



**Investigation of Vortex-Induced-Vibration  
of Self-Elevating Offshore Platforms with  
Tubular Legs under Combined Waves and  
Currents**

**By**

**©2020 Sudheesh Ramadasan**

**A Thesis submitted for the degree of Doctor of Philosophy**

**School of Engineering, Marine Technology**

**Newcastle University**

**Singapore**

**June 2020**



## Abstract

The effects of the oscillatory lift forces acting on the legs and the consequent Vortex-Induced-Vibration (VIV) are customarily neglected in the structural design of self-elevating offshore platforms, hereinafter called jack-ups. Severe vibrations of shallow water jack-ups due to vortex shedding about its circular cylindrical legs have led to many unsuccessful operations at aggressive tidal locations. This research project aims to understand the intricacies involved with the VIV of the cylindrical legged jack-ups and investigate the effect of vortex induced forces on its strength and life.

This PhD project consists of analysis of industry design data, development of a simplified single-degree-of-freedom (SDOF) analysis methodology, physical experiments, numerical simulations and propositions towards VIV suppression. The analysis of the design data revealed that many of the jack-ups currently in commission are vulnerable to inline, crossflow and yaw VIV in currents and regular waves. A simple mathematical model is developed based on the SDOF analogy and principle of conservation of energy evaluating various modes of VIV of the jack-up with cylindrical legs in uniform current and regular waves. Mass ratio, damping ratio and mode factor are found to be the important parameters controlling the crossflow VIV and radius of gyration also for the yaw VIV. Criteria for the initiation of the multiple VIV modes are also developed for the jack-up experiencing current and regular waves. SDOF analysis of the jack-ups indicated extreme yield and fatigue strength utilisations during lock-in vibrations.

The newly developed mathematical VIV model is validated by a set of experiments conducted in a wind, wave and current flume. Model tests revealed that the sway (crossflow) and yaw (torsional) modes of the jack-up VIV could be dynamically excited by the vortex shedding. The experimental investigation further revealed that jack-up experiences significant crossflow VIV in uniform currents and regular waves, and yaw VIV in uniform currents. The jack-up is found not to experience any significant VIV during tests in irregular waves. In regular waves with imposed current also, the jack-up is found to experience crossflow and yaw VIV. The force tests revealed considerable drag and lift amplifications, and additional inertial loading on the legs during VIV. 2D Fluid-Structure Interaction (FSI) simulations carried out in model scale under uniform currents have also resulted in similar response behaviour. It is demonstrated by means of mathematical investigation and physical experiments that

streamlined leg fairing can be used as an excellent vortex suppression device for the jack-ups. Designs of two optimum fairing profiles are developed based on NACA0018 profile and successfully tested on the cylindrical legs of the scaled jack-up model, achieving substantial reduction of VIV amplitudes.

The finding of the jack-ups experiencing VIVs in currents and regular waves well within its certified operating envelopes is a matter of significant concern. The mathematical method will equip engineers to consider the effect of VIV in jack-up designs. The two fairing section offsets presented can be readily used by Industry for practical applications. Moreover, the comprehensive results from the numerical simulation and experimental measurements will provide reliable benchmark for future study on the topic.

## Acknowledgements

First and foremost, I would like to thank Almighty for giving me the strength, knowledge, ability and opportunity to undertake this research and persevere till its completion. I express my sincere thanks to Newcastle University for giving me an opportunity to pursue a PhD in Marine Technology.

I profoundly thank my supervisors, Prof. Longbin Tao and Dr. Arun Dev for their unconditional support and continuous guidance throughout the research and their precious time spent towards this. It is only because of their support and motivation I was able to manage the research in spite of many unexpected situations.

I also thank my co-supervisor, Dr. Yongchang Pu for his support and Prof. Grant Burgess for his advice and encouragement. I extend my appreciation to Mr. John Garside for his invaluable guidance right from the beginning of my research.

I express my immense gratitude to my employers, Mr. Bhasker Rao and Mr. Arvind Dhupkar of M/s Cybermarine Technologies Pte. Ltd., Singapore for their invaluable technical, monetary and emotional support during the PhD. It is my greatest fortune to have them as my employers, who are incredibly understanding of all the hardships associated with a research degree.

I am extremely indebted to the staff of the Hydrodynamic Laboratory, Mr. Peter Bowes, Mr. Robert Hindhaugh, Mr. Ian Howard-Row, Mr. Phil Letouze, Mr. Kieron Fallows and Ms Leena for their unreserved support and guidance during the design, setting up and execution of the physical experiments at the Newcastle University. I also thank the apprentices, Tom and the late Kieran for their support during my experimental work.

My special thanks to the staff of the Student Wellbeing Service of the Newcastle University, especially Mr. Liam Southam for their excellent emotional support which helped me to manage with all the extenuating circumstances, I faced during the programme.

I sincerely thank all my friends at the Marine Technology research group at Newcastle University, with the special mention of Ceasar Edward, Jaime Lopez, Martin Nuernberg, Putu Wibawa and Yibo Liang, for not only helping me with their knowledge but also for making the journey utmost memorable. I would also like to thank the teachers and staff of the School of Engineering, Marine Technology, Newcastle University and NUIS for helping me throughout the programme.

I am extremely grateful to my family, my wife Remya Thalappil and my daughter Daksha Sudheesh for accompanying me in this adventure. Without their emotional support, I would not have been able to overcome both the personal and professional hardships faced during the research.

I would also like to thank my parents, Mr. Ramadasan and Mrs. Sudha for giving me the strength and courage to undertake this journey and strive for continuous development.

Finally, I thank all those whose names may have escaped the attention here but have in one way or the other contributed to my work.

## Table of Contents

Abstract .....	iii
Acknowledgements .....	v
Table of Contents .....	vii
List of Figures .....	xv
List of Tables .....	xxvi
Nomenclature .....	xxix
List of Publications .....	xli
Chapter 1. Introduction.....	1
1.1 Background and Motivation .....	2
1.1.1 Vortex Induced Vibration .....	2
1.1.2 Jack-up Platforms.....	5
1.1.3 Jack-up VIV .....	7
1.1.4 Lack of regulations .....	9
1.1.5 Limited Research.....	10
1.2 Aim and Objectives of the Research .....	10
1.3 Contributions of the Research .....	11
Chapter 2. Research Methodology.....	13
2.1 State-of-the-Art.....	13
2.1.1 Rules and Regulations .....	13
2.1.2 VIV Prediction.....	13
2.1.3 Jack-up VIV in Waves .....	15
2.2 Research Methodology and General Approach.....	15
2.2.1 Step 1: Literature Survey / Review .....	15
2.2.2 Step 2: Studies on Flow-Based Models and Research Tools.....	16
2.2.3 Step 3: Data Analysis of Existing Jack-ups .....	17
2.2.4 Step 4: Theoretical Investigation .....	17
2.2.5 Step 5: Experimental Investigation .....	18
2.2.6 Step 6: Numerical Investigation (CFD Simulations).....	18
2.2.7 Step 7: Structure Response, Yield and Fatigue Strength .....	19
2.2.8 Step 8: Suppression of Jack-up VIV .....	20
2.2.9 Step 9: Discussion, Conclusions and Recommendations.....	20
2.3 Flow Chart of Research Methodology and Approach .....	20
Chapter 3. Literature Review .....	22
3.1 VIV of Multi-Cylinder Structures .....	22
3.2 Vortex Induced Motion.....	24
3.3 VIV models .....	25

3.4	VIV Criteria.....	28
3.5	Fatigue Strength and VIV.....	28
3.6	Jack-up Platforms .....	29
3.6.1	Dynamics of Jack-ups.....	30
3.6.2	Jack-up SDOF .....	30
3.6.3	Jack-up Damping.....	31
3.6.4	Jack-up VIV.....	32
3.6.5	Jack-up Experimental Investigations.....	33
3.6.6	Jack-up Numerical Investigations .....	35
3.7	Fluid Structure Interaction Simulations of VIV.....	36
3.8	Summary .....	37
Chapter 4.	VIV Assessment of Existing Jack-ups.....	38
4.1	Design Load and Environment.....	38
4.2	Leg Diameter .....	38
4.3	Mass Ratio.....	38
4.4	Structural Dynamics.....	42
4.4.1	VIV Modes .....	43
4.4.2	Leg Mode Shape.....	43
4.4.3	Mass for Surge / Sway modes .....	45
4.4.4	Inertia for Yaw mode.....	48
4.4.5	Stiffness.....	48
4.4.6	Natural Frequency .....	49
4.5	Crossflow VIV in Current.....	51
4.6	Crossflow VIV in Regular Waves .....	52
4.7	Inline VIV in Current.....	53
4.8	Yaw VIV in Current .....	55
4.9	Yaw VIV in Regular Waves.....	56
4.10	Discussion .....	58
Chapter 5.	Theoretical Investigation .....	60
5.1	Dynamic Damping Stiffness.....	60
5.1.1	Resonant Response of a Linear Mass Spring System.....	60
5.1.2	Low damping and dynamic damping stiffness.....	61
5.2	VIV of 2D circular cylinders in a steady flow .....	62
5.2.1	Inline/Surge VIV of a single cylinder .....	62
5.2.2	Crossflow/Sway VIV of a single cylinder .....	64
5.2.3	Yaw VIV of a system of four 2D cylinders in a rectangular configuration under inline excitation.....	65
5.2.4	Yaw VIV of a system of four 2D cylinders in a rectangular configuration under crossflow excitation.....	67

5.3	VIV of Jack-up with four Circular Cylindrical Legs in Uniform Current .....	69
5.3.1	Inline / Surge VIV.....	69
5.3.2	Crossflow / Sway VIV .....	71
5.3.3	Yaw/Torsional VIV due to inline excitation.....	71
5.3.4	Yaw VIV due to crossflow excitation.....	73
5.4	Mean Drag Amplification in Uniform Current .....	74
5.4.1	Crossflow VIV .....	75
5.4.2	Yaw VIV.....	76
5.5	VIV of 2D Circular Cylinders in a Planar Oscillatory Flow.....	78
5.5.1	Crossflow / Sway VIV of a single cylinder.....	78
5.5.2	Crossflow VIV of a system of four 2D cylinders in a rectangular configuration .....	82
5.5.3	Yaw VIV of a system of four 2D cylinders in a rectangular configuration.	85
5.6	VIV of Jack-up with four Circular Cylindrical Legs in Regular Waves .....	87
5.6.1	Crossflow VIV .....	87
5.6.2	Yaw VIV.....	92
5.7	Mean Drag Amplification in Regular waves .....	94
5.7.1	Crossflow VIV .....	94
5.7.2	Yaw VIV.....	95
5.8	Reduced Velocity during VIV in an Oscillatory Flow .....	97
5.9	Jack-up Damping.....	98
5.9.1	Inline/Surge damping.....	98
5.9.2	Crossflow damping .....	100
5.9.3	Effective Damping for Yaw Mode .....	101
5.10	Lift Amplification with Response .....	103
5.10.1	Crossflow/Sway VIV of a single cylinder.....	104
5.10.2	Yaw VIV of a system of four 2D cylinders in a rectangular configuration under crossflow excitation.....	106
5.11	Jack-up VIV Response Prediction in Uniform Current.....	107
5.11.1	Inline / Surge VIV .....	107
5.11.2	Crossflow / Sway VIV .....	108
5.11.3	Yaw VIV due to inline excitation .....	112
5.11.4	Yaw VIV due to crossflow excitation.....	115
5.12	Jack-up VIV Response Prediction in Regular Waves .....	118
5.12.1	Crossflow / Sway VIV .....	118
5.12.2	Yaw VIV.....	119
5.13	Leg Yield Augmentation .....	122
5.13.1	Dynamic Stresses due to VIV.....	122
5.13.2	Mean Stresses due to Drag Amplification.....	124

5.14	Leg Fatigue Strength .....	126
5.15	VIV of Jack-up in Regular Wave with Imposed Uniform Current.....	129
5.15.1	Lift Force in Regular Wave with imposed Current.....	129
5.15.2	Response in Regular Wave with imposed Uniform Current .....	137
5.16	Discussion .....	138
Chapter 6.	Experimental Investigation.....	139
6.1	Experimental Setup.....	139
6.1.1	Model .....	139
6.1.2	WWC tank.....	141
6.1.3	Jack-up and Leg Axis Systems .....	142
6.1.4	Global Headings .....	142
6.1.5	Leg Designs and Local Headings .....	144
6.1.6	Test Cases.....	145
6.1.7	Current Profile and Turbulence .....	145
6.1.8	Test Procedure .....	147
6.2	Mass property test .....	148
6.3	Stiffness Tests .....	148
6.3.1	Leg stiffness.....	149
6.3.2	Leg-Hull Interface.....	150
6.3.3	Jack-up Model.....	152
6.4	Leg Footing (Ball Joint) Friction Test .....	156
6.5	Free Decay Tests.....	156
6.5.1	Tests in Air and Still Water.....	157
6.5.2	Tests in Current .....	163
6.6	Response Test in Current and Wind .....	172
6.6.1	Inline/Surge Response.....	172
6.6.2	Crossflow/Sway Response .....	174
6.6.3	Yaw Response.....	177
6.6.4	Combined Response .....	180
6.6.5	Mean Response.....	181
6.6.6	Effect of Environmental Headings and Leg Orientation .....	182
6.7	Response Test in Regular Waves.....	189
6.7.1	Inline / Surge Response.....	190
6.7.2	Crossflow/Sway Response .....	192
6.7.3	Yaw Response.....	196
6.7.4	Combined Response .....	200
6.7.5	Mean Response.....	201
6.7.6	Effect of Environmental Headings and Leg Orientation .....	201

6.8	Response Test in Irregular Waves .....	202
6.8.1	Inline Response.....	203
6.8.2	Crossflow Response.....	205
6.8.3	Yaw Response .....	207
6.9	Response Test in Regular Waves with imposed Current .....	209
6.9.1	Amplitude Response .....	209
6.9.2	Frequency Response .....	211
6.10	Response Tests with various Leg Designs.....	216
6.10.1	Inline Response.....	217
6.10.2	Crossflow Response.....	217
6.10.3	Yaw Response .....	219
6.11	Force Tests .....	222
6.11.1	Inline Force.....	224
6.11.2	Crossflow Force .....	227
6.12	Discussion .....	231
6.12.1	Experimental Challenges.....	232
6.12.2	Experimental Uncertainty .....	233
6.12.3	Model Nonlinearities .....	234
Chapter 7.	Numerical Investigation .....	235
7.1	ANSYS Fluent .....	235
7.2	Reynolds Averaged Navier Stokes Equations .....	235
7.3	SST $k\omega$ Turbulence Model.....	236
7.4	Transition SST Model.....	237
7.4.1	Wall Modelling .....	237
7.4.2	Inlet Turbulence.....	238
7.5	Pressure Velocity Coupling .....	238
7.6	Discretisation Scheme and Solver.....	239
7.7	Mesh Independence .....	240
7.7.1	Computational Domain.....	240
7.7.2	Numerical Mesh.....	241
7.7.3	Mesh Convergence Study .....	242
7.7.4	Time Step Convergence Study.....	244
7.7.5	Numerical uncertainty.....	244
7.8	Steady Flow around Cylindrical Legs of the Jack-up.....	245
7.8.1	Computational Domain .....	245
7.8.2	Numerical Mesh.....	246
7.8.3	Dynamic Mesh.....	249
7.8.4	Rigid Body (Jack-up) Modelling.....	250

7.8.5	Response in Steady flow .....	251
7.8.6	Forces in Steady Flow .....	261
7.8.7	Vortex Synchronisation about the Legs .....	268
7.8.8	Vortex Pattern about the Legs .....	271
7.9	Discussion .....	276
Chapter 8.	Suppression of Jack-up VIV.....	279
8.1	Fairing Theory.....	279
8.1.1	Sway Mode of the Jack-up in Uniform Current.....	279
8.1.2	Yaw Mode of the Jack-up with four cylindrical legs in Uniform Current.	284
8.2	Fairing Profiles .....	287
8.3	Fairing Models .....	288
8.4	Physical Experiments.....	290
8.4.1	Experimental Setup.....	290
8.4.2	Test Procedures.....	290
8.4.3	Mass and Stiffness Tests .....	291
8.4.4	Free Decay Tests with Fairings.....	292
8.4.5	Weathervaning Stability Tests.....	297
8.4.6	Response Test with Fairings in Steady Current .....	298
8.5	Effect of Fairing Depth Ratio .....	303
8.5.1	Amplitude Response.....	304
8.5.2	Frequency Response.....	305
8.5.3	Mean Response.....	308
8.5.4	Optimum Fairing Depth .....	309
8.6	Fairing Offsets.....	310
8.7	Detachable Fairing Concept .....	310
8.8	VIV Suppression by means of Leg Diameter Selection.....	311
8.8.1	Steady Current.....	311
8.8.2	Regular Waves .....	312
8.9	Jack-up with Fixed Footing .....	314
8.10	Discussion .....	314
Chapter 9.	Conclusions and Recommendations.....	316
9.1	Conclusions .....	316
9.1.1	Design Data Analysis.....	316
9.1.2	Theoretical Investigation .....	316
9.1.3	Experimental Investigation.....	317
9.1.4	Numerical Investigation.....	318
9.1.5	Investigations on Suppression of Jack-up VIV .....	318
9.1.6	Cross-Validation of Theoretical, Experimental and Numerical Models..	318

9.1.7	Design Recommendations for Jack-ups .....	319
9.2	Recommendations for Future Work.....	321
9.2.1	Theoretical Investigation.....	321
9.2.2	Experimental Investigation .....	322
9.2.3	Numerical Investigation .....	323
9.2.4	Investigations on Jack-up Design.....	324
9.3	Concluding Note.....	326
References	.....	327
Appendix A. Generic Literature Review on VIV	.....	339
A.1	Vortex Shedding around Bluff Bodies.....	339
A.1.1	Steady Flow around a Circular Cylinder .....	339
A.1.2	Oscillatory Flow around a Circular Cylinder.....	340
A.2	VIV in Steady Flow .....	341
A.2.1	Strouhal Relation.....	342
A.2.2	Excitation / Vortex Induced Forces.....	343
A.2.3	Inline VIV .....	349
A.2.4	Crossflow VIV.....	350
A.2.5	Spanwise Correlation .....	353
A.2.6	Surface Roughness.....	354
A.2.7	Response Branches and Vortex Modes .....	355
A.2.8	Fluid Damping .....	357
A.2.9	Mass Ratio .....	359
A.2.10	Added Mass .....	361
A.2.11	Mass Damping Parameter.....	364
A.2.12	VIV frequency.....	366
A.2.13	Force amplification .....	367
A.2.14	Reynolds Number Dependence .....	371
A.3	VIV in Oscillatory Flow.....	372
A.3.1	Lift force.....	372
A.3.2	Crossflow VIV.....	376
A.3.3	Spanwise Correlation. ....	378
A.4	VIV in Regular Waves .....	379
A.5	VIV in sheared current.....	383
A.6	VIV Suppression.....	385
A.7	Structural Dynamics .....	387
A.7.1	Conservation of Energy .....	387
A.7.2	SDOF Approximation.....	387
A.8	CFD Investigations on Flow around Circular Cylinders .....	388

A.9	Physical Experiments with Scaled Models .....	395
A.9.1	Laws of Similitude .....	395
A.9.2	Model Scale Selection .....	397
A.9.3	Model Scale Effect .....	397
A.9.4	Data Acquisition and Instrumentation .....	397

## List of Figures

Figure 1-1: Jack-up with cylindrical legs (M/s Cybermarine Technologies Pte. Ltd.)...	1
Figure 1-2: Vortex shedding about a cylinder (Williamson, 1996) .....	2
Figure 1-3: Vortex induced forces on a cylinder (Sumer and Fredsøe, 2006) .....	3
Figure 1-4: Crossflow amplitude, frequency and phase response of a spring mounted cylinder in wind (Feng, 1968) .....	4
Figure 1-5: Velocity field in a shallow water wave (Journée and Massie, 2001).....	6
Figure 1-6: Lift coefficient versus $KC$ number in planar oscillatory flow (Sarpkaya, 1975) .....	6
Figure 1-7: Jack-up with leg fairings (European Commission, 2005) .....	8
Figure 1-8: Mean drag amplification with crossflow vibration amplitude (Blevins, 2001) .....	8
Figure 2-1: Variation of $St$ with $Re$ (DNV GL, 2017b) .....	15
Figure 2-2: Research flow and approach .....	21
Figure 3-1: Cylinder interference regions (Zdravkovich, 1985).....	23
Figure 3-2: Crossflow response of the downstream cylinder for various longitudinal pitch ratios (Zdravkovich, 1985) .....	24
Figure 3-3: Comparison of the harmonic and empirical models with experimental data (Sumer and Fredsøe, 2006) .....	26
Figure 3-4: Typical natural and excitation frequencies of offshore structures (Sumer and Fredsøe, 2006).....	29
Figure 3-5: Jack-up SDOF Idealisation (PANEL OC-7, 2008).....	31
Figure 3-6: Typical jack-up model with instrumentation (Johnson and Patel, 1992)..	34
Figure 3-7: Experimental setup for the jack-up model in a wave basin (Grundlehner, 1997) .....	35
Figure 3-8: Crossflow response of the derrick of jack-ups with 3 and 6 legs (Van Den Abeele and Vande Voorde, 2011a) .....	36
Figure 4-1: Variation of leg diameter, a) with water depth, b) with elevated load .....	40
Figure 4-2: Leg diameter versus design parameter .....	40
Figure 4-3: Variation of mass ratio with water depth .....	41
Figure 4-4: Jack-up VIV modes, a) inline (surge), b) crossflow (sway), c) yaw (torsional) .....	43
Figure 4-5: Jack-up leg mode shape .....	44
Figure 4-6: Variation of natural periods with design parameter .....	51
Figure 5-1: Linear mass spring system .....	60
Figure 5-2: Inline VIV excitation of a cylinder .....	62
Figure 5-3: Crossflow excitation of a cylinder.....	64
Figure 5-4: Yaw due to inline excitation.....	65

Figure 5-5: Yaw due to crossflow excitation.....	68
Figure 5-6: Jack-up a) mean drag amplification and b) OTM amplification in crossflow VIV.....	77
Figure 5-7: Crossflow excitation in a planar oscillatory flow.....	79
Figure 5-8: Flow and lift oscillations for various lift frequency factors .....	80
Figure 5-9: Sway due to crossflow excitation in a planar oscillatory flow .....	83
Figure 5-10: Yaw due to crossflow excitation in a planar oscillatory flow.....	85
Figure 5-11: Critical reduced velocity versus $KC$ number in oscillatory flow .....	98
Figure 5-12: Leg deflection due to small angle of Yaw .....	102
Figure 5-13: Lift variation with crossflow response .....	105
Figure 5-14: Validation of quartile polynomial lift expression with published data...	106
Figure 5-15: Variation of effective leg lift coefficient with amplitude ratio and depth ratio .....	111
Figure 5-16: Cylindrical leg of a jack-up with the pin holes .....	128
Figure 5-17: Flow speed variation for current speed less than wave particle velocity .....	131
Figure 5-18: Lift force in an oscillatory flow with the horizontal particle velocity greater than the imposed current velocity .....	135
Figure 5-19: Flow speed variation for current speed greater than wave particle velocity .....	135
Figure 5-20: Lift force in an oscillatory flow with the wave horizontal particle velocity greater than the imposed current velocity .....	137
Figure 6-1: Jack-up Model .....	139
Figure 6-2: Leg-hull interface; a) O rings for moment transfer, b) Bolts for weight transfer.....	140
Figure 6-3: Experimental Setup .....	142
Figure 6-4: Jack-up and leg axis systems.....	143
Figure 6-5: Turntable arrangement .....	143
Figure 6-6: Global heading definition of the jack-up model.....	144
Figure 6-7: Leg designs and local headings .....	145
Figure 6-8: Instrumentation plan for the kinematics measurement .....	146
Figure 6-9: Current profiles from kinematics measurement .....	147
Figure 6-10: Yaw table swing test.....	149
Figure 6-11: Leg stiffness test setup .....	150
Figure 6-12: Force deflection curve for leg stiffness test .....	150
Figure 6-13: Force deflection curve for leg-hull interface stiffness test.....	151
Figure 6-14: Stiffness test set-ups for a) sway/crossflow and b) yaw .....	152
Figure 6-15: Model sway stiffness test; VL, Dry, a) force deflection curve, b) sway stiffness versus deflection.....	153

Figure 6-16: Model sway force versus deflection curve for various load cases .....	154
Figure 6-17: Model yaw stiffness test; VL, Dry, a) force deflection curve, b) yaw stiffness versus deflection .....	154
Figure 6-18: Model yaw moment versus deflection curve for various load cases....	155
Figure 6-19: Sway static and dynamic stiffnesses versus deflection for NVL, 890WD .....	155
Figure 6-20: Setup for ball joint friction test .....	156
Figure 6-21: Support moment versus rotation .....	157
Figure 6-22: a) Free decay time series of sway free decay test; NVL, 890WD b) Sway natural frequency variation with amplitude; NVL, 890WD c) Variation of sway damping ratio with sway frequency; NVL, 890WD. ....	159
Figure 6-23: FFT of surge and sway free decay tests for the test case, VL, Dry .....	161
Figure 6-24: FFT of sway free decay tests for all test cases .....	161
Figure 6-25: a) Free decay time series of yaw free decay test; VL, 890WD b) Yaw natural frequency variation with displacement; VL, 890WD c) Variation of yaw damping ratio with yaw frequency; VL, 890WD.....	162
Figure 6-26: FFT of yaw free decay tests for all test cases .....	163
Figure 6-27: Sway natural frequency versus reduced velocity in current .....	165
Figure 6-28: Leg sway added mass versus reduced velocity in current .....	165
Figure 6-29: Sway fluid damping versus reduced velocity.....	167
Figure 6-30: Yaw natural frequency versus reduced velocity in current .....	168
Figure 6-31: Yaw added mass versus reduced velocity in current .....	168
Figure 6-32: Yaw fluid damping versus reduced velocity in current.....	169
Figure 6-33: Natural frequency variation a) with respect to sway reduced velocity b) with respect to yaw reduced velocity. ....	170
Figure 6-34: Added mass variation with sway reduced velocity .....	171
Figure 6-35: Fluid damping variation with sway reduced velocity.....	171
Figure 6-36: Inline amplitude response with corresponding reduced velocity ( $U/f_{Nx}D$ ) .....	173
Figure 6-37: Time series of crossflow response for 'NVL, 890WD' at a reduced velocity of 4.84 .....	174
Figure 6-38: Crossflow amplitude response with corresponding reduced velocity ( $U/f_{Ny}D$ ).....	175
Figure 6-39: Crossflow frequency response with corresponding reduced velocity ( $U/f_{Ny}D$ ).....	176
Figure 6-40: Crossflow amplitude response with the inverse of modified mass damping parameter.....	177
Figure 6-41: Time series of yaw response for 'VL, 890WD' at a yaw reduced velocity of 5.15 .....	178

Figure 6-42: Yaw amplitude response with corresponding reduced velocity ( $U/f_{N\phi}D$ )	179
Figure 6-43: Yaw frequency response with corresponding reduced velocity ( $U/f_{N\phi}D$ )	180
Figure 6-44: Yaw amplitude response with the inverse of inertia damping parameter	181
Figure 6-45: Combined crossflow amplitude response of the jack-up leg with current	181
Figure 6-46: Inline mean response of the model with current	182
Figure 6-47: Inline amplitude response versus reduced velocity for various headings	183
Figure 6-48: Inline frequency response versus reduced velocity for various headings	184
Figure 6-49: Crossflow amplitude response versus reduced velocity for various headings	185
Figure 6-50: Crossflow frequency response versus reduced velocity for various headings	186
Figure 6-51: Yaw response versus reduced velocity for various headings	187
Figure 6-52: Yaw frequency response versus reduced velocity for various headings	187
Figure 6-53: Combined crossflow response versus current for various headings...	188
Figure 6-54: Mean inline response versus current for various headings	189
Figure 6-55: Inline/surge response, a) versus reduced velocity, b) versus $KC$ number	191
Figure 6-56: Inline frequency response normalised with the wave frequency and plotted against the $KC$ number	192
Figure 6-57: Crossflow amplitude response with reduced velocity ( $U_O/f_{Ny}D$ )	193
Figure 6-58: Model crossflow response time series in regular waves for NVL, at a reduced velocity of 4.52	194
Figure 6-59: Crossflow amplitude response with $KC$ number	194
Figure 6-60: Crossflow frequency response normalised with wave frequency against $KC$ number	195
Figure 6-61: Crossflow frequency response normalised with natural frequency against reduced velocity ( $U_O/f_{Ny}D$ )	196
Figure 6-62: Crossflow amplitude response with the inverse of modified mass damping parameter	197
Figure 6-63: Yaw amplitude response with reduced velocity ( $U_O/f_{N\phi}D$ )	197
Figure 6-64: Yaw amplitude response with corresponding $KC$ numbers	198
Figure 6-65: Yaw frequency response normalised with wave frequency against $KC$ number	199

Figure 6-66: Yaw frequency response normalised with natural frequency against reduced velocity ( $U_0/f_{N\phi}D$ ) .....	199
Figure 6-67: Yaw amplitude response with the inverse of inertia damping parameter .....	200
Figure 6-68: Leg crossflow combined amplitude response due to sway and yaw with KC number .....	201
Figure 6-69: Crossflow relative response in regular waves for various global headings .....	202
Figure 6-70: Inline amplitude response in irregular waves versus effective KC number .....	203
Figure 6-71: Inline frequency response in irregular waves versus effective KC number, a) natural frequency ratio, b) wave frequency ratio .....	204
Figure 6-72: Crossflow amplitude response in irregular waves versus effective KC number .....	205
Figure 6-73: Crossflow frequency response in irregular waves versus effective KC number, a) natural frequency ratio, b) wave frequency ratio .....	206
Figure 6-74: Yaw amplitude response in irregular waves versus effective KC number .....	207
Figure 6-75: Yaw frequency response in irregular waves versus effective KC number, a) natural frequency ratio, b) wave frequency ratio .....	208
Figure 6-76: Inline, crossflow and yaw amplitude response in regular wave with imposed current, a) against sway reduced velocity based on current only, b) against sway reduced velocity based on maximum horizontal particle velocity ( $(U+U_0)/f_{Ny}D$ ) .....	210
Figure 6-77: Inline, crossflow and yaw amplitude response in regular wave with imposed current, a) against yaw reduced velocity based on current only, b) against yaw reduced velocity based on maximum horizontal particle velocity ( $(U+U_0)/f_{N\phi}D$ ) .....	213
Figure 6-78: Inline, crossflow and yaw frequency response in regular wave with imposed current versus sway reduced velocity, a) natural frequency ratio, b) wave frequency ratio.....	214
Figure 6-79: Yaw frequency response in regular wave with imposed current, a) against yaw reduced velocity based on current only, b) against yaw reduced velocity based on maximum horizontal particle velocity ( $(U+U_0)/f_{N\phi}D$ ) .....	215
Figure 6-80: Inline, crossflow and yaw frequency response (wave frequency ratio) in regular wave with imposed current versus effective KC number based on maximum horizontal particle velocity. ....	216
Figure 6-81: Inline amplitude response versus reduced velocity for various leg designs .....	218
Figure 6-82: Crossflow amplitude response versus reduced velocity for various leg designs.....	218
Figure 6-83: Crossflow frequency response versus reduced velocity for various leg designs.....	219

Figure 6-84: Yaw amplitude response versus yaw reduced velocity for various leg designs .....	220
Figure 6-85: Yaw frequency response versus yaw reduced velocity for various leg designs .....	221
Figure 6-86: Combined crossflow response versus current for various leg designs	221
Figure 6-87: Inline mean response versus current for various leg designs .....	222
Figure 6-88: a) Model setup for force tests, b) leg footing fitted with load cell, c) electric cabling for load cell leading to the amplifier .....	223
Figure 6-89: a) Transversely constrained model configuration, b) Forward starboard transverse guy line.....	225
Figure 6-90: Inline base shear force time series in steady current for NVL around a reduced velocity of 5, for the free and constrained models.....	226
Figure 6-91: Inline force response versus reduced velocity .....	227
Figure 6-92: Mean drag amplification with crossflow response.....	227
Figure 6-93: Crossflow base shear force time series in steady current for the test case, NVL at a reduced velocity approximately 5.....	228
Figure 6-94: Crossflow average oscillatory force response of the legs versus reduced velocity.....	229
Figure 6-95: Crossflow oscillatory force response of the leg versus reduced velocity .....	230
Figure 6-96: Crossflow mean oscillatory force coefficient versus amplitude ratio. ..	230
Figure 7-1: Decay of inlet turbulence intensity with the streamwise distance (ANSYS, 2013b).....	238
Figure 7-2: Computational Domain for 2D single cylinder.....	241
Figure 7-3: Typical numerical mesh for 2D single cylinder.....	242
Figure 7-4: Unstructured mesh, a) boundary layer inflation and near cylinder, b) wake .....	243
Figure 7-5: Computational Domain for 2D jack-up legs .....	246
Figure 7-6: Numerical Mesh for the jack-up cylindrical legs.....	247
Figure 7-7: Unstructured mesh around jack-up legs, a) boundary layer inflation, b) near cylindrical legs and wake .....	248
Figure 7-8: Deformed dynamic mesh around the jack-up legs.....	250
Figure 7-9: Inline amplitude response of the jack-up in steady flow, with corresponding reduced velocity ( $U/f_{Nx}D$ ) .....	253
Figure 7-10: Inline frequency response of the jack-up in steady flow .....	254
Figure 7-11: Crossflow amplitude response of the jack-up in steady flow, with corresponding reduced velocity ( $U/f_{Ny}D$ ).....	255
Figure 7-12: Crossflow frequency response of the jack-up in steady flow .....	256
Figure 7-13: Crossflow amplitude response with effective mass damping parameter .....	256

Figure 7-14: Yaw amplitude response of the jack-up in steady flow, with corresponding reduced velocity ( $U/f_{N\phi}D$ ) .....	257
Figure 7-15: Yaw frequency response of the jack-up in steady flow.....	258
Figure 7-16: Yaw amplitude response with effective inertia damping parameter ....	259
Figure 7-17: Mean inline response of the jack-up versus steady flow speed .....	260
Figure 7-18: Combined crossflow response of the leg in steady flow.....	260
Figure 7-19: Average lift coefficient of the leg in steady flow, a) versus crossflow reduced velocity, b) versus yaw reduced velocity.....	262
Figure 7-20: Lift frequency in steady flow for the jack-up legs.....	263
Figure 7-21: Average oscillatory drag coefficient of the leg in steady flow .....	264
Figure 7-22: Oscillatory drag frequency in steady flow for the jack-up legs.....	265
Figure 7-23: Average mean drag coefficient of the leg in steady flow .....	266
Figure 7-24: Force amplification on the jack-up during crossflow VIV in steady flow .....	267
Figure 7-25: Force amplification on the jack-up under yaw VIV in steady flow.....	268
Figure 7-26: FFT of the total lift coefficient of the stationary jack-up corresponding to crossflow VIV, steady flow speed 0.25 m/s, reduced velocity of 5.82.....	269
Figure 7-27: FFT of the total lift coefficient of the stationary jack-up corresponding to yaw VIV, steady flow speed 0.35 m/s, yaw reduced velocity of 5.28.....	269
Figure 7-28: FFT of the total lift coefficient of the freely vibrating jack-up during crossflow VIV, steady flow speed 0.25 m/s, reduced velocity of 5.82.....	270
Figure 7-29: FFT of the total lift coefficient of the freely vibrating jack-up during yaw VIV, steady flow speed 0.35 m/s, yaw reduced velocity of 5.28 .....	271
Figure 7-30: Vortex swirling strength contours colour coding scheme .....	272
Figure 7-31: Vortex pattern about the jack-up legs during crossflow VIV, steady flow speed 0.25 m/s, reduced velocity of 5.82, a) $t = 53.5$ s, b) $t = 53.6$ s, c) $t = 53.7$ s, d) $t = 53.8$ s, e) $t = 53.9$ s, f) $t = 54$ s, g) $t = 54.1$ s, h) $t = 54.2$ s , i) $t = 54.3$ s, j) $t = 54.4$ s .....	274
Figure 7-32: Vortex pattern about the jack-up legs during yaw VIV, steady flow speed 0.35 m/s, yaw reduced velocity of 5.28, a) $t = 48.6$ s, b) $t = 48.7$ s, c) $t = 48.8$ s, d) $t = 48.9$ s, e) $t = 49$ s, f) $t = 49.1$ s, g) $t = 49.2$ s, h) $t = 49.3$ s.....	275
Figure 7-33: Vortex pattern for the VIV modes, a) crossflow, b) yaw .....	278
Figure 8-1: Jack-up with leg fairings.....	280
Figure 8-2: Relative response ratio versus fairing depth ratio of a fully immersed vertical cylinder with negligible structural damping .....	283
Figure 8-3: Fairing Profile/Design 1 in the model scale .....	288
Figure 8-4: Fairing Profile/Design 2 in the model scale .....	288
Figure 8-5: a) Fairing models, b) Fairing design 2 with draft marks and lead ballast .....	289
Figure 8-6: Experimental setup for VIV test of the jack-up model fitted with fairings .....	291

Figure 8-7: Stiffness tests a) sway, b) yaw .....	292
Figure 8-8: Sway deflections of the jack-up model with and without fairings .....	292
Figure 8-9: Surge free decay test in still water with fairing design 1, a) free decay time series, b) natural frequency versus amplitude, c) damping ratio versus frequency. ....	293
Figure 8-10: FFT of the free decay tests with fairings, a) surge, fairing design1, b) surge, fairing design 2, c) sway, fairing design1, d) sway, fairing design 2, e) yaw, fairing design1, f) yaw, fairing design 2.....	296
Figure 8-11: Weathervaning test.....	297
Figure 8-12: Model sway response at a reduced velocity of around 5 (0.225 m/s current) .....	298
Figure 8-13: Model yaw response at a yaw reduced velocity of around 5 (0.325 m/s current) .....	299
Figure 8-14: Inline and crossflow amplitude responses for the fairing profiles.....	300
Figure 8-15: Yaw amplitude response versus yaw reduced velocity.....	300
Figure 8-16: Inline and crossflow frequency responses for the fairing profiles.....	301
Figure 8-17: Yaw frequency response versus yaw reduced velocity .....	302
Figure 8-18: Mean inline and crossflow responses versus current .....	303
Figure 8-19: Mean yaw response versus current.....	303
Figure 8-20: Crossflow amplitude response for various fairing depth ratios .....	305
Figure 8-21: Yaw amplitude response for various fairing depth ratios .....	305
Figure 8-22: Crossflow frequency response for various fairing depth ratios .....	306
Figure 8-23: Yaw frequency response for various fairing depth ratios .....	307
Figure 8-24: Yaw frequency response normalised with bare model parameters for various fairing depth ratios.....	307
Figure 8-25: Mean inline and crossflow response for various fairing depth ratios... ..	308
Figure 8-26: Mean yaw response for various fairing depths .....	309
Figure 8-27: VIV and galloping responses versus fairing depth ratios; a) crossflow b) yaw .....	310
Figure 9-1: Recommended tank plan for a typical jack-up.....	321
Figure 9-2: Splitter plate fairing comparison, a) splitter plate, b) fairing (Blevins, 2001) .....	325
Figure 9-3: Spudcan soil rotational stiffness (ABS, 2018b).....	326
Figure A-1: Von Karman vortex street (Blevins, 2001).....	339
Figure A-2: Flow regimes around a cylinder in steady flow (Blevins, 2001).....	340
Figure A-3: Flow regimes around a smooth circular cylinder in an oscillatory flow (Sumer and Fredsøe, 2006).....	341
Figure A-4: $St$ versus $Re$ (Blevins, 2001).....	342
Figure A-5: Pressure distribution in a vortex (Blevins, 2001) .....	343

Figure A-6: Mean drag coefficient of a smooth cylinder as a function of $Re$ (Sumer and Fredsøe, 2006).....	344
Figure A-7: Oscillatory drag coefficient of a smooth cylinder as a function of $Re$ (Sumer and Fredsøe, 2006).....	345
Figure A-8: Lift coefficient versus $Re$ from various sources (Blevins, 2001).....	346
Figure A-9: Lift coefficient versus $Re$ , a) (Barltrop and Adams, 1991), b) (Sumer and Fredsøe, 2006).....	346
Figure A-10: Sectional lift coefficient versus $Re$ (Norberg, 2001).....	347
Figure A-11: Spanwise correlation length versus $Re$ (Norberg, 2001).....	347
Figure A-12: Reduction in lift force due to finite aspect ratios (Barltrop and Adams, 1991).....	348
Figure A-13: Base bending moment response of a model pile due to inline VIV (King <i>et al.</i> , 1973).....	349
Figure A-14: Crossflow amplitude and frequency response for low mass and damping (Khalak and Williamson, 1997a).....	351
Figure A-15: Crossflow VIV of small roughness cylinder in critical regime (Ding <i>et al.</i> , 2004).....	352
Figure A-16: Correlation length versus amplitude ratio (Sumer and Fredsøe, 2006).....	353
Figure A-17: Crossflow VIV of smooth and rough cylinders (Ding <i>et al.</i> , 2004).....	354
Figure A-18: Response branches and vortex modes from the wake mode map (Govardhan and Williamson, 2004).....	356
Figure A-19: Vortex modes of a vibrating cylinder (Bearman, 2009).....	357
Figure A-20: Fluid damping of a vibrating cylinder at an amplitude ratio of 0.50 (Sarpkaya, 1995).....	358
Figure A-21: Effect of mass ratio ( $m^*$ ) on crossflow amplitude response (Sumer and Fredsøe, 2006).....	360
Figure A-22: Effect of mass ratio ( $m^*$ ) on crossflow frequency response (Khalak and Williamson, 1997b).....	361
Figure A-23: Added mass of a vibrating cylinder at an amplitude ratio of 0.50 (Sarpkaya, 1995).....	362
Figure A-24: Effect of mass ratio ( $m^*$ ) on synchronisation regime (Morse and Williamson, 2009).....	363
Figure A-25: Effect of mass damping parameter ( $m^*\zeta$ ) on crossflow amplitude ratio (Morse and Williamson, 2009).....	364
Figure A-26: Crossflow amplitude ratio as a function of stability parameter (Sumer and Fredsøe, 2006).....	365
Figure A-27: Inline amplitude response versus mass-damping parameter (Xu <i>et al.</i> , 2012).....	366
Figure A-28: Natural frequency ratio versus reduced velocity for various mass ratios (Sumer and Fredsøe, 2006).....	368

Figure A-29: Variation of lift coefficient with crossflow amplitude ratio (Barltrop and Adams, 1991) .....	370
Figure A-30: Drag amplification due to VIV in steady flow (Sarpkaya, 1995).....	370
Figure A-31: Crossflow amplitude response versus $Re$ (Sumer and Fredsøe, 2006) .....	371
Figure A-32: Lift forces in oscillatory flow with $KC$ (Sumer and Fredsøe, 2006) .....	373
Figure A-33: Lift coefficient versus $KC$ number (Sumer and Fredsøe, 2006).....	373
Figure A-34: Oscillatory lift histogram in oscillatory flow (Sumer and Fredsøe, 2006) .....	374
Figure A-35: Lift force coefficient of a smooth cylinder in oscillatory flow (Sumer and Fredsøe, 2006) .....	375
Figure A-36: Crossflow amplitude and frequency response with reduced velocity in planar oscillatory flow (Sumer and Fredsøe, 1988).....	377
Figure A-37: Correlation coefficient for a cylinder undergoing self-induced vibrations in oscillatory flow (Sumer <i>et al.</i> , 1994).....	379
Figure A-38: Correlation coefficient of the lift forces on a cylinder in oscillatory flow (Sumer and Fredsøe, 2006).....	379
Figure A-39: Lift coefficient of a vertical cylinder in waves (Barltrop and Adams, 1991) .....	380
Figure A-40: Distribution of $KC$ with depth in regular waves (Barltrop and Adams, 1991) .....	381
Figure A-41: Crossflow amplitude response a vertical pile in regular waves versus reduced velocity (Zedan <i>et al.</i> , 1981).....	381
Figure A-42: Crossflow response parameter of a vertical pile in regular waves versus frequency ratio (Zedan <i>et al.</i> , 1981).....	382
Figure A-43: Drag coefficient versus crossflow amplitude ratio in regular waves (Barltrop and Adams, 1991).....	383
Figure A-44: Effect of shear on the crossflow response of a flexible cylinder (Vandiver <i>et al.</i> , 1996).....	384
Figure A-45: Crossflow VIV in sheared current, amplitude ratio versus reduced velocity (Humphries and Walker, 1988) .....	384
Figure A-46: Drag coefficient of vortex suppression devices (Zdravkovich, 1981)..	386
Figure A-47: SDOF approximation of an MDOF system (Barltrop and Adams, 1991) .....	388
Figure A-48: Displacement of discrete and distributed MDOF systems and effective mass, damping, stiffness and excitation of an SDOF (Barltrop and Adams, 1991).	389
Figure A-49: Turbulent shear stress profiles of various turbulence models (Menter, 1996).....	390
Figure A-50: Comparison of the vortex contours of LES and RANS at $Re 1 \times 10^6$ (Catalano <i>et al.</i> , 2003) .....	391

Figure A-51: $C_D$ versus $Re$ , RANS predictions and measurements .....	392
Figure A-52: Computational mesh for LES (Chen <i>et al.</i> , 2009) .....	393
Figure A-53: Near wall and boundary layer meshing (Stringer <i>et al.</i> , 2014) .....	395

## List of Tables

Table 4-1: Jack-up design data from industry (M/s Cybermarine Technologies Pte. Ltd.).....	39
Table 4-2: Effective mass ratio .....	41
Table 4-3: Jack-up structural properties and natural periods .....	42
Table 4-4: Potential crossflow VIV excitation in current .....	52
Table 4-5: Potential crossflow VIV excitation in regular waves, 90-degree heading .	54
Table 4-6: Potential crossflow VIV excitation in regular waves, 0-degree heading ...	55
Table 4-7: Potential inline VIV excitation in current.....	56
Table 4-8: Potential yaw VIV excitation in current.....	57
Table 4-9: Potential yaw VIV excitation in regular waves.....	58
Table 5-1: Lift amplitude factors and lift frequency factors.....	80
Table 5-2: Inline VIV response of jack-ups in longitudinal critical uniform current ..	109
Table 5-3: Crossflow VIV response of jack-ups in longitudinal critical uniform currents .....	113
Table 5-4: Yaw VIV of jack-ups due to inline excitation in longitudinal critical uniform currents.....	114
Table 5-5: Yaw VIV of jack-ups due to crossflow excitation in longitudinal critical uniform currents.....	117
Table 5-6: Crossflow or sway response of jack-ups in head critical regular waves.	121
Table 5-7: Leg dynamic bending stresses under inline VIV in critical uniform currents .....	124
Table 5-8: Leg dynamic bending stresses under crossflow VIV in critical regular waves .....	125
Table 5-9: Drag amplification and yield strength under crossflow VIV in critical uniform currents.....	126
Table 5-10: Drag amplification and yield strength under yaw VIV in critical uniform currents.....	127
Table 5-11: Nominal fatigue life of the jack-ups under inline VIV in critical uniform currents.....	129
Table 5-12: Nominal fatigue life of the jack-ups under crossflow VIV in critical uniform currents.....	130
Table 5-13: Nominal fatigue life of the jack-ups under yaw VIV in critical uniform currents.....	131
Table 5-14: Nominal fatigue life of the jack-ups under crossflow VIV in critical regular waves.....	132
Table 6-1: Model and prototype properties .....	140
Table 6-2: WWC particulars.....	141
Table 6-3: Basic test cases.....	146

Table 6-4: Inlet turbulence.....	148
Table 6-5: Model mass properties .....	149
Table 6-6: Model natural frequency, added mass and damping from sway free decay tests.....	160
Table 6-7: Model natural frequency, added mass and damping from yaw free decay tests.....	160
Table 6-8: Results of free decay test in current a) sway, b) yaw .....	164
Table 6-9: Response test results in current, and wind, a) sway, b) yaw .....	173
Table 6-10: Details of the test cases with various headings .....	183
Table 6-11: Test cases in regular waves .....	190
Table 6-12: Response test results in regular waves, a) sway, b) yaw .....	190
Table 6-13: Free decay test results with various leg designs .....	217
Table 6-14: Response tests results with various leg designs in uniform current .....	217
Table 6-15: Summary of force test results.....	224
Table 7-1: Discretisation scheme for the numerical simulations.....	239
Table 7-2: Summary of mesh convergence study a) without inlet turbulence, b) with 6% turbulence intensity in way of the cylinder, wake refinement, c) with 13% turbulence intensity in way of the cylinder .....	244
Table 7-3: Summary of time step convergence study .....	245
Table 7-4: Summary of mesh convergence study with 13% turbulence intensity in way of the upstream cylinders .....	249
Table 7-5: Properties of the jack-up rigid body .....	251
Table 7-6: Jack-up crossflow and yaw responses from the numerical simulations (CFD) .....	252
Table 7-7: Jack-up average leg forces from numerical simulations, a) crossflow VIV, b) yaw VIV .....	261
Table 7-8: Jack-up leg force amplification from numerical simulations, a) crossflow VIV, b) yaw VIV .....	266
Table 8-1: Fairing properties .....	290
Table 8-2: Fairing added mass and damping from surge free decay tests.....	294
Table 8-3: Fairing added mass and damping from sway free decay tests.....	294
Table 8-4: Fairing added mass and damping from yaw free decay tests .....	294
Table 8-5: Weathervaning performance of fairings.....	298
Table 8-6: Details of fairing depth test.....	304
Table 8-7: Nondimensionalised offset table of fairing design 1 .....	311
Table 8-8: Nondimensionalised offset table of fairing design 2 .....	311
Table 8-9: Minimum leg diameter in deep water for vortex suppression in regular waves. ....	313

Table A-1: Vortex shedding regimes versus <i>KC</i> number in an oscillatory flow (Sumer and Fredsøe, 2006) .....	342
Table A-2: Scaling laws in offshore engineering (Chakrabarti, 2005) .....	395
Table A-3: Froude scaling of model parameters (Chakrabarti, 2005) .....	396
Table A-4: Scaling of stiffness parameters for combined Froude-Cauchy similarity (Chakrabarti, 2005) .....	396
Table A-5: Typical instrumentation for offshore model testing (Chakrabarti, 2005)	398

## Nomenclature

$a$	Longitudinal or inline spacing of cylinders/legs
$A$	Leg deflection coefficient/constant
ABS	American Bureau of Shipping
$A_F$	Fatigue strength coefficient
ASTM	American Society for Testing and Materials
$b$	Transverse or crossflow spacing of cylinders/legs
$B$	Leg deflection coefficient/constant
$BM_{Dx}(z)$	Leg inline dynamic bending moment about transverse (y) axis
$BM_{Mx}(z)$	Leg inline mean bending moment about transverse (y) axis
$c_{Lx}(z)$	Inline damping coefficient distribution along the leg
$c_{Lfx}(z)$	Inline fluid damping coefficient distribution along the leg
$c_{Lfy}(z)$	Crossflow fluid damping coefficient distribution along the leg
$C$	Damping coefficient
$C_A$	Added mass coefficient
$C_{EA}$	Effective added mass coefficient due to vortex dynamics
$C_L$	Lift coefficient
$C_{Le}$	Effective lift coefficient of the leg
$C_{LO}$	Lift coefficient of a nonvibrating (stationary) cylinder
COG	Centre of Gravity
$C_D$	Mean drag coefficient
$C_{DW}$	Mean drag coefficient in oscillatory flow or regular wave
$C_{DA}$	Amplified mean drag coefficient of a vibrating cylinder
$C_{DAL}$	Amplified mean drag coefficient of the leg

$C_{DO}$	Oscillatory drag coefficient
$C_{\phi}$	Yaw damping coefficient
$C_{eL}$	Effective SDOF damping coefficient per leg
$C_{eLx}$	Effective SDOF inline damping coefficient per leg
$C_{eLy}$	Effective SDOF crossflow damping coefficient per leg
$C_{eLfx}$	Effective SDOF inline fluid damping coefficient per leg
$C_{eLfy}$	Effective SDOF crossflow fluid damping coefficient per leg
$C_{eLsx}$	Effective SDOF inline structural damping coefficient per leg
$C_{eLsy}$	Effective SDOF crossflow structural damping coefficient per leg
$C_{eLfx\phi x}$	Effective SDOF yaw damping coefficient per leg due to inline fluid drag
$C_{eLfy\phi y}$	Effective SDOF yaw damping coefficient per leg due to crossflow fluid drag
$C_{e\phi}$	Effective SDOF yaw damping coefficient
$C_{es\phi}$	Effective SDOF yaw structural damping coefficient
$C_{ef\phi}$	Effective SDOF yaw fluid damping coefficient
$C_{ex}$	Effective SDOF surge/inline damping coefficient
$C_{ey}$	Effective SDOF sway/crossflow damping coefficient
$C_{FX}$	Inline force coefficient
$C_{FX0}$	Amplitude of inline force coefficient
$C_{FY}$	Amplitude of crossflow force coefficient
$C_{FY}$	Crossflow force coefficient
$C_{FYL}$	Crossflow force coefficient of the leg
$\bar{C}_{FX}$	Inline steady force coefficient
CFD	Computational Fluid Dynamics

CEL	Coupled Eulerian Lagrangian
$C_x$	Damping coefficient along inline direction
$C_y$	Damping coefficient along crossflow direction
$d$	Distance travelled by the flow
$d'$	Effective water depth considering penetration
$D$	Diameter of the cylinder/leg
DAF	Dynamic Amplification Factor
DAS	Data Acquisition System
DES	Detached Eddy Simulation
DNS	Direct Numerical Simulation
DOF	Degrees of Freedom
DP	Dynamic Positioning
$D_\omega$	Cross-diffusion of turbulence kinetic energy
$E$	Leg deflection coefficient/constant
$E_L$	Modulus of elasticity of leg material
ELES	Embedded Large Eddy Simulation
$f$	Vibration frequency of the cylinder
$f_{cLfx}(z)$	Inline quadratic fluid damping force distribution along leg
$f_{DO}$	Oscillatory drag frequency
$f_{lower}$	Vibration frequency in the lower branch
$f_L$	Lift frequency
$f_N$	Natural frequency of the cylinder
$f_v$	Vortex shedding frequency of the cylinder
$f_w$	Wave frequency

$f_{oLx}(z)$	Oscillatory drag force distribution along leg
$f_{ox}(z)$	Oscillatory drag force distribution along legs
$f_{oy}(z)$	Oscillatory lift force distribution along legs
$F(t)$	Time dependent excitation force
$F_D$	Drag force
$F_{DAL}$	Amplified mean drag force per leg
$F_{DO}$	Amplitude of oscillatory drag force
$F_{ey}$	Effective SDOF crossflow excitation
$F_{eL}$	Effective SDOF force excitation per leg
$F_{eLx}$	Effective SDOF inline excitation force per leg
$F_{eLy}$	Effective SDOF crossflow excitation force per leg
FFT	Fast Fourier Transform
$F_L$	Lift force
$F_{Lo}$	Amplitude of lift force
$FL$	Fatigue life
$F_o$	Amplitude of excitation force
$F_{ox}$	Amplitude of inline excitation force
$F_{oy}$	Amplitude of crossflow excitation force
FSI	Fluid Structure Interaction
FSM	Fractional Step Method
$F_X$	Inline force
$F_Y$	Crossflow force
$F_{YL}$	Leg crossflow force
$g$	Acceleration due to gravity
$G_k$	Production of turbulence kinetic energy

$G_\omega$	Production of specific dissipation rate
$h$	Water depth
HPC	High Performance Computing
HTS	High Tensile Steels
$H_{W,crit}$	Critical wave height for VIV
$H_W$	Wave height
$I$	Inertia of leg section
$I_{e\phi}$	Effective yaw inertia of the jack-up SDOF
$I_x$	Inertia of leg section along inline direction (about transverse axis)
$I_y$	Inertia of leg section along crossflow direction (about longitudinal axis)
$I_r$	Inertia of the leg section about the radial axis passing through yaw centre
$I_\phi$	Yaw moment of inertia
JIS	Japanese Industrial Standards
$k$	Turbulence kinetic energy
$k_\phi$	Yaw radius of gyration of the jack-up SDOF
$k_{\phi H}$	Yaw radius of gyration of the hull
$K$	Stiffness of a linear mass spring system
$K_S$	Stability parameter
$K_x$	Stiffness of the cylinder along inline direction
$K_y$	Stiffness of the cylinder along crossflow direction
$KC$	Keulegan Carpenter number ( $KC$ number)
$KC(z)$	Variation of $KC$ number along legs
$K_{eL}$	Effective lateral stiffness of the leg in way of the hull interface

$K_{ex}$	Surge stiffness of jack-up
$K_{ey}$	Sway stiffness of jack-up
$K_{e\phi}$	Effective yaw stiffness of jack-up
$K_{eLx}$	Leg stiffness along inline direction
$K_{eLy}$	Leg stiffness along crossflow direction
$K_{rH}$	Rotational stiffness of the leg-hull interface
$K_{\phi}$	Yaw stiffness
$L$	Length of the cylinder, effective leg length (from leg bottom to hull interface)
LES	Large Eddy Simulation
LHI	Leg-Hull Interface
$m^*$	Mass ratio (mass per displaced mass) of the cylinder
$m^*_{crit}$	Critical mass ratio of the cylinder
$m(z)$	Mass distribution along leg
$m_F$	Fatigue strength exponent
$m_{LbH}(z)$	Mass distribution of the leg below the hull interface
$m_{LAM}(z)$	Added mass distribution of the leg
$m_{LEM}(z)$	Entrapped mass distribution of the leg
$m_{o\phi}(z)$	Oscillatory yaw moment distribution along leg
$M$	Mass of a linear mass spring system / cylinder
MDOF	Multi-Degree-of-Freedom
$M_e$	Effective mass of jack-up SDOF
$M_{el}$	Elevated mass of jack-up
$M_{eL}$	Effective SDOF mass per leg at hull interface level
$M_{eAM}$	Effective added mass of jack-up SDOF
$M_{eEM}$	Effective entrapped mass of jack-up SDOF

$M_{eH}$	Effective mass of jack-up elevated hull
$M_{eLaH}$	Effective SDOF mass of legs above hull interface level
$M_{LaH}$	Mass of a leg above hull interface level
$M_{eLbH}$	Effective SDOF mass of legs below hull interface level
$MF$	Mode Factor
$M_H$	Mass of jack-up elevated hull
$M_{o\phi}$	Amplitude of oscillatory yaw moment
$M_{oe\phi}$	Effective SDOF yaw excitation
$M_{oe\phi L}$	Effective SDOF yaw excitation per leg
MS	Mild Steel
$M_\phi$	Yaw moment
$n_L$	Number of legs
NA	Not Applicable
$N_L$	Lift frequency factor, ratio of lift frequency to flow frequency
$N_F$	Number of cycles to failure
$N_V$	Number of vortices shed in an oscillatory flow half cycle
$OTM$	Overturning moment
$OTM_A$	Amplified overturning moment
$OTM_{AL}$	Amplified overturning moment per leg
$OTM_L$	Unamplified overturning moment per leg
$P$	Static vertical load acting on the leg
$P_{EL}$	Euler's buckling load of the leg
$P_{ELx}$	Euler's buckling load of the leg along inline direction
$P_{ELY}$	Euler's buckling load of the leg along crossflow direction
PISO	Pressure-Implicit with Splitting of Operators
PIV	Particle Image Velocimetry

PVC	Polyvinyl Chloride
$r_\phi$	Radial distance of the cylinder from yaw centre
rms	Root-Mean-Square
RANS	Reynolds Averaged Navier-Stokes
RSS	Root-Sum-Square
$Re$	Reynolds Number
RHS	Right Hand Side
RNG	Renormalisation Group
RSM	Reynolds Stress Model
$R_\phi$	Radial distance of the leg from yaw centre
SA	Spalart–Allmaras
SAS	Scale Adaptive Simulation
SCF	Stress Concentration Factor
$S_D$	Dynamic stress range
SDOF	Single-Degree-of-Freedom
SGS	Sub-Grid Scale
$S_k$	Source of turbulence kinetic energy
SST	Shear-Stress Transport
$St$	Strouhal number
$S_\omega$	Source of specific dissipation rate
$t$	Time
$t_0$	Time instant of flow reversal
$T$	Vibration period

TLP	Tension Leg Platform
$T_N$	Natural period
$T_W$	Oscillatory flow or wave period
$T_{W,crit,y}$	Critical wave period for crossflow VIV
$T_{W,crit,\phi}$	Vritical wave period for yaw VIV
$T_L$	Lift period
$T_{Nx}$	Surge/inline natural period
$T_{Ny}$	Sway/crossflow natural period
$T_{N\phi}$	Yaw natural period
$u_i$	Velocity component
$\bar{u}_i$	Mean velocity component
$u'_i$	Fluctuating velocity component
$U$	2D steady flow or uniform current velocity
$U(z)$	Flow velocity variation along the leg
$U_{crit,y}$	Critical current speed for crossflow VIV
$U_{crit,x}$	Critical current speed for inline VIV
$U_{crit,\phi}$	Critical current speed for yaw VIV
UDF	User Defined Function
$U_o$	Amplitude of the oscillatory flow horizontal velocity, wave particle horizontal velocity
$U_o(z)$	Variation of the amplitude of the wave particle horizontal velocity along legs
URANS	Unsteady RANS
VCG	Vertical Centre of Gravity
VIM	Vortex Induced Motion
VIV	Vortex Induced Vibration

VIY	Vortex Induced Yaw Motion
$V_r$	Reduced velocity
WL	Waterline
WIV	Wake Induced Vibration
WWC	Wind Wave Current
$x$	Inline direction / response
$\bar{x}$	Mean inline response
$x_o$	Displacement amplitude / amplitude of inline VIV response
$x_o(z)$ along leg	Inline VIV response amplitude variation (deflection profile)
$x_L$ interface	Inline VIV response amplitude of leg in way of the hull
$y$	Crossflow direction / response
$y^*$	Combined crossflow response considering sway and yaw
$y_e$	Effective jack-up SDOF crossflow displacement
$y_o$	Amplitude of crossflow VIV response
$y_o(z)$ profile) along leg	Crossflow VIV response amplitude variation (deflection
$y_L$ interface	Crossflow VIV response amplitude of leg in way of the hull
$Y_k$	Dissipation of turbulence kinetic energy
$Y_\omega$	Dissipation of specific dissipation rate
$z$	Elevation w.r.t to leg bottom, positive upwards; 0 at seabed
$Z$	Section modulus of the leg section
$Z_r$ through yaw centre	Section modulus of the leg about the radial axial passing
$Z_x$	Section modulus of the leg about transverse (y) axis

$Z_y$	Section modulus of the leg bout longitudinal (x) axis
2D	Two Dimensional
3D	Three Dimensional
$\alpha$	Lift amplitude factor
$\varepsilon$	Phase difference between displacement and force
$\varepsilon$	Turbulence dissipation rate
$\phi$	Yaw direction / response
$\phi_o$	Amplitude of yaw response
$\phi_o(z)$ along leg	Yaw VIV response amplitude variation (deflection profile)
$\phi_L$	Yaw VIV response of leg in way of the hull interface
$\Gamma_k$	Effective diffusivity of turbulence kinetic energy
$\Gamma_\omega$	Effective diffusivity of specific dissipation rate
$\kappa_L$	Structural mode number of the leg
$\kappa_W$	Wave number of the leg
$\rho$	Density of the fluid
$\sigma_{Dx}$	Leg dynamic bending stress due to inline VIV
$\sigma_{Dy}$	Leg dynamic bending stress due to crossflow VIV
$\sigma_{D\phi}$	Leg dynamic bending stress due to yaw VIV
$\sigma_{Mx}$	Leg mean bending stress
$\sigma_Y$	Yield Strength
$\omega$	Turbulence specific dissipation rate
$\omega$	Vibration angular frequency
$\omega_L$	Lift force frequency
$\omega_N$	Natural angular frequency
$\omega_{Nx}$	Surge / inline natural angular frequency

$\omega_{Ny}$	Sway / crossflow natural angular frequency
$\omega_{N\phi}$	Yaw natural angular frequency
$\omega_v$	Vortex shedding angular frequency
$\omega_W$	Oscillatory flow or wave angular frequency
$\zeta$	Damping ratio
$\zeta_{fy}$	Fluid damping ratio along crossflow/sway direction
$\zeta_{f\phi}$	Fluid damping ratio of the yaw mode
$\zeta_{sx}$	Structural damping ratio along inline direction
$\zeta_{sy}$	Structural damping ratio along crossflow/sway direction
$\zeta_{s\phi}$	Structural damping ratio of the yaw mode
$\zeta_x$	Damping ratio along inline direction
$\zeta_y$	Damping ratio along crossflow direction
$\zeta_\phi$	Damping ratio of yaw mode

## List of Publications

Ramadasan, S., Tao, L. and Dev, A. (2018) 'Antinode Fairings: An Optimum Solution for Reduction of Vortex Induced Vibration', *Offshore Technology Conference Asia*. Kuala Lumpur, Malaysia, 2018/3/20/. OTC: Offshore Technology Conference.

Ramadasan, S., Tao, L. and Dev, A. (2019) ' Vortex-Induced-Vibration of Jack-Ups With Cylindrical Legs in Regular Waves', *OMAE 2019*. Glasgow, UK, June 9-14. ASME.

Ramadasan, S., Tao, L. and Dev, A.K. (2019) 'Vortex-Induced-Vibration of jack-ups with cylindrical legs in multiple modes', *Marine Structures*, 67, p. 102637



## Chapter 1. Introduction

Self-elevating offshore platforms or jack-up platforms, hereinafter called jack-ups typically have three or four legs that are either designed as cylindrical or lattice structures (DNV GL, 2015). Circular cylindrical legs are widely used for shallow water jack-up concepts like construction jack-ups and lift boats owing to its minimum drag coefficient, multidirectional symmetry and ease of fabrication. Small jack-ups with cylindrical legs are also used extensively for geotechnical investigation, platform support and installation of renewable energy devices. Mat-type jack-ups with cylindrical legs attached to a large bottom mat are usually deployed in water depths in the order of 80m for oil and gas drilling operations (Hirst *et al.*, 1976). Jack-ups with independent cylindrical legs are typically deployed in shallow and intermediate waters up to around 50m depth. Figure 1-1 illustrates a jack-up with cylindrical legs performing geotechnical investigation in coastal waters (M/s Cybermarine Technologies Pte. Ltd).



Figure 1-1: Jack-up with cylindrical legs (M/s Cybermarine Technologies Pte. Ltd.)

Vortex Induced Vibration (VIV) is an extensively researched classical fluid structure interaction problem known to cause severe yield and fatigue failures of marine and offshore structures. Jack-up VIV has led to abortion of various operations in UK coastal waters due to the loss of platform stability and eventually resulted in the mobilisation of expensive alternatives like dynamic positioning (DP) vessels (Thake, 2005). Not only the present classification society rules and industry standards tend to ignore the phenomenon of jack-up VIV, but also there is a lack of dedicated guidelines or

regulations addressing this issue. This situation is compounded by the inadequacy of published literature and the lack of comprehensive investigations on the subject. Department of Trade and Industry, UK categorically called for new design guidelines to address this issue (Thake, 2005), making this research relevant at this juncture.

## 1.1 Background and Motivation

The effects of oscillatory lift forces are customarily neglected in the structural design of jack-ups due to its zero-mean value. However, the effect of the lift forces may not be negligible in the case of jack-ups with cylindrical legs when it comes to its dynamic response, fatigue strength and the increase in drag due to vortex induced vibrations.

### 1.1.1 Vortex Induced Vibration

#### 1.1.1.1 Flow around Cylinders

The alternate shedding of vortices from either side of a circular cylinder results in a periodic pressure field causing oscillating forces along inline and crossflow directions to the incoming flow. These forces are called vortex induced forces or flow induced forces and the inline and crossflow forces are called drag and lift respectively. As the frequency of the vortex induced forces approaches the natural frequency of the cylinder, severe vibration is experienced by the cylinder which is called VIV (Sumer and Fredsøe, 2006). Figure 1-2 illustrates the Von Karman vortex street behind a stationary circular cylinder at a Reynolds Number ( $Re$ ) of 4000 (Williamson, 1996). The turbulent vortex shedding and the alternate vortices of opposite signs are clearly visible in the figure.



Figure 1-2: Vortex shedding about a cylinder (Williamson, 1996)

Figure 1-3 displays the vortex induced forces acting on a circular cylinder in steady flow (Sumer and Fredsøe, 2006). It can be observed that the lift period is same as the vortex shedding period and the oscillatory drag period is half the shedding period. It can also be observed that the amplitude of the lift force is much higher than the amplitude of the oscillatory drag. The drag and lift forces induce inline and crossflow VIV respectively.

#### 1.1.1.2 Cylinder Vibrations

The phenomenon of lock-in occurs when the VIV is locked on to the natural vibration of the cylinder. It causes the natural vibration mode of the cylinder to take control over the vortex shedding process and the shedding frequency follows the vibration frequency. This phenomenon happens over a range of frequency around the natural frequency, also referred to as wake capture and involves increased vibration amplitude in the order of  $0.1D$ , where  $D$  is the diameter of the cylinder. (Halse, 1997).

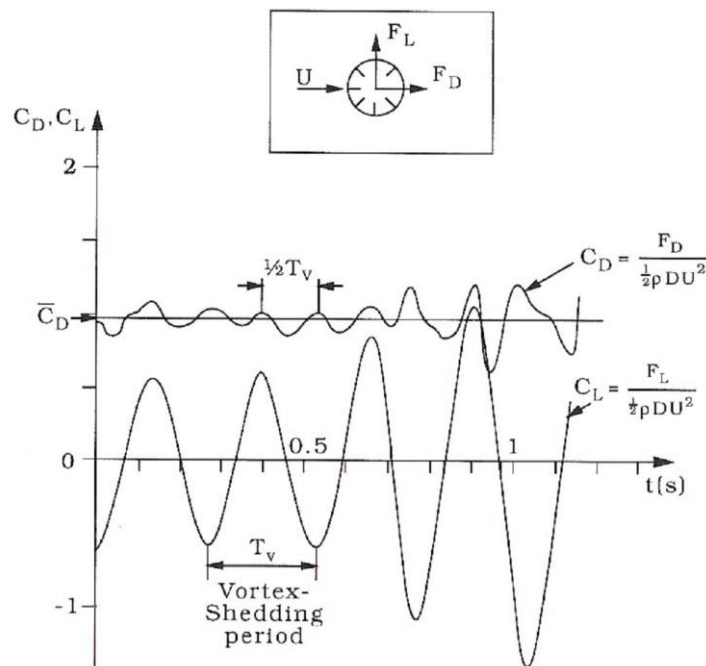


Figure 1-3: Vortex induced forces on a cylinder (Sumer and Fredsøe, 2006)

Figure 1-4 demonstrates the typical crossflow response amplitude ratio ( $\bar{Y} = \frac{y_0}{D}$ ), frequency ratio ( $\frac{f_c}{f_n}$ ) and phase angle ( $\phi$ ) of a spring supported circular cylinder freely oscillating in air, with a mass ratio ( $m^*$ ) of 248 (Feng, 1968). The responses are plotted

against the normalised wind velocity ( $U = \frac{U}{2\pi f_n D}$ ) in the figure, which also illustrates the vortex shedding frequency ratio ( $\frac{f_v}{f_n}$ );  $y_o$ ,  $D$ ,  $f_c$ ,  $f_n$ ,  $f_v$ , and  $U$  represent the crossflow vibration amplitude, cylinder diameter, vibration frequency, natural frequency, vortex shedding frequency and wind velocity respectively. It can be observed from the figure that during lock-in both the cylinder vibration frequency and vortex shedding frequency are equal and lock on to the cylinder's natural frequency while the cylinder vibrates with large amplitudes.

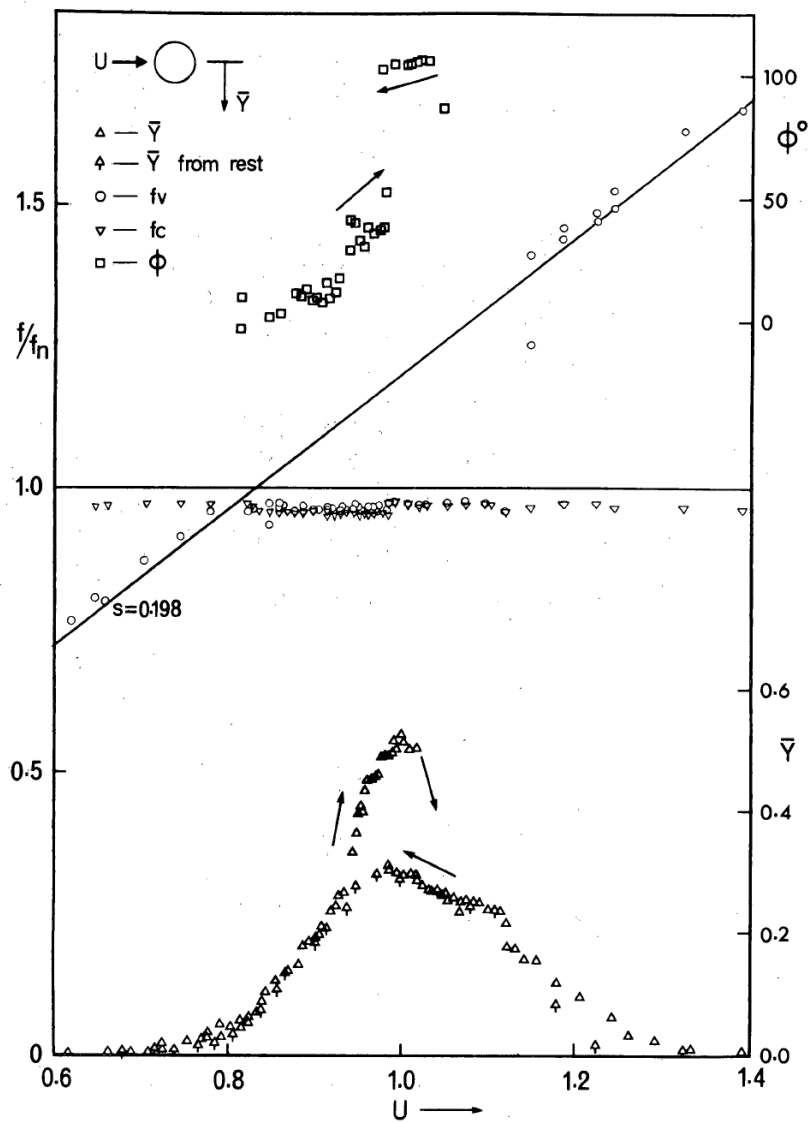


Figure 1-4: Crossflow amplitude, frequency and phase response of a spring mounted cylinder in wind (Feng, 1968)

### 1.1.2 *Jack-up Platforms*

#### 1.1.2.1 *Natural Periods*

The typical natural periods of the fundamental modes of jack-ups are in the range of 5 to 15 seconds (ABS, 2017), which correspond to natural frequencies in the range of 0.06 to 0.20 Hertz. For small jack-ups, the fundamental modes can have natural periods in the order of less than 5 seconds (DNV GL, 2015). Van Den Abeele and Vande Voorde (2011a) performed the modal analysis of typical jack-up barges with 50m leg length and found that the natural period of the first two modes were in the order of 2 seconds.

#### 1.1.2.2 *Cylindrical Legs in Shallow Waters*

Jack-ups constructed of multiple cylindrical legs with diameters up to 4.00 m are usually deployed at various coastal or offshore locations. It is very likely for these sites to have currents up to 5 knots and wave heights up to 10 metres. Under these conditions, it is quite possible for the legs to have vortex shedding frequencies in the range of 0.05 to 0.30 Hertz, or even higher. This situation can potentially lead to large resonant and lock-in lateral vibrations of the jack-up when the vortex shedding frequency approaches its natural frequency.

Moreover, the exponential decay of wave motion with the vertical distance from the water surface at such depths is minimal and the effect of waves is experienced till the sea bed (Barltrop and Adams, 1991). Figure 1-5 illustrates the velocity field of particles in a shallow water wave (Journée and Massie, 2001). It can be observed that though the vertical particle velocity declines with distance from the water line, the variation of horizontal particle velocity is minimal, and the horizontal particle velocity is experienced even at the seabed. Consequently, the vortex shedding will be closely correlated over the water depth and the magnitude of lift forces can be expected to follow the behaviour expected in planar oscillatory flow. Hence in shallow waters, the jack-up legs can experience synchronised vortex shedding along the legs throughout the water depth making them highly vulnerable to VIV.

Further, the lift forces in waves are uncharacteristically high at Keulegan-Carpenter (*KC*) numbers less than 20, which is an additional concern since the wave flows about jack-up legs fall in this range. It is observed that crossflow forces can be as large as

the inline forces and the lift coefficient can reach a value as high as 3 at  $KC$  numbers less than 20 (Sarpkaya, 1975). Figure 1-6 displays the variation of the lift coefficient with  $KC$  number in a planar oscillatory flow (Sarpkaya, 1975). It can be observed that the lift coefficient has very high values, even greater than the drag coefficient in the  $KC$  number range from 7 to 24.

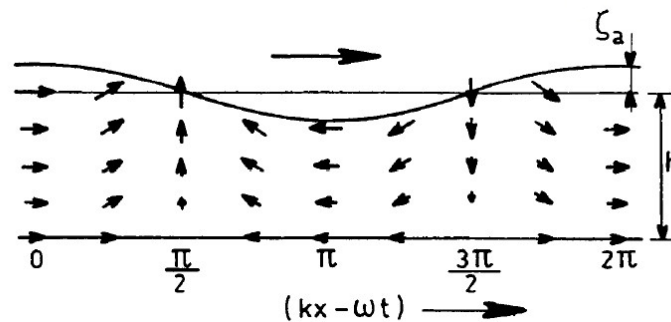


Figure 1-5: Velocity field in a shallow water wave (Journée and Massie, 2001)

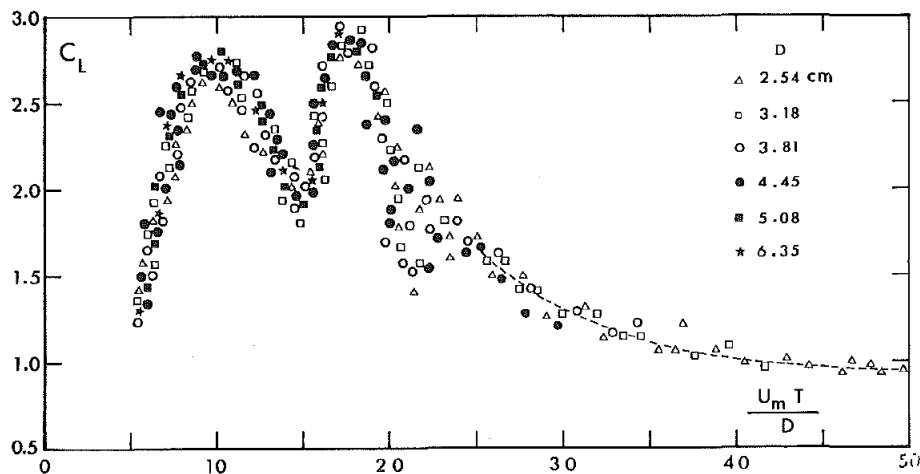


Figure 1-6: Lift coefficient versus  $KC$  number in planar oscillatory flow (Sarpkaya, 1975)

Experiments on roughened vertical cylinders conducted in shallow waters showed that the wave flow closely approximates the planar oscillatory flow and lift forces had a high degree of span wise coherence (Wolfram, 1991). The legs being stiff cylinders, the VIV response can be a single mode response with large correlation length exhibiting pronounced lock-in vibrations with large amplitudes. The oscillatory drag force can also

cause in-line resonant vibrations of the jack-ups at low currents when the vortex shedding frequency is near to half the natural frequency.

### 1.1.3 **Jack-up VIV**

Jack-ups are predominantly drag loaded and are also dynamically responsive (Barltrop and Adams, 1991). The conventional dynamic analysis of a jack-up covers only the inline dynamic response to the waves as the natural period is typically excited by wave frequencies (ABS, 2017). The dynamics of jack-up VIV is usually disregarded as a structural design requirement.

Nicholls-Lee *et al.* (2013a) reported the instability of the jack-ups in high tidal currents and associated VIV causing large topside motions leading to the abortion of operations. Severe vibrations of jack-up barges due to vortex shedding about the cylindrical legs have led to many unsuccessful operations at aggressive tidal locations in UK waters (Thake, 2005). Detailed studies were conducted by the marine construction company, Seacore and special leg fairings were fitted on their jack-up to prevent resonant vibrations due to vortex shedding during the installation of tidal turbines off Foreland Point, near Lynmouth, on the North Devon coast of England (European Commission, 2005). Figure 1-7 illustrates the special fairings fitted on the leg of their jack-up, Deep Diver to reduce the drag and suppress VIV.

VIV not only increases the forces on the legs but also can initiate inline and crossflow dynamic motions of the jack-up, which can lead to large inertial accelerations of the elevated mass. The combined effect of the above-mentioned behaviours can result in static and cyclic stresses of considerable magnitude in the legs which can eventually affect its yield and fatigue strength.

#### 1.1.3.1 *Force Amplification*

VIV can increase the drag loads acting on the legs and thereby affect the structural strength of the jack-up. The mean drag increases almost linearly with the crossflow vibration amplitude, as demonstrated in Figure 1-8 (Blevins, 2001). It can be observed that the mean drag even increases threefold with large vibration amplitudes. Lateral vibrations can also cause large values of lift coefficients as even small vibrations will tune vortex shedding and separation points along the legs (DNV GL, 2017b).



Figure 1-7: Jack-up with leg fairings (European Commission, 2005)

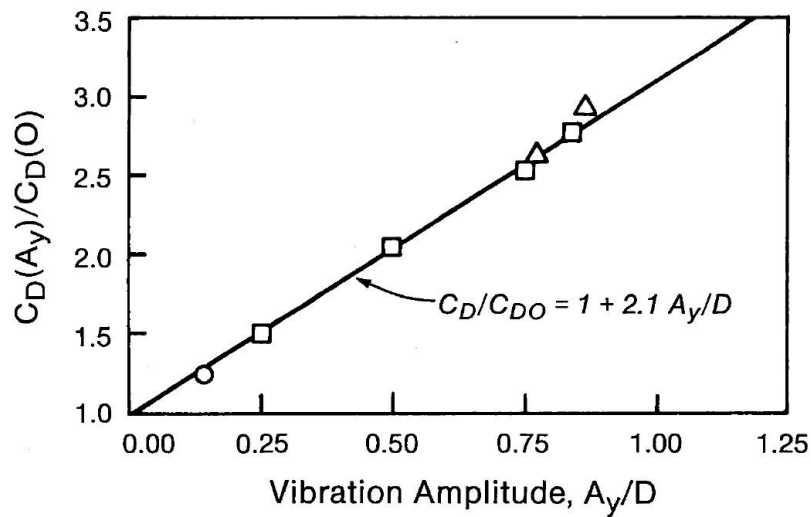


Figure 1-8: Mean drag amplification with crossflow vibration amplitude (Blevins, 2001)

### 1.1.3.2 Fatigue Strength

The high frequent nature of VIV can significantly affect the fatigue life of the marine structures. The conventional fatigue analysis assumes that the vortex shedding

induced lift forces are not sufficiently coherent over the whole span of a tubular member to cause considerable damage. Walker and Brazier (1980) carried out the fatigue analysis of a jacket structure considering the vortex induced lift forces along with the wave forces and based on the results concluded that the effects of vortex shedding should be considered in the fatigue life of the offshore structures.

#### 1.1.4 *Lack of regulations*

The latest American Bureau of Shipping (ABS) Rules for Building and Classing Mobile Offshore Drilling Units (ABS, 2018d) vaguely mentions about the vortex shedding in general but lacks necessary formulations for its assessment. ABS Guidance Notes (ABS, 2016; ABS, 2017) on the analysis of jack-ups also do not mention about VIV. DNV Rules for Classification (DNV GL, 2018), DNV Offshore Standard (DNV GL, 2017a) and Recommended Practice (DNV GL, 2015) on jack-ups ambiguously mention about the potential fatigue effects due to vortex shedding in current but does not contain any concrete guideline or formulation for its evaluation. American Petroleum Institute (2000) recommends to investigate the effect of VIV in the design of local members near to the free surface but neglects the global effect of lift forces due to its mean zero nature, random phasing, higher frequency and lack of correlation. PANEL OC-7 (2008), which contains exhaustive guidelines on the site specific analysis of jack-ups also mentions only about the local VIV of the members of lattice legs.

ISO (2016) explicitly mentions that VIV should be evaluated for jack-ups with large diameter cylindrical legs in currents outside design limits but refers to generic literature including DNV GL (2017b), Blevins (2001) for verification procedure. Further, it is incorrectly assumed that the VIV due to currents within design limits is already verified during classification. DNV GL (2017b) clearly describes various technical aspects of Vortex Induced Oscillations, recommends a generic response based model for evaluating various modes of VIV and Vortex Induced Motion (VIM) of offshore structures under various flow scenarios and contains general guidelines on vortex suppression. Thake (2005) describes evidently about the VIV and associated problems faced by jack-ups working in deep and fast currents, the lack of established design guidelines to address this issue and the need of developing new methods. It is recommended to develop special design guidelines for this shallow water problem.

### 1.1.5 *Limited Research*

There are limited model tests results on jack-ups available in the published literature, and almost none of them pertains to jack-up VIV. Most of the studies (Bennett Jr and Patel, 1989; Johnson and Patel, 1992; Grundlehner, 1997) on the jack-ups pertained to understanding the dynamics in regular waves and evaluating the dynamic response. Cammaert et al. (2014) carried out model tests of an arctic jack-up with cylindrical legs to verify the ice loads and leg sheltering factor. Journee et al. (1988) had carried out experiments with simplified jack-up models with cylindrical legs and investigated the hydrodynamic and structural nonlinearities in the fluid-structure interaction.

Van Den Abeele and Vande Voorde (2011a) performed the modal analysis of a typical jack-up barge with 50m leg length to evaluate the susceptibility to VIV. The modal analysis was performed for the number of legs in the range of 3 to 6, and it was found that the natural periods of the first two modes were in the range of 1 - 2 seconds. It was observed that legs had limited effects on the natural frequencies, and VIV was mainly governed by flow conditions and leg diameter. The stability of the jack-up barges against vortex shedding in combined current and wave flow was also evaluated, and it was found that the jack-ups with more number of legs exhibited higher stability (Van Den Abeele and Vande Voorde, 2011a; Van Den Abeele and Vande Voorde, 2011b).

## 1.2 **Aim and Objectives of the Research**

The aim of this research is to carry out a thorough scientific investigation on the effect of oscillatory lift forces on the yield and fatigue strength of self-elevating offshore platforms with cylindrical legs under various operating flows. This research is expected to result in a comprehensive understanding of the phenomenon of jack-up VIV as well as possible solutions for its mitigation.

The objectives of this research can be summarised as follows.

1. Systematic evaluation of various working and in progress designs of jack-ups with cylindrical legs based on the data provided by the industry to verify the vulnerability to vortex excitations in combined current and waves.

2. Identifying critical flow regimes of the jack-ups considering the practical combinations of leg diameter, current speed, wave height, wave period and operating water depth.
3. Identifying significant range of natural time periods of the jack-ups with cylindrical legs from various combinations of elevated mass, water depth and leg flexural stiffness.
4. Arriving at the range of critical cylinder diameters corresponding to various combinations of flow regimes, water depth and elevated mass.
5. Theoretical investigation of various modes and scenarios of jack-up VIV towards a better analytical understanding of the phenomena.
6. Development of simplified analytical methods or response based mathematical models to evaluate the various modes of jack-up VIV under various flow scenarios.
7. Development of criteria for the occurrence of various modes of jack-up VIV under various flow scenarios.
8. Experimental investigation of the various modes and flow scenarios of jack-up VIV by means of a scaled model and validation of the theoretical investigation.
9. Numerical investigation of the various modes of Jack-up VIV by Computational Fluid Dynamics (CFD).
10. Evaluation of the effect of VIV on the structural yield strength and fatigue strength of the Jack-up.
11. Understanding the physics of streamlined fairing as a vortex suppression device, creating optimum leg fairing sections for the suppression of jack-up VIV and developing a simplified mathematical model for its application.
12. Recommendations and design guidelines for accounting the effect of oscillatory lift excitations in the structural design of jack-ups with cylindrical legs.

### **1.3 Contributions of the Research**

The main contributions of this research project can be listed as follows.

1. Discovery of the concept of dynamic damping stiffness as the critical parameter controlling the resonant response of a single-degree-of-freedom (SDOF) system.

2. Development of a harmonic model for the evaluation of yaw VIV of rigidly coupled 2D cylinders in a rectangular configuration.
3. Development of response-based models for VIV assessment of jack-ups under various modes and flow scenarios.
4. Formulation of VIV Criteria for quick verification of the occurrence of various VIV modes for 2D cylinders and jack-ups.
5. Conceptualisation of the SDOF idealisation of the yaw mode of the jack-up.
6. Creation of a mathematical model to design and optimise streamlined fairings for VIV suppression.
7. Design of two leg fairing profiles for ready industrial application towards suppression of jack-up VIV.
8. Pioneering comprehensive experimental investigation on jack-up VIV
9. Presentation of holistic design recommendations for jack-ups towards alleviating VIV.
10. Creation of a benchmark for future investigations on jack-up VIV.

## Chapter 2. Research Methodology

### 2.1 State-of-the-Art

Circular sections are widely used in marine and offshore engineering applications owing to its minimum drag coefficient and multidirectional symmetry. Most of the slender elastic marine structures like risers, mooring lines, umbilicals are found to be vulnerable to VIV and the associated fatigue failures. Jack-ups with tubular legs are also found to experience aggressive VIV in high tidal currents (see Section 1.1.3).

Almost none of the limited model test results on jack-ups available in the published literature pertains to jack-up VIV. Most of these works were intended towards understanding the dynamics and associated response of jack-ups in regular waves. There are also very limited published theoretical and numerical investigations on the jack-up VIV (see Section 1.1.5). However, there are published investigations on VIM, a low frequency rigid body equivalent of VIV, experienced by floating single (spar) or multi-cylinder structures like semi-submersibles and TLPs. The available literature on VIM (Gonçalves *et al.*, 2011a; Gonçalves *et al.*, 2011b; Fajarra *et al.*, 2012; Gonçalves *et al.*, 2018a) can be used effectively to draw relevant insights to the jack-up VIV.

#### 2.1.1 Rules and Regulations

The present classification society rules and industry standards neither mention about the jack-up VIV nor contain necessary guidelines for its evaluation (see Section 1.1.4). DNV GL (2017b), though presents an elaborate response-based model for the evaluation of VIV and VIM, it is too generic and its specific application warrants very high theoretical proficiency. UK Department of Trade and Industry had categorically sought the development of new evaluation methods and special design guidelines towards this coastal engineering problem (Thake, 2005).

#### 2.1.2 VIV Prediction

DNV GL (2017b) classifies the current prediction methods of VIV into response-based, force-based and flow-based computational models. Response based models are empirical models based on hydrodynamic and structural parameters for the prediction of steady state VIV amplitudes while force-based models depend on integrated force coefficients from empirical data and structural parameters for the computation of the

hydrodynamic forces and VIV response respectively. Flow-based models perform direct computation of hydrodynamic forces from fluid flow quantities, and structural response is calculated from the structural parameters.

Response based models are simple in nature and can be used for initial screening. There are adequate published literatures (Blevins, 2001; Sumer and Fredsøe, 2006; DNV GL, 2017b) on generic response based models which can be applied to cylindrical structures experiencing VIV. Most of the VIV programs used in the industry for evaluating VIV of risers and other cylindrical structures are built on force based models. Some of these programs are limited by the scale effects of the empirical data and exclusion of inline oscillatory drag coefficient (DNV GL, 2017b).

CFD, based on the solution of Navier Stokes equations, is the typical example for flow based model. However, direct 3D CFD simulations are not feasible at present, due to high demands in terms of computational grid, time and resources. Hence, 2D CFD simulations and use of the strip theory is regarded as a more feasible approach for slender cylindrical structures. Moreover, at high  $Re$ , the flow becomes turbulent, and as the Direct Numerical Simulation (DNS) is practically unfeasible, the flow fluctuations are modelled by using appropriate turbulence models. As there is not a single universally acknowledged turbulence model, results vary among simulations (DNV GL, 2017b). Further, widely used turbulence model based two-dimensional unsteady Reynold's Averaged Navier Stokes (URANS) simulations are found to have limitations in capturing the drag crisis phenomenon (Qiu *et al.*, 2017).

Hydrodynamic model testing, though a well-established tool for design verification of marine structures, can be affected by the scale effects when viscous forces are significant. As vortex shedding is a  $Re$  dependent phenomenon for circular cylinders, model test results should be corrected for scale effects during prototype scaling. However, DNV GL (2017b) considers  $St$  to be relatively insensitive to  $Re$  for stationary rough cylinders and vibrating cylinders as illustrated in Figure 2-1. The publication also recommends a value of 0.9 for lift coefficient ( $C_L$ ) in current, irrespective of  $Re$  because even small vibrations tune vortex shedding and separation points. The correlation length of vortex shedding is also considered to be independent of  $Re$  in the mentioned standard. Hence, scale effects are regarded as relatively insignificant for the rough and vibrating cylinders when compared to the stationary cylinders.

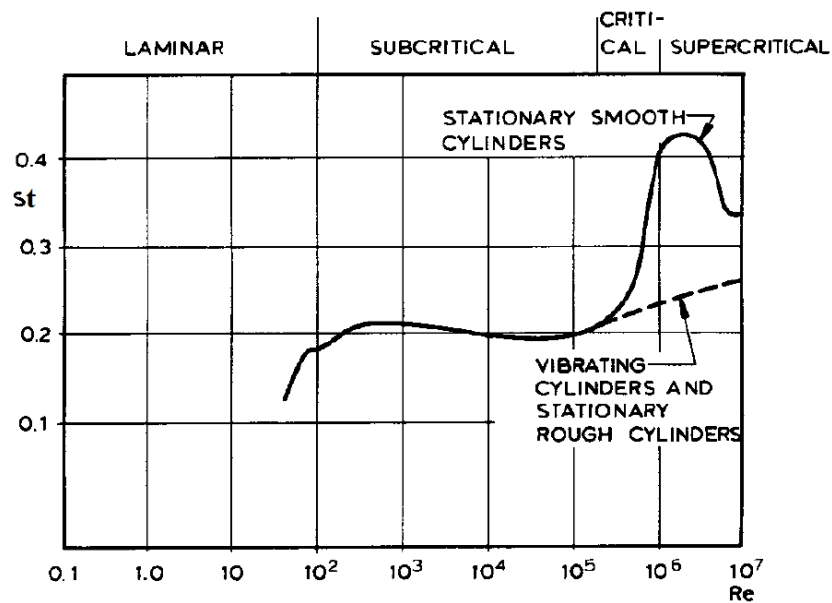


Figure 2-1: Variation of  $St$  with  $Re$  (DNV GL, 2017b)

### 2.1.3 Jack-up VIV in Waves

Though there are barely any published literatures on jack-up VIV in waves or waves with imposed current, extensive studies are available on VIV of vertical cylinders or piles in planar oscillatory flows and regular waves (Sarpkaya, 1975; Zedan *et al.*, 1981; Angrilli and Cossalter, 1982; Bearman *et al.*, 1984; Williamson, 1985; Sarpkaya, 1987; Sumer and Fredsøe, 1988; Longoria *et al.*, 1991; Sumer *et al.*, 1994; Sumer and Kozakiewicz, 1995; Fu *et al.*, 2013). These literatures along with limited studies on VIV of vertical cylinders or piles and VIM of cylindrical structures in regular waves and imposed current (Tsayalis, 1987; Moreau and Huang, 2010; Gonçalves *et al.*, 2012; Gonçalves *et al.*, 2018b) may be effectively used to understand the jack-up VIV under these flow conditions. DNV GL (2017b) recommends a high lift coefficient ( $C_L$ ) of 3 for  $KC$  numbers less than 20 in regular waves. However, the response-based model contained within does not cater to VIV in regular waves with imposed current.

## 2.2 Research Methodology and General Approach

### 2.2.1 Step 1: Literature Survey / Review

The investigation will start with literature surveys towards understanding the behaviour of wake behind circular cylinders, vortex shedding phenomenon, flow induced forces, vortex modes, span wise correlation, the effect of free stream turbulence and the effect

of  $Re$  on the steady flow around circular cylinders. Similar studies will be carried out for the oscillatory flow about the circular cylinder as well, with special emphasis on the effect of  $KC$  number on vortex modes and flow induced forces, the effect of flow reversal, the effect of imposed current, the cylinder in regular waves and cylinder in irregular waves.

This will be followed by literature studies on VIV of cylinders in steady flow, oscillatory flow, regular wave, regular wave with imposed current and irregular waves. Literature reviews will also cover the hydrodynamic damping, added mass and vortex modes during cylinder VIV and the force (drag and lift) amplification due to VIV. The literatures on flow around multiple cylinders, the significance of inline and crossflow spacing of cylinders, wake-induced vibration of the leeward cylinders, VIV of rigidly coupled multiple cylinders and vortex synchronization among multiple cylinders will also be subjected to exhaustive reviews. The studies will also cover the published mathematical and empirical models for the prediction of VIV under various flow scenarios and the vast literature available on the experimental and numerical studies on the subject. Typical experimental setups and numerical models used for such investigation will also be subjected to special studies.

The studies will subsequently extend to self-elevating offshore platforms, accentuating the critical aspects like structural dynamics, nonlinear behaviour, environmental loading and the yield and fatigue strength of the legs. Special attention will be given to the experimental studies conducted with jack-up models, the experimental setups and the intricacies associated with scaling. The latest rules and regulations for the design of the jack-ups and the reported cases of jack-up VIV will also be subjected to rigorous studies.

### **2.2.2 Step 2: Studies on Flow-Based Models and Research Tools**

Comprehensive studies will be carried out on flow-based models, CFD, turbulence modelling, modelling wall boundary layer, modelling flow around vibrating structures and coupling between multiple bodies. Studies on CFD will be followed by studies on fluid structure interaction (FSI). CFD and 2D FSI will be carried out by using the widely acclaimed solvers ANSYS FLUENT. Studies will also cover acquaintance with programming languages including C++ and MATLAB. C++ is required towards generating and compiling User Defined Functions (UDF) in FLUENT while MATLAB is

required towards post processing the results of numerical and experimental investigations.

### **2.2.3 Step 3: Data Analysis of Existing Jack-ups**

Data Analysis of various working designs of jack-ups with cylindrical legs and the respective operating environments will be carried out to verify the vulnerability to various modes of VIV under various flow scenarios. The typical ranges of physical parameters important to jack-up VIV including leg diameter, natural periods, practical flow regimes and elevated mass will be arrived at from this analysis. The variation of natural periods, leg diameter and mass ratio, as a function of water depth and elevated load will be analysed, and the critical flow regimes will be identified for various leg diameters.

### **2.2.4 Step 4: Theoretical Investigation**

Theoretical investigation will be carried to understand the mathematics of jack-up VIV. The studies will produce mathematical response-based models for predicting VIV response of the jack-ups in steady uniform current, regular waves and regular waves with imposed current. Criteria for the occurrence of jack-up VIV in uniform current and regular waves will also be developed. Theoretical evaluation will start with the simple case of a single 2D cylinder, followed with four 2D cylinders in a rectangular configuration and subsequently jack-up with four cylindrical legs. The studies will cover the various modes of jack-up VIV, namely inline, crossflow and yaw VIV.

The importance of various parameters such as the mode shape, mass ratio, damping ratio in VIV suppression will be covered in the study. Empirical formulations will be proposed based on the above studies for verifying and predicting the jack-up VIV under the mentioned flow scenarios. The mathematical solutions will be validated by using physical experiments. Theoretical investigation will also be carried out on the suppression of Jack-up VIV. A mathematical model will be proposed for the application of leg fairings or other vortex suppression devices for various VIV modes. Design of leg fairing sections for practical application will be developed based on the theoretical studies. Formulations shall also be developed for calculating the additional yield and fatigue strength utilisation of the legs under jack-up VIV.

### 2.2.5 **Step 5: Experimental Investigation**

Experimental investigation will be carried out with a scaled jack-up model under various flow scenarios. Experiments involve primarily the measurement of the VIV response of the jack-ups exposed to uniform current and regular waves. The VIV of a jack-up under regular waves with imposed current and irregular waves will also be investigated. The effect of various water depths and mass ratios on the jack-up VIV will be investigated experimentally. The effect of the global heading of the jack-up and the local heading of the legs with respect to the direction of the flow, on the VIV response will be examined. The experimental investigation will also cover the effect of various leg designs on the jack-up VIV.

Prior to the experiments, the scaled model will be calibrated with mass tests, stiffness tests and free decay tests under various scenarios, towards verifying the jack-up mass properties, leg stiffness, natural frequency, added mass and hydrodynamic damping. Force tests will be carried out where the leg base shear due to hydrodynamic forces acting on the legs are measured. The physical phenomena such as drag amplification, lift amplification, transverse inertial loading will be studied based on the experimental results. The experimental data is also intended to serve as a reliable source for validation of mathematical models. The behaviour of the leg fairing designs developed and its efficacy in vortex suppression will be tested on the scaled model of the jack-up.

### 2.2.6 **Step 6: Numerical Investigation (CFD Simulations)**

The VIV of jack-ups will be further investigated by means of CFD, one of the widely accepted flow-based models. The fluid flow around the jack-up will be modelled, and the response and forces characteristics of the legs will be deduced by the numerical solution of Navier Stokes equations. The turbulence at high  $Re$  flows shall be modelled by using the shear-stress transport (SST) models, owing to their high reliability for adverse pressure gradient flows (Menter, 1996) and capability to capture laminar turbulent transition in the boundary layers (Benim *et al.*, 2007). 2D CFD and FSI simulations shall be carried out for the steady flow conditions. The numerical simulations will be carried out for various damped and undamped scenarios to study the effect of damping ratio on VIV response.

As one of the strengths of CFD simulation, the detailed vortex shedding patterns around the legs for various VIV modes, the corresponding oscillatory forces and the jack-up response shall be found from the numerical investigation. The modes of vortex shedding about the legs corresponding to various modes of jack-up VIV can be understood from the CFD results. The effect of damping ratios on the response characteristics of the jack-up, vortex synchronization among the legs, lift and drag amplification, jack-up added mass, hydrodynamic damping, and the self-limiting nature of the jack-up VIV will also be investigated.

### **2.2.7 Step 7: Structure Response, Yield and Fatigue Strength**

From the resulting response time history from the experiments, the amplitude response and frequency response of the jack-up will be studied for various flow scenarios; uniform current, regular waves, irregular waves and regular waves with imposed current. The effect of water depth, mass ratio, damping ratio, mass damping parameter and leg mode shape on the VIV response will be evaluated consequently. The response time history will reveal the response of the jack-up along all the three VIV modes; inline, crossflow and yaw. The added mass and damping of the jack-ups undergoing VIV will be analysed from the free decay and response test results.

The time series of the leg base shear will be studied to understand the vortex induced and inertial forces acting on the leg during various modes of jack-up VIV. The spanwise correlation and the amplification of the lift and drag forces will be evaluated from the time history of leg base shear. The vortex modes corresponding to various modes of VIV and the vortex synchronization among the legs can be understood by analysing the results of CFD. The effect of damping ratio, the scenario of undamped jack-up VIV and the force amplification due to VIV will also be studied from CFD results.

Based on the design data analysis of jack-ups, the trend in variation of natural periods with respect to water depths and leg diameter will be identified. The resulting responses will be converted to dynamic leg stresses to investigate the effect on the structural yield and fatigue strength of the platform. The cyclic stresses reflect the linear effect of lift forces, the effect of lift amplification, the inertial effects caused by the jack-up's dynamic motions and the additional bending moments due to large deflections. The increase in mean stresses due to drag amplification shall also be evaluated.

Fatigue life of the jack-ups under prolonged action of the environment shall be evaluated by choosing an appropriate SN curve.

### **2.2.8 Step 8: Suppression of Jack-up VIV**

A simplified mathematical model will be developed based on the principle of conservation of energy, which can be used to decide the optimum location and depth of the vortex suppression devices for the cylinders undergoing VIV in a uniform flow. Two newly developed leg fairing sections based on NACA0018 profiles will be tested on cylindrical legs of a Jack-up model in the uniform current, and the results will be compared with the predicted behaviour, particularly the effect of selected fairlead depth and location. The free decay tests will reveal the added mass and damping of the fairings, and the response test results will be used to study the effect of leg fairings on jack-up response. The VIV reduction achievable and the effect of fairings on the mean drag of the jack-up will also be ascertained from the test results. The weathervaning stability of both the fairing designs will be tested to verify the efficacy for practical applications.

### **2.2.9 Step 9: Discussion, Conclusions and Recommendations**

Detailed analysis and discussions based on the results obtained at the various stages of research will be carried out. The main conclusions drawn from the results of the present research will be presented in the thesis, recommendations for practical designs will be made for the offshore industry and future research will be proposed with potential problems identified. The research will culminate with design recommendations for the jack-ups, towards alleviating problems due to VIV.

## **2.3 Flow Chart of Research Methodology and Approach**

Figure 2-2 illustrates the research flow and approach adopted for the project.

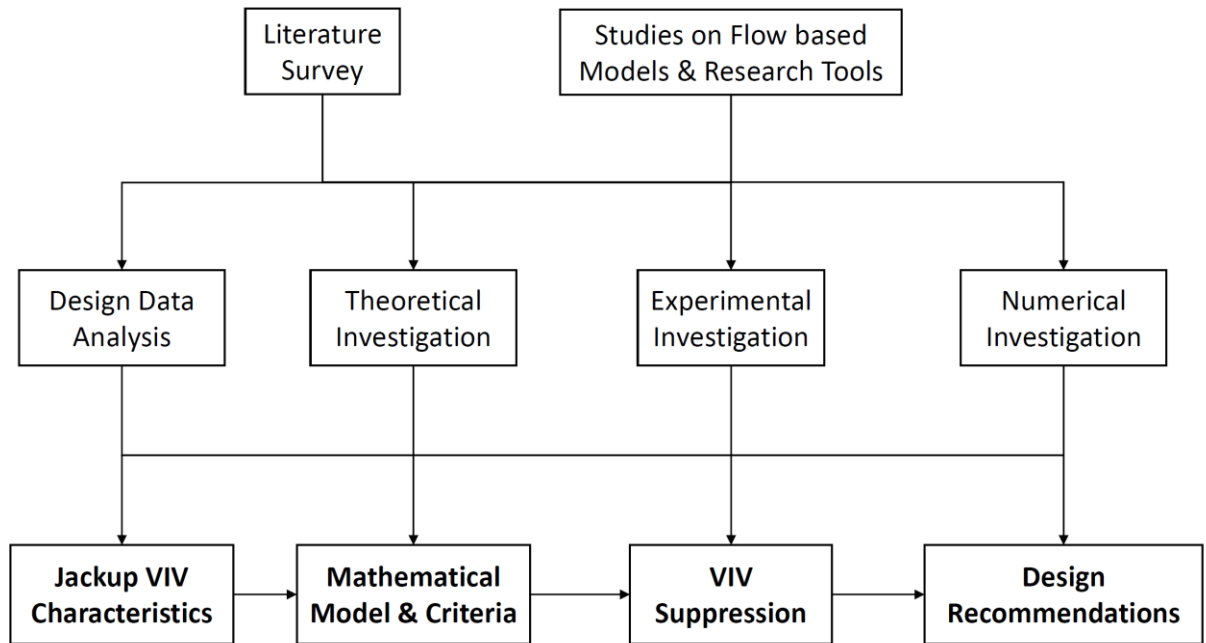


Figure 2-2: Research flow and approach

## Chapter 3. Literature Review

Flow around circular cylinders is an extensively researched subject all over the world. It is well known that alternate shedding of vortices about the cylinders due to flow separation causes VIV, which can lead to structural yield and fatigue failures. This chapter endeavours to comprehensively understand the fundamental aspects of VIV under various flow scenarios, experimental and numerical investigations on VIV, prediction models for VIV, structural dynamics of jack-ups and eventually the state of the art of jack-up VIV.

### 3.1 VIV of Multi-Cylinder Structures

Multi-cylinder structures like jacket platforms, semi submersibles, jack-ups, etc. are extensively used in marine and offshore applications. The spacing between the cylinders is a significant parameter for multi-cylinder VIV as the cylinders are strongly influenced by wake and proximity interference effects. Sumner (2010) presented an exhaustive review of literature on the flow around two identical circular cylinders in a steady flow, covering the three main configurations, namely tandem, side by side and staggered. Bearman (2011) has reviewed and summarised the recent research on VIV of isolated circular cylinders and circular cylinders in tandem arrangement.

Zdravkovich (1985) conducted extensive wind tunnel experiments with two identical cylinders in tandem, side by side and staggered arrangements. The investigation covered the proximity interference, wake interference and no interference regions as depicted in Figure 3-1. It was concluded that when the transverse pitch ratio was above 4, the coupling between cylinders disappeared and when the longitudinal pitch ratio was greater than 7, the wake interference gradually diminished. Wang et al. (2013) conducted an experimental study of the flow around four circular cylinders in square configuration and reconfirmed that depending on the pitch ratio, the inline flow could be broadly classified as shielding regime, shear layer reattachment regime and vortex impinging regime. It was observed that for transverse spacing ratios above 4, the four-cylinder array could be regarded as two isolated parallel rows of two cylinders in tandem. It was found that for large pitch ratios (greater than 5), the vortex shedding from all the four cylinders is fully synchronised with constant frequency and definite phase relationships.

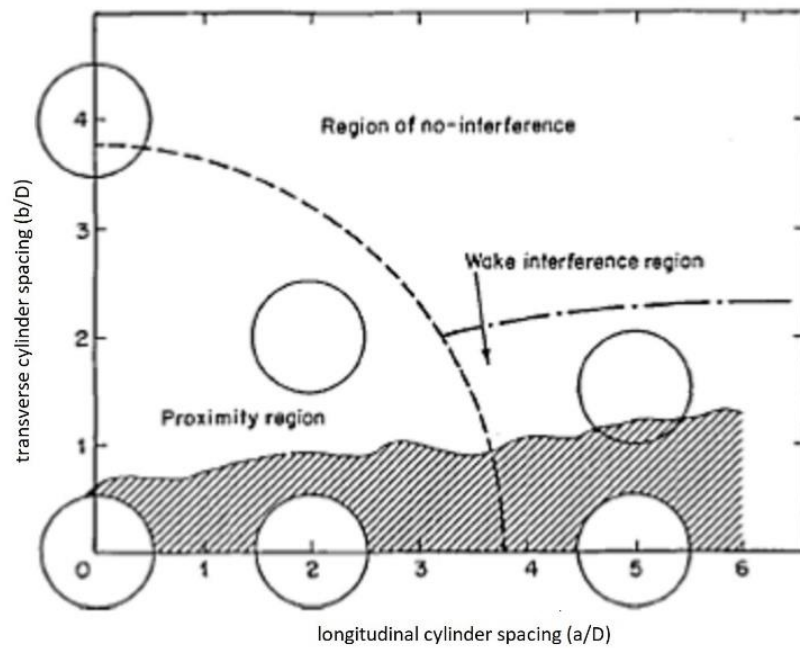


Figure 3-1: Cylinder interference regions (Zdravkovich, 1985)

Assi *et al.* (2010) studied the wake induced vibration (WIV) response of a downstream cylinder for various longitudinal pitch ratios and found that the downstream cylinder experienced vibrations with increasing amplitudes at higher reduced velocities for the pitch ratios lesser than 8. It was found that for pitch ratios greater than 8, the WIV progressively reduced and the response amplitude peak corresponded to that of VIV resonance. Jiang (2012) numerically studied flow induced crossflow vibrations of two tandem cylinders between two parallel walls and the effect of pitch ratios ranging from 1.1 to 10. It was found that the cylinders decouple and behave as two isolated cylinders for larger pitch ratios above 8.

Han *et al.* (2015b) numerically investigated the VIV of four uncoupled identical circular cylinders placed in a square arrangement subjected to uniform flow. It was found that dual resonance or cylinder synchronised vibrations along both inline and crossflow directions occurred during lock-in for a pitch ratio of 5. Zhao and Cheng (2012) performed a numerical simulation of VIV of four rigidly coupled square cylinders in a square configuration with a pitch ratio of 3. It was found that there are two modes of vortex shedding, symmetrical, with cylinders on either side shedding vortices symmetrically about the longitudinal centre line, and synchronised, with aggressive lock-in vibrations due to the synchronisation of vortex shedding about all the four cylinders.

Bearman (2011) states with reference to the study from Assi *et al.* (2010), that in a multi-cylinder arrangement, in addition to the VIV response the downstream cylinder experiences a wake-induced vibration caused by interactions between vortices shed from both cylinders. Figure 3-2 presented by him, originally from Assi demonstrates double peaks, in the rear cylinder response ( $\frac{A}{D} = \frac{y_o}{D}$ ); one at a reduced velocity of about 5 due to own vortex shedding and the other at a higher reduced velocity. It can be observed that the high reduced velocity peak decreases steadily as the separation is increased.

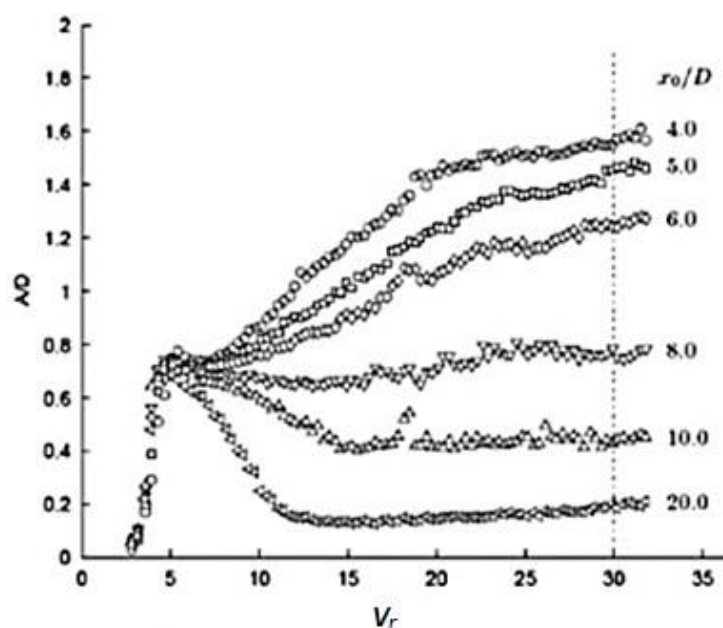


Figure 3-2: Crossflow response of the downstream cylinder for various longitudinal pitch ratios (Zdravkovich, 1985)

Bearman (2011) challenged the argument that the rear cylinder response experienced at higher reduced velocity is galloping on account of the transverse hydrodynamic stability of the cylinder and claimed that the phenomenon is another type of VIV.

### 3.2 Vortex Induced Motion

Floating multi-cylinder structures like semi-submersibles and TLPs are found to experience VIM, a low frequency equivalent of VIV. The mass ratio of unity and low slenderness ratio of the cylinders can be regarded as the main differences of VIM with the jack-up VIV. However, as published works are limited for the VIV of a jack-up, available literature on VIM and VIV of rigidly coupled multiple cylinders can be used to

draw relevant insights on the jack-up VIV. A comprehensive review of the research developments on VIM was presented by Fujarra et al. (2012). Gonçalves et al. (2011b) conducted experimental studies on VIM with a scaled model of the semisubmersible and found that inline, crossflow and yaw vibrations were experienced. Lock-in was observed for both the crossflow and yaw vibrations, and the later was named as vortex induced yaw motion (VIY). It was stated that VIY occurred when vortex shedding frequency about the columns approached the natural frequency of yaw of the semisubmersible.

Gonçalves et al. (2018a) conducted experiments on deep draft semi-submersible models to investigate the effects of the column shape and the surface roughness on VIM. It was found that the circular column experienced higher VIM amplitudes in both transverse and yaw motions and confirmed the existence of lock-in ranges for both these modes. The dynamic amplification of drag, lift and yaw moment coefficients were observed during lock-in. Gonçalves et al. (2011a) conducted VIV experiments with cantilevered bar and pivoted pendulum having low mass and aspect ratios and compared the results with the published literature on VIM to establish similarity between VIM and VIV. Similarity in trends and values were observed between both the phenomena, and it was noticed that higher aspect ratios experienced higher amplitudes due to enhanced vortex correlation.

### **3.3 VIV models**

The VIV analysis models can be divided into three types, 1) harmonic model predominantly for two-dimensional cases, 2) non-linear oscillator model based on Van der Pol equations and 3) CFD for complete solutions (Barltrop and Adams, 1991). In the harmonic model, the excitation is expressed in terms of the sinusoidal variation of a lift coefficient and any change in added mass with amplitude and frequency is neglected. It is assumed that at lock-in, the frequency of excitation matches with the natural frequency.

Vickery and Watkins (1964) derived the dependence of response amplitude on mass damping parameter (reduced damping) by considering the energy balance between excitation and damping at resonance, and presented conditions of similarity between model and prototype for VIV experiments. Griffin (1980) proposed an analytical model based on the assumption that the fluid forces are independent of the resonant

vibrations of the cylinder. The model predicted the maximum displacement as a function of mass damping parameter. The simplest analytical model (Blevins, 2001) even though does not incorporate the nonlinearities, serves as a reliable tool to develop the appropriate nondimensional parameters. The limitation of the harmonic model is that it cannot capture the self-limiting nature of VIV, which is overcome by other nonlinear oscillator models.

Sumer and Fredsøe (2006) developed a simplified harmonic model and found an expression for the maximum vibration amplitude ratio  $\left(\frac{y_o}{D}\right)$  as a function of the stability parameter ( $K_s = \pi^2 m^* \zeta$ ); for  $K_s > 5$  corresponding to  $\frac{y_o}{D} < 0.2$ ,

$$\frac{y_o}{D} = \frac{0.85}{K_s} \quad \text{Equation 3-1}$$

Further, for  $K_s < 5$  ( $\frac{y_o}{D} > 0.2$ ), the following empirical equation is proposed.

$$\frac{y_o}{D} = \frac{3}{K_s + 1.5} \quad \text{Equation 3-2}$$

The results were found to have reasonably good agreement with the experimental data as illustrated in Figure 3-3.

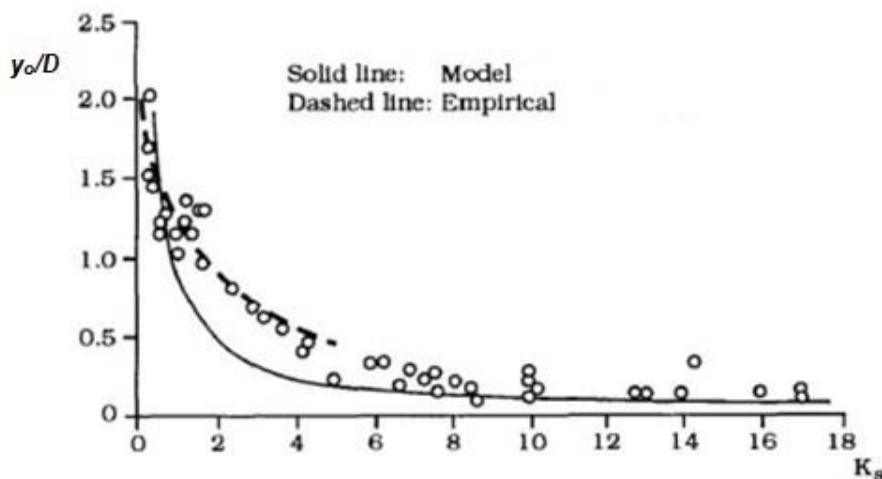


Figure 3-3: Comparison of the harmonic and empirical models with experimental data (Sumer and Fredsøe, 2006)

The simplest nonlinear model is the one which incorporates the amplitude dependence of the lift using a three term polynomial fit to the experimental data (Blevins and Burton, 1976). The polynomial fit captures the initial amplification of the lift coefficient with the response amplitude as well as subsequent decline and disappearance at larger amplitudes. The model represents the spanwise vortex correlation by a characteristic correlation length, which increases uniformly with the cylinder amplitude until the two-dimensional flow is achieved. The model is limited to the resonance of a single mode and  $Re$  range,  $2 \times 10^3$  to  $2 \times 10^5$  with a well formed vortex street. The self-limiting amplitude ratios of three typical mode shapes, rigid cylinder, pivoted cantilever and sine mode are predicted as 1, 1.4 and 1.2 respectively with the model. The aspect ratio is considered to affect the cylinder response only when the response is below the amplitude required for fully correlated flow. The model predicts the response as a function of the damping, mode shape, and aspect ratio. At amplitudes in the order of  $1D$ , the lift forces tend to zero producing a self-limiting amplitude independent of damping. There are also more complex wake oscillator models which represent the fluid behaviour as a nonlinear self-excited oscillator (Skop and Griffin, 1973; Iwan and Blevins, 1974).

Xu *et al.* (2012) state that there is no efficient analytical model for predicting pure inline VIV currently. A wake oscillator model capable of analysing the inline VIV is proposed with two different kinds of Van der Pol equations describing wake dynamics related to the symmetric vortex shedding in the first excitation region and alternate vortex shedding in the second one. The model is based on the assumption that the mean drag force provides fluid damping while the fluctuating drag excites the structure.

Verley (1982) proposed a simple mathematical model based on instantaneous Strouhal relationship to calculate the lift forces on a cylinder due to vortex shedding in oscillatory flows. The quasi-steady model was based on the assumption that the instantaneous velocity is zero at the start of every half cycle and could predict that the lift forces due to vortex shedding spread over several multiples of wave frequencies on either side of the fundamental frequency. Bearman *et al.* (1984) presented a quasi-steady model to predict the lift forces acting on cylinders in waves and oscillating flows. The model was based on a constant  $St$  of 0.20 and on the assumption that the lift coefficient is constant over the half cycle of flow. Experiments were conducted with circular cylinders in planar oscillatory flow, and the results agreed well with the quasi-

steady model at  $KC$  greater than 15. McConnell and Park (1982) presented a theoretical model for oscillatory flows which predicted three frequency components for the lift forces in terms of vortex shedding frequency ( $f_v$ ) and flow frequency ( $f_w$ ),  $f_v$ ,  $f_v+2f_w$  and  $f_v-2f_w$ .

Angrilli and Cossalter (1982) proposed a simplified harmonic model for the evaluation of the resonant crossflow VIV in regular waves and found that the response  $\left(\frac{y_D}{D}\right)$  is inversely proportional to the mass-damping parameter, similar to the steady flow. Hayashi *et al.* (2003) presented a simple mathematical model for VIV in regular waves, derived based on the equations of motions and demonstrated the importance of frequency ratio and the inverse proportionality of the amplitudes with the mass-damping or stability parameter. It was demonstrated that the VIV response of the cylinder is a function of its ratio of natural frequency to wave frequency,  $KC$  number and damping coefficient in air.

### 3.4 VIV Criteria

The harmonic model was used to develop criteria (Barltrop and Adams, 1991; Blevins, 2001) for the occurrence of VIV. It can be seen that various modes of VIV can be suppressed by increasing mass damping parameter above certain threshold values. The inline VIV can be prevented if the mass damping parameter is greater than 1.8 and for cylinders in air, crossflow VIV can be suppressed if the mass damping parameter is greater than about 25 (Barltrop and Adams, 1991). King *et al.* (1973) conducted experiments on modal piles in water and developed stability criteria for the occurrence of VIV; stability parameters 1.2 and 17 for inline and crossflow mode respectively. Sakai *et al.* (2002) conducted an experimental study with cantilever cylinders with various reduced damping and confirmed the criteria of reduced damping of 1.2 for the inline direction.

### 3.5 Fatigue Strength and VIV

Halse (1997) expressed serious concerns on the fatigue strength of the marine structures experiencing VIV, due to the latter's high frequency nature. Figure 3-4 shows the range of the fundamental lift frequency in the ocean environment along with the natural frequency of the offshore structures (Sumer and Fredsøe, 2006). It can be

seen that the fundamental lift frequency has a higher range than the wave frequency and can potentially excite fixed structures.

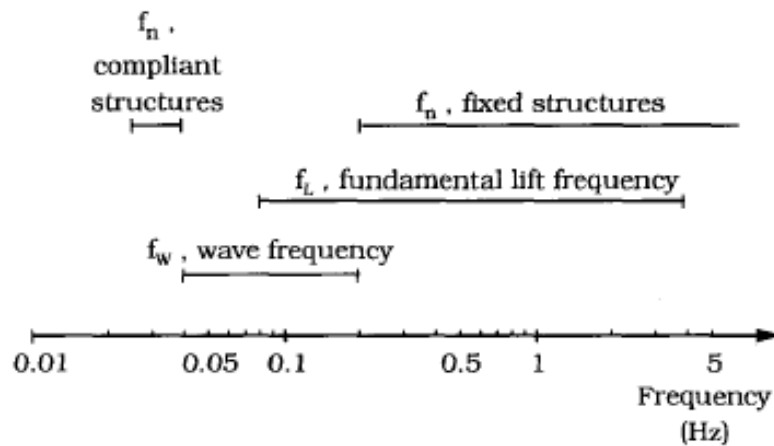


Figure 3-4: Typical natural and excitation frequencies of offshore structures (Sumer and Fredsøe, 2006)

Walker and Brazier (1980) stated based on experimental evidence that the fatigue rates are greater than predicted by conventional fatigue studies considering only direct wave loading. The authors carried out the fatigue analysis of a jacket structure and demonstrated that the effect of vortex shedding on the structural fatigue life is substantial. Wolfram (1991) highlights the limitation of the conventional fatigue analysis, which assumes that the vortex induced lift forces are not sufficiently coherent over the whole span of a tubular. It was demonstrated that the cumulative fatigue damage increased multifold with the consideration of vortex induced lift forces. Bearman (2011) cautions that the contribution of the inline VIV to the fatigue damage can also be substantial since it occurs at the double the shedding frequency. Xu *et al.* (2012) note that the inline VIV occurs frequently and may cause severe fatigue damages in slender marine structures.

### 3.6 Jack-up Platforms

Van Den Abeele and Vande Voorde (2011b) mention that jack-ups can be used as drilling rigs or service vessels to install offshore windmills and decommission platforms. Nicholls-Lee *et al.* (2013b) regard jack-ups as one of the most ecofriendly options for marine operations, concerning both noise generation and physical interaction with marine life. Harding (2013) and Thake (2005) acknowledge the importance of jack-ups

for installation processes requiring high accuracy like monopile and tidal turbine installations.

### 3.6.1 *Dynamics of Jack-ups*

Morandi *et al.* (1999) performed a comparative study of the jack-up and jacket platforms about strength and reliability. It was observed that dynamic effects could be ignored for the jacket as the maximum natural period did not exceed 2.5 s. It was argued that the critical failure probabilities of the jack-up are about an order of magnitude greater than the corresponding jacket, and hence the dynamic effects are unignorable. The natural period of the jack-ups is typically in the range of 5 to 15 seconds and are subject to dynamic amplification (resonance) with waves (ABS, 2017).

Johnson and Patel (1992) explain about the nonlinearities in jack-up response due to the variation in drag coefficient, wave current interactions, leg-hull/mud line interactions, nonlinear waves and P-delta effect. Time domain analysis is regarded as the ideal method for the structural analysis of a jack-up though quicker deterministic and spectral analysis methods are used with additional techniques to account for dynamics (Bartrop and Adams, 1991).

### 3.6.2 *Jack-up SDOF*

The first and second vibrational modes of the jack-up are the surge and sway modes, with the natural periods usually very close to each other. The third vibrational mode is the torsional or yaw mode, which is significant for the oblique environmental headings. In the SDOF analysis, the jack-up on its foundation is represented as an equivalent mass-spring-damper system. The periods of the fundamental modes are estimated based on an equivalent mass and equivalent spring. The equivalent mass is located at the centre of gravity (COG) of the elevated hull and consists of the mass of the hull and contributions from the mass and added mass of the legs. The equivalent spring represents the combined effect of the contributions from the flexural, shear and axial stiffnesses of the legs, and the stiffnesses of the leg to hull connections and leg foundations (PANEL OC-7, 2008). Figure 3-5 illustrates the schematic representation of the jack-up SDOF. The system is idealised as pinned at the footing level and supported by rollers at the hull level.

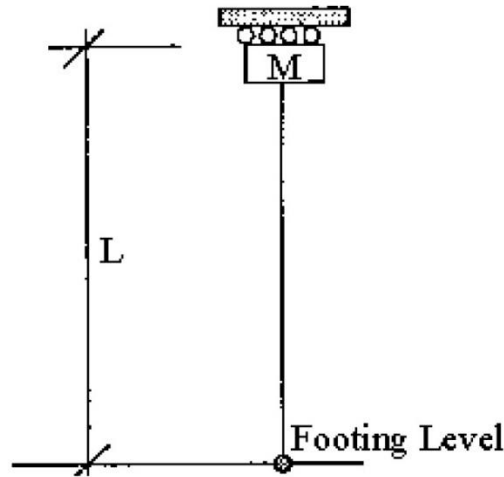


Figure 3-5: Jack-up SDOF Idealisation (PANEL OC-7, 2008)

The natural period is determined from the following equation applied to one leg.

$$T_N = 2\pi \sqrt{\frac{M_e}{K_e}}$$

Equation 3-3

where,  $T_N$  is the natural period and  $M_e$  and  $K_e$  are the effective mass and stiffness respectively associated with one leg. The SDOF method can be further used to predict dynamic responses in the respective modes, by means of appropriate pseudo static analysis considering equivalent excitation and equivalent damping. The SDOF method is not applied to the yaw mode presently (PANEL OC-7, 2008).

### 3.6.3 Jack-up Damping

Accurate consideration of the damping of the jack-up is highly important since the dynamic response and the fatigue life are highly dependent on it. For an offshore structure like jack-up, there are four kinds of damping: structural, material, foundation and fluid damping (Barltrop and Adams, 1991). Structural damping is generated by the friction between the parts of the structure while the material damping is due to internal energy dissipation. Foundation and fluid damping are due to energy dissipation into the soil and fluid respectively by the vibrating structure. Structural (including material) damping and foundation (soil) damping are usually determined using the free decay test in air and field measurements respectively. Fluid or hydrodynamic damping is usually accounted in the computations by using the relative velocity in the Morison equation.

The current regulations and guidelines (PANEL OC-7, 2008; DNV GL, 2015; ISO, 2016; ABS, 2017; ABS, 2018d; DNV GL, 2018) consider jack-up damping to comprise of structural, foundation and hydrodynamic damping, and prescribe typical contributions as percentage of critical damping. Alternatively, the foundation damping and hydrodynamic damping are also considered in the dynamic analysis by means of a nonlinear foundation model and relative velocity formulation in Morrison's equation respectively (PANEL OC-7, 2008). ABS (2017) recommends a total damping ratio not exceeding 7% for independent leg jack-ups, with typical maximum values of 2%, 2% and 3% for structural, foundation and hydrodynamic damping respectively. It is further recommended to preferably account the hydrodynamic damping directly in the fluid load formulations by considering the relative velocity.

#### 3.6.4 *Jack-up VIV*

Nicholls-Lee *et al.* (2013b) presented the results of a numerical analysis carried out for a jack-up barge operating in extreme tidal conditions. The analysis yielded potential large motions in the order of few metres during operation as a result of the VIV in strong currents. The authors mentioned about VIV in very high tidal currents and in water depths greater than 20m resulting in abortion of operations. Thake (2005) discussed about the installation of a large tidal current turbine done by a jack-up barge in high currents of 4 -6 knots, operating over long periods. It was highlighted that limitations were imposed on the operating envelope restricting the depth of installation and special fairings were fitted on the legs to lower the drag and suppress VIV.

Directorate-General for Research (2005) mentions the VIV faced by the jack-ups, and the need for larger jack-ups and special leg fairings to work in higher currents and greater depths. The official launch magazine of the conference; All-ENERGY 2013, reported another instance of Jack-up VIV where the installation of the foundation of a tidal turbine was aborted at the Orkney Islands, UK ([www.all-energy.co.uk](http://www.all-energy.co.uk), 2012). The installation was carried out by a specialised DP vessel as the experts were certain about the recurrence of the problem irrespective of the jack-up size. Harding (2013) mentions about the VIV caused due to the cyclic vortex shedding about the cylindrical legs, potentially subjecting the jack-up to aggressive resonant vibrations.

Van Den Abeele and Vande Voorde (2011b) state that offshore structures in shallow water depths (up to 100 metres) require a unique dedicated approach as they are

subjected to higher flow velocities, induced by both tides and waves. Morse (2011) identifies that most tidal sites are near land in relatively shallow waters, suitable for jack-up operations. Thake (2005) further discusses the uniqueness of the challenges associated with deep and fast-moving currents with regards to the stability and strength of jack-ups and about the lack of directly applicable design guidelines for such cases. The author calls for the development of new methods which can ensure adequate safety in the design against VIV and the need for accepted design criteria for certification to obtain liability insurance for operations.

### 3.6.5 *Jack-up Experimental Investigations*

Journee *et al.* (1988) carried out experiments with simplified jack-up models with cylindrical legs and investigated the hydrodynamic and structural nonlinearities in the FSI. The platform behaviour was investigated for wave frequencies in the vicinity of the resonance. Pinned support was provided at the leg footing and based on the elastic similarity, large diameter polyvinyl chloride (PVC) legs and small diameter copper legs were selected. It was observed that the model experienced wave forces not only at the wave frequency but also at its higher harmonics. This indicated a nonlinear behaviour that was attributed to nonlinearities like the quadratic drag. Bennett Jr and Patel (1989) tested the scaled model of a jack-up and confirmed that the behaviour was similar to a classical SDOF system. The 1: 48 scale model was tested in the elevated condition with the legs pinned at the bottom with ball joints. It was found that both the natural period and damping are higher in the presence of current. The Dynamic Amplification Factor (DAF) values for the random waves were found to be one-half that of the regular waves. Further, it was observed that the DAF values decreased with increasing significant wave height.

Johnson and Patel (1992) carried out the comparison of the test results of jack-up models to evaluate the DAF due to resonance. Two models with 1: 80 and 1: 48 scales were tested, and the legs were fabricated using plexiglass and acrylic rod material respectively to ensure elastic similarity. Tests with legs pinned and fixed at the bottom were performed, and test conditions included regular and random waves, and with and without current. Tests were conducted in deck fixed and free conditions. Figure 3-6 illustrates the 1:80 model with the instrumentation. It was found that a change from 2% to 10% damping approximately halved the DAF, and as wave height increased DAF reduced. Further, the presence of current was found to increase the loading on the

jack-up and as current speed increased DAF reduced. Significant damping (2% - 5%) was observed in the leg-hull interface during large displacements due to the slip friction. Further, surge was found to be the predominant motion when the heading was 0 degrees. The authors conclude that DAF can be reliably predicted by model tests.

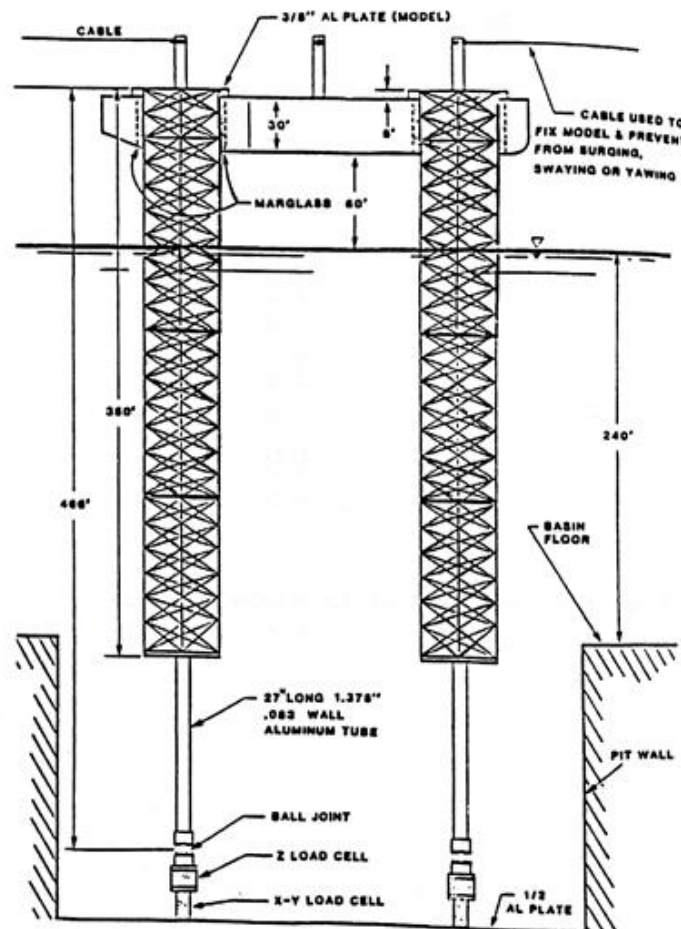


Figure 3-6: Typical jack-up model with instrumentation (Johnson and Patel, 1992)

Grundlehner (1997) performed tests with the restrained and free models to measure the quasi-static wave current loading and the dynamic response. The test set-up in the wave basin is summarised in Figure 3-7. The legs were supported by ball joints and were constructed of aluminium. A relatively large flexibility was introduced at the leg-hull interface to obtain overall stiffness similitude. The tests covered regular and irregular waves, presence and absence of current, normal and additional hull mass, uni-(2D) and multi-directional (3D) sea states. It was observed that the hydrodynamic damping increased with the increasing wavelength or height and with the presence of current. The hydrodynamic damping was found to increase further during resonance with regular waves. It was concluded that the relative velocity effects could be

expressed as a fixed (hydrodynamic) damping added to the structural damping; a total value of 5 to 7% for the design storm conditions.

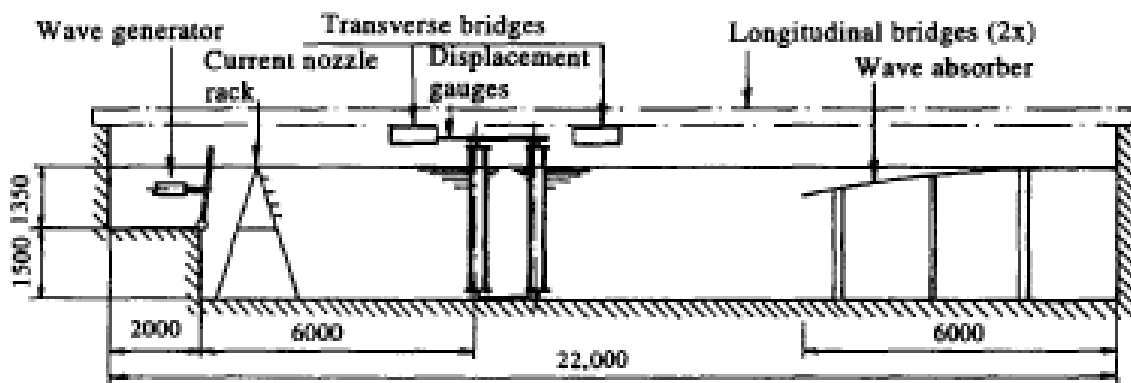


Figure 3-7: Experimental setup for the jack-up model in a wave basin (Grundlehner, 1997)

(Cammaert *et al.*, 2014) carried out model tests of an arctic jack-up with cylindrical legs to verify the ice loads and leg sheltering factor. It was observed that downstream legs in the wake of the upstream cylinder experienced sheltering and reduced loading.

### 3.6.6 Jack-up Numerical Investigations

Van Den Abeele and Vande Voorde (2011a) carried out the modal analysis of simplified jack-up barges with 3 – 6 legs to evaluate the susceptibility to VIV. It was found that the natural periods of the first two modes are between 1.5 – 2 s and the effect of the platform legs on the natural frequencies is limited, though the natural frequency increases with the number of legs. Further, VIV is found to be mainly driven by the leg diameter and flow conditions. The authors state that the problem warrants FSI simulations.

Van Den Abeele and Vande Voorde (2011b; 2011a) has pursued a Coupled Eulerian Lagrangian (CEL) approach to simulate jack-up movements in strong tidal flows. The fluid flow is modelled in a Eulerian framework where the water flows freely through a fixed mesh. The jack-up is modelled as a compliant structure in a Lagrangian formulation where the nodes move with the underlying material. The interaction between the fluid domain and the structure is enforced using general contact conditions, and the response is calculated by the principle of virtual work. It was found that though all designs are structurally adequate, the platform with six legs has much

higher stability, as evident from the transverse displacements of the top of the derrick illustrated in Figure 3-8.

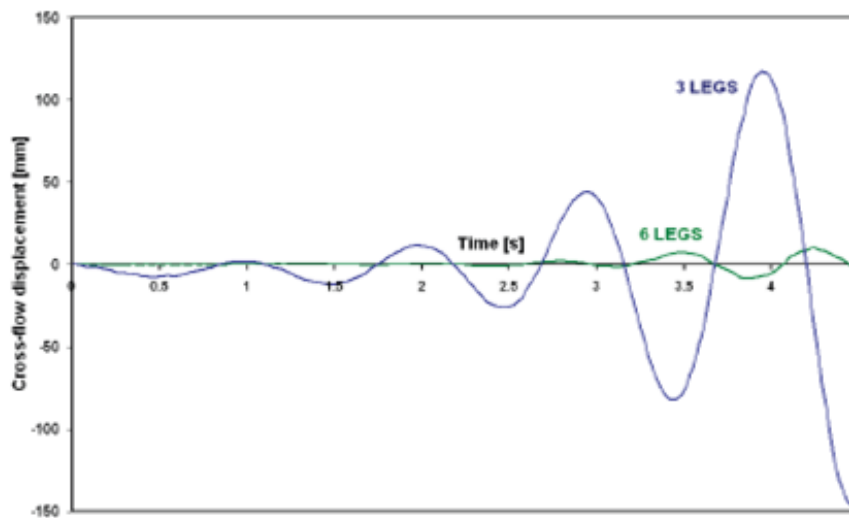


Figure 5: Cross-flow displacements of the derrick for both jack-up barges

Figure 3-8: Crossflow response of the derrick of jack-ups with 3 and 6 legs (Van Den Abeele and Vande Voorde, 2011a)

Johnson and Patel (1992) performed numerical simulations and correlated the results with that of the model test. The regular and random wave time domain analyses were carried out, and it was found that surge amplitude lags the passing wave by 60 to 70 degrees at the most critical wave period. In long period waves, there observed no phase difference, and in short period waves, the phase difference was approximately 180 degrees. Further, it was confirmed that the DAF could be reliably predicted from the model tests. Grundlehner (1997) confirmed using numerical simulations that the use of the relative velocity formulation agrees well with the measured fluid damping.

### 3.7 Fluid Structure Interaction Simulations of VIV

Han *et al.* (2015a) simulated the VIV of a circular cylinder at  $Re$  of 200 by using transient FSI computations by coupling ANSYS with Fluent. The inlet, side wall and outlet distance from the cylinder were at 5D, 5D and 15D respectively. Two way coupling technique was employed to transfer the fluid loads and structural response to ANSYS and Fluent respectively. Dynamic meshing with diffusion based smoothing was employed to update the computational mesh with the cylinder motion. The simulations captured the lock-in phenomenon successfully.

Botterill *et al.* (2013) investigated the effect of the drag crisis on the VIV of a circular cylinder using CFD and rigid body FSI simulations in ANSYS CFX. Large Eddy Simulations (LES) were performed for the stationary cylinder and the cylinder with two degrees of freedom (DOF). The inlet, side wall and outlet distances were at 4D, 4D and 14D from the cylinder respectively and the spanwise domain size was 2.5D. Hexagonal meshing was used with a  $y^+$  around 1 near the wall, and the total number of cells was around 2.5 million. It was found that the stationary cylinder simulation predicted the drag crisis reasonably well when corrected for the blockage effect. It was observed that cylinder motions increased the mean drag even in the critical regime and drag crisis increased the streamwise amplitude response due to the reduction in fluid damping.

### 3.8 Summary

Jack-ups with tubular legs are found to experience aggressive VIV. There is scarcely any published literature pertaining to theoretical, numerical, and experimental investigations on jack-up VIV. The present classification society rules and industry standards also do not seem to address jack-up VIV adequately. Nevertheless, the published literature on VIV of multi-cylinder structures, VIM, VIV analysis models and dynamics of jack-ups can be used effectively to draw relevant insights into the phenomenon of jack-up VIV.

## Chapter 4. VIV Assessment of Existing Jack-ups

Assessment of various working designs of jack-ups with circular cylindrical legs, provided by M/s Cybermarine Technologies is carried out to verify the vulnerability to VIV in currents and regular waves. The typical ranges of leg diameter, natural periods, practical flow regimes and mass ratio are derived from this analysis. The variation of leg diameter, natural periods and mass ratio, as a function of water depth are also analysed, and the critical flow regimes are identified for various leg diameters.

### 4.1 Design Load and Environment

The details of the working designs of jack-ups, provided by M/s Cybermarine Technologies Pte. Ltd., are displayed in Table 4-1. It can be seen that the cylindrical legs are being used for water depths up to 50 m, design current up to 10 knots and design waves up to 9.50 m. The elevated load of the jack-ups are in the range of 100 – 6700 t.

### 4.2 Leg Diameter

The variations of the leg diameter of the jack-up with respect to the water depth and elevated load are shown in Figure 4-1, a) and b) respectively. It can be observed that the leg diameter generally increases with the water depth and the elevated load. Figure 4-2 illustrates the leg diameter plotted against an empirical design parameter  $\sqrt{\frac{M_e g h}{\sigma_Y}}$ , square root of the product of elevated mass ( $M_e$ ), acceleration due to gravity ( $g$ ), water depth ( $h$ ) and inverse of yield strength ( $\sigma_Y$ ). It can be observed that the leg diameter fits well on a straight line as shown in the figure.

### 4.3 Mass Ratio

Table 4-2 displays the mass ratio (mass over the fluid mass displaced by the legs) of the jack-up designs. The leg penetration to the seabed is accounted in the calculation of effective water depth to consider the most onerous scenario of hard soil. The effective leg associated mass has contributions from the leg structural, added and entrapped masses apart from the elevated hull mass as explained in Section 4.4.3. It can be observed that the mass ratio ranges from 2.50 to 20.

The variation of mass ratio with effective water depth is illustrated in Figure 4-3. It can be seen that the mass ratio exponentially declines with increasing water depth and tends to converge towards a value of around 2 at water depths around 50m. The mass ratios are found to be much lower than the typical values in air, which can cause crossflow VIV with very high response amplitudes, large lock-in ranges and substantial force amplification (Khalak and Williamson, 1997a), making the jack-up practically inoperable. Further, low mass ratios are found to cause large natural frequency variation during lock-in, effectively increasing the excitation regime. Such low mass ratios are also found to cause inline VIV in water (King *et al.*, 1973).

Table 4-1: Jack-up design data from industry (M/s Cybermarine Technologies Pte. Ltd.)

Sr. No	Project Name	Water Depth (m)	Leg Diameter (m)	Elevated Load (t)	Design Current (knots)	Design Wave (m)	Wave Period (s)
1	12-1012	6.00	0.508	114	4.00	1.00	5.00
2	09-1027	12.50	0.53	170	4.00	1.00	3.00
3	08-1016	14.00	0.61	80	2.50	1.00	7.00
4	10-1046	18.00	0.61	155	4.00	1.00	3.00
5	12-1013	9.00	0.64	161	4.00	1.25	6.00
6	03-51	12.50	0.70	143	2.00	1.50	3.00
7	9931	12.00	0.70	170	4.00	1.00	6.00
8	9921	20.00	0.94	400	4.00	2.00	7.00
9	10-1024	15.00	0.95	450	5.00	1.00	3.00
10	05-1022	14.00	1.20	523.37	5.83	3.00	3.00
11	9928	18.00	1.40	619.51	6.00	2.00	7.00
12	07-1015A	15.00	1.45	1009	10.00	3.00	8.00
13	07-1015B	30.00	1.45	1009	2.50	1.50	8.00
14	12-1005	20.00	1.50	795	4.00	2.00	8.00
15	200046	10.00	1.60	674	4.00	2.50	6.00
16	07-1031	20.00	2.00	710	6.00	2.00	6.00
17	9724	40.00	2.00	710	6.00	2.00	4.00
18	13-1010A	40.00	2.20	1400	8.00	1.50	8.00
19	13-1010B	30.00	2.20	1400	8.00	1.50	8.00
20	09-4040	28.50	2.60	3402	2.00	9.50	10.50
21	07-5020	30.00	2.60	3402	2.00	5.00	10.00
22	11-4035	46.83	4.00	6744	3.30	9.14	10.00

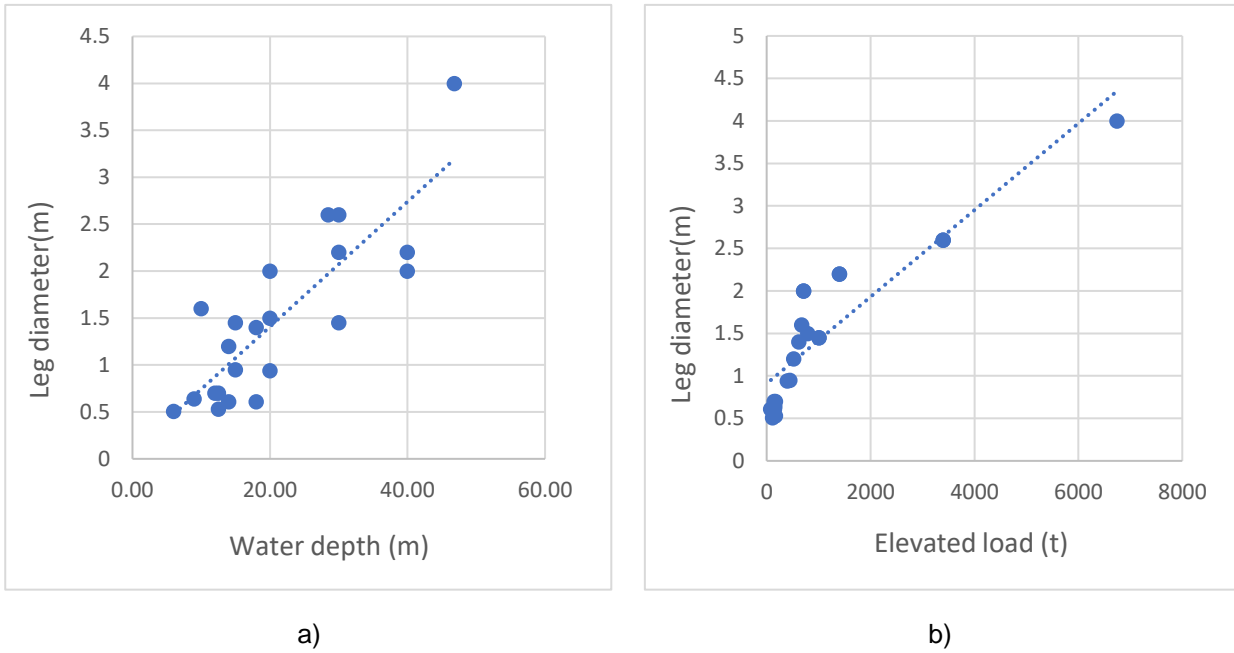


Figure 4-1: Variation of leg diameter, a) with water depth, b) with elevated load

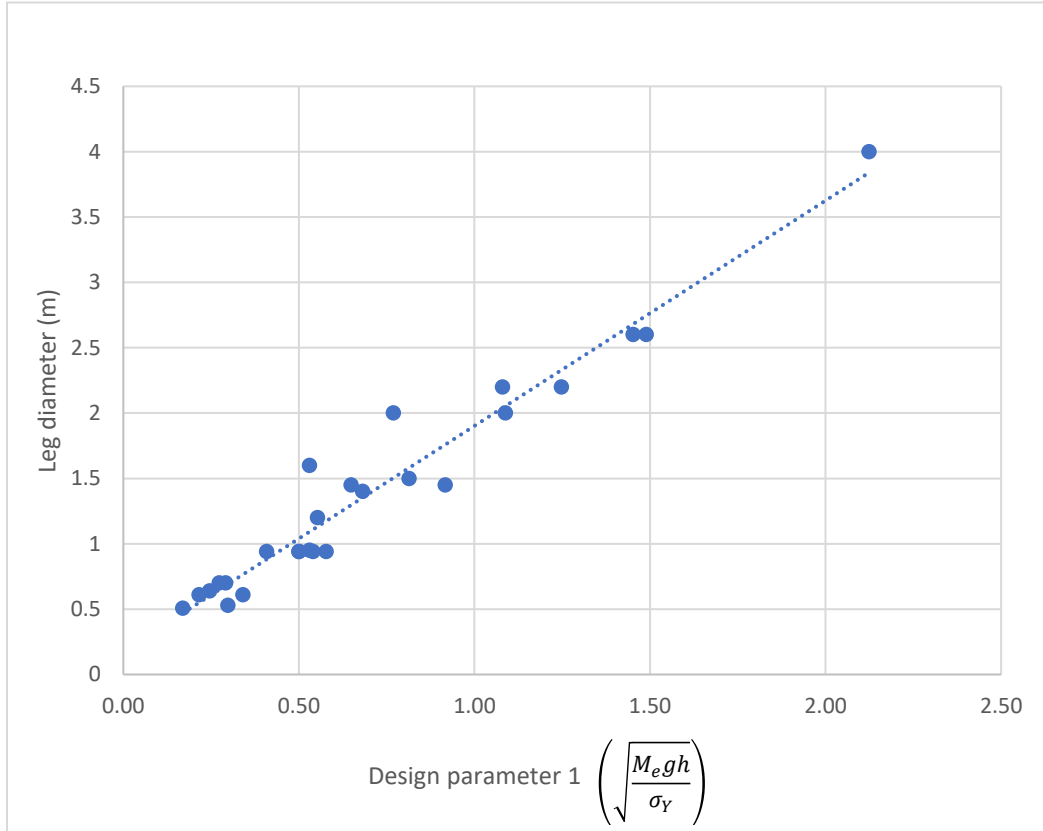


Figure 4-2: Leg diameter versus design parameter

Table 4-2: Effective mass ratio

Sr. No	Project Name	Effective Water Depth (m)	Effective Leg Associated Mass (t)	Effective Mass Ratio
1	12-1012	8.00	32.93	19.82
2	09-1027	14.50	50.48	15.40
3	08-1016	16.00	29.47	6.15
4	10-1046	20.00	51.45	8.59
5	12-1013	12.00	47.75	12.07
6	03-51	15.50	48.97	8.01
7	9931	17.00	55.00	8.20
8	9921 M	22.00	129.85	8.30
9	10-1024	17.00	137.06	11.10
10	05-1022	16.00	155.94	8.41
11	9928	20.00	211.77	6.71
12	07-1015A	21.00	321.09	9.03
13	07-1015B	33.00	322.15	5.77
14	12-1005	22.00	263.75	6.62
15	200046	14.00	218.60	7.58
16	07-1031	25.00	289.08	3.59
17	9724	42.00	356.50	2.64
18	13-1010A	43.00	537.95	3.21
19	13-1010B	33.00	534.09	4.15
20	09-4040	31.50	1198.68	6.99
21	07-5020	33.00	1142.00	6.36
22	11-4035	49.83	2616.59	4.08

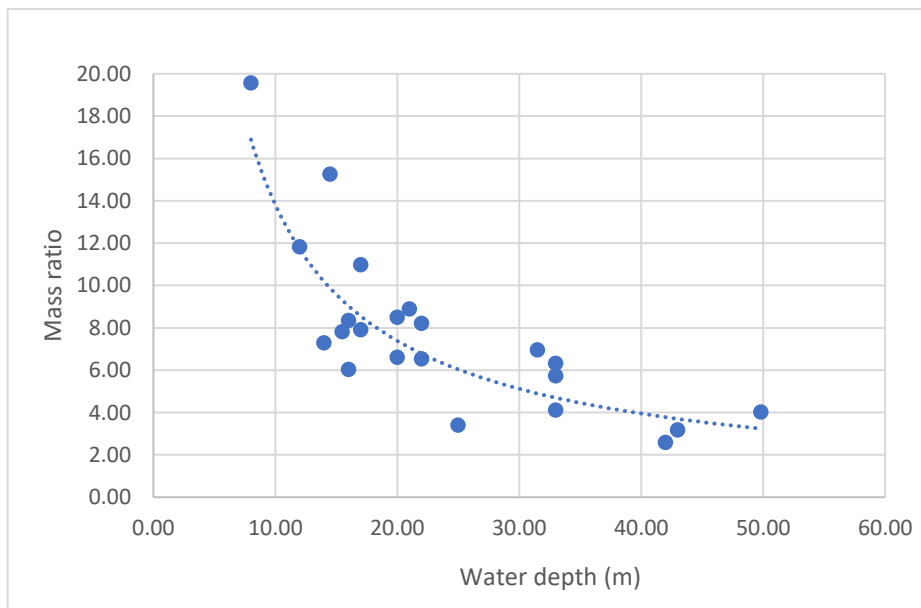


Figure 4-3: Variation of mass ratio with water depth

#### 4.4 Structural Dynamics

The structural and dynamic properties of the jack-up designs are summarised in Table 4-3. It can be observed that the yield strength of the leg materials can be as high as 7 t/cm<sup>2</sup>. The natural periods of surge, sway and yaw modes of the jack-ups are in the range of 1.5 to 6 s, which is sufficiently large to be excited by vortex shedding from the legs. The natural period is computed as explained in Section 4.4.6.

Table 4-3: Jack-up structural properties and natural periods

Sr. No	Project Name	Effective Leg Length (m)	Elevated Load (t)	No of Legs	Leg Material	Yield Stress (t/cm <sup>2</sup> )	T <sub>x</sub> (Surge) (s)	T <sub>y</sub> (Sway) (s)	T <sub>φ</sub> (Yaw) (s)
1	12-1012	10.13	114	4	MS	2.40	1.92	1.76	1.43
2	09-1027	16.40	170	4	MS	2.40	4.72	4.63	3.66
3	08-1016	18.90	80	4	MS	2.40	3.64	3.64	3.19
4	10-1046	21.90	155	4	MS	2.40	5.87	5.38	4.34
5	12-1013	14.25	161	4	MS	2.40	2.85	3.09	2.30
6	03-51	17.65	143	4	MS	2.40	3.39	2.83	2.50
7	9931	18.88	170	4	MS	2.40	3.44	4.20	3.09
8	9921 M	27.35	400	4	MS	2.40	4.86	4.86	3.91
9	10-1024	18.85	450	4	MS	2.40	3.33	3.33	2.49
10	05-1022	19.36	523.37	4	MS	2.40	2.28	2.28	1.85
11	9928	25.08	619.51	4	MS	2.40	3.14	3.14	2.47
12	07-1015A	26.83	1009	4	H36	3.60	3.29	3.29	2.56
13	07-1015B	38.08	1009	4	H36	3.60	5.89	5.89	4.60
14	12-1005	24.63	795	4	MS	2.40	3.03	3.03	2.38
15	200046	25.35	674	4	MS	2.40	2.94	2.94	2.62
16	07-1031	28.00	710	4	MS	2.40	2.35	2.35	1.97
17	9724	45.00	710	4	MS	2.40	5.60	5.60	4.90
18	13-1010A	53.33	1400	4	H36	3.60	5.72	5.72	4.88
19	13-1010B	43.33	1400	4	H36	3.60	4.09	4.09	3.48
20	09-4040	41.75	3402	4	JIS SM58	4.60	4.74	3.60	3.25
21	07-5020	43.25	3402	4	JIS SM59	4.60	4.89	3.71	3.32
22	11-4035	59.15	6744	4	ASTM A 514	7.00	4.54	5.13	4.43

#### 4.4.1 VIV Modes

Severe vibrations of jack-up barges due to vortex shedding about the cylindrical legs have led to instability and abortion of operations (Nicholls-Lee *et al.*, 2013a). Dynamic analysis of the global model of the jack-ups can reveal the modes of vibration having time periods which can be excited by vortex shedding. The first three modes of jack-up, derived from the dynamic analysis of a structural model are demonstrated in Figure 4-4. The first two modes are the surge (inline) and sway (crossflow) modes with nearly identical natural periods while the third one is the yaw (torsional) mode with a lower natural period.

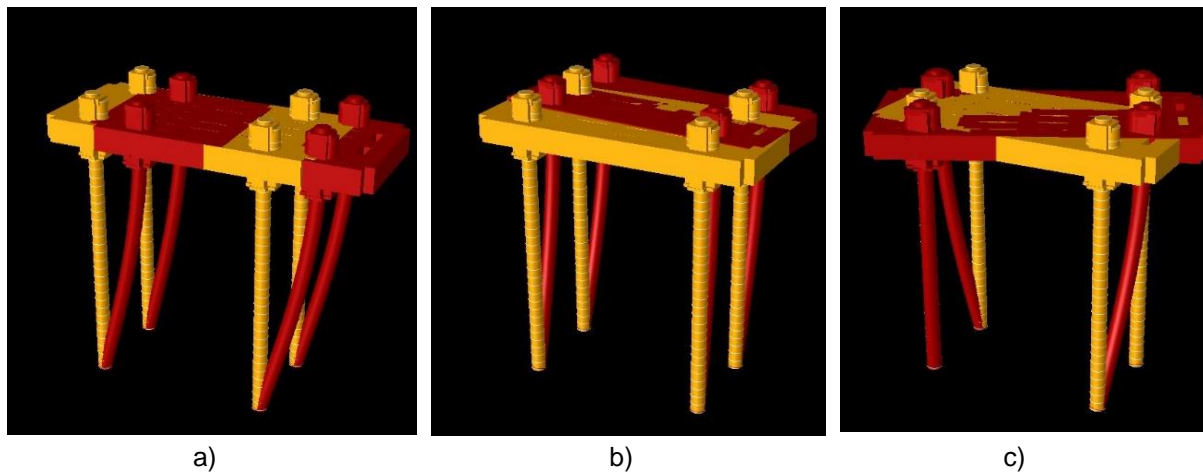


Figure 4-4: Jack-up VIV modes, a) in-line (surge), b) crossflow (sway), c) yaw (torsional)

#### 4.4.2 Leg Mode Shape

Figure 4-5 illustrates the typical leg mode shape. The jack-up is idealised as a single elevated mass at the hull level with the legs providing necessary stiffness along the various modes, as illustrated in Figure 3-5.

The mode shape or deflected profile of the leg of an independent leg type jack-up undergoing resonant vibration can be idealised as a generalised sinusoidal wave (PANEL OC-7, 2008).

For in-line vibration, based on Ramadasan *et al.* (2018),

$$x_o(z) = \left[ \frac{x_L}{A \sin(\kappa_L L + B) + E} \right] [A \sin(\kappa_L z + B) + E] \quad \text{Equation 4-1}$$

where  $x_o(z)$ ,  $x_L$ ,  $\kappa_L$ ,  $L$  represent the inline deflection profile, inline response in way of the hull interface, mode number and effective length of the leg respectively,  $A$ ,  $B$  and  $E$  are constants depending on boundary conditions, and  $z$  represents the elevation with respect to leg bottom with positive direction pointing upwards; at leg bottom,  $z = 0$  and at hull interface,  $z = L$ .

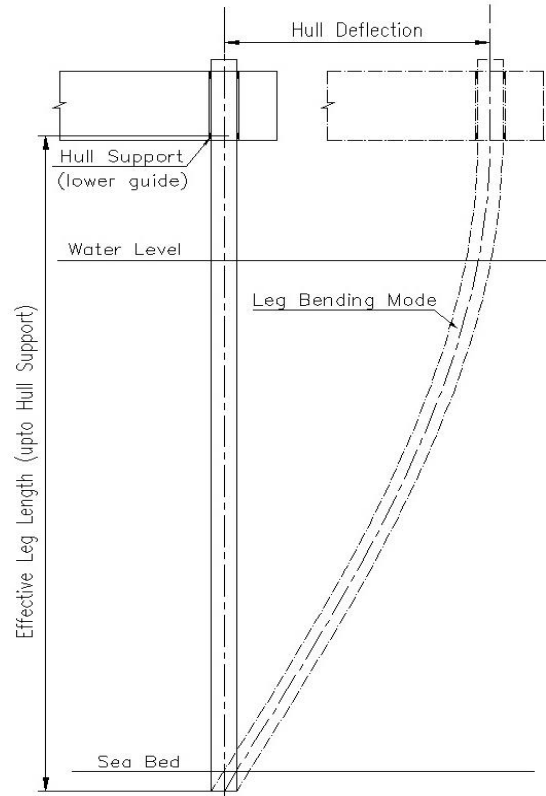


Figure 4-5: Jack-up leg mode shape

Similarly, for crossflow vibration (Ramadasan *et al.*, 2018),

$$y_o(z) = \left[ \frac{y_L}{A \sin(\kappa_L L + B) + E} \right] [A \sin(\kappa_L z + B) + E] \quad \text{Equation 4-2}$$

where  $y_o(z)$  and  $y_L$  represent the crossflow deflection profile and crossflow response in way of the hull interface respectively.

And for yaw vibration (Ramadasan *et al.*, 2019),

$$\phi_o(z) = \left[ \frac{\phi_L}{A \sin(\kappa_L L + B) + E} \right] [A \sin(\kappa_L z + B) + E] \quad \text{Equation 4-3}$$

where  $\phi_o(z)$  and  $\phi_L$  represent the yaw deflection profile and yaw response in way of the hull interface respectively

For small jack-ups, the leg is generally rigidly connected to the hull and for the independent cylindrical legs typically without the spud can, the leg footing can be considered as a pinned support (ABS, 2016).

Hence, the deflected leg profile can be considered as a perfect quarter sine wave and the coefficients,  $A = 1$ ,  $B = E = 0$  and mode number,  $\kappa_L = \frac{\pi}{2L}$ .

#### 4.4.3 Mass for Surge / Sway modes

The effective kinetic energy of the jack-up SDOF undergoing resonant crossflow vibration can be expressed based on Energy Principle (Bartrop and Adams, 1991) as,

$$\frac{1}{2} \omega^2 M_e y_e^2 = \int_0^L \frac{1}{2} \omega^2 m(z) [y_o(z)]^2 dz \quad \text{Equation 4-4}$$

where  $\omega$ ,  $M_e$ ,  $y_e$  and  $m(z)$  represent the vibration frequency, effective SDOF mass, effective SDOF crossflow displacement and the mass distribution along the leg respectively

The effective mass of the SDOF idealised at the leg-hull interface level can be derived from Equation 4-4 by considering Equation 4-2 and  $y_e = y_L$  as,

$$M_e = \int_0^L m(z) \left[ \frac{A \sin(\kappa_L z + B) + E}{A \sin(\kappa_L L + B) + E} \right]^2 dz \quad \text{Equation 4-5}$$

As evident from the above equation, the contributions from the individual mass components (elevated hull and leg structural, added and entrapped masses) depend on the leg mode shape and the respective locations along the leg.

##### 4.4.3.1 Elevated Hull Mass

The leg-hull interface usually has a reasonably high rotational stiffness to ensure almost a zero-slope condition at the legs. As the dynamic displacement of the elevated

hull is same as that in way of the leg-hull interface, the effective contribution of the elevated hull mass to the SDOF ( $M_{eH}$ ) shall be,

$$M_{eH} = M_H \quad \text{Equation 4-6}$$

where  $M_H$  represents the mass of the elevated hull.

#### 4.4.3.2 Leg Mass above Hull Interface

Similar to elevated hull mass, the effective SDOF mass contribution from the leg mass above hull interface ( $M_{eLaH}$ ),

$$M_{eLaH} = n_L M_{LaH} \quad \text{Equation 4-7}$$

where  $n_L$  and  $M_{LaH}$  represent the number of legs and mass of the leg above the hull interface respectively.

#### 4.4.3.3 Leg Mass below Hull Interface

The effective contribution to the SDOF from the leg mass below leg-hull interface ( $M_{eLbH}$ ) can be expressed based on Equation 4-5,

$$M_{eLbH} = \int_0^L n_L m_{LbH}(z) \left[ \frac{A \sin(\kappa_L z + B) + E}{A \sin(\kappa_L L + B) + E} \right]^2 dz \quad \text{Equation 4-8}$$

where  $m_{LbH}(z)$  represents the mass distribution of the leg below the hull interface.

#### 4.4.3.4 Leg Added Mass

Similarly,

$$M_{eAM} = \int_0^h n_L m_{LAM}(z) \left[ \frac{A \sin(\kappa_L z + B) + E}{A \sin(\kappa_L L + B) + E} \right]^2 dz \quad \text{Equation 4-9}$$

where  $M_{eAM}$ ,  $h$  and  $m_{LAM}(z)$  represent the effective contribution of the leg added mass to the SDOF, water depth and added mass distribution of the leg respectively.

## 4.4.3.5 Leg Entrapped Mass

Similarly, for nonbuoyant cylindrical legs, the effective entrapped mass shall be,

$$M_{eEM} = \int_0^h n_L m_{LEM}(z) \left[ \frac{A \sin(\kappa_L z + B) + E}{A \sin(\kappa_L L + B) + E} \right]^2 dz \quad \text{Equation 4-10}$$

where  $M_{eEM}$ , and  $m_{LEM}(z)$  represent the effective contribution of the leg entrapped mass to the SDOF and the entrapped mass distribution of the leg respectively.

## 4.4.3.6 SDOF Effective Mass

The effective SDOF mass can be expressed as the summation of the individual mass contributions.

$$M_e = M_H + M_{eLaH} + M_{eLbH} + M_{eAM} + M_{eEM} \quad \text{Equation 4-11}$$

For independent jack-ups, the deflected leg profile can be considered as a perfect quarter sine wave and  $A = 1$ ,  $B = E = 0$  and  $\kappa_L = \frac{\pi}{2L}$ .

Approximating a uniform leg structural mass, added mass and entrapped mass distribution,

$$M_{eLbH} = n_L m_{LbH} \frac{L}{2} \quad \text{Equation 4-12}$$

$$M_{eAM} = \frac{n_L m_{LAM} L}{2\pi} (2\kappa_L h - \sin(2\kappa_L h)) \quad \text{Equation 4-13}$$

$$M_{eEM} = \frac{n_L m_{LEM} L}{2\pi} (2\kappa_L h - \sin(2\kappa_L h)) \quad \text{Equation 4-14}$$

Considering the similarity and parallelism of legs, the effective SDOF mass per leg ( $M_{eL}$ ) for the sway mode shall be,

$$M_{eL} = \frac{M_e}{n_L} \quad \text{Equation 4-15}$$

Similarly, it can be demonstrated that the effective mass for the surge mode is identical to the sway mode.

#### 4.4.4 *Inertia for Yaw mode*

Similarly, the effective yaw inertia of the jack-up SDOF can be expressed as the summation from the individual mass contributions.

$$I_{e\phi} = M_H k_{\phi H}^2 + (n_L M_{LaH} + M_{eLbH} + M_{eAM} + M_{eEM}) \frac{(a^2 + b^2)}{4} = M_e k_{\phi}^2 \quad \text{Equation 4-16}$$

where  $I_{e\phi}$ ,  $a$ ,  $b$ ,  $k_{\phi H}^2$ , and  $k_{\phi}$  represent the effective yaw inertia of the SDOF, longitudinal distance between legs, transverse distance between legs, hull yaw radius of gyration and the SDOF yaw radius of gyration respectively.

#### 4.4.5 *Stiffness*

##### 4.4.5.1 *Surge / Sway Modes*

For a jack-up with independent legs, the leg can be assumed to be pinned to the seabed as the soil foundation rotational stiffness is usually very low (ABS, 2016). Further, neglecting the axial and shear effects of the legs, the effective lateral stiffness of the leg in way of the hull interface ( $K_{eL}$ ) can be expressed as per PANEL OC-7 (2008) as,

$$K_{eL} = \frac{3EI}{L^3} \frac{(1 - \frac{P}{P_{EL}})}{(1 + \frac{3EI}{L K_{rH}})} \quad \text{Equation 4-17}$$

where  $E$ ,  $I$ ,  $P$ ,  $P_{EL}$  and  $K_{rH}$  represent the modulus of elasticity, inertia of the leg section, the static vertical load acting on the leg, Euler's buckling load of the leg and rotational stiffness of the leg-hull interface respectively.

As the leg-hull interface stiffness can be regarded as a very high value which is generally true for coastal jack-ups, the effective stiffness of the leg can be,

$$K_{eL} = \frac{3EI}{L^3} \left(1 - \frac{P}{P_{EL}}\right) \quad \text{Equation 4-18}$$

The surge stiffness of the jack-up SDOF ( $K_{ex}$ ) shall be,

$$K_{ex} = n_L \frac{3EI_x}{L^3} \left(1 - \frac{P}{P_{ELx}}\right) \quad \text{Equation 4-19}$$

where  $I_x$  and  $P_{ELx}$  represent the effective leg section inertia and Euler buckling load along the inline direction.

Similarly, the sway stiffness of the jack-up SDOF ( $K_{ey}$ ) shall be,

$$K_{ey} = n_L \frac{3EI_y}{L^3} \left(1 - \frac{P}{P_{ELy}}\right) \quad \text{Equation 4-20}$$

where  $I_y$  and  $P_{ELy}$  represent the effective leg section inertia and Euler buckling load along crossflow direction.

#### 4.4.5.2 Yaw Mode

Similarly, the effective yaw stiffness ( $K_{e\phi}$ ) of the Jack-up SDOF idealization can be expressed as,

$$K_{e\phi} = K_{ex} \frac{(b^2)}{4} + K_{ey} \frac{(a^2)}{4} \quad \text{Equation 4-21}$$

### 4.4.6 Natural Frequency

#### 4.4.6.1 Surge/Sway

The surge natural frequency ( $\omega_{Nx}$ ) can be expressed as,

$$\omega_{Nx} = \sqrt{\frac{K_{ex}}{M_e}} = \sqrt{\frac{K_{eLx}}{M_{eL}}} \quad \text{Equation 4-22}$$

where  $K_{eLx}$  is the effective stiffness of the leg along the inline direction.

Similarly, the sway natural frequency ( $\omega_{Ny}$ ) shall be expressed as,

$$\omega_{Ny} = \sqrt{\frac{K_{ey}}{M_e}} = \sqrt{\frac{K_{eLy}}{M_{eL}}} \quad \text{Equation 4-23}$$

where  $K_{eLy}$  is the effective stiffness of the leg along the crossflow direction.

#### 4.4.6.2 Yaw

The yaw natural frequency ( $\omega_{N\phi}$ ) of the jack-up shall be expressed as,

$$\omega_{N\phi} = \sqrt{\frac{K_{e\phi}}{I_{e\phi}}} \quad \text{Equation 4-24}$$

The natural periods can be calculated from the respective natural frequencies. The natural periods of the jack-up designs derived from the natural frequency calculated using the above formulation is tabulated in Table 4-3. It can be observed that the natural period of the jack-up increase with increasing water depth.

Even though there is an increasing trend for natural periods with the increasing leg diameter, the same is less pronounced. It can be observed from Table 4-3 that the natural periods of the first two fundamental modes, surge and sway of the cylindrical legged jack-ups are in the range of 1.5 s – 6 s. The yaw mode is also found to have a natural period in the range of 1 to 5 s, very much excitable by the vortex shedding around the legs.

Figure 4-6 illustrates the variation of natural periods of the VIV modes with another empirical design parameter,  $\sqrt{\frac{M_e h^3}{D^4}}$ ; the square root of the product of elevated mass, cube of water depth and inverse of the fourth power of diameter ( $D$ ). It can be observed that the variation is fairly linear, and the empirical parameter can be considered as a governing parameter in determining the natural periods of jack-ups.

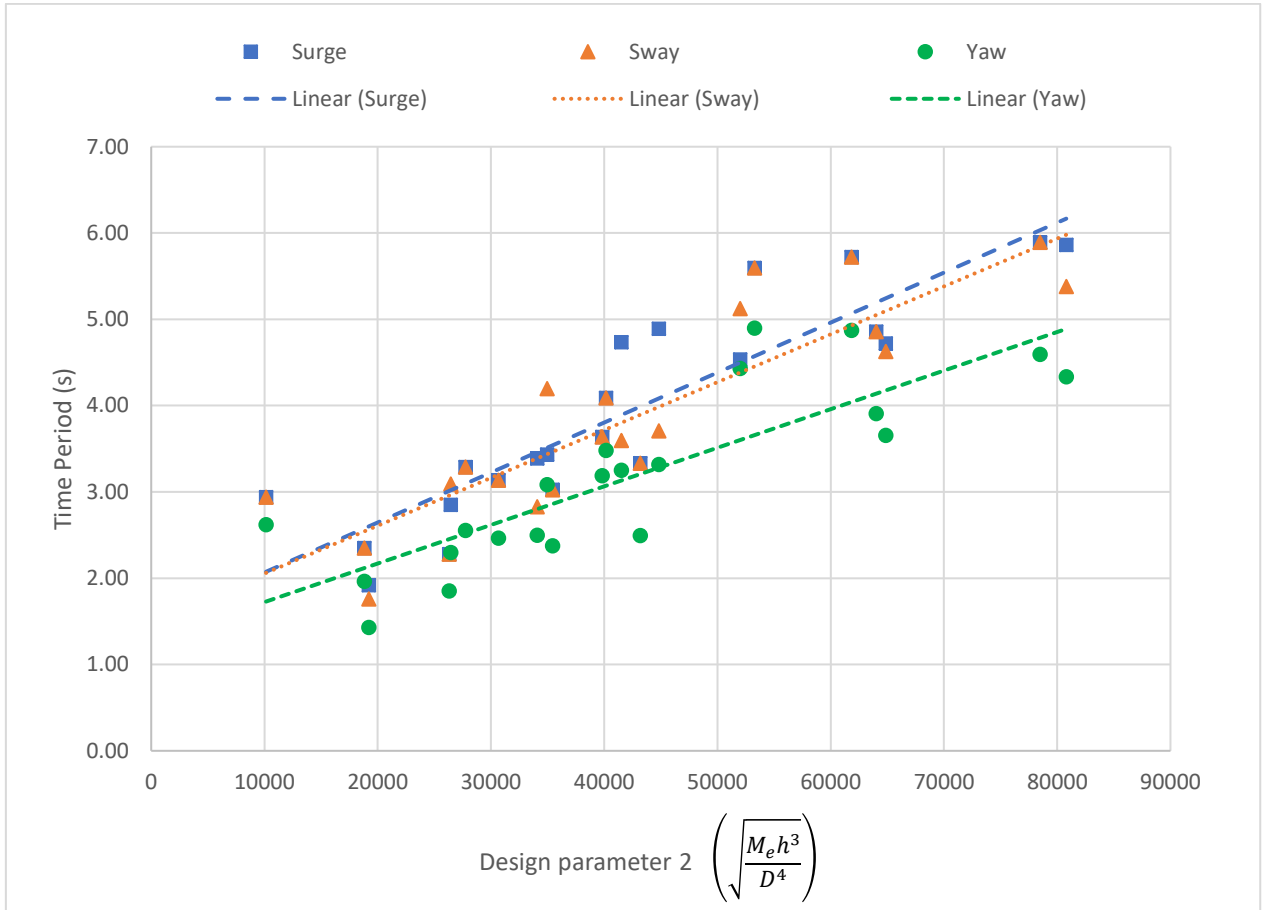


Figure 4-6: Variation of natural periods with design parameter

#### 4.5 Crossflow VIV in Current

The critical current speed at which vortex shedding or lift force can cause resonant crossflow VIV ( $U_{crit,y}$ ) of the jack-up can be found by equating the vortex shedding frequency with the crossflow natural frequency and using the Strouhal relationship.

$$U_{crit,y} = \frac{f_v D}{St} = \frac{\omega_{Ny} D}{2\pi St} \tag{Equation 4-25}$$

where  $f_v$ ,  $D$ ,  $St$  and  $\omega_{Ny}$  represent vortex shedding frequency, leg diameter, Strouhal number and crossflow natural frequency respectively.

The critical current speeds can be found by using the calculated natural frequency and selecting a suitable value of  $St$ . Table 4-4 contains the critical current speeds calculated for the jack-up designs for two global environmental headings, 0 degree and 90 degrees, considering a  $St$  of 0.20. The 0 and 90 degree headings correspond to head and beam environment respectively. The designs which are found to be excited

at a critical current less than the design current are highlighted with pink shade in the table.

It can be observed that most of the designs are vulnerable to crossflow VIV in currents having magnitudes lesser than the design limits. The  $Re$  of flow during crossflow VIV is found to be in the range of  $2 \times 10^5$  to  $7 \times 10^6$ , subcritical to transcritical regimes.

Table 4-4: Potential crossflow VIV excitation in current

Sr. No	Project Name	Critical current (90 degrees) (knots)	Critical current (0 degree) (knots)	$Re$ critical (90 degrees)	$Re$ critical (0 degree)	Design Current (knots)
1	12-1012	2.57	2.80	4.80E+05	5.23E+05	4.00
2	09-1027	1.09	1.11	2.13E+05	2.17E+05	4.00
3	08-1016	1.63	1.63	3.65E+05	3.65E+05	2.50
4	10-1046	1.01	1.10	2.27E+05	2.47E+05	4.00
5	12-1013	2.18	2.01	5.13E+05	4.73E+05	4.00
6	03-51	2.01	2.41	5.16E+05	6.19E+05	2.00
7	9931	1.98	1.62	5.09E+05	4.17E+05	4.00
8	9921	1.88	1.88	6.50E+05	6.50E+05	4.00
9	10-1024	2.77	2.77	9.67E+05	9.67E+05	5.00
10	05-1022	5.11	5.11	2.25E+06	2.25E+06	5.83
11	9928	4.34	4.34	2.23E+06	2.23E+06	6.00
12	07-1015A	4.28	4.28	2.28E+06	2.28E+06	10.00
13	07-1015B	2.39	2.39	1.27E+06	1.27E+06	2.50
14	12-1005	4.82	4.82	2.66E+06	2.66E+06	4.00
15	200046	5.29	5.29	3.11E+06	3.11E+06	4.00
16	07-1031	8.27	8.27	6.08E+06	6.08E+06	6.00
17	9724	3.47	3.47	2.55E+06	2.55E+06	6.00
18	13-1010A	3.74	3.74	3.02E+06	3.02E+06	8.00
19	13-1010B	5.23	5.23	4.23E+06	4.23E+06	8.00
20	09-4040	5.34	7.03	5.10E+06	6.71E+06	2.00
21	07-5020	5.16	6.81	4.93E+06	6.51E+06	2.00
22	11-4035	8.57	7.58	1.26E+07	1.11E+07	3.30

#### 4.6 Crossflow VIV in Regular Waves

The critical wave periods ( $T_{W,crit,y}$ ) can be found by equating the lift frequency in the waves to the crossflow natural frequency of the jack-up, where lift frequency is a function of the  $KC$  number ( $KC$ ) of the flow. As the lift frequency has its principal component at double the wave frequency for the practical  $KC$  range of 4 – 16

(Williamson, 1985), the critical wave period can be considered as twice the natural period,

$$T_{W,crit,y} = 2T_L = 2T_{Ny} \quad \text{Equation 4-26}$$

where  $T_L$  and  $T_{Ny}$  represent the lift period and the crossflow natural period respectively.

The critical wave heights ( $H_{W,crit}$ ) can be calculated corresponding to the  $KC$  range by the relationship,

$$H_{W,crit} = \frac{KC D \tanh(\kappa_W h)}{\pi} \quad \text{Equation 4-27}$$

where  $KC$  and  $\kappa_W$  represent the  $KC$  number and wave number respectively.

Table 4-5 and Table 4-6 contain the critical regular waves calculated for the jack-up designs for two global headings, 0 and 90 degrees respectively considering a  $KC$  range of 4 - 16. The designs which are found to be excited by waves less than the design waves are highlighted with pink shade in the table.

It can be observed that most of the designs are vulnerable to crossflow VIV in regular waves lesser than the design limits. The  $Re$  of flow during crossflow VIV is found to be in the range of  $8.5 \times 10^4$  to  $9.5 \times 10^6$ , subcritical to transcritical regimes. It can be observed that the critical  $KC$  numbers for the jack-up VIV are in the range of 4 – 13.

#### 4.7 Inline VIV in Current

The critical current speed at which oscillatory drag force can cause inline VIV ( $U_{crit,x}$ ) of the jack-up is found by equating the oscillatory drag frequency with the inline natural frequency and using the Strouhal relationship.

As the drag force oscillates at twice the vortex shedding frequency,

$$U_{crit,x} = \frac{f_v D}{2 St} = \frac{\omega_{Nx} D}{4\pi St} \quad \text{Equation 4-28}$$

where  $\omega_{Nx}$  represents the inline natural frequency of the jack-up.

Table 4-5: Potential crossflow VIV excitation in regular waves, 90-degree heading

Sr. No	Project Name	Critical Wave Period (s)	Critical Wave (KC=4) (m)	Re (KC = 4)	Critical Max Wave (KC<=16) (m)	Re Max wave	KC Max wave	Design Wave (m)
1	12-1012	3.84	0.61	1.92E+05	1.00	3.16E+05	6.58	1.00
2	09-1027	9.44	0.46	8.50E+04	1.00	1.85E+05	8.71	1.00
3	08-1016	7.28	0.66	1.46E+05	1.00	2.22E+05	6.07	1.00
4	10-1046	11.73	0.51	9.06E+04	1.00	1.76E+05	7.78	1.00
5	12-1013	5.70	0.70	2.05E+05	1.25	3.66E+05	7.13	1.25
6	03-51	6.78	0.76	2.07E+05	1.50	4.06E+05	7.86	1.50
7	9931	6.87	0.75	2.04E+05	1.00	2.72E+05	5.35	1.00
8	9921	9.72	0.95	2.60E+05	2.00	5.48E+05	8.44	2.00
9	10-1024	6.67	1.09	3.87E+05	NA	NA	NA	1.00
10	05-1022	4.56	1.51	9.01E+05	3.00	1.79E+06	7.92	3.00
11	9928	6.28	1.71	8.92E+05	2.00	1.05E+06	4.69	2.00
12	07-1015A	6.58	1.68	9.13E+05	3.00	1.63E+06	7.14	3.00
13	07-1015B	11.78	1.47	5.10E+05	1.50	5.20E+05	4.08	1.50
14	12-1005	6.05	1.87	1.06E+06	2.00	1.14E+06	4.28	2.00
15	200046	5.88	1.77	1.24E+06	2.50	1.75E+06	5.64	2.50
16	07-1031	4.70	2.54	2.43E+06	NA	NA	NA	2.00
17	9724	11.19	2.27	1.02E+06	NA	NA	NA	2.00
18	13-1010A	11.44	2.48	1.21E+06	NA	NA	NA	1.50
19	13-1010B	8.18	2.68	1.69E+06	NA	NA	NA	1.50
20	09-4040	9.47	2.95	2.04E+06	9.50	6.56E+06	12.86	9.50
21	07-5020	9.79	2.94	1.97E+06	5.00	3.35E+06	6.80	5.00
22	11-4035	9.07	5.00	5.04E+06	9.14	9.21E+06	7.32	9.14

Table 4-7 contains the critical speeds calculated for the jack-up designs for two global headings, 0 degree and 90 degrees considering a  $St$  of 0.20. The designs which are found to be excited at a critical current speed less than the design current are highlighted with pink shade in the table. It can be observed that most of the designs are vulnerable to inline VIV in currents lesser than the design limits. The  $Re$  of flow during inline VIV is found to be in the range  $1 \times 10^5$  to  $3.5 \times 10^6$ , subcritical to upper transitional regimes.

The scenario of inline VIV in regular waves is not considered for the analysis as principal inline frequency component is the wave frequency itself and the inline vibrations are observed to occur at this frequency (Blevins, 2001).

Table 4-6: Potential crossflow VIV excitation in regular waves, 0-degree heading

Sr. No	Project Name	Critical Wave Period (s)	Critical Wave (KC=4) (m)	Re (KC = 4)	Critical Max Wave (KC<=16) (m)	Re Max wave	KC Max wave	Design Wave (m)
1	12-1012	3.53	0.62	2.09E+05	1.00	3.35E+05	6.41	1.00
2	09-1027	9.26	0.47	8.67E+04	1.00	1.86E+05	8.58	1.00
3	08-1016	7.28	0.66	1.46E+05	1.00	2.22E+05	6.07	1.00
4	10-1046	10.76	0.55	9.88E+04	1.00	1.80E+05	7.28	1.00
5	12-1013	6.19	0.67	1.89E+05	1.25	3.54E+05	7.49	1.25
6	03-51	5.66	0.83	2.47E+05	1.50	4.46E+05	7.21	1.50
7	9931	8.39	0.65	1.67E+05	1.00	2.55E+05	6.12	1.00
8	9921	9.72	0.95	2.60E+05	2.00	5.48E+05	8.44	2.00
9	10-1024	6.67	1.09	3.87E+05	NA	NA	NA	1.00
10	05-1022	4.56	1.51	9.01E+05	3.00	1.79E+06	7.92	3.00
11	9928	6.28	1.71	8.92E+05	2.00	1.05E+06	4.69	2.00
12	07-1015A	6.58	1.68	9.13E+05	3.00	1.63E+06	7.14	3.00
13	07-1015B	11.78	1.47	5.10E+05	1.50	5.20E+05	4.08	1.50
14	12-1005	6.05	1.87	1.06E+06	2.00	1.14E+06	4.28	2.00
15	200046	5.88	1.77	1.24E+06	2.50	1.75E+06	5.64	2.50
16	07-1031	4.70	2.54	2.43E+06	NA	NA	NA	2.00
17	9724	11.19	2.27	1.02E+06	NA	NA	NA	2.00
18	13-1010A	11.44	2.48	1.21E+06	NA	NA	NA	1.50
19	13-1010B	8.18	2.68	1.69E+06	NA	NA	NA	1.50
20	09-4040	7.19	3.24	2.68E+06	9.50	7.87E+06	11.73	9.50
21	07-5020	7.42	3.24	2.60E+06	5.00	4.02E+06	6.18	5.00
22	11-4035	10.25	4.86	4.46E+06	9.14	8.38E+06	7.52	9.14

#### 4.8 Yaw VIV in Current

The critical current speed at which lift force can cause yaw VIV ( $U_{crit,\phi}$ ) of the jack-up is found by equating the vortex shedding frequency with the yaw natural frequency and using the Strouhal relationship,

$$U_{crit,\phi} = \frac{f_v D}{St} = \frac{\omega_{N\phi} D}{2\pi St} \quad \text{Equation 4-29}$$

where  $\omega_{N\phi}$  represents the yaw natural frequency.

Table 4-8 contains the critical speeds calculated for the jack-up designs considering a  $St$  of 0.20. The designs which are found to be excited at a critical current speed less than the design current are highlighted with pink shade in the table. It can be observed that most of the designs are vulnerable to yaw VIV in currents having magnitudes lesser than the design limits. The  $Re$  during yaw VIV is found to be in the range 2.5 x

$10^5 - 5 \times 10^6$ , subcritical to transcritical regimes. Further, the critical speed for the yaw VIV is found to be independent of the heading directions.

Table 4-7: Potential inline VIV excitation in current

Sr. No	Project Name	Critical current (0 degree) (knots)	Critical current (90 degrees) (knots)	Re critical (0 degree)	Re critical (90 degrees)	Design Current (knots)
1	12-1012	1.29	1.40	2.40E+05	2.61E+05	4.00
2	09-1027	0.55	0.56	1.06E+05	1.08E+05	4.00
3	08-1016	0.81	0.81	1.83E+05	1.83E+05	2.50
4	10-1046	0.51	0.55	1.13E+05	1.23E+05	4.00
5	12-1013	1.09	1.01	2.56E+05	2.36E+05	4.00
6	03-51	1.00	1.20	2.58E+05	3.09E+05	2.00
7	9931	0.99	0.81	2.55E+05	2.08E+05	4.00
8	9921 M	0.94	0.94	3.25E+05	3.25E+05	4.00
9	10-1024	1.38	1.38	4.83E+05	4.83E+05	5.00
10	05-1022	2.56	2.56	1.13E+06	1.13E+06	5.83
11	9928	2.17	2.17	1.12E+06	1.12E+06	6.00
12	07-1015A	2.14	2.14	1.14E+06	1.14E+06	10.00
13	07-1015B	1.20	1.20	6.37E+05	6.37E+05	2.50
14	12-1005	2.41	2.41	1.33E+06	1.33E+06	4.00
15	200046	2.64	2.64	1.55E+06	1.55E+06	4.00
16	07-1031	4.14	4.14	3.04E+06	3.04E+06	6.00
17	9724	1.74	1.74	1.28E+06	1.28E+06	6.00
18	13-1010A	1.87	1.87	1.51E+06	1.51E+06	8.00
19	13-1010B	2.61	2.61	2.11E+06	2.11E+06	8.00
20	09-4040	2.67	3.51	2.55E+06	3.36E+06	2.00
21	07-5020	2.58	3.41	2.47E+06	3.25E+06	2.00
22	11-4035	4.28	3.79	6.30E+06	5.57E+06	3.30

The designs are not analysed for yaw VIV due to inline excitation since the magnitude of the oscillatory drag is considerably lesser than the lift. Further, based on the studies on the VIM of multi-cylinder structures, it can be inferred that the yaw oscillations are due to lift excitation (Gonçalves *et al.*, 2011b).

#### 4.9 Yaw VIV in Regular Waves

The critical wave periods ( $T_{W,crit,\phi}$ ) can be found by equating the lift frequency in the waves to the yaw natural frequency of the jack-up. For the practical  $KC$  range of 4 – 16, the lift frequency has its principal component at double the wave frequency. Hence the critical wave period can be considered as twice the natural period,

$$T_{W,crit,\phi} = 2T_L = 2T_{N\phi}$$

Equation 4-30

where  $T_{N\phi}$  represents the yaw natural period of the jack-up.

Table 4-8: Potential yaw VIV excitation in current

Sr. No	Project Name	Critical current (knots)	Re critical	Design Current (knots)
1	12-1012	3.45	6.45E+05	4.00
2	09-1027	1.41	2.74E+05	4.00
3	08-1016	1.86	4.17E+05	2.50
4	10-1046	1.37	3.06E+05	4.00
5	12-1013	2.71	6.36E+05	4.00
6	03-51	2.72	7.00E+05	2.00
7	9931	2.20	5.67E+05	4.00
8	9921 M	2.34	8.08E+05	4.00
9	10-1024	3.70	1.29E+06	5.00
10	05-1022	6.30	2.78E+06	5.83
11	9928	5.52	2.84E+06	6.00
12	07-1015A	5.51	2.94E+06	10.00
13	07-1015B	3.07	1.63E+06	2.50
14	12-1005	6.13	3.38E+06	4.00
15	200046	5.93	3.49E+06	4.00
16	07-1031	9.89	7.26E+06	6.00
17	9724	3.97	2.92E+06	6.00
18	13-1010A	4.39	3.55E+06	8.00
19	13-1010B	6.14	4.97E+06	8.00
20	09-4040	7.77	7.42E+06	2.00
21	07-5020	7.61	7.27E+06	2.00
22	11-4035	8.77	1.29E+07	3.30

The critical wave heights can be calculated corresponding to the mentioned  $KC$  range by using Equation 4-27. Table 4-9 contains the critical regular waves calculated for the jack-up designs considering a  $KC$  range, 4 - 16. The designs which are found to be excited by waves less than the design waves are highlighted with pink shade in the table.

It can be observed that many of the designs are vulnerable to yaw VIV also in regular waves within the design limits. The critical waves for the yaw VIV are found to be independent of the wave heading. The  $Re$  of flow during crossflow VIV is found to be

in the range  $1 \times 10^5 - 5.5 \times 10^6$ , subcritical to transcritical regimes. The critical  $KC$  numbers for yaw VIV are in the range 4 to 12.

Table 4-9: Potential yaw VIV excitation in regular waves

Sr. No	Project Name	Critical Wave Period (s)	Critical Wave ( $KC=4$ ) (m)	$Re$ ( $KC = 4$ )	Critical Max Wave ( $KC \leq 16$ ) (m)	$Re$ , Max wave	$KC$ Max wave
1	12-1012	2.86	0.64	2.58E+05	1.00	4.01E+05	6.22
2	09-1027	7.31	0.55	1.10E+05	1.00	1.99E+05	7.25
3	08-1016	6.38	0.71	1.67E+05	1.00	2.36E+05	5.66
4	10-1046	8.67	0.64	1.23E+05	1.00	1.92E+05	6.25
5	12-1013	4.60	0.77	2.55E+05	1.25	4.12E+05	6.47
6	03-51	5.00	0.86	2.80E+05	1.50	4.86E+05	6.95
7	9931	6.17	0.79	2.27E+05	1.00	2.86E+05	5.04
8	9921 M	7.82	1.08	3.23E+05	2.00	6.01E+05	7.44
9	10-1024	4.99	1.19	5.17E+05	NA	NA	NA
10	05-1022	3.71	1.53	1.11E+06	3.00	2.18E+06	7.86
11	9928	4.93	1.77	1.14E+06	2.00	1.28E+06	4.51
12	07-1015A	5.11	1.81	1.17E+06	3.00	1.94E+06	6.62
13	07-1015B	9.19	1.69	6.54E+05	NA	NA	NA
14	12-1005	4.76	1.91	1.35E+06	2.00	1.42E+06	4.20
15	200046	5.25	1.87	1.39E+06	2.50	1.86E+06	5.33
16	07-1031	3.93	2.55	2.91E+06	NA	NA	NA
17	9724	9.80	2.40	1.17E+06	NA	NA	NA
18	13-1010A	9.75	2.65	1.42E+06	NA	NA	NA
19	13-1010B	6.96	2.77	1.99E+06	NA	NA	NA
20	09-4040	6.51	3.28	2.97E+06	9.50	8.59E+06	11.58
21	07-5020	6.64	3.28	2.91E+06	5.00	4.43E+06	6.09
22	11-4035	8.87	5.02	5.16E+06	9.14	9.40E+06	7.29

#### 4.10 Discussion

The analysis of the design data of the jack-ups provided by the industry reveals that most of the designs are vulnerable to various modes of VIV in both current and waves. It is found that the jack-ups can potentially experience VIV about the inline, crossflow and yaw modes in both currents and regular waves within the design limits. The vulnerability of the jack-ups to various VIV modes is found to be less dependent on the environment heading as the shedding frequency is independent of the directions for circular legs. The natural periods of the surge and sway modes of the cylindrical legged jack-ups are in the range of 1.5 - 6 s while that of yaw mode is in the range of 1 - 5 s. As the natural periods of the surge, sway and yaw modes are very close to each other,

various modes of VIV can be experienced by the jack-up throughout its operating environment.

The leg diameter is found to be determined by an empirical design parameter which is a function of water depth, elevated load and yield strength of the leg material. The leg diameter is found to increase with the water depth and the elevated load but to reduce with the leg yield strength. The natural period is also found to be predominantly dependent on the elevated mass per unit water depth. The effective mass ratios of the analysed designs are found to be in the range of 2.5 – 20, much lesser than structures in air and very close to the floating structure's value of 1. Such low mass ratios not only increase the lock-in range and amplitude response of crossflow VIV but also induce inline VIV at low current speeds (see Sections A.2.3 and A.2.9).

The results of the design data analysis validate the field experiences reported (Thake, 2005). The  $Re$  range of the jack-up VIV is found to span over subcritical to transcritical regimes. The  $KC$  range of the VIV in regular waves spans over the asymmetric vortex regime or single pair regime, where fundamental lift frequency is at twice the wave frequency and lift coefficient is of considerable magnitude (Williamson, 1985). The scenario of ideal resonance or lock-in only is considered in this analysis. However, it can be inferred from the results that the lock-in regimes of one mode can span over a range of operating currents and also overlap with lock-in regimes of other modes, making the jack-up practically redundant. Hence, the VIV of jack-up is of considerable significance and should be subjected to further investigation.

## Chapter 5. Theoretical Investigation

This chapter mathematically investigates various modes of jack-up VIV. Simple criteria and response-based models are developed based on the SDOF analogy and principle of conservation of energy, for evaluating multiple modes of jack-up VIV in uniform current, regular waves and regular waves with imposed uniform current. Criteria for the initiation of various VIV modes are also developed for the cases of a single 2D cylinder and four rigidly coupled 2D cylinders in a rectangular configuration experiencing uniform and planar oscillatory flows. Based on the proposed formulations, designs of jack-ups provided by the industry are evaluated for the potential yield and fatigue implications due to various modes of VIV. The mathematical formulations presented in this chapter were derived as part of this research.

### 5.1 Dynamic Damping Stiffness

#### 5.1.1 Resonant Response of a Linear Mass Spring System

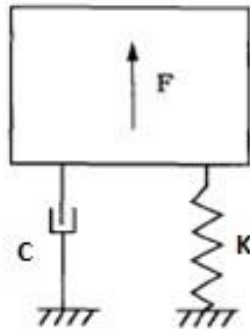


Figure 5-1: Linear mass spring system

The equation of motion for a linear mass spring SDOF system, illustrated in Figure 5-1, under dynamic excitations shall be expressed as,

$$M\ddot{x} + C\dot{x} + Kx = F(t)$$

Equation 5-1

where  $M, C, K$  represent the mass, damping and the stiffness respectively;  $x, \dot{x}, \ddot{x}$  represent the displacement, velocity and acceleration respectively and  $F(t)$  represents the time varying excitation force.

For a periodic excitation,  $F(t) = F_0 \cos(\omega t)$ , the time varying displacement can be expressed as,

$$x(t) = x_0 \cos(\omega t - \varepsilon) \quad \text{Equation 5-2}$$

where  $F_0, x_0, \omega, \varepsilon$  and  $t$  represent the excitation force amplitude, response or displacement amplitude, excitation frequency, phase difference and time respectively.

The response amplitude ( $x_0$ ) can be derived as (Sumer and Fredsøe, 2006),

$$x_0 = \frac{F_0}{K} \frac{1}{\sqrt{\left[1 - \left(\frac{\omega}{\omega_N}\right)^2\right]^2 + \left[\left(\frac{C}{M\omega_N}\right)^2 \left(\frac{\omega}{\omega_N}\right)^2\right]}} \quad \text{Equation 5-3}$$

where  $\omega_N$  represents the natural frequency of the SDOF.

The phase difference ( $\varepsilon$ ) between the displacement and force shall be expressed as,

$$\varepsilon = \tan^{-1} \left[ \frac{\left(\frac{C}{M\omega_N}\right) \left(\frac{\omega}{\omega_N}\right)}{1 - \left(\frac{\omega}{\omega_N}\right)^2} \right] \quad \text{Equation 5-4}$$

### 5.1.2 Low damping and dynamic damping stiffness

For a lightly damped system, the natural frequency shall be approximated as,

$$\omega_N = \sqrt{\frac{K}{M}} \quad \text{Equation 5-5}$$

At resonance  $\omega = \omega_N$  and Equation 5-3 becomes

$$x_0 = \frac{F_0}{K} \frac{1}{\left(\frac{C}{M\omega_N}\right)} \quad \text{Equation 5-6}$$

Substituting Equation 5-5 in Equation 5-6 and further simplifying,

$$x_o = \frac{F_o}{C\omega_N} \quad \text{Equation 5-7}$$

The product  $C\omega_N$  is analogous to structural stiffness and controls the resonance amplitude. Hence the same can be termed as **Dynamic Damping Stiffness**.

## 5.2 VIV of 2D circular cylinders in a steady flow

### 5.2.1 Inline/Surge VIV of a single cylinder

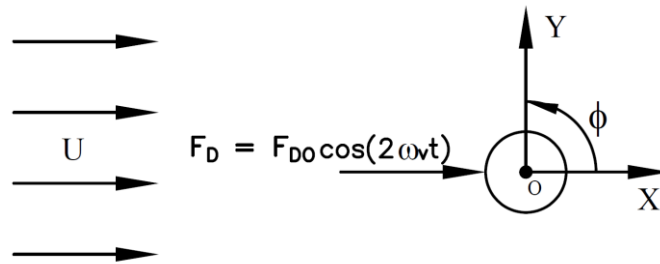


Figure 5-2: Inline VIV excitation of a cylinder

The inline resonant response amplitude,  $x_o$  of a lightly damped linear mass spring SDOF cylinder, illustrated in Figure 5-2, under dynamic excitations can be expressed based on Equation 5-7 as (Ramadasan *et al.*, 2018).

$$x_o = \frac{F_{ox}}{C_x \omega_{Nx}} \quad \text{Equation 5-8}$$

where  $F_{ox}$ ,  $C_x$  and  $\omega_{Nx}$  represent the amplitude of the excitation force, damping coefficient and natural angular frequency respectively along the inline direction.

The inline excitation due to oscillatory drag ( $F_{ox}$ ) (King *et al.*, 1973) can be expressed as,

$$F_{ox} = \frac{1}{2} \rho C_{D0} D U^2 L \quad \text{Equation 5-9}$$

where  $\rho$ ,  $C_{D0}$ ,  $D$ ,  $U$  and  $L$  denote the density of the fluid, oscillatory drag coefficient, diameter of the cylinder, flow velocity and length of the cylinder respectively

The flow velocity shall be expressed in terms of the Strouhal relationship as,

$$U = \frac{f_v D}{St} = \frac{\omega_v D}{2\pi St} \quad \text{Equation 5-10}$$

where  $f_v$ ,  $\omega_v$  and  $St$  represent the vortex shedding frequency, vortex shedding angular frequency and Strouhal number respectively.

The damping coefficient can be expressed in terms of a damping ratio ( $\zeta_x$ ) as,

$$\zeta_x = \frac{C_x}{2\sqrt{MK_x}} \quad \text{Equation 5-11}$$

where  $M$  and  $K_x$  represent the mass and inline stiffness respectively of the cylinder.

During inline resonance / lock-in,

$$\omega_v = \frac{\omega_{Nx}}{2} = \frac{1}{2}\sqrt{\frac{K_x}{M}} \quad \text{Equation 5-12}$$

Defining mass ratio ( $m^*$ ) of the cylinder as the ratio of mass over displaced mass,

$$m^* = \frac{M}{\frac{\pi}{4}D^2L\rho} \quad \text{Equation 5-13}$$

Substituting Equation 5-9 to Equation 5-13 in Equation 5-8 and after some mathematics, the amplitude ratio of the inline VIV response can be derived as,

$$\frac{x_O}{D} = \frac{C_{D0}}{16\pi^3 St^2 \zeta_x m^*} \quad \text{Equation 5-14}$$

It can be seen from Equation 5-14 that the inline response amplitude ratio of a cylinder undergoing inline VIV in steady flow is inversely proportional to the product of mass and damping ratios as noted by many researchers. The  $Re$  dependence of the inline VIV is also visible from the presence of  $St$  and drag coefficient in the above expression.

A criterion for the occurrence of the inline VIV can be derived by considering 1% amplitude ratio (Barltrop and Adams, 1991).

$$\zeta_x m^* \leq \frac{25 C_{D0}}{4\pi^3 St^2} \quad \text{Equation 5-15}$$

Considering a  $St$  of 0.20 and a maximum stationary oscillatory drag coefficient of 0.10 (see Figure A-7) for the practical  $Re$  range, the criterion for the inline VIV can be derived as

$$\zeta_x m^* \leq 0.50 \quad \text{Equation 5-16}$$

### 5.2.2 Crossflow/Sway VIV of a single cylinder

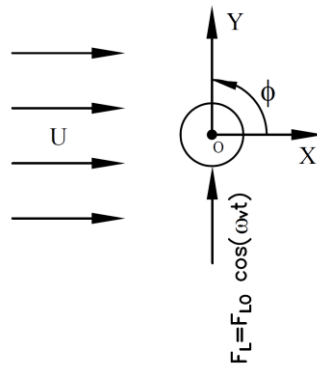


Figure 5-3: Crossflow excitation of a cylinder

During crossflow resonance / lock-in,

$$\omega_V = \omega_{Ny} = \sqrt{\frac{K_y}{M}} \quad \text{Equation 5-17}$$

where  $\omega_{Ny}$  and  $K_y$  represent the natural frequency and stiffness respectively of the cylinder in the crossflow direction.

Like the inline response, the amplitude ratio of the crossflow VIV response ( $y_0$ ) of a 2D cylinder in a steady flow, illustrated in Figure 5-3 can be derived as,

$$\frac{y_0}{D} = \frac{C_L}{4\pi^3 St^2 \zeta_y m^*} \quad \text{Equation 5-18}$$

where  $C_L$  and  $\zeta_y$  represent the lift coefficient and crossflow damping ratio of the cylinder.

The equation also explains the inverse proportionality to the product of mass and damping ratios and the  $Re$  dependence of the crossflow VIV.

Similar to inline VIV, the criterion for the occurrence of the crossflow VIV can also be derived by considering 1% amplitude ratio (Barltrop and Adams, 1991).

$$\zeta_y m^* \leq \frac{25C_L}{\pi^3 St^2} \quad \text{Equation 5-19}$$

Considering a  $St$  of 0.20 and a maximum stationary lift coefficient of 0.85 (see Figure A-9) for the practical  $Re$  range, the crossflow VIV criterion can be derived as,

$$\zeta_y m^* \leq 17.20 \quad \text{Equation 5-20}$$

### 5.2.3 Yaw VIV of a system of four 2D cylinders in a rectangular configuration under inline excitation

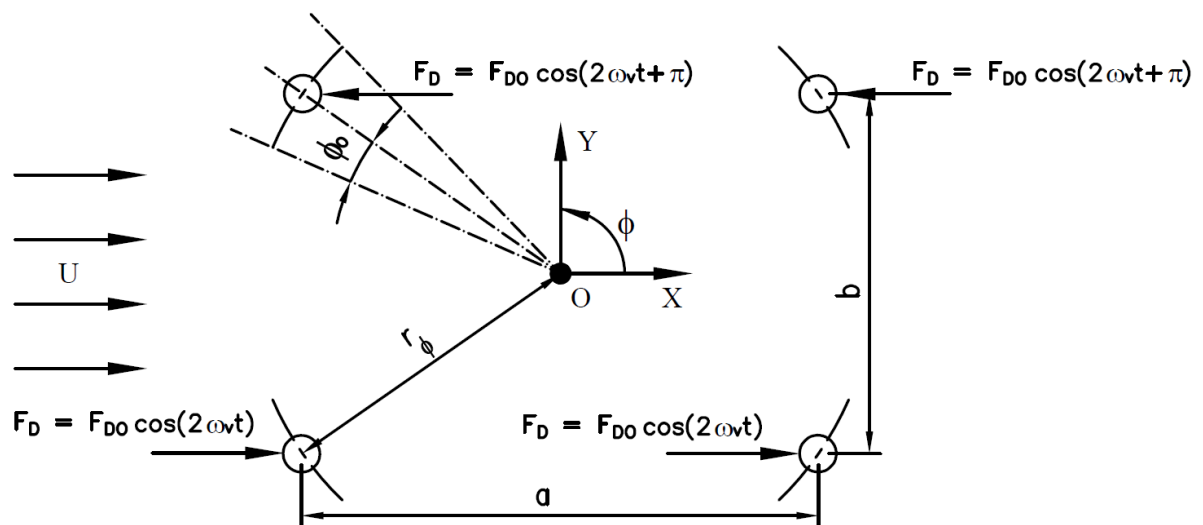


Figure 5-4: Yaw due to inline excitation

Like the single cylinder VIV, the amplitude of yaw VIV response ( $\phi_o$ ) of a system of four 2D cylinders in a steady flow under inline or drag excitation can be expressed as,

$$\phi_o = \frac{M_{o\phi}}{C_\phi \omega_{N\phi}} \quad \text{Equation 5-21}$$

where  $M_{o\phi}$ ,  $C_\phi$  and  $\omega_{N\phi}$  represent the amplitude of yaw excitation moment, yaw damping coefficient and yaw natural frequency respectively.

The yaw excitation due to oscillatory drag, considering the vortex synchronisation between cylinders as shown in Figure 5-4 can be,

$$M_{o\phi} = 2 \times \frac{1}{2} \rho C_{D0} D U^2 L \times b \quad \text{Equation 5-22}$$

where  $b$  represents the crossflow or transverse cylinder spacing.

During resonance/lock-in under inline excitation,

$$\omega_V = \frac{\omega_{N\phi}}{2} = \frac{1}{2} \sqrt{\frac{K_\phi}{I_\phi}} \quad \text{Equation 5-23}$$

where  $K_\phi$  and  $I_\phi$  represent the yaw stiffness and yaw moment of inertia respectively.

Considering the Strouhal relationship, mass ratio, damping ratio and the radial distance of the cylinders from the yaw centre ( $r_\phi$ ) which is also the yaw radius of gyration, the amplitude ratio of yaw VIV resonant response can be derived as,

$$\frac{\phi_o}{D} = \frac{C_{D0} b}{32 \pi^3 St^2 \zeta_\phi m^* r_\phi^2} \quad \text{Equation 5-24}$$

where  $\zeta_\phi$  represents the yaw damping ratio of the cylinders.

Equation 5-24 explains the inverse proportionality of the yaw response to the product of mass and damping ratios and the  $Re$  dependence of the yaw VIV. The

proportionality with the leg transverse spacing and inverse proportionality with the square of yaw radius of gyration are also captured.

Similar to inline and crossflow VIV, considering a 1 % amplitude ratio to represent VIV suppression,

$$\frac{r_\phi \phi_0}{D} \leq \frac{1}{100} \quad \text{Equation 5-25}$$

The criterion for the occurrence of yaw VIV under drag excitation shall be derived as,

$$\zeta_\phi m^* \leq \frac{25 C_{D0} b}{8 \pi^3 St^2 r_\phi} \quad \text{Equation 5-26}$$

Considering a  $St$  of 0.20 and a maximum stationary cylinder oscillatory drag coefficient of 0.10 for the practical  $Re$  range, the criterion becomes,

$$\zeta_\phi m^* r_\phi \leq 0.25 b \quad \text{Equation 5-27}$$

#### 5.2.4 ***Yaw VIV of a system of four 2D cylinders in a rectangular configuration under crossflow excitation***

The yaw excitation due to lift, considering the vortex synchronisation between cylinders as shown in Figure 5-5 can be expressed as,

$$M_{o\phi} = 2 \times \frac{1}{2} \rho C_L D U^2 L \times a \quad \text{Equation 5-28}$$

where  $a$  is the inline or longitudinal cylinder spacing.

During resonance/lock-in under lift excitation,

$$\omega_V = \omega_{N\phi} = \sqrt{\frac{K_\phi}{I_\phi}} \quad \text{Equation 5-29}$$

Like yaw due to drag excitation, the amplitude ratio of the yaw VIV resonant response due to lift excitation can be derived as,

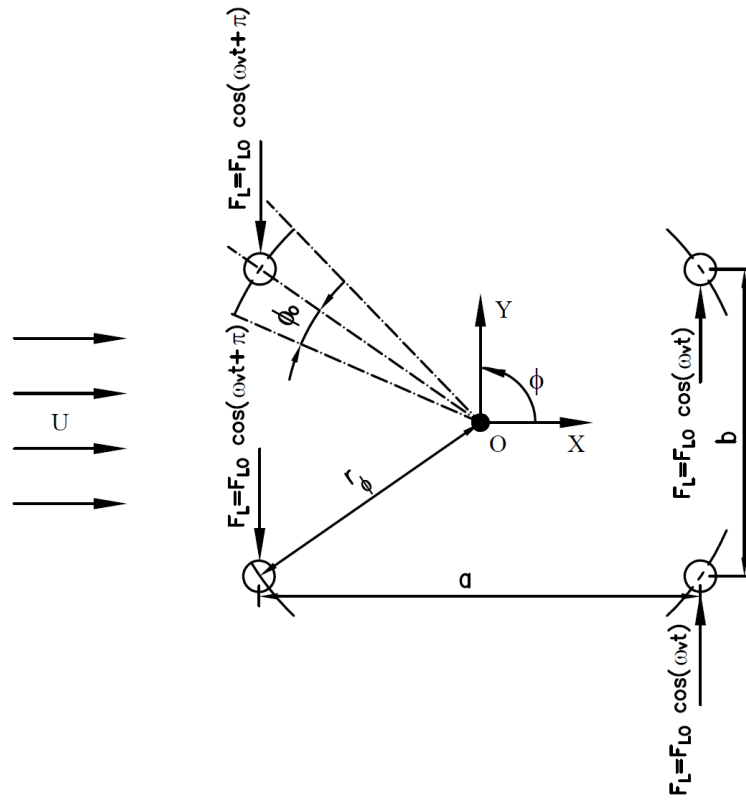


Figure 5-5: Yaw due to crossflow excitation

$$\frac{\phi_0}{D} = \frac{C_L a}{8 \pi^3 St^2 \zeta_\phi m^* r_\phi^2}$$

Equation 5-30

Equation 5-30 explains the inversely proportionality of the response with the product of cylinder mass ratio, damping ratio and the square of the yaw radius of gyration.  $Re$  dependence and linear proportionality with the longitudinal leg spacing are also reflected.

Similarly, the criterion for the occurrence of yaw VIV under lift excitation shall be derived as,

$$\zeta_\phi m^* \leq \frac{25 C_L a}{2 \pi^3 St^2 r_\phi}$$

Equation 5-31

Considering a  $St$  of 0.20 and a maximum stationary cylinder lift coefficient of 0.85 for the practical  $Re$  range, the criterion becomes,

$$\zeta_{\phi} m^* r_{\phi} \leq 8.60 a$$

Equation 5-32

### 5.3 VIV of Jack-up with four Circular Cylindrical Legs in Uniform Current

#### 5.3.1 Inline / Surge VIV

The effective inline excitation force per leg ( $F_{eLx}$ ) of the SDOF system of the jack-up can be expressed based on Energy Principle (Barltrop and Adams, 1991) as,

$$F_{eLx} = \int_0^h f_{ox}(z) \frac{A \sin(\kappa_L z + B) + E}{A \sin(\kappa_L L + B) + E} dz \quad \text{Equation 5-33}$$

where  $f_{ox}$  represents the distribution of the oscillatory excitation force along the leg.

The resonant inline response ( $x_L$ ) of the SDOF can be expressed like Equation 5-8 and considering the similarity, parallelism and vortex synchronisation of the legs.

$$x_L = \frac{F_{eLx}}{C_{eLx} \omega_{Nx}} \quad \text{Equation 5-34}$$

where  $C_{eLx}$  represents the effective inline damping coefficient per leg.

The simplest inline VIV model for a jack-up can be developed by neglecting the effect of drag interaction with the response,

$$f_{ox} = \frac{1}{2} \rho C_{D0} D U^2 \quad \text{Equation 5-35}$$

where  $f_{ox}$  represents the distribution of the oscillatory drag force amplitude along the leg.

Defining the oscillatory drag force as  $F_{D0} = f_{ox} h$ , the response, Equation 5-34 can be simplified as,

$$x_L = \frac{F_{DO}}{C_{eLx} \omega_{Nx}} \left( \frac{1}{h[A \sin(\kappa_L L + B) + E]} \right) \int_0^h [A \sin(\kappa_L z + B) + E] dz \quad \text{Equation 5-36}$$

where  $x_L$  and  $h$  represent the inline response of the leg in way of hull interface and the effective water depth (considering leg penetration in the soil) respectively.

Considering the Strouhal relationship, resonance/lock-in under inline excitation,

$$\frac{x_L}{D} = \frac{C_{DO}}{16\pi^3 St^2 \zeta_x m^*} \left( \frac{1}{h[A \sin(\kappa_L L + B) + E]} \right) \int_0^h [A \sin(\kappa_L z + B) + E] dz \quad \text{Equation 5-37}$$

Equation 5-37 explains clearly the inverse proportionality with the mass damping parameter (product of mass ratio and damping ratio), the effect of leg mode shape and the  $Re$  dependence of the inline VIV.

Considering a 1 % amplitude ratio to represent VIV suppression, the criterion for the occurrence of inline VIV of a jack-up shall be derived as,

$$\zeta_x m^* \leq \frac{25 C_{DO}}{4 \pi^3 St^2} \left( \frac{1}{h[A \sin(\kappa_L L + B) + E]} \right) \int_0^h [A \sin(\kappa_L z + B) + E] dz \quad \text{Equation 5-38}$$

Considering a  $St$  of 0.20 and a maximum stationary oscillatory drag coefficient of 0.10 for the practical  $Re$  range, the criterion becomes.

$$\zeta_x m^* \left( \frac{h [A \sin(\kappa_L L + B) + E]}{\int_0^h [A \sin(\kappa_L z + B) + E] dz} \right) \leq 0.50 \quad \text{Equation 5-39}$$

The expression inside parentheses can be defined as the mode factor (MF). The product of MF with mass damping parameter can be the effective (or modified) mass damping parameter for a jack-up. The criterion becomes,

$$\zeta_x m^* MF \leq 0.50 \quad \text{Equation 5-40}$$

### 5.3.2 Crossflow / Sway VIV

Like the inline response, the crossflow response can also be derived considering Strouhal relationship and lock-in conditions as below,

$$\frac{y_L}{D} = \frac{C_L}{4\pi^3 St^2 \zeta_y m^*} \left( \frac{1}{h[A \sin(\kappa_L L + B) + E]} \right) \int_0^h [A \sin(\kappa_L z + B) + E] dz \quad \text{Equation 5-41}$$

where  $y_L$  represents the crossflow response of the leg in way of hull interface.

It can be observed that the inverse proportionality with mass damping parameter, the effect of leg mode shape and the  $Re$  dependence are applicable also for crossflow VIV.

Considering a 1 % amplitude ratio for VIV suppression, the criterion for the crossflow jack-up VIV is,

$$\zeta_y m^* \leq \frac{25 C_L}{\pi^3 St^2} \left( \frac{1}{h[A \sin(\kappa_L L + B) + E]} \right) \int_0^h [A \sin(\kappa_L z + B) + E] dz \quad \text{Equation 5-42}$$

Considering a  $St$  of 0.20 and a maximum stationary cylinder Lift coefficient of 0.85 for the practical  $Re$  range, the criterion becomes,

$$\zeta m^* MF \leq 17.20 \quad \text{Equation 5-43}$$

### 5.3.3 Yaw/Torsional VIV due to inline excitation

The total effective yaw excitation moment per leg ( $M_{oe\phi L}$ ) of the equivalent SDOF system of a Jack-up is,

$$M_{oe\phi L} = \int_0^h m_{o\phi}(z) \left[ \frac{A \sin(\kappa_L z + B) + E}{A \sin(\kappa_L L + B) + E} \right] dz \quad \text{Equation 5-44}$$

where  $m_{o\phi}(z)$  represents the distribution of the yaw excitation moment amplitude along the leg.

The total yaw excitation on the jack-up ( $M_{oe\phi}$ ) shall be expressed as,

$$M_{oe\phi} = 4 M_{oe\phi L} \quad \text{Equation 5-45}$$

The yaw resonant response of the SDOF ( $\phi_L$ ) can be expressed similar to Equation 5-21 and considering the similarity and vortex synchronisation of the legs.

$$\phi_L = \frac{M_{oe\phi}}{C_{e\phi} \omega_{N\phi}} \quad \text{Equation 5-46}$$

where  $C_{e\phi}$  represents the effective yaw damping coefficient of the jack-up SDOF.

The yaw excitation per unit leg length shall be,

$$m_{o\phi}(z) = f_{ox}(z) \frac{b}{2} \quad \text{Equation 5-47}$$

where  $b$  represents the crossflow or transverse spacing of legs.

Considering Strouhal relationship and lock-in condition, Equation 5-46 can be further simplified as,

$$\frac{\phi_L}{D} = \frac{C_{DO} b}{32\pi^3 St^2 \zeta_\phi m^* k_\phi^2} \left( \frac{1}{h [A \sin(\kappa_L L + B) + E]} \right) \int_0^h [A \sin(\kappa_L z + B) + E] dz$$

$$\text{Equation 5-48}$$

where  $k_\phi$  represents the yaw radius of gyration of the jack-up SDOF

Equation 5-48 explains the inverse proportionality of the yaw response with the product of cylinder mass ratio, damping ratio and the square of the yaw radius of gyration, the effect of mode shape,  $Re$  dependence and linear proportionality with the transverse leg spacing.

Considering a 1 % amplitude ratio, the criterion for the occurrence of yaw VIV of a Jack-up under drag excitation shall be derived as,

$$\zeta_{\phi} m^* k_{\phi}^2 \leq \frac{25 C_{DO} b \sqrt{a^2 + b^2}}{16 \pi^3 St^2} \left( \frac{1}{h[A \sin(\kappa_L L + B) + E]} \right) \int_0^h [A \sin(\kappa_L z + B) + E] dz$$

Equation 5-49

Considering a  $St$  of 0.20 and a maximum stationary cylinder oscillatory drag coefficient of 0.10 for the practical  $Re$  range, the criterion becomes,

$$\zeta_{\phi} m^* MF k_{\phi}^2 \leq 0.13 b \sqrt{a^2 + b^2}$$

Equation 5-50

### 5.3.4 Yaw VIV due to crossflow excitation

The yaw excitation per leg shall be,

$$m_{\phi}(z) = f_{oy}(z) \frac{a}{2}$$

Equation 5-51

where  $f_{oy}$  and  $a$  represent the distribution of the oscillatory lift force amplitude along the leg and inline or longitudinal spacing of legs respectively.

Like yaw due to drag excitation, the amplitude ratio of the yaw VIV resonant response due to lift excitation can be derived as,

$$\frac{\phi_L}{D} = \frac{C_L a}{8 \pi^3 St^2 \zeta_{\phi} m^* k_{\phi}^2} \left( \frac{1}{h[A \sin(\kappa_L L + B) + E]} \right) \int_0^h [A \sin(\kappa_L z + B) + E] dz$$

Equation 5-52

Equation 5-52 explains the inverse proportionality of the yaw response with the product of cylinder mass ratio, damping ratio and the square of the yaw radius of gyration, the effect of mode shape,  $Re$  dependence and linear proportionality with the longitudinal leg spacing.

Considering a 1 % amplitude ratio to represent VIV suppression, the criterion for Yaw VIV of a Jack-up under lift excitation shall be,

$$\zeta_{\phi} m^* k_{\phi}^2 \leq \frac{25 C_L a \sqrt{a^2 + b^2}}{4 \pi^3 S t^2} \left( \frac{1}{h [A \sin(\kappa_L L + B) + E]} \right) \int_0^h [A \sin(\kappa_L z + B) + E] dz$$

Equation 5-53

Considering a  $St$  of 0.20 and a maximum stationary cylinder lift coefficient of 0.85 for the practical  $Re$  range, the criterion becomes,

$$\zeta_{\phi} m^* MF k_{\phi}^2 \leq 4.30 a \sqrt{a^2 + b^2}$$

Equation 5-54

#### 5.4 Mean Drag Amplification in Uniform Current

As discussed in Section A.2.13.2, VIV significantly increases the drag force acting on the cylinder. The amplified mean drag coefficient ( $C_{DA}$ ) of a 2D circular cylinder undergoing crossflow vibration shall be expressed as (Blevins, 2001),

$$C_{DA} = C_D \left( 1 + \frac{2.1 y_0}{D} \right)$$

Equation 5-55

where  $C_D$  is the mean drag coefficient of a stationary cylinder.

Accordingly, the amplified mean drag force acting on a jack-up leg ( $F_{DAL}$ ) experiencing crossflow vibrations can be expressed as,

$$F_{DAL} = \frac{1}{2} \rho C_D D \int_0^h \left( 1 + \frac{2.1 y_L [A \sin(\kappa_L z + B) + E]}{D [A \sin(\kappa_L L + B) + E]} \right) (U(z))^2 dz$$

Equation 5-56

where  $U(z)$  represents the variation of the flow velocity along the leg.

The amplified drag coefficient of the vibrating leg ( $C_{DAL}$ ) can be expressed as,

$$C_{DAL} = C_D \left[ \frac{\int_0^h \left( 1 + \frac{2.1 y_L [A \sin(\kappa_L z + B) + E]}{D [A \sin(\kappa_L L + B) + E]} \right) (U(z))^2 dz}{\int_0^h (U(z))^2 dz} \right]$$

Equation 5-57

Similarly, the increased inline overturning moment ( $OTM$ ) per leg ( $OTM_{AL}$ ) shall be derived as,

$$OTM_{AL} = \frac{1}{2} \rho C_D D \int_0^h \left( 1 + \frac{2.1 y_L [A \sin(\kappa_L z + B) + E]}{D [A \sin(\kappa_L L + B) + E]} \right) (U(z))^2 z dz \quad \text{Equation 5-58}$$

#### 5.4.1 Crossflow VIV

In the uniform current, the increased mean drag force on the leg of a jack-up undergoing crossflow VIV becomes,

$$F_{DAL} = \frac{1}{2} \rho C_D D U^2 \int_0^h \left( 1 + \frac{2.1 y_L [A \sin(\kappa_L z + B) + E]}{D [A \sin(\kappa_L L + B) + E]} \right) dz \quad \text{Equation 5-59}$$

The amplified mean drag coefficient becomes,

$$C_{DAL} = C_D \left[ \frac{\int_0^h \left( 1 + \frac{2.1 y_L [A \sin(\kappa_L z + B) + E]}{D [A \sin(\kappa_L L + B) + E]} \right) dz}{h} \right] \quad \text{Equation 5-60}$$

The inline OTM per leg becomes.

$$OTM_{AL} = \frac{1}{2} \rho C_D D U^2 \int_0^h \left( 1 + \frac{2.1 y_L [A \sin(\kappa_L z + B) + E]}{D [A \sin(\kappa_L L + B) + E]} \right) z dz \quad \text{Equation 5-61}$$

For jack-ups with independent legs, the deflected leg profile can be considered as a perfect quarter sine wave and  $A = 1$ ,  $B = E = 0$  and  $\kappa_L = \frac{\pi}{2L}$ .

The increased mean drag force on the leg becomes,

$$F_{DAL} = \frac{1}{2} \rho C_D D U^2 h \left( 1 + \frac{2.1 y_L}{D h \kappa_L} (1 - \cos(\kappa_L h)) \right) \quad \text{Equation 5-62}$$

The effective drag coefficient shall be,

$$C_{DAL} = C_D \left( 1 + \frac{2.1 y_L}{D h k_L} (1 - \cos(\kappa_L h)) \right) \quad \text{Equation 5-63}$$

Similarly, the increased OTM per leg shall be derived as,

$$OTM_{AL} = \frac{1}{4} \rho C_D D U^2 h^2 \left( 1 + \frac{4.2 y_L}{D h^2 k_L^2} (\sin(\kappa_L h) - k_L h \cos(\kappa_L h)) \right) \quad \text{Equation 5-64}$$

Considering the similarity and parallelism of legs, the total amplified OTM ( $OTM_A$ ) on the jack-up along the direction of current shall be,

$$OTM_A = n_L \frac{1}{4} \rho C_D D U^2 h^2 \left( 1 + \frac{4.2 y_L}{D h^2 k_L^2} (\sin(\kappa_L h) - k_L h \cos(\kappa_L h)) \right) \quad \text{Equation 5-65}$$

3D graphs in Figure 5-6 illustrate the increase in mean drag force and OTM on the jack-up respectively as a function of crossflow amplitude and depth ratios. It can be observed that the drag force and OTM acting on the jack-up increases with both amplitude and depth ratios. The increase in OTM is much higher than the increase in mean drag, which explains the instability of the jack-up observed during VIV.

#### 5.4.2 Yaw VIV

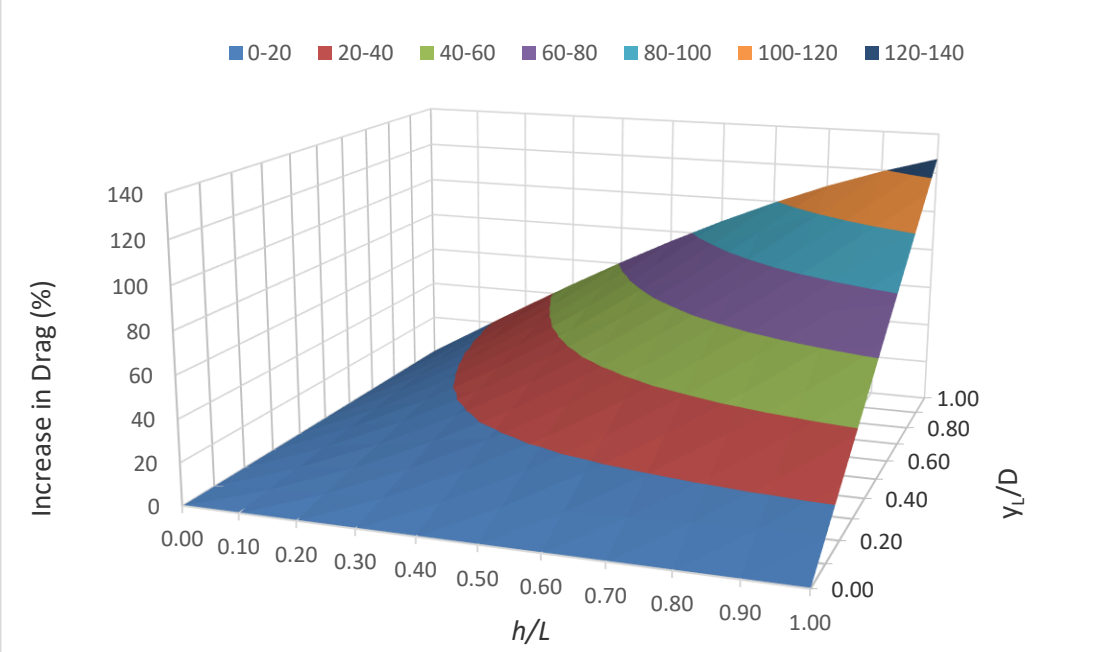
In the uniform current, the increased mean drag force on the leg of a jack-up undergoing yaw VIV can be,

$$F_{DAL} = \frac{1}{2} \rho C_D D U^2 \int_0^h \left( 1 + \frac{2.1 \left( \frac{\alpha}{2} \phi_L \right) [A \sin(\kappa_L z + B) + E]}{D [A \sin(\kappa_L L + B) + E]} \right) dz \quad \text{Equation 5-66}$$

The amplified mean drag coefficient becomes

$$C_{DAL} = C_D \left[ \frac{\int_0^h \left( 1 + \frac{1.05 (\alpha \phi_L) [A \sin(\kappa_L z + B) + E]}{D [A \sin(\kappa_L L + B) + E]} \right) dz}{h} \right] \quad \text{Equation 5-67}$$

a)



b)

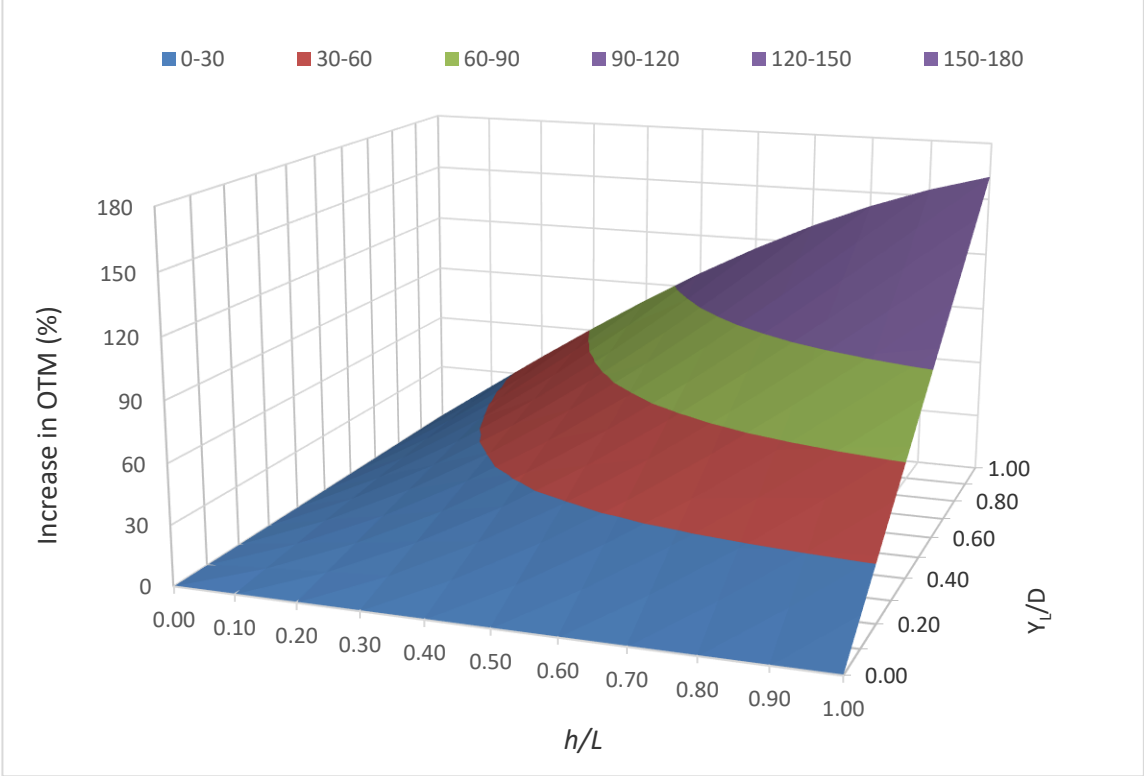


Figure 5-6: Jack-up a) mean drag amplification and b) OTM amplification in crossflow VIV

The inline OTM per leg becomes.

$$OTM_{AL} = \frac{1}{2} \rho C_D D U^2 \int_0^h \left( 1 + \frac{1.05 (a \phi_L) [A \sin(\kappa_L z + B) + E]}{D [A \sin(\kappa_L L + B) + E]} \right) z dz \quad \text{Equation 5-68}$$

For jack-ups with independent legs,  $A = 1$ ,  $B = E = 0$  and  $\kappa_L = \frac{\pi}{2L}$

$$F_{DAL} = \frac{1}{2} \rho C_D D U^2 h \left( 1 + \frac{1.05 a \phi_L}{D h \kappa_L} (1 - \cos(\kappa_L h)) \right) \quad \text{Equation 5-69}$$

$$C_{DAL} = C_D \left( 1 + \frac{1.05 a \phi_L}{D h \kappa_L} (1 - \cos(\kappa_L h)) \right) \quad \text{Equation 5-70}$$

$$OTM_{AL} = \frac{1}{4} \rho C_D D U^2 h^2 \left( 1 + \frac{2.1 a \phi_L}{D h^2 \kappa_L^2} (\sin(\kappa_L h) - \kappa_L h \cos(\kappa_L h)) \right) \quad \text{Equation 5-71}$$

Similarly, the total amplified OTM along the direction of flow shall be,

$$OTM_A = n_L \frac{1}{4} \rho C_D D U^2 h^2 \left( 1 + \frac{2.1 a \phi_L}{D h^2 \kappa_L^2} (\sin(\kappa_L h) - \kappa_L h \cos(\kappa_L h)) \right) \quad \text{Equation 5-72}$$

It can be inferred that the percentage increase in drag force and OTM will be similar to that of crossflow VIV.

## 5.5 VIV of 2D Circular Cylinders in a Planar Oscillatory Flow

### 5.5.1 Crossflow / Sway VIV of a single cylinder

The crossflow resonant response amplitude,  $y_0$  of a lightly damped linear mass spring SDOF cylinder, illustrated in Figure 5-7, under dynamic excitations can be expressed based on Equation 5-7 as,

$$y_0 = \frac{F_{oy}}{C_y \omega_{Ny}} \quad \text{Equation 5-73}$$

where  $F_{oy}$ ,  $C_y$  and  $\omega_{Ny}$  represent the amplitude of the excitation force, damping coefficient and natural angular frequency respectively along the crossflow direction.

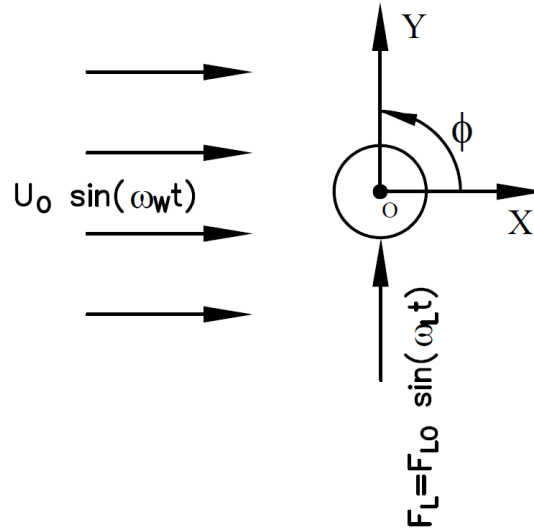


Figure 5-7: Crossflow excitation in a planar oscillatory flow

As lift frequency is a multiple of flow frequency (Williamson, 1985), the oscillatory lift excitation ( $F_L$ ) in a planar oscillatory flow can be expressed as,

$$F_L = \frac{1}{2} \rho C_L D [U_o \sin(\omega_w t)]^2 L \sin(N_L \omega_w t) \quad \text{Equation 5-74}$$

where  $\rho$ ,  $C_L$ ,  $D$ ,  $U_o$ ,  $L$ ,  $\omega_w$ ,  $t$  and  $N_L$  denote the density of the fluid, oscillatory lift coefficient, diameter of the cylinder, amplitude of flow velocity, length of the cylinder, oscillatory flow angular frequency, time instant and lift frequency factor respectively.

The lift frequency factor can be defined as the ratio of the fundamental lift frequency ( $\omega_L$ ) with the flow frequency,

$$N_L = \frac{\omega_L}{\omega_w} \quad \text{Equation 5-75}$$

Figure 5-8 illustrates the time series of the lift forces normalised with the maximum value for the lift frequency factors from 2 to 4, along with the normalised oscillatory flow velocity. It can be observed that the condition of zero lift force at zero flow velocity is satisfied by Equation 5-74.

The amplitude of the lift excitation ( $F_{Lo}$ ) can be derived as,

$$F_{Lo} = \alpha \left[ \frac{1}{2} \rho C_L D U_o^2 L \right] \quad \text{Equation 5-76}$$

where  $\alpha$  denotes the lift amplitude factor, which can be calculated by finding the maxima of Equation 5-74. The lift amplitude factors calculated corresponding to various values of lift frequency factor are shown in Table 5-1.

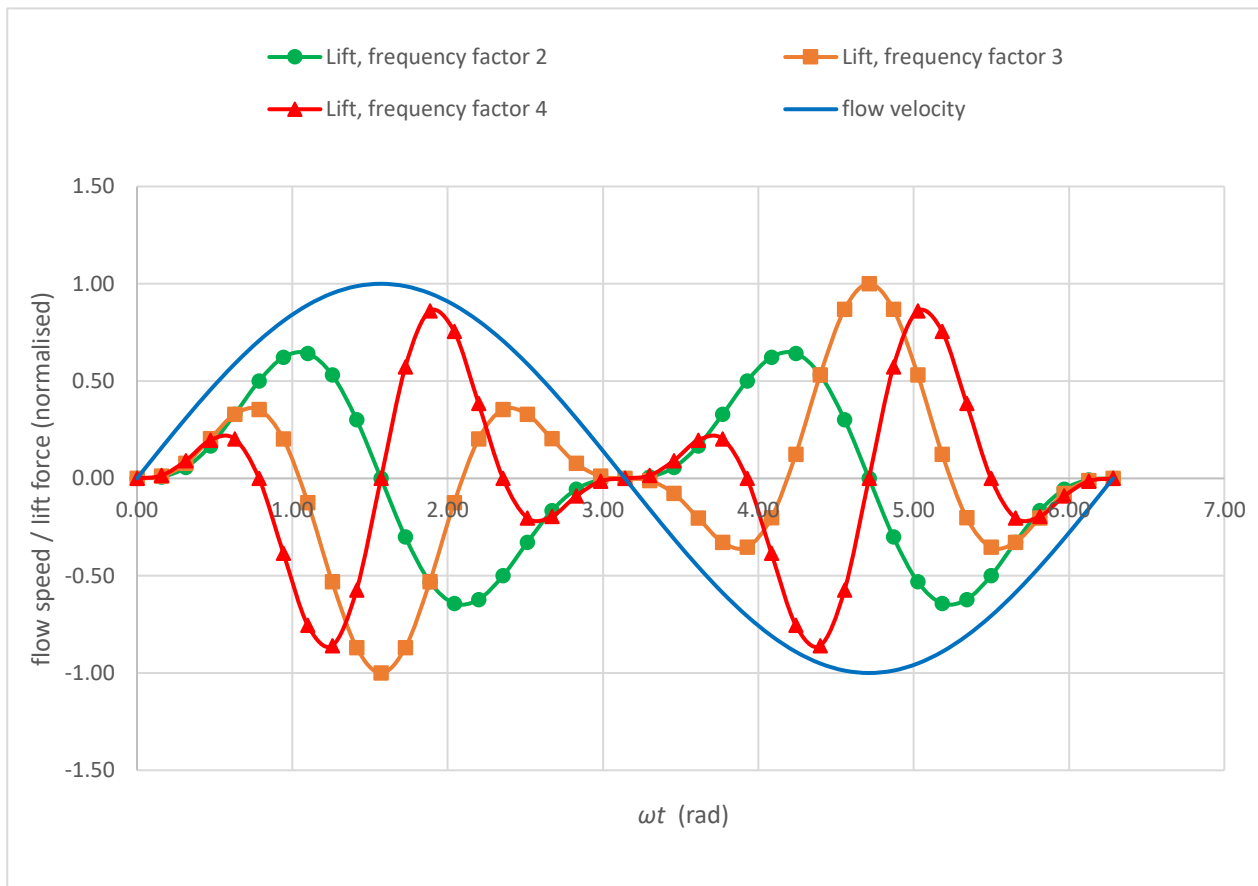


Figure 5-8: Flow and lift oscillations for various lift frequency factors

Table 5-1: Lift amplitude factors and lift frequency factors.

$N_L$	1	2	3	4	5	6	7	8	9	10
$\alpha$	1	0.65	1	0.87	1	0.94	1	0.96	1	0.98

The frequency components of oscillatory lift force in a planar oscillatory flow can be derived by performing trigonometric operations on Equation 5-74,

$$F_L = \frac{1}{8} \rho C_L D U_o^2 L [2 \sin(N_L \omega_W t) - \sin((N_L - 2) \omega_W t) - \sin((N_L + 2) \omega_W t)]$$

*Equation 5-77*

It can be seen from Equation 5-77 that lift force in oscillatory flow has three frequency components which are higher harmonics of flow frequency;  $(N_L - 2)\omega_W$ ,  $N_L \omega_W$  and  $(N_L + 2)\omega_W$ .

Considering fundamental lift frequency ( $N_L \omega_W$ ) only,

$$F_L = \frac{1}{4} \rho C_L D U_o^2 L \sin(N_L \omega_W t)$$

*Equation 5-78*

During crossflow resonance or lock-in,

$$F_{oy} = \frac{1}{4} \rho C_L D U_o^2 L$$

*Equation 5-79*

$$\omega_L = N_L \omega_W = \omega_{Ny} = \sqrt{\frac{K_y}{M}}$$

*Equation 5-80*

Defining  $KC$  number ( $KC$ ) of the flow as,

$$KC = \frac{U_o}{f_w D}$$

*Equation 5-81*

where  $f_w$  represents the frequency of the flow.

Equation 5-79 to Equation 5-81 in Equation 5-73, assuming that the cylinder responds to fundamental lift frequency only during resonance, the amplitude ratio of the crossflow VIV response can be derived as,

$$\frac{y_o}{D} = \frac{C_L KC^2}{8 \pi^3 N_L^2 \zeta_y m^*} \quad \text{Equation 5-82}$$

where  $\zeta_y$  and  $m^*$  represent the crossflow damping ratio and the mass ratio of the cylinder respectively.

It can be seen from Equation 5-82 that the response amplitude ratio of a cylinder undergoing crossflow VIV in a planar oscillatory flow is inversely proportional to the product of mass and damping ratios (mass damping parameter) similar to the steady flow. The  $KC$  number dependence of the crossflow VIV is visible from the presence of lift coefficient, lift frequency factor and  $KC$  number itself in the above expression.

A criterion for the occurrence of the crossflow VIV can be derived by considering 1% amplitude ratio (Barltrop and Adams, 1991).

$$\zeta_y m^* \leq \frac{25 C_L KC^2}{2 \pi^3 N_L^2} \quad \text{Equation 5-83}$$

Considering the  $KC$  number of 10 at which the maximum lift is observed, the corresponding maximum stationary cylinder lift coefficient of 3 (Sarpkaya, 1975; DNV GL, 2017b) and corresponding lift frequency factor of 2 (Williamson, 1985), the crossflow VIV criterion in a planar oscillatory flow can be derived as,

$$\zeta m^* \leq 30.23 \quad \text{Equation 5-84}$$

It can be seen from Equation 5-84 that crossflow VIV in a planar oscillatory flow can be initiated at a much higher mass damping parameter than a steady flow. Hence structures which do not experience crossflow VIV in a steady flow may respond aggressively under planar oscillatory flow conditions.

### 5.5.2 **Crossflow VIV of a system of four 2D cylinders in a rectangular configuration**

The sway excitation due to lift force ( $F_L$ ) in a planar oscillatory flow, illustrated in Figure 5-9 can be expressed as,

$$F_L = 2 \times \frac{1}{2} \rho C_L D L U_o^2 \{ [\sin(\omega_W t)]^2 \sin(N_L \omega_W t) + [\sin(\omega_W t + \kappa_W a)]^2 \sin(N_L (\omega_W t + \kappa_W a)) \}$$

Equation 5-85

where  $a$  is the inline or longitudinal cylinder spacing and  $\kappa_W$  is the wave number of flow.

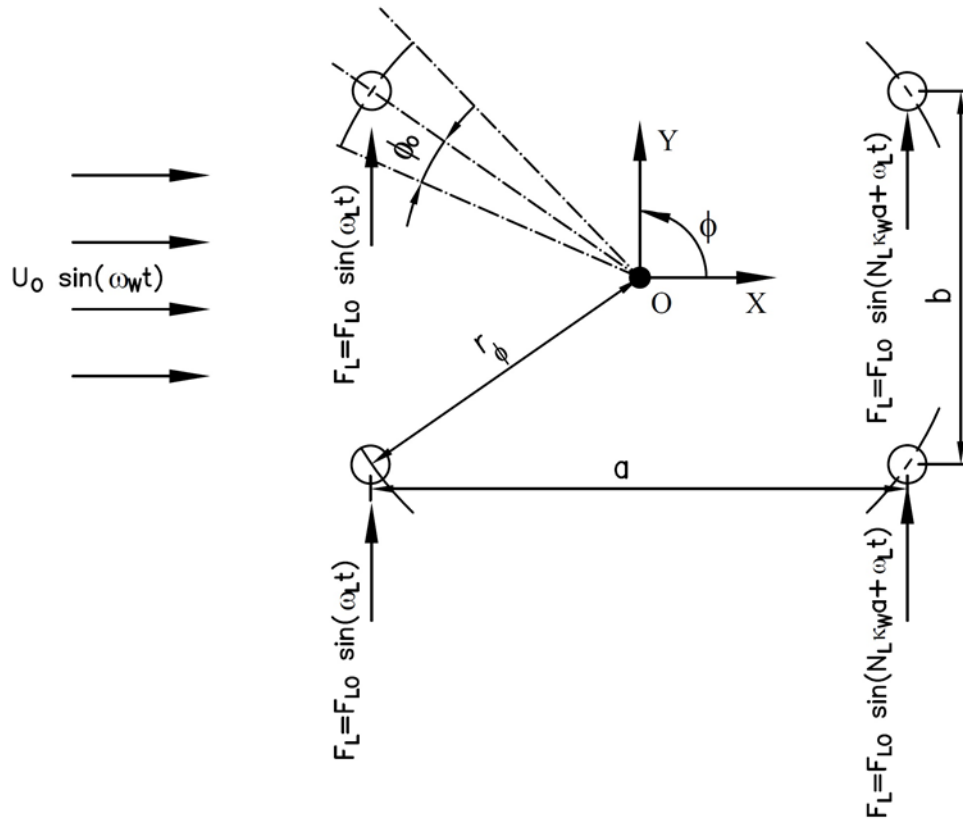


Figure 5-9: Sway due to crossflow excitation in a planar oscillatory flow

Equation 5-85 when expanded in terms of component frequencies becomes,

$$F_L = 2 \times \frac{1}{2} \rho C_L D L U_o^2 \times \frac{1}{4} \{ [2 \sin(N_L \omega_W t) - \sin((N_L - 2)\omega_W t) - \sin((N_L + 2)\omega_W t)] + [2 \sin(N_L (\omega_W t + \kappa_W a)) - \sin((N_L - 2)(\omega_W t + \kappa_W a)) - \sin((N_L + 2)(\omega_W t + \kappa_W a))] \}$$

Equation 5-86

Considering the fundamental lift frequency only,

$$F_L = 2 \times \frac{1}{4} \rho C_L D L U_o^2 [\sin(N_L \omega_W t) + \sin(N_L (\omega_W t + \kappa_W a))] \quad \text{Equation 5-87}$$

Which can be further simplified as,

$$F_L = 2 \times \frac{1}{2} \rho C_L D L U_o^2 \cos\left(N_L \frac{\kappa_W a}{2}\right) \sin\left(N_L \left(\omega_W t + \frac{\kappa_W a}{2}\right)\right) \quad \text{Equation 5-88}$$

The amplitude of the lift excitation is,

$$F_{Lo} = 2 \times \frac{1}{2} \rho C_L D L U_o^2 \cos\left(N_L \frac{\kappa_W a}{2}\right) \quad \text{Equation 5-89}$$

Considering the  $KC$  relationship, crossflow lock-in condition, mass ratio, damping ratio and the amplitude ratio, the crossflow VIV resonant response can be derived as,

$$\frac{y_o}{D} = \frac{C_L K C^2}{8 \pi^3 N_L^2 \zeta_y m^*} \cos\left(N_L \frac{\kappa_W a}{2}\right) \quad \text{Equation 5-90}$$

Equation 5-90 shows the inverse proportionality of the crossflow response to the mass damping parameter and the  $KC$  number dependence of the sway VIV. The significance of cylinder longitudinal spacing is also captured in the equation.

Considering 1% amplitude ratio to represent VIV occurrence (Bartrop and Adams, 1991), the criterion for the occurrence of the crossflow VIV under planar oscillatory flow can be derived as,

$$\zeta m^* \leq \frac{25 C_L K C^2}{2 \pi^3 N_L^2} \cos\left(N_L \frac{\kappa_W a}{2}\right) \quad \text{Equation 5-91}$$

Considering a  $KC$  number of 10, the corresponding maximum stationary cylinder lift coefficient of 3 and corresponding lift frequency factor of 2, the crossflow VIV criterion in a planar oscillatory flow becomes,

$$\zeta m^* \leq 30.23 \cos\left(N_L \frac{\kappa_W a}{2}\right) \quad \text{Equation 5-92}$$

## 5.5.3 Yaw VIV of a system of four 2D cylinders in a rectangular configuration

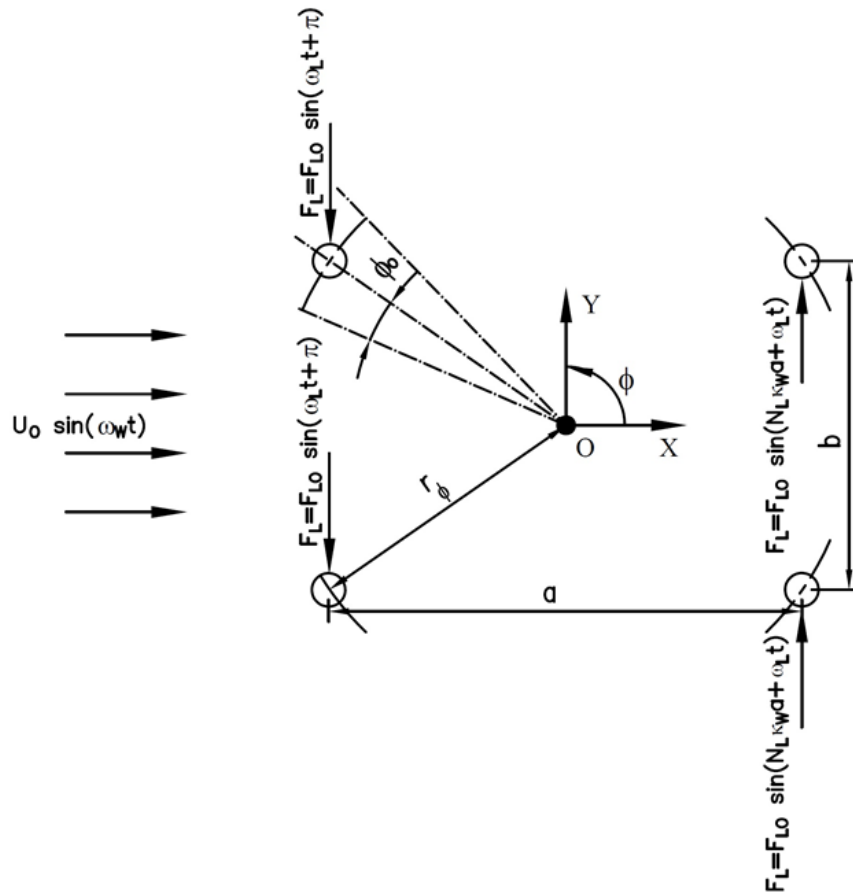


Figure 5-10: Yaw due to crossflow excitation in a planar oscillatory flow

The amplitude of yaw VIV response ( $\phi_o$ ) of a system of four 2D cylinders in a planar oscillatory flow under crossflow or lift excitation can be expressed as,

$$\phi_o = \frac{M_{o\phi}}{C_\phi \omega_{N\phi}} \quad \text{Equation 5-93}$$

The yaw excitation due to lift ( $M_\phi$ ), considering the vortex synchronisation between cylinders as shown in Figure 5-10 can be expressed as,

$$M_\phi = 2 \times \frac{1}{2} \rho C_L D L U_o^2 \{ [\sin(\omega_W t)]^2 \sin(N_L \omega_W t) + [\sin(\omega_W t + \kappa_W a)]^2 \sin(N_L (\omega_W t + \kappa_W a)) \} \times \frac{a}{2}$$

$$\text{Equation 5-94}$$

Equation 5-94 when expanded in terms of component frequencies become,

$$M_{\phi} = 2 \times \frac{1}{2} \rho C_L D L U_o^2 \times \frac{1}{4} \{ [2 \sin(N_L \omega_W t) - \sin((N_L - 2)\omega_W t) - \sin((N_L + 2)\omega_W t)] + [2 \sin(N_L(\omega_W t + \kappa_W a)) - \sin((N_L - 2)(\omega_W t + \kappa_W a)) - \sin((N_L + 2)(\omega_W t + \kappa_W a))] \} \times \frac{a}{2}$$

Equation 5-95

Considering the fundamental lift frequency only,

$$M_{\phi} = 2 \times \frac{1}{4} \rho C_L D L U_o^2 [\sin(N_L \omega_W t) + \sin(N_L(\omega_W t + \kappa_W a))] \times \frac{a}{2}$$

Equation 5-96

Equation 5-96 can be further simplified as,

$$M_{\phi} = 2 \times \frac{1}{2} \rho C_L D L U_o^2 \cos\left(N_L \frac{\kappa_W a}{2}\right) \sin\left(N_L \left(\omega_W t + \frac{\kappa_W a}{2}\right)\right) \times \frac{a}{2}$$

Equation 5-97

During resonance/lock-in under lift excitation,

$$\omega_L = N_L \omega_W = \omega_{N\phi} = \sqrt{\frac{K_{\phi}}{I_{\phi}}}$$

Equation 5-98

Considering the  $KC$  relationship, lock-in condition, mass ratio, damping ratio and the radial distance of the cylinders from the yaw centre ( $r_{\phi}$ ) which is also the yaw radius of gyration, the amplitude ratio of yaw VIV resonant response can be derived from Equation 5-93 as,

$$\frac{\phi_o}{D} = \frac{C_L K C^2 a}{16 \pi^3 N_L^2 \zeta_{\phi} m^* r_{\phi}^2} \cos\left(N_L \frac{\kappa_W a}{2}\right)$$

Equation 5-99

Equation 5-99 shows the inverse proportionality of the yaw response to the mass damping parameter and the  $KC$  number dependence of the yaw VIV. The effect of cylinder longitudinal spacing and the inverse proportionality with the square of yaw radius of gyration are also captured in the equation.

Similar to crossflow VIV, considering a 1 % amplitude ratio to represent VIV occurrence,

$$\frac{r_\phi \phi_0}{D} \leq \frac{1}{100} \quad \text{Equation 5-100}$$

The criterion for the occurrence of yaw VIV under lift excitation in a planar oscillatory flow can be derived as,

$$\zeta_\phi m^* \leq \frac{25 C_L KC^2 a}{4 \pi^3 N_L^2 r_\phi} \cos\left(N_L \frac{\kappa_W a}{2}\right) \quad \text{Equation 5-101}$$

Considering a  $KC$  number of 10, the corresponding maximum stationary cylinder lift coefficient of 3 and the corresponding lift frequency factor of 2, the yaw VIV criterion in planar oscillatory flow becomes,

$$\zeta_\phi m^* r_\phi \leq 15.12 a \cos\left(N_L \frac{\kappa_W a}{2}\right) \quad \text{Equation 5-102}$$

## 5.6 VIV of Jack-up with four Circular Cylindrical Legs in Regular Waves

### 5.6.1 Crossflow VIV

The effective crossflow excitation force ( $F_{ey}$ ) of the SDOF system of the jack-up can be expressed based on energy principle (Bartrop and Adams, 1991) as,

$$F_{ey} = \int_0^h f_{oy}(z) \frac{A \sin(\kappa_L z + B) + E}{A \sin(\kappa_L L + B) + E} dz \quad \text{Equation 5-103}$$

where  $f_{oy}(z)$  represents the distribution of the amplitude of the total oscillatory lift excitation force along the legs.

The resonant crossflow response ( $y_L$ ) of the SDOF can be expressed similar to Equation 5-34 as,

$$y_L = \frac{F_{ey}}{C_{ey} \omega_{Ny}} \quad \text{Equation 5-104}$$

where  $C_{ey}$  represents the effective damping coefficient of the jack-up SDOF along the crossflow direction.

The simplest crossflow VIV model for a jack-up can be developed by considering the oscillatory lift excitation in a regular wave, based on Equation 5-89 as,

$$f_{oy}(z) = 2 \times \frac{1}{2} \rho C_L D U_o(z)^2 \cos\left(N_L \frac{\kappa_W a}{2}\right) \quad \text{Equation 5-105}$$

The horizontal particle velocity amplitude distribution along the legs ( $U_o(z)$ ) in the regular wave can be expressed as,

$$U_o(z) = \frac{\pi H_W \cosh(\kappa_W z)}{T_W \sinh(\kappa_W h)} \quad \text{Equation 5-106}$$

where  $H_W, T_W, \kappa_W$  and  $h$  represent the wave height, wave period, wave number and the effective water depth respectively.

Equation 5-105 and Equation 5-106 in Equation 5-103,

$$F_{ey} = \rho C_L D \left[ \frac{\pi H_W}{T_W \sinh(\kappa_W h)} \right]^2 \frac{\cos\left(N_L \frac{\kappa_W a}{2}\right)}{A \sin(\kappa_L L + B) + E} \int_0^h [\cosh(\kappa_W z)]^2 [A \sin(\kappa_L z + B) + E] dz \quad \text{Equation 5-107}$$

Accordingly, Equation 5-104 becomes,

$$y_L = \frac{\rho C_L D}{C_{ey} \omega_{Ny}} \left[ \frac{\pi H_W}{T_W \sinh(\kappa_W h)} \right]^2 \left( \frac{\cos\left(N_L \frac{\kappa_W a}{2}\right)}{[A \sin(\kappa_L L + B) + E]} \right) \int_0^h [\cosh(\kappa_W z)]^2 [A \sin(\kappa_L z + B) + E] dz \quad \text{Equation 5-108}$$

Defining  $KC$  number of the regular wave at the water level,

$$KC(h) = \frac{U_o(h)}{f_w D} \quad \text{Equation 5-109}$$

where  $f_w$  represents the wave frequency.

Considering the  $KC$  relationship and the crossflow resonance lock-in condition in Equation 5-108, the crossflow response can be derived as,

$$\frac{y_L}{D} = \frac{C_L KC(h)^2}{8 \pi^3 N_L^2 \zeta_y m^*} \left[ \frac{1}{\cosh(\kappa_W h)} \right]^2 \left( \frac{\cos\left(N_L \frac{\kappa_W a}{2}\right)}{h [A \sin(\kappa_L L + B) + E]} \right) \int_0^h [\cosh(\kappa_W z)]^2 [A \sin(\kappa_L z + B) + E] dz$$

$$\text{Equation 5-110}$$

Equation 5-110 shows clearly the inverse proportionality with the mass damping parameter, the effect of longitudinal leg spacing and mode shape,  $KC$  dependence and the effect of horizontal velocity profile on the crossflow VIV response.

It needs to be noted that the integration on the right-hand side of the Equation 5-110 should be performed only over the extent of leg length experiencing the crossflow excitation. The extent of cylinder length experiencing crossflow excitation can be found from the variation of  $KC$  along the leg. The integration shall be performed over the leg length falling in the  $KC$  range, 4 to 16.

Considering a 1% amplitude ratio, the criterion for the occurrence of crossflow VIV of a jack-up in regular waves can be derived as,

$$\zeta_y m^* \leq \frac{25 C_L KC(h)^2}{2 \pi^3 N_L^2} \left[ \frac{1}{\cosh(\kappa_W h)} \right]^2 \left( \frac{\cos\left(N_L \frac{\kappa_W a}{2}\right)}{h [A \sin(\kappa_L L + B) + E]} \right) \int_0^h [\cosh(\kappa_W z)]^2 [A \sin(\kappa_L z + B) + E] dz$$

$$\text{Equation 5-111}$$

Considering a  $KC$  number of 10, corresponding maximum stationary cylinder lift coefficient of 3 and corresponding lift frequency factor of 2, the crossflow VIV criterion of a jack-up in regular wave becomes,

$$\zeta_y m^* \left( \frac{h [\cosh(\kappa_W h)]^2 [A \sin(\kappa_L L + B) + E]}{\int_0^h [\cosh(\kappa_W z)]^2 [A \sin(\kappa_L z + B) + E] dz} \right) \leq 30.23 \cos \left( N_L \frac{\kappa_W a}{2} \right) \quad \text{Equation 5-112}$$

The expression inside parentheses on the left-hand side can be defined as the mode factor (MF). It can be observed that the MF is not only dependent on the leg mode shape but also on the wave horizontal particle kinematics. The product of MF with mass damping parameter can be the effective mass damping parameter for a jack-up. Thus, the criterion becomes,

$$\zeta_y m^* MF \leq 30.23 \cos \left( N_L \frac{\kappa_W a}{2} \right) \quad \text{Equation 5-113}$$

#### 5.6.1.1 Crossflow / Sway VIV in Shallow Water

In shallow water,

$$(\kappa_W h \rightarrow 0, \kappa_W z \rightarrow 0, \sinh(\kappa_W h) \rightarrow \kappa_W h, \cosh(\kappa_W h) \rightarrow 1, \cosh(\kappa_W z) \rightarrow 1),$$

$$U_o(z) = U_o = \frac{\pi H_W}{T_W \kappa_W h} \quad \text{Equation 5-114}$$

$$KC(z) = KC = \frac{U_o}{f_w D} \quad \text{Equation 5-115}$$

where  $KC(z)$  is the variation of  $KC$  number along legs.

Accordingly, the crossflow response in shallow water can be derived from Equation 5-110 as,

$$\frac{y_L}{D} = \frac{C_L KC^2}{8 \pi^3 N_L^2 \zeta_y m^*} \left( \frac{\cos \left( N_L \frac{\kappa_W a}{2} \right)}{h [A \sin(\kappa_L L + B) + E]} \right) \int_0^h [A \sin(\kappa_L z + B) + E] dz$$

Equation 5-116

Consequently, the criterion for the occurrence of crossflow jack-up VIV in shallow water becomes,

$$\zeta_y m^* \left( \frac{h [A \sin(\kappa_L L + B) + E]}{\int_0^h [A \sin(\kappa_L z + B) + E] dz} \right) \leq 30.23 \cos \left( N_L \frac{\kappa_W a}{2} \right) \quad \text{Equation 5-117}$$

It can be seen from Equation 5-117 that the MF becomes independent of the velocity profile and is same as that of uniform current in shallow waters.

#### 5.6.1.2 Crossflow / Sway VIV in Deep Water

In deep water,

$$(\kappa_W h \rightarrow \infty, \kappa_W z \rightarrow \infty, \sinh(\kappa_W h) \rightarrow \cosh(\kappa_W h) \rightarrow e^{\kappa_W h},$$

$$\sinh(\kappa_W z) \rightarrow \cosh(\kappa_W z) \rightarrow e^{\kappa_W z}),$$

$$U_o(z) = \frac{\pi H_W}{T_W} e^{\kappa_W(z-h)} \quad \text{Equation 5-118}$$

The crossflow response in deep water can be derived from Equation 5-110 as,

$$\frac{y_L}{D} = \frac{C_L KC(h)^2}{8 \pi^3 N_L^2 \zeta_y m^*} \left( \frac{1}{e^{(2\kappa_W h)}} \right) \left( \frac{\cos \left( N_L \frac{\kappa_W a}{2} \right)}{h [A \sin(\kappa_L L + B) + E]} \right) \int_0^h e^{(2\kappa_W z)} [A \sin(\kappa_L z + B) + E] dz$$

Equation 5-119

Accordingly, the criterion for the occurrence of crossflow jack-up VIV in deep water becomes,

$$\zeta_y m^* \left( \frac{e^{(2\kappa_W h)} h [A \sin(\kappa_L L + B) + E]}{\int_0^h e^{(2\kappa_W z)} [A \sin(\kappa_L z + B) + E] dz} \right) \leq 30.23 \cos \left( N_L \frac{\kappa_W a}{2} \right) \quad \text{Equation 5-120}$$

It can be seen from Equation 5-120 that in deep water, MF is significantly affected by the exponential horizontal particle velocity profile in a regular wave.

### 5.6.2 Yaw VIV

The effective yaw excitation on the jack-up ( $M_{oe\phi}$ ) can be expressed based on Equation 5-44, Equation 5-45 and Equation 5-94 as,

$$M_{oe\phi} = \frac{\rho C_L D a}{2} \left[ \frac{\pi H_W}{T_W \sinh(\kappa_W h)} \right]^2 \frac{\cos\left(N_L \frac{\kappa_W a}{2}\right)}{A \sin(\kappa_L L + B) + E} \int_0^h [\cosh(\kappa_W z)]^2 [A \sin(\kappa_L z + B) + E] dz$$

Equation 5-121

Equation 5-121 in Equation 5-46, and considering  $KC$  relationship and lock-in condition, the yaw response can be derived as,

$$\frac{\phi_L}{D} = \frac{C_L KC(h)^2 a}{16 \pi^3 N_L^2 \zeta_\phi m^* k_\phi^2} \left[ \frac{1}{\cosh(\kappa_W h)} \right]^2 \left( \frac{\cos\left(N_L \frac{\kappa_W a}{2}\right)}{h [A \sin(\kappa_L L + B) + E]} \right) \int_0^h [\cosh(\kappa_W z)]^2 [A \sin(\kappa_L z + B) + E] dz$$

Equation 5-122

Equation 5-122 shows the inverse proportionality of the yaw response with the mass damping parameter and the square of the yaw radius of gyration. The effects of mode shape, horizontal particle velocity profile,  $KC$  number and longitudinal leg spacing are also captured in the equation.

Considering a 1% amplitude ratio, the criterion for the occurrence of yaw VIV of a Jack-up in regular waves can be derived as,

$$\zeta_\phi m^* k_\phi^2 \left( \frac{h [\cosh(\kappa_W h)]^2 [A \sin(\kappa_L L + B) + E]}{\int_0^h [\cosh(\kappa_W z)]^2 [A \sin(\kappa_L z + B) + E] dz} \right) \leq \frac{25 C_L KC(h)^2 a \sqrt{a^2 + b^2}}{8 \pi^3 N_L^2} \cos\left(N_L \frac{\kappa_W a}{2}\right)$$

Equation 5-123

Considering a  $KC$  number of 10, corresponding to the maximum stationary cylinder lift coefficient of 3.00 and the corresponding lift frequency factor of 2, the criterion becomes,

$$\zeta_{\phi} m^* M F k_{\phi}^2 \leq 7.56 a \sqrt{a^2 + b^2} \cos\left(N_L \frac{\kappa_W a}{2}\right) \quad \text{Equation 5-124}$$

#### 5.6.2.1 Yaw VIV in Shallow Water

In shallow water, the yaw crossflow response ratio can be derived as,

$$\frac{\phi_L}{D} = \frac{C_L KC^2 a}{16 \pi^3 N_L^2 \zeta_{\phi} m^* k_{\phi}^2} \left( \frac{\cos\left(N_L \frac{\kappa_W a}{2}\right)}{h [A \sin(\kappa_L L + B) + E]} \right) \int_0^h [A \sin(\kappa_L z + B) + E] dz$$

$$\text{Equation 5-125}$$

The criterion for the occurrence of crossflow jack-up VIV in shallow water becomes,

$$\zeta_{\phi} m^* k_{\phi}^2 \left( \frac{h [A \sin(\kappa_L L + B) + E]}{\int_0^h [A \sin(\kappa_L z + B) + E] dz} \right) \leq 7.56 \cos\left(N_L \frac{\kappa_W a}{2}\right) a \sqrt{a^2 + b^2} \quad \text{Equation 5-126}$$

#### 5.6.2.2 Yaw VIV in Deep Water

In deep water, the crossflow response can be derived as,

$$\frac{\phi_L}{D} = \frac{C_L KC(h)^2 a}{16 \pi^3 N_L^2 \zeta_{\phi} m^* k_{\phi}^2} \left( \frac{1}{e^{(2\kappa_W h)}} \right) \left( \frac{\cos\left(N_L \frac{\kappa_W a}{2}\right)}{h [A \sin(\kappa_L L + B) + E]} \right) \int_0^h e^{(2\kappa_W z)} [A \sin(\kappa_L z + B) + E] dz$$

$$\text{Equation 5-127}$$

The criterion for the occurrence of crossflow jack-up VIV in deep water becomes,

$$\zeta_{\phi} m^* k_{\phi}^2 \left( \frac{e^{(2\kappa_W h)} h [A \sin(\kappa_L L + B) + E]}{\int_0^h e^{(2\kappa_W z)} [A \sin(\kappa_L z + B) + E] dz} \right) \leq 7.56 \cos\left(N_L \frac{\kappa_W a}{2}\right) a \sqrt{a^2 + b^2}$$

Equation 5-128

## 5.7 Mean Drag Amplification in Regular waves

In regular waves, the variation of velocity along the leg is,

$$U(z) = \frac{\pi H_W \cosh(\kappa_W z)}{T_W \sinh(\kappa_W h)} \quad \text{Equation 5-129}$$

### 5.7.1 Crossflow VIV

Neglecting the variation of the mean drag coefficient along the legs; Equation 5-129 in Equation 5-56 yields the amplified mean drag force acting on a jack-up leg,

$$F_{DAL} = \frac{1}{2} \rho C_{DW} D \left( \frac{\pi H_W}{T_W \sinh(\kappa_W h)} \right)^2 \int_0^h \left( 1 + \frac{2.1 y_L [A \sin(\kappa_L z + B) + E]}{D [A \sin(\kappa_L L + B) + E]} \right) (\cosh(\kappa_W z))^2 dz$$

Equation 5-130

where  $C_{DW}$  represents the mean drag coefficient in regular wave or oscillatory flow

The amplified drag coefficient of the vibrating leg can be expressed as,

$$C_{DAL} = C_{DW} \left[ \frac{\int_0^h \left( 1 + \frac{2.1 y_L [A \sin(\kappa_L z + B) + E]}{D [A \sin(\kappa_L L + B) + E]} \right) (\cosh(\kappa_W z))^2 dz}{\int_0^h (\cosh(\kappa_W z))^2 dz} \right] \quad \text{Equation 5-131}$$

The increased inline OTM per leg shall be,

$$OTM_{AL} = \frac{1}{2} \rho C_{DW} D \left( \frac{\pi H_W}{T_W \sinh(\kappa_W h)} \right)^2 \int_0^h \left( 1 + \frac{2.1 y_L [A \sin(\kappa_L z + B) + E]}{D [A \sin(\kappa_L L + B) + E]} \right) (\cosh(\kappa_W z))^2 z dz$$

Equation 5-132

For jack-ups with independent legs, the deflected leg profile can be considered as a perfect quarter sine wave and  $A = 1$ ,  $B = E = 0$  and  $\kappa_L = \frac{\pi}{2L}$ .

$$F_{DAL} = \frac{1}{2} \rho C_{DW} D \left( \frac{\pi H_W}{T_W \sinh(\kappa_W h)} \right)^2 \int_0^h \left( 1 + \frac{2.1 y_L}{D} \sin(\kappa_L z) \right) (\cosh(\kappa_W z))^2 dz$$

Equation 5-133

$$C_{DAL} = C_{DW} \left[ \frac{\int_0^h \left( 1 + \frac{2.1 y_L}{D} \sin(\kappa_L z) \right) (\cosh(\kappa_W z))^2 dz}{\int_0^h (\cosh(\kappa_W z))^2 dz} \right]$$

Equation 5-134

$$OTM_{AL} = \frac{1}{2} \rho C_{DW} D \left( \frac{\pi H_W}{T_W \sinh(\kappa_W h)} \right)^2 \int_0^h \left( 1 + \frac{2.1 y_L}{D} \sin(\kappa_L z) \right) (\cosh(\kappa_W z))^2 z dz$$

Equation 5-135

The total amplified OTM on the jack-up along the direction of regular wave shall be,

$$OTM_A = n_L \frac{1}{2} \rho C_{DW} D \left( \frac{\pi H_W}{T_W \sinh(\kappa_W h)} \right)^2 \int_0^h \left( 1 + \frac{2.1 y_L}{D} \sin(\kappa_L z) \right) (\cosh(\kappa_W z))^2 z dz$$

Equation 5-136

It can be inferred that in shallow water, the flow velocity becomes independent of the water depth and the equations converge to that of uniform current.

### 5.7.2 Yaw VIV

Similarly, for Yaw VIV in regular waves,

$$F_{DAL} = \frac{1}{2} \rho C_{DW} D \left( \frac{\pi H_W}{T_W \sinh(\kappa_W h)} \right)^2 \int_0^h \left( 1 + \frac{1.05 a \phi_L [A \sin(\kappa_L z + B) + E]}{D [A \sin(\kappa_L L + B) + E]} \right) (\cosh(\kappa_W z))^2 dz$$

Equation 5-137

$$C_{DAL} = C_{DW} \left[ \frac{\int_0^h \left( 1 + \frac{1.05 a\phi_L [A \sin(\kappa_L z + B) + E]}{D [A \sin(\kappa_L L + B) + E]} \right) (\cosh(\kappa_W z))^2 dz}{\int_0^h (\cosh(\kappa_W z))^2 dz} \right] \quad \text{Equation 5-138}$$

$$OTM_{AL} = \frac{1}{2} \rho C_{DW} D \left( \frac{\pi H_W}{T_W \sinh(\kappa_W h)} \right)^2 \int_0^h \left( 1 + \frac{1.05 a\phi_L [A \sin(\kappa_L z + B) + E]}{D [A \sin(\kappa_L L + B) + E]} \right) (\cosh(\kappa_W z))^2 z dz \quad \text{Equation 5-139}$$

For jack-ups with independent legs,  $A = 1$ ,  $B = E = 0$  and  $\kappa_L = \frac{\pi}{2L}$

$$F_{DAL} = \frac{1}{2} \rho C_{DW} D \left( \frac{\pi H_W}{T_W \sinh(\kappa_W h)} \right)^2 \int_0^h \left( 1 + \frac{1.05 a\phi_L \sin(\kappa_L z)}{D} \right) (\cosh(\kappa_W z))^2 dz \quad \text{Equation 5-140}$$

$$C_{DAL} = C_{DW} \left[ \frac{\int_0^h \left( 1 + \frac{1.05 a\phi_L \sin(\kappa_L z)}{D} \right) (\cosh(\kappa_W z))^2 dz}{\int_0^h (\cosh(\kappa_W z))^2 dz} \right] \quad \text{Equation 5-141}$$

$$OTM_{AL} = \frac{1}{2} \rho C_{DW} D \left( \frac{\pi H_W}{T_W \sinh(\kappa_W h)} \right)^2 \int_0^h \left( 1 + \frac{1.05 a\phi_L \sin(\kappa_L z)}{D} \right) (\cosh(\kappa_W z))^2 z dz \quad \text{Equation 5-142}$$

Similarly, the total amplified OTM along the direction of flow shall be,

$$OTM_A = n_L \frac{1}{2} \rho C_{DW} D \left( \frac{\pi H_W}{T_W \sinh(\kappa_W h)} \right)^2 \int_0^h \left( 1 + \frac{1.05 a\phi_L \sin(\kappa_L z)}{D} \right) (\cosh(\kappa_W z))^2 z dz \quad \text{Equation 5-143}$$

It can be inferred that the increase in drag force and OTM will be similar to that of crossflow VIV.

### 5.8 Reduced Velocity during VIV in an Oscillatory Flow

The reduced velocity ( $V_r$ ) in an oscillatory flow can be expressed as,

$$V_r = \frac{U_o}{f_N D} \quad \text{Equation 5-144}$$

where  $f_N$  represents the natural frequency of the cylinder.

During ideal lock-in vibrations in oscillatory flow,

$$f_N = f_L = N_L f_w \quad \text{Equation 5-145}$$

where  $f_L$  represents the fundamental lift frequency in the oscillatory flow.

Substituting Equation 5-145 in Equation 5-144, the relationship between the critical reduced velocity ( $V_{r,crit}$ ) and the  $KC$  number during VIV in oscillatory flow can be expressed as,

$$V_{r,crit} = \frac{KC}{N_L} \quad \text{Equation 5-146}$$

It is to be noted that the lift frequency factor ( $N_L$ ) is also a function of  $KC$  number (Williamson, 1985). Figure 5-11 illustrates the variation of  $V_{r,crit}$  with respect to  $KC$  in an oscillatory flow. It can be seen that the upper limit of the reduced velocity is 8 during lock-in, for all  $KC$  ranges. Further, the lower limit is found to increase with increasing  $KC$  and tend towards 8 at high  $KC$  values. This behaviour can be attributed to the increase in  $N_L$  by a value of 1, corresponding to an increase in  $KC$  number by a value of 8.

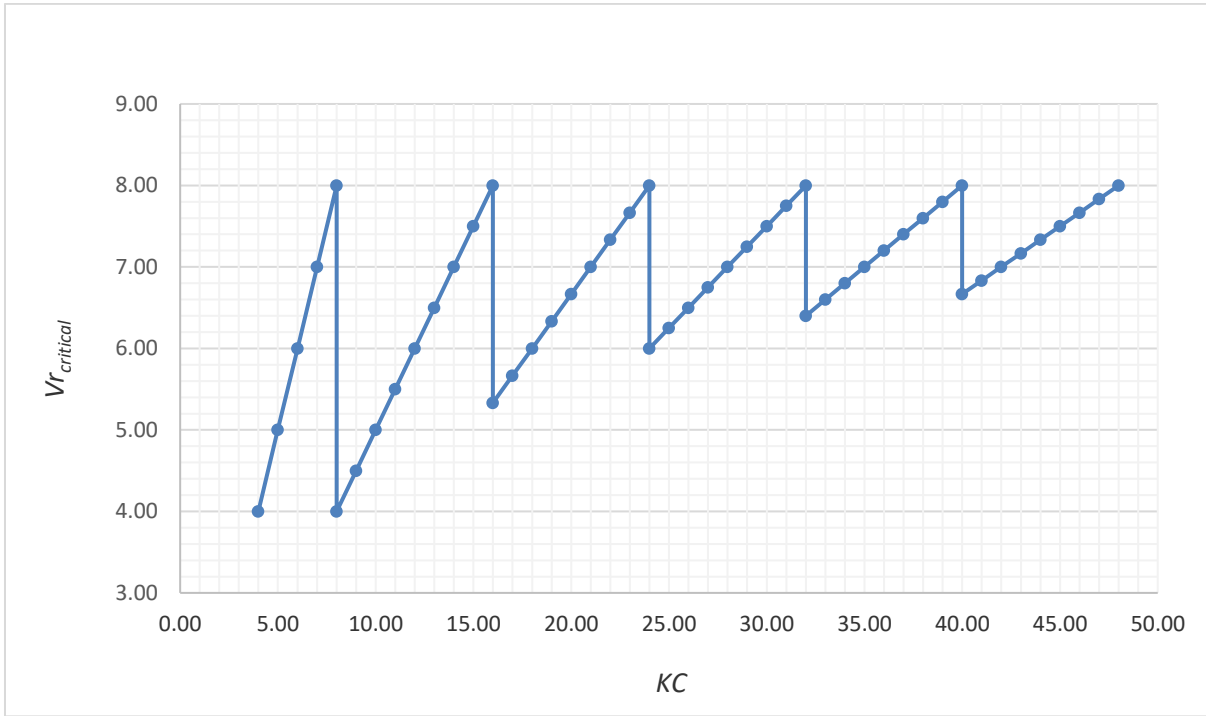


Figure 5-11: Critical reduced velocity versus  $KC$  number in oscillatory flow

## 5.9 Jack-up Damping

The damping of a jack-up comprises structural, foundation and hydrodynamic or fluid damping (PANEL OC-7, 2008; DNV GL, 2015; ABS, 2017). The following sections explain mathematically damping for various modes of VIV. Foundation damping is neglected as small jack-ups with independent legs have low soil penetrations and are not usually fitted with large diameter spud cans causing insignificant soil internal and radiation damping (Bartrop and Adams, 1991).

### 5.9.1 Inline/Surge damping

The effective inline damping coefficient ( $C_{eLx}$ ) per leg of the equivalent SDOF of a Jack-up can be expressed based on Energy Principle (Bartrop and Adams, 1991) as,

$$\pi \omega C_{eLx} x_L^2 = \int_0^h \pi \omega c_{Lx}(z) (x_o(z))^2 dz \quad \text{Equation 5-147}$$

where  $x_o(z)$  and  $c_{Lx}(z)$  represent the distribution of inline displacement amplitude and damping coefficient respectively along the legs.

Considering leg deflected mode shape  $x_o(z)$ , and simplifying,

$$C_{eLx} = \int_0^h c_{Lx}(z) \left[ \frac{A \sin(\kappa_L z + B) + E}{A \sin(\kappa_L L + B) + E} \right]^2 dz \quad \text{Equation 5-148}$$

Neglecting soil and radiation damping, the damping coefficient consists predominantly of contributions from fluid drag, material and structural damping.

#### 5.9.1.1 Fluid damping

The inline quadratic fluid damping force distribution on a leg ( $f_{CLfx}(z)$ ) of a Jack-up undergoing inline vibration can be expressed as (Xu *et al.*, 2012),

$$f_{CLfx}(z) = \frac{1}{2} \rho C_D D \left[ (\omega x_o(z))^2 \cos(\omega t) |\cos(\omega t)| - 2U(z) (\omega x_o(z)) |\cos(\omega t)| \right]$$

$$\text{Equation 5-149}$$

After linearisation of the quadratic damping and considering the deflected mode shape ( $x_o(z)$ ), the inline fluid damping force per leg can be represented in terms of an effective linear drag coefficient variation ( $c_{Lfx}(z)$ ) as,

$$c_{Lfx}(z) = \frac{4}{3\pi} \rho C_D D \omega x_L \left[ \frac{A \sin(\kappa_L z + B) + E}{A \sin(\kappa_L L + B) + E} \right] \quad \text{Equation 5-150}$$

Equation 5-150 in Equation 5-148 provides the effective inline fluid damping coefficient ( $C_{eLfx}$ ) per leg,

$$C_{eLfx} = \frac{4}{3\pi [A \sin(\kappa_L L + B) + E]^3} \rho C_D D \omega x_L \int_0^h [A \sin(\kappa_L z + B) + E]^3 dz \quad \text{Equation 5-151}$$

#### 5.9.1.2 Structural damping

The structural and material dampings are usually collectively termed as structural damping and the coefficient ( $C_{eLsx}$ ) is assumed as a certain percentage of the critical damping coefficient,  $2\sqrt{M_{eL}K_{eLx}}$ .

$$C_{eLsx} = \zeta_{sx} 2\sqrt{M_{eL}K_{eLx}} \quad \text{Equation 5-152}$$

where  $\zeta_{sx}$  is the structural damping ratio along inline direction.

### 5.9.1.3 Effective Inline Damping

The effective inline SDOF damping coefficient per leg shall be,

$$C_{eLx} = C_{eLfx} + C_{eLsx} \quad \text{Equation 5-153}$$

The effective inline damping coefficient ( $C_{ex}$ ) of the jack-up SDOF shall be,

$$C_{ex} = n_L C_{eLx} \quad \text{Equation 5-154}$$

where  $n_L$  represents the number of legs.

## 5.9.2 Crossflow damping

The crossflow damping of the jack-up can be expressed similar to the inline damping, neglecting the damping contributions from soil foundation and radiation.

### 5.9.2.1 Fluid Damping

After linearization of the quadratic damping, the crossflow fluid damping force per leg can be represented in terms of an effective linear drag coefficient variation ( $c_{Lfy}(z)$ ) as,

$$c_{Lfy}(z) = \frac{4}{3\pi} \rho C_{DW} D \omega y_L \left[ \frac{A \sin(\kappa_L z + B) + E}{A \sin(\kappa_L L + B) + E} \right] \quad \text{Equation 5-155}$$

where  $C_{DW}$  represents the drag coefficient in oscillatory flow.

Consequently, the linear crossflow fluid damping coefficient per leg ( $C_{eLfy}$ ) becomes,

$$C_{eLfy} = \frac{4}{3\pi [A \sin(\kappa_L L + B) + E]^3} \rho C_{DW} D \omega y_L \int_0^h [A \sin(\kappa_L z + B) + E]^3 dz$$

Equation 5-156

The crossflow fluid drag coefficient is applicable only outside the extend of leg length experiencing lock-in excitation since the fluid damping is found to be negative during lock-in (Sarpkaya, 1995) and is implicitly accounted as the lift amplification.

#### 5.9.2.2 Structural Damping

The structural crossflow damping coefficient ( $C_{eLsy}$ ) per leg shall be,

$$C_{eLsy} = \zeta_{sy} 2\sqrt{M_{eL}K_{eLy}} \quad \text{Equation 5-157}$$

where  $\zeta_{sy}$  is the structural damping ratio along crossflow direction.

#### 5.9.2.3 Effective Crossflow Damping

The effective crossflow SDOF damping coefficient per leg ( $C_{eLy}$ ) shall be,

$$C_{eLy} = C_{eLfy} + C_{eLsy} \quad \text{Equation 5-158}$$

Within the lock-in crossflow extend,

$$C_{eLy} = C_{eLsy} \quad \text{Equation 5-159}$$

The effective crossflow damping coefficient ( $C_{ey}$ ) of the jack-up SDOF shall be,

$$C_{ey} = n_L C_{eLy} \quad \text{Equation 5-160}$$

### 5.9.3 Effective Damping for Yaw Mode

The effective yaw damping per leg of the equivalent SDOF of a Jack-up can be derived from the fluid and structural damping components, neglecting the foundation and radiation damping.

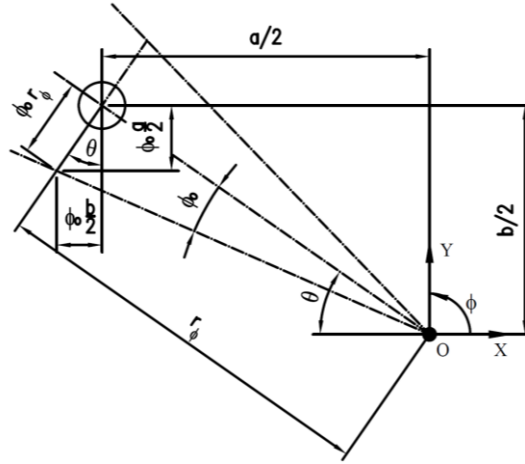


Figure 5-12: Leg deflection due to small angle of Yaw

### 5.9.3.1 Fluid Damping due to Inline Drag

The effective fluid yaw damping coefficient per leg due to inline drag force ( $C_{eLf\phi x}$ ) can be expressed in terms of the effective inline fluid damping coefficient ( $C_{eLfx}$ ) as,

$$C_{eLf\phi x} = C_{eLfx} \left(\frac{b}{2}\right)^2 \quad \text{Equation 5-161}$$

Equation 5-151 in Equation 5-161 and considering  $x_L = \frac{b}{2} \phi_L$  based on Figure 5-12, and after some mathematics,

$$C_{eLf\phi x} = \frac{b}{2} \left[ \frac{1}{3\pi [A \sin(\kappa_L L + B) + E]^3} b^2 \rho C_D D \omega \phi_L \int_0^h [A \sin(\kappa_L z + B) + E]^3 dz \right]$$

$$\text{Equation 5-162}$$

### 5.9.3.2 Fluid Damping due to Crossflow Drag

Similarly, the effective yaw damping coefficient per leg due to crossflow fluid drag force ( $C_{eLf\phi y}$ ) can be derived from the effective crossflow fluid damping coefficient as,

$$C_{eLf\phi y} = \frac{a}{2} \left[ \frac{1}{3\pi [A \sin(\kappa_L L + B) + E]^3} a^2 \rho C_{DW} D \omega \phi_L \int_0^h [A \sin(\kappa_L z + B) + E]^3 dz \right]$$

Equation 5-163

The yaw damping coefficient due to crossflow fluid drag is applicable only outside the extend of leg length experiencing lock-in, since the fluid damping is found to be negative during crossflow lock-in and is implicitly accounted as lift amplification.

#### 5.9.3.3 Structural Damping

The structural yaw damping coefficient of the jack-up SDOF ( $C_{es\phi}$ ) can be expressed as,

$$C_{es\phi} = \zeta_{s\phi} 2 \sqrt{I_{e\phi} K_{e\phi}} \quad \text{Equation 5-164}$$

where  $\zeta_{s\phi}$  is the structural damping ratio of the yaw mode.

#### 5.9.3.4 Effective Yaw Damping

The effective yaw damping coefficient ( $C_{e\phi}$ ) of the jack-up SDOF shall be,

$$C_{e\phi} = C_{es\phi} + n_L (C_{eLf\phi x} + C_{eLf\phi y}) \quad \text{Equation 5-165}$$

### 5.10 Lift Amplification with Response

It has been shown by many researchers that the lift excitation during crossflow lock-in is highly amplitude dependent. Pantazopoulos (1994) compiled a number of published data from various experiments and demonstrated that the lift excitation initially increases with response amplitude, peaks around an amplitude ratio of 0.50, subsequently decreases with further increase in amplitude and finally becomes zero at an amplitude ratio between 1 to 2. Sarpkaya (1995) demonstrated that the lift excitation peaks at around an amplitude ratio of 0.50 and showed that the fluid damping during lock-in is negative, increasing the lift force. It is concluded that the lift excitation approached to zero at the self-limiting amplitude, near an amplitude ratio of 1. Khalak and Williamson (1997b) plotted the maximum transverse amplitude ratios obtained from their experiments with an elastically mounted cylinder of low mass and damping

and demonstrated that the amplitude ratio of the upper branch converges towards a self-limiting value of around 1.2 as the mass damping parameter approaches a value of 0.

Khalak and Williamson (1999) did a critical review of the published results and demonstrated that the large variation in the self-limiting amplitudes obtained by various authors is due to the fact that the data comprised not only elastically mounted cylinders but also cantilevers, pivoted cylinders, etc. It was further observed that for elastically mounted rigid cylinders, the maximum peak amplitude ratio achieved was 1.13 while for cantilevers and pivoted cylinders greater self-limiting amplitude ratios in the order of 1.50 was achievable. This is expected behaviour as for cantilevers and pivoted cylinders, though the amplitude ratio exceeds the 2D self-limiting value near antinodes, vortex excitation can still be experienced at other locations resulting in a net positive lift force. Fluctuating pressure measurements by Bearman and Currie (1979) at a point 90° from the forward stagnation point on a transversely oscillating circular cylinder also revealed that the lift force reaches a maximum at an amplitude ratio of around 0.5. It was postulated that the self-limiting amplitudes of undamped vibrations would be between 1.5 to 2 diameters.

Based on the pressure fluctuation measurements (Bearman and Currie, 1979), the variation of the lift force with the amplitude ratio can be approximated as,

$$C_L = C_{L0} \left[ -2.99 \left( \frac{y_o}{D} \right)^4 + 14.70 \left( \frac{y_o}{D} \right)^3 - 25.90 \left( \frac{y_o}{D} \right)^2 + 15.30 \left( \frac{y_o}{D} \right) + 1 \right] \quad \text{Equation 5-166}$$

where  $C_{L0}$  represents the lift coefficient of the non-vibrating (stationary) cylinder

The variation of normalized lift coefficient with the crossflow amplitude ratio as per the Equation 5-166 is illustrated in Figure 5-13. It can be seen that the lift coefficient is dependent on the response amplitude, peaking and vanishing at amplitude ratios around 0.50 and 1.50 respectively.

### 5.10.1 *Crossflow/Sway VIV of a single cylinder*

Substituting Equation 5-166 in Equation 5-18,

$$\frac{y_o}{D} = \frac{C_{LO} \left[ -2.99 \left( \frac{y_o}{D} \right)^4 + 14.70 \left( \frac{y_o}{D} \right)^3 - 25.90 \left( \frac{y_o}{D} \right)^2 + 15.30 \left( \frac{y_o}{D} \right) + 1 \right]}{4\pi^3 St^2 \zeta_y m^*} \quad \text{Equation 5-167}$$

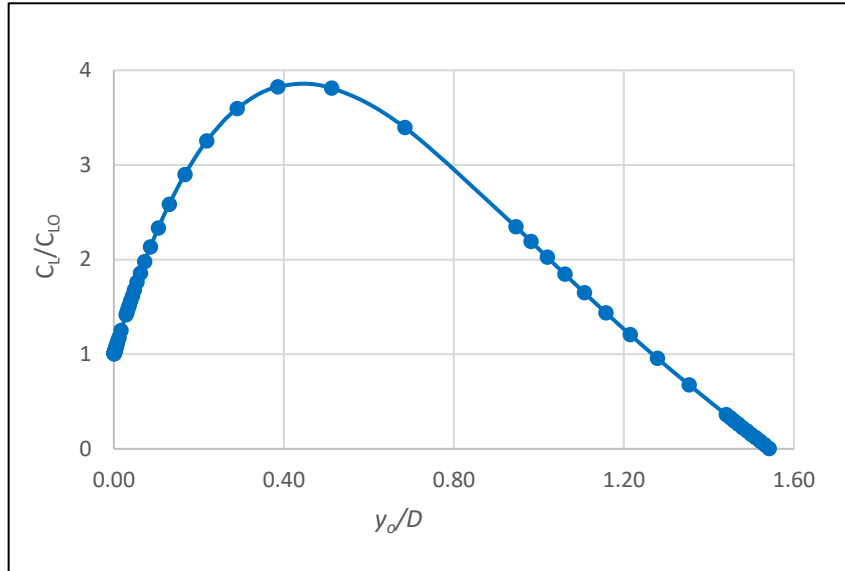


Figure 5-13: Lift variation with crossflow response

Defining,

$$\left( \frac{y_o}{D} \right)_o = \frac{C_{LO}}{4\pi^3 St^2 \zeta_y m^*} \quad \text{Equation 5-168}$$

Equation 5-167 can be rearranged to a quartile equation, which can be solved to obtain the amplitude response,

$$\left[ -2.99 \left( \frac{y_o}{D} \right)_o \right] \left( \frac{y_o}{D} \right)_o^4 + \left[ 14.70 \left( \frac{y_o}{D} \right)_o \right] \left( \frac{y_o}{D} \right)_o^3 + \left[ -25.90 \left( \frac{y_o}{D} \right)_o \right] \left( \frac{y_o}{D} \right)_o^2 + \left[ 15.30 \left( \frac{y_o}{D} \right)_o - 1 \right] \left( \frac{y_o}{D} \right)_o + \left( \frac{y_o}{D} \right)_o = 0$$

$$\text{Equation 5-169}$$

The crossflow response amplitude ratio calculated from Equation 5-169 as a function of the mass-damping parameter is illustrated in Figure 5-14. The amplitude ratios calculated are also compared with the experimental values obtained for the elastically mounted cylinders by Khalak and Williamson (1997b) and Griffin (1980) at the low values of mass-damping parameters. It can be observed from the comparison that

Equation 5-169 serves as a conservative mathematical lift model to predict the VIV of cylindrical structures.

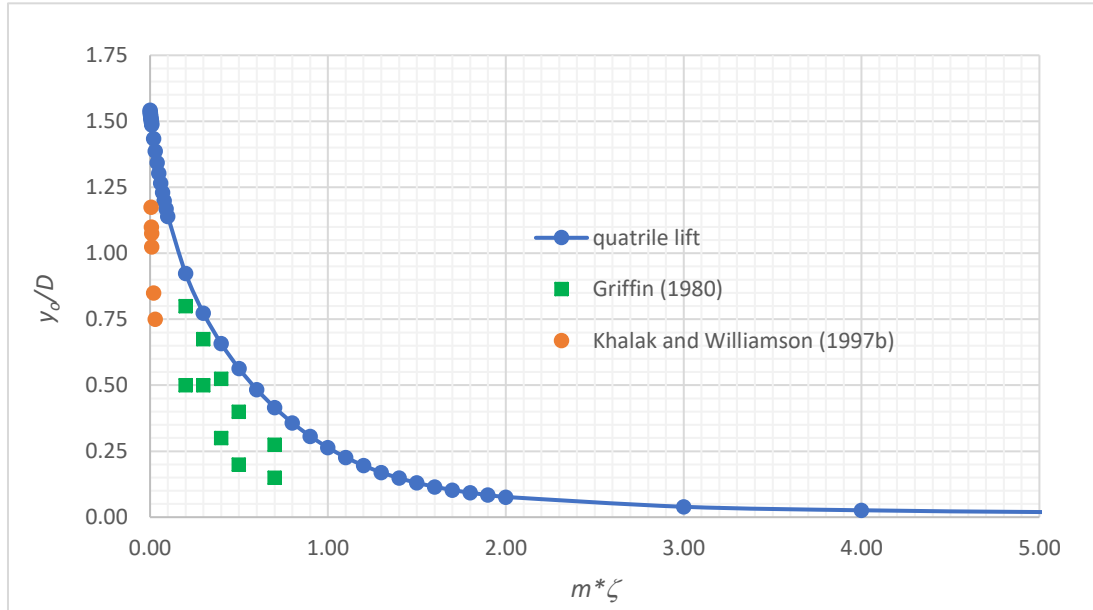


Figure 5-14: Validation of quartile polynomial lift expression with published data

It can be observed that the quadrille expression, Equation 5-169 provides a conservative engineering envelope for the response values at low mass-damping parameters, practically accounting for the upper branch of VIV as well.

### 5.10.2 Yaw VIV of a system of four 2D cylinders in a rectangular configuration under crossflow excitation

For small amplitude yaw motion,

$$y_o = \frac{a}{2} \phi_o \quad \text{Equation 5-170}$$

$$x_o = \frac{b}{2} \phi_o \quad \text{Equation 5-171}$$

Substituting Equation 5-166 and Equation 5-170 in Equation 5-30,

$$\frac{\phi_o}{D} = \frac{C_{Lo} \left[ -2.99 \left( \frac{a \phi_o}{2D} \right)^4 + 14.70 \left( \frac{a \phi_o}{2D} \right)^3 - 25.90 \left( \frac{a \phi_o}{2D} \right)^2 + 15.30 \left( \frac{a \phi_o}{2D} \right) + 1 \right] a}{8 \pi^3 St^2 \zeta_\phi m^* r_\phi^2}$$

Equation 5-172

Defining,

$$\left(\frac{\phi_o}{D}\right)_o = \frac{C_{LO} a}{8 \pi^3 St^2 \zeta_\phi m^* r_\phi^2} \quad \text{Equation 5-173}$$

Equation 5-172 can be rearranged to the quartile equation, which can be solved to obtain the yaw amplitude response,

$$\begin{aligned} & \left[-2.99 \left(\frac{a}{2}\right)^4 \left(\frac{\phi_o}{D}\right)_o\right] \left(\frac{\phi_o}{D}\right)_o^4 + \left[14.70 \left(\frac{a}{2}\right)^3 \left(\frac{\phi_o}{D}\right)_o\right] \left(\frac{\phi_o}{D}\right)_o^3 + \left[-25.90 \left(\frac{a}{2}\right)^2 \left(\frac{\phi_o}{D}\right)_o\right] \left(\frac{\phi_o}{D}\right)_o^2 \\ & + \left[15.30 \left(\frac{a}{2}\right) \left(\frac{\phi_o}{D}\right)_o - 1\right] \left(\frac{\phi_o}{D}\right)_o + \left(\frac{\phi_o}{D}\right)_o = 0 \end{aligned}$$

Equation 5-174

## 5.11 Jack-up VIV Response Prediction in Uniform Current

This section proposes response based models for predicting the VIV response of various modes of the jack-up in the uniform current.

### 5.11.1 *Inline / Surge VIV*

Substituting Equation 5-151 and Equation 5-153 in Equation 5-36 and further simplification yields a quadratic equation which can be solved to obtain the inline response.

$$[a_1 x_L^2 + a_2 x_L + a_3] = 0 \quad \text{Equation 5-175}$$

where,

$$a_1 = \frac{4}{3\pi [A \sin(\kappa_L L + B) + E]^3} \rho C_D D \omega \int_0^h [A \sin(\kappa_L z + B) + E]^3 dz \quad \text{Equation 5-176}$$

$$a_2 = C_{eLsx} \quad \text{Equation 5-177}$$

$$\mathbf{a}_3 = -\frac{F_{DO}}{\omega_{Nx}} \left( \frac{1}{h[A \sin(\kappa_L L + B) + E]} \right) \int_0^h [A \sin(\kappa_L z + B) + E] dz \quad \text{Equation 5-178}$$

The real and positive root of Equation 5-175 is the response of the Jack-up under the inline excitation. Table 5-2 contains the calculated inline responses of the vulnerable jack-up designs in a longitudinal uniform current, considering 2% maximum structural damping (PANEL OC-7, 2008; ABS, 2017). The legs are assumed to be pinned at the seabed for the calculations, and the corresponding leg mode shape is a quarter sine wave. It can be observed from the amplitude ratios that the designs at lower water depths are generally unresponsive to inline excitation. However, the jack-ups show a tendency to exhibit inline VIV at higher water depths with low effective mass damping parameters, with amplitudes in the order of 10% of the leg diameter.

### 5.11.2 Crossflow / Sway VIV

#### 5.11.2.1 Crossflow Vortex Excitation

By defining,

$$(f_{oy})_o = \frac{1}{2} \rho C_{LO} D U^2 \quad \text{Equation 5-179}$$

The simplest expression for the distribution of the oscillatory lift excitation ( $f_{oy}(z)$ ) along the leg shall be,

$$f_{oy}(z) = (f_{oy})_o \left[ -2.99 \left( \frac{y_o(z)}{D} \right)^4 + 14.70 \left( \frac{y_o(z)}{D} \right)^3 - 25.90 \left( \frac{y_o(z)}{D} \right)^2 + 15.30 \left( \frac{y_o(z)}{D} \right) + 1 \right]$$

$$\text{Equation 5-180}$$

The effective crossflow excitation force per leg ( $F_{eLy}$ ) of the SDOF system of the jack-up can be derived based on Energy Principle as,

Table 5-2: Inline VIV response of jack-ups in longitudinal critical uniform current

Sr. No	Project Name	$f_{Nx}$ (Hz)	Critical Current (knots)	Drag Coefficient ( $C_{D0}$ )	Amplitude Ratio ( $x_L/D$ )	Inline Response (m)	Total Damping (%)	MF	$\zeta_x m^* MF$
1	12-1012	0.52	1.29	0.10	0.01	0.00	2.00%	1.84	0.72
2	09-1027	0.21	0.55	0.10	0.01	0.01	2.01%	1.70	0.52
3	08-1016	0.27	0.81	0.10	0.02	0.01	2.04%	1.75	0.21
4	10-1046	0.17	0.51	0.10	0.02	0.01	2.02%	1.66	0.29
5	12-1013	0.35	1.09	0.10	0.01	0.01	2.01%	1.75	0.42
6	03-51	0.30	1.00	0.10	0.02	0.01	2.03%	1.70	0.27
7	9931	0.29	0.99	0.10	0.02	0.01	2.03%	1.68	0.27
8	9921 M	0.21	0.94	0.10	0.02	0.02	2.01%	1.81	0.30
9	10-1024	0.30	1.38	0.10	0.01	0.01	2.01%	1.67	0.37
10	05-1022	0.44	2.56	0.10	0.02	0.02	2.01%	1.78	0.30
11	9928	0.32	2.17	0.10	0.02	0.03	2.01%	1.82	0.24
12	07-1015A	0.30	2.14	0.10	0.02	0.02	2.01%	1.85	0.33
13	07-1015B	0.17	1.20	0.10	0.03	0.04	2.02%	1.72	0.20
14	12-1005	0.33	2.41	0.10	0.02	0.03	2.02%	1.68	0.22
15	200046	0.34	2.64	0.10	0.01	0.02	2.00%	2.46	0.36
16	07-1031	0.43	4.14	0.10	0.04	0.09	2.07%	1.68	0.12
17	9724	0.18	1.74	0.10	0.06	0.11	2.13%	1.64	0.09
18	13-1010A	0.17	1.87	0.10	0.04	0.09	2.06%	1.81	0.12
19	13-1010B	0.24	2.61	0.10	0.03	0.07	2.03%	1.89	0.16
20	09-4040	-	-	-	-	-	-	-	-
21	07-5020	-	-	-	-	-	-	-	-
22	11-4035	-	-	-	-	-	-	-	-

$$F_{ely} = \frac{(f_{oy})_o}{[A \sin(\kappa_L L + B) + E]} \left[ a_1 \left(\frac{y_L}{D}\right)^4 + a_2 \left(\frac{y_L}{D}\right)^3 + a_3 \left(\frac{y_L}{D}\right)^2 + a_4 \left(\frac{y_L}{D}\right) + a_5 \right]$$

Equation 5-181

where,

$$a_1 = \frac{-2.99}{[A \sin(\kappa_L L + B) + E]^4} \int_0^h [A \sin(\kappa_L z + B) + E]^5 dz$$

Equation 5-182

$$a_2 = \frac{14.70}{[A \sin(\kappa_L L + B) + E]^3} \int_0^h [A \sin(\kappa_L z + B) + E]^4 dz \quad \text{Equation 5-183}$$

$$a_3 = \frac{-25.90}{[A \sin(\kappa_L L + B) + E]^2} \int_0^h [A \sin(\kappa_L z + B) + E]^3 dz \quad \text{Equation 5-184}$$

$$a_4 = \frac{15.30}{[A \sin(\kappa_L L + B) + E]} \int_0^h [A \sin(\kappa_L z + B) + E]^2 dz \quad \text{Equation 5-185}$$

$$a_5 = \int_0^h [A \sin(\kappa_L z + B) + E] dz \quad \text{Equation 5-186}$$

The effective lift coefficient ( $C_{Le}$ ) of the leg shall be defined based on Equation 5-181 as,

$$C_{Le} = C_{LO} \left( \frac{1}{h [A \sin(\kappa_L L + B) + E]} \right) \left[ a_1 \left( \frac{y_L}{D} \right)^4 + a_2 \left( \frac{y_L}{D} \right)^3 + a_3 \left( \frac{y_L}{D} \right)^2 + a_4 \left( \frac{y_L}{D} \right) + a_5 \right]$$

$$\text{Equation 5-187}$$

The variation of the normalized effective lift coefficient  $\left( \frac{C_{Le}}{C_{LO}} \right)$  with respect to the depth ratio  $\left( \frac{h}{L} \right)$  and amplitude ratio  $\left( \frac{y_L}{D} \right)$  is illustrated in Figure 5-15 for the classical pinned footing assumption with a mode shape of the quarter sine wave. It can be observed that the lift coefficient tends to zero value at large response amplitudes ratios, representing the self-limiting nature of the vibrations.

#### 5.11.2.2 Crossflow Damping

In the uniform current, as the whole cylinder is experiencing uniform lock-in,

$$C_{eLy} = 0 \quad \text{Equation 5-188}$$

$$C_{eLy} = C_{eLsy} \quad \text{Equation 5-189}$$

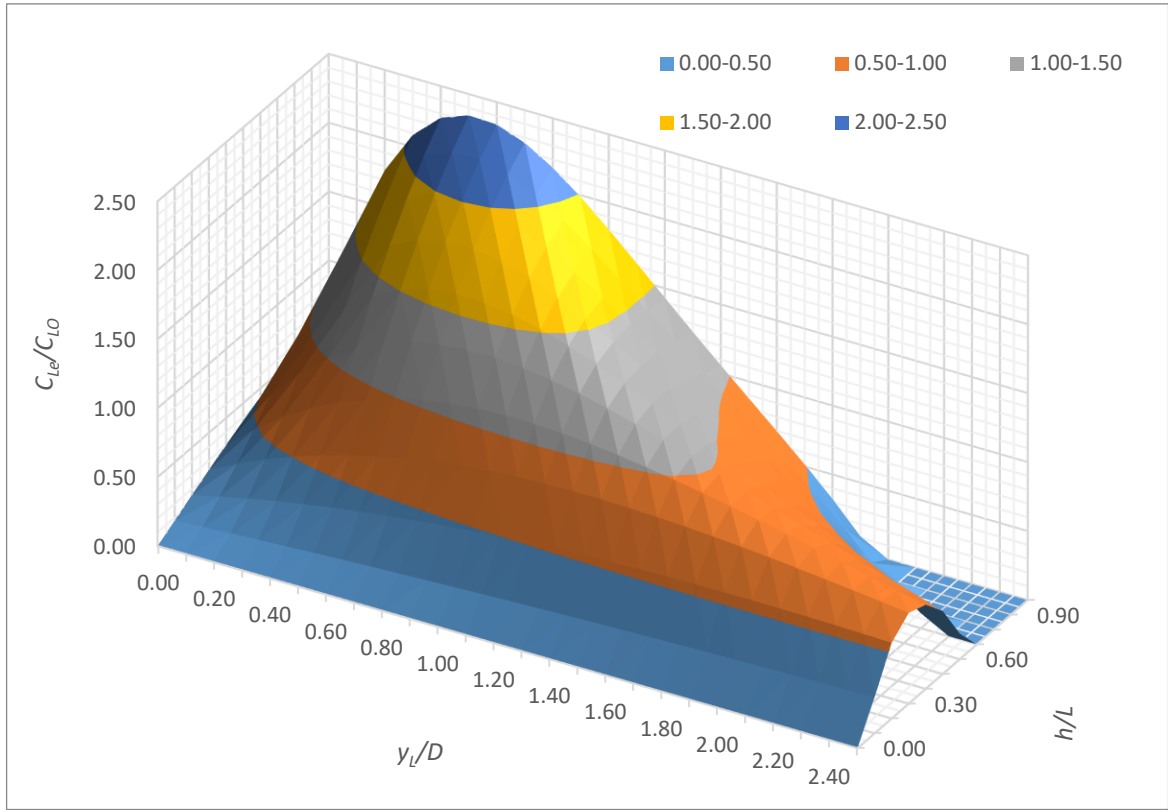


Figure 5-15: Variation of effective leg lift coefficient with amplitude ratio and depth ratio

### 5.11.2.3 Crossflow Response

Equation 5-41 becomes,

$$\frac{y_L}{D} = \frac{C_{LO}}{4\pi^3 St^2 \zeta_{sy} m^*} \left( \frac{1}{h [A \sin(\kappa_L L + B) + E]} \right) \left[ a_1 \left( \frac{y_L}{D} \right)^4 + a_2 \left( \frac{y_L}{D} \right)^3 + a_3 \left( \frac{y_L}{D} \right)^2 + a_4 \left( \frac{y_L}{D} \right) + a_5 \right]$$

Equation 5-190

Which can be simplified to a quartile equation,

$$\left[ a_1 \left( \frac{y_L}{D} \right)^4 + a_2 \left( \frac{y_L}{D} \right)^3 + a_3 \left( \frac{y_L}{D} \right)^2 + a_4' \left( \frac{y_L}{D} \right) + a_5 \right] = 0$$

Equation 5-191

where,

$$a_4' = \left[ a_4 - \frac{4\pi^3 St^2 \zeta_{sy} m^*}{C_{LO}} (h [A \sin(\kappa_L L + B) + E]) \right] \quad \text{Equation 5-192}$$

where  $\zeta_{sy}$  represents the structural damping ratio of the sway mode.

The real and positive root of Equation 5-191 is the response of the Jack-up under the crossflow excitation. Table 5-3 contains the calculated crossflow VIV response of the vulnerable jack-up designs in a longitudinal uniform current, considering 2% structural damping and neglecting lift amplification. The legs are assumed to be pinned at the seabed for the calculations. It can be observed from the amplitude ratios that most jack-ups experience aggressive crossflow VIV with large amplitudes of vibration. It can be inferred from the results that jack-ups with low effective mass damping parameters can even experience crossflow vibrations with amplitudes greater than 50% of the leg diameter in uniform currents at higher water depths.

### 5.11.3 Yaw VIV due to inline excitation

#### 5.11.3.1 Damping

The fluid damping coefficient of the typical four legged jack-up ( $C_{ef\phi}$ ) can be expressed based on Equation 5-162, Equation 5-163 and Equation 5-165 as,

$$C_{ef\phi} = 4 (C_{eLf\phi x} + C_{eLf\phi y}) \quad \text{Equation 5-193}$$

$$C_{ef\phi} = \frac{4}{6\pi [A \sin(\kappa_L L + B) + E]^3} \rho D \omega \phi_L [C_D b^3 + C_{DW} a^3] \int_0^h [A \sin(\kappa_L z + B) + E]^3 dz$$

$$\text{Equation 5-194}$$

$$C_{e\phi} = C_{es\phi} + C_{ef\phi} \quad \text{Equation 5-195}$$

Table 5-3: Crossflow VIV response of jack-ups in longitudinal critical uniform currents

Sr. No	Project Name	$f_{Ny}$ (Hz)	Critical Current (knots)	Lift Coefficient ( $C_L$ )	Amplitude Ratio ( $y_L/D$ )	Crossflow Response (m)	Total Damping	$\zeta_y m^* MF$
1	12-1012	0.57	2.80	0.24	0.07	0.03	2.00%	0.72
2	09-1027	0.22	1.11	0.71	0.28	0.15	2.00%	0.52
3	08-1016	0.27	1.63	0.28	0.27	0.17	2.00%	0.21
4	10-1046	0.19	1.10	0.57	0.40	0.25	2.00%	0.28
5	12-1013	0.32	2.01	0.25	0.12	0.08	2.00%	0.41
6	03-51	-	-	-	-	-	-	-
7	9931	0.24	1.62	0.27	0.20	0.14	2.00%	0.26
8	9921	0.21	1.88	0.25	0.17	0.16	2.00%	0.30
9	10-1024	0.30	2.77	0.27	0.15	0.14	2.00%	0.37
10	05-1022	0.44	5.11	0.31	0.21	0.25	2.00%	0.30
11	9928	0.32	4.34	0.31	0.26	0.36	2.00%	0.24
12	07-1015A	0.30	4.28	0.31	0.19	0.28	2.00%	0.33
13	07-1015B	0.17	2.39	0.28	0.29	0.42	2.00%	0.20
14	12-1005	-	-	-	-	-	-	-
15	200046	-	-	-	-	-	-	-
16	07-1031	-	-	-	-	-	-	-
17	9724	0.18	3.47	0.30	0.71	1.41	2.00%	0.08
18	13-1010A	0.17	3.74	0.28	0.50	1.09	2.00%	0.11
19	13-1010B	0.24	5.23	0.27	0.35	0.77	2.00%	0.15
20	09-4040	-	-	-	-	-	-	-
21	07-5020	-	-	-	-	-	-	-
22	11-4035	-	-	-	-	-	-	-

## 5.11.3.2 Response

Equation 5-195 in Equation 5-46 and some simplifications yield a quadratic equation which can be solved to obtain the yaw response,

$$\left[ a_1 \left( \frac{\phi_L}{D} \right)^2 + a_2 \left( \frac{\phi_L}{D} \right) + a_3 \right] = 0 \quad \text{Equation 5-196}$$

where,

$$a_1 = \frac{4 \pi St^2 [C_D b^3 + C_{DW} a^3]}{6 C_{D0} b [A \sin(\kappa_L L + B) + E]^2} \int_0^h [A \sin(\kappa_L z + B) + E]^3 dz \quad \text{Equation 5-197}$$

Table 5-4: Yaw VIV of jack-ups due to inline excitation in longitudinal critical uniform currents

Sr. No	Project Name	$f_{N\phi}$ (Hz)	Critical Current (knots)	Drag Coefficient ( $C_{D0}$ )	Yaw Response (degree)	Amplitude Ratio ( $\frac{r_{\phi} \theta_0}{D}$ )	Total Damping	$\zeta_{\phi} m^* MF$
1	12-1012	0.70	1.73	0.10	0.01	0.00	2.00%	0.72
2	09-1027	0.27	0.70	0.10	0.00	0.00	2.00%	0.52
3	08-1016	0.31	0.93	0.10	0.01	0.00	2.00%	0.21
4	10-1046	0.23	0.68	0.10	0.00	0.00	2.00%	0.28
5	12-1013	0.43	1.35	0.10	0.01	0.00	2.00%	0.41
6	03-51	0.40	1.36	0.10	0.01	0.00	2.00%	0.27
7	9931	0.32	1.10	0.10	0.01	0.00	2.00%	0.27
8	9921 M	0.26	1.17	0.10	0.00	0.00	2.00%	0.30
9	10-1024	0.40	1.85	0.10	0.00	0.00	2.00%	0.37
10	05-1022	0.54	3.15	0.10	0.01	0.00	2.00%	0.30
11	9928	0.41	2.76	0.10	0.01	0.00	2.00%	0.24
12	07-1015A	0.39	2.76	0.10	0.00	0.00	2.00%	0.33
13	07-1015B	0.22	1.53	0.10	0.00	0.00	2.00%	0.20
14	12-1005	0.42	3.07	0.10	0.01	0.00	2.00%	0.22
15	200046	0.38	2.96	0.10	0.00	0.00	2.00%	0.36
16	07-1031	0.51	4.94	0.10	0.01	0.00	2.00%	0.11
17	9724	0.20	1.98	0.10	0.01	0.00	2.00%	0.08
18	13-1010A	0.21	2.19	0.10	0.01	0.00	2.00%	0.11
19	13-1010B	0.29	3.07	0.10	0.01	0.00	2.00%	0.16
20	09-4040	-	-	-	-	-	-	-
21	07-5020	-	-	-	-	-	-	-
22	11-4035	-	-	-	-	-	-	-

$$a_2 = \frac{C_{es\phi} \omega_{N\phi} [A \sin(\kappa_L L + B) + E]}{\rho C_{D0} U^2 b} \quad \text{Equation 5-198}$$

$$a_3 = - \int_0^h [A \sin(\kappa_L z + B) + E] dz \quad \text{Equation 5-199}$$

The real and positive root of Equation 5-196 is the yaw response of the Jack-up under the inline excitation. Table 5-4 demonstrates the yaw VIV of the jack-up designs due to inline excitation in a longitudinal uniform current. The legs are assumed to be pinned at the seabed in the calculations. It can be observed from the results that jack-ups do not experience yaw VIV due to inline excitation irrespective of the water depths, as expected.

### 5.11.4 Yaw VIV due to crossflow excitation

#### 5.11.4.1 Damping

In the uniform current, as the whole cylinder is experiencing uniform lock-in,

$$C_{eLf\phi y} = 0 \quad \text{Equation 5-200}$$

$$C_{ef\phi} = 4C_{eLf\phi x}$$

$$= \frac{4}{6\pi[A \sin(\kappa_L L + B) + E]^3} \rho C_D D b^3 \omega \phi_L \int_0^h [A \sin(\kappa_L z + B) + E]^3 dz \quad \text{Equation 5-201}$$

#### 5.11.4.2 Response

The yaw excitation per unit leg length shall be,

$$m_{o\phi}(z) =$$

$$\frac{1}{2} \rho C_{Lo} DU^2 \left[ -2.99 \left( \frac{a \phi_o(z)}{2D} \right)^4 + 14.70 \left( \frac{a \phi_o(z)}{2D} \right)^3 - 25.90 \left( \frac{a \phi_o(z)}{2D} \right)^2 + 15.30 \left( \frac{a \phi_o(z)}{2D} \right) + 1 \right] \frac{a}{2}$$

$$\text{Equation 5-202}$$

Defining,

$$M_{o\phi L} = \frac{1}{2} \rho C_{Lo} DU^2 h \frac{a}{2}$$

$$\text{Equation 5-203}$$

The effective yaw excitation moment can be expressed based on Equation 5-44 and Equation 5-45 as,

$$M_{oe\phi} = \frac{4 M_{o\phi L}}{h [A \sin(\kappa_L L + B) + E]} \left[ a_1 \left( \frac{\phi_L}{D} \right)^4 + a_2 \left( \frac{\phi_L}{D} \right)^3 + a_3 \left( \frac{\phi_L}{D} \right)^2 + a_4 \left( \frac{\phi_L}{D} \right) + a_5 \right]$$

$$\text{Equation 5-204}$$

where,

$$a_1 = \frac{-2.99}{[A \sin(\kappa_L L + B) + E]^4} \left(\frac{a}{2}\right)^4 \int_0^h [A \sin(\kappa_L z + B) + E]^5 dz \quad \text{Equation 5-205}$$

$$a_2 = \frac{14.70}{[A \sin(\kappa_L L + B) + E]^3} \left(\frac{a}{2}\right)^3 \int_0^h [A \sin(\kappa_L z + B) + E]^4 dz \quad \text{Equation 5-206}$$

$$a_3 = \frac{-25.90}{[A \sin(\kappa_L L + B) + E]^2} \left(\frac{a}{2}\right)^2 \int_0^h [A \sin(\kappa_L z + B) + E]^3 dz \quad \text{Equation 5-207}$$

$$a_4 = \frac{15.30}{[A \sin(\kappa_L L + B) + E]} \left(\frac{a}{2}\right) \int_0^h [A \sin(\kappa_L z + B) + E]^2 dz \quad \text{Equation 5-208}$$

$$a_5 = \int_0^h [A \sin(\kappa_L z + B) + E] dz \quad \text{Equation 5-209}$$

Substituting Equation 5-204 in Equation 5-46

$$\phi_L = \frac{4 M_{o\phi L}}{(C_{es\phi} + C_{ef\phi}) \omega_N} \left( \frac{1}{h [A \sin(\kappa_L L + B) + E]} \right) \left[ a_1 \left(\frac{\phi_L}{D}\right)^4 + a_2 \left(\frac{\phi_L}{D}\right)^3 + a_3 \left(\frac{\phi_L}{D}\right)^2 + a_4 \left(\frac{\phi_L}{D}\right) + a_5 \right]$$

$$\text{Equation 5-210}$$

Which can be further simplified into a quartile equation,

$$\left[ a_1 \left(\frac{\phi_L}{D}\right)^4 + a_2 \left(\frac{\phi_L}{D}\right)^3 + a_3' \left(\frac{\phi_L}{D}\right)^2 + a_4' \left(\frac{\phi_L}{D}\right) + a_5 \right] = 0 \quad \text{Equation 5-211}$$

where,

$$a_3' = \left[ a_3 - \left( \frac{8\pi St^2 b^3 C_D \int_0^h [A \sin(\kappa_L z + B) + E]^3 dz}{3 C_{LO} a [A \sin(\kappa_L L + B) + C]^2} \right) \right] \quad \text{Equation 5-212}$$

$$a_4' = \left[ a_4 - \left( \frac{C_{es\phi} \omega_N [A \sin(\kappa_L L + B) + E]}{\rho C_{LO} U^2 a} \right) \right] \quad \text{Equation 5-213}$$

Table 5-5: Yaw VIV of jack-ups due to crossflow excitation in longitudinal critical uniform currents

Sr. No	Project Name	$f_{N\phi}$ (Hz)	Critical Current (knots)	Lift Coefficient ( $C_L$ )	Yaw Response (degree)	Amplitude Ratio ( $\frac{r_{\phi} \theta_0}{D}$ )	Total Damping	$\zeta_{\phi} m^* MF$
1	12-1012	0.70	3.45	0.24	0.40	0.08	2.00%	0.72
2	09-1027	0.27	1.41	0.71	1.39	0.34	2.02%	0.52
3	08-1016	0.31	1.86	0.28	1.40	0.20	2.03%	0.21
4	10-1046	0.23	1.37	0.57	2.18	0.49	2.03%	0.29
5	12-1013	0.43	2.71	0.25	0.98	0.17	2.01%	0.42
6	03-51	-	-	-	-	-	-	-
7	9931	0.32	2.20	0.27	1.33	0.25	2.02%	0.27
8	9921 M	0.26	2.34	0.25	1.13	0.21	2.01%	0.30
9	10-1024	0.40	3.70	0.27	0.92	0.19	2.01%	0.37
10	05-1022	-	-	-	-	-	-	-
11	9928	0.41	5.52	0.31	1.94	0.33	2.02%	0.24
12	07-1015A	0.39	5.51	0.31	1.34	0.25	2.01%	0.33
13	07-1015B	-	-	-	-	-	-	-
14	12-1005	-	-	-	-	-	-	-
15	200046	-	-	-	-	-	-	-
16	07-1031	-	-	-	-	-	-	-
17	9724	0.20	3.97	0.30	5.22	0.64	2.09%	0.09
18	13-1010A	0.21	4.39	0.28	3.64	0.52	2.05%	0.12
19	13-1010B	0.29	6.14	0.27	2.68	0.38	2.02%	0.16
20	09-4040	-	-	-	-	-	-	-
21	07-5020	-	-	-	-	-	-	-
22	11-4035	-	-	-	-	-	-	-

The real and positive root of Equation 5-211 gives the yaw response of the Jack-up under the crossflow excitation. Table 5-5 displays the calculated yaw VIV of the jack-ups due to crossflow excitation in longitudinal uniform currents, considering a 2% structural damping. The legs are assumed to be pinned at the seabed, and the lift amplification is neglected in the calculations. It can be observed that the jack-ups can experience aggressive yaw VIV across all water depths with response amplitudes greater than even 50% of the diameter.

## 5.12 Jack-up VIV Response Prediction in Regular Waves

This section proposes response based models for predicting the VIV response of various modes of the jack-up in regular waves.

### 5.12.1 Crossflow / Sway VIV

Considering lift amplification, the crossflow response amplitude ratio in regular waves can be derived like that in uniform current from Equation 5-104 as,

$$\frac{y_L}{D} = \frac{C_{LO} KC(h)^2}{8 \pi^3 N_L^2 \zeta_y m^*} \left[ \frac{1}{\cosh(\kappa_W h)} \right]^2 \left( \frac{\cos\left(N_L \frac{\kappa_W a}{2}\right)}{h [A \sin(\kappa_L L + B) + E]} \right) \left[ a_1 \left(\frac{y_L}{D}\right)^4 + a_2 \left(\frac{y_L}{D}\right)^3 + a_3 \left(\frac{y_L}{D}\right)^2 + a_4 \left(\frac{y_L}{D}\right) + a_5 \right]$$

Equation 5-214

$$a_1 = \frac{-2.99}{[A \sin(\kappa_L L + B) + E]^4} \int_0^h [\cosh(\kappa_W z)]^2 [A \sin(\kappa_L z + B) + E]^5 dz$$

Equation 5-215

$$a_2 = \frac{14.70}{[A \sin(\kappa_L L + B) + E]^3} \int_0^h [\cosh(\kappa_W z)]^2 [A \sin(\kappa_L z + B) + E]^4 dz$$

Equation 5-216

$$a_3 = \frac{-25.90}{[A \sin(\kappa_L L + B) + E]^2} \int_0^h [\cosh(\kappa_W z)]^2 [A \sin(\kappa_L z + B) + E]^3 dz$$

Equation 5-217

$$a_4 = \frac{15.30}{[A \sin(\kappa_L L + B) + E]} \int_0^h [\cosh(\kappa_W z)]^2 [A \sin(\kappa_L z + B) + E]^2 dz$$

Equation 5-218

$$a_5 = \int_0^h [\cosh(\kappa_W z)]^2 [A \sin(\kappa_L z + B) + E] dz$$

Equation 5-219

Equation 5-214 can be simplified to a quartile equation,

$$\left[ a_1 \left(\frac{y_L}{D}\right)^4 + a_2 \left(\frac{y_L}{D}\right)^3 + a_3 \left(\frac{y_L}{D}\right)^2 + a_4' \left(\frac{y_L}{D}\right) + a_5 \right] = 0$$

Equation 5-220

where,

$$a_4' = \left[ a_4 - \frac{8 \pi^3 N_L^2 \zeta_y m^*}{C_{LO} KC(h)^2} [\cosh(\kappa_W h)]^2 \left( \frac{h [A \sin(\kappa_L L + B) + E]}{\cos\left(N_L \frac{\kappa_W a}{2}\right)} \right) \right]$$

Equation 5-221

The real and positive root of Equation 5-220 is the response of the Jack-up under the crossflow excitation. Equation 5-220 can be solved iteratively by calculating the fluid damping contribution and the response amplitude till convergence.

If the whole cylinder is experiencing crossflow lock-in, the fluid damping can be neglected,

$$\zeta_y = \zeta_{sy}$$

Equation 5-222

The calculated crossflow VIV response of the jack-up designs in head regular waves is documented in Table 5-6. The leg bottom is assumed as pin supported, and the lift amplification is neglected for the calculations. It can be observed that the  $KC$  numbers during lock-in are low in nature, causing high lift coefficients and the jack-ups do exhibit aggressive lock-in sway vibrations with amplitudes up to 40% of the leg diameter.

### 5.12.2 Yaw VIV

Similarly, the yaw response amplitude ratio in regular waves can be derived from Equation 5-46 as,

$$\frac{\phi_L}{D} = \frac{C_{LO} KC(h)^2 a}{16 \pi^3 N_L^2 \zeta_\phi m^* k_\phi^2} \left[ \frac{1}{\cosh(\kappa_W h)} \right]^2 \left( \frac{\cos\left(N_L \frac{\kappa_W a}{2}\right)}{h [A \sin(\kappa_L L + B) + E]} \right) \left[ a_1 \left(\frac{\phi_L}{D}\right)^4 + a_2 \left(\frac{\phi_L}{D}\right)^3 + a_3 \left(\frac{\phi_L}{D}\right)^2 + a_4 \left(\frac{\phi_L}{D}\right) + a_5 \right]$$

Equation 5-223

$$a_1 = \frac{-2.99}{[A \sin(\kappa_L L + B) + E]^4} \left(\frac{a}{2}\right)^4 \int_0^h [\cosh(\kappa_W z)]^2 [A \sin(\kappa_L z + B) + E]^5 dz$$

Equation 5-224

$$a_2 = \frac{14.70}{[A \sin(\kappa_L L + B) + E]^3} \left(\frac{a}{2}\right)^3 \int_0^h [\cosh(\kappa_W z)]^2 [A \sin(\kappa_L z + B) + E]^4 dz$$

Equation 5-225

$$a_3 = \frac{-25.90}{[A \sin(\kappa_L L + B) + E]^2} \left(\frac{a}{2}\right)^2 \int_0^h [\cosh(\kappa_W z)]^2 [A \sin(\kappa_L z + B) + E]^3 dz$$

Equation 5-226

$$a_4 = \frac{15.30}{[A \sin(\kappa_L L + B) + E]} \left(\frac{a}{2}\right) \int_0^h [\cosh(\kappa_W z)]^2 [A \sin(\kappa_L z + B) + E]^2 dz$$

Equation 5-227

$$a_5 = \int_0^h [\cosh(\kappa_W z)]^2 [A \sin(\kappa_L z + B) + E] dz$$

Equation 5-228

Which can be simplified to a quartile equation,

$$\left[ a_1 \left(\frac{\phi_L}{D}\right)^4 + a_2 \left(\frac{\phi_L}{D}\right)^3 + a_3 \left(\frac{\phi_L}{D}\right)^2 + a_4' \left(\frac{\phi_L}{D}\right) + a_5 \right] = 0$$

Equation 5-229

where,

$$a_4' = \left[ a_4 - \frac{16 \pi^3 N_L^2 \zeta_\phi m^* k_\phi^2}{C_{Lo} [KC(h)]^2 a} [\cosh(\kappa_W h)]^2 \left( \frac{h [A \sin(\kappa_L L + B) + E]}{\cos\left(N_L \frac{\kappa_W a}{2}\right)} \right) \right]$$

Equation 5-230

The real and positive root of Equation 5-229 gives the yaw response of the Jack-up under the crossflow excitation. Equation 5-229 can be solved iteratively by calculating the fluid damping contribution and the response amplitude till convergence.

Table 5-6: Crossflow or sway response of jack-ups in head critical regular waves

Sr. No	Project Name	$f_{Ny}$ (Hz)	Wave Height (m)	KC	Lift Coefficient ( $C_L$ )	Amplitude Ratio ( $y_L/D$ )	Crossflow Response (m)	Total Damping
1	12-1012	0.57	1.00	6.41	1.56	0.02	0.01	2.00%
2	09-1027	0.22	1.00	8.58	2.43	0.13	0.07	2.00%
3	08-1016	0.27	1.00	6.07	1.43	0.10	0.06	2.00%
4	10-1046	0.19	1.00	7.28	1.91	0.17	0.11	2.00%
5	12-1013	0.32	1.25	7.49	2.00	0.03	0.02	2.00%
6	03-51	0.35	1.50	7.21	1.88	0.01	0.00	2.00%
7	9931	0.24	1.00	6.12	1.45	0.05	0.03	2.00%
8	9921	0.21	2.00	8.44	2.38	0.20	0.19	2.00%
9	10-1024	-	-	-	-	-	-	-
10	05-1022	0.44	3.00	7.92	2.17	0.11	0.14	2.00%
11	9928	0.32	2.00	4.69	0.87	0.02	0.03	2.00%
12	07-1015A	0.30	3.00	7.14	1.85	0.08	0.12	2.00%
13	07-1015B	0.17	1.50	4.08	0.63	0.02	0.02	2.00%
14	12-1005	0.33	2.00	4.28	0.71	0.01	0.02	2.00%
15	200046	0.34	2.50	5.64	1.26	0.04	0.06	2.00%
16	07-1031	-	-	-	-	-	-	-
17	9724	-	-	-	-	-	-	-
18	13-1010A	-	-	-	-	-	-	-
19	13-1010B	-	-	-	-	-	-	-
20	09-4040	0.28	9.50	11.73	3.00	0.44	1.14	2.00%
21	07-5020	0.27	5.00	6.18	1.47	0.06	0.16	2.00%
22	11-4035	0.20	9.14	7.52	2.01	0.03	0.11	2.00%

If the whole cylinder is experiencing crossflow lock-in, the crossflow component of the fluid damping can be neglected ( $C_{eLf\phi y} = 0$ ) and Equation 5-229 can be converted to an alternative quartile equation,

$$\left[ a_1 \left( \frac{\phi_L}{D} \right)^4 + a_2 \left( \frac{\phi_L}{D} \right)^3 + a_3' \left( \frac{\phi_L}{D} \right)^2 + a_4' \left( \frac{\phi_L}{D} \right) + a_5 \right] = 0 \quad \text{Equation 5-231}$$

where,

$$a_3' = \left[ a_3 - \left\{ \frac{16 \pi N_L^2 b^3 C_D \int_0^h [A \sin(\kappa_L z + B) + E]^3 dz}{3 C_{LO} a [KC(h)]^2 [A \sin(\kappa_L L + B) + E]^2 \cos \left( N_L \frac{\kappa_W a}{2} \right)} \right\} \right] \quad \text{Equation 5-232}$$

$$a_4' = \left[ a_4 - \left( \frac{2 C_{es\phi} \omega_N [A \sin(\kappa_L L + B) + E]}{\rho C_{LO} a \left[ \frac{\pi H_W}{T_W \sinh(\kappa_W h)} \right]^2 \cos \left( N_L \frac{\kappa_W a}{2} \right)} \right) \right] \quad \text{Equation 5-233}$$

The real and positive root of Equation 5-231 is the yaw response of the Jack-up under the crossflow excitation.

### 5.13 Leg Yield Augmentation

#### 5.13.1 Dynamic Stresses due to VIV

The dynamic stresses induced due to VIV can be computed from the leg bending moment variation along the legs.

##### 5.13.1.1 Inline VIV

The dynamic inline bending moment ( $BM_{Dx}(z)$ ) at any section along the leg shall be calculated by using the classical Euler-Bernoulli beam theory (Timoshenko, 1937),

$$BM_{Dx}(z) = -E_L I_x \frac{d^2}{dz^2} x_o(z) \quad \text{Equation 5-234}$$

Substituting for mode shape in Equation 5-234, the leg bending moment shall be,

$$BM_{Dx}(z) = E_L I_x \left[ \frac{x_L}{A \sin(\kappa_L L + B) + E} \right] \kappa_L^2 [A \sin(\kappa_L z + B)] \quad \text{Equation 5-235}$$

For independent legs, the maximum leg bending moment is experienced in way of leg-hull interface ( $z = L$ ),

$$BM_{Dx}(L) = E_L I_x \left[ \frac{x_L}{A \sin(\kappa_L L + B) + E} \right] \kappa_L^2 [A \sin(\kappa_L L + B)] \quad \text{Equation 5-236}$$

For the classical bottom pinned idealisation,  $A = 1, B = E = 0$  and,  $\kappa_L = \frac{\pi}{2L}$ ,

$$BM_{Dx}(L) = \frac{\pi^2 E_L I_x x_L}{4L^2} \quad \text{Equation 5-237}$$

The maximum dynamic bending stresses ( $\sigma_{Dx}(L)$ ) can be computed from Equation 5-236 as,

$$\sigma_{Dx}(L) = \frac{BM_{Dx}(L)}{Z_x} = \frac{E_L I_x x_L \kappa_L^2}{Z_x} \left[ \frac{A \sin(\kappa_L L + B)}{A \sin(\kappa_L L + B) + E} \right] \quad \text{Equation 5-238}$$

where  $Z_x$  is the section modulus of the leg about the transverse ( $y$ ) axis.

Table 5-7 shows the dynamic bending stresses in the legs of the jack-up and the corresponding yield strength utilisation due to inline VIV in the uniform current. It can be noted that at higher water depths, the strength utilisation is as high as 50% of the yield stress, revealing potential fatigue implications.

#### 5.13.1.2 Crossflow VIV

Similarly, the maximum leg dynamic bending stress due to crossflow VIV ( $\sigma_{Dy}(L)$ ) shall be,

$$\sigma_{Dy}(L) = \frac{E_L I_y y_L \kappa_L^2}{Z_y} \left[ \frac{A \sin(\kappa_L L + B)}{A \sin(\kappa_L L + B) + E} \right] \quad \text{Equation 5-239}$$

where  $Z_y$  is the section modulus of the leg about the longitudinal ( $x$ ) axis.

#### 5.13.1.3 Yaw VIV

Similarly, the maximum leg dynamic bending stress due to yaw VIV ( $\sigma_{D\phi}(L)$ ) shall be,

$$\sigma_{D\phi}(L) = \frac{E_L I_r \sqrt{a^2 + b^2} \phi_L \kappa_L^2}{2 Z_r} \left[ \frac{A \sin(\kappa_L L + B)}{A \sin(\kappa_L L + B) + E} \right] \quad \text{Equation 5-240}$$

where  $I_r$  and  $Z_r$  are the inertia and section modulus of the leg about the radial axis passing through yaw centre.

Table 5-8 shows the dynamic bending stresses in the legs of the jack-up and the corresponding yield strength utilisation due to crossflow VIV in regular waves. It can be seen that the dynamic stresses are of considerable magnitudes, with the strength utilisation as high as 95% of the yield stress. The cells corresponding to designs with

yield strength utilisation more than 75% are highlighted with a different colour in the table. This can also have significant bearing on the fatigue strength of the legs.

Table 5-7: Leg dynamic bending stresses under inline VIV in critical uniform currents

Sr. No	Project Name	Leg Dynamic Bending Moment (tm)	Dynamic Bending Stress (t/cm <sup>2</sup> )	Dynamic Yield utilisation (%)
1	12-1012	1.15	0.05	2
2	09-1027	0.85	0.03	1
3	08-1016	2.24	0.06	3
4	10-1046	1.57	0.04	1
5	12-1013	2.41	0.06	3
6	03-51	3.64	0.08	3
7	9931	4.24	0.07	3
8	9921 M	9.39	0.05	2
9	10-1024	11.34	0.09	4
10	05-1022	41.30	0.17	7
11	9928	55.59	0.17	7
12	07-1015A	63.04	0.12	3
13	07-1015B	51.84	0.10	3
14	12-1005	85.62	0.22	9
15	200046	49.61	0.14	6
16	07-1031	405.19	0.56	23
17	9724	205.41	0.29	12
18	13-1010A	301.05	0.19	5
19	13-1010B	343.13	0.21	6
20	09-4040	-	-	-
21	07-5020	-	-	-
22	11-4035	-	-	-

### 5.13.2 Mean Stresses due to Drag Amplification

The increase in leg mean stresses due to drag amplification can be calculated from the increase in the static leg bending moment.

The increase in mean inline bending moment ( $\Delta BM_{Mx}(L)$ ) due to drag amplification can be calculated from the increase in OTM,

$$\Delta BM_{Mx}(L) = (OTM_{AL} - OTM_L) \quad \text{Equation 5-241}$$

where  $OTM_L$  represent the unamplified OTM per leg respectively.

Table 5-8: Leg dynamic bending stresses under crossflow VIV in critical regular waves

Sr. No	Project Name	Leg Dynamic Bending Moment (tm)	Dynamic Bending Stress (t/cm <sup>2</sup> )	Dynamic Yield utilisation (%)
1	12-1012	3.97	0.13	6
2	09-1027	12.04	0.36	15
3	08-1016	9.53	0.27	11
4	10-1046	17.70	0.35	15
5	12-1013	5.18	0.16	7
6	03-51	1.56	0.02	1
7	9931	7.66	0.17	7
8	9921	113.43	0.62	26
9	10-1024	-	-	-
10	05-1022	278.00	1.13	47
11	9928	52.34	0.16	7
12	07-1015A	329.39	0.60	17
13	07-1015B	34.79	0.06	2
14	12-1005	53.67	0.14	6
15	200046	129.84	0.38	16
16	07-1031	-	-	-
17	9724	-	-	-
18	13-1010A	-	-	-
19	13-1010B	-	-	-
20	09-4040	15404.58	4.39	95
21	07-5020	2002.75	0.57	12
22	11-4035	2294.79	0.33	5

The increase in mean bending stress ( $\Delta\sigma_{Mx}(L)$ ) can be computed as,

$$\Delta\sigma_{Mx}(L) = \frac{\Delta BM_{Mx}(L)}{Z_x} \quad \text{Equation 5-242}$$

Table 5-9 and Table 5-10 show the additional dynamic and mean bending stresses in the legs of the jack-up and the corresponding yield strength utilisation due to crossflow and yaw VIV respectively in longitudinal currents. The cells corresponding to designs with yield strength utilisation more than 75% are highlighted with a different colour in the table. It can be noted that the dynamic stresses in legs are considerable and even exceed the yield strength of the legs. The OTMs due to current are also found to increase significantly, even up by around 100%, which could jeopardise the stability of the jack-ups. However, the increase in mean bending stresses is found to be generally insignificant except for one of the designs, where the yield strength utilisation was

around 10 - 20%. Hence, both the crossflow and yaw VIV are of greater significance both from strength and fatigue perspectives. Yaw VIV due to inline excitation is not considered as it was found to be insignificant.

Table 5-9: Drag amplification and yield strength under crossflow VIV in critical uniform currents

Sr. No	Project Name	Leg Dynamic Bending Moment (tm)	Dynamic Bending Stress (t/cm <sup>2</sup> )	Dynamic Yield utilisation (%)	Increase in Mean Drag	Increase in OTM	Increase in Mean Bending Stress (t/cm <sup>2</sup> )	Mean Yield Utilisation (%)
1	12-1012	13	0.44	18	7.35%	9.54%	0.01	0
2	09-1027	25	0.75	31	32.49%	41.82%	0.01	1
3	08-1016	26	0.73	30	31.02%	40.06%	0.03	1
4	10-1046	41	0.81	34	48.75%	62.59%	0.03	1
5	12-1013	21	0.65	27	14.13%	18.25%	0.01	1
6	03-51	-	-	-	-	-	-	-
7	9931	33	0.73	30	24.41%	31.38%	0.02	1
8	9921	96	0.53	22	19.06%	24.69%	0.02	1
9	10-1024	122	0.97	40	17.61%	22.64%	0.03	1
10	05-1022	517	2.10	88	23.81%	30.80%	0.07	3
11	9928	697	2.10	88	28.56%	37.02%	0.08	3
12	07-1015A	788	1.44	40	20.66%	26.81%	0.04	1
13	07-1015B	594	1.09	30	33.73%	43.49%	0.05	1
14	12-1005	-	-	-	-	-	-	-
15	200046	-	-	-	-	-	-	-
16	07-1031	-	-	-	-	-	-	-
17	9724	2,603	3.61	151	86.28%	110.58%	0.45	19
18	13-1010A	3,516	2.19	61	54.91%	71.13%	0.17	5
19	13-1010B	3,750	2.33	65	37.06%	48.17%	0.14	4
20	09-4040	-	-	-	-	-	-	-
21	07-5020	-	-	-	-	-	-	-
22	11-4035	-	-	-	-	-	-	-

#### 5.14 Leg Fatigue Strength

The leg fatigue strength can be found from the VIV induced dynamic stresses by means of an appropriate SN curve and Stress Concentration Factor (SCF).

The number of cycles to failure ( $N_F$ ) based on SN curves (ABS, 2018a),

$$N_F = A_F S_D^{m_F} \quad \text{Equation 5-243}$$

where  $A_F, m_F$  are the fatigue strength coefficient and exponent respectively and  $S_D$  represents the dynamic stress range.

Table 5-10: Drag amplification and yield strength under yaw VIV in critical uniform currents

Sr. No	Project Name	Leg Dynamic Bending Moment (tm)	Dynamic Bending Stress (t/cm <sup>2</sup> )	Dynamic Yield utilisation (%)	Increase in Mean Drag	Increase in OTM	Increase in Mean Bending Stress (t/cm <sup>2</sup> )	Mean Yield Utilisation (%)
1	12-1012	13.7	0.71	29	5.75%	7.46%	0.00	0
2	09-1027	30	1.30	54	32.36%	41.66%	0.02	1
3	08-1016	19	0.75	31	13.72%	17.72%	0.01	0
4	10-1046	48	1.39	58	47.41%	60.87%	0.03	1
5	12-1013	30	1.22	51	15.19%	19.62%	0.01	1
6	03-51	-	-	-	-	-	-	-
7	9931	47	1.24	52	23.79%	30.58%	0.02	1
8	9921 M	116	0.90	37	18.47%	23.94%	0.01	1
9	10-1024	159	1.79	74	17.21%	22.12%	0.03	1
10	05-1022	-	-	-	-	-	-	-
11	9928	879	3.70	154	29.13%	37.76%	0.08	3
12	07-1015A	1,050	2.68	74	22.61%	29.35%	0.04	1
13	07-1015B	-	-	-	-	-	-	-
14	12-1005	-	-	-	-	-	-	-
15	200046	-	-	-	-	-	-	-
16	07-1031	-	-	-	-	-	-	-
17	9724	2,351	4.54	189	63.95%	81.96%	0.26	11
18	13-1010A	3,687	3.18	88	47.91%	62.07%	0.13	3
19	13-1010B	4,114	3.55	99	33.83%	43.97%	0.10	3
20	09-4040	-	-	-	-	-	-	-
21	07-5020	-	-	-	-	-	-	-
22	11-4035	-	-	-	-	-	-	-

The dynamic stress range shall be calculated as,

$$S = 2 \sigma_D SCF \quad \text{Equation 5-244}$$

where  $\sigma_D$  and  $SCF$  represent the dynamic leg stress as relevant and stress concentration factor respectively.

The fatigue life ( $FL$ ) can be determined considering lock-in as,

$$FL = N_F T_N = \frac{N_F \omega_N}{2\pi} \quad \text{Equation 5-245}$$

Table 5-11 to Table 5-14 present the fatigue life of the legs at the leg-hull interface (LHI) and the waterline (WL) for inline, crossflow and yaw VIV in critical uniform current

and crossflow VIV in critical regular waves respectively. An SCF of 2.50 is considered to account for the stress concentration due to pin holes (Pilkey, 2008) in the legs, shown in Figure 5-16. Nominal stress method is employed for the fatigue assessment and the SN curves considered are the ABS Offshore SN curves for nontubular details and non-intersection tubular connections; plain steel with cleaned surfaces but with the edges machine flame-cut by a controlled procedure to ensure that the cut surface is free from cracks (ABS, 2018a). The corrosive environment considered are 'In-Air' for the leg-hull interface and 'Free Corrosion' for the waterline.

It can be observed from the tables that the jack-ups are highly vulnerable to fatigue damage under all the VIV modes. The fatigue life is found to be negligible or only a few days or even hours during prolonged crossflow and yaw VIV in steady currents. It can also be noted that during inline VIV in steady current at higher water depths and crossflow VIV in regular waves, the fatigue lives of many designs are found to be considerably less than practically essential. The cells corresponding to designs with fatigue lives less than a year are highlighted with a different colour in the table.



Figure 5-16: Cylindrical leg of a jack-up with the pin holes

Table 5-11: Nominal fatigue life of the jack-ups under inline VIV in critical uniform currents

Sr. No	Project Name	LHI Stress Range (MPa)	Cycles to failure at LHI	Life at Leg-hull interface (days)	WL Stress Range (MPa)	Cycles to failure	Life at Waterline (days)
1	12-1012	22.41	9.68E+09	215,154	21.20	3.21E+08	7,139
2	09-1027	12.88	2.04E+11	11,133,147	12.67	1.95E+09	106,547
3	08-1016	31.06	1.61E+09	67,655	30.17	9.35E+07	3,938
4	10-1046	17.41	3.88E+10	2,633,327	17.25	6.61E+08	44,901
5	12-1013	31.01	1.62E+09	53,541	30.06	9.47E+07	3,125
6	03-51	37.33	5.85E+08	22,937	36.65	4.73E+07	1,856
7	9931	32.79	1.19E+09	47,454	32.39	7.29E+07	2,899
8	9921	25.32	4.95E+09	278,172	24.13	2.04E+08	11,483
9	10-1024	44.10	2.34E+08	9,025	43.58	2.58E+07	996
10	05-1022	82.53	8.28E+06	219	79.48	3.15E+06	83
11	9928	82.23	8.39E+06	305	78.11	3.35E+06	122
12	07-1015A	56.73	5.86E+07	2,229	53.46	1.26E+07	481
13	07-1015B	46.65	1.72E+08	11,702	45.63	2.20E+07	1,498
14	12-1005	107.00	3.34E+06	117	105.50	1.17E+06	41
15	200046	71.10	1.69E+07	576	54.23	1.20E+07	409
16	07-1031	275.94	1.21E+05	3	272.04	4.25E+04	1
17	9724	139.89	1.31E+06	85	139.12	4.44E+05	29
18	13-1010A	91.94	5.68E+06	376	87.72	2.23E+06	148
19	13-1010B	104.79	3.59E+06	170	97.53	1.54E+06	73
19	09-4040	-	-	-	-	-	-
20	07-5020	-	-	-	-	-	-
23	11-4035	-	-	-	-	-	-

## 5.15 VIV of Jack-up in Regular Wave with Imposed Uniform Current

### 5.15.1 Lift Force in Regular Wave with imposed Current

The horizontal particle velocity in a regular wave with imposed uniform current  $U(z, t)$  shall be expressed as,

$$U(z, t) = U + U_o(z) \cos(\omega_w t)$$

Equation 5-246

Table 5-12: Nominal fatigue life of the jack-ups under crossflow VIV in critical uniform currents

Sr. No	Project Name	LHI Stress Range (MPa)	Cycles to failure at LHI	Life at Leg-hull interface (days)	WL Stress Range (MPa)	Cycles to failure	Life at Waterline (days)
1	12-1012	215.86	2.86E+05	6	204.23	1.16E+05	2
2	09-1027	365.56	4.53E+04	2	359.52	1.60E+04	1
3	08-1016	358.66	4.84E+04	2	348.29	1.79E+04	1
4	10-1046	398.90	3.34E+04	2	395.20	1.15E+04	1
5	12-1013	317.44	7.42E+04	3	307.73	2.76E+04	1
6	03-51	-	-	-	-	-	-
7	9931	357.32	4.90E+04	2	352.98	1.71E+04	1
8	9921	259.08	1.51E+05	8	246.94	5.96E+04	3
9	10-1024	475.71	1.80E+04	1	470.07	6.26E+03	0
10	05-1022	1032.35	1.20E+03	0	994.18	4.55E+02	0
11	9928	1030.95	1.20E+03	0	979.29	4.80E+02	0
12	07-1015A	708.70	4.46E+03	0	667.88	1.83E+03	0
13	07-1015B	534.23	1.20E+04	1	522.56	4.32E+03	0
14	12-1005	-	-	-	-	-	-
15	200046	-	-	-	-	-	-
16	07-1031	-	-	-	-	-	-
17	9724	1772.98	1.80E+02	0	1763.27	6.12E+01	0
18	13-1010A	1073.71	1.04E+03	0	1024.43	4.10E+02	0
19	13-1010B	1145.15	8.32E+02	0	1065.85	3.57E+02	0
20	09-4040	-	-	-	-	-	-
21	07-5020	-	-	-	-	-	-
22	11-4035	-	-	-	-	-	-

As the wave horizontal particle velocity decays with the distance from the water level, two different flow conditions can be experienced by a vertical cylinder, with and without flow reversal depending on the net horizontal velocity of the flow.

#### 5.15.1.1 Case1: Wave horizontal particle velocity greater than the current velocity; $U_o(z) > U$

This scenario is typically experienced near the water level. Figure 5-17 illustrates the variation of the flow velocity when the current speed is lesser than horizontal particle velocity in the regular wave. The net flow can be idealized as an oscillatory flow with two asymmetric half cycles of different frequency.

Table 5-13: Nominal fatigue life of the jack-ups under yaw VIV in critical uniform currents

Sr. No	Project Name	LHI Stress Range (MPa)	Cycles to failure at LHI	Life at Leg-hull interface (days)	WL Stress Range (MPa)	Cycles to failure	Life at Waterline (days)
1	12-1012	346.32	5.47E+04	1	327.67	2.21E+04	0
2	09-1027	637.20	6.48E+03	0	626.68	2.29E+03	0
3	08-1016	370.19	4.33E+04	2	359.49	1.60E+04	1
4	10-1046	683.57	5.07E+03	0	677.23	1.74E+03	0
5	12-1013	597.32	8.12E+03	0	579.04	3.02E+03	0
6	03-51	-	-	-	-	-	-
7	9931	609.44	7.57E+03	0	602.04	2.63E+03	0
8	9921 M	439.52	2.38E+04	1	418.93	9.37E+03	0
9	10-1024	875.72	2.13E+03	0	865.33	7.40E+02	0
10	05-1022	-	-	-	-	-	-
11	9928	1816.33	1.66E+02	0	1725.31	6.61E+01	0
12	07-1015A	1314.83	5.13E+02	0	1239.08	2.11E+02	0
13	07-1015B	-	-	-	-	-	-
14	12-1005	-	-	-	-	-	-
15	200046	-	-	-	-	-	-
16	07-1031	-	-	-	-	-	-
17	9724	2228.24	8.10E+01	0	2216.03	2.75E+01	0
18	13-1010A	1561.38	2.81E+02	0	1489.72	1.10E+02	0
19	13-1010B	1742.37	1.92E+02	0	1621.71	8.21E+01	0
20	09-4040	-	-	-	-	-	-
21	07-5020	-	-	-	-	-	-
22	11-4035	-	-	-	-	-	-

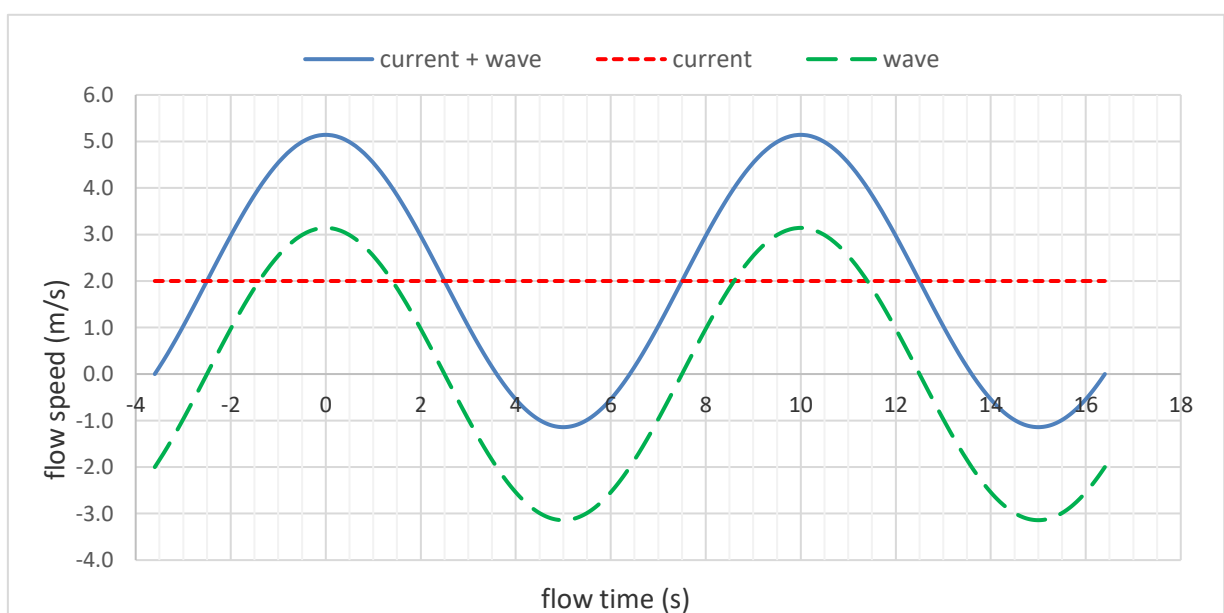


Figure 5-17: Flow speed variation for current speed less than wave particle velocity

Table 5-14: Nominal fatigue life of the jack-ups under crossflow VIV in critical regular waves

Sr. No	Project Name	LHI Stress Range (MPa)	Cycles to failure at LHI	Life at Leg-hull interface (days)	WL Stress Range (MPa)	Cycles to failure	Life at Waterline (days)
1	12-1012	65.85	2.58E+07	526	62.30	7.39E+06	151
2	09-1027	178.20	5.60E+05	30	175.25	1.98E+05	11
3	08-1016	132.21	1.59E+06	67	128.39	5.88E+05	25
4	10-1046	172.29	6.30E+05	39	170.69	2.17E+05	14
5	12-1013	76.73	1.11E+07	398	74.38	3.97E+06	142
6	03-51	11.60	3.62E+11	11,841,015	11.39	2.83E+09	92,552
7	9931	82.97	8.13E+06	395	81.96	2.83E+06	137
8	9921	305.70	8.47E+04	5	291.38	3.34E+04	2
9	10-1024	-	-	-	-	-	-
10	05-1022	555.54	1.05E+04	0	535.00	3.98E+03	0
11	9928	77.43	1.06E+07	384	73.55	4.13E+06	150
12	07-1015A	296.41	9.43E+04	4	279.33	3.87E+04	1
13	07-1015B	31.31	1.54E+09	104,928	30.63	8.87E+07	6,049
14	12-1005	67.06	2.33E+07	816	66.12	6.00E+06	210
15	200046	186.10	4.81E+05	16	141.94	4.14E+05	14
16	07-1031	-	-	-	-	-	-
17	9724	-	-	-	-	-	-
18	13-1010A	-	-	-	-	-	-
19	13-1010B	-	-	-	-	-	-
20	09-4040	2152.44	9.14E+01	0	1994.36	3.98E+01	0
21	07-5020	279.84	1.15E+05	5	260.67	4.93E+04	2
22	11-4035	159.62	8.23E+05	49	154.76	3.06E+05	18

At a given elevation ( $z$ ), the time instant of flow reversal ( $t_o$ ) can be derived from Equation 5-246 as,

$$t_o = \frac{1}{\omega_w} \cos^{-1} \left( \frac{U}{U_o} \right) \quad \text{Equation 5-247}$$

The distance travelled by the flow in the positive asymmetric half cycle can be,

$$d_+ = 2 \int_0^{t_o} U(t) dt = 2 \left( Ut_o + \frac{U_o}{\omega_w} \sin(\omega_w t_o) \right) \quad \text{Equation 5-248}$$

Similarly, the distance travelled by the flow in the negative asymmetric half cycle is,

$$d_- = 2 \left( U \frac{T_W}{2} - Ut_0 - \frac{U_o}{\omega_W} \sin(\omega_W t_0) \right) \quad \text{Equation 5-249}$$

Two equivalent  $KC$  numbers can be defined for the asymmetric half cycles,

For the positive half cycle,

$$KC^+ = \frac{2\pi}{D} \left( Ut_0 + \frac{U_o}{\omega_W} \sin(\omega_W t_0) \right) \quad \text{Equation 5-250}$$

For the negative half cycle,

$$KC^- = \frac{2\pi}{D} \left( U \frac{T_W}{2} - Ut_0 - \frac{U_o}{\omega_W} \sin(\omega_W t_0) \right) \quad \text{Equation 5-251}$$

The number of vortices shed in the respective half cycle can be found from the distance travelled by the steady flow to shed one vortex;  $\frac{D}{2St}$ .

Accordingly, the number of vortices shed in the positive half cycle can be derived from Equation 5-248 by considering  $St = 0.2$  as,

$$N_{V+} = \frac{4St}{D} \left( Ut_0 + \frac{U_o}{\omega_W} \sin(\omega_W t_0) \right) = \frac{KC^+}{8} \quad \text{Equation 5-252}$$

Similarly, for negative half cycles from Equation 5-249,

$$N_{V-} = \frac{4St}{D} \left( U \frac{T_W}{2} - Ut_0 - \frac{U_o}{\omega_W} \sin(\omega_W t_0) \right) = \frac{KC^-}{8} \quad \text{Equation 5-253}$$

The number of vortices as calculated above shall be rounded to the lower integer for applications. It can be inferred that the direction of vortex shedding alternates between along and against the direction of wave propagation, during the positive and negative half cycles respectively.

The effective Time Periods of the flow for the positive half cycle shall be,

$$T_+ = 4t_0 \quad \text{Equation 5-254}$$

Consequently, for the negative half cycle,

$$T_- = 2(T_w - 2t_0) \quad \text{Equation 5-255}$$

Hence, the oscillatory lift frequency in the positive half cycle shall be (Sumer and Fredsøe, 2006),

$$f_{L+} = (N_{V+} + 1) \frac{1}{T_+} \quad \text{Equation 5-256}$$

Similarly, lift frequency for the negative half cycle,

$$f_{L-} = (N_{V-} + 1) \frac{1}{T_-} \quad \text{Equation 5-257}$$

The above lift frequencies shall be used in the lift force model for this type of flow. Figure 5-18 shows the typical variation of the lift force in an oscillatory flow with the horizontal particle velocity greater than the imposed current velocity.

#### 5.15.1.2 Case2: Wave horizontal particle velocity less than the current velocity; $U_o(z) < U$

This flow condition will be experienced typically near to the seabed in regular waves with imposed current. Figure 5-19 illustrates the typical flow speed variation when the current speed is greater than the horizontal particle velocity. The flow can be idealized as a sinusoidally varying flow with a high velocity and a low velocity half cycles.

The distance travelled by the flow in the high velocity half cycle can be expressed as,

$$d_h = T_w \left( \frac{U}{2} + \frac{U_o}{\pi} \right) \quad \text{Equation 5-258}$$

Similarly, for the low velocity half cycle,

$$d_l = T_w \left( \frac{U}{2} - \frac{U_o}{\pi} \right)$$

Equation 5-259

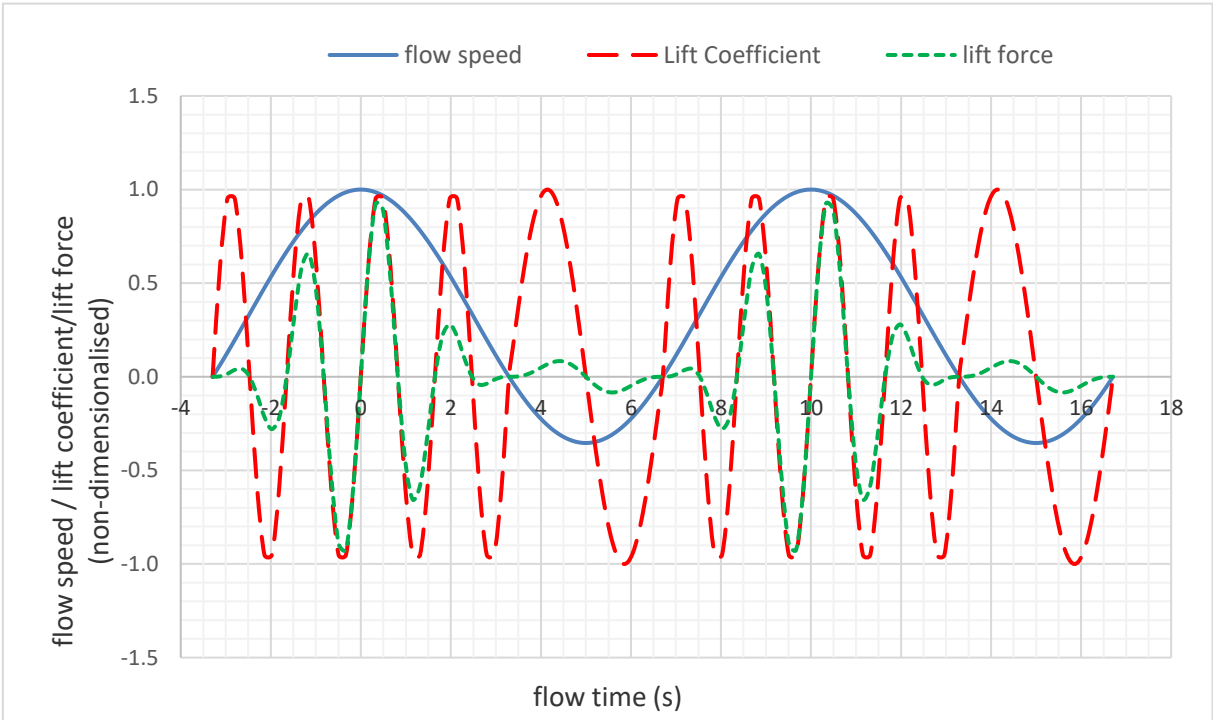


Figure 5-18: Lift force in an oscillatory flow with the horizontal particle velocity greater than the imposed current velocity

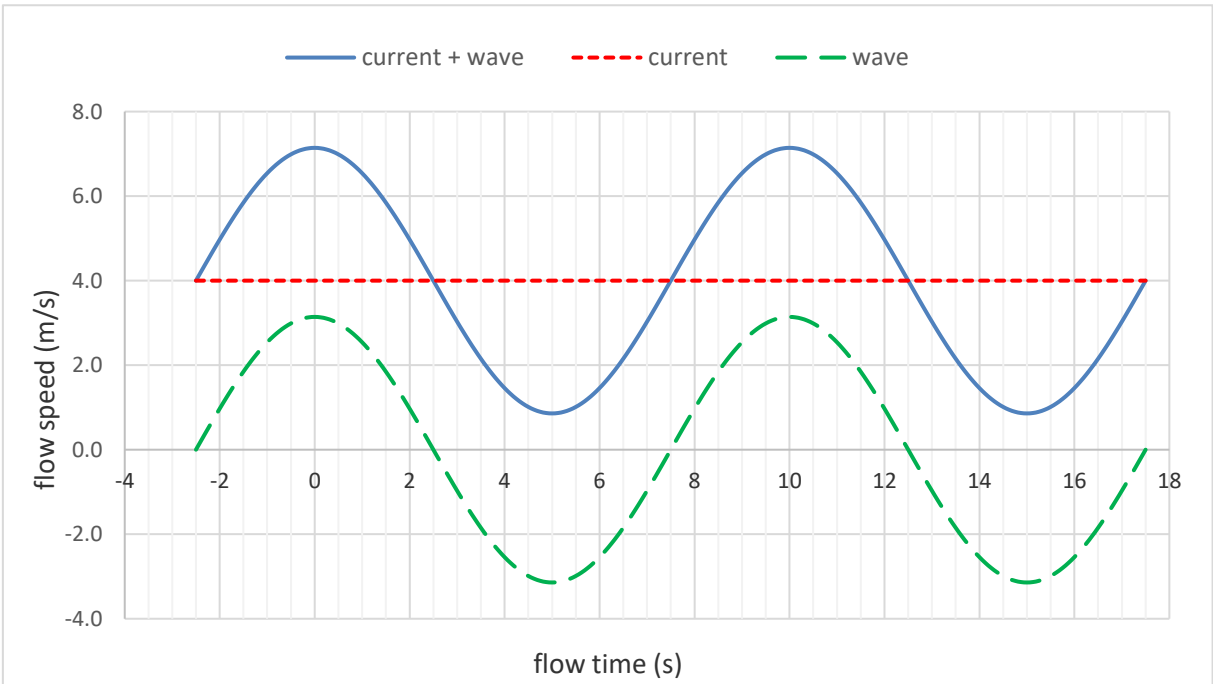


Figure 5-19: Flow speed variation for current speed greater than wave particle velocity

The equivalent  $KC$  number for the high velocity half cycle can be expressed as,

$$KC^h = \frac{\pi T_W}{D} \left( \frac{U}{2} + \frac{U_o}{\pi} \right) \quad \text{Equation 5-260}$$

Similarly, for the low velocity half cycle,

$$KC^l = \frac{\pi T_W}{D} \left( \frac{U}{2} - \frac{U_o}{\pi} \right) \quad \text{Equation 5-261}$$

The number of vortices shed in the high velocity half cycle shall be,

$$N_{Vh} = \frac{2St T_W}{D} \left( \frac{U}{2} + \frac{U_o}{\pi} \right) = \frac{KC^h}{8} \quad \text{Equation 5-262}$$

Similarly, the number of vortices shed in the low velocity half cycle shall be,

$$N_{Vl} = \frac{2St T_W}{D} \left( \frac{U}{2} - \frac{U_o}{\pi} \right) = \frac{KC^l}{8} \quad \text{Equation 5-263}$$

The number of vortices calculated above shall be rounded to the nearest integer. As there is no flow reversal, the direction of vortex shedding will always be along the direction of the current.

The average oscillatory lift frequency of the high velocity half cycles shall be,

$$f_{Lh} = \frac{N_{Vh}}{T_W} \quad \text{Equation 5-264}$$

Similarly, the lift frequency in the low velocity half cycle,

$$f_{Ll} = \frac{N_{Vl}}{T_W} \quad \text{Equation 5-265}$$

The above frequencies can be used with the appropriate force model to generate the lift time series. Figure 5-20 illustrates the typical variation of the lift force in an

oscillatory flow with the horizontal particle velocity less than the imposed current velocity.

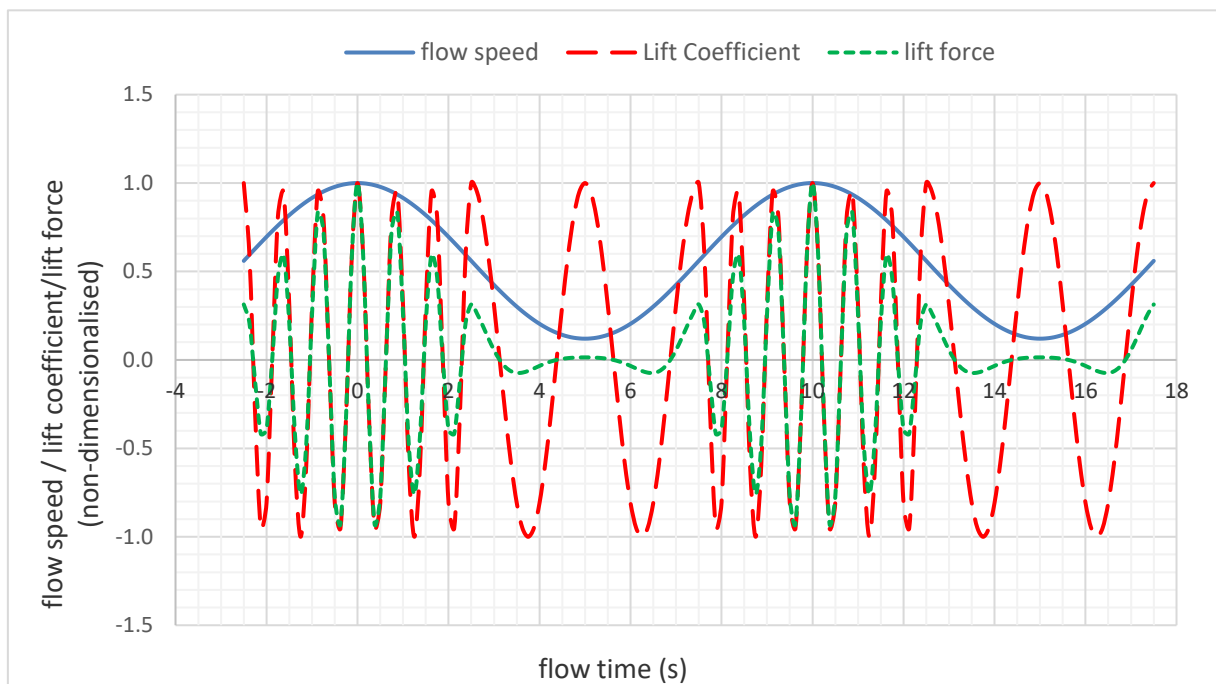


Figure 5-20: Lift force in an oscillatory flow with the wave horizontal particle velocity greater than the imposed current velocity

### 5.15.2 Response in Regular Wave with imposed Uniform Current

#### 5.15.2.1 Shallow Water Waves

It can be observed that in shallow water regular waves, the horizontal water particle velocity will tend towards a constant value, and the flow will be very close to a typical planar oscillatory flow. Consequently, the flow scenario will fall into either of the cases explained in Section 5.15.1, and the VIV response can be calculated individually for the half cycles, like VIV in regular waves. This gives a conservative assessment of the VIV response since the effect of discontinuity in the excitation due to alternating lift frequencies with the flow half cycles is neglected.

#### 5.15.2.2 Intermediate and Deep Water Waves

In intermediate and deep water waves, the excitation frequencies not only vary with the half cycles but also with the distance from the waterline, making the flow scenario highly complex. This can be simplified by dividing the distance from the seabed to the

waterline to various frequency blocks where the lift frequency is nearly constant within a half cycle. The response due to a particular frequency block can then be evaluated individually for the half cycles, similar to the shallow water wave case.

### 5.16 Discussion

This chapter mathematically explains various modes of jack-up VIV, building from the simple case of 2D cylinders. Simple criteria and response-based models were developed based on SDOF analogy and principle of conservation of energy, for evaluating the inline, crossflow and yaw modes of jack-up VIV in uniform current, regular waves and regular waves with imposed uniform current. Similar criteria were also developed for the cases of a single 2D cylinder and four 2D cylinders in a rectangular configuration, in steady and planar oscillatory flows. Mass damping parameter (product of mass ratio and damping ratio) and mode factor were found to be the important parameters controlling the inline and crossflow VIV and additionally radius of gyration also for the yaw VIV.

A polynomial expression is proposed for the lift coefficient as a function of the crossflow amplitude ratio for providing the observed self-limiting characteristics to the response-based models. It is found that the jack-ups are vulnerable to inline, crossflow and yaw VIV with response amplitude ratios up to the order of  $0.10D$ ,  $0.70D$  and  $0.70D$  respectively. It must be noted that the present assumption of coefficients in the polynomial expression for lift-response interaction is expected to provide a conservative prediction of response amplitude. If experiments can be carried out at various  $Re$  to find the variation of the polynomial coefficients, the expression can be used as a universal lift amplification model.

The SDOF formulations are further elaborated to cover the potential consequences of VIV like drag amplification, dynamic stresses and fatigue life. It is found that the dynamic stresses due to crossflow VIV can be as high as 150% and 95% of the yield stress in uniform current and regular waves respectively. The increase in mean leg stresses due to drag amplification is found to be relatively lesser, up to 20%. However, this can be of significant concern since the allowable mean stresses are usually fully utilised during design. The fatigue strength of the jack-ups was found to be as low as few days under sustained crossflow and yaw vibrations in both uniform current and regular waves, attributable to the high frequency nature of the jack-up VIV.

## Chapter 6. Experimental Investigation

This chapter describes the experimental investigation conducted with a scaled jack-up model to understand the intricacies of the jack-up VIV. The investigation was carried out in current, regular waves, regular waves with imposed current and irregular waves. The natural frequency, jack-up responses and leg forces were measured and analysed to understand the various VIV modes and associated phenomena. The added mass and damping of the jack-up exhibiting VIV were also evaluated with the physical experiments.

### 6.1 Experimental Setup

#### 6.1.1 Model

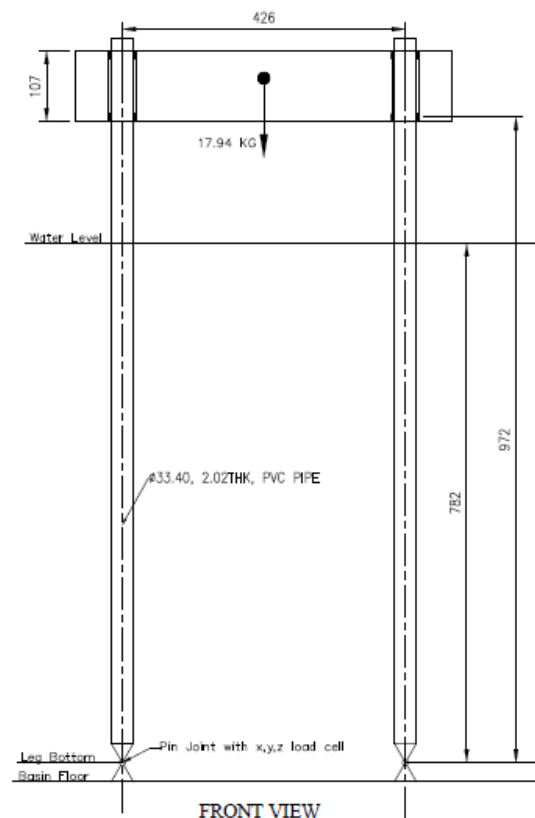


Figure 6-1: Jack-up Model

Figure 6-1 illustrates the jack-up model used for the experiments. The model is based on jack-up 9921, Sr. No 8 presented in Table 4-1. A model scale of 1: 28 was adopted to suit the tank dimensions. PVC was selected as the model material as per Cauchy scaling to satisfy the law of similitude of structural deflections (also see Sections A.9.1 and A.9.2). Ball joints were provided at the leg footings to simulate the typical pinned

boundary conditions in the soil. The similitude of mass was achieved by means of lead ballast plates mounted on the model deck. The elevated mass was free to vibrate in all the 6 DOF under the leg excitation. The principal properties of the model and prototype are displayed in Table 6-1.

Table 6-1: Model and prototype properties

Particulars	Prototype	Model
Length (m)	20.00	0.71
Breadth (m)	16.00	0.57
Longitudinal leg spacing (m)	16.00	0.57
Transverse Leg Spacing (m)	12.00	0.43
Elevated Load (kg)	400,000	17.94
Leg cantilever length (m)	27.35	0.97
Leg Diameter (m)	0.94	0.03
Leg Material	Mild Steel	PVC
Hull Material	Mild Steel	PVC
Water Depth (m)	20.00	0.78
Maximum Current (knots)	4.00	0.75
Associated Wave Height (m)	2.00	0.07

#### 6.1.1.1 Leg-hull interface

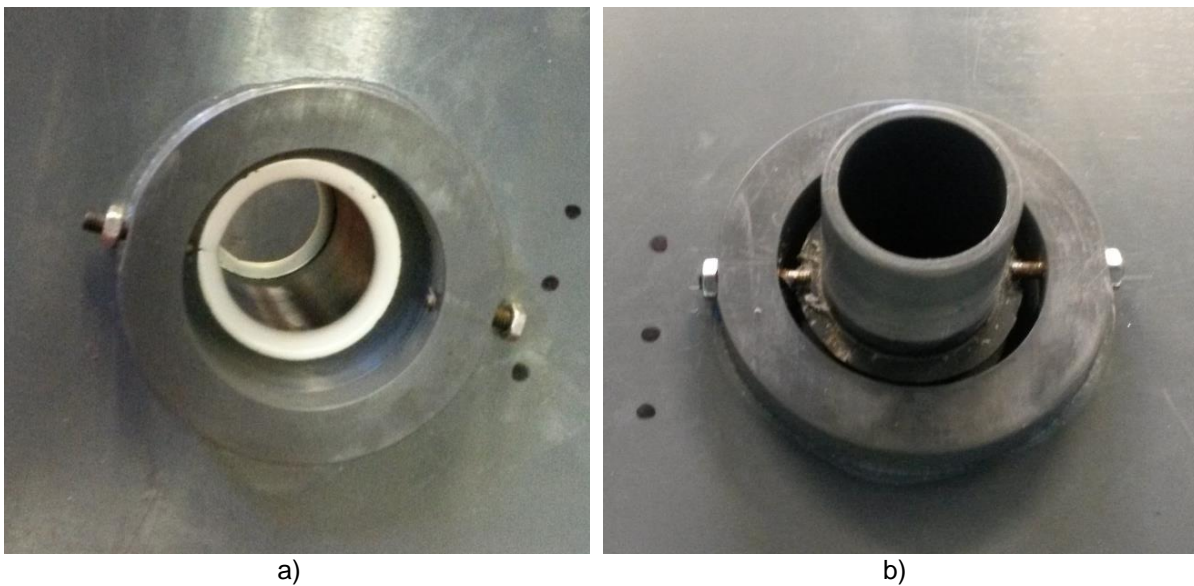


Figure 6-2: Leg-hull interface; a) O rings for moment transfer, b) Bolts for weight transfer

Figure 6-2 illustrates the leg-hull interface of the model. The leg well in the model is provided with two O-rings made of silicone rubber solid cords, with the diameter and shore hardness of 7mm and 60 respectively, for transferring the leg moments to the hull, as displayed in Figure 6-2, a). The weight of the hull is transferred to the legs by

means of two hull bolts resting on a concentric plastic pad glued to the leg, as shown in Figure 6-2, b).

### 6.1.2 *WWC tank*

The experiments were conducted in the wind wave current (WWC) tank at the hydrodynamic laboratory of the School of Marine Science and Technology, Newcastle University. The main particulars of the WWC tank are displayed in Table 6-2.

The model was fixed to the tank bottom, positioned at the measuring section of the WWC tank and was exposed to various flows, wind, current, regular waves, irregular waves and regular waves with imposed current. The model was mounted on a turntable base which can be rotated by predefined angular displacements to simulate various environmental headings. The local heading of the legs can be varied by rotating the legs about its own vertical axis. The responses of the model along the 6 DOF were measured by means of 2 Qualisys motion tracking cameras installed on either side of the model.

Table 6-2: WWC particulars

<b>WWC Tank Specification</b>	
Length (m)	11.00
Width (m)	1.80
Maximum Water Depth (m)	1.00
Maximum Wave Height (m)	0.12
Maximum Current (knots)	1.94
Maximum Wind (knots)	38.88

The tank blockage is 3.78%, and the distance of the model leg from the nearest side wall is around 20 times its diameter, ensuring insignificant flow blockage and boundary effects respectively on the test results (Chakrabarti, 2005). The scale effect due to the difference in model and prototype  $Re$  is expected to be minimal due to the free vibrations of the legs, as even small vibrations tend to synchronise vortex shedding and separation points (DNV GL, 2017b). Further, the  $Re$  influence experienced by a smooth stationary cylinder in an incoming laminar flow is not significantly felt in real flow conditions with substantial incoming turbulence, as verified with full scale piles experiencing aggressive crossflow VIV, even in critical and supercritical regimes

(Sainsbury and King, 1971). The high turbulence intensity of around 13% generated by the inlet grid ensures a turbulent boundary layer during test conditions in the subcritical flow regime, similar to the realistic prototype conditions (Chakrabarti, 2005). The experimental setup is illustrated in Figure 6-3.



Figure 6-3: Experimental Setup

### 6.1.3 *Jack-up and Leg Axis Systems*

The axis systems adopted for the jack-up and the leg are illustrated in Figure 6-4. The origin of the jack-up axis system lies at the geometric centre of the hull, and the  $x$  and  $y$  axes coincide with its longitudinal and transverse centre lines respectively as shown in the figure. The origin of the axis system of the leg coincides with the centre of the bottom most section or ball joint, and the  $x$  and  $y$  axes are parallel to the respective jack-up axes. The vertical  $z$  axes of both the jack-up and the leg are positive upwards.

### 6.1.4 *Global Headings*

The global heading is defined as the relative angular separation between the direction of the environment with the longitudinal centre line of the jack-up. The different global headings of the model with respect to the environment is accomplished in the WWC tank by means of the turntable base with locking pins. The turntable arrangement and

definition of the global heading of the jack-up model are shown in Figure 6-5 and Figure 6-6 respectively.

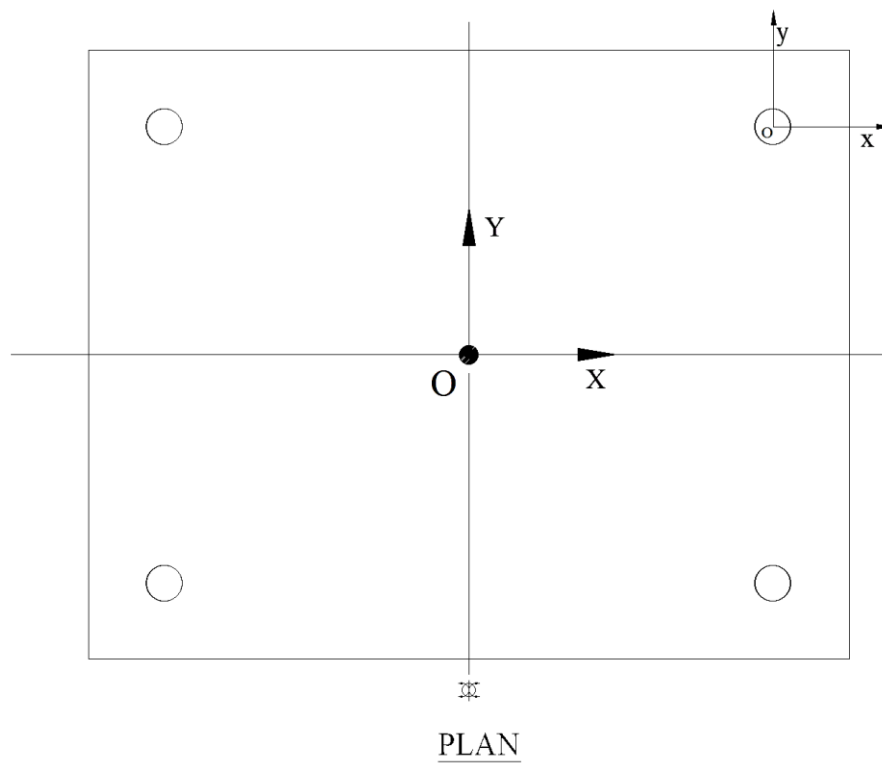


Figure 6-4: Jack-up and leg axis systems

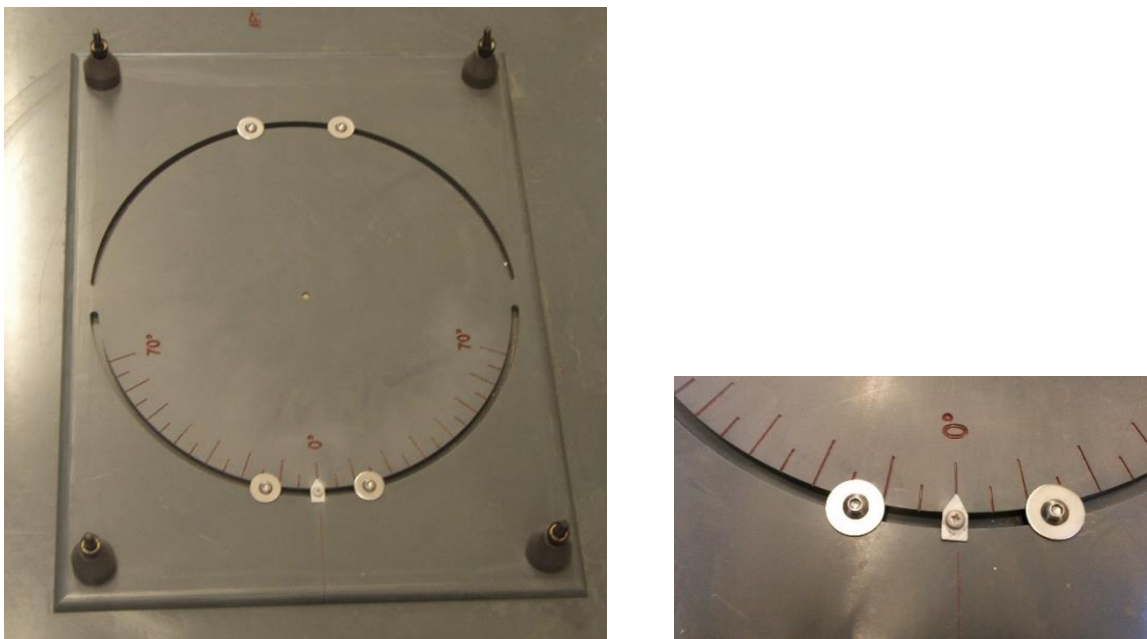


Figure 6-5: Turntable arrangement

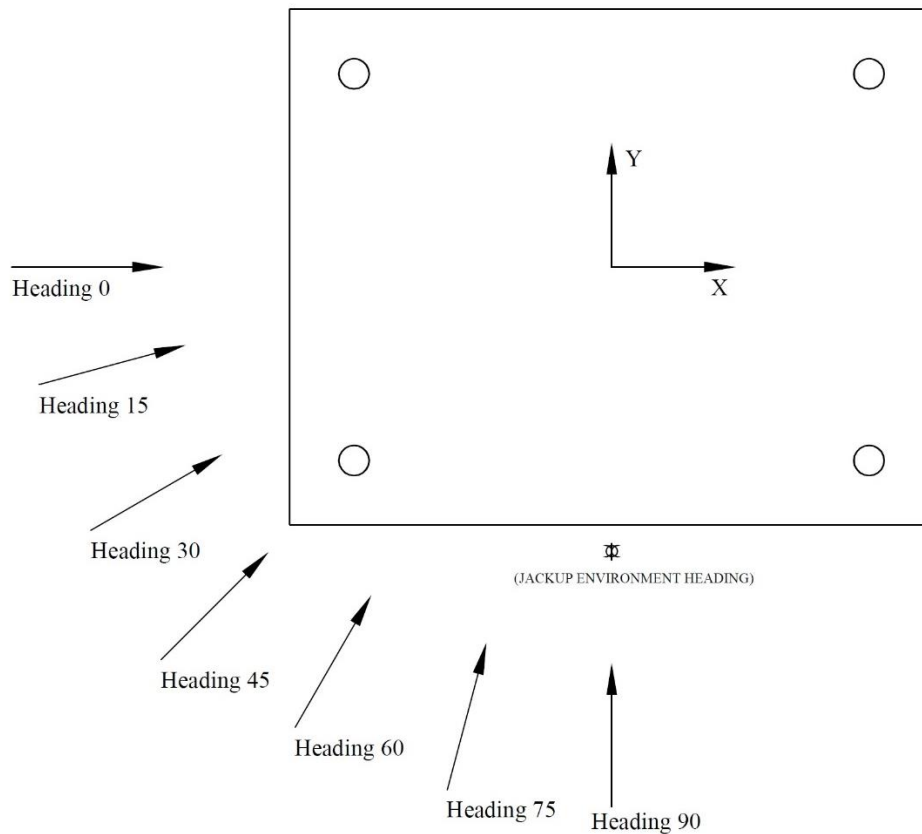


Figure 6-6: Global heading definition of the jack-up model

### 6.1.5 Leg Designs and Local Headings

Figure 6-7 illustrates various leg designs tested along with the respective leg local headings. Local heading is the relative orientation of the leg with respect to the longitudinal centre line of the jack-up. Local heading defines the relative orientation of the appurtenances like pin holes with the incoming flow. The various local headings of the legs were achieved by rotating the leg about its own vertical axis by a known angular distance.

LD1H3 and LD1H4 correspond to leg designs with three and four holes respectively, for the hydraulic pins performing self-elevating operation. LD1H0 corresponds to the leg design without pin holes that uses doubler pads or grippers for self-elevating operation. The LD1H3 is tested for two local headings of  $0^\circ$  and  $180^\circ$  due to the dissimilarity in pin hole disposition with the flow. The model leg for the design LD1H0 was furnished from the leg model LD1H4 by blanking the pinholes with cello tapes effectively retaining the leg stiffness.

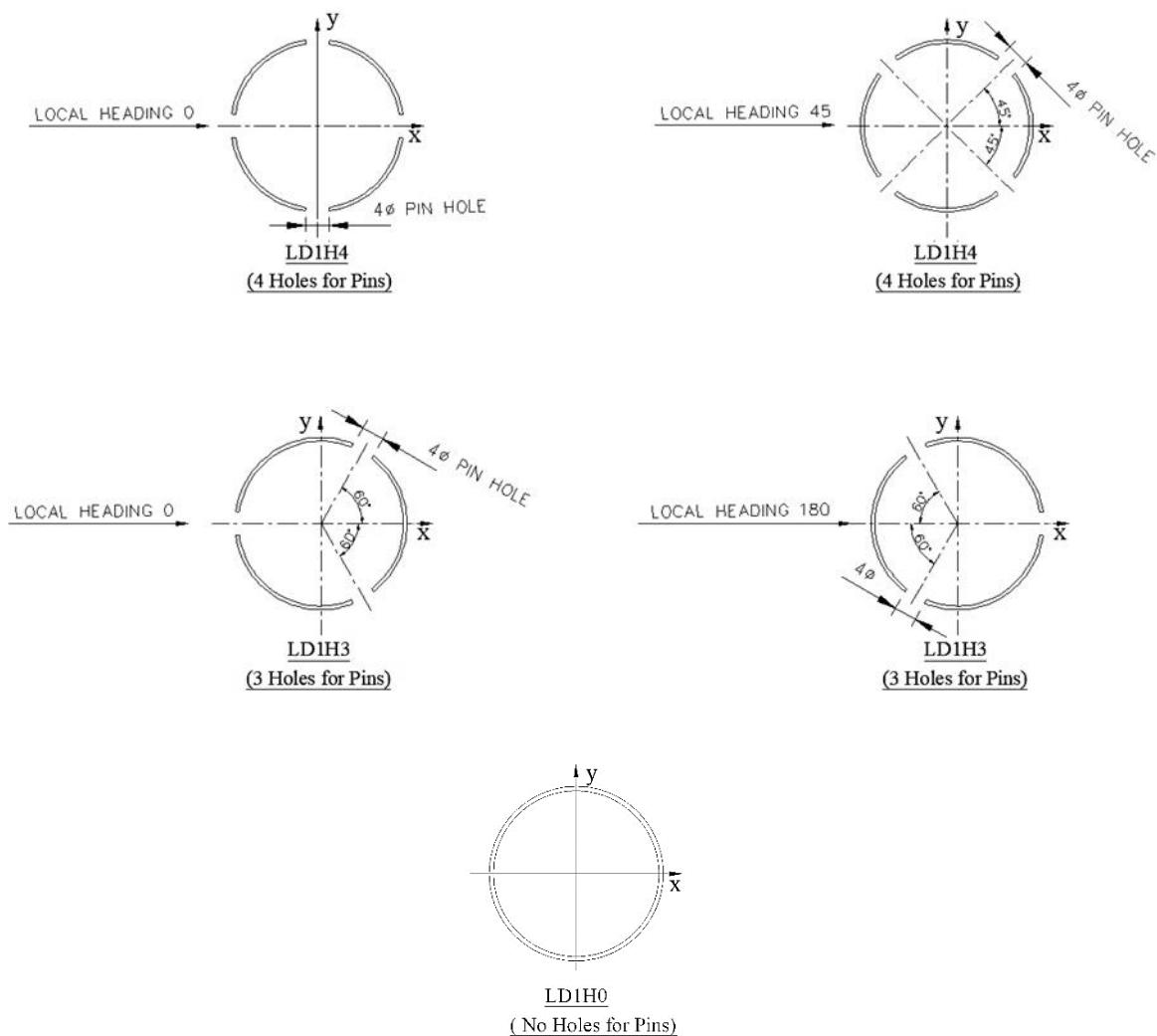


Figure 6-7: Leg designs and local headings

### 6.1.6 Test Cases

The details of the basic test cases are presented in Table 6-3. The effective water depth can be defined as the height of the water level above the leg ball joint. The commonly used leg design LD1H4 is selected for the basic test cases, and the jack-up global and leg local headings are kept at 0 degrees.

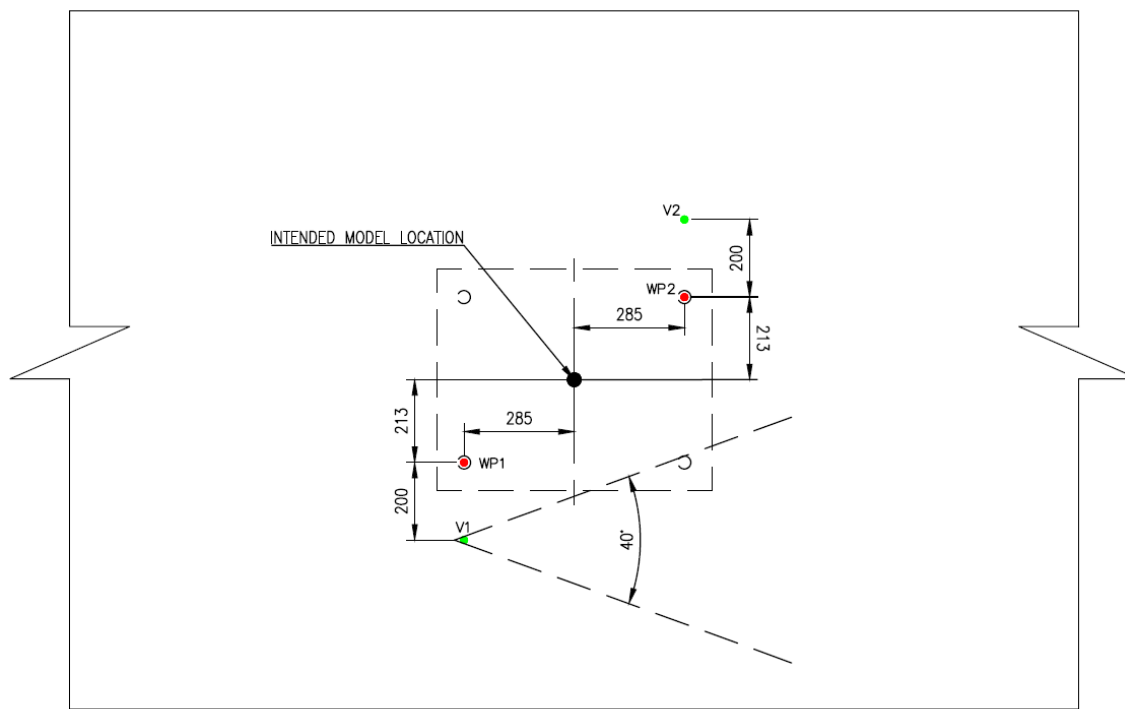
### 6.1.7 Current Profile and Turbulence

Measurements were carried out to verify the current profile and the inlet turbulence. The velocity time series were measured by means of two velocity profilers fitted at the intended model location inside the WWC tank. The measurements were taken at four

vertical locations for a given water depth, and the test was conducted for two water depths of 0.50 m and 0.89 m. The vertical profile and inlet turbulence were obtained by post processing the results. Figure 6-8 illustrates the instrumentation plan followed for the kinematics measurement. V1 and V2 indicate the velocity profilers and WP1 and WP2 indicates wave probes used for measuring the velocity and water surface elevation respectively.

Table 6-3: Basic test cases

Test Case	Description	Hull Mass (kg)	Fluid Medium	Water Depth (m)	Effective Water Depth (m)
NVL, Dry	No Variable Load	10.65	Air	-	-
VL, Dry	Full Variable Load	18.05	Air	-	-
VL, 500WD	Full Variable Load	18.05	Water	0.50	0.39
VL, 700WD	Full Variable Load	18.05	Water	0.70	0.59
NVL, 890WD / NVL	No Variable Load	10.65	Water	0.89	0.78
RVL, 890WD / RVL	Reduced Variable Load	14.08	Water	0.89	0.78
VL, 890WD / VL	Full Variable Load	18.05	Water	0.89	0.78



WWC Tank Plan

Figure 6-8: Instrumentation plan for the kinematics measurement

It is found that the velocity profile can be regarded as reasonably uniform up to a current of around 0.50 m/s, which is used as the test current range for the experiments. The normalised velocity profiles obtained as a result of the kinematics measurement are illustrated in Figure 6-9. It can be observed that at higher currents, the profile is significantly parabolic.

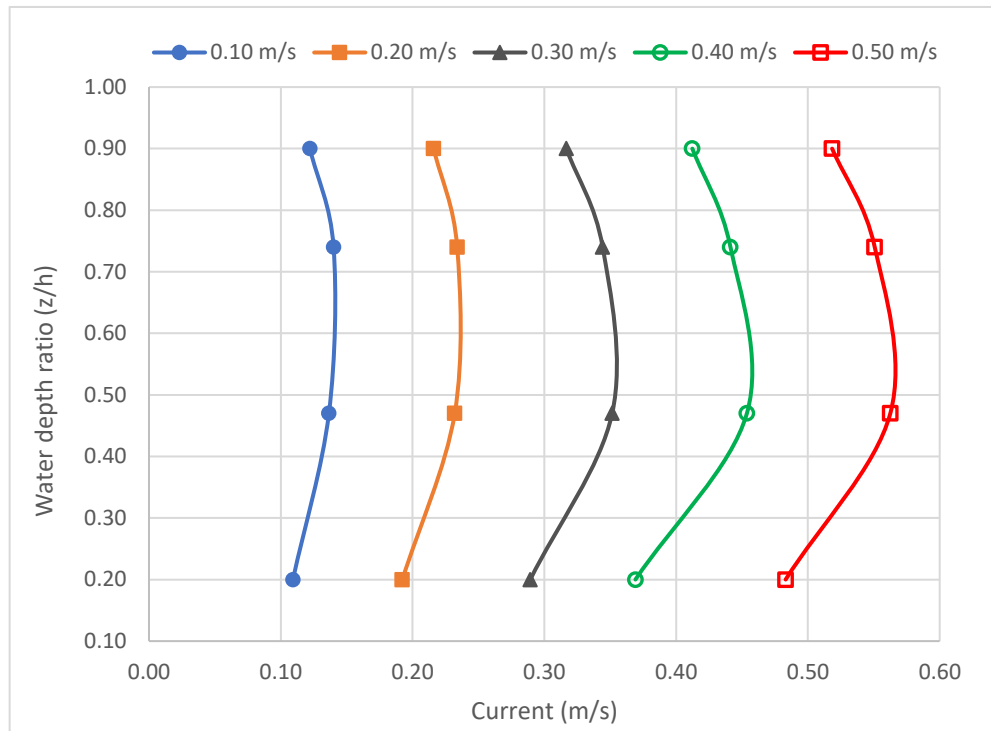


Figure 6-9: Current profiles from kinematics measurement

The inlet turbulence is found to be considerably high in the order of 12 - 13% as demonstrated in Table 6-4 due to the presence of an inlet grid. The high turbulence effectively increases the  $Re$  of the model and minimise the scale effect.

### 6.1.8 Test Procedure

The tests involved mass tests, stiffness tests, ball joint friction tests, free decay tests, response tests and force tests. Mass tests yielded the mass, inertia and COG details of the model. Friction tests were carried out to quantify the friction in the ball joints provided in way of the leg footings. Stiffness tests verified the stiffness of the model, the effect of ball joint friction on the model stiffness and associated nonlinearities. Natural frequencies, damping properties and the dynamic properties of the models were established with the free decay tests.

Table 6-4: Inlet turbulence

<b>Current (m/s)</b>	<b>Turbulence Intensity</b>
0.10	13.15%
0.20	12.21%
0.30	12.33%
0.40	11.49%
0.50	12.89%

Response tests were carried out to evaluate the modes, amplitudes and frequencies of the VIV responses experienced by the model. Response tests were conducted for three water depths and three elevated loads to capture the operational envelope of a jack-up. Response tests were carried out both in uniform current as well as wind to verify the effect of mass ratio and to validate the criteria developed. Response tests were also carried out in regular waves, irregular waves and regular waves with imposed current. The effect of the VIV on the mean drag force acting on the model was also established with the response tests. Force tests were conducted in uniform current to investigate the drag and lift amplification on the jack-up due to VIV.

## 6.2 Mass property test

The mass properties of the model hull and legs were measured by means of the conventional weighing test. The COG of the leg was found by means of an edge test; the point about which the leg is balanced is the COG. The vertical centre of gravity (VCG) and yaw inertia properties of the model were derived by means of a swing test with a yaw table. The sway and yaw natural periods of the yaw table with and without the model were found, and the VCG and yaw inertia of the model were derived respectively from the difference in the natural periods. The net mass properties of the model hull were found by means of moment additions. The yaw table inertia test is illustrated in Figure 6-10, and the model mass and inertia properties are displayed in Table 6-5.

## 6.3 Stiffness Tests

The stiffnesses of the bare leg and leg in hull interface were measured to evaluate the effect of leg interface. The tests were followed by stiffness test of the model along various VIV modes.



Figure 6-10: Yaw table swing test

Table 6-5: Model mass properties

Item	Mass (g)	VCG (mm)	k (m)	I (gm <sup>2</sup> )
Hull	10,650	1,025	0.24	636
legs	1,520	512	0.38	214
Ballast	7,400	1,053	0.13	123
Total, model	19,570	996	0.22	973

### 6.3.1 Leg stiffness

The stiffness test of the individual leg was performed to find the leg flexural properties. The individual leg was clamped on one end to form a cantilever with a span equal to the effective length of the leg. Incremental static weights were applied, and the deflections were measured at a location near to the leg footing. Figure 6-11 and Figure 6-12 illustrate the leg stiffness test setup and the force deflection curve obtained from

the leg stiffness test respectively. It can be observed that the leg stiffness is linear with a nominal hysteresis (see Figure 6-12).



Figure 6-11: Leg stiffness test setup

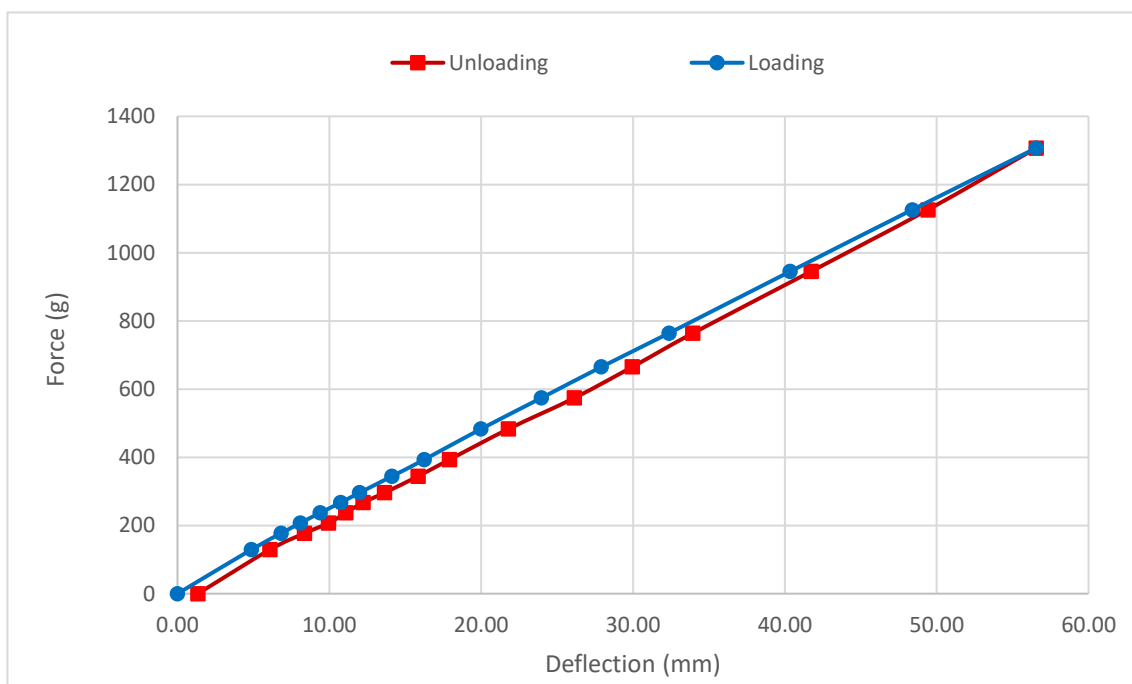


Figure 6-12: Force deflection curve for leg stiffness test

### 6.3.2 *Leg-Hull Interface*

The stiffness of the leg in the leg-hull interface was tested similar to the legs by placing the model horizontally. Similar incremental loads were used for the test, and the deflections of the leg were observed. The deflections were then corrected with the

corresponding leg deflections from the leg stiffness tests to arrive at the pure interface deflections. The interface deflections were then analysed to find the interface stiffness of the model.

Figure 6-13 illustrates the force deflection curve obtained from the test. It can be observed that the leg interface stiffness is fairly linear for small deflections but exhibits a hardening nonlinearity at large deflection, possibly due to the limiting compression of the interface O-rings. The leg interface is also found to exhibit a rather significant hysteresis as evident in the figure.

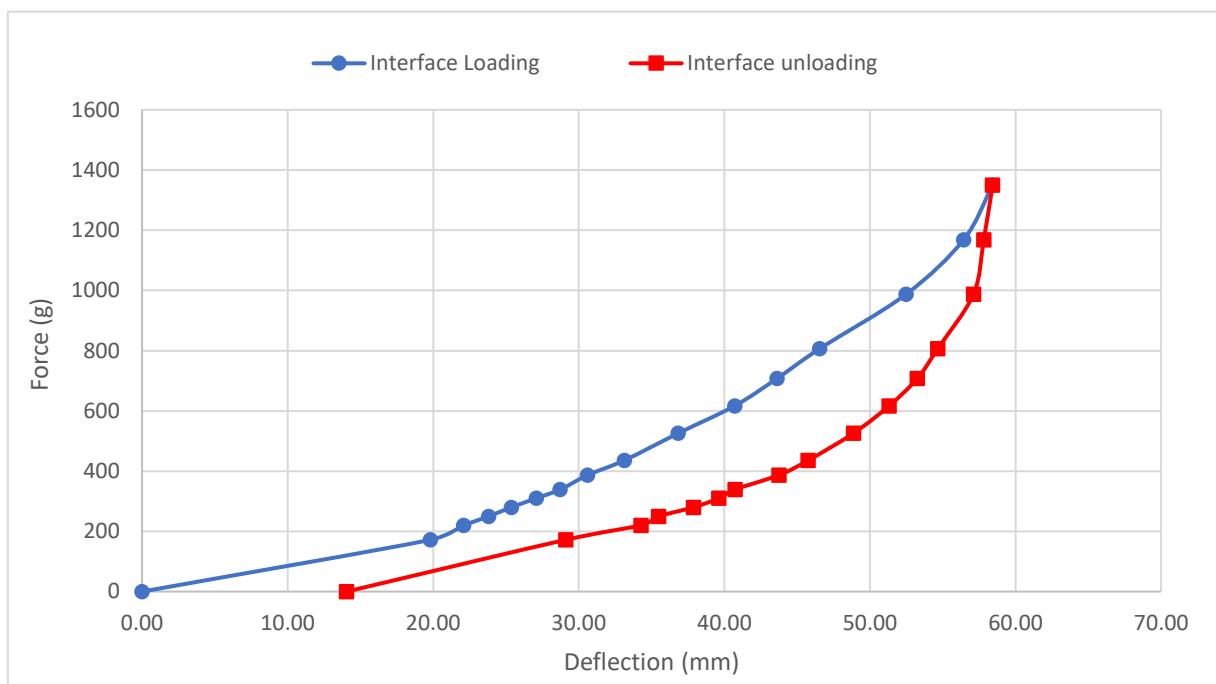


Figure 6-13: Force deflection curve for leg-hull interface stiffness test

### 6.3.2.1 Leg and Leg-Hull Interface Hysteresis

The leg material and leg-hull interface are found to have nominal and significant hysteresis respectively. The source of the leg-hull interface hysteresis is attributed to the O-rings made of silicone rubber solid cords, fitted inside the leg wells for absorbing leg moments and having a specified compression set of 20%. The hysteresis is expected to act as one of the major sources of material damping during vibrations.

### 6.3.3 *Jack-up Model*

The model was subjected to incremental static forces or moments along the respective VIV modes. The static responses of the model against the known forces or moments were measured by means of 2 Qualisys motion tracking cameras installed on either side of the model. The time series obtained were processed to find the static stiffness properties of the model. Stiffness test was carried out both in the air as well as in still water to ascertain the effect of the fluid medium on model stiffness. Stiffness test was also carried out for various loading conditions, to evaluate the P Delta effect on the model. Figure 6-14 a) and b) illustrates the sway and yaw stiffness tests respectively of the model. The rope and pulley arrangement, fitted on the model and WWC side wall to apply a horizontal force or moment by means of known weights is visible in the figures.

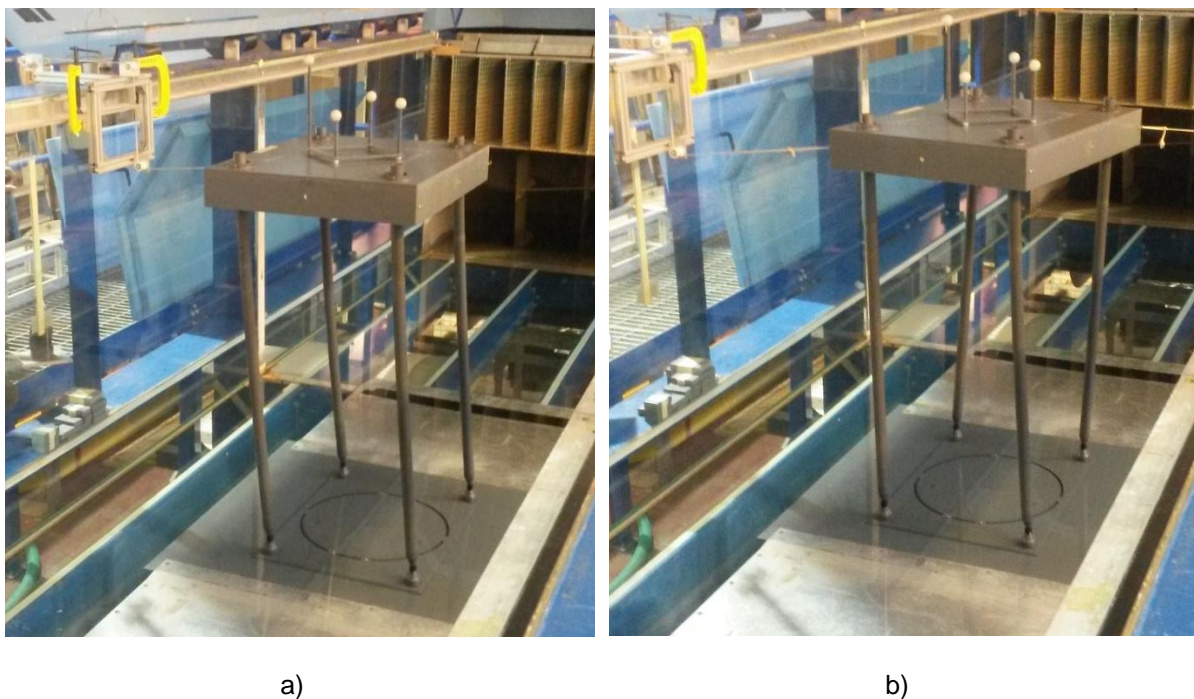


Figure 6-14: Stiffness test set-ups for a) sway/crossflow and b) yaw

The force deflection curve and the corresponding sway stiffness curve obtained from the stiffness test in the air for the full variable load condition (VL) is illustrated in Figure 6-15 a) and b) respectively. The sway deflection demonstrated in the figure is the mean of the results of the port and starboard sides. The model stiffness test reveals a softening nonlinearity with initial deflections, during the loading cycle. It was further revealed that the ball joint friction was influencing the rotational fixity of the leg footing

(see Figure 6-15 b)). Leg bottom behaved as a fixed footing for very small initial deflections and pinned footing for reasonably large deflections. For intermediate deflections, the footing was found to exhibit decreasing rotational stiffness.

It can be observed in Figure 6-15 b) that during the unloading cycle, the model stiffness increases with the deflection. This phenomenon can be attributed to the reversal of ball joint friction during the unloading cycle. It can be further observed in Figure 6-15 a) that the model exhibits significant hysteresis due to both the leg interface hysteresis and ball joint friction.

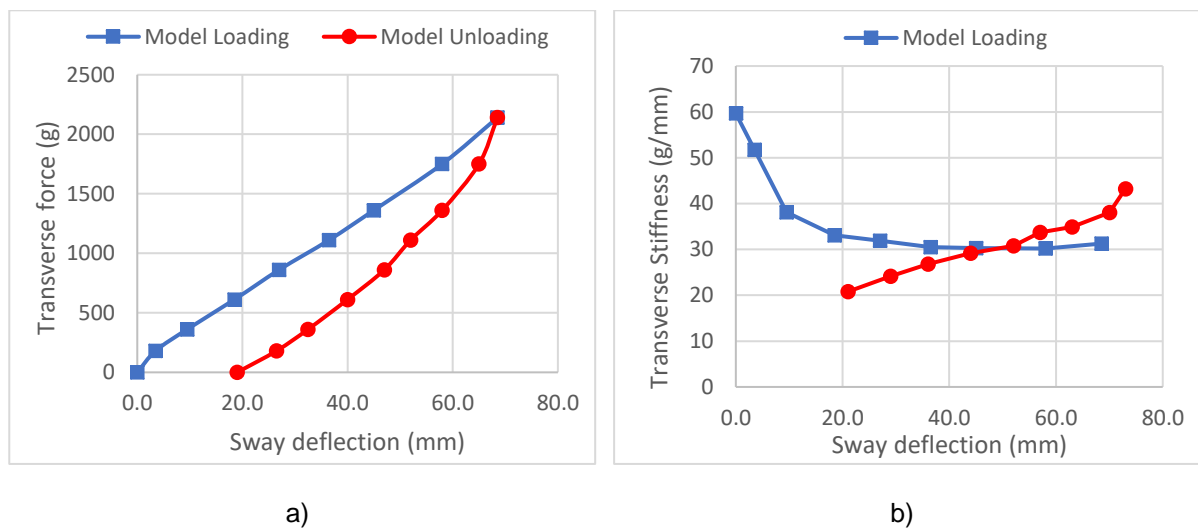


Figure 6-15: Model sway stiffness test; VL, Dry, a) force deflection curve, b) sway stiffness versus deflection

Figure 6-16 illustrates the force versus deflection curve during the loading cycle of the model along the sway mode for various load cases. It can be inferred that in general, the sway stiffness is constant for very small initial deflections. However, the sway stiffness reduces nominally in still water for intermediate deflections, possibly due to the reduction in ball joint friction. The sway stiffness was also found to reduce nominally with the increase of elevated load at intermediate to large deflections, possibly due to the increase in P delta effect. The surge and sway stiffnesses of the model were found to be identical as expected.

Yaw stiffness tests also exhibited behaviours including softening nonlinearity during loading, reduced stiffness during unloading, footing fixity, high hysteresis, similar to the sway results as illustrated in Figure 6-17a) and b). However, the reduction of stiffness with the increase in elevated load due to the P delta effect was not observed for the

yaw mode, as evident in Figure 6-18. Further, the yaw stiffness is found to reduce nominally in water similar to sway, possibly due to the reduction in ball joint friction.

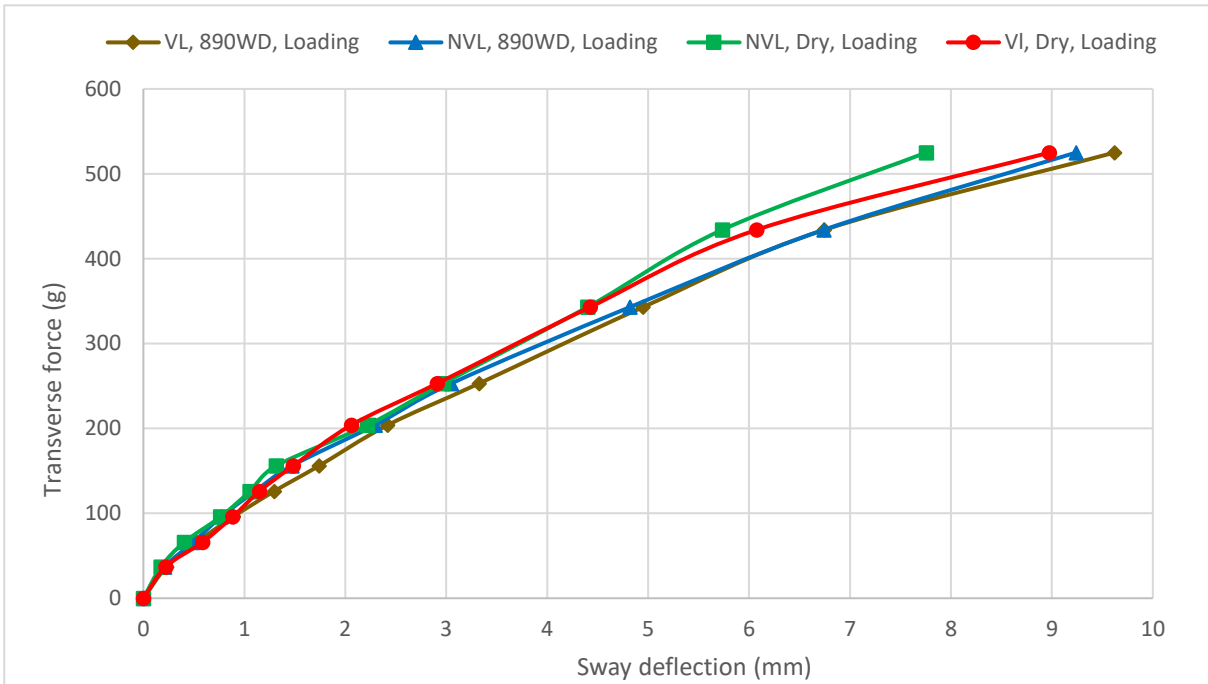


Figure 6-16: Model sway force versus deflection curve for various load cases

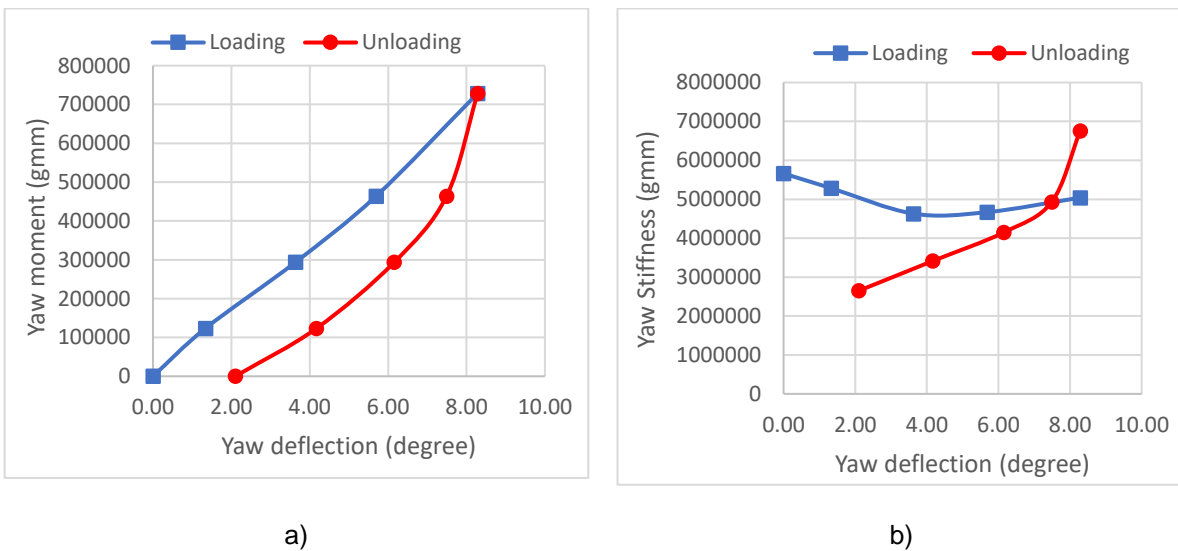


Figure 6-17: Model yaw stiffness test; VL, Dry, a) force deflection curve, b) yaw stiffness versus deflection

Figure 6-19 demonstrates the variation of sway stiffness with the deflection for the test case NVL, 890WD and the corresponding dynamic sway stiffnesses for the port (P) and starboard (S) sides, derived from the free decay tests. It can be observed that the

dynamic stiffness is less dependent on the deflections and nearly corresponds to that of pinned footing. Hence, it can be inferred that the support rotational stiffness due to the ball joint friction has an insignificant bearing on the leg mode shape and the natural frequency during vibrations and contributes more towards the damping of the system.

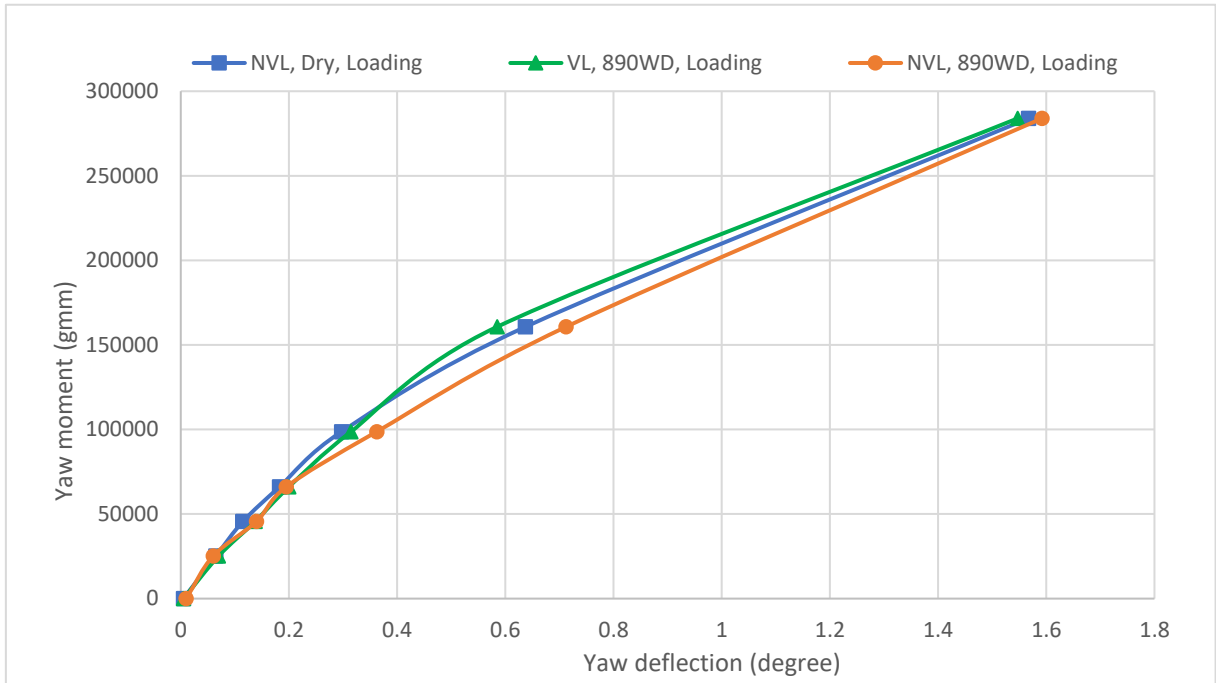


Figure 6-18: Model yaw moment versus deflection curve for various load cases

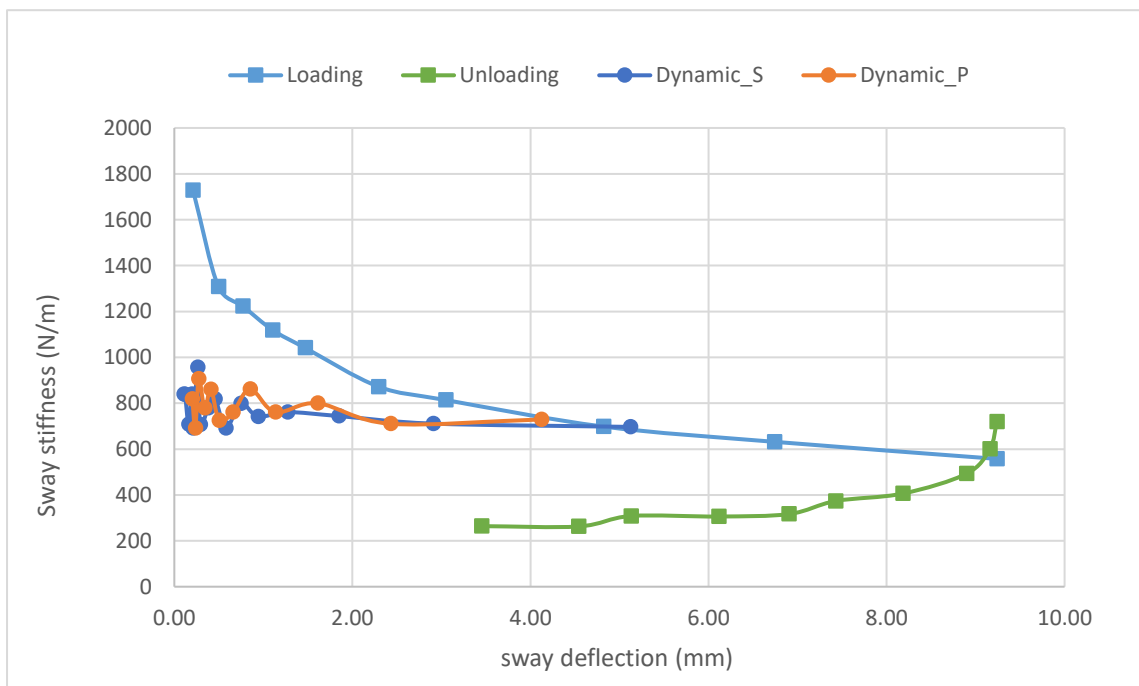


Figure 6-19: Sway static and dynamic stiffnesses versus deflection for NVL, 890WD

#### 6.4 Leg Footing (Ball Joint) Friction Test

The ball joints provided in way of leg bottoms were tested for the presence of any dry friction. The ball joints were mounted horizontally, and given loads are applied on the connecting nut at a known distance to find out the existence of any friction moment. It was found that the ball joints do experience Coulomb or dry friction, which can be inferred as the source of model nonlinearity observed during the stiffness tests. Figure 6-20 and Figure 6-21 illustrate the ball joint friction test setup and the results obtained from the test respectively.

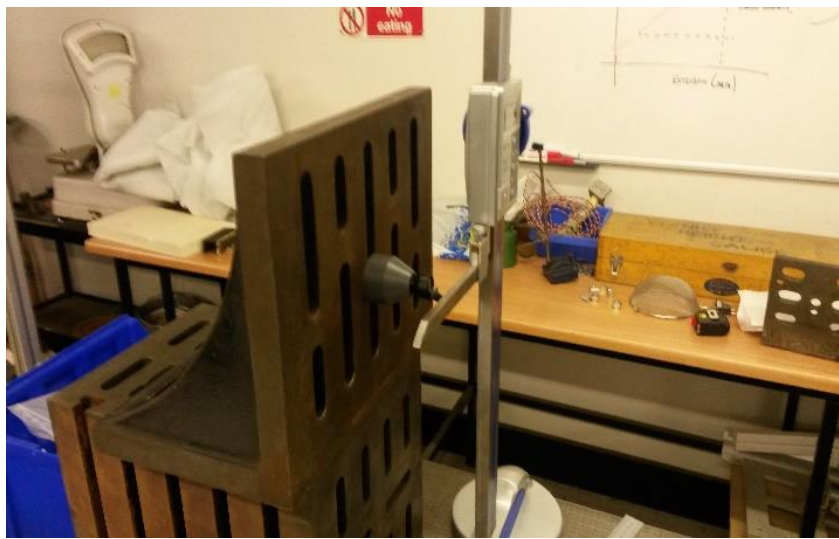


Figure 6-20: Setup for ball joint friction test

It can be observed in Figure 6-21 that the support moment is insignificant and corresponds to even less than 10 g of horizontal loading in way of the jack-up hull. However, the value may be higher once fitted with the model due to the increase in the normal reaction caused by the model's weight. The ball joint dry friction can be regarded as the source of footing rotational fixity at small initial deflections, causing the bimodal response during the stiffness tests. Further, the Coulomb friction will also act as an additional source of nonlinear damping during vibrations.

#### 6.5 Free Decay Tests

Free decay tests were carried out with the model in the air as well as in still water. The tests were intended to establish the natural frequency, added mass, damping and the nonlinearities of the system. The tests were also carried out in uniform current to investigate added mass and damping of a freely vibrating jack-up. The tests were

carried out by applying predefined initial displacements along various response modes and introducing free vibrations.

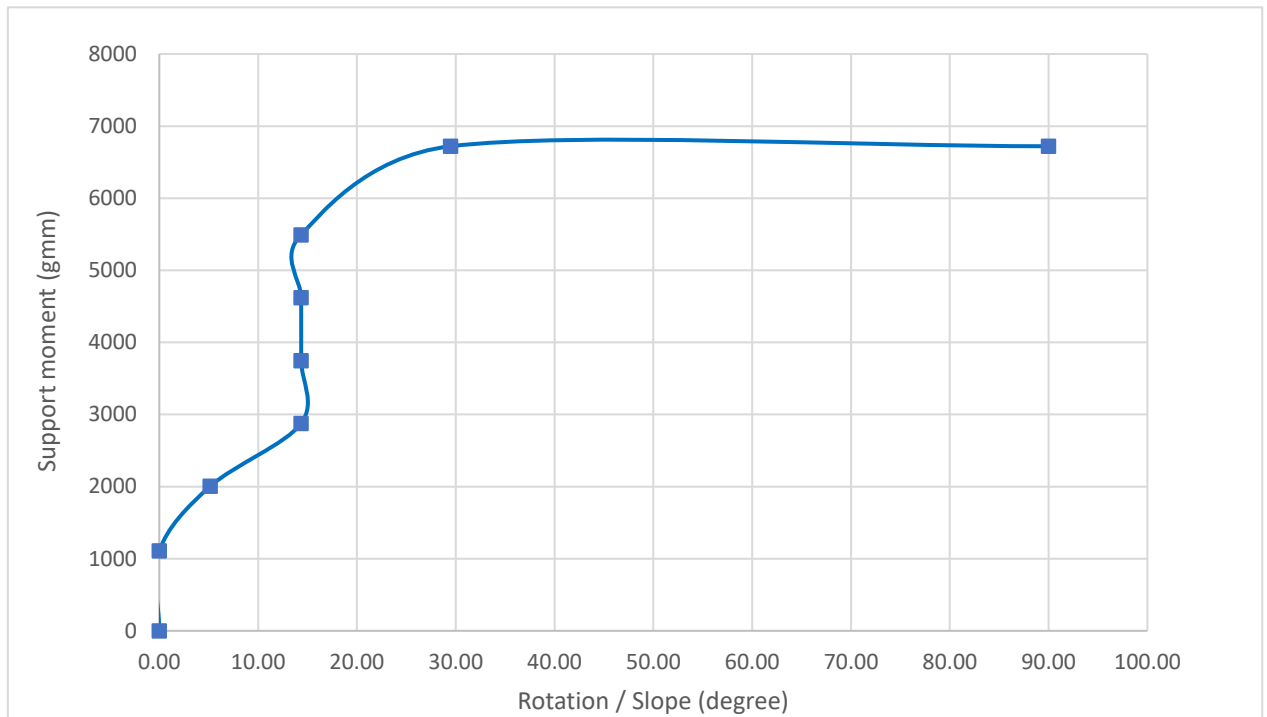


Figure 6-21: Support moment versus rotation

As the model was found to exhibit softening nonlinearity at large deflections due to the ball joint friction or support rotational stiffness, the free decay time series was truncated to remove large amplitudes. Subsequently, Fast Fourier Transform (FFT) analysis of the truncated time series was carried out to establish the natural frequencies. The added mass of the legs was calculated from differences in natural frequencies of the model in air and water. The variation of the damping ratio with the frequency was calculated from the successive amplitude decays, and the trend obtained was used to calculate the damping ratio corresponding to the natural frequency. Similarly, the variation of the damping ratio with the vibration amplitude was also generated.

### 6.5.1 Tests in Air and Still Water

Model free decay tests revealed a softening nonlinearity in the system, where the natural frequency decreased with the increasing amplitudes. This confirmed the bimodal response of the system observed during stiffness tests, due to the presence of ball joint friction.

Free decay tests revealed that the damping of the system had increased in still water due to the additional fluid damping. It was also found that the damping of the model was increasing with the vibration amplitudes. However, the damping ratios obtained from the tests were found to exhibit considerable scatter, possibly due to the effect of ball joint friction which influenced the results as dry friction or coulomb damping.

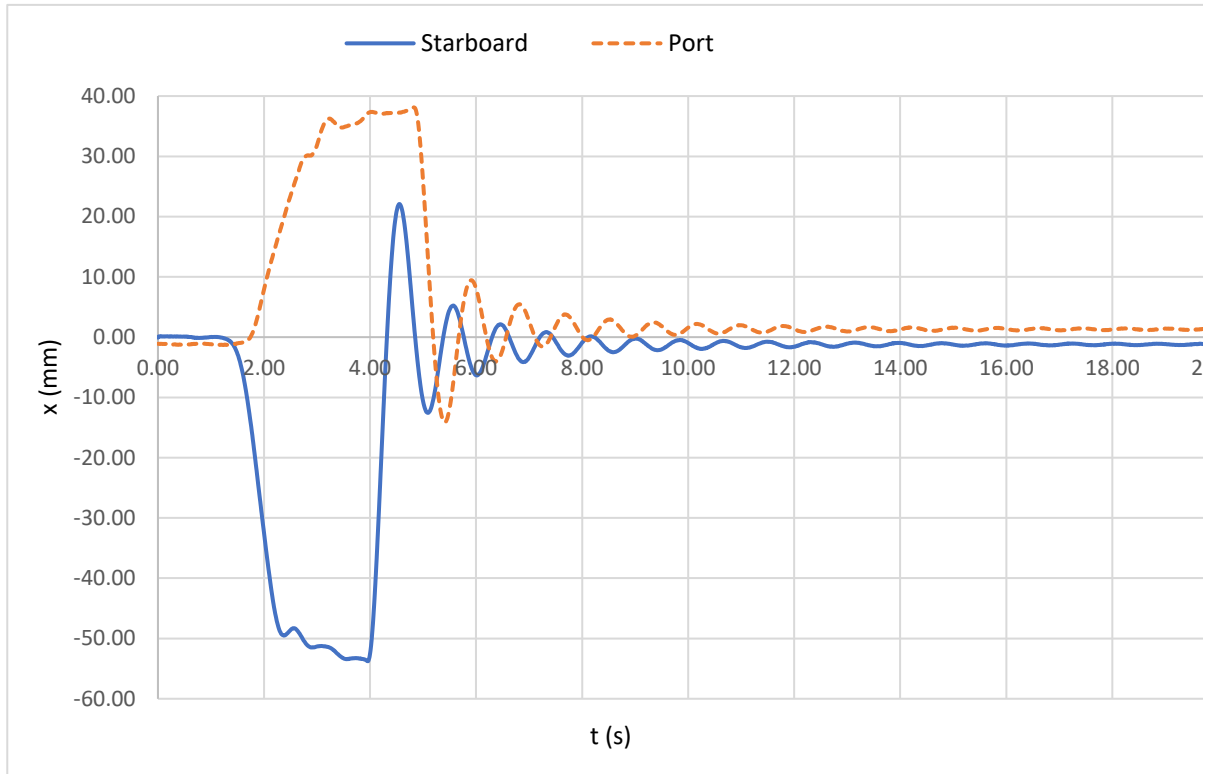
Figure 6-22 a), b) and c) illustrate the free decay time series, natural frequency variation with the amplitude and the damping factor variation with the natural frequency respectively resulted from the sway free decay test for NVL, 890WD. The test case, NVL, 890WD represents the lightest operating condition of the jack-up at the maximum water depth. Figure 6-22 b) evidently shows the slight reduction in sway frequency with the amplitudes. It can be observed in Figure 6-22 c) that the damping ratio generally decreases with increasing sway frequency, though considerable scatter is observed.

From free decay tests, the added mass coefficient of the legs in still water was found to be around 1, the theoretical value. The corresponding mode shape was found to that of pinned footing, quarter sinusoid. This indicates that for the practical vibration amplitudes, the model legs were vibrating with a mode shape near that of pinned footing and the effect of the ball joint friction was negligible. Table 6-6 and Table 6-7 summarise the results of sway and yaw free decay tests respectively. The leg design selected for the test was LD1H4.

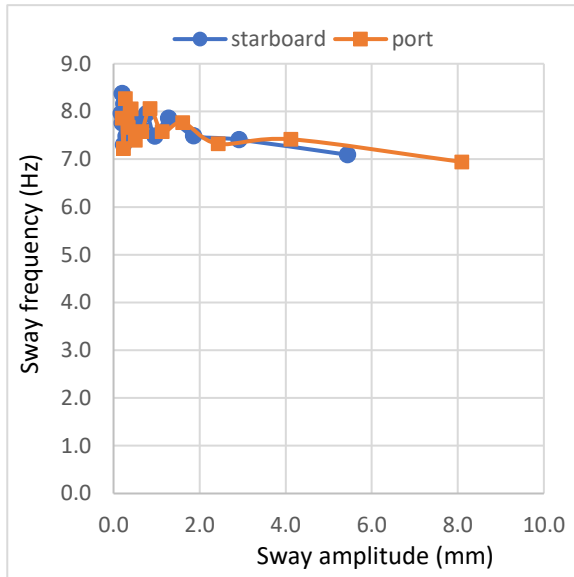
Figure 6-23 compares the FFT of the surge and sway free decay test results in air for the test case, VL. It can be seen in the figure that the surge and sway natural frequencies are almost identical, as observed for typical jack-ups and attributable to the similarity in the effective mass and stiffness of these two modes. Consequently, further free decay tests were not carried out for the surge mode.

#### 6.5.1.1 Sway

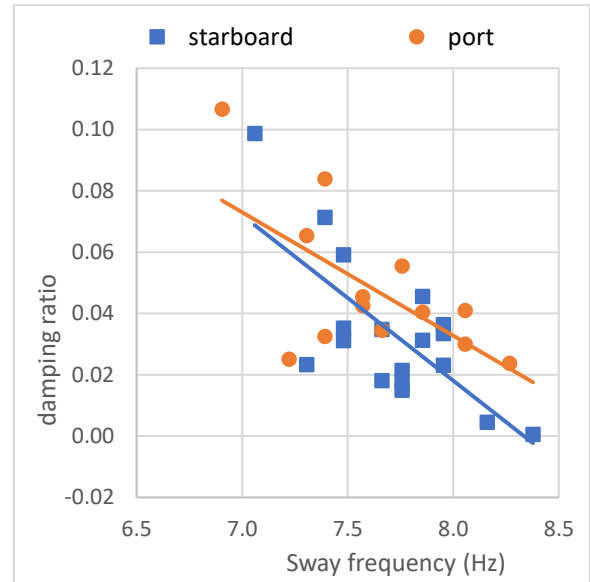
The FFT of the sway free decay signals of the test cases in air and at the maximum water depth are illustrated in Figure 6-24. It can be observed that the test cases with full variable load (VL) exhibit the lowest sway frequencies while the cases with no variable load (NVL) have the highest. The test case with reduced variable load (RVL) is found to have an intermediate sway frequency.



a)



b)



c)

Figure 6-22: a) Free decay time series of sway free decay test; NVL, 890WD b) Sway natural frequency variation with amplitude; NVL, 890WD c) Variation of sway damping ratio with sway frequency; NVL, 890WD.

Table 6-6: Model natural frequency, added mass and damping from sway free decay tests

Sway							
Test Case	Damping Ratio	Natural Frequency (Hz)	Natural Period (s)	Added Mass (kg)	Leg Added Mass Coefficient	Fluid Damping (Ns/m)	Fluid damping ratio
NVL, Dry	0.036	1.37	0.73	0.00	-	0.00	0.00
VL, Dry	0.031	1.03	0.97	0.00	-	0.00	0.00
VL, 500WD	0.041	1.00	1.00	0.12	0.71	2.09	0.01
VL, 700WD	0.035	0.98	1.02	0.56	1.06	1.00	0.00
NVL, 890WD	0.040	1.22	0.82	1.46	1.35	1.15	0.01
RVL, 890WD	0.044	1.08	0.93	1.40	1.29	2.87	0.01
VL, 890WD	0.038	0.95	1.05	1.19	1.10	1.97	0.01

Table 6-7: Model natural frequency, added mass and damping from yaw free decay tests

Yaw							
Test Case	Damping Ratio	Natural Frequency (Hz)	Natural Period (s)	Added Mass Inertia (kgm <sup>2</sup> )	Leg Added Mass Coefficient	Fluid Damping (Nms/rad)	Fluid damping ratio
NVL, Dry	0.037	2.05	0.49	0.00	-	0.00	0.00
VL, Dry	0.040	1.91	0.52	0.00	-	0.00	0.00
VL, 500WD	0.041	1.86	0.54	0.02	1.00	0.04	0.00
VL, 700WD	0.042	1.78	0.56	0.07	1.00	0.10	0.00
NVL, 890WD	0.038	1.81	0.55	0.13	0.88	0.11	0.00
RVL, 890WD	0.043	1.74	0.58	0.14	0.95	0.21	0.01
VL, 890WD	0.043	1.72	0.58	0.12	0.82	0.15	0.01

#### 6.5.1.2 Yaw

Figure 6-25 a), b) and c) illustrate the free decay time series, natural frequency variation with the amplitude and the damping factor variation with the natural frequency respectively resulted from the yaw free decay test for VL, 890WD. The test case, VL, 890WD represents the heaviest operating condition of the jack-up at the maximum water depth. It can be observed in Figure 6-25 b) that the softening nonlinearity is rather insignificant for the yaw mode. It can be observed in Figure 6-25 c) that the damping ratio generally reduces with increasing yaw frequency, in spite of considerable scatter.

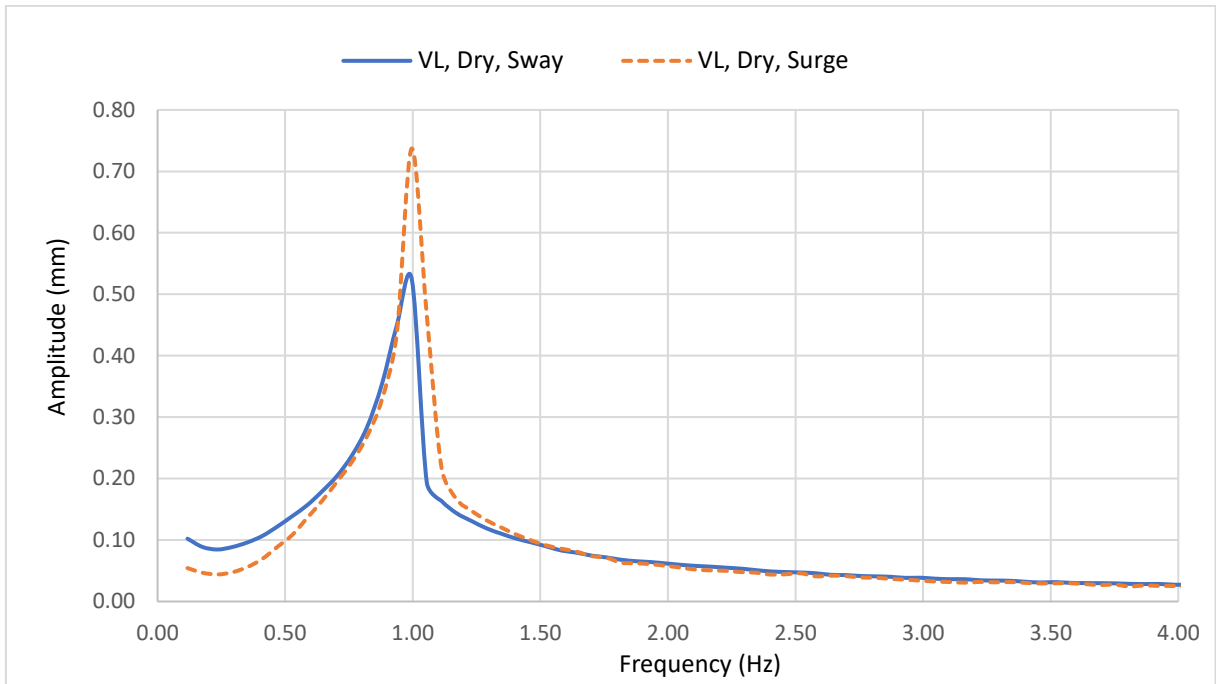


Figure 6-23: FFT of surge and sway free decay tests for the test case, VL, Dry

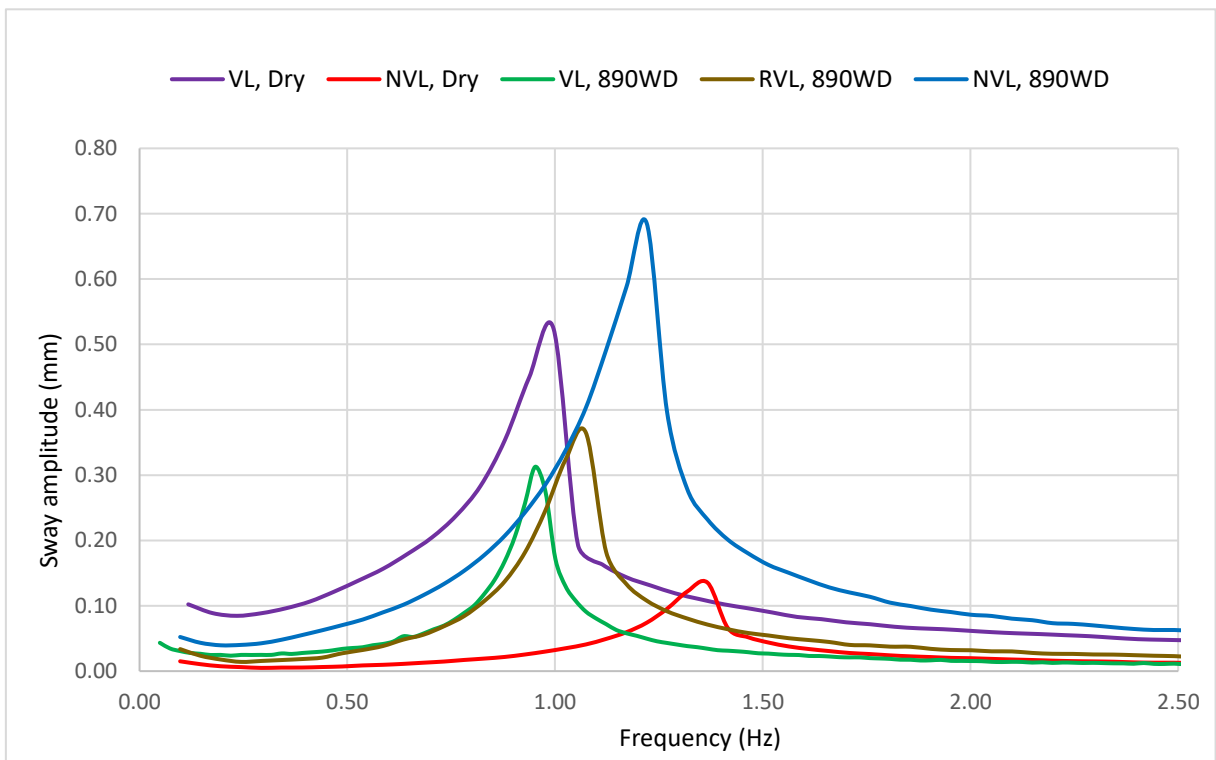
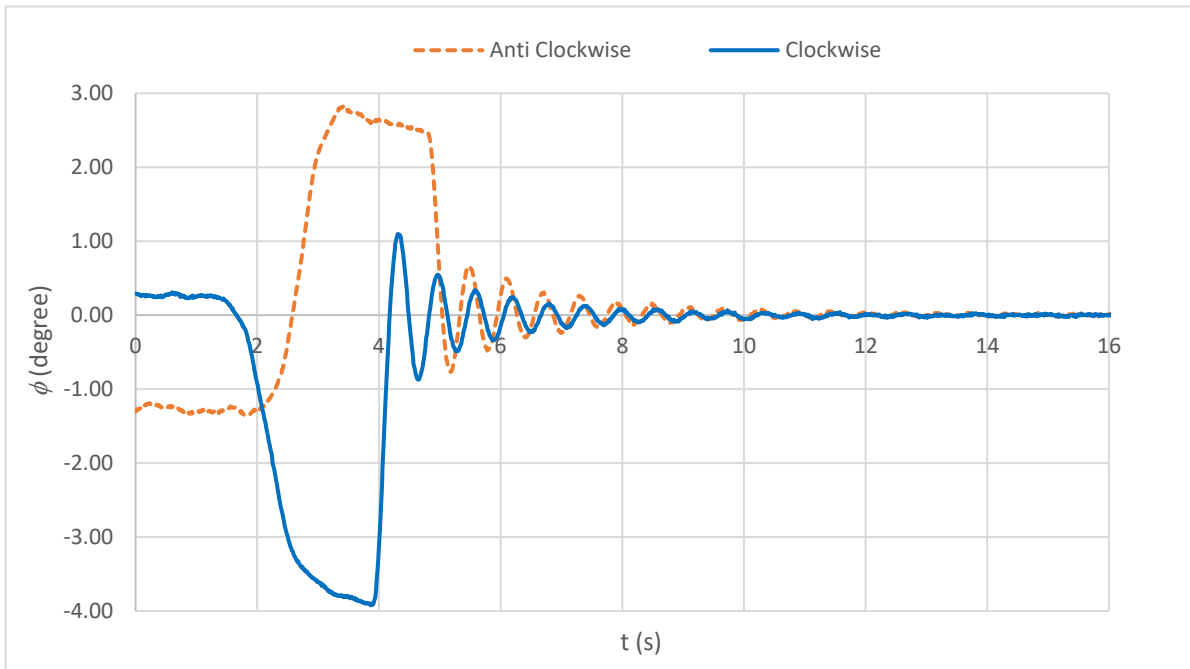


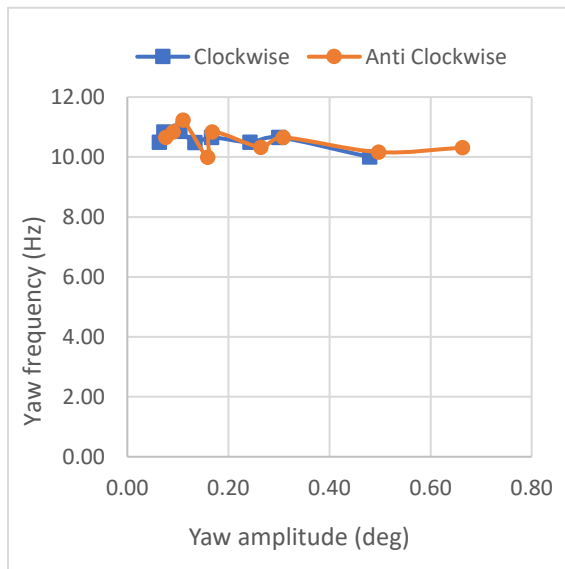
Figure 6-24: FFT of sway free decay tests for all test cases

Figure 6-26 illustrates the FFT of the yaw free decay signals for the test cases in air and in water at the maximum water depth. It can be observed that the test cases with full variable load (VL) exhibit the lowest yaw frequencies, the cases with no variable

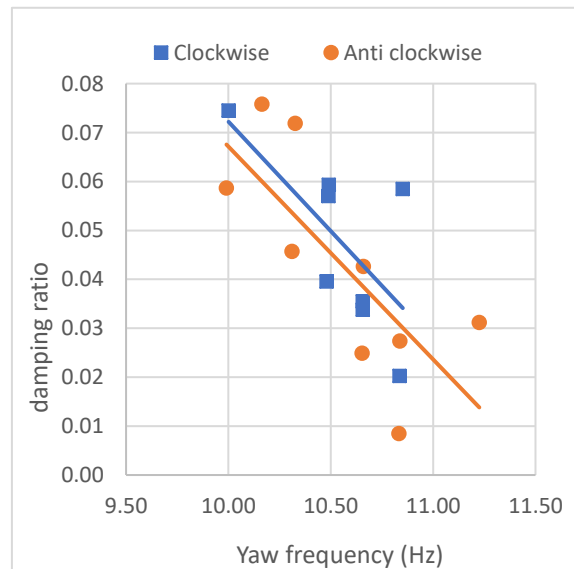
load (NVL) exhibit the highest and the test case with reduced variable load (RVL) being intermediate. However, all three test cases at the maximum water depth are found to have yaw frequencies very close to each other.



a)



b)



c)

Figure 6-25: a) Free decay time series of yaw free decay test; VL, 890WD b) Yaw natural frequency variation with displacement; VL, 890WD c) Variation of yaw damping ratio with yaw frequency; VL, 890WD.

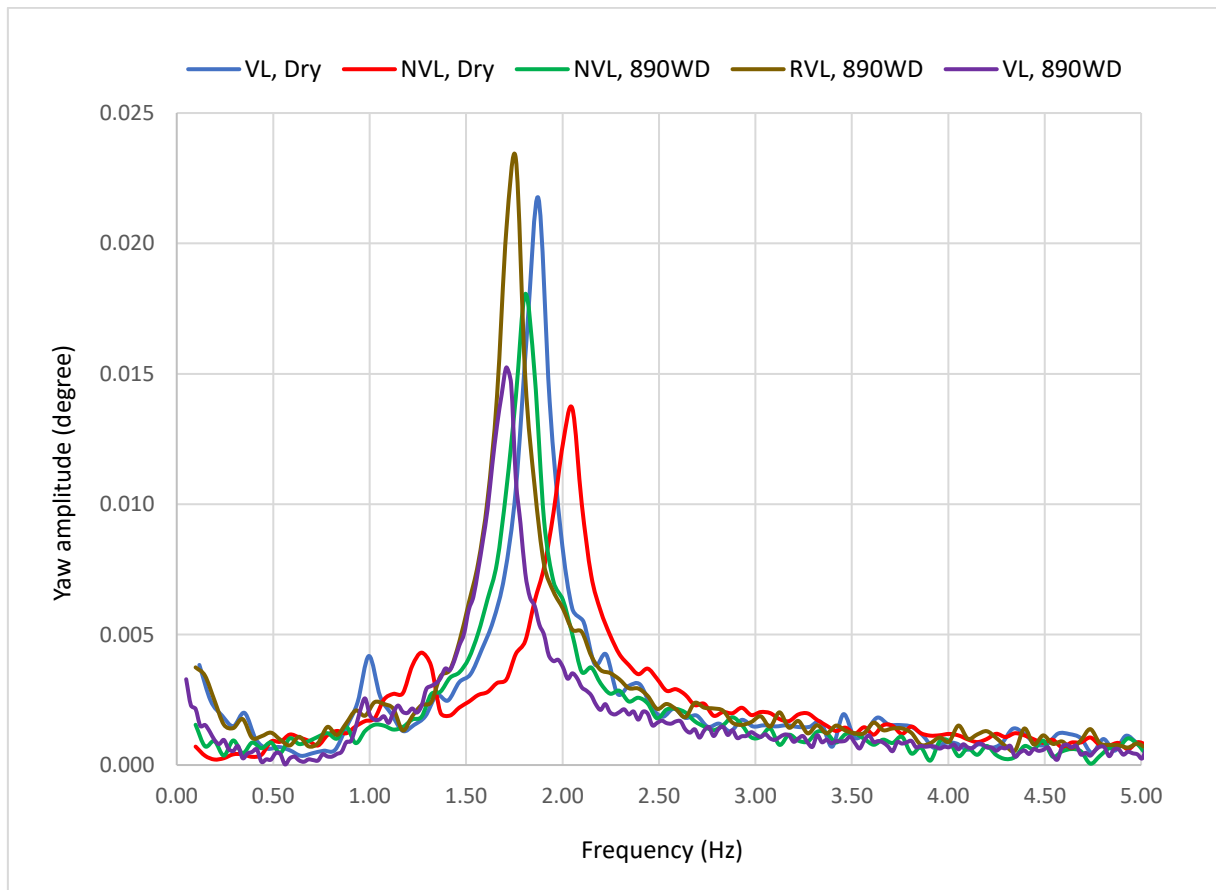


Figure 6-26: FFT of yaw free decay tests for all test cases

### 6.5.2 Tests in Current

Free decay tests of the sway and yaw modes were conducted in incremental current to investigate the effect of cylinder vibrations on natural frequency and fluid damping. The effective water depth for the test was considered at 0.78 m, and the loading condition corresponded to full variable load, VL. The leg design considered was LD1H4, and the global heading and local heading of the model and legs were kept at 0 degrees. The details and results of the free decay tests in current are summarised in Table 6-8. It can be observed that the natural frequencies of the sway and yaw modes vary with the reduced velocity. The natural frequencies of both the modes are found to be higher than the corresponding still water values in the lock-in regime (reduced velocity range, 5 - 8), revealing lower and even negative added mass. The fluid damping is also found to be negative in the vicinity of resonance.

Table 6-8: Results of free decay test in current a) sway, b) yaw

a)							
Sway							
Loading Condition	Current (m/s)	$V_{ry}$	Natural Frequency (Hz)	Natural Period (s)	Leg Added Mass Coefficient	Fluid damping ratio	Natural frequency ratio
VL, 890WD_SW	0.00	0.00	0.94	1.07	0.93	0.012	1.00
VL, 890WD_0p05	0.05	1.58	0.93	1.08	1.19	0.014	0.99
VL, 890WD_0p10	0.10	3.16	0.93	1.08	1.19	0.020	0.99
VL, 890WD_0p15	0.15	4.75	0.92	1.08	1.48	-0.007	0.99
VL, 890WD_0p175	0.18	5.54	0.95	1.05	0.24	-0.015	1.02
VL, 890WD_0p20	0.20	6.33	0.98	1.02	-0.67	-0.001	1.04
VL, 890WD_0p25	0.25	7.91	0.98	1.02	-0.71	0.023	1.05
VL, 890WD_0p30	0.30	9.49	0.95	1.05	0.17	0.034	1.02
VL, 890WD_0p35	0.35	11.07	0.98	1.02	-0.76	0.039	1.05
VL, 890WD_0p40	0.40	12.66	0.98	1.02	-0.79	0.053	1.05
VL, 890WD_0p45	0.45	14.24	0.97	1.04	-0.26	0.019	1.03
VL, 890WD_0p50	0.50	15.82	0.91	1.10	2.10	0.066	0.97

b)							
Yaw							
Loading Condition	Current (m/s)	$V_{r\phi}$	Natural Frequency (Hz)	Natural Period (s)	Leg Added Mass Coefficient	Fluid damping ratio	Natural frequency ratio
VL, 890WD_SW	0.000	0.00	1.70	0.59	0.77	0.012	1.00
VL, 890WD_0p05	0.050	0.87	1.69	0.59	0.87	0.012	0.99
VL, 890WD_0p10	0.100	1.74	1.68	0.60	0.97	0.021	0.99
VL, 890WD_0p15	0.150	2.61	1.66	0.60	1.14	0.019	0.98
VL, 890WD_0p20	0.200	3.48	1.64	0.61	1.30	0.033	0.97
VL, 890WD_0p25	0.250	4.35	1.67	0.60	0.99	0.003	0.99
VL, 890WD_0p30	0.300	5.22	1.68	0.59	0.89	-0.025	0.99
VL, 890WD_0p35	0.350	6.10	1.80	0.56	0.00	0.021	1.06
VL, 890WD_0p40	0.400	6.97	1.83	0.55	-0.25	0.011	1.08
VL, 890WD_0p45	0.450	7.84	1.83	0.55	-0.25	0.019	1.08
VL, 890WD_0p50	0.500	8.71	1.69	0.59	0.84	0.040	1.00

### 6.5.2.1 Sway Mode

Figure 6-27 illustrates the variation of the sway natural frequency ( $f_{Ny, current}$ ) normalised with the sway natural frequency in still water ( $f_{Ny}$ ), plotted against the corresponding reduced velocity. The vortex shedding frequency ( $f_v$ ) normalised with the sway natural frequency in still water is also illustrated in the figure. It can be observed that the natural frequency is almost same as the still water value at low reduced velocities and increases above the natural frequencies post the resonance point at a reduced velocity of 5, till a very high reduced velocity. The natural frequency variation shows double hump behaviour, which is further investigated in the following sections.

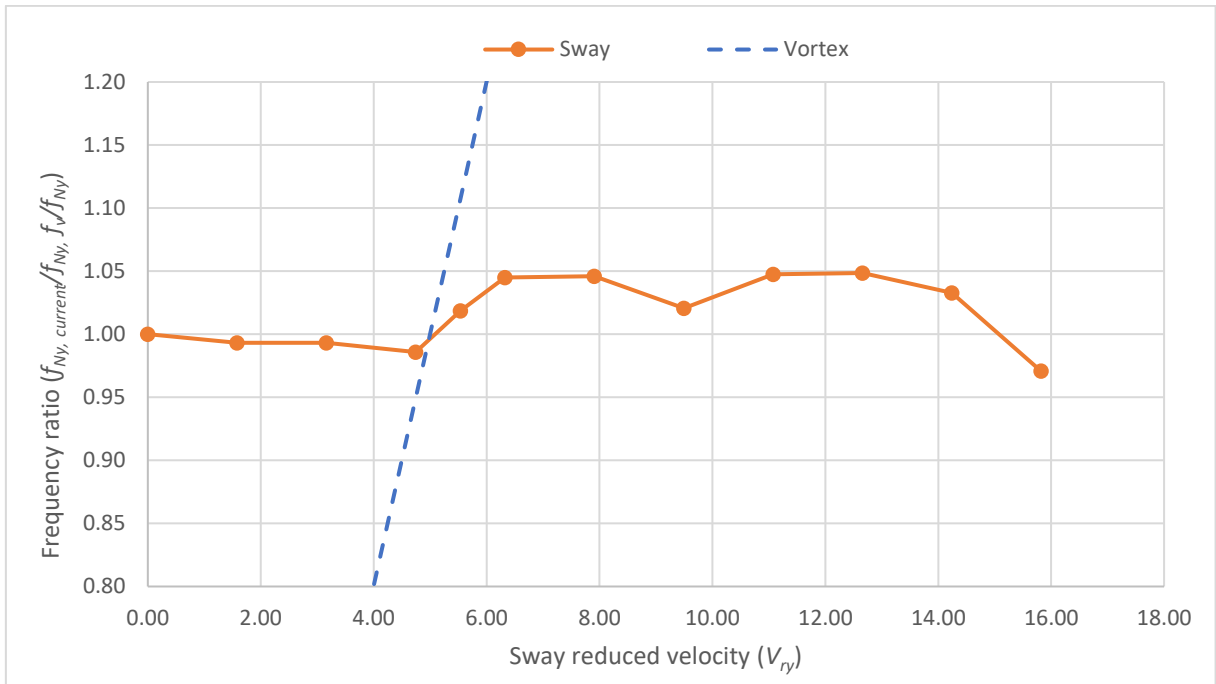


Figure 6-27: Sway natural frequency versus reduced velocity in current

It can be inferred from Figure 6-27 that the added mass is not a constant for the jack-up free to vibrate in sway or crossflow mode. Figure 6-28 illustrates the variation of the leg added mass coefficient ( $C_A$ ) with the sway reduced velocity, as derived from the frequency variation displayed in Figure 6-27. The natural frequency variation is also demonstrated in the secondary vertical axis.

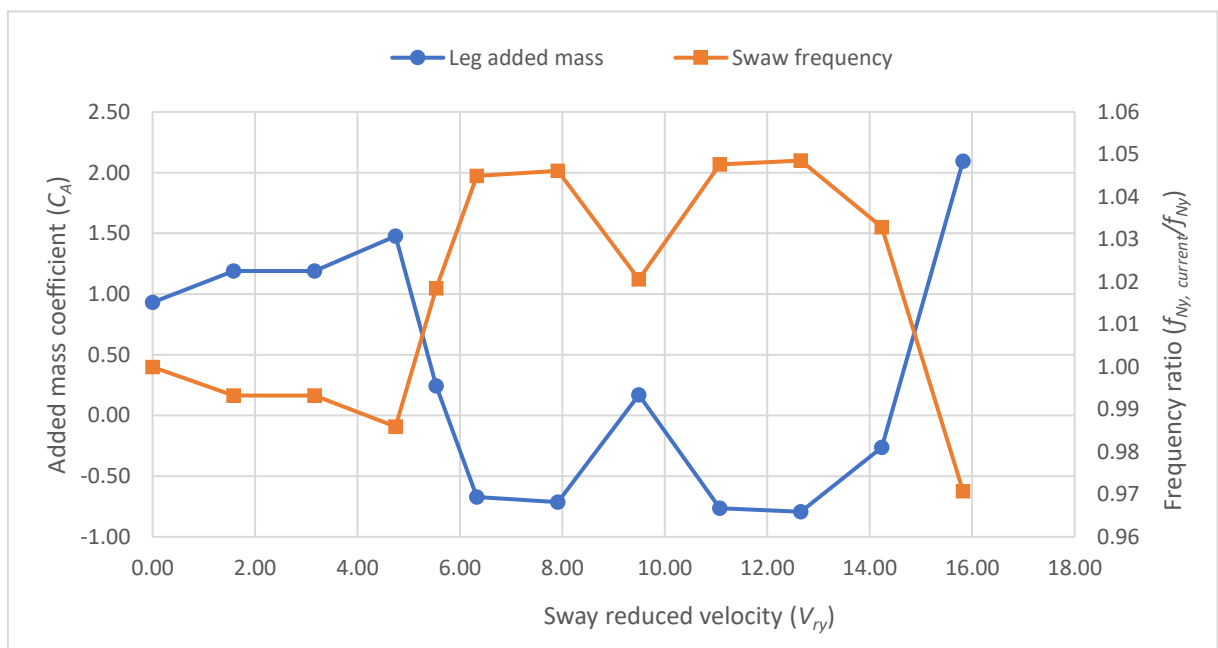


Figure 6-28: Leg sway added mass versus reduced velocity in current

It can be observed in Figure 6-28 that the added mass varies considerably in the lock-in range and even attains negative values over a considerable current range. This can be attributed to the effect of the vortex modes around the vibrating legs on the still water added mass, similar to a vibrating single cylinder. This is in line with the findings of many researchers with freely vibrating single cylinder experiment (Sarpkaya, 1995; Govardhan and Williamson, 2004). The added mass also exhibits the double hump behaviour similar to the natural frequency variation. It can be inferred that the second hump at post lock-in reduced velocities is due to the coupling with the yaw lock-in vibrations. However, this phenomenon warrants further investigation.

The fluid damping of the jack-up undergoing sway vibrations in current is calculated by subtracting the structural damping from the total damping found from the free decay tests. Figure 6-29 illustrates the variation of the fluid damping in sway ( $\zeta_{fy}$ ) with the corresponding reduced velocity. The frequency variation is also demonstrated in the secondary vertical axis. It can be seen that the fluid damping reduced to low values, even negative in the vicinity of sway resonance, around a reduced velocity of 5. This is analogous to the lift amplification established by other researchers with single cylinder experiments (Sarpkaya, 1995). Hence it can be noted that the results of a single cylinder can be applied to jack-up as well. However, it is observed that the damping was positive at reduced velocities above 9, though the natural frequency and added mass still exhibited higher values. This further indicates that the phenomenon represented by the second hump is related to yaw coupling rather than sway lock-in. On either side of the resonance point, the sway damping is found to generally increase with the current, except for the anomalous behaviour at a reduced velocity around 14.

#### 6.5.2.2 Yaw Mode

Figure 6-30 illustrates the variation of the normalised yaw frequency ( $f_{N\phi, current}/f_{N\phi}$ ) with the corresponding reduced velocity. The vortex shedding frequency normalised with the still water yaw natural frequency is also indicated in the figure. It can be observed that the natural frequency is less than the corresponding still water value in the pre-resonance regime. However, the natural frequency increases above the still water frequency post the resonance point at the reduced velocity of 5, till a high reduced velocity. Unlike sway, yaw frequency variation shows a single hump behaviour corresponding to the yaw lock-in.

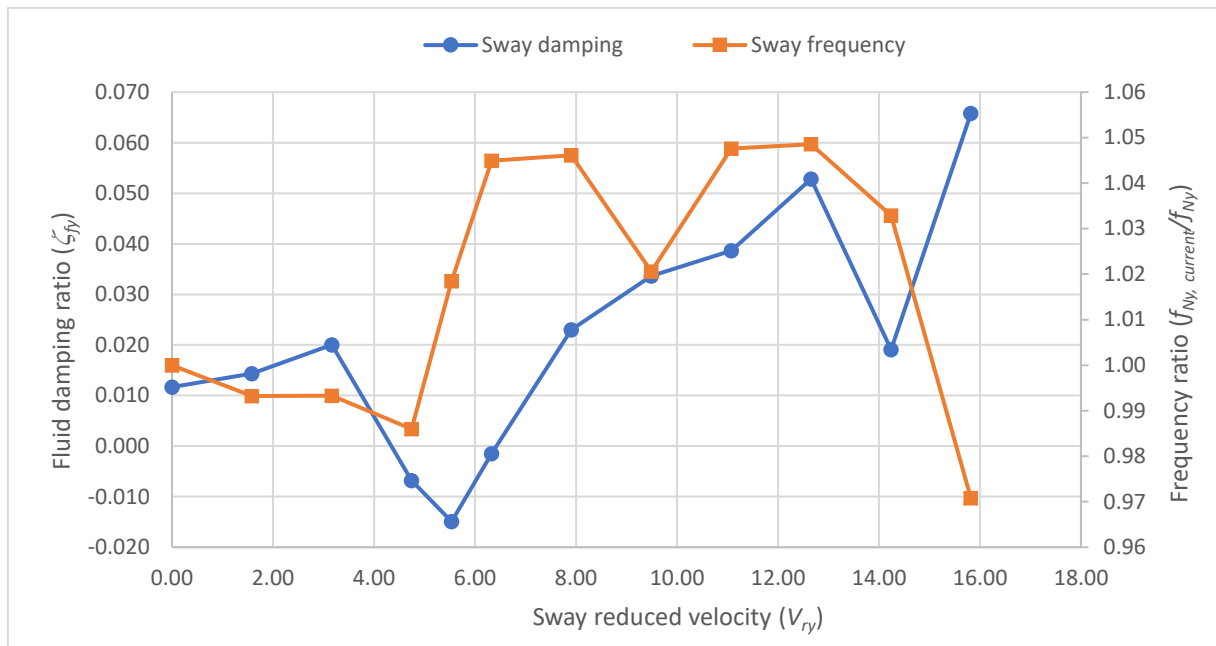


Figure 6-29: Sway fluid damping versus reduced velocity

The added mass coefficient in yaw is derived from the natural frequency and illustrated in Figure 6-31, against the yaw reduced velocity. The natural frequency variation is also demonstrated in the secondary vertical axis. Similar to sway, it can be observed that the added mass varies considerably with yaw vibrations attaining negative values in the lock-in range. This indicates that the physics of flow around a single leg follows that of an isolated cylinder irrespective of the global VIV mode. However, unlike sway vibrations, the added mass is found to increase in the pre-resonance regime, which can be attributed to the coupling effect due to sway lock-in.

The yaw fluid damping of the jack-up is derived by subtracting the structural damping from the results of the free decay tests in current. Figure 6-32 displays the variation of the yaw fluid damping ( $\zeta_{f\phi}$ ) with the corresponding reduced velocity. The natural frequency variation is also illustrated in the secondary vertical axis. It can be seen that the fluid damping attains negative values in the vicinity of yaw resonance region, around a reduced velocity of 5. This is analogous to lift amplification, and accordingly, it can be inferred that the phenomenon is applicable to yaw vibrations of the jack-up as well. This further verifies that the physics of flow around a single leg follows that of an isolated cylinder irrespective of the global VIV mode. However, it is observed that the damping attains positive values quickly with the increase in reduced velocity, though natural frequency exhibits high values. In pre-resonance and post resonance regimes, the yaw damping is found to increase with increasing current.

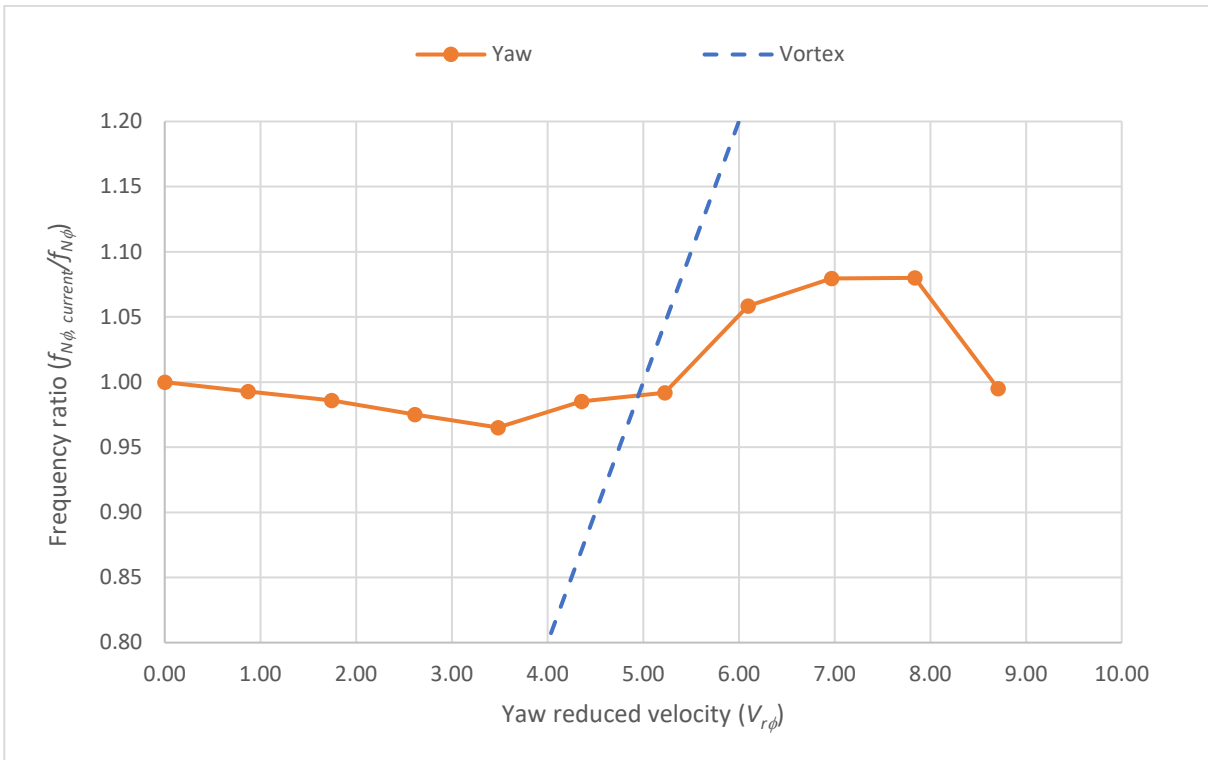


Figure 6-30: Yaw natural frequency versus reduced velocity in current

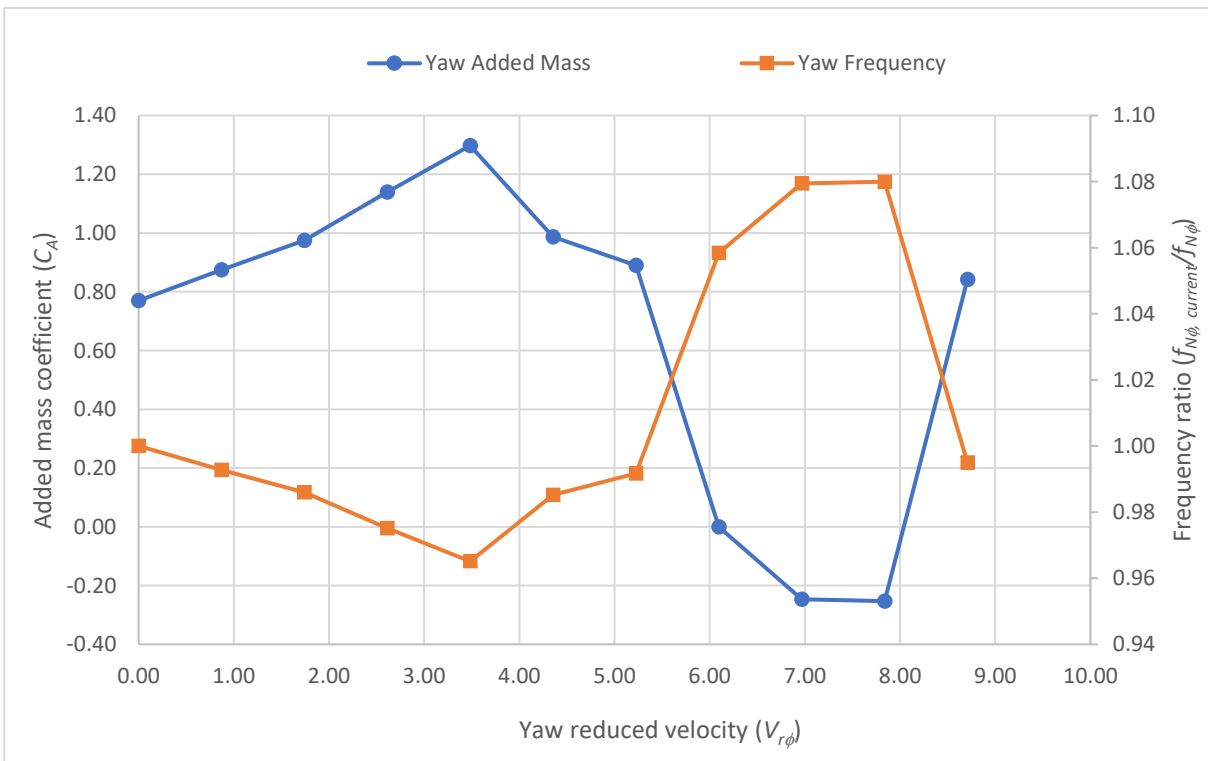


Figure 6-31: Yaw added mass versus reduced velocity in current

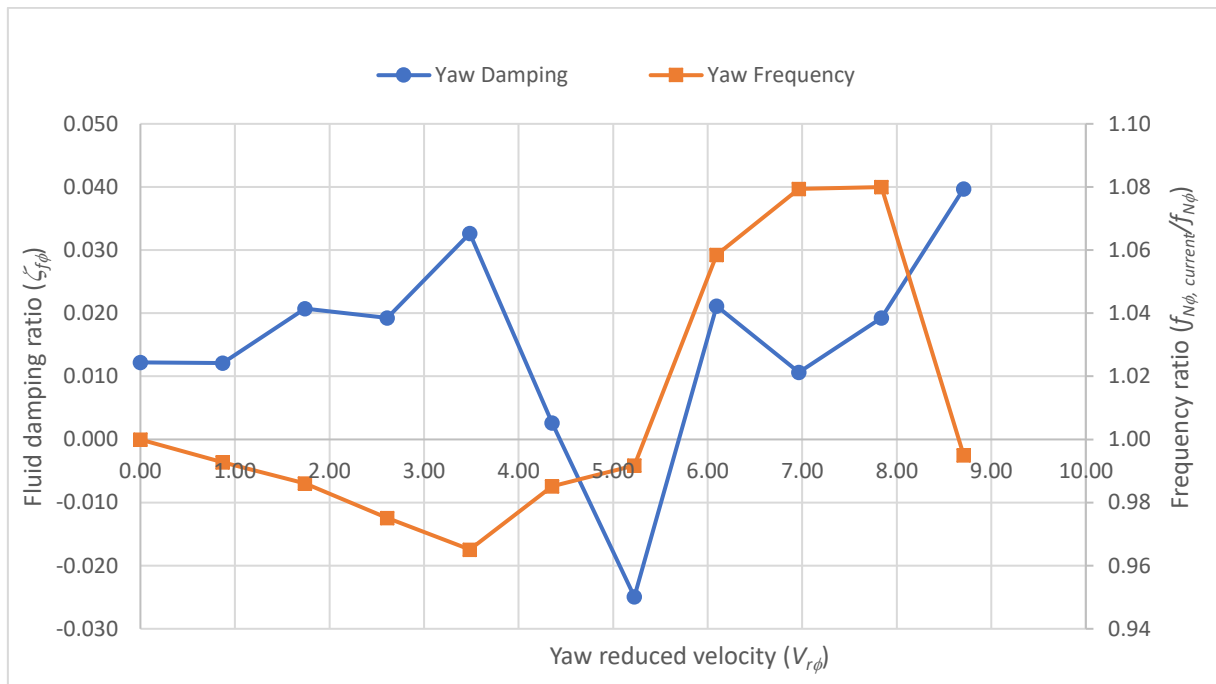


Figure 6-32: Yaw fluid damping versus reduced velocity in current

#### 6.5.2.3 Sway – Yaw Coupling

The effect of coupling between sway and yaw vibrations is further investigated by superimposing the mentioned properties with respect to any single mode reduced velocity. Figure 6-33 a) and b) illustrates the variation of the natural frequency of both the mentioned modes with sway reduced velocity and yaw reduced velocity respectively. It can be inferred from Figure 6-33 a) that in the sway lock-in regime, the yaw frequency is reduced due to the coupling with the sway lock-in vibrations. Figure 6-33 b) reveals that in the yaw lock-in regime, the sway natural frequency is increased due to the coupling with the yaw vibrations. From these observations, it can be concluded that the twin hump behaviour in the sway frequency variation is due to sway lock-in and sway coupling with the yaw lock-in.

The effect of coupling on the added mass can be evaluated by plotting both the sway and yaw added mass variation against the sway reduced velocity, as illustrated in Figure 6-34. The normalised natural frequency variation is also illustrated in the secondary vertical axis. It can be seen that in the first hump sway lock-in regime, the sway added mass assumes negative values as expected. Further, yaw added mass is found to slightly increase in the mentioned regime due to the reduction in yaw frequency caused by the coupling due to sway lock-in. In the second hump yaw lock-in regime, the yaw added mass is negative as expected, while the sway added mass

also exhibits negative values due to the increase in sway frequencies from the coupling effect of the yaw mode.

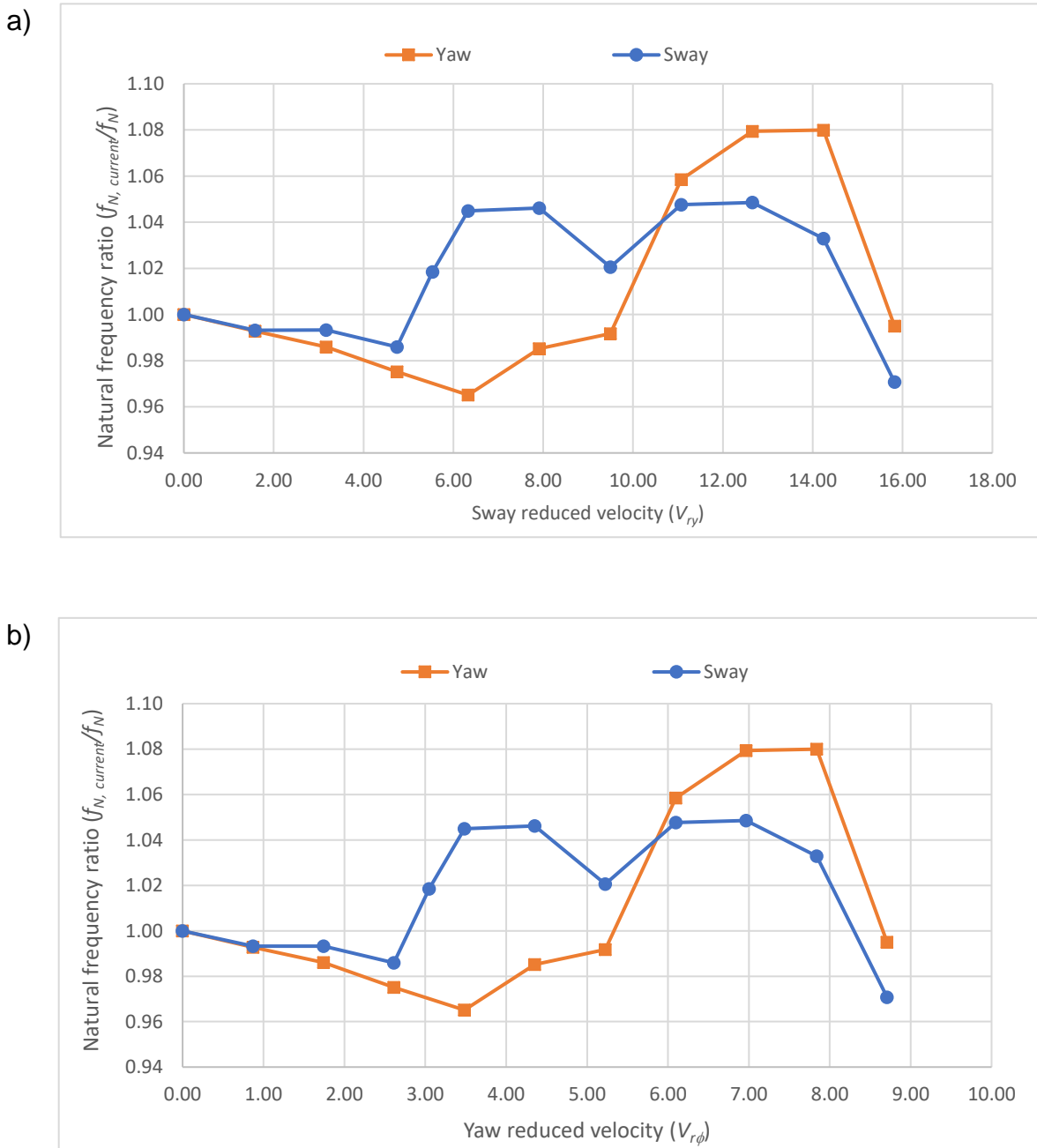


Figure 6-33: Natural frequency variation a) with respect to sway reduced velocity b) with respect to yaw reduced velocity.

The variation of the fluid damping ratios ( $\zeta_f$ ) of both the sway and yaw modes are plotted with respect to the sway reduced velocities in Figure 6-35. It can be observed that sway and yaw damping are negative in the vicinity of sway and yaw resonance

respectively. However, sway damping is found to increase in the yaw lock-in region, probably due to coupling effects. Similarly, yaw damping is also found to increase in the sway lock-in region due to coupling effects.

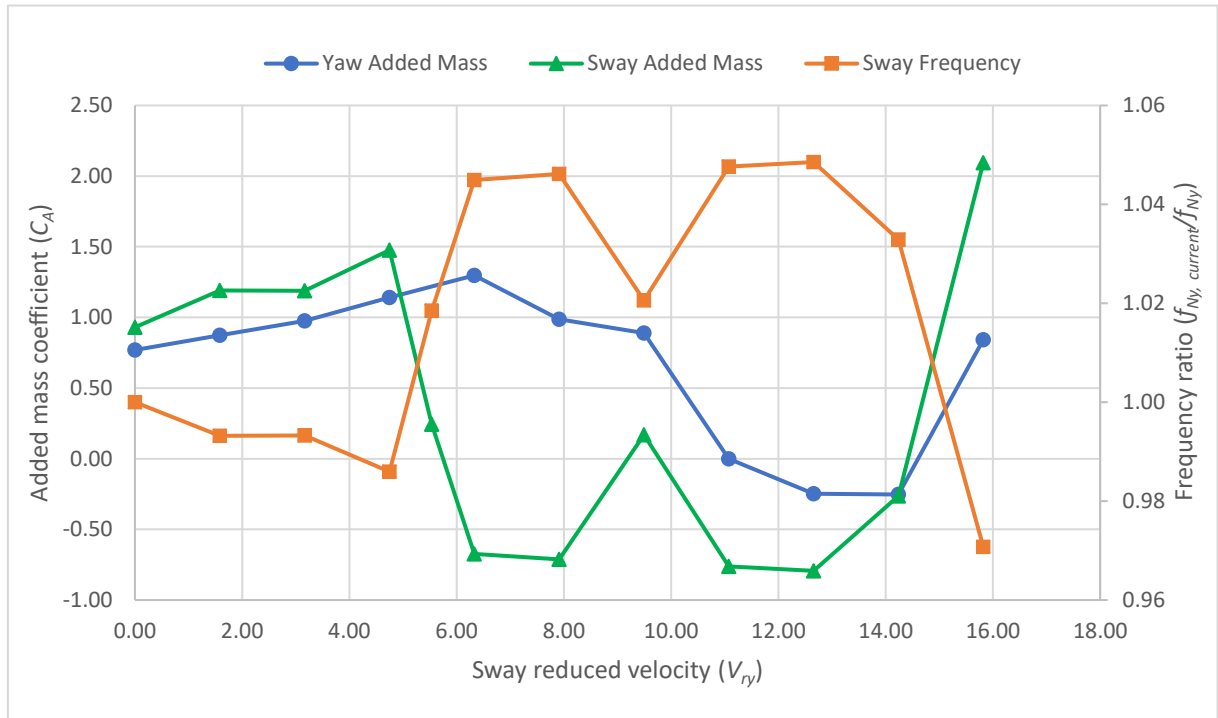


Figure 6-34: Added mass variation with sway reduced velocity

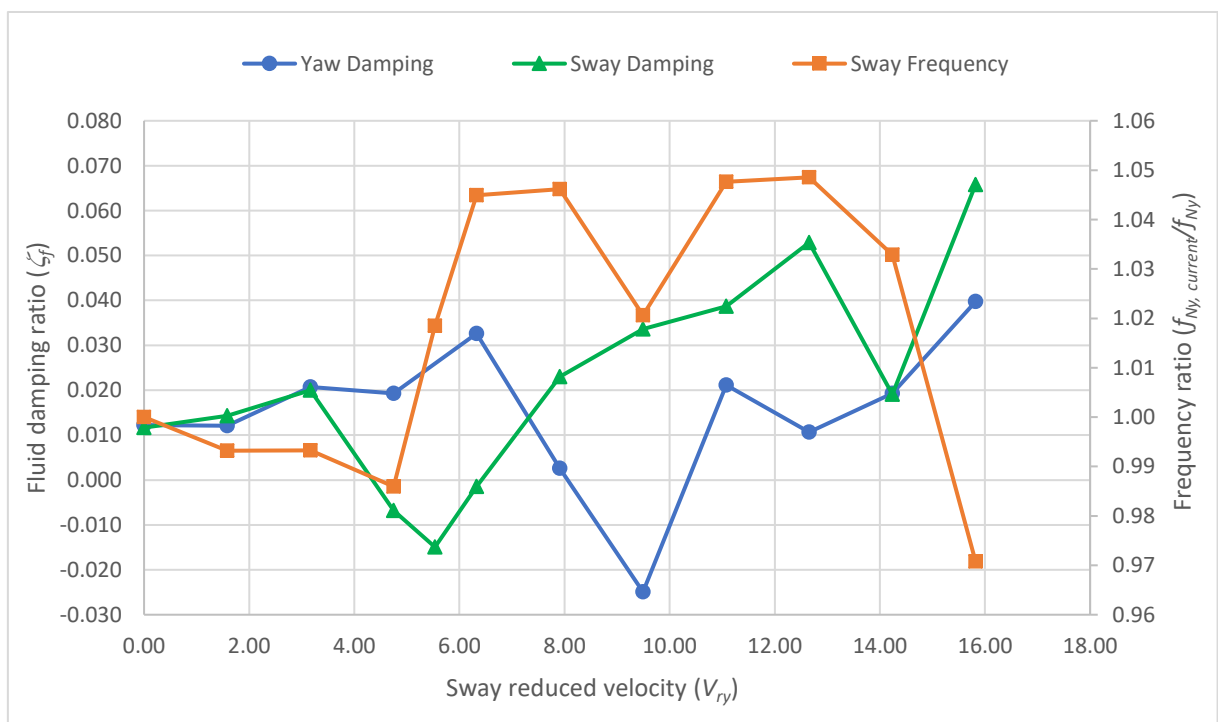


Figure 6-35: Fluid damping variation with sway reduced velocity

## 6.6 Response Test in Current and Wind

Response tests were carried out by exposing the model to incremental current or wind from the head direction (0 global heading). Three drafts and three loading conditions were considered for the tests to cover the realistic operating scenarios and the practical operating ranges of the mass ratio and the mass damping parameters. The responses of the elevated hull along the 6 DOF were measured and recorded as individual time series. The inline, crossflow and yaw time series were post processed, and the rms amplitudes and vibration frequencies were calculated for various flow speeds. The leg design considered for the test was LD1H4 with a local heading of 0. The tests in the wind were intended to validate the crossflow and yaw VIV criteria developed in Section 5.3.

The results of the response tests are summarised in Table 6-9. On verifying against the jack-up VIV criteria developed in Section 5.3, it can be conservatively inferred that only the test case, 'NVL, 890WD' is vulnerable to inline VIV while all the test cases in water are vulnerable to crossflow and yaw VIV. Added mass may not be considered in the mass ratio of the sway mode as the same is found to be negative during crossflow lock-in (Govardhan and Williamson, 2004).

### 6.6.1 *Inline/Surge Response*

As per the VIV criteria developed in Section 5.3.1, inline surge vibrations were not expected for the model in most of the test cases due to the high values of mass-damping parameters. The model tests also confirmed that the jack-up did not experience any inline VIV. The inline rms amplitude response of the model normalised with the leg diameter and plotted against the corresponding reduced velocity is displayed in Figure 6-36, for all the test cases. The model did not exhibit inline VIV response for any of the test cases as evident in Figure 6-36.

It can be observed that the inline response amplitude ratios are rather trivial except at large reduced velocities greater than 8, which can be traced to the galloping response observed in high currents. This validates the mathematical model and the effect of high inherent mass ratios of the jack-ups. These results verified the significance of mass damping parameter in suppressing VIV.

Table 6-9: Response test results in current, and wind, a) sway, b) yaw

a)

Sway							
Case	$m^*$	MF	$\zeta$	$m^*\zeta MF$	$V_{ry}$	$y_{O,rms}/D$	$y_{O,max}/D$
VL, Dry	6719.10	1.571	0.031	328	4.80	0.00	0.00
VL, 500WD	13.65	3.274	0.041	1.82	4.80	0.02	0.03
VL, 700WD	9.38	2.276	0.035	0.75	4.92	0.04	0.06
VL, 890WD	7.38	1.812	0.038	0.51	5.05	0.06	0.10
RVL, 890WD	5.96	1.812	0.044	0.47	4.82	0.07	0.11
NVL, 890WD	4.73	1.812	0.040	0.34	4.84	0.08	0.13

b)

Yaw								
Case	$m^*$	MF	$\zeta$	$k_\phi (m)$	$m^*\zeta MF k_\phi^2 (m^2)$	$V_{r\phi}$	$R_{\phi\phi O,rms}/D$	$R_{\phi\phi O,max}/D$
VL, Dry	6719.10	1.571	0.040	0.215	19.2911	4.96	0.00	0.00
VL, 500WD	13.65	3.274	0.041	0.218	0.0863	4.96	0.02	0.04
VL, 700WD	9.38	2.276	0.042	0.224	0.0447	5.40	0.04	0.08
VL, 890WD	7.38	1.812	0.043	0.233	0.0310	5.15	0.07	0.13
RVL, 890WD	5.96	1.812	0.043	0.252	0.0293	5.54	0.06	0.12
NVL, 890WD	4.73	1.812	0.038	0.275	0.0245	5.32	0.06	0.11

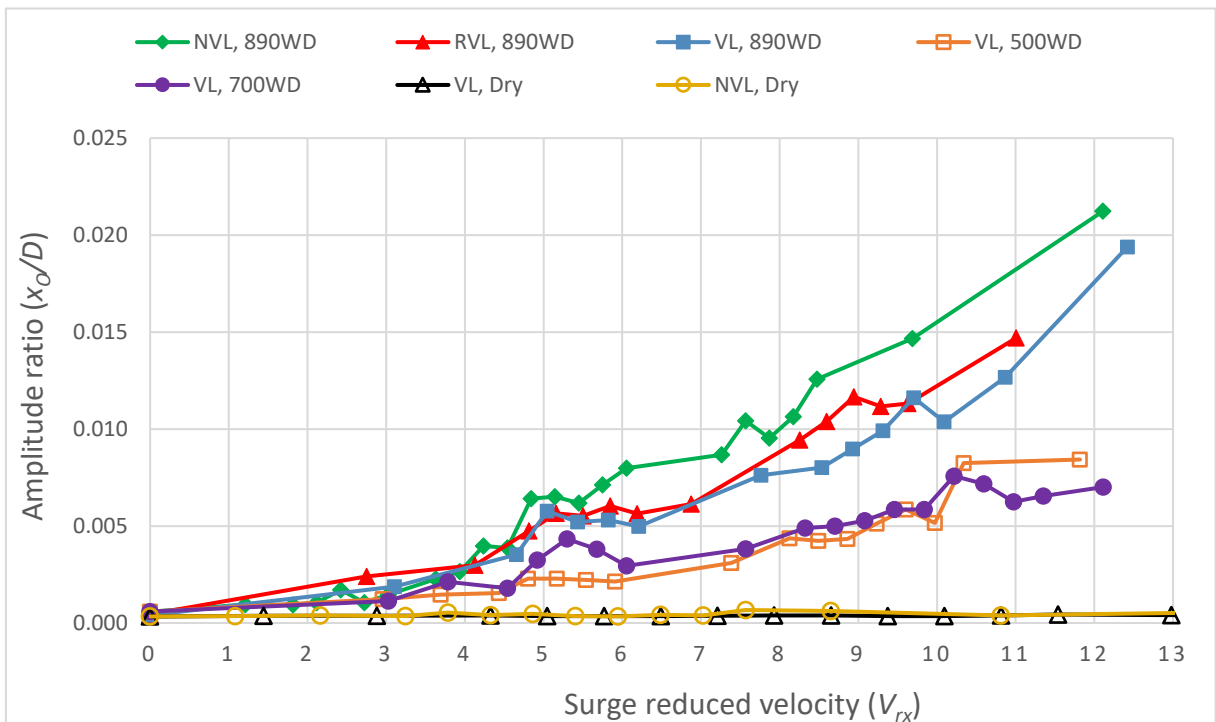


Figure 6-36: Inline amplitude response with corresponding reduced velocity ( $U/f_{Nx}D$ )

### 6.6.2 Crossflow/Sway Response

As per the crossflow VIV criteria developed in Section 5.3.2, the model was expected to undergo significant crossflow VIV for all the test cases in water. Further, crossflow VIV was expected to be very aggressive for the test case 'NVL, 890WD' corresponding to no variable load due to the lowest mass ratio. Crossflow VIV is not expected to occur for the test cases in the wind. Figure 6-37 illustrates the time series of the crossflow response for the test case, 'NVL, 890WD' at a reduced velocity around 5.

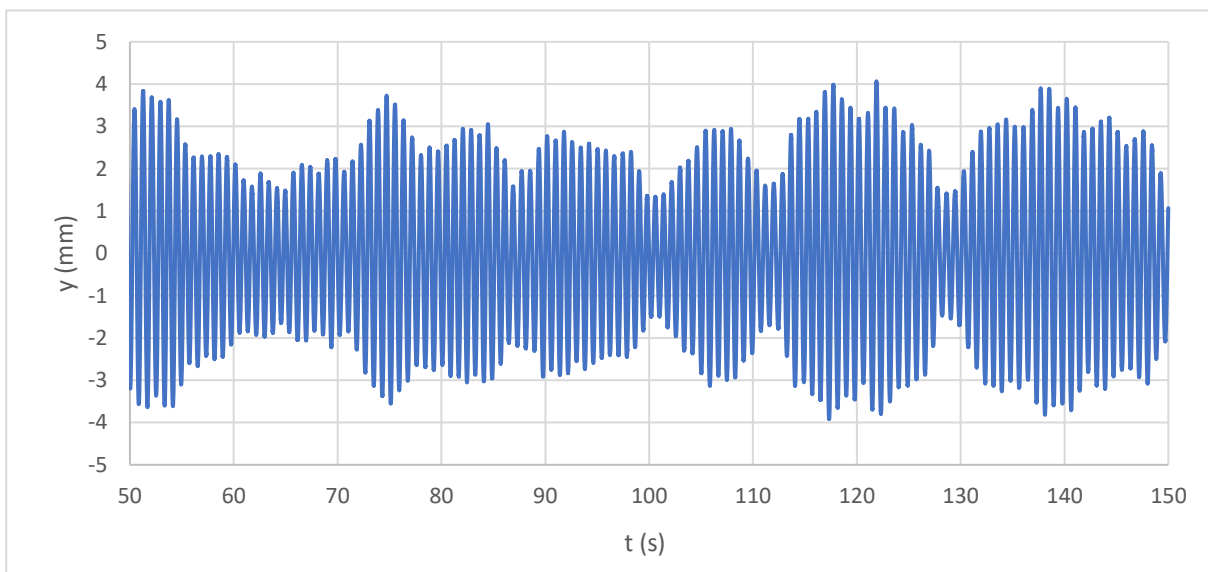


Figure 6-37: Time series of crossflow response for 'NVL, 890WD' at a reduced velocity of 4.84

Figure 6-38 shows the variation of the normalised crossflow rms amplitude responses, plotted with respect to the corresponding reduced velocities. The theoretically predicted crossflow resonance amplitudes (see Section 5.11.2) of the model, corresponding to various test cases are also demonstrated against a reduced velocity of 5 in the figure. As the damping of the jack-up model was found to be nonlinear and increasing with the amplitude ratio (see Section 6.5), the damping ratio considered for the theoretical prediction was calculated iteratively corresponding to the amplitude ratio.

It can be inferred that the model was highly vulnerable to crossflow VIV with large lock-in regimes, as evident in Figure 6-38. The rms response amplitudes were found to be approximately  $0.08D$ , and the maximum response amplitude was observed to be as high as  $0.13D$ . The sway lock-in regime was found to extend between reduced

velocities of 3 to 8. The response amplitude and lock-in range were found to increase with increase in water depth and reduction in elevated load; the test case with the lowest mass ratio exhibits the largest crossflow response amplitude and lock-in regime.

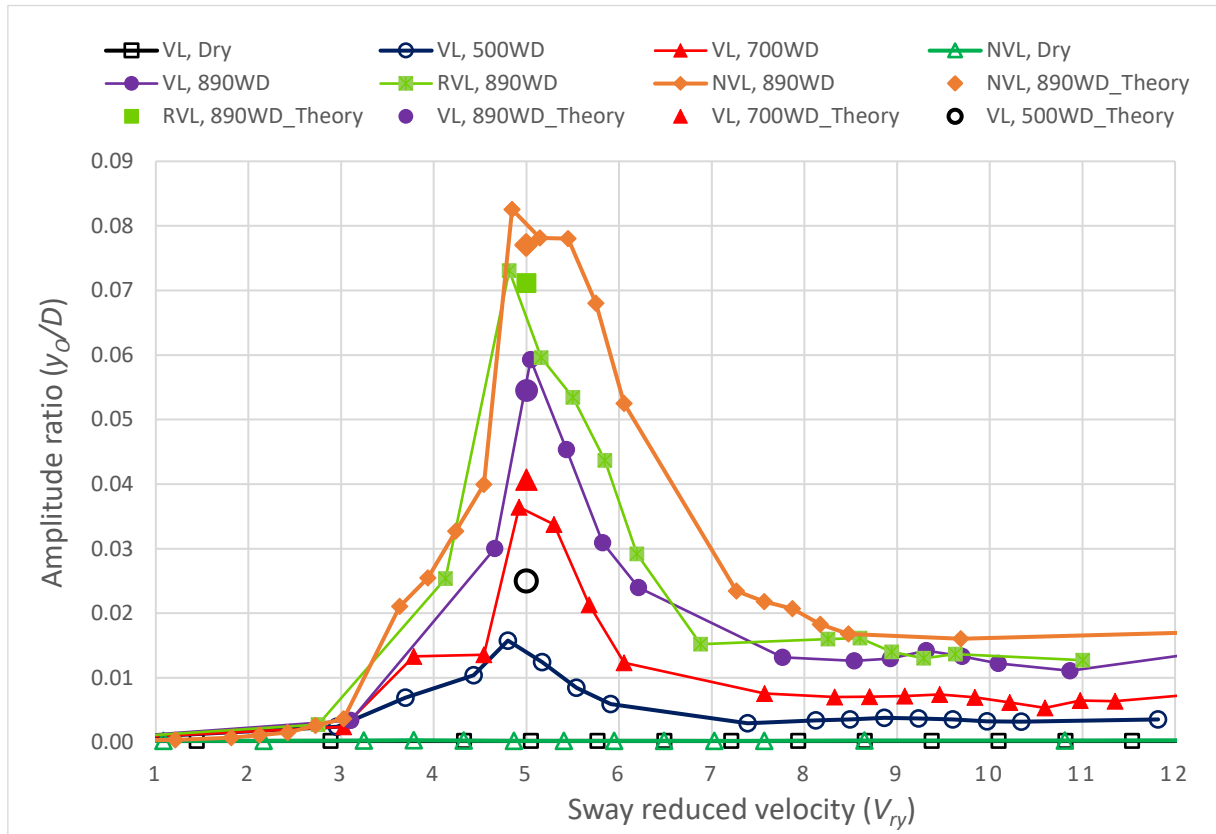


Figure 6-38: Crossflow amplitude response with corresponding reduced velocity ( $U/f_{Ny}D$ )

It can be observed that the peaks in the crossflow response curve are consistently around a reduced velocity of 5, which correspond to lift excitation. Further, the model did not exhibit any crossflow VIV during the response tests in wind, as predicted by the VIV criteria (see Table 6-9). The theoretical predictions also correlated well with the experimental results except for the test case at 590mm water depth, where the effect of the WWC tank bottom on the uniform current profile was significant. This validated the mathematical model, crossflow VIV criteria and the significance of the mass ratios in containing the VIV of the jack-ups.

The frequency responses of the models were calculated from the time series, normalised with the respective natural frequencies and plotted against the corresponding reduced velocities. Figure 6-39 illustrates the crossflow frequency

responses of the model for all the test cases. It can be observed that the crossflow frequency response of the model reveals two separated lock-in regimes, a lower regime with a frequency ratio of around unity and an upper regime with a frequency ratio above 1.40. Comparing with Figure 6-38, it can be revealed that the lower regime corresponds to the crossflow lock-in responses in the sway mode. An in-depth study on the frequency further revealed that the upper regime corresponds to lock-in responses in the yaw or torsional mode (also see Section 6.6.3). It can be observed that the crossflow vibrations in the upper regime are coupled vibrations with the yaw lock-in frequencies. It is noted that the coupling is strong and continuous for the lightest test case while weak and intermittent for the other cases.

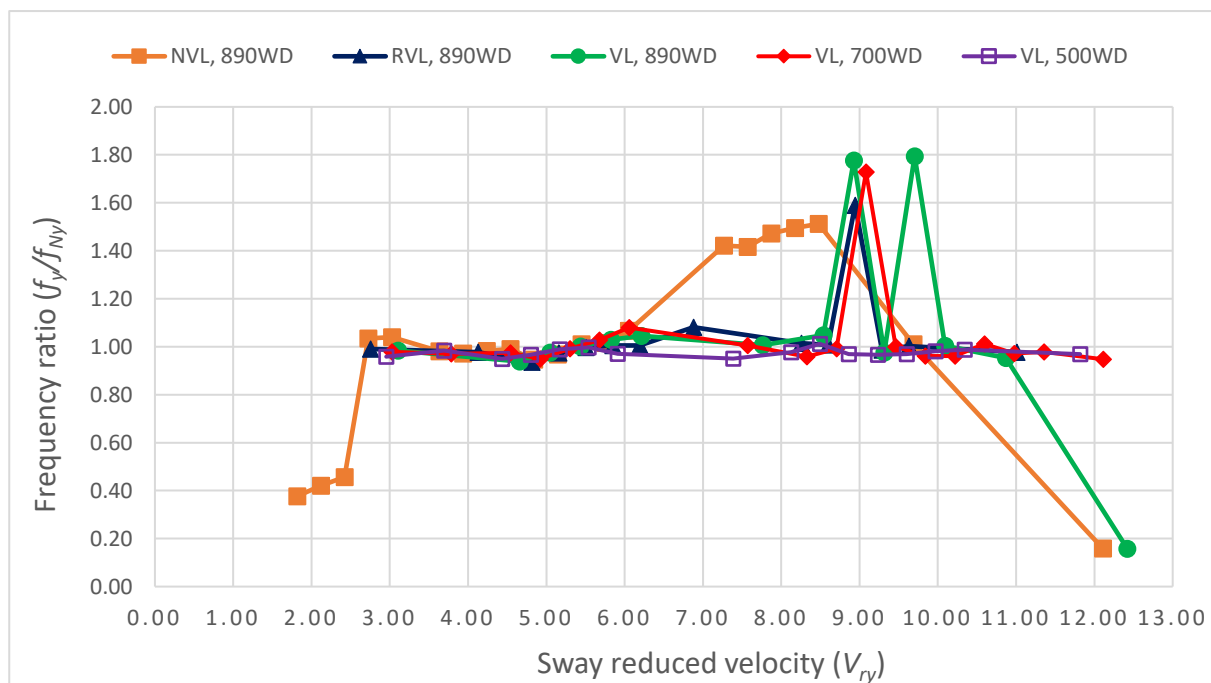


Figure 6-39: Crossflow frequency response with corresponding reduced velocity ( $U/f_{Ny}D$ )

#### 6.6.2.1 Effect of Mass Ratio

It was observed that the increase in mass ratio reduces the amplitude response and the lock-in range. The normalised crossflow rms response amplitude ratios fitted reasonably well in a straight line, when plotted against the inverse of the product of mass damping parameter and mode factor (MF), as revealed in Figure 6-40. This reemphasised the significance of mass damping parameter and MF in controlling the crossflow VIV response. The product of mass damping parameter with the MF can be

called modified or effective mass damping parameter, which can be considered as a universal parameter governing crossflow VIV across various mode shapes and water depths.

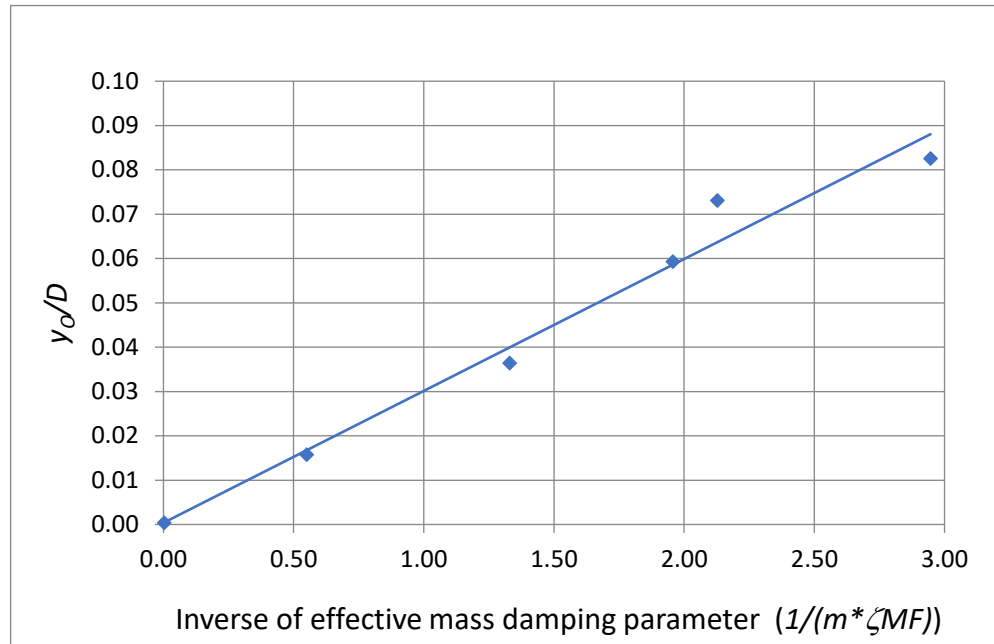


Figure 6-40: Crossflow amplitude response with the inverse of modified mass damping parameter.

### 6.6.3 Yaw Response

The model was expected to undergo significant yaw VIV also as per the criteria developed in Section 5.3.4. Similar to crossflow VIV, the yaw VIV during the test case NVL with the lowest variable load was expected to be severest. The test cases in the wind were not expected to exhibit any yaw VIV. Figure 6-41 illustrates the time series of the yaw response of the test case, 'VL, 890WD' corresponding to a yaw reduced velocity of approximately 5.

The model was found to experience significant torsional or yaw VIV response at higher currents. The normalised yaw rms amplitude response as a function of yaw reduced velocity is plotted in Figure 6-42. The theoretically predicted yaw resonance amplitudes (see Section 5.11.4) corresponding to various test cases are also demonstrated against a reduced velocity of 5 in the figure. As the damping of the jack-up model was found to be nonlinear and increasing with the amplitude ratio (see Section 6.5), the damping ratio considered for the theoretical prediction was calculated iteratively. It can

be observed that the peak yaw response occurs around a yaw reduced velocity of 5, which confirms that the yaw VIV is due to crossflow lift excitation. The rms response amplitudes were found to be around  $0.07D$ , and the maximum response amplitude was around  $0.13D$ . The lock-in regime was found to extend between the yaw reduced velocities of 3 to 7.

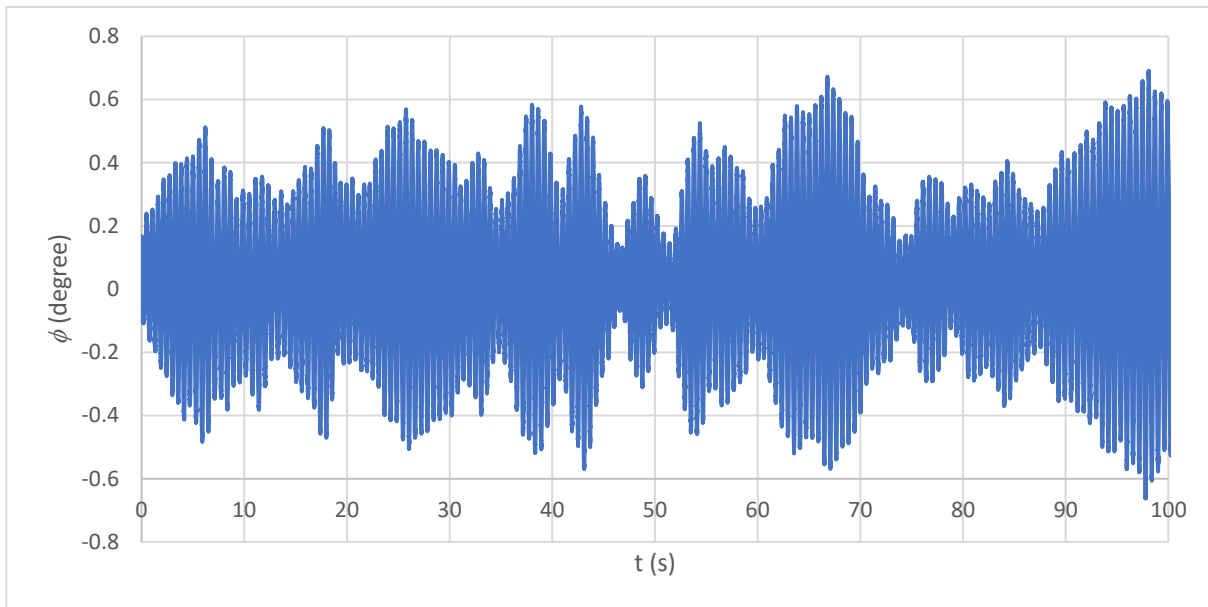


Figure 6-41: Time series of yaw response for 'VL, 890WD' at a yaw reduced velocity of 5.15

The response amplitude and lock-in range are found to increase generally with an increase in water depth. However, the amplitude and lock-in range did not increase as expected with the reduction in elevated load, with the response amplitudes displaying saturation in the lighter test cases. This unexpected behaviour may be attributed to the concurrent coupled sway vibrations with significant amplitudes at low mass ratios, drawing away a considerable portion of the excitation energy. Further, there is also the possibility of an increase in the yaw radius of gyration and damping ratio of the model with the reduction in the elevated load, due to the removal of the lead ballast plates having low radii of gyration (see Table 6-5). Hence, it is recommended to conduct similar experiments with the model experiencing pure yaw vibrations and constrained along the sway mode to have a further understanding of the phenomenon.

As evident from Figure 6-42, the model did not exhibit any yaw VIV during the response tests in the wind. The theoretical predictions also correlated reasonably well with the

experimental results except for the test cases at 700mm and 590mm water depths. The conservative nature of the theoretical predictions at lower water depths can be attributed to the effect of the WWC tank bottom on the current profile, aggravated by the higher current speeds (see Section 6.1.7). This validated the mathematical model and the yaw VIV criteria developed in Sections 5.3.3 and 5.3.4, and the significance of the mass ratios in containing the VIV of the jack-ups.

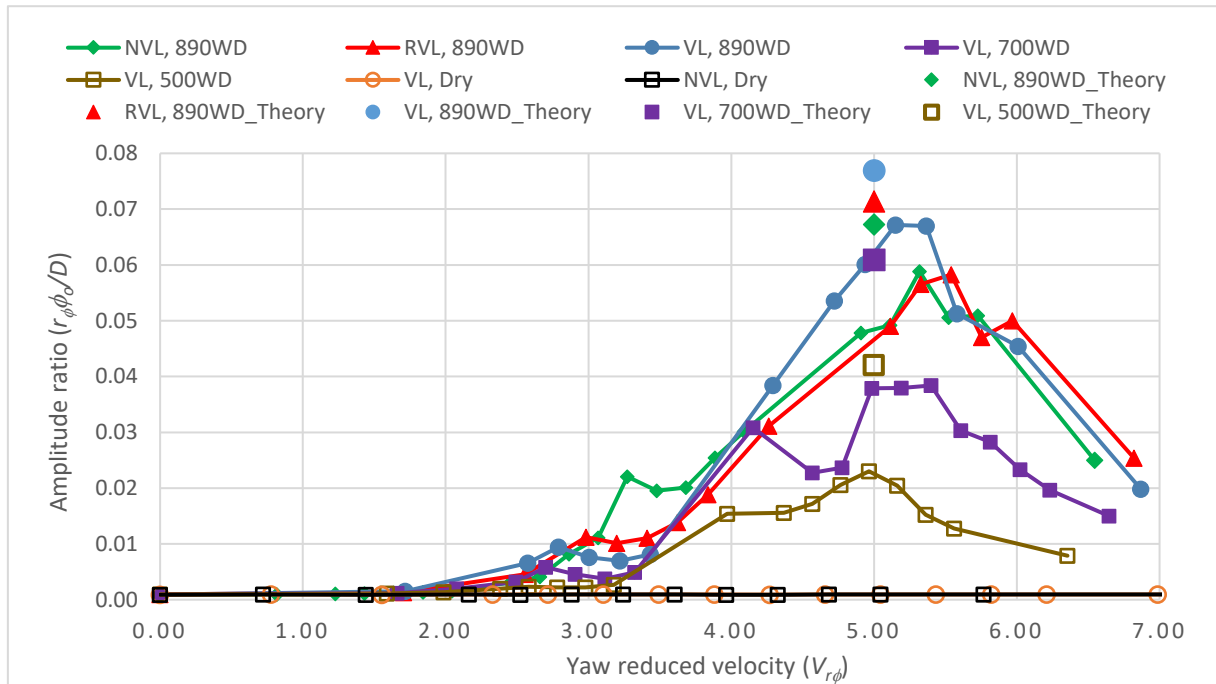


Figure 6-42: Yaw amplitude response with corresponding reduced velocity ( $U/f_{N\phi}D$ )

The yaw frequency responses of the model, normalised with the corresponding natural frequencies are plotted against the yaw reduced velocities in Figure 6-43. Similar to crossflow frequency response, the yaw frequency response of the model also revealed two separated lock-in regimes, a lower regime with a frequency ratio below 0.70 and an upper regime with a frequency ratio of around 1. On comparison with Figure 6-39 and Figure 6-42, it can be understood that the lower regime corresponds to the coupled yaw vibrations due to crossflow lock-in and the upper regime represents lock-in responses in the model's yaw mode.

#### 6.6.3.1 Effect of Mass Ratio

It was observed that an increase in mass ratio generally reduced the amplitude response and the lock-in range except for the test cases at maximum VL water depth. The

response amplitude ratio fitted reasonably well in a straight line except for the lighter test cases, when plotted against the inverse of an effective inertia damping parameter as illustrated in Figure 6-44. Effective inertia damping parameter is the product of mass damping parameter, MF and square of yaw radius of gyration and can be considered as the universal parameter determining the yaw VIV response of jack-ups. The deviation of the lightest test cases from the expected behaviour may be attributed to the coupled crossflow vibrations of significant amplitudes extracting energy from the lift forces inducing yaw lock-in vibrations.

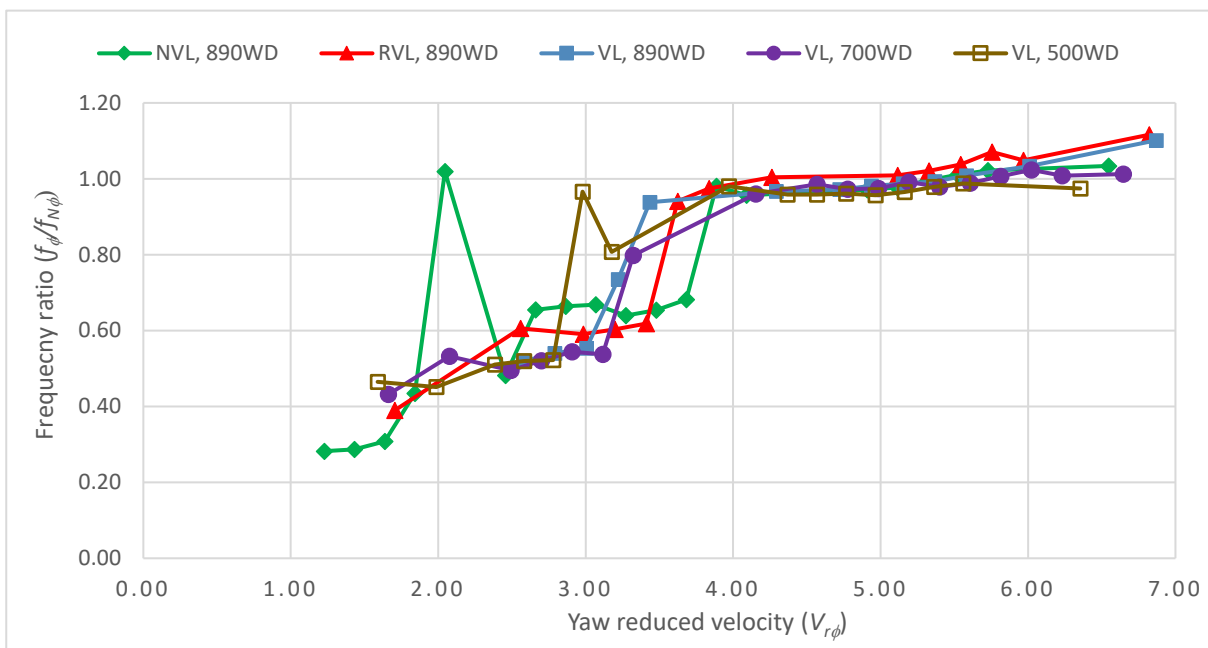


Figure 6-43: Yaw frequency response with corresponding reduced velocity ( $U/f_{N\phi}D$ )

#### 6.6.4 Combined Response

It was noted that the yaw response range overlaps with the crossflow response range particularly for low mass ratios, causing a combined lock-in range throughout the operating current speeds. The combined crossflow amplitude response ( $y^*$ ) of the leg derived from the corresponding crossflow and yaw responses is plotted against the current speeds in Figure 6-45. The combined vibrations achieved higher response amplitudes (up to 0.10D) than the individual values (maximum 0.08D for crossflow and 0.07D for yaw vibrations, see Figure 6-38 and Figure 6-42 respectively), particularly for low mass ratios. Further the combined lock-in range was extending over almost throughout the operating current range (0.10 m/s to 0.40 m/s) making the jack-up practically redundant, except at low currents.

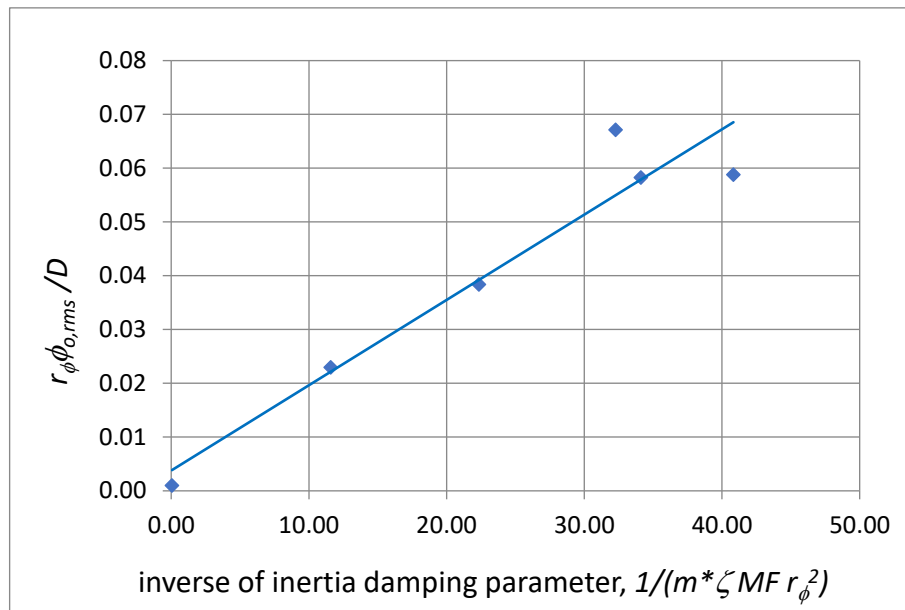


Figure 6-44: Yaw amplitude response with the inverse of inertia damping parameter

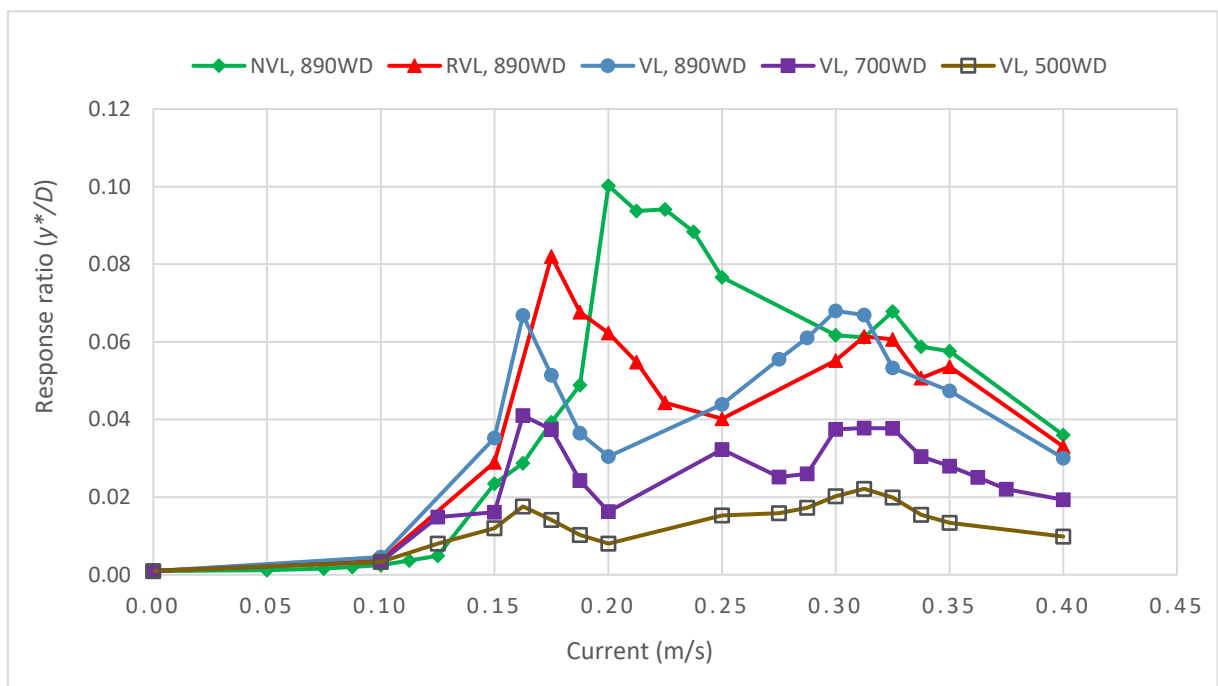


Figure 6-45: Combined crossflow amplitude response of the jack-up leg with current

### 6.6.5 Mean Response

The mean or steady inline responses ( $\bar{x}$ ) were also measured as a function of current speeds, and the normalised results are plotted in Figure 6-46. It can be observed that the mean inline response roughly follows a quadratic variation with the current speeds and hence is a good representation of the mean drag force acting on the model. The

fitted quadratic curve for the case, NVL, 890WD is also presented in the figure along with the mathematical expression, showing negligible contributions from the nonquadratic terms. The lightest operating condition (NVL, 890WD) at the maximum water depth exhibited the highest mean inline response despite having a greater stiffness due to lesser P delta effect. It is evident that the jack-up VIV amplified the mean drag and consequently, the mean inline responses at almost the entire practical speed range. The mean crossflow and yaw responses were found to be insignificant throughout the tested current speeds.

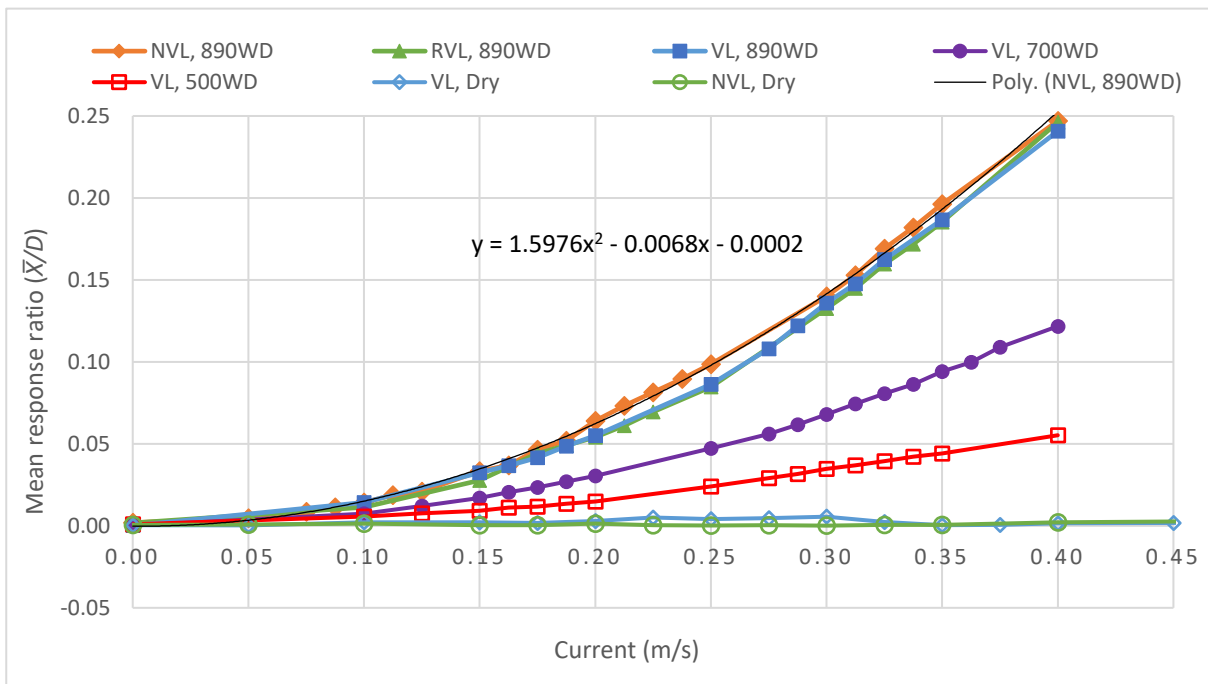


Figure 6-46: Inline mean response of the model with current

### 6.6.6 Effect of Environmental Headings and Leg Orientation

Response tests were conducted in current with various global headings of the model and local headings of the leg to investigate the effect of environment heading and leg orientation on the jack-up VIV. The tests were intended to account the real sea conditions of a jack-up. The full variable load condition was selected for the tests at the maximum effective water depth of 0.78m, corresponding to the test case 'VL' mentioned in Table 6-3. The leg design selected for the test is LD1H4. The details of the various tests cases and the summary of the results are displayed in Table 6-10.

Table 6-10: Details of the test cases with various headings

Case	Global Heading	Local Heading	$x_{O, rms}/D$	$y_{O, rms}/D$	$y_{O, max}/D$	$R_{\phi\phi, rms}/D$	$R_{\phi\phi, max}/D$
VL_GH0_LH0	0	0	0.006	0.06	0.10	0.067	0.127
VL_GH21_LH0	21	0	0.021	0.06	0.09	0.053	0.118
VL_GH37_LH0	37	0	0.019	0.04	0.07	0.045	0.093
VL_GH45_LH0	45	0	0.037	0.07	0.11	0.045	0.098
VL_GH0_LH45	0	45	0.004	0.05	0.09	0.083	0.146

### 6.6.6.1 Inline VIV

Figure 6-47 illustrates the normalised inline VIV amplitude response of the model for various global and local headings, plotted against the reduced velocity. It can be observed that the jack-up is vulnerable to aggressive inline VIV under oblique environmental headings. The jack-up exhibited significant inline VIV for the global environmental headings of 21, 37 and 45 degrees, with 45-degree heading being most severe. As the inline vibrations are observed approximately at a reduced velocity of 4.7, it can be evidently inferred as coupled VIV due to the crossflow lock-in. Further, both the test cases with the global heading of zero are found not experiencing inline VIV. The jack-up was found to experience galloping at large current speeds in all the test cases.

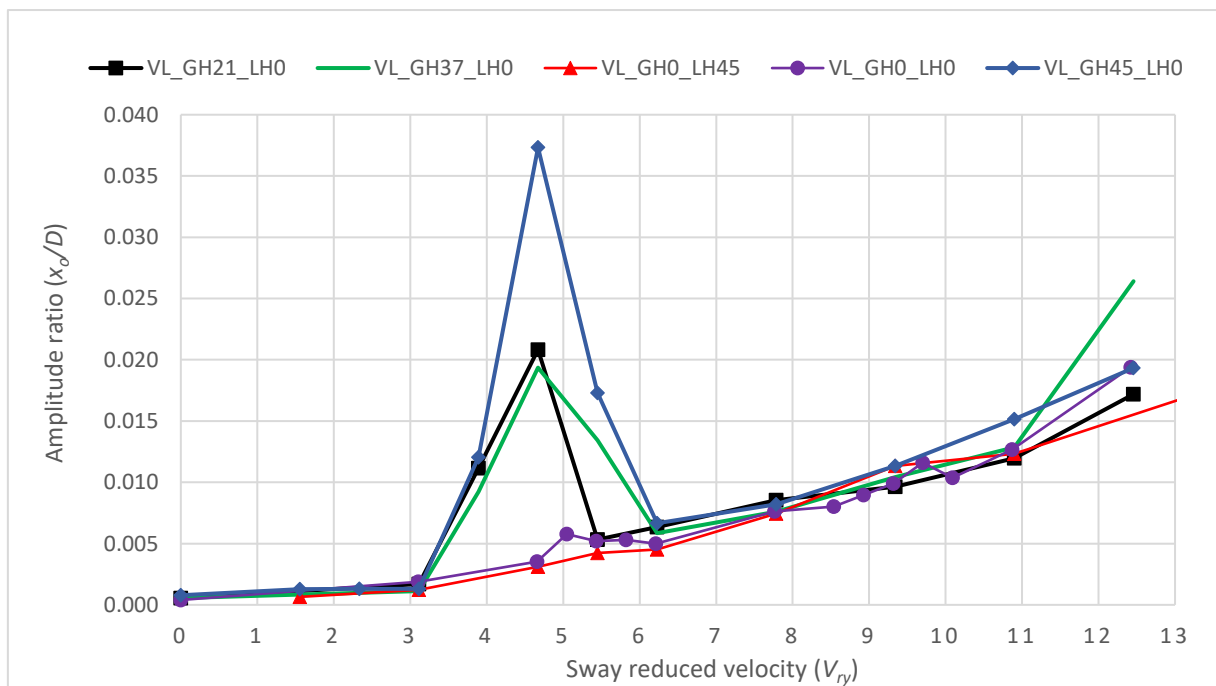


Figure 6-47: Inline amplitude response versus reduced velocity for various headings

The normalised inline frequency response of the jack-up plotted with respect to the reduced velocity for various headings is illustrated in Figure 6-48. It can be observed that a clear lock-in regime with a frequency ratio of 1 is observed for all the test cases except the one with a global heading of 37 degrees. As the surge and sway natural frequencies of a jack-up are nearly equal, a frequency ratio of 1 corresponds to the sway lock-in regime, and it can be inferred that the inline VIV is due to coupling with sway lock-in vibrations. Sway coupling is also observed for the cases with zero global heading though the vibration amplitudes are insignificant. The case with a global heading of zero and a local heading of 45 degrees is also found to couple weakly with yaw lock-in.

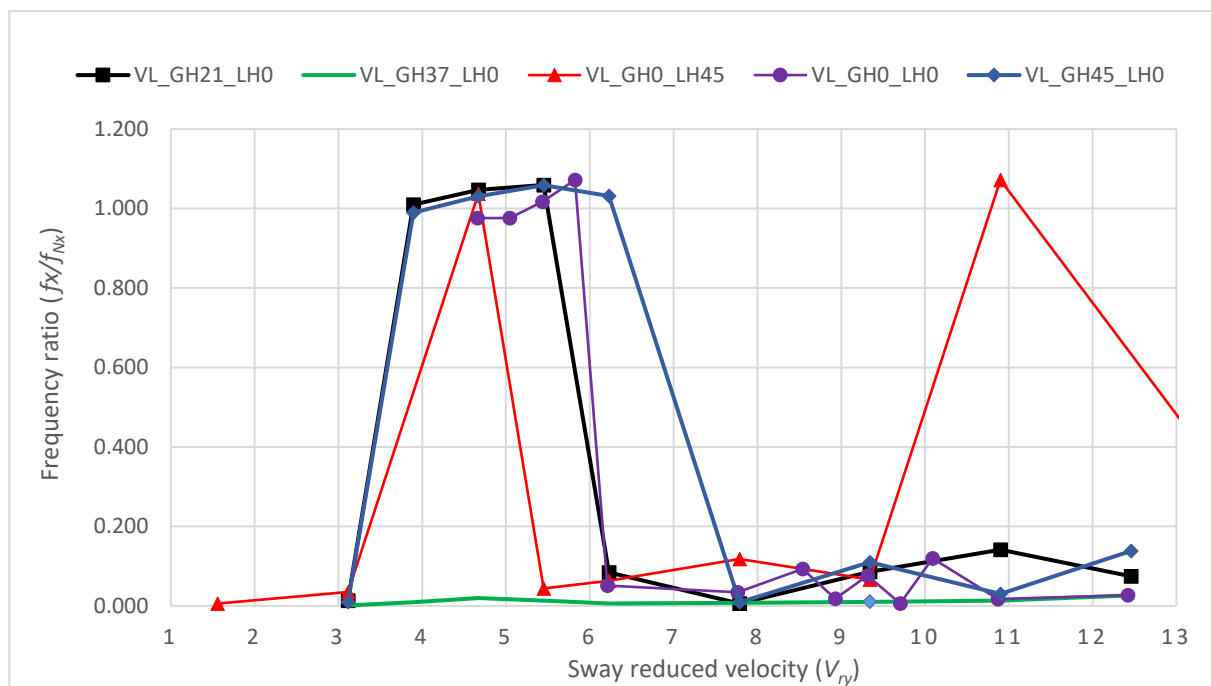


Figure 6-48: Inline frequency response versus reduced velocity for various headings

#### 6.6.6.2 Crossflow VIV

Figure 6-49 illustrates the crossflow VIV response of the jack-up model for various headings in uniform current plotted with respect to the corresponding reduced velocity. It can be observed that all the test cases exhibit crossflow VIV with significant amplitudes up to the order of  $0.07D$ . The cases with the global headings of 0, 21 and 45 degrees were found to experience the aggressive vibration of high amplitudes. Surprisingly, the crossflow response is found to be considerably lesser for the global heading of 37 degrees. This can be probably attributed to the disruption of the

synchronised vortex shedding along the legs due to the presence of one of the pin holes of LD1H4 at 127 degrees from the forward stagnation point, which is very near to the separation points (also see Section 6.10.2). The test case with leg local heading 0 is also found to exhibit significant crossflow VIV.

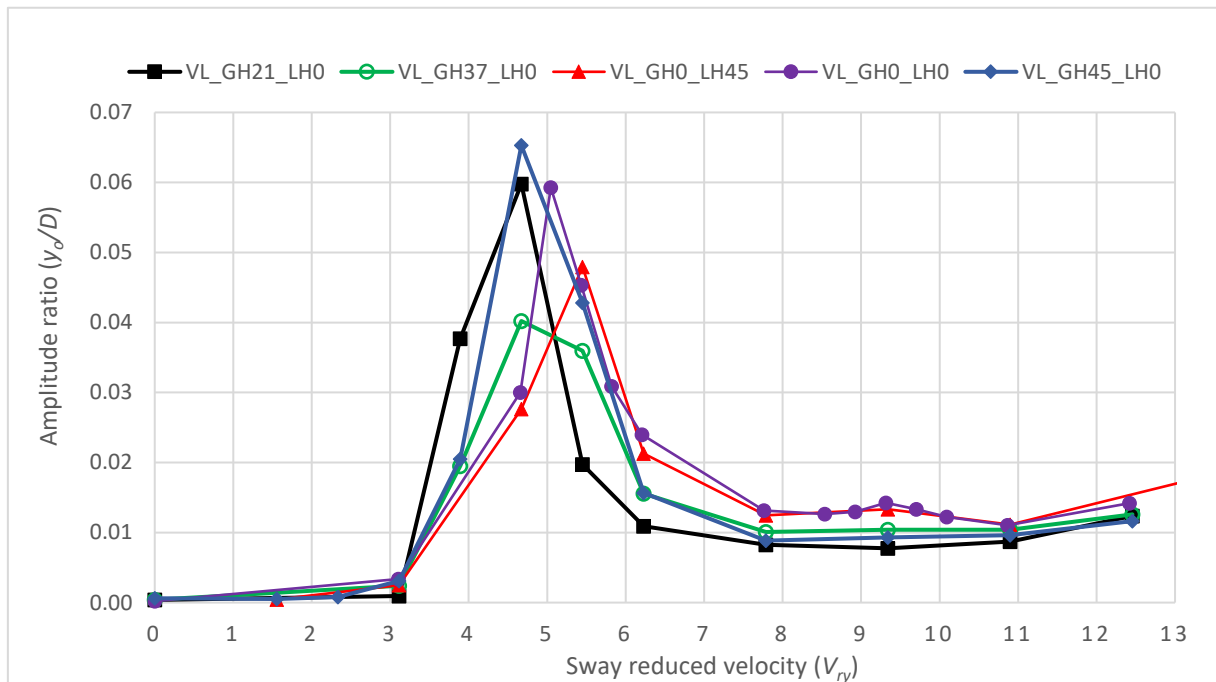


Figure 6-49: Crossflow amplitude response versus reduced velocity for various headings

The crossflow frequency response of the model normalised with the natural frequency is plotted against the reduced velocity for various headings, as illustrated in Figure 6-50. It can be observed that most of the crossflow vibrations occur at a frequency ratio of 1, representing sway lock-in regime. A weak upper sway coupling regime due to yaw lock-in can also be observed for the load cases with zero global heading. The sway lock-in regime extends almost throughout the reduced velocity range for the oblique global headings. It can be inferred that the crossflow vibrations occur predominantly at the natural frequency only for the oblique global headings.

#### 6.6.6.3 Yaw VIV

The normalised yaw VIV response of the jack-up for various headings in uniform current is illustrated in Figure 6-51. All the headings are found to experience significant yaw VIV with amplitudes up to the order of 0.08D. The cases with the global heading

of zero degrees are found to be the most vulnerable ones with the local heading of 45 degrees exhibiting highest yaw lock-in vibrations. The yaw vibrations are found to be relatively lesser for the oblique headings, which can be attributed to the occurrence of concurrent inline coupled vibrations drawing up a considerable amount of the excitation energy. It should be pointed out that, in the case of oblique headings, the responses may have been relatively higher with more measurement points. The yaw reduced velocity of the peak vibrations is found to be around 5, indicating that the excitation source is oscillatory lift forces.

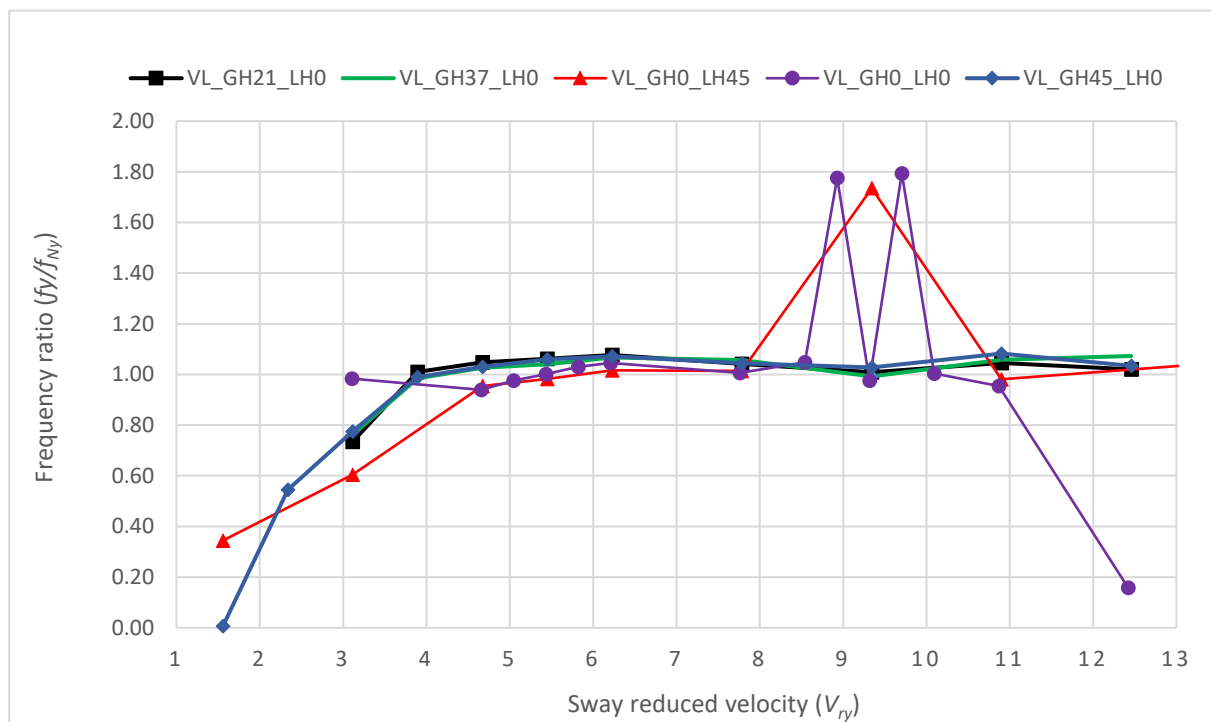


Figure 6-50: Crossflow frequency response versus reduced velocity for various headings

The yaw frequency response of the jack-up for various headings is illustrated in Figure 6-52, plotted against the corresponding reduced velocity. A yaw lock-in regime with a frequency ratio of 1 is clearly visible for all the headings. A lower regime with a frequency ratio of around 0.60 is also observed for all the test cases between the reduced velocities of 2 to 3, where coupled yaw vibrations are experienced due to crossflow lock-in.

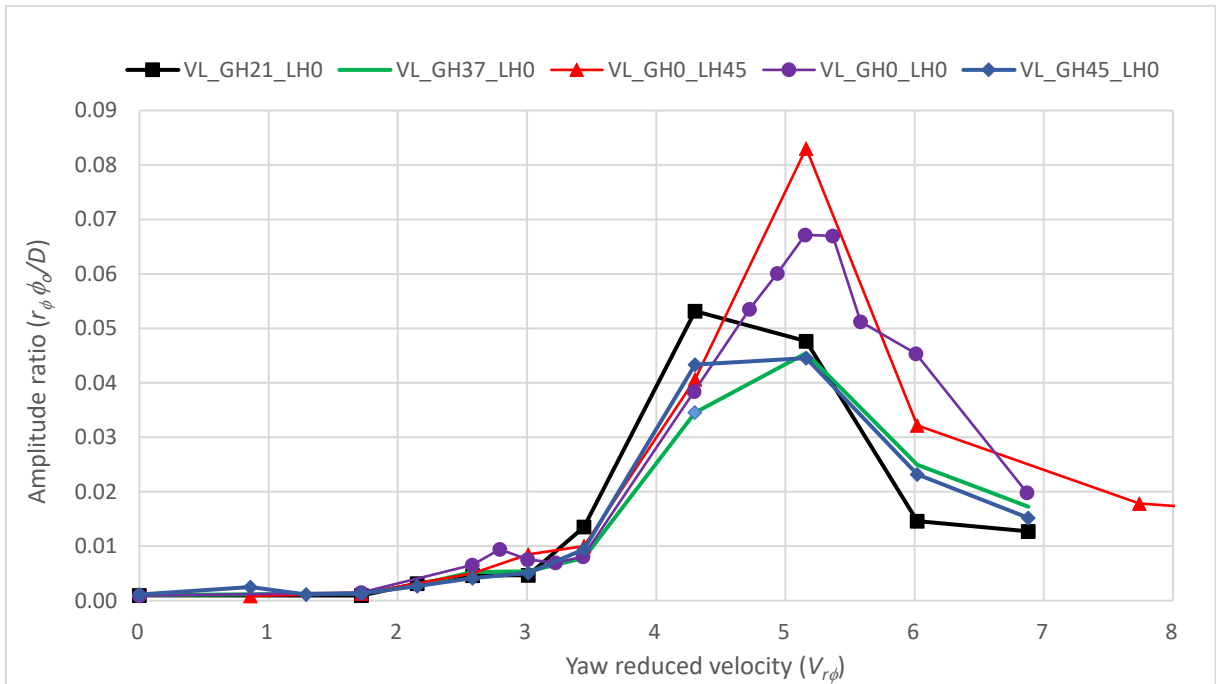


Figure 6-51: Yaw response versus reduced velocity for various headings

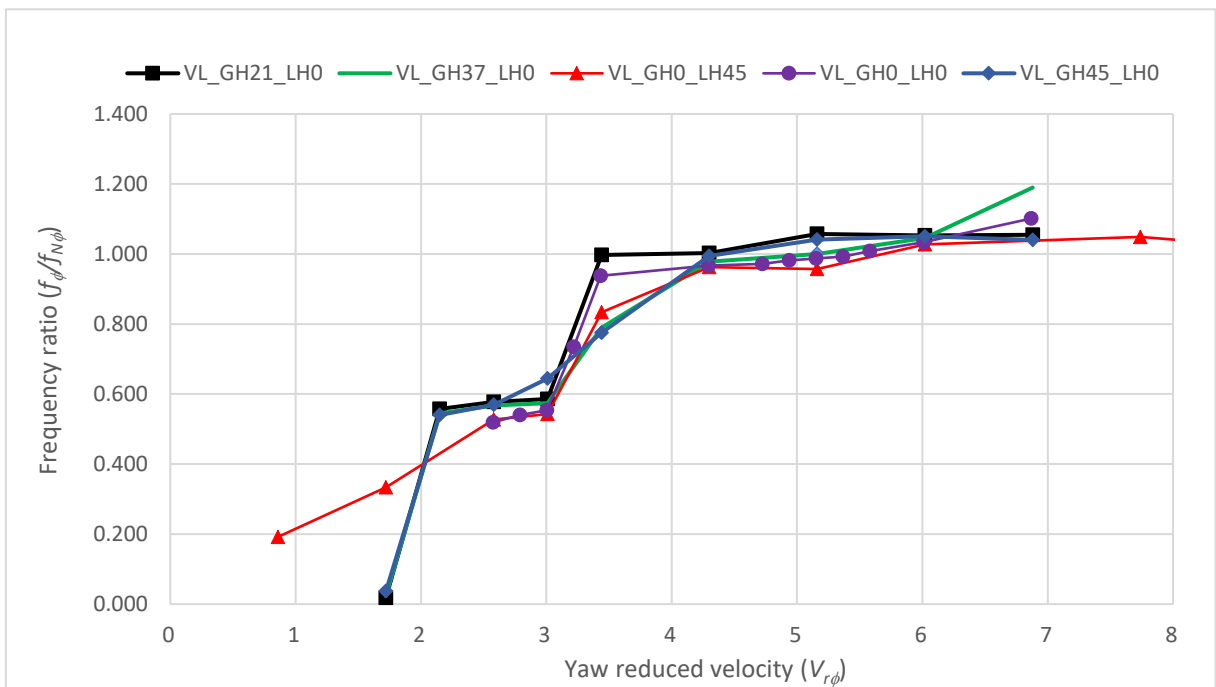


Figure 6-52: Yaw frequency response versus reduced velocity for various headings

6.6.6.4 Combined Response

Figure 6-53 illustrates the combined crossflow response of the leg ( $y^*$ ) of the jack-up model considering the concurrent crossflow and yaw vibrations, plotted against the current speed from an operational perspective, for all the headings. It can be observed

that the jack-up experiences resultant responses of considerable magnitudes for all the headings making the jack-up practically redundant, except for low currents (< 0.10 m/s). A global heading of 37 degrees, is found to cause the minimum combined response among all the cases tested. Though global heading of 0 along with leg local headings of 45 degrees was able to substantially reduce the crossflow response, the yaw lock-in response increased considerably.

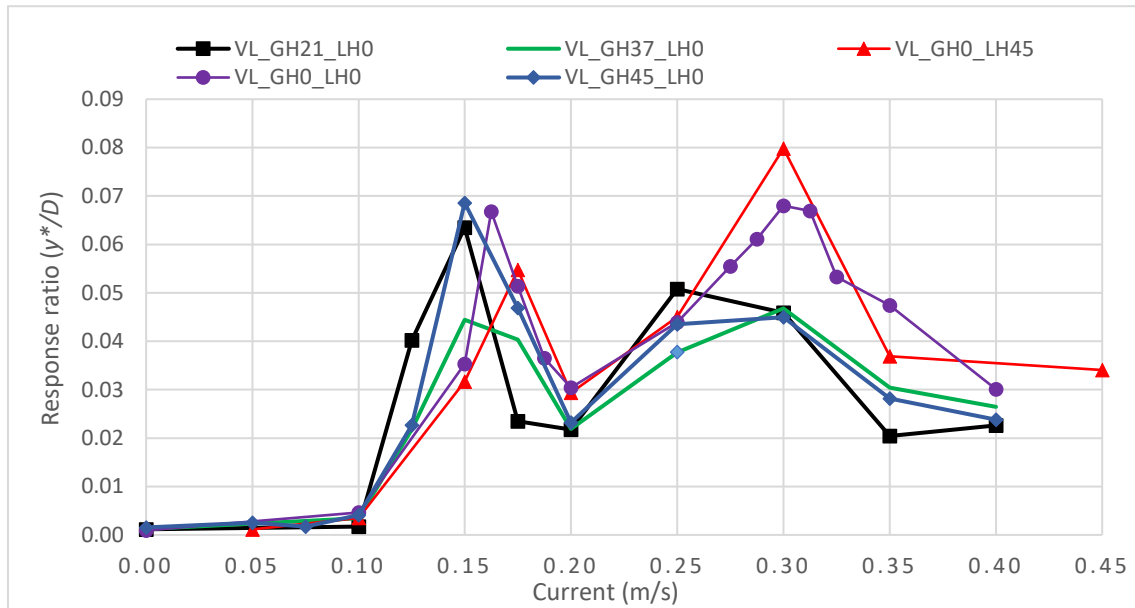


Figure 6-53: Combined crossflow response versus current for various headings

#### 6.6.6.5 Mean Response

Figure 6-54 demonstrates the mean inline response ( $\bar{x}$ ) of the jack-up for various headings, plotted against the current speed to evaluate the operational significance of drag amplification. It can be seen that the mean inline response is higher for the oblique headings than a global heading of 0 degrees. This indicates that the legs experience a higher mean drag in oblique seas due to a higher drag amplification, attributable to the vibrations along all the three modes. Further, in oblique seas, none or utmost only one of the legs experience wake flow from the ahead legs leading to higher drag forces on the leeward legs. The case with 0 degree global heading and leg local heading of 45 degrees is found to have a high mean inline response in the yaw lock-in regime, possibly due to aggressive yaw vibrations. It can be concluded that maintaining global and local headings at zero degrees can be an effective way of reducing mean drag forces on jack-ups.

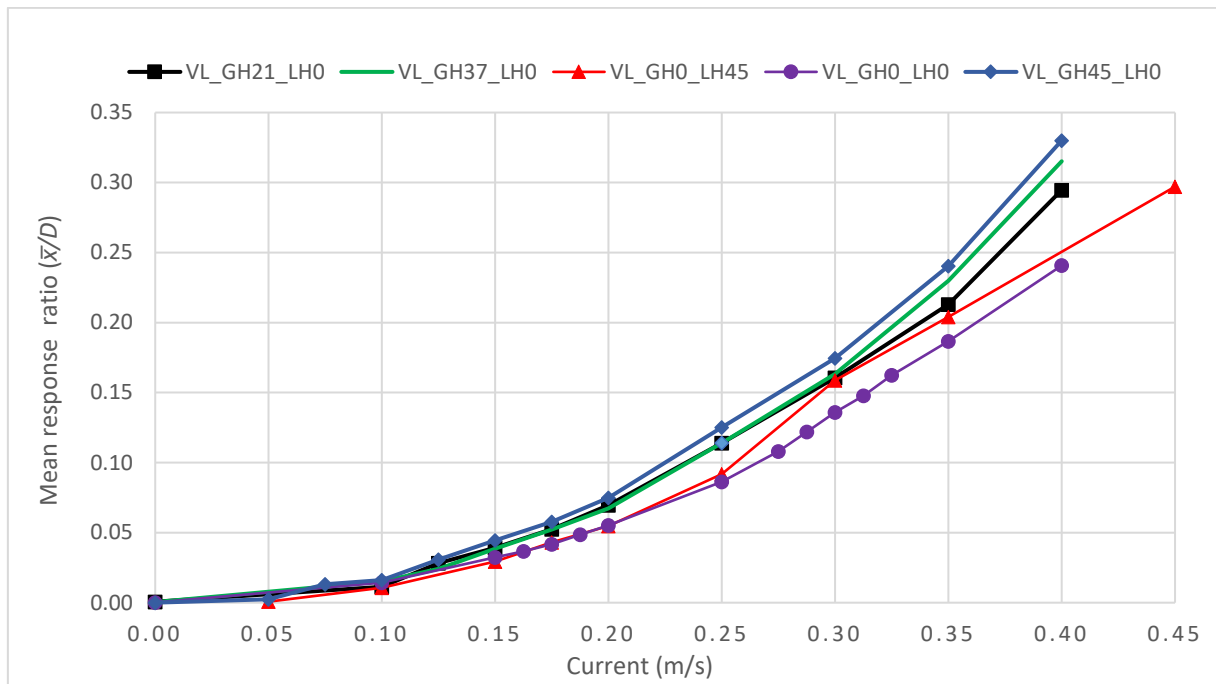


Figure 6-54: Mean inline response versus current for various headings

## 6.7 Response Test in Regular Waves

Wave is one of the primary forms of oscillatory flow impact on jack-ups operating at sea. Response tests were carried out in regular waves by exposing the model to incremental wave periods from head direction (0 global heading). The wave height selected was 92 mm at an effective water depth of 0.78m. The leg design considered was LD1H4, and the local heading of the legs was maintained at 0 degrees. The tests were carried out for three loading conditions covering the realistic operation scenarios and the practical ranges of the mass ratio and the mass damping parameter. The full variable load condition (VL) was also tested for various combinations of wave heights and periods for a constant  $KC$  number of 5. The test case with a  $KC$  of 5 is considered to investigate the VIV at the wave frequency, due to the asymmetry of the two attached vortices, observed for  $4 < KC < 8$  (Sumer and Fredsøe, 1988). The responses of the hull along the 6 DOF were measured and recorded as individual time series. The surge, sway and yaw time series were post processed and the rms amplitudes and vibration frequencies were calculated for the corresponding regular waves. Rms amplitudes were considered due to the modulations inherent to VIV amplitudes. The details of the test cases are presented in Table 6-11.

Table 6-11: Test cases in regular waves

Test Case	Load Description	Hull Mass (kg)	Effective Water Depth (m)
NVL	No Variable Load	10.65	0.78
RVL	Reduced Variable Load	14.08	0.78
VL	Full Variable Load	18.05	0.78

The response tests were conducted for three elevated loads to cover the operational envelope of a jack-up. However, the response tests for the intermediate elevated load condition (RVL) was carried out for a smaller wave period range corresponding to the crossflow lock-in range only. The results of the response tests are summarised in Table 6-12. Added mass is not considered in the mass ratio of the sway mode as the same is found to be negative during crossflow lock-in (Govardhan and Williamson, 2004).

Table 6-12: Response test results in regular waves, a) sway, b) yaw

a)

Sway				
Case	$m^*$	$MF$	$y_{O, rms}/D$	$y_{O, max}/D$
VL	6.99	2.457	0.05	0.08
RVL	5.57	2.701	0.06	0.11
NVL	4.35	3.091	0.13	0.17

b)

Yaw					
Case	$m^*$	$MF$	$k_{\phi}$ (m)	$R_{\phi\phi, rms}/D$	$R_{\phi\phi, max}/D$
VL	7.38	5.026	0.233	0.032	0.058
NVL	4.73	3.091	0.275	0.042	0.072

Note:  $R_{\phi}$  represents the radial distance of leg from yaw centre.

### 6.7.1 Inline / Surge Response

Figure 6-55 a) and b) display the variation of the normalised inline rms amplitude response plotted with respect to the corresponding reduced velocities and the  $KC$  numbers respectively. It can be observed in Figure 6-55 a) that the model exhibits inline response with large amplitudes in the order of  $0.18D$  at a reduced velocity of around 9. Additional inline peaks of significant amplitudes are also observed at a reduced velocity of 4 and 5 for the test cases NVL and VL respectively. In comparison with Figure 6-55 b), it can be inferred that the peaks at the reduced velocity of 9, correspond to  $KC$  around 9 revealing inline resonance response with wave frequency.

The peaks at the reduced velocities of 4 and 5 corresponded to a  $KC$  around 12. The inline response in the regular wave is also characterised by the multiple peaks in the response curve.

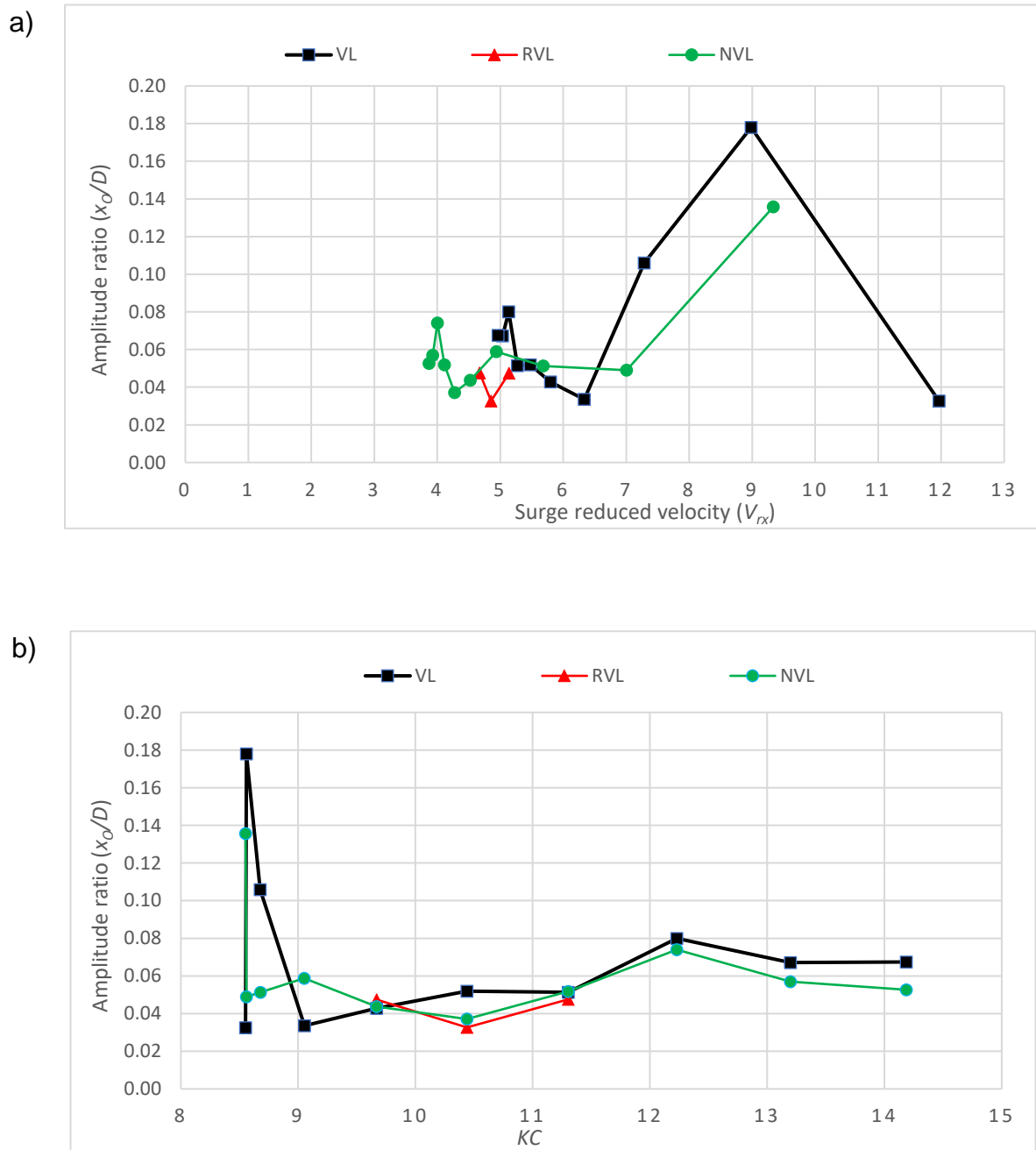


Figure 6-55: Inline/surge response, a) versus reduced velocity, b) versus  $KC$  number

Figure 6-56 illustrates the inline frequency responses of the model normalised with the wave frequency and plotted against the respective  $KC$  numbers for the test cases. It can be observed that the drag excitation is predominantly at the wave frequency. However, it is interesting to note that the inline drag excitation is also found to be

present at the second and third multiples of the wave frequency at certain  $KC$  (e.g.,  $KC = 9.05$  and  $10.44$  respectively). In comparison with Figure 6-55 b), it can be observed that these points do not exhibit any significant response and can be inferred as weak coupling with the multiples of lift excitations.

### 6.7.2 Crossflow/Sway Response

Figure 6-57 shows the variation of the normalised crossflow rms amplitude response plotted with respect to the corresponding reduced velocities. It is evidently revealed that the model is highly vulnerable to crossflow VIV with large amplitude lock-in vibrations. The response amplitudes (rms) were found to be around  $0.13 D$ , which corresponded to maximum response amplitudes of approximately  $0.17D$ . Crossflow VIV was found to be insignificant during the test at the low  $KC$  of 5.

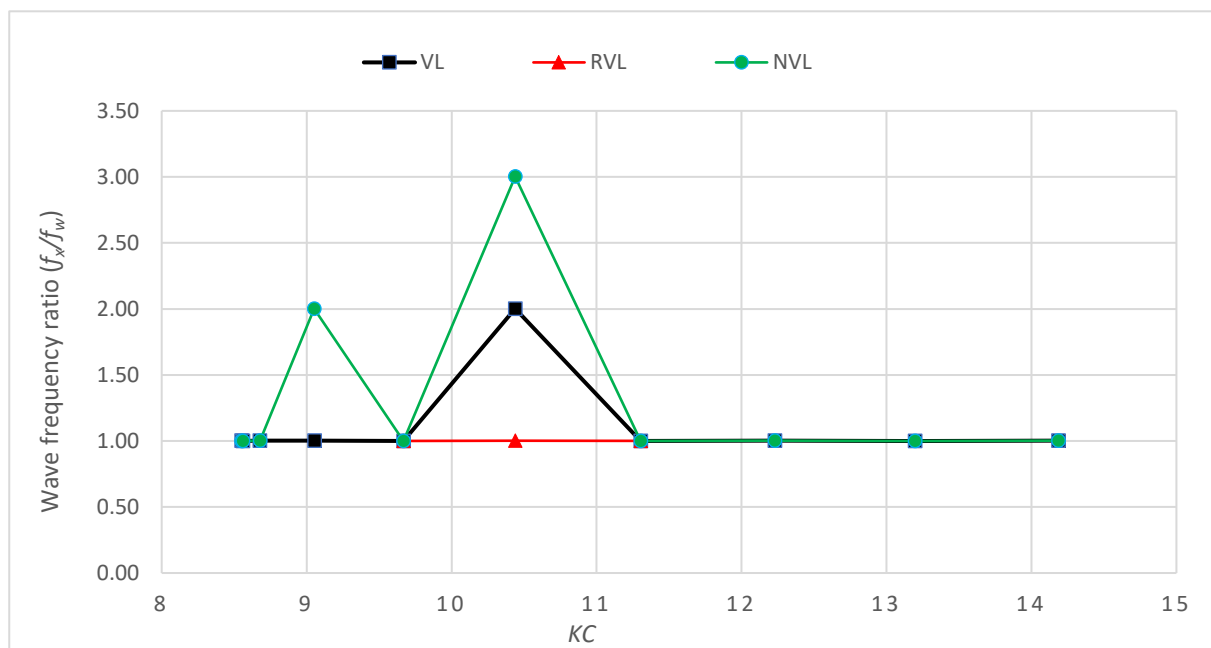


Figure 6-56: Inline frequency response normalised with the wave frequency and plotted against the  $KC$  number

It can be observed that the peak crossflow response occurs around a reduced velocity of 5, similar to the case under uniform current. However, the lock-in regime is found to be narrow and confined around the peak response. The response amplitude and the lock-in range are found to increase with a reduction in elevated load, with the lightest load test case exhibiting the largest crossflow response amplitude and lock-in regime. However, the observed increase in lock-in regime is found to be rather insignificant.

Figure 6-57 also demonstrates the crossflow response of the loading condition, NVL in uniform current for comparison. It can be observed that the amplitude response is considerably higher than in uniform current while the lock-in range is considerably smaller. The higher crossflow response than in steady current can be attributed to a  $KC$  during lock-in of approximately 10, where the vortex correlation and lift coefficient are found to be the highest in waves (Barltrop and Adams, 1991). The crossflow response in the regular wave is also characterised by the classical twin peaks in the response curve for the cases, VL and NVL; the range of the test case RVL is too small to capture the second peak

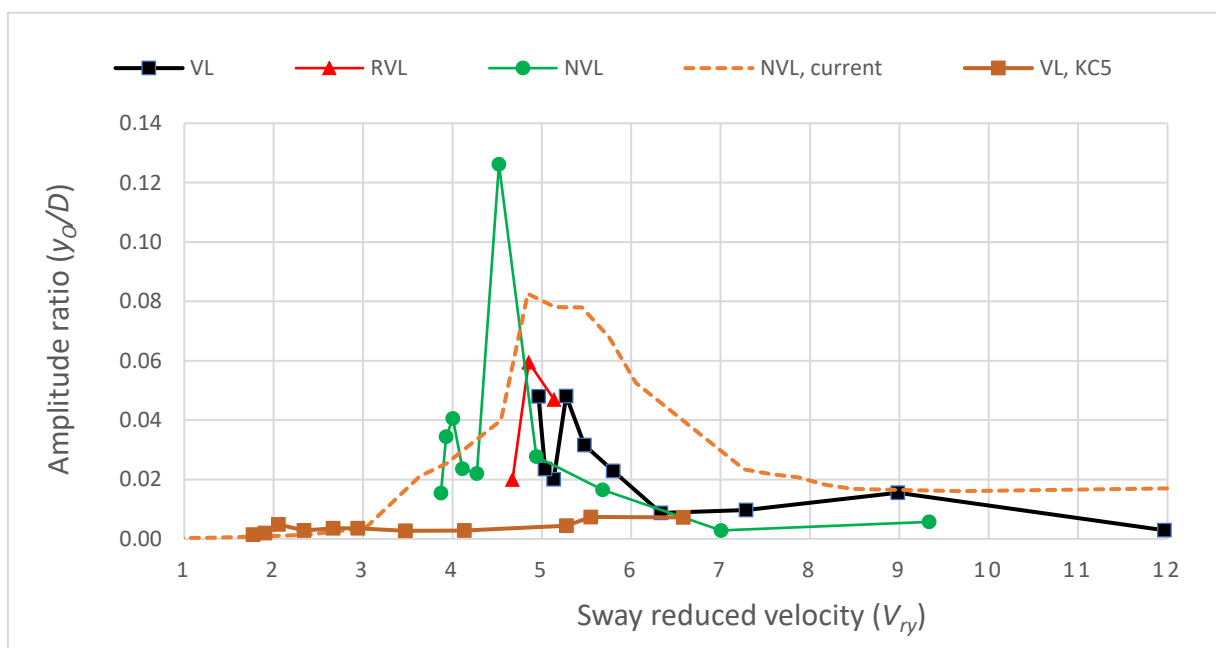


Figure 6-57: Crossflow amplitude response with reduced velocity ( $U_o / f_{Ny}D$ )

Figure 6-58 displays the time series of the crossflow response of the model, for the test case NVL, corresponding to a reduced velocity of 4.52. It can be observed that aggressive crossflow vibrations are exhibited by the model with amplitudes up to the order of 6mm (0.18 D). It is further revealed in Figure 6-58 that the crossflow VIV exhibits significant amplitude modulations even in regular waves.

Figure 6-59 shows the variation of the crossflow rms amplitude responses, plotted against the  $KC$  number of the flow. It can be observed that the peak crossflow responses correspond to the  $KC$  number around 10. As the value of the  $KC$  number at resonance is approximately twice of the respective reduced velocity, it can be inferred that the crossflow lock-in is occurring at double the wave frequency, corresponding to

the fundamental lift frequency at these  $KC$  numbers. It can be further inferred that the primary response peak corresponds to lock-in with the lift component at double wave frequency while the second peak appears to correspond to lock-in with the lift component at triple wave frequency. This phenomenon is visible for two test cases, VL and NVL in the figure, while the range of the test case RVL is too small to capture the second peak.

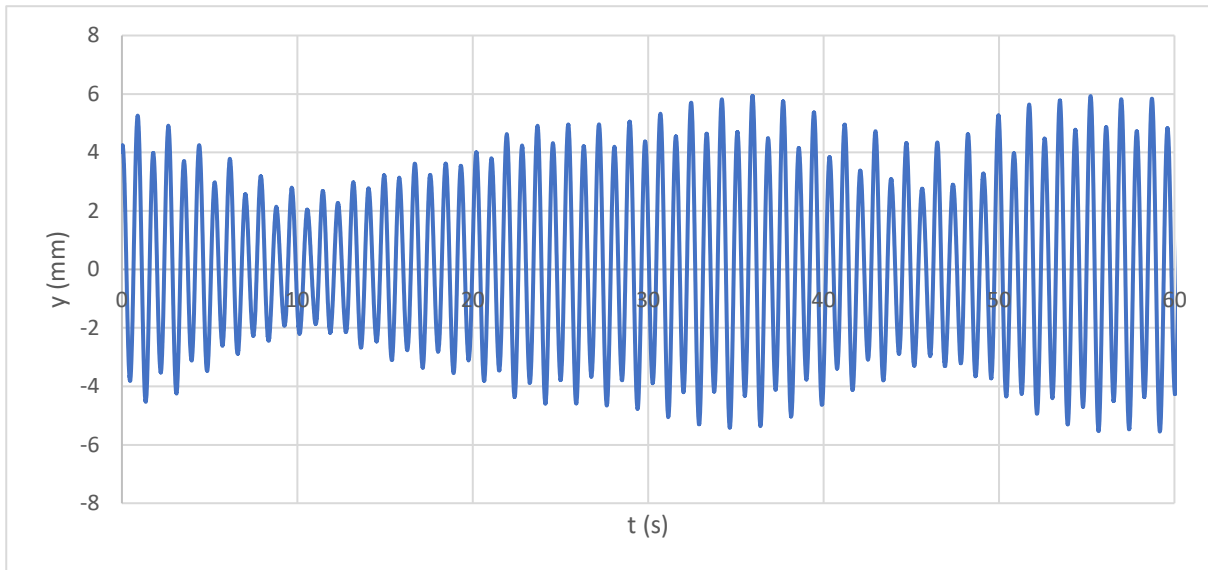


Figure 6-58: Model crossflow response time series in regular waves for NVL, at a reduced velocity of 4.52

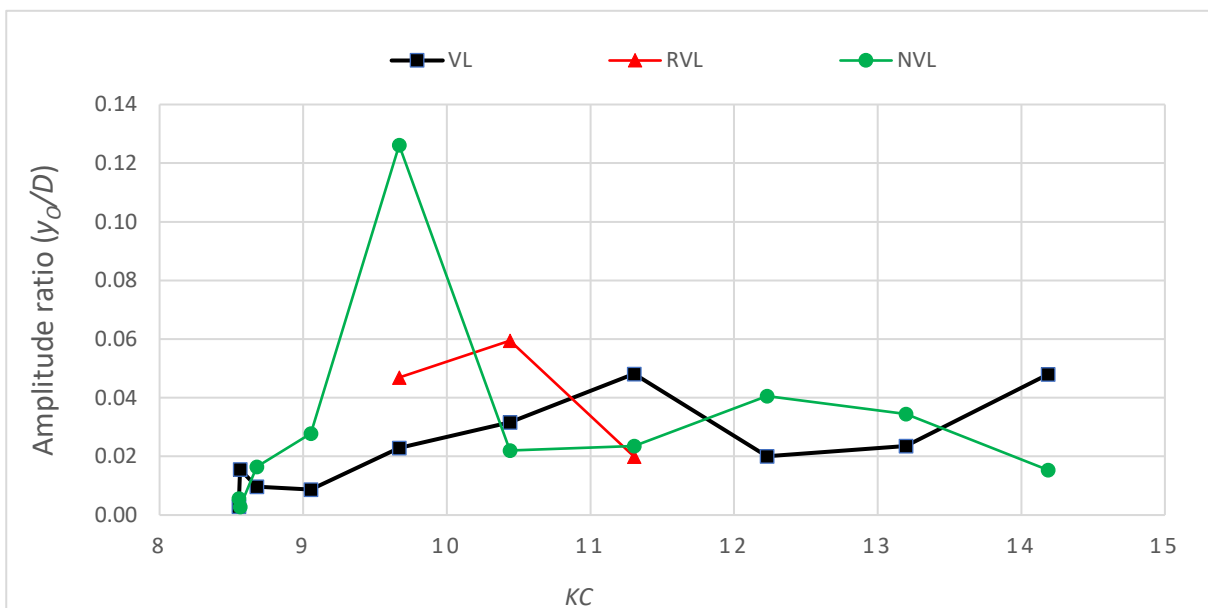


Figure 6-59: Crossflow amplitude response with  $KC$  number

Figure 6-60 illustrates the crossflow frequency responses of the model normalised with the wave frequency and plotted against the respective  $KC$  numbers for the test cases. It can be observed in Figure 6-60 that the lift excitation is present at various multiples of wave frequency as also observed by other researchers (Sarpkaya, 1975; Maull and Milliner, 1978; McConnell and Park, 1982; Williamson, 1985; Sarpkaya, 1987) with oscillatory flows. Further, during crossflow resonance, the lift frequency is found to be twice the wave frequency. From the frequency response, it can be observed that the lift excitation is also present at the wave frequency for low  $KC$  number. The lift frequency is found to be at 3<sup>rd</sup> and 4<sup>th</sup> multiples of wave frequency at high  $KC$ .

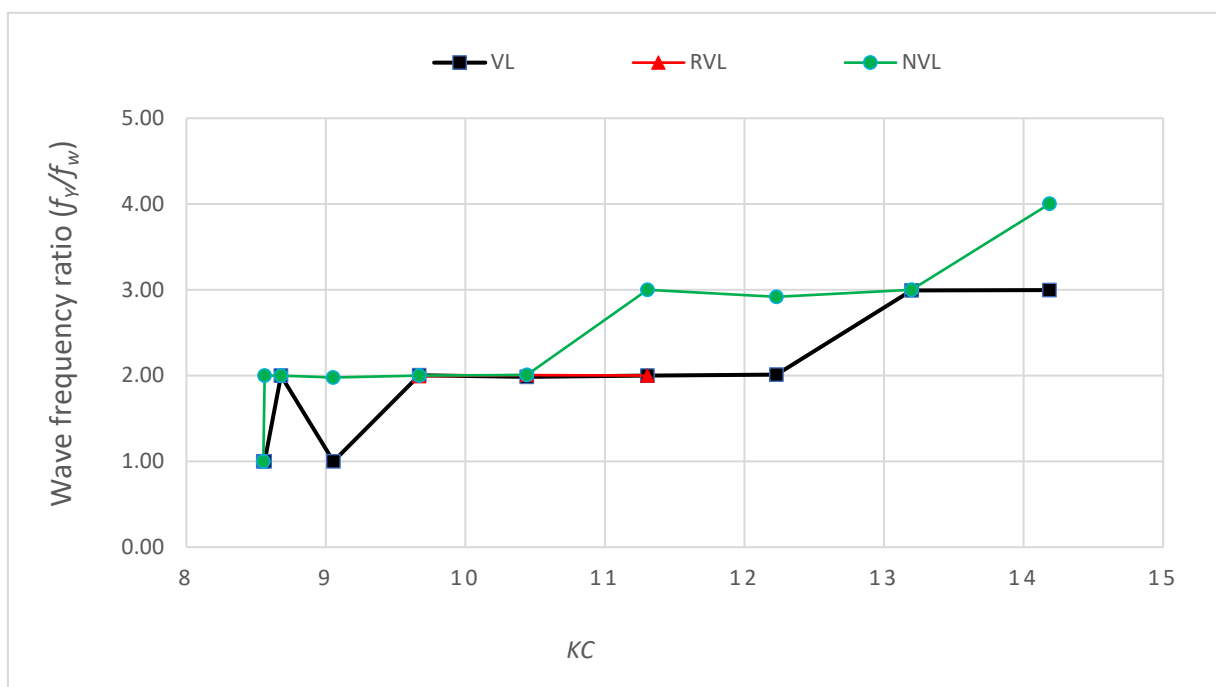


Figure 6-60: Crossflow frequency response normalised with wave frequency against  $KC$  number

Figure 6-61 illustrates the crossflow frequency responses of the model normalised with the natural frequency and plotted against the corresponding reduced velocities. It can be observed that the natural frequency ratio tends to oscillate around a value of 1, causing the jack-up to respond to the frequency component of the lift force that is close to its natural frequency. In comparing Figure 6-57 with Figure 6-61, it can be noted that the peak amplitude responses occur at those reduced velocities when the natural frequency ratio is coinciding with or near a value of unity.

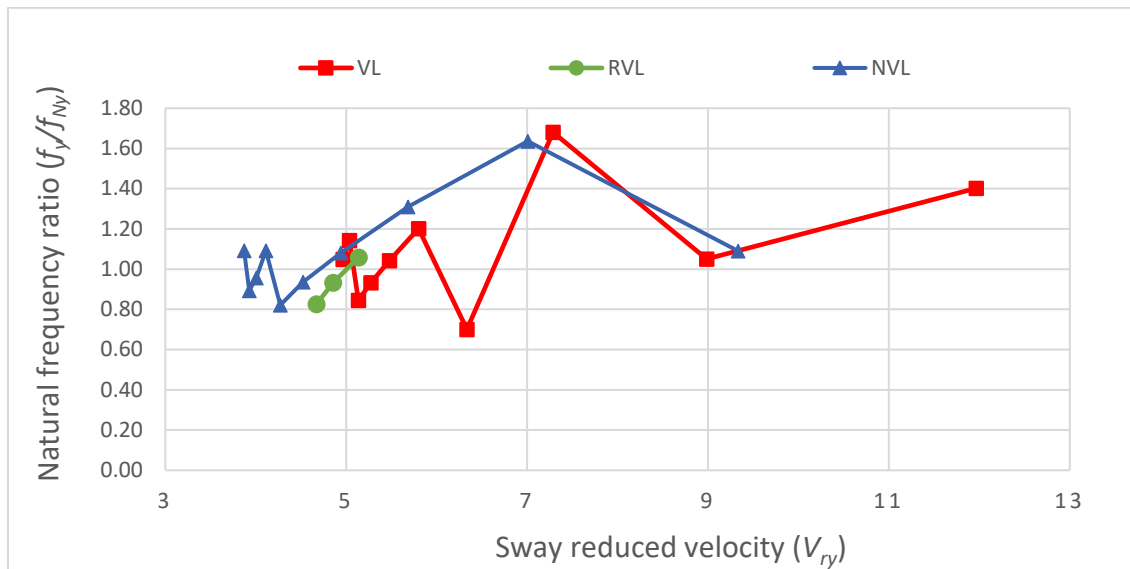


Figure 6-61: Crossflow frequency response normalised with natural frequency against reduced velocity ( $U_0/f_{Ny}D$ )

#### 6.7.2.1 Effect of Mass ratio

The increase in response amplitude with the reduction in model mass validated the inverse proportionality established in the mathematical model developed in Section 5.6.1. It was observed that the increase in mass ratio reduces not only the amplitude response but also the lock-in range. The normalised crossflow rms response amplitude ratios displayed an increasing trend, when plotted against the inverse of effective mass damping parameter (mass damping parameter multiplied with the MF), as shown in Figure 6-62. This demonstrated the significance of effective mass damping parameter in controlling the crossflow VIV response in regular waves. Thus, the effective mass damping parameter can be considered as the universal parameter governing the crossflow VIV across various mode shapes and water depths in regular waves.

#### 6.7.3 Yaw Response

The response tests revealed that the model jack-up experienced torsional or yaw VIV responses in regular waves. The yaw amplitude responses as a function of yaw reduced velocity are plotted in Figure 6-63. It can be observed that the peak yaw response occurs at a yaw reduced velocity less than 5, indicating that the yaw VIV is due to higher multiples of lift excitation. The rms response amplitudes are found to be around  $0.04D$ , with the maximum response amplitude around  $0.07D$ . The lock-in regime is found to be very small with triple response peaks for yaw VIV, though the  $KC$

range of the test case RVL was too small to capture the triple peak response. It can be observed in Figure 6-63 that the yaw response is less aggressive compared to the crossflow response in regular waves. The yaw response in regular waves is also found to be significantly less than that in a steady current. The model jack-up was found not to experience any yaw VIV during the tests at the  $KC$  of 5.

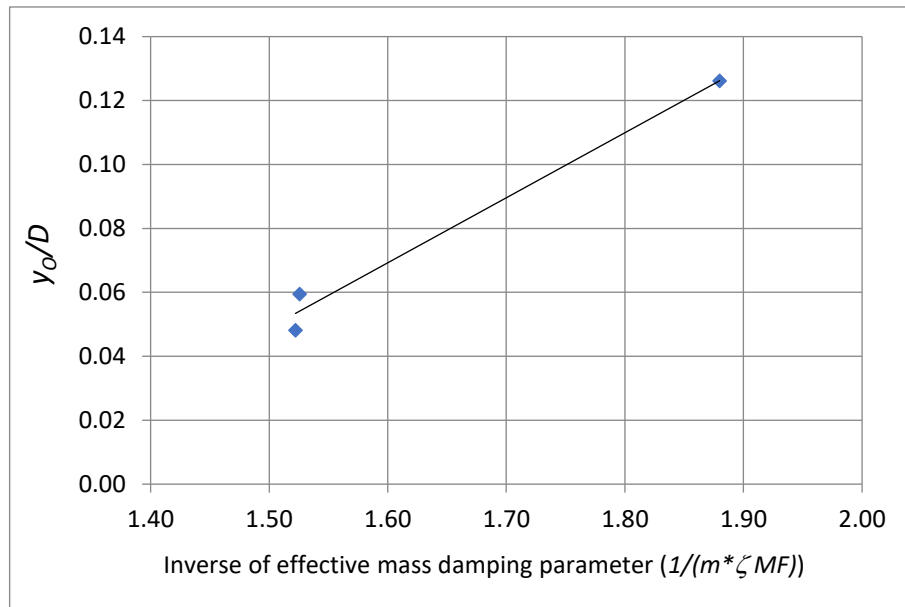


Figure 6-62: Crossflow amplitude response with the inverse of modified mass damping parameter

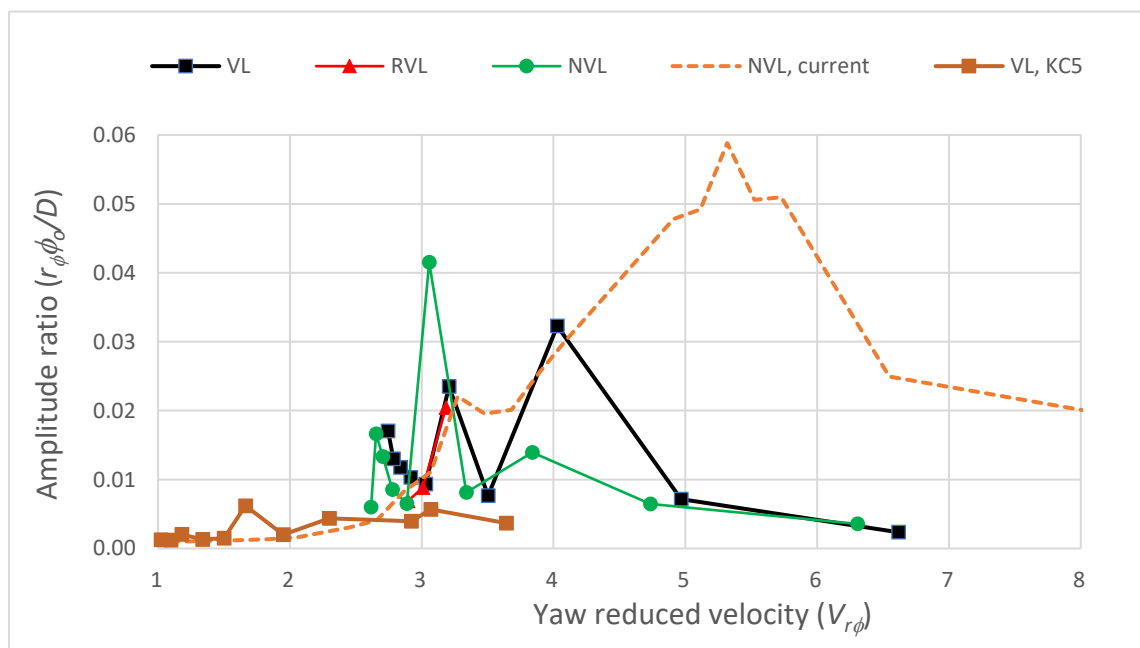


Figure 6-63: Yaw amplitude response with reduced velocity ( $U_0/f_{N\phi}D$ )

Figure 6-64 demonstrates the yaw amplitude response in regular waves plotted as a function of the  $KC$  number. The response amplitude is found to increase with the reduction in elevated load, though there is hardly any difference in the lock-in range. It can be inferred that the increase in mass ratio reduces the yaw amplitude response as demonstrated mathematically in Section 5.6.2. It is noted that the  $KC$  number range of RVL is not large enough to capture the fundamental response peak and triple peak response of the yaw VIV.

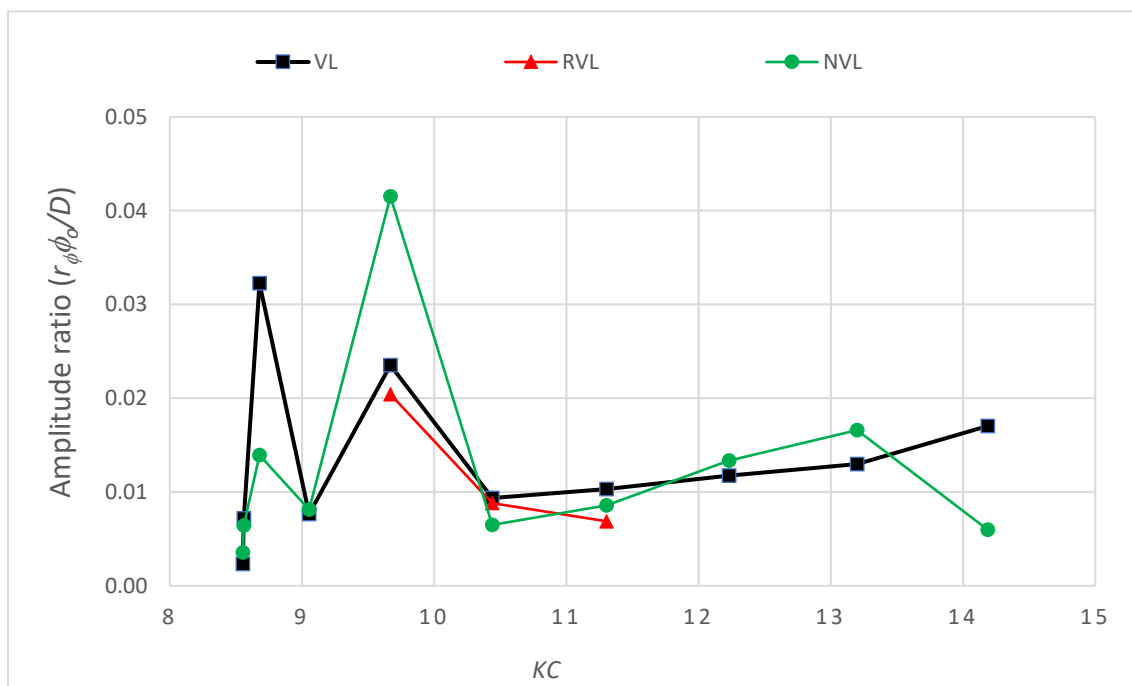


Figure 6-64: Yaw amplitude response with corresponding  $KC$  numbers

Figure 6-65 illustrates the yaw frequency responses of the model in regular waves normalised with the wave frequencies and plotted against the  $KC$  number. It can be observed that the lift excitation is present at higher multiples of wave frequency. It can be inferred that during the highest yaw resonance peaks, the lift frequency is twice the wave frequency, same as the fundamental lift frequency at these  $KC$ . It can be observed that the lift excitation is present at the wave frequency also for low  $KC$  number. The lift frequencies are also found to be present even at the 5<sup>th</sup> multiples of wave frequency at high  $KC$ .

The yaw frequency responses of the model, normalised with the corresponding natural frequencies are plotted against the yaw reduced velocities in Figure 6-66. Similar to crossflow response, the natural frequency ratio is found to oscillate around a value of

unity causing the model to respond to that lift frequency component near to its natural frequency. Comparison with Figure 6-63 reveals that the peak amplitude responses occur at those reduced velocities when the natural frequency ratio is near to a value of unity.

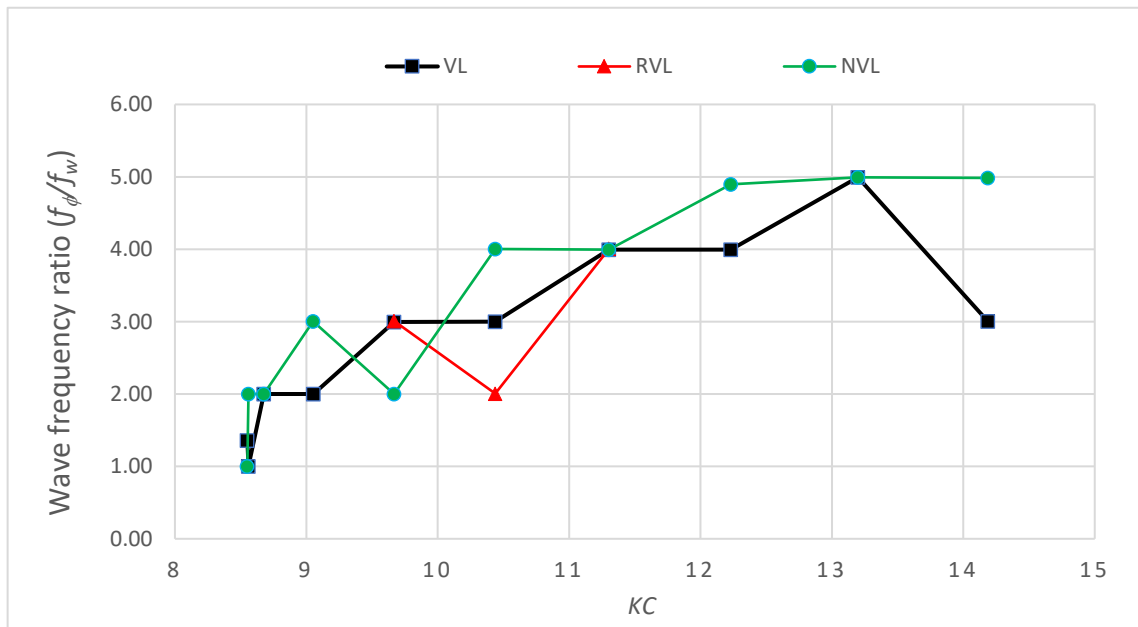


Figure 6-65: Yaw frequency response normalised with wave frequency against  $KC$  number

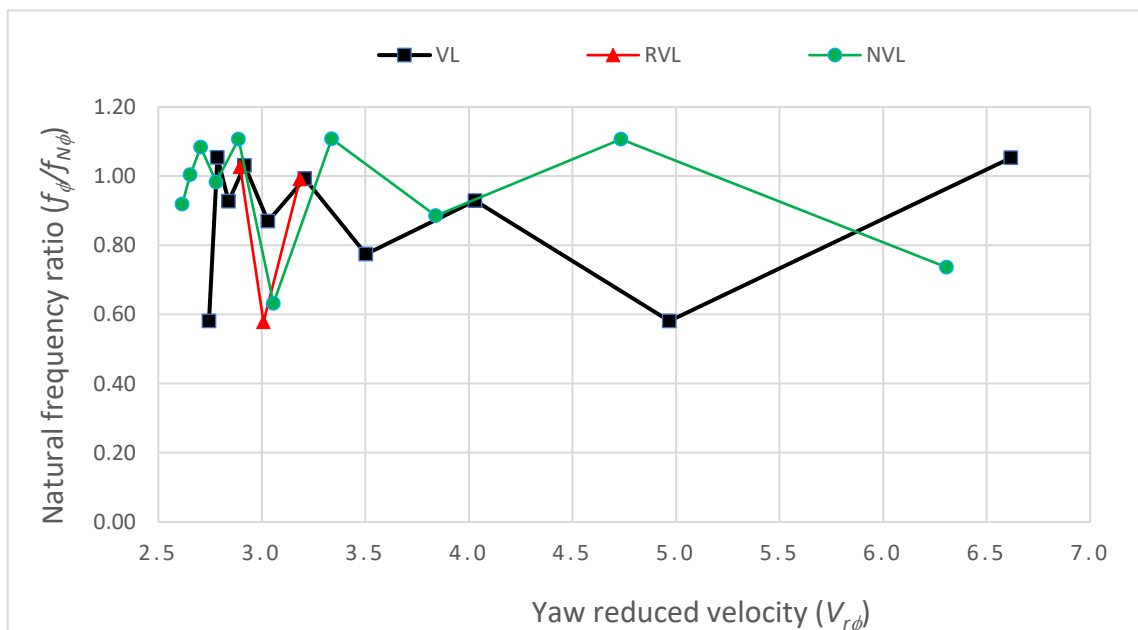


Figure 6-66: Yaw frequency response normalised with natural frequency against reduced velocity ( $U_0/f_{N\phi}D$ )

### 6.7.3.1 Effect of Mass ratio

Figure 6-67 illustrates the yaw response amplitude ratios of the two load cases, NVL and VL plotted against the inverse of effective inertia damping parameter defined as the product of mass damping parameter, MF and square of yaw radius of gyration. It can be observed that the yaw response increases with the inverse of effective inertia damping parameter and thus can be considered as the universal parameter determining the yaw VIV response. This agrees generally with the mathematical model derived in Section 5.6.2.

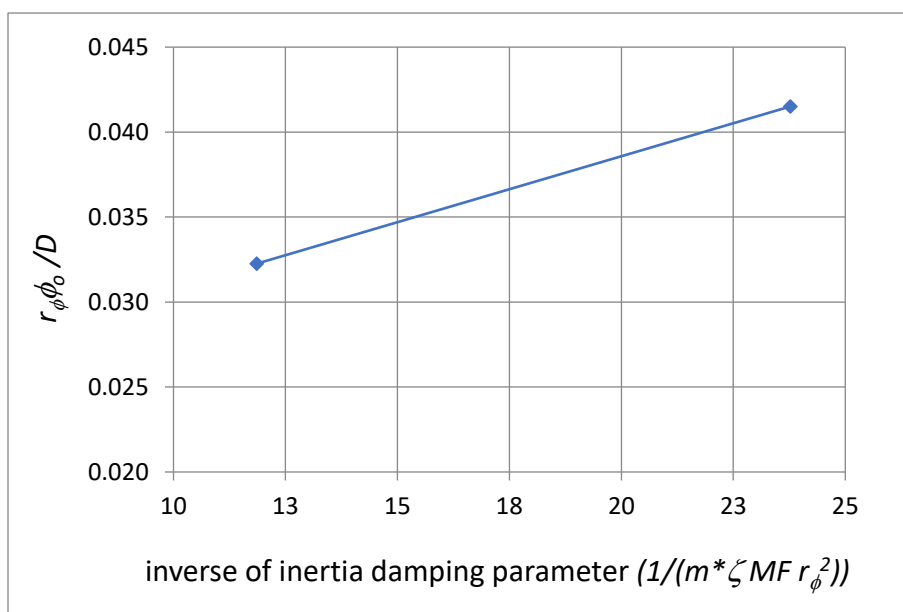


Figure 6-67: Yaw amplitude response with the inverse of inertia damping parameter

### 6.7.4 Combined Response

The combined crossflow amplitude response of the leg derived from the corresponding crossflow and yaw responses is plotted in Figure 6-68, against the  $KC$  number. On analysing Figure 6-68 along with Figure 6-59 and Figure 6-64, it can be observed that the range of the yaw response coincides with that of the crossflow response for the lowest mass ratio (NVL), causing a combined lock-in range ( $8.56 < KC < 10.44$ ) with response amplitudes (0.16D) higher than the respective individual values (0.13D and 0.04D). The crossflow and yaw lock-in ranges of VL and RVL also overlap to cause a larger combined lock-in range ( $8.56 < KC < 11.30$ ) with effective amplitude ratio in the order of 0.04D to 0.06D. The high combined response rms amplitude can be quite detrimental when it comes to leg strength.

### 6.7.5 Mean Response

The mean or steady inline, crossflow and yaw responses were also measured in regular waves and were found to be insignificant throughout the wave periods. This was the expected behaviour since the mean flow speed is zero in regular waves.

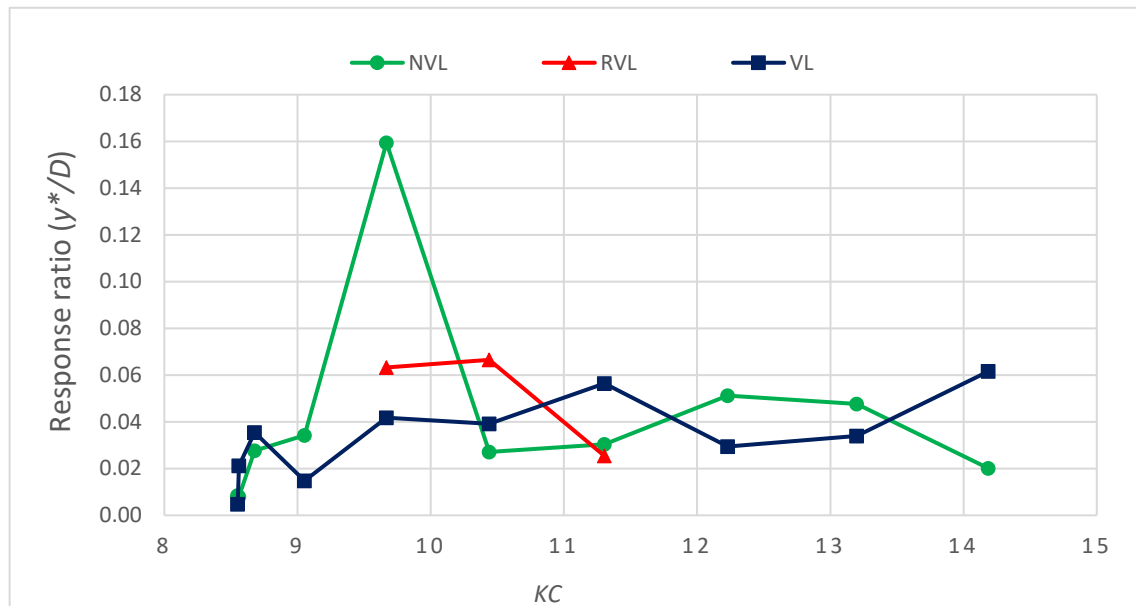


Figure 6-68: Leg crossflow combined amplitude response due to sway and yaw with KC number

### 6.7.6 Effect of Environmental Headings and Leg Orientation

Response tests were conducted in regular waves with various global and local headings to investigate the effect of environment heading and leg orientation on the jack-up VIV. However, the investigation was limited to crossflow VIV as the yaw VIV in regular waves is found to be relatively insignificant. The test cases were retained same as the experiments in current, displayed in Table 6-10.

Figure 6-69 illustrates the relative crossflow amplitude ratio of various headings plotted against the global headings. The relative amplitude ratio is calculated by normalising the respective amplitude ratios with the amplitude ratio at a global and local heading of 0. It can be observed that the crossflow response reduced by around 60% at a global heading of 21 degrees and by around 30% for both the global headings of 37 and 45 degrees. However, the crossflow response is found to increase by around 60% when the local heading of the leg design LD1H4 is changed to 45 degrees. This is a clear

indication that the crossflow VIV response of a jack-up can be minimised by selecting a heading close to quartering seas.

## 6.8 Response Test in Irregular Waves

Response test was carried out in irregular waves also for the test case VL, with full variable load and at the maximum effective water depth of 780mm. The Pierson Moskowitz spectrum was selected for the irregular waves, and the significant wave height was kept at a constant 92 mm. The mean zero crossing period of the wave spectrum was varied to study the effect of the irregular wave frequencies on the jack-up VIV. Mean zero crossing period was considered for the investigation since vortex shedding is a viscous phenomenon dependent on the instantaneous flow reversal. The effective  $KC$  number of the wave spectrum was calculated based on the significant wave height and the mean zero crossing frequency. The amplitude and frequency response measured is compared with the respective results in regular waves. The global and the local headings of the model and the leg respectively were maintained at 0 degrees during the tests, and the leg design selected was LD1H4. The test case corresponds to 'VL' mentioned in Table 6-3.

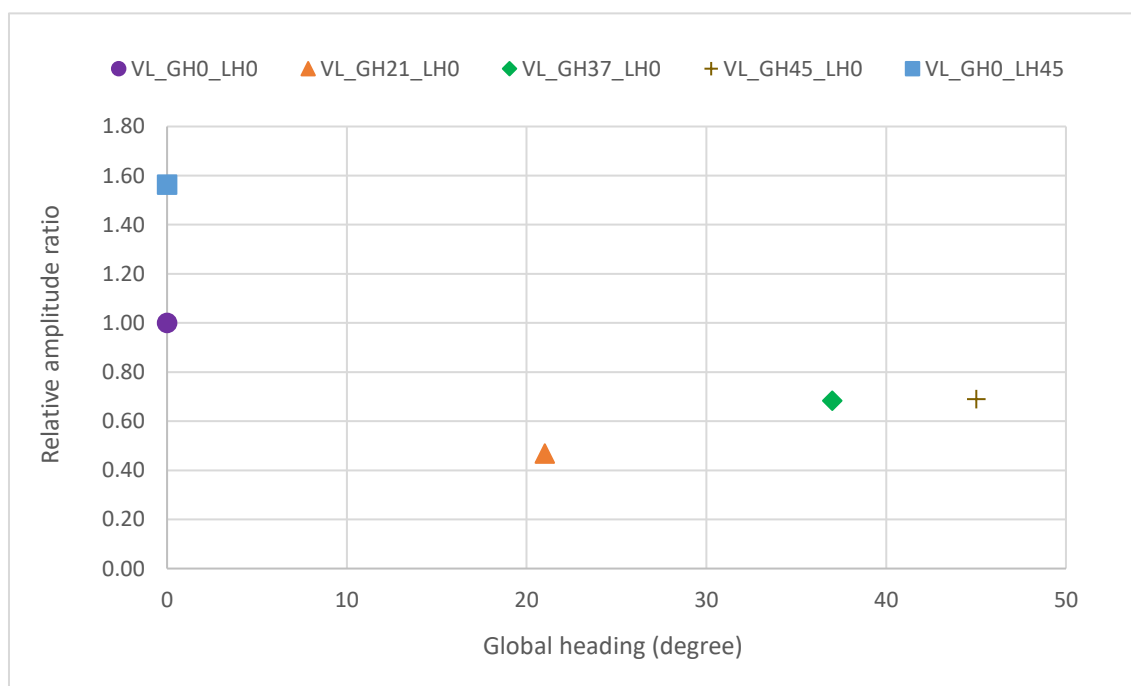


Figure 6-69: Crossflow relative response in regular waves for various global headings

### 6.8.1 *Inline Response*

Figure 6-70 illustrates the inline amplitude response of the model in the irregular waves, plotted against the effective  $KC$  numbers. The corresponding response in regular waves of height 92mm is also shown for comparison. It can be observed that significant inline vibrations with amplitude ratios up to the order of 0.08  $D$  occurs in irregular waves. The peak inline response in irregular waves corresponded well with the surge resonance in regular waves. However, in irregular seas, the response is more homogenised with trimmed peaks and continuous variation with the  $KC$  numbers.

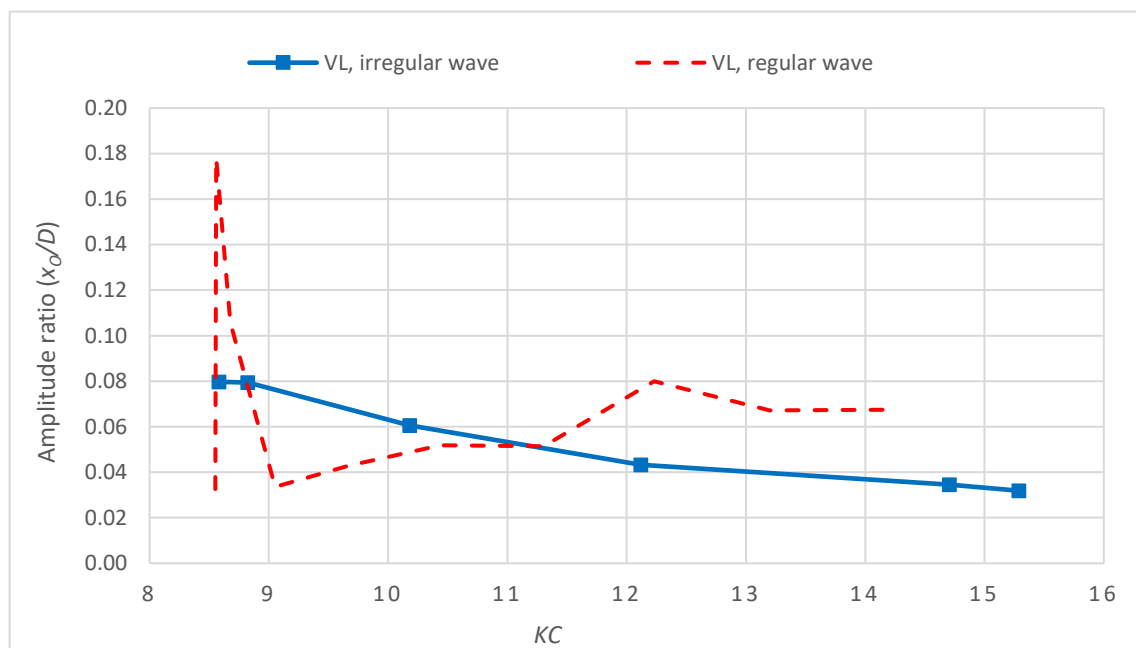


Figure 6-70: Inline amplitude response in irregular waves versus effective  $KC$  number

Figure 6-71 a) and b) demonstrates the inline frequency response of the model in terms of the natural frequency ratio and wave (mean zero crossing) frequency ratio respectively. It can be seen that in irregular waves, the inline response occurs at the natural frequency irrespective of the wave frequencies. This is in drastic contrast with the behaviour of the jack-up in regular waves where the inline response predominantly occurs at the wave frequency except at specific  $KC$  numbers experiencing coupled vibrations due to crossflow lock-in (for example,  $KC = 10.4$ ). It can be inferred that in irregular waves, the jack-up is in resonance with the frequency component of the inline force close to the surge natural frequency. It is further evident in Figure 6-71 b) that the inline vibration frequencies are unrelated to the mean zero crossing frequencies of irregular waves.

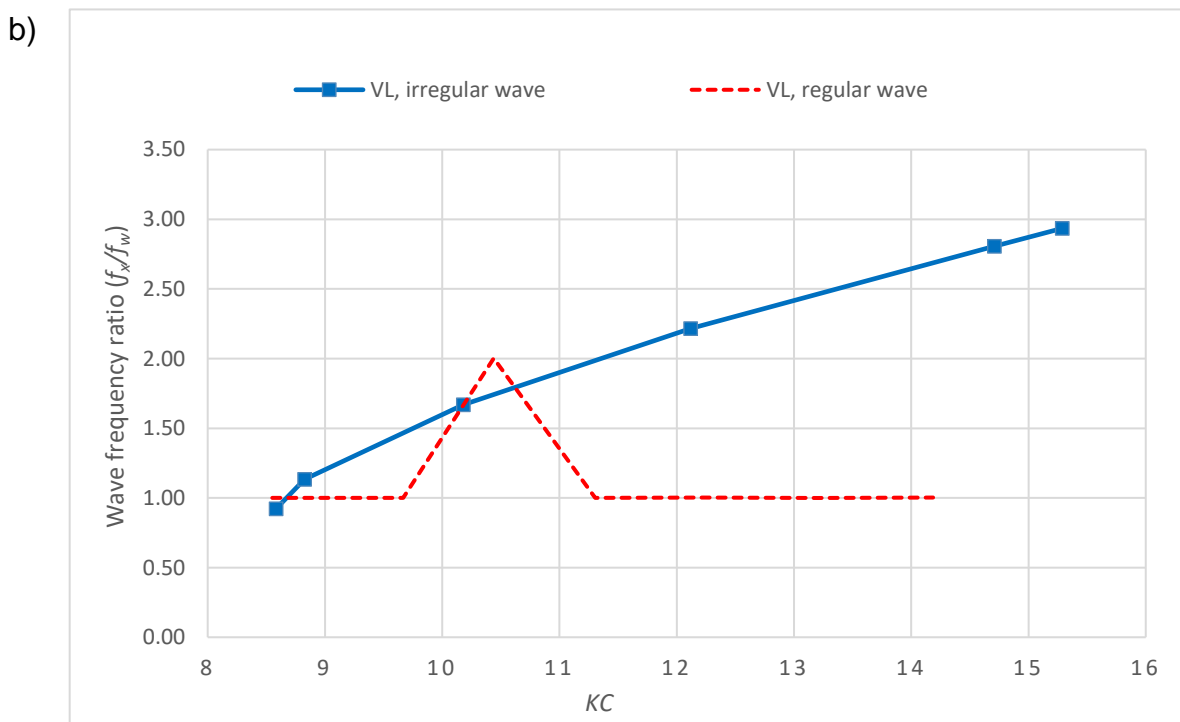
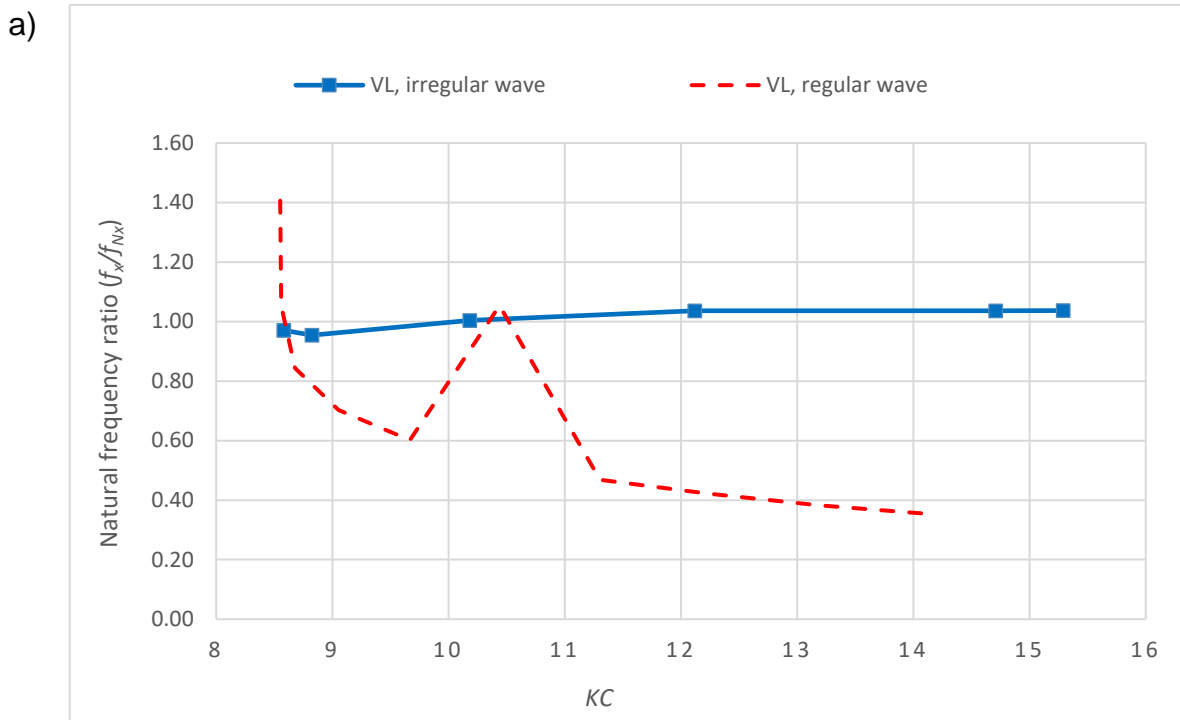


Figure 6-71: Inline frequency response in irregular waves versus effective  $KC$  number, a) natural frequency ratio, b) wave frequency ratio

### 6.8.2 Crossflow Response

Figure 6-72 illustrates the crossflow amplitude response of the model in the irregular waves plotted against the effective  $KC$ . It is clearly evident that the crossflow response is reduced to nominal values in irregular waves. The classical multiple peak behaviour in regular waves is also found to disappear in irregular waves. The low crossflow response can be attributed to the irregularities in the successive wave amplitudes and frequencies leading to irregular vortex shedding and random lift oscillations with low axial correlation, incapable of causing sustained resonance (Barltrop and Adams, 1991).

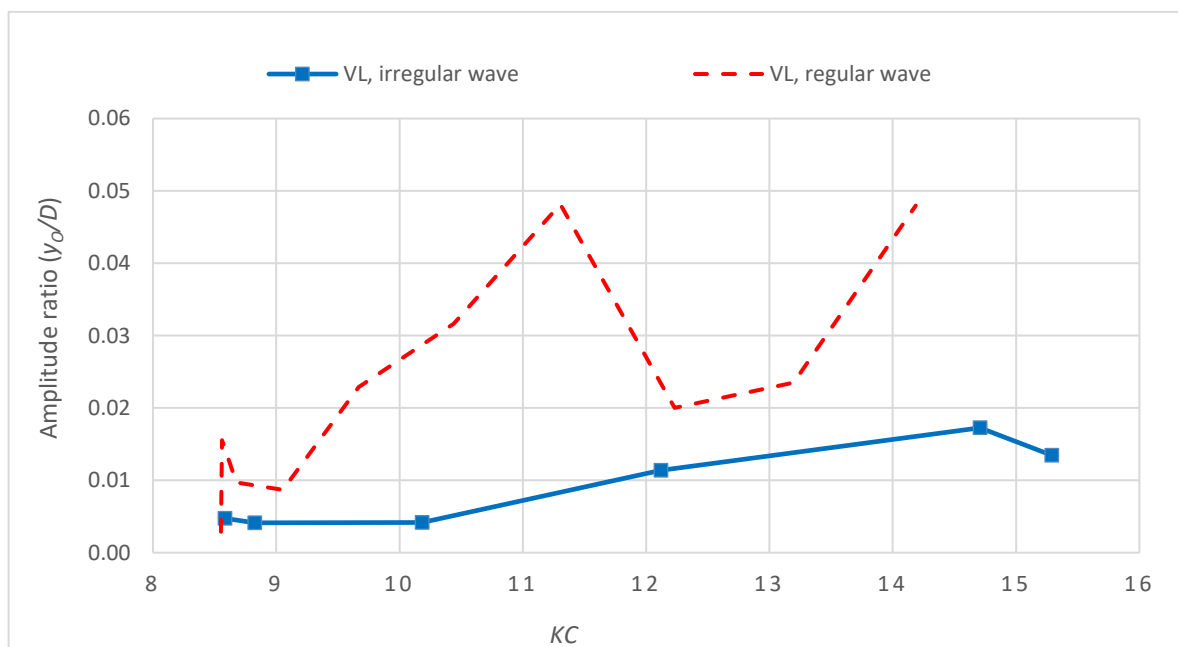


Figure 6-72: Crossflow amplitude response in irregular waves versus effective  $KC$  number

Figure 6-73 a) and b) demonstrates the crossflow frequency response of the model in irregular waves, in terms of the natural frequency ratio and wave frequency ratios respectively. It can be observed in Figure 6-73 a) that in irregular waves, the crossflow response occurs at the sway natural frequency of the jack-up irrespective of the wave frequency. This can be inferred as tuning of the jack-up with the lift frequency component present in the irregular waves near to its natural frequency. Figure 6-73 b) reveals that in irregular seas lift frequency is independent of the spectral mean crossing frequency.

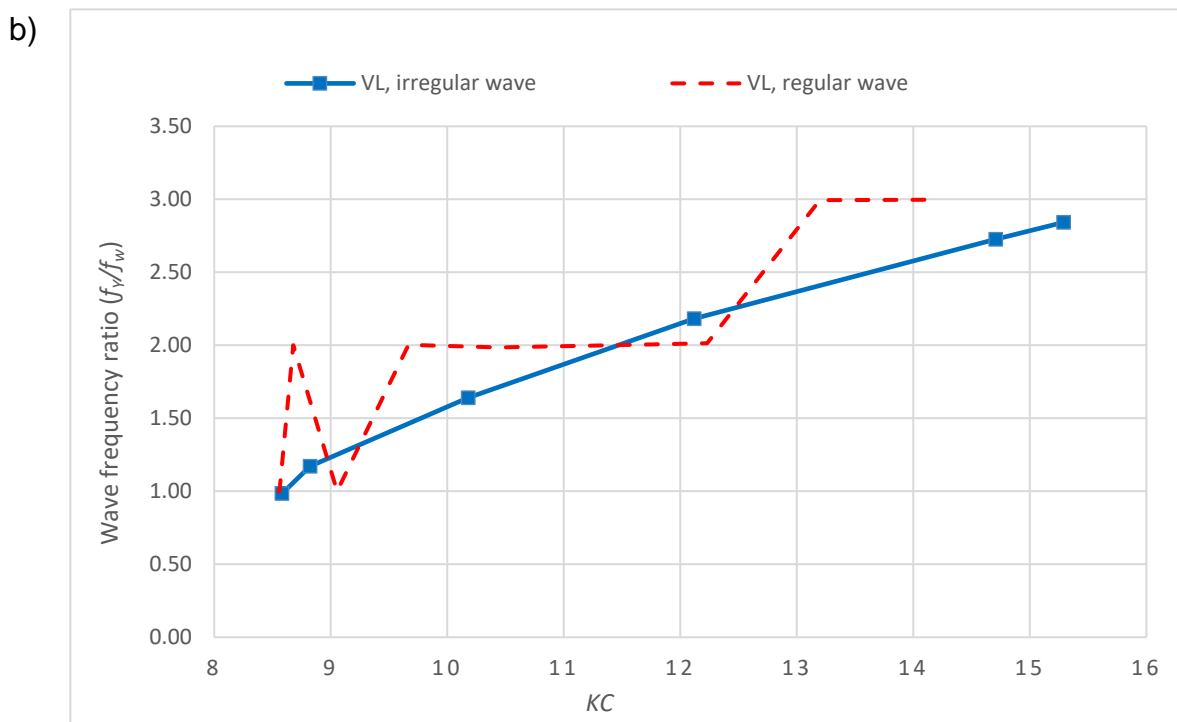
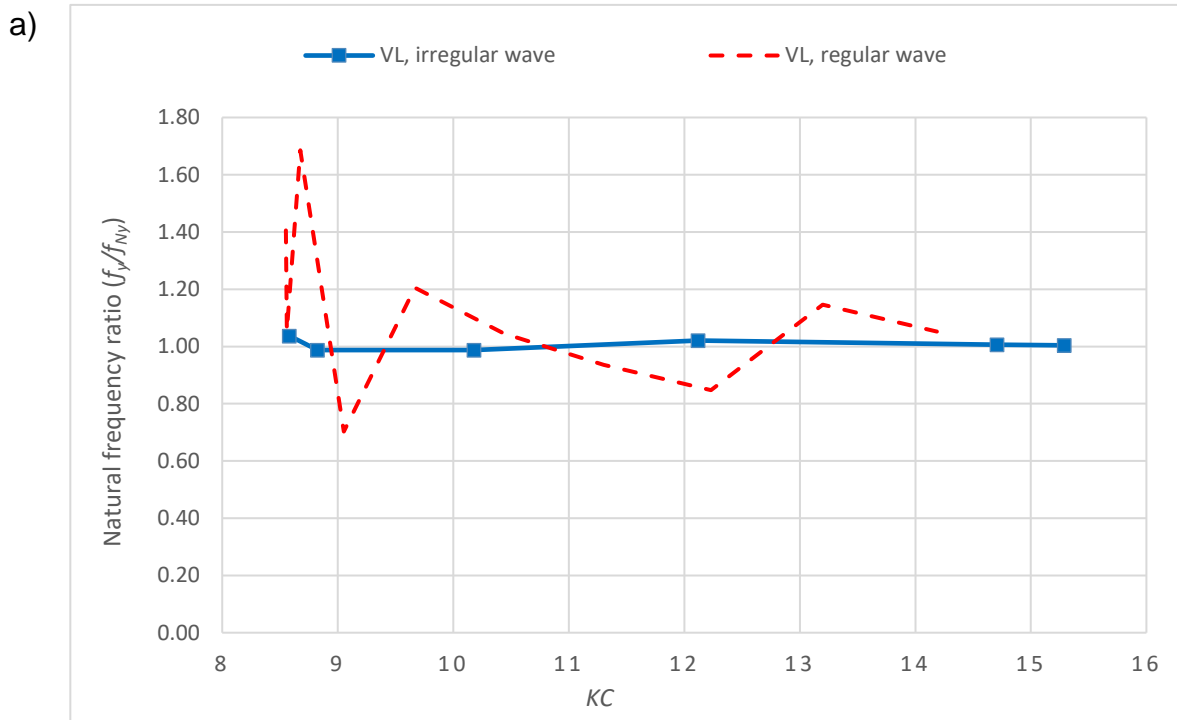


Figure 6-73: Crossflow frequency response in irregular waves versus effective  $KC$  number, a) natural frequency ratio, b) wave frequency ratio

### 6.8.3 Yaw Response

Figure 6-74 shows the yaw response of the model in the irregular waves. As evident in the figure, yaw VIV was not experienced in irregular waves. Similar to the crossflow response, the multiple peak behaviour in regular waves was also found to disappear completely. This can be attributed to the irregularities in the lift force oscillations due to the irregular and less correlated vortex shedding in a random sea, incapable of causing sustained lock-in vibrations (Barltrop and Adams, 1991).

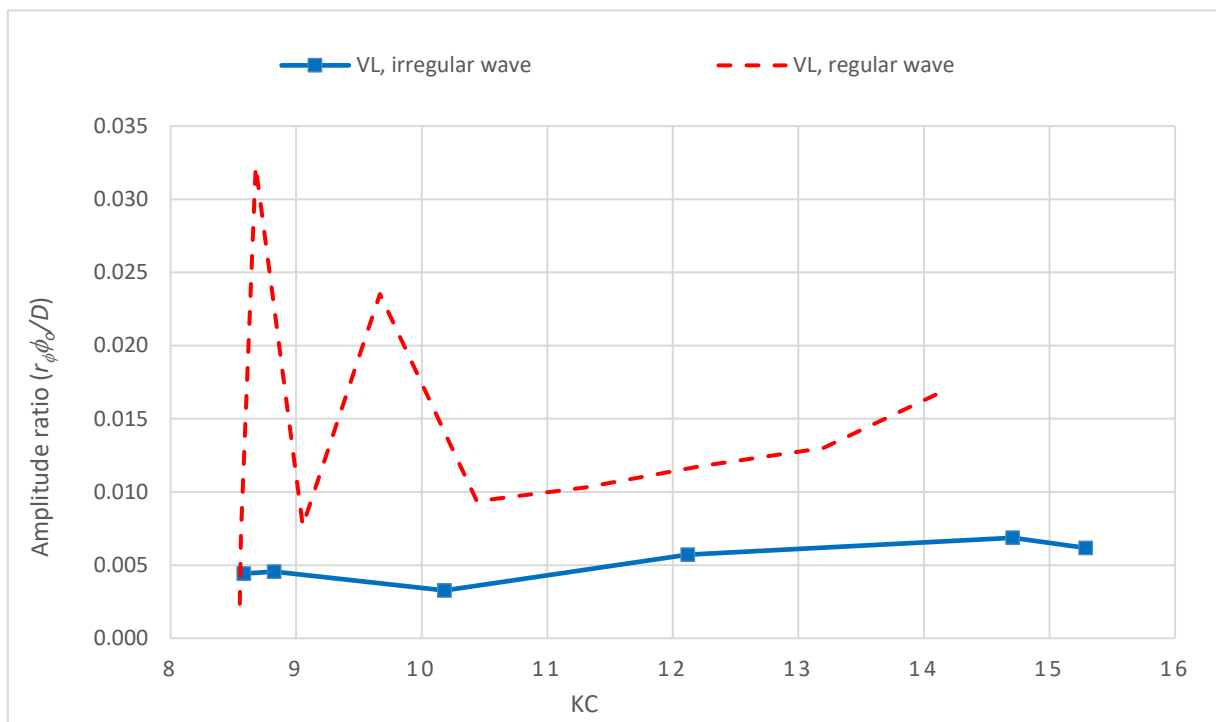


Figure 6-74: Yaw amplitude response in irregular waves versus effective  $KC$  number

Figure 6-75 a) and b) demonstrates the yaw frequency response of the model in terms of the natural frequency ratio and wave frequency ratio respectively in irregular waves. It can be observed that the yaw response happens at the natural frequency irrespective of the wave frequencies except around a low  $KC$  of 9. At this low  $KC$ , the model is found to exhibit yaw vibrations at the wave frequency demonstrating coupled vibrations with the aggressive inline resonant vibrations. Similar to crossflow VIV, it can be argued that the jack-up is in a continuous state of yaw resonance with the lift component near to its natural frequency, though the response is less.

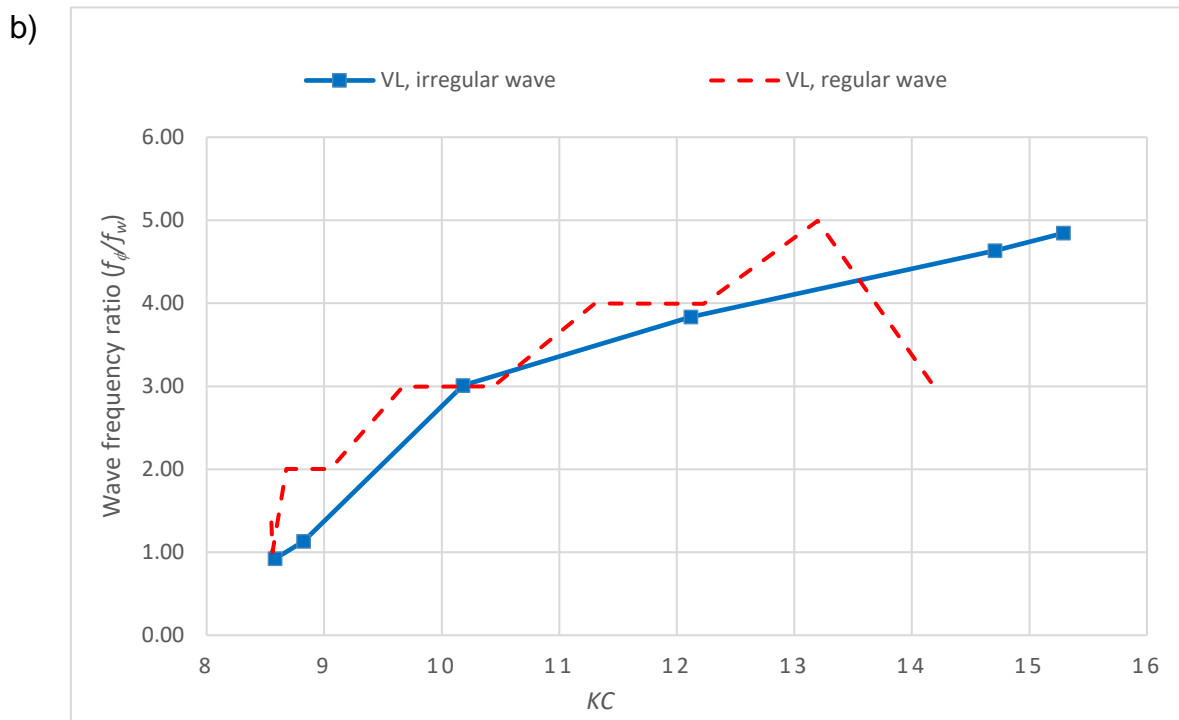
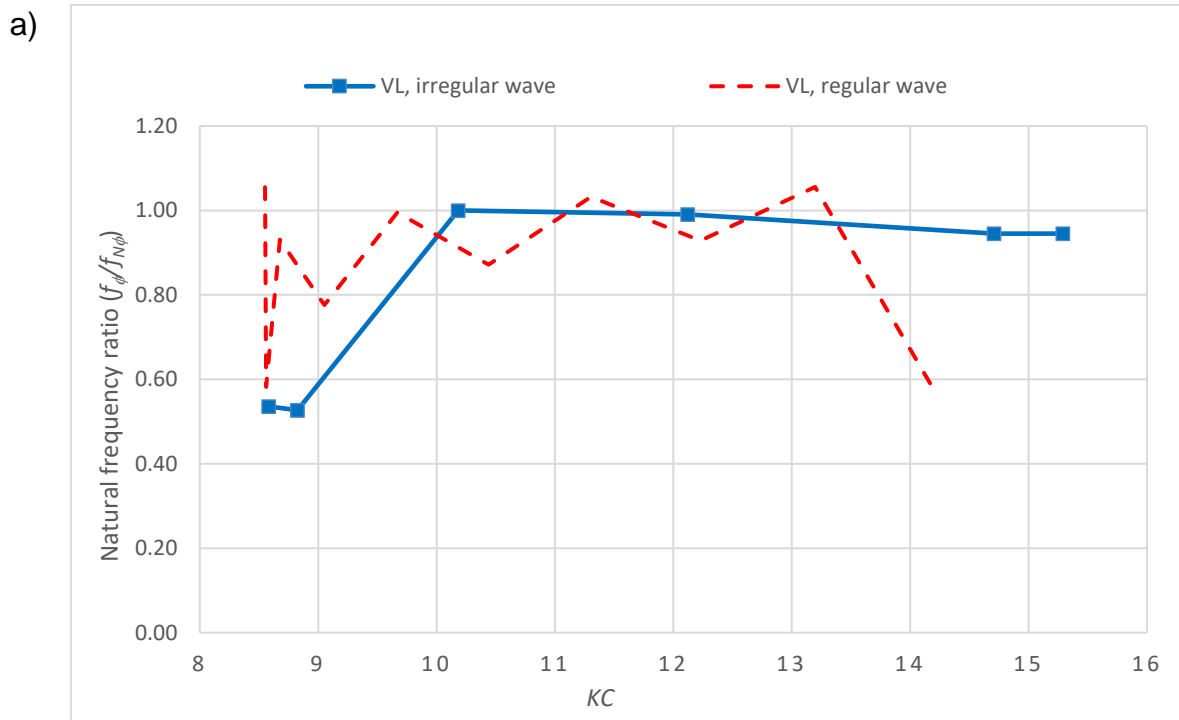


Figure 6-75: Yaw frequency response in irregular waves versus effective  $KC$  number, a) natural frequency ratio, b) wave frequency ratio

## 6.9 Response Test in Regular Waves with imposed Current

Further response tests were carried out in regular waves with imposed current. A regular wave height and period of 92mm and 2.25s respectively were selected for the tests, corresponding to the crossflow lock-in or sway resonance. The effective water depth was selected at the maximum 0.78m, and the loading condition corresponded to VL, full variable load. The model was exposed to regular waves along with incremental current from the head direction, and the responses along the inline, crossflow and yaw directions were measured and compared with the regular wave results. The global and local headings of the model and the legs were kept at zero, and the leg design selected was LD1H4. The test case corresponds to 'VL' presented in Table 6-3 and is identified as 'VL\_RWC' in the following sections.

### 6.9.1 Amplitude Response

Figure 6-76 a) illustrates the relative response ratios of the inline, crossflow and yaw VIV modes with respect to the sway reduced velocity calculated considering only the respective current. The relative amplitude ratio is calculated by normalising the amplitude ratios with the respective amplitude ratio at zero reduced velocity, corresponding to zero current or regular wave alone. The amplitude ratio at zero reduced velocity can be found from the results of response tests in regular waves, demonstrated in Table 6-12. The velocity ratio, current velocity upon wave horizontal particle velocity is also plotted in the figure for understanding the physics of the flow. From the velocity ratio, it can be inferred that flow reversal occurs at all the reduced velocities with velocity ratio less than 1.

It can be observed that the inline response increases almost linearly with the imposed current. This can be attributed to the effect of current speed on the horizontal particle velocity and consequently on the inline oscillatory drag (Barltrop and Adams, 1991; ABS, 2016; ABS, 2017). Crossflow response is observed to be high for nil and very low currents with an additional high peak at a sway reduced velocity around 3. The crossflow response is found to reduce subsequently and saturate at low values as reduced velocity increases further. The yaw response is found to be high at zero and low imposed currents, around a sway reduced velocity of 3 and at high sway reduced velocities above 7.5. It can be inferred from the velocity ratio that the sway and yaw

peaks at reduced velocities less than around 5, are experienced under flow reversal conditions.

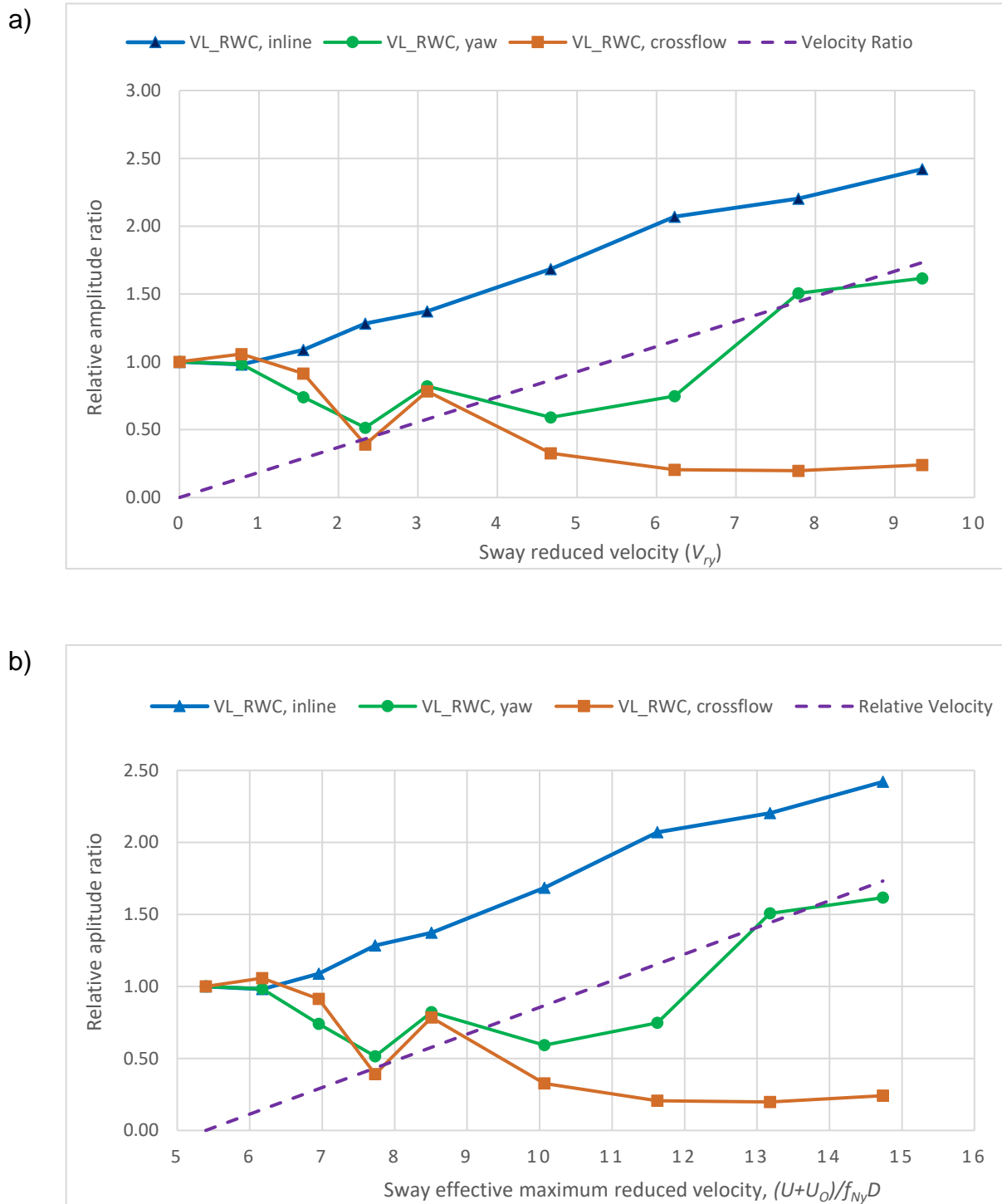


Figure 6-76: Inline, crossflow and yaw amplitude response in regular wave with imposed current, a) against sway reduced velocity based on current only, b) against sway reduced velocity based on maximum horizontal particle velocity  $((U+U_0)/f_N D)$

The effect of the combined flow velocity due to wave and current on the jack-up VIV can be better analysed by defining an effective reduced velocity based on the combined horizontal particle velocity. Figure 6-76 b) illustrates the relative amplitude ratios of the three modes plotted against the effective maximum sway reduced velocity calculated based on the maximum horizontal particle velocity. It can be noticed that the crossflow response peak at zero and low currents occurs around an effective reduced velocity of 5, which indicates that the peak corresponds to sway lock-in. The concurrent yaw peak around the effective sway reduced velocity of 5 can be attributed to the coupled yaw vibrations due to sway lock-in.

Figure 6-77 a) and b) displays the relative amplitude responses of the three modes plotted with respect to the yaw reduced velocity and effective maximum yaw reduced velocity respectively. It can be seen from Figure 6-77 a) that the highest yaw peak at high current corresponds to a yaw reduced velocity of around 5, indicating yaw resonance or lock-in. This implicitly implies that under high imposed currents eliminating flow reversal scenarios in regular waves, lock-in or resonance is controlled by current speed only. This can be explained by the argument that in high imposed current, the flow is oscillatory but unidirectional as the flow reversal is absent, and the vortex shedding process follows that of an unsteady current.

Figure 6-77 b) illustrates the relative amplitude responses plotted against the effective yaw maximum reduced velocity, calculated based on the maximum horizontal particle velocity. It can be observed that the middle yaw peak at moderate current corresponds to an effective yaw maximum reduced velocity of around 5, indicating a yaw resonance or lock-in response. Consequently, the concurrent crossflow VIV peak can be deciphered as coupled sway VIV due to yaw lock-in. This implies that under flow reversal scenarios in regular waves with low imposed currents, lock-in or resonant yaw VIV is a function of the maximum or minimum horizontal particle velocity.

### 6.9.2 *Frequency Response*

Figure 6-78 a) and b) illustrates the natural frequency ratio and wave frequency ratio respectively of the various modes of vibrations with the sway reduced velocity. It can be observed that the inline and crossflow responses occur at around half the natural frequency and natural frequency respectively. The yaw frequency is found to switch between half the natural frequency and the natural frequency. Comparing figures, a)

and b), it is evident that the inline vibrations occur at the wave frequency irrespective of the imposed current speed. Similarly, crossflow vibrations are also found to occur at double the wave frequency irrespective of the imposed current speed. It further indicates that the crossflow response is in a continuous state of lock-in with the lift component at double the wave frequency that is very near natural sway frequency.

Figure 6-78 b) indicates that the yaw frequency is switching between double and quadruple times the wave frequency. In comparison with Figure 6-78 a), it can be seen that during yaw lock-in, the wave frequency ratio is 2 or 4, ensuring that the component lift frequency resonates with the natural frequency. It is also evident from the frequency ratios in Figure 6-78 that the yaw peak around the sway reduced velocity of zero is caused by coupled vibrations due to sway lock-in. Similarly, the crossflow peak around the sway reduced velocity of 3 can be attributed to coupling with yaw lock-in.

Figure 6-79 a) and b) demonstrates the yaw frequency response plotted against the yaw reduced velocity and effective yaw maximum reduced velocity respectively. In comparing a) and b) it can be inferred that the yaw peak at the yaw reduced velocity of around 1.5 is due to yaw lock-in with the lift component at four times the wave frequency. It can be revalidated from Figure 6-79 b) that the effective reduced velocity or horizontal particle velocity is the governing parameter controlling lock-in vibrations in regular waves with imposed current experiencing flow reversal. Figure 6-79 a) further reveals that the yaw peak around the reduced velocity of 5 is due to yaw lock-in under flow scenarios not experiencing flow reversal. It can be concluded that in the absence of flow reversal, current speed or reduced velocity is the governing parameter controlling lock-in response.

Figure 6-80 illustrates the wave frequency ratios of the responses plotted against the effective  $KC$  number based on the maximum horizontal particle velocity, as derived in Section 5.15.1. The  $KC$  number of the regular wave is around 12, corresponding to zero current. It is evident in the figure that the frequency components of the lift force in regular waves are considerably affected by the presence of imposed current. Lift components are observed to be present up to the fourth multiple of the wave frequency, even in high imposed currents eliminating flow reversal. The presence of the lift component even at the fourth multiple of the wave frequency reveals that the effective  $KC$  number of the flow is increased by the imposed current, as evident from the yaw lock-in at a  $KC+$  (Section 5.15.1, Equation 5-250) of around 20. It may be inferred that

the jack-up responds to the lift frequency component closest to the natural frequency, originating from either of the half cycles.

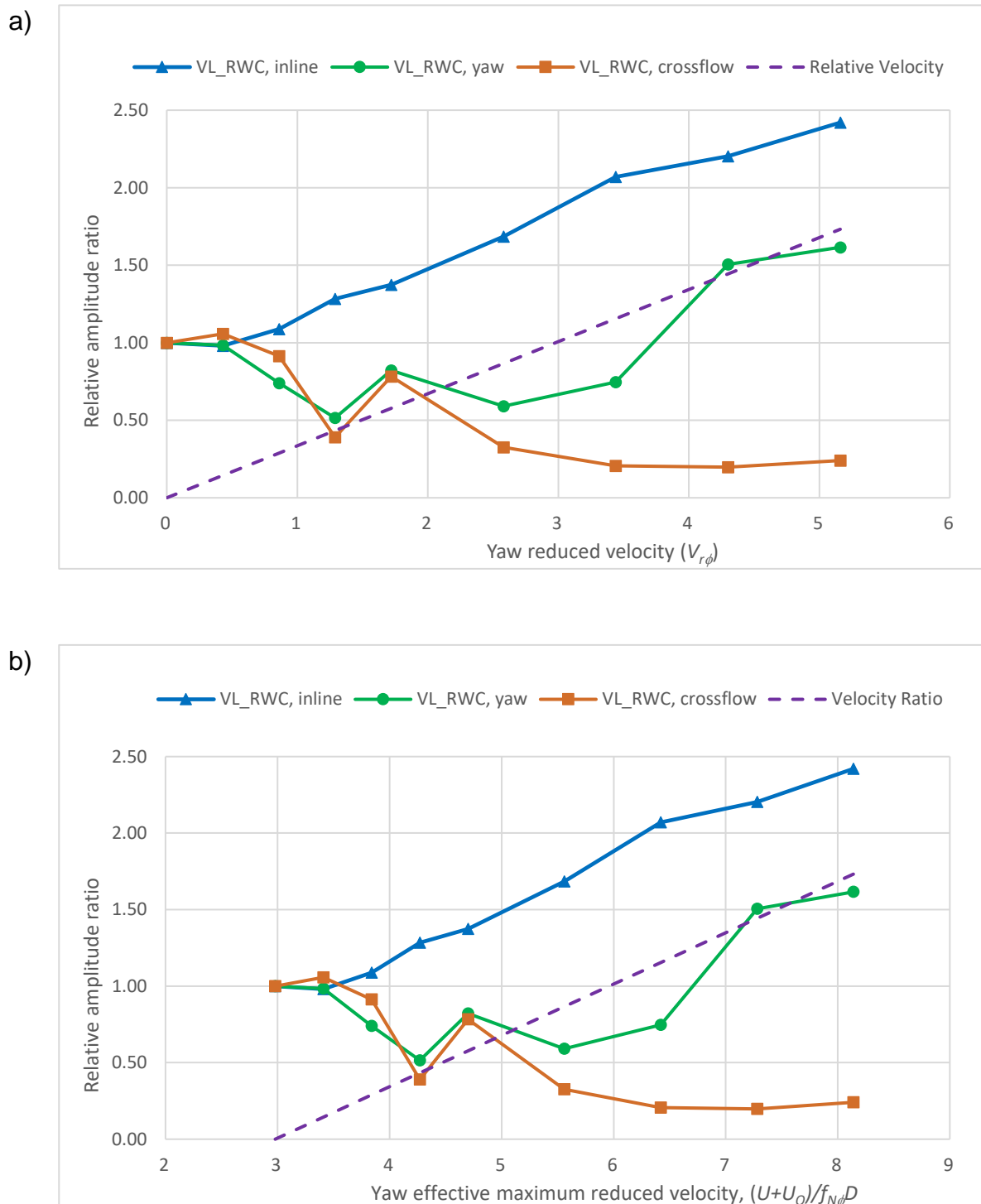


Figure 6-77: Inline, crossflow and yaw amplitude response in regular wave with imposed current, a) against yaw reduced velocity based on current only, b) against yaw reduced velocity based on maximum horizontal particle velocity  $((U+U_O)/f_{N\phi}D)$

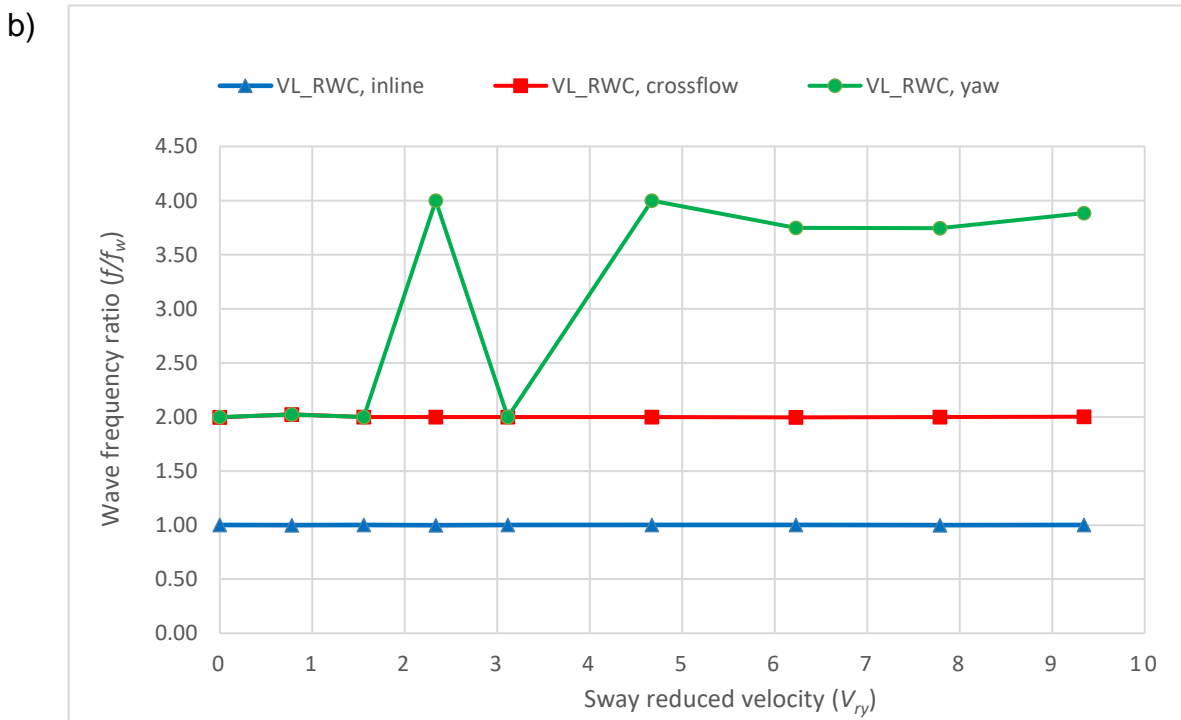
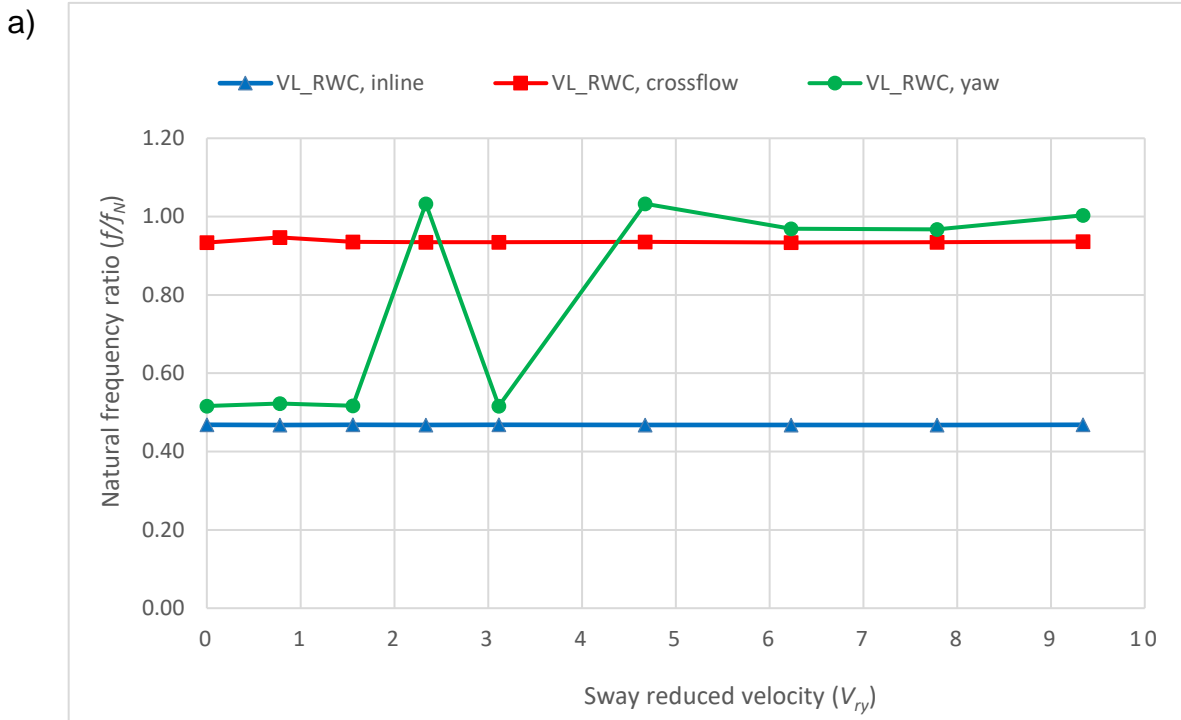


Figure 6-78: Inline, crossflow and yaw frequency response in regular wave with imposed current versus sway reduced velocity, a) natural frequency ratio, b) wave frequency ratio

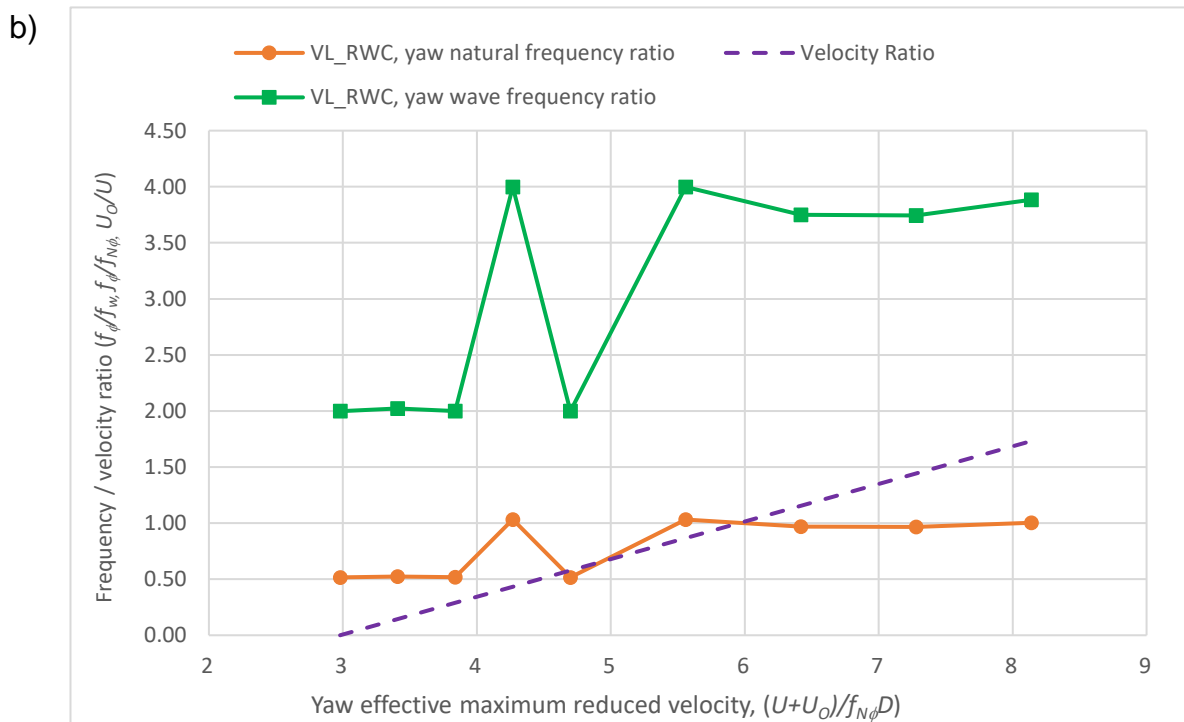
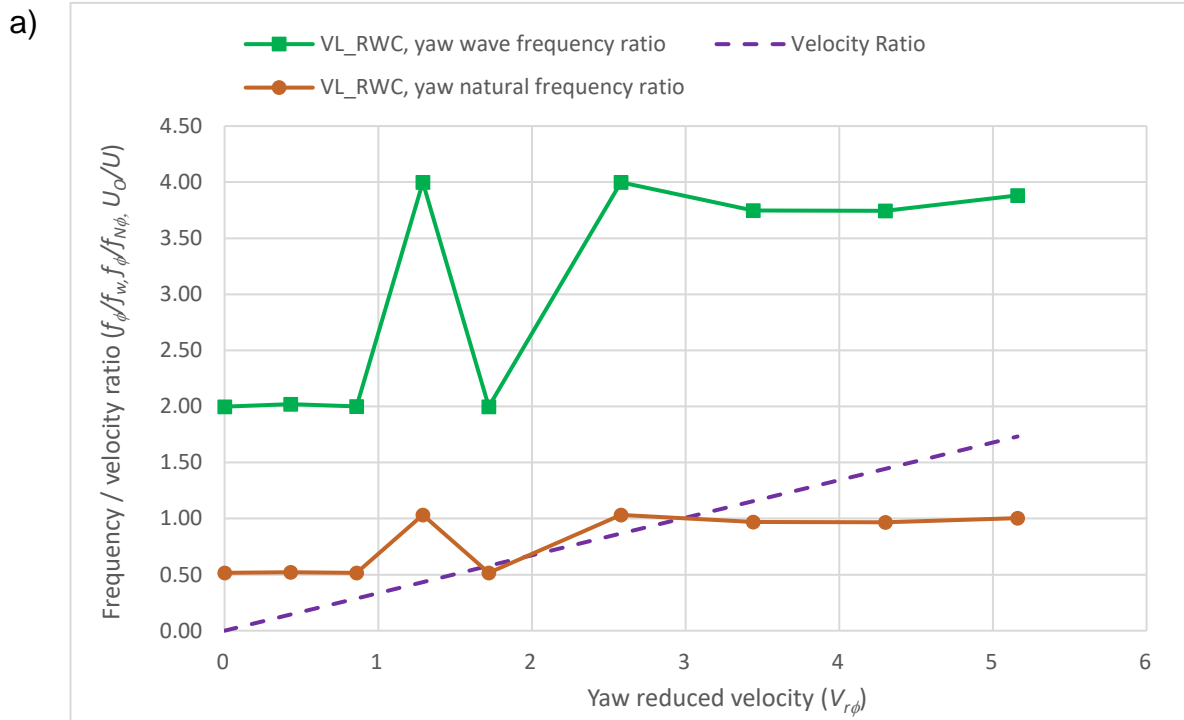


Figure 6-79: Yaw frequency response in regular wave with imposed current, a) against yaw reduced velocity based on current only, b) against yaw reduced velocity based on maximum horizontal particle velocity ( $(U+U_0)/f_{N\phi}D$ )

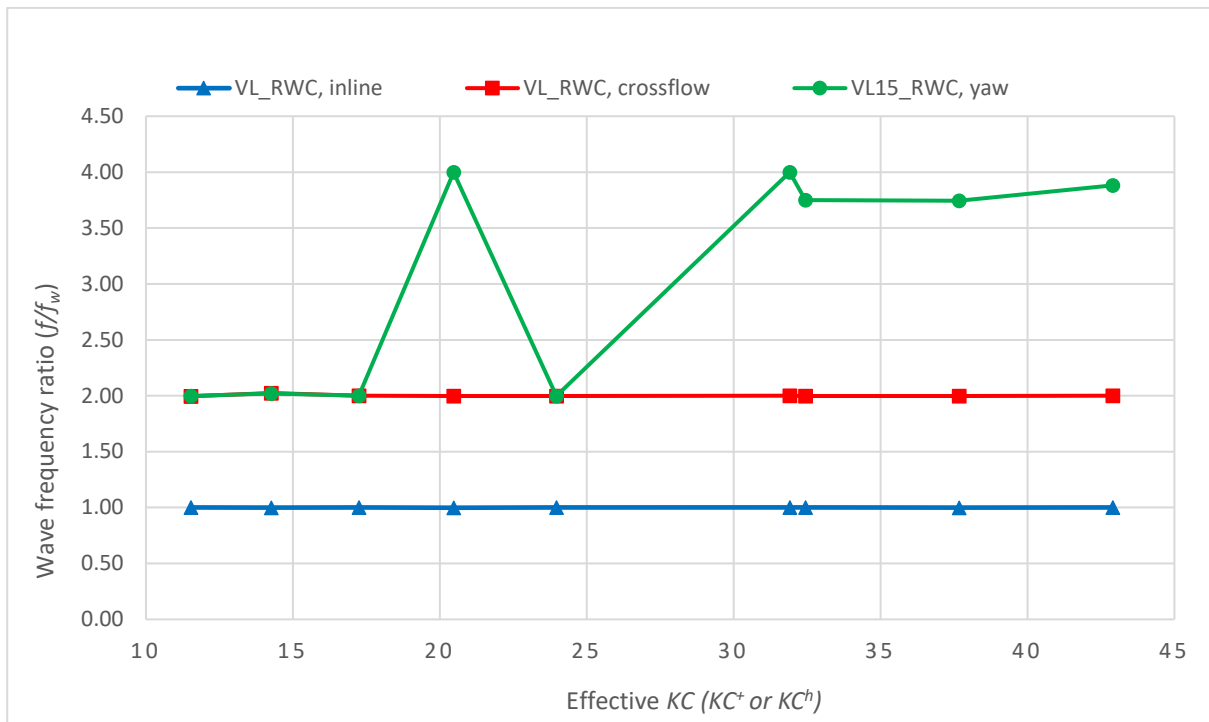


Figure 6-80: Inline, crossflow and yaw frequency response (wave frequency ratio) in regular wave with imposed current versus effective  $KC$  number based on maximum horizontal particle velocity.

### 6.10 Response Tests with various Leg Designs

Response tests were carried out in uniform current with various prevalent leg designs mentioned in Section 6.1.5 to ascertain the effect on jack-up VIV. Free decay tests were also carried out with the leg designs, LD1H3 and LD1H0 in water to account for the effect of the difference in stiffness and added mass respectively. The results of the free decay tests are presented in Table 6-13.

It can be seen in Table 6-13 that the sway and yaw natural frequencies of the model increased when fitted with the mentioned leg designs. This can be attributed to the absence of entrapped mass in the case of LD1H0 and increase in stiffness due to a lesser number of leg holes in the case of LD1H3. The stiffness of LD1H0 has not increased since the design was furnished from LD1H4 by blanking the holes with cello tape, retaining the stiffness. The response test results with various leg designs are summarised in Table 6-14.

Table 6-13: Free decay test results with various leg designs

<b>Sway</b>							
Test Case	Damping Ratio	Natural Frequency (Hz)	Natural Period (s)	Added Mass (kg)	Leg Added Mass Coefficient	Fluid Damping (Ns/m)	Fluid damping ratio
NVL, 890WD, LD1H0	0.059	1.27	0.79	1.17	1.08	4.64	0.02
NVL, 890WD, LD1H3	0.047	1.27	0.79	1.07	0.99	2.32	0.01
<b>Yaw</b>							
Test Case	Damping Ratio	Natural Frequency (Hz)	Natural Period (s)	Added Mass MI (kgm <sup>2</sup> )	Leg Added Mass Coefficient	Fluid Damping (Nms/rad)	Fluid damping ratio
NVL, 890WD, LD1H0	0.083	1.96	0.51	0.10	0.69	0.95	0.04
NVL, 890WD, LD1H3	0.061	1.92	0.52	0.11	0.70	0.50	0.02

Table 6-14: Response tests results with various leg designs in uniform current

Case	Leg Design	Local Heading	$m^*$	$k_\phi$	$y_{O,rms}/D$	$y_{O,max}/D$	$R_{\phi\phi_{O,rms}}/D$	$R_{\phi\phi_{O,max}}/D$
NVL16_LD1H4_LH0	LD1H4	0	4.73	0.275	0.08	0.12	0.059	0.11
NVL16_LD1H3_LH0	LD1H3	0	4.73	0.275	0.05	0.09	0.033	0.06
NVL16_LD1H3_LH180	LD1H3	180	4.73	0.275	0.08	0.15	0.065	0.13
NVL16_LD1H10	LD1H0	-	4.46	0.268	0.11	0.18	0.061	0.13

### 6.10.1 Inline Response

Figure 6-81 illustrates the inline amplitude response of the model for various leg designs in the uniform current. It can be observed that none of the leg designs experiences inline VIV though galloping is observed at large current speeds.

### 6.10.2 Crossflow Response

Figure 6-82 demonstrates the crossflow VIV amplitude response of the jack-up for various leg designs in the uniform current. All three leg designs are found to experience crossflow VIV with rms amplitudes in the order of 0.10 D. It is noted that LD1H0 exhibits the highest sway response which can be attributed to the reduction in mass ratio due to the buoyant legs. The response of LD1H3 at a local heading of 180 degrees is comparable with that of LD1H4, though the responses are slightly higher for the former at higher reduced velocities. Surprisingly, the crossflow response is found to be

considerably lesser for LD1H3 at a local heading of zero degrees. This may be attributed to the possible disruption of the synchronised vortex shedding along the legs due to the presence of pin holes at 120 degrees from the forward stagnation point on either side of the leg, near to the separation points under high incoming turbulence (Sadeh and Saharon, 1982). Hence the leg design LD1H3 with a local heading of 0 degrees to the flow can be considered as a practical solution for VIV reduction.

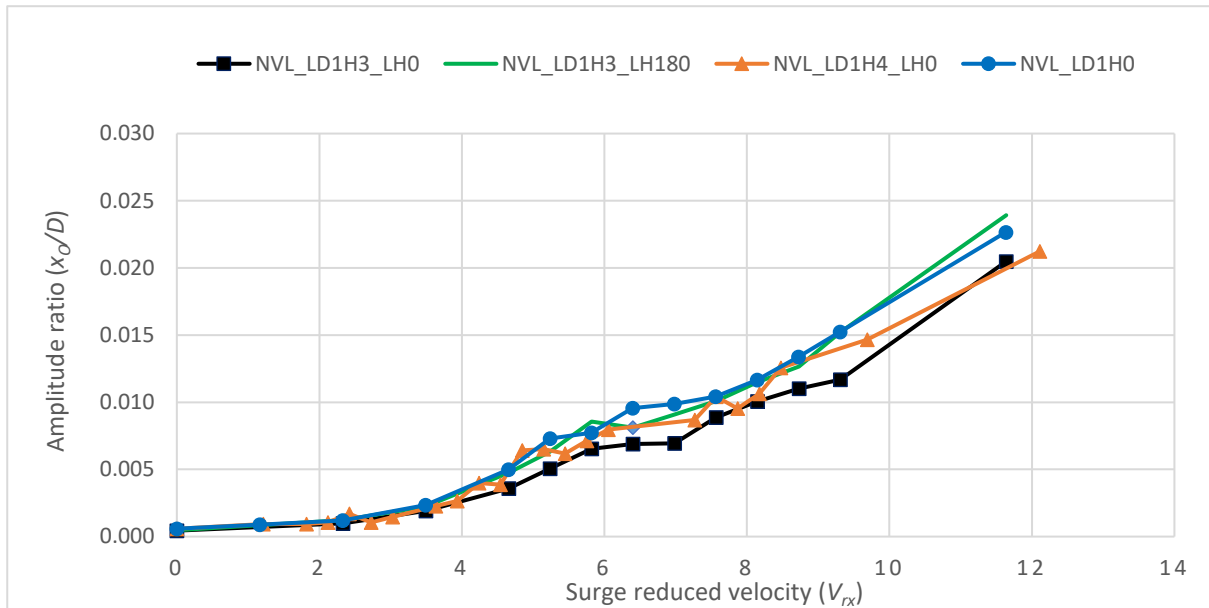


Figure 6-81: Inline amplitude response versus reduced velocity for various leg designs

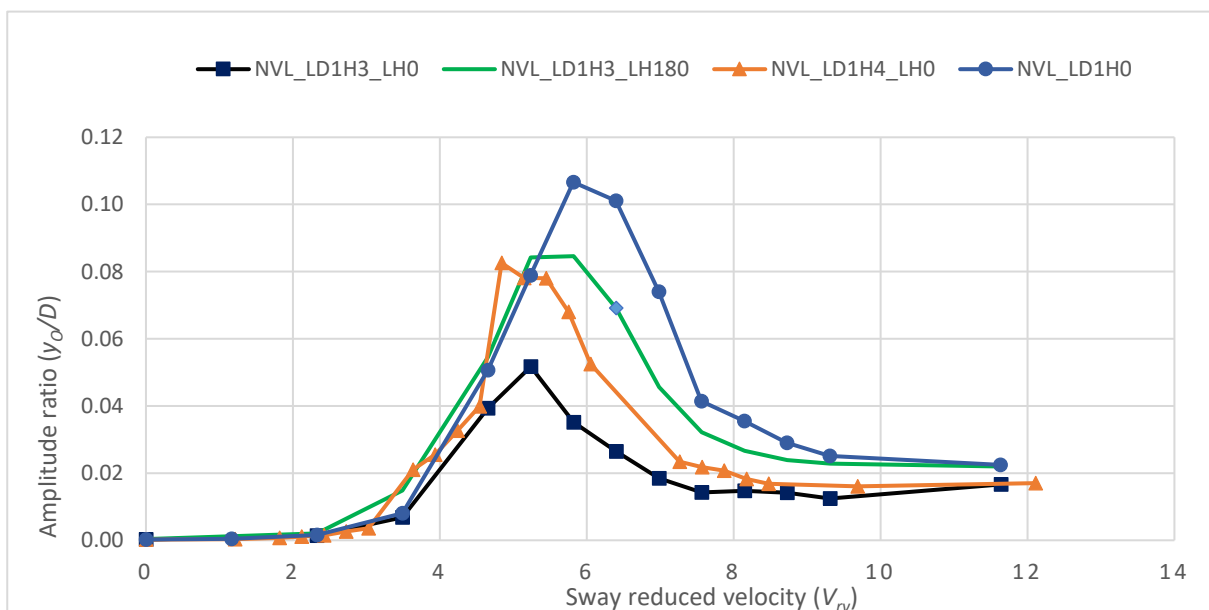


Figure 6-82: Crossflow amplitude response versus reduced velocity for various leg designs

The crossflow frequency responses of the various leg designs plotted against the respective reduced velocities are illustrated in Figure 6-83. It can be observed that a lower sway lock-in regime with a frequency ratio of 1 is experienced by all the leg designs. However, the upper yaw coupling regime with a frequency ratio around 1.50 is experienced only by LD1H4 and LD1H3 at a local heading of 180 degrees, though the regime is too small for the later. The sway lock-in regime is found to be quite large for LD1H0 and LD1H3 at a local heading of zero degrees.

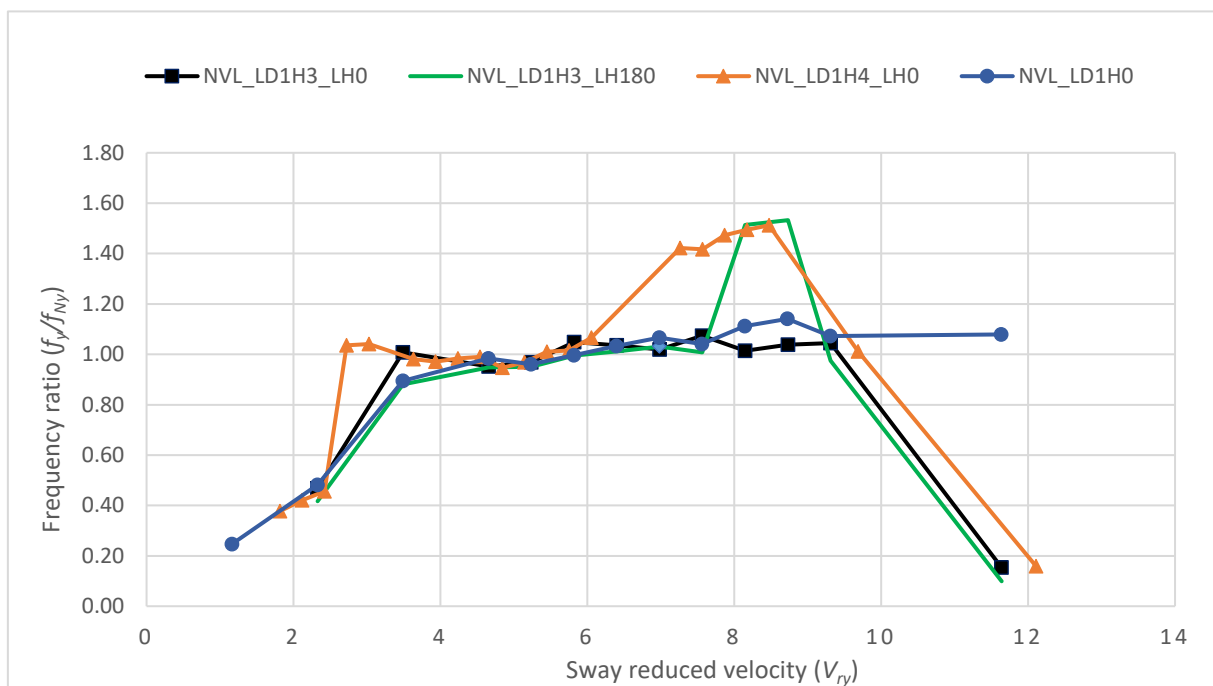


Figure 6-83: Crossflow frequency response versus reduced velocity for various leg designs

### 6.10.3 Yaw Response

Figure 6-84 displays the yaw VIV response of the jack-up for various leg designs in uniform current, plotted against the yaw reduced velocity. All three leg designs are found to experience yaw VIV with rms amplitudes in the order of  $0.06D$ . The designs, LD1H0 and LD1H3 at a local heading of 180 degrees exhibit the highest yaw response with large lock-in regimes. The yaw response of LD1H4 is also found to be quite significant. Like the crossflow response, the yaw response is found to be considerably lesser for LD1H3 at a local heading of zero, which can be attributed again to the disruption of synchronised vortex shedding due to the presence of pin holes. The

mentioned observation reconfirms that the leg design LD1H3 at a local heading of 0 degrees to the flow can be used as a practical solution for the reduction of jack-up VIV.

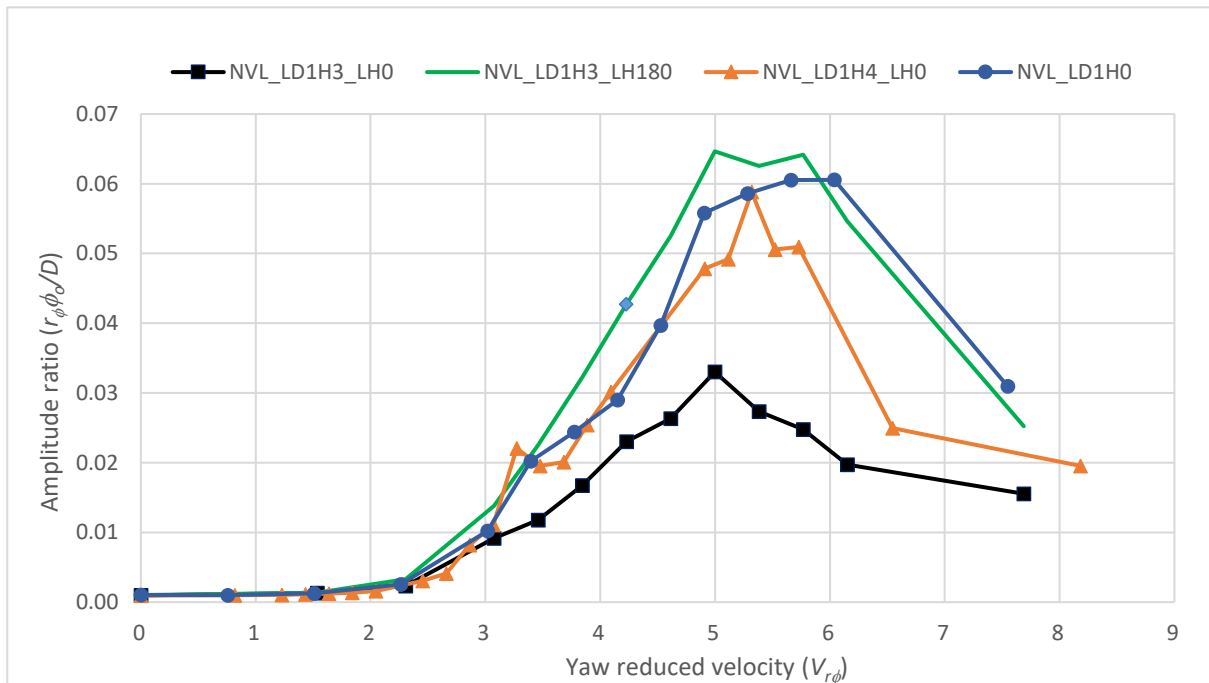


Figure 6-84: Yaw amplitude response versus yaw reduced velocity for various leg designs

The yaw frequency response of the leg designs is illustrated in Figure 6-85. It can be noticed that all the designs exhibit prolonged upper yaw lock-in regime with a frequency ratio of 1. All the designs are also found to exhibit the lower sway coupling regime with a frequency ratio of around 0.60. The leg design, LD1H4 is found to exhibit a weak yaw lock-in due to inline excitation at a reduced velocity around 2, though the corresponding amplitude response is negligible.

The combined crossflow response of the model considering both the sway and yaw vibrations plotted against the current is illustrated in Figure 6-86. The leg design with no holes, LD1H0 experiences resultant response of considerable magnitudes making the jack-up practically redundant, except at low currents. LD1H4 and LD1H3 at 180 degrees local heading are also found to exhibit considerable combined response with large combined lock-in regimes. LD1H3 at 0 local headings is found to have a considerably low VIV response throughout the currents except at the crossflow resonance point.

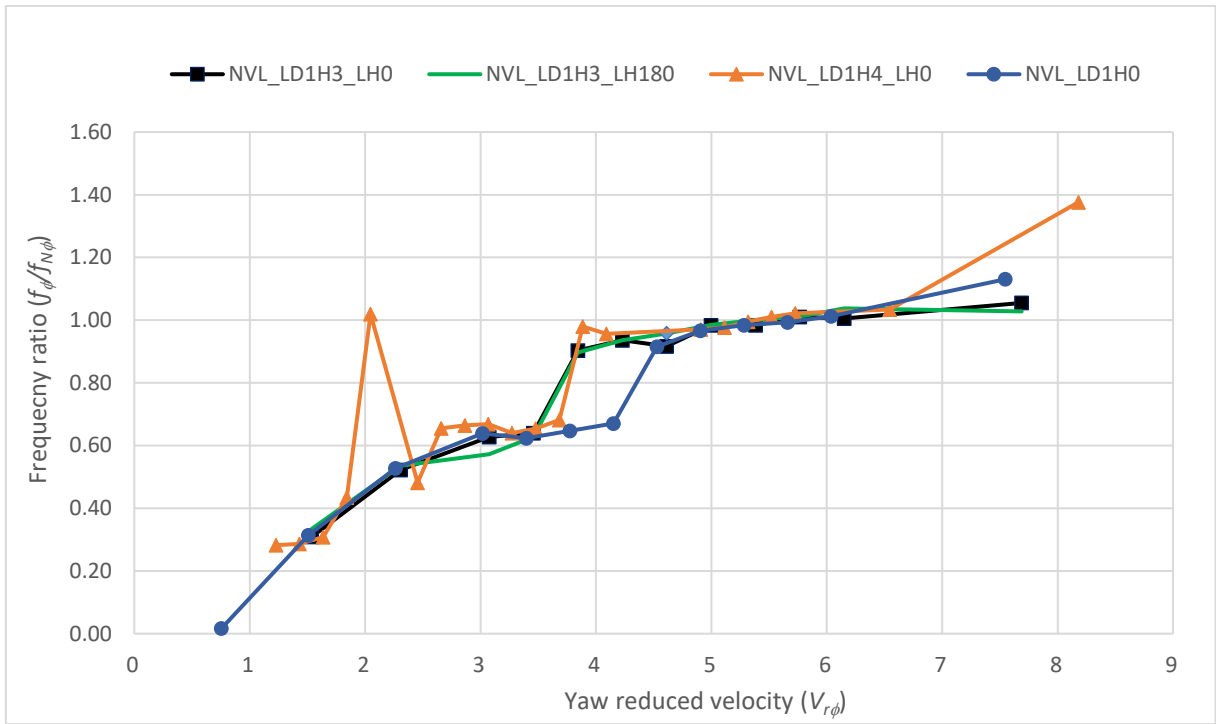


Figure 6-85: Yaw frequency response versus yaw reduced velocity for various leg designs

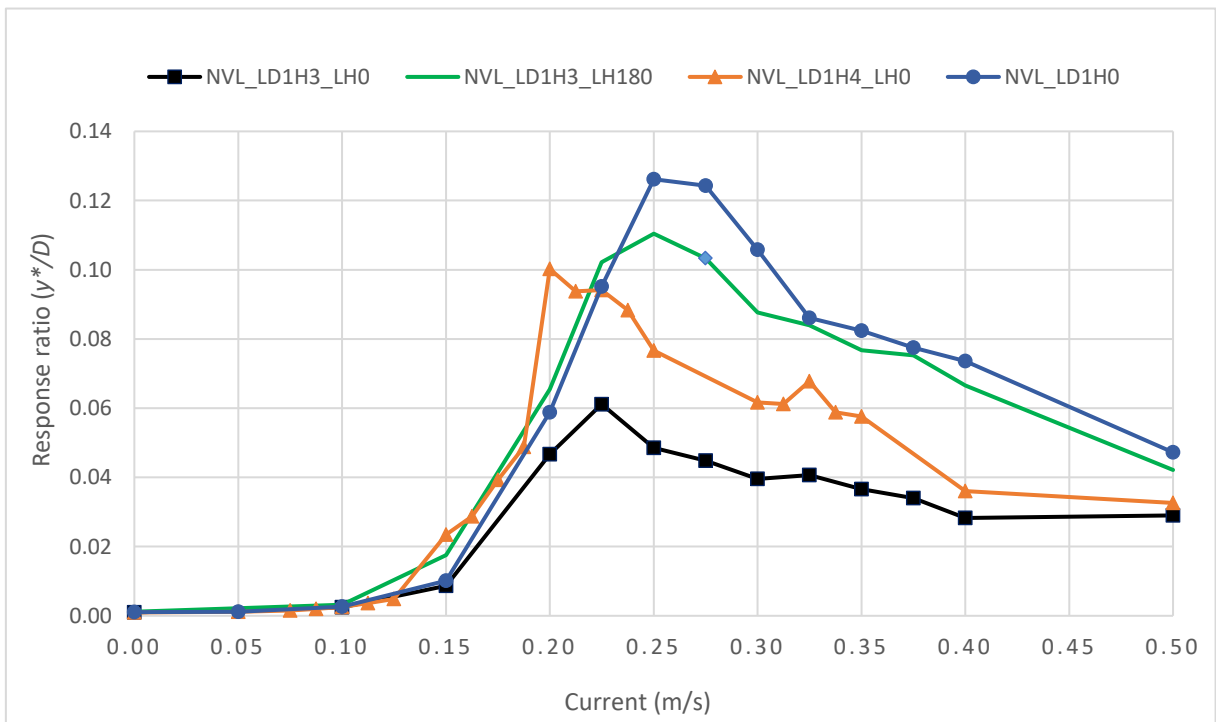


Figure 6-86: Combined crossflow response versus current for various leg designs

Figure 6-87 demonstrates the steady or mean inline response of the jack-up model corresponding to various leg designs. It can be seen that the mean inline response of

LD1H0, with no leg holes, is considerably higher than that of other designs. This can be attributed to the higher mean drag amplification experienced by LD1H0 due to aggressive crossflow and combined vibrations with amplitudes and lock-in range considerably higher than other designs, as evident in Figure 6-82 and Figure 6-86 (also see Section 6.6.5). The inline response of the design, LD1H4 is also found to be nominally higher than LD1H3, possibly due to a lower leg stiffness.

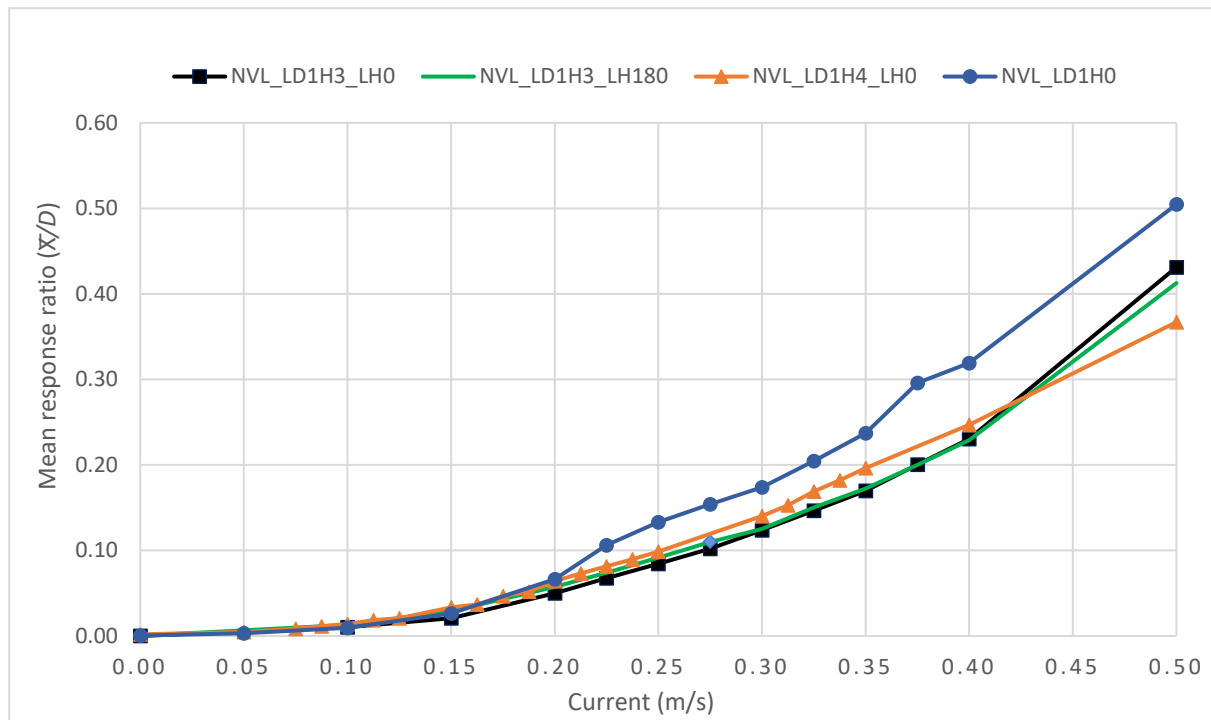
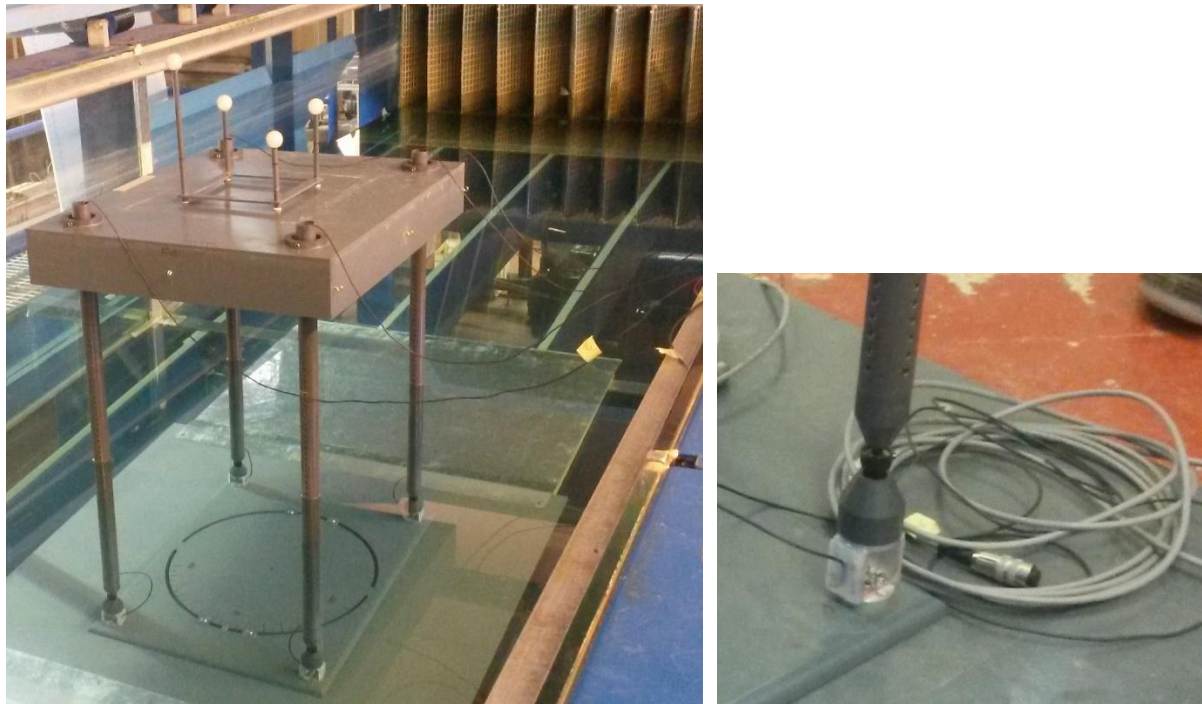


Figure 6-87: Inline mean response versus current for various leg designs

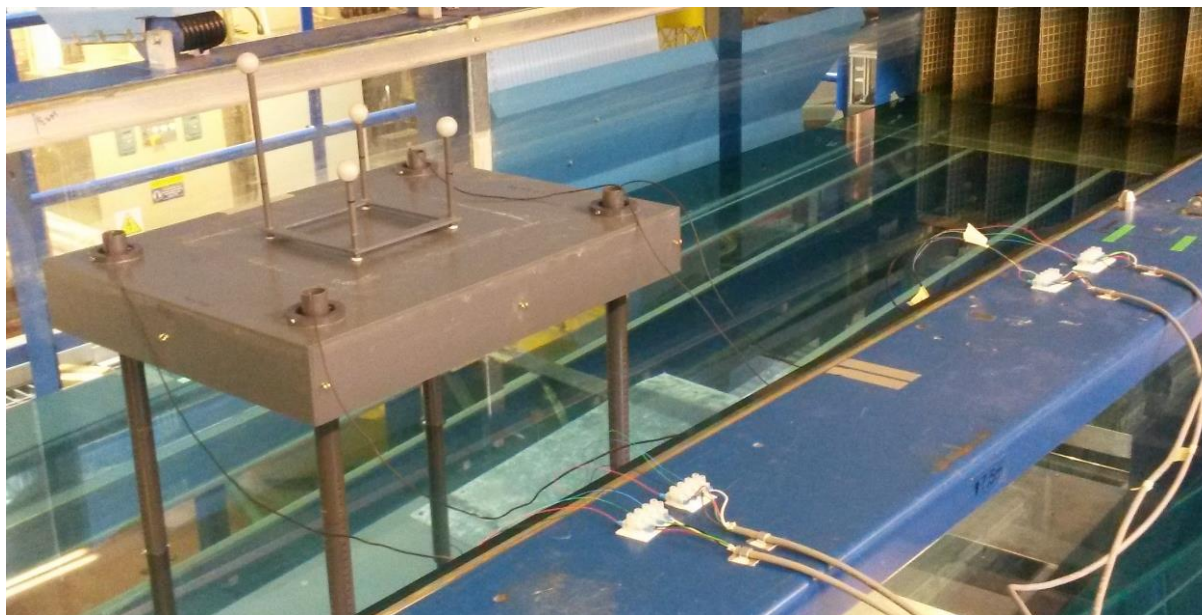
### 6.11 Force Tests

Force tests were carried out with the jack-up model fitted with load cells below leg footings. The load cells were made of strain gauges mounted on aluminium frames and waterproofed by coating with a transparent silicone sealant. The load cells were carefully calibrated prior to installation. The necessary cabling of the load cells is routed through the cylindrical legs, and excess length of the cables was maintained to ensure adequate slackness and thereby minimum effect on the model stiffness and damping. Simultaneous to the force measurement, the responses of the model were also measured to correlate between the forces and the displacements. Figure 6-88 displays the model fitted with the load cells and the experimental setup for the force tests.



a)

b)



c)

Figure 6-88: a) Model setup for force tests, b) leg footing fitted with load cell, c) electric cabling for load cell leading to the amplifier

The load cells measure the base shear force acting on the leg footings. Base shear provides adequate quantification of the forces acting on the legs and includes the effect of the vortex induced forces as well as inertial forces due to dynamic accelerations. As

the load cells were able to measure forces along only one of the horizontal axes at a time due to the limitations of available data channels, the experiments were carried out for the inline and crossflow directions separately. The force tests were carried out in steady current at a water depth of 940mm, which corresponded to an effective water depth of 780 mm from the leg ball joint to the still water surface. The global and local headings of the model and leg respectively are kept at zero, and the leg design was LD1H4. The details of the force tests are shown in Table 6-15.

Table 6-15: Summary of force test results

Test Case	Description	Constraint	Load cell	$y_0, rms/D$	$C_{Fy_0, rms}$	$C_{Fxo, rms}$	$C_{Fx, mean}$
NVL_LCx_Fix	NVL	y	x	0.01	-	0.10	1.07
NVL_LCx	NVL	Free	x	0.08	-	0.31	1.20
VL_LCy	VL	Free	y	0.03	0.52	-	-
RVL_LCy	RVL	Free	y	0.05	0.55	-	-
NVL_LCy	VL	Free	y	0.07	0.59	-	-

### 6.11.1 *Inline Force*

The inline force tests were carried out with both free and transversely constrained model. In the constrained model set up, the motion response in the crossflow direction is limited by means of four transverse polyester guy lines at the four corners, effectively making the model free to respond only along the inline direction. The guy lines were terminated to a specially designed clamping arrangement on the tank sides by means of the coil springs of high stiffness. The spring stiffness was high enough to ensure that the model is sufficiently constrained transversely at least in the crossflow lock-in range without affecting the inline response. Figure 6-89 a) demonstrates the configuration of the transversely constrained model. The forward and aft transverse guy lines with coil springs on the starboard side are clearly visible along with the cabling arrangement and the load cells. Figure 6-89 b) illustrates the enlarged view of the forward starboard guy line.

Figure 6-90 illustrates the time series of the total inline base shear ( $F_x$ ) of the free model and the one constrained in the crossflow direction. The test was carried out for the lightest operating condition of the jack-up, NVL. It can be seen that the magnitude

of the inline forces is considerably high for the model, which is free to move along the crossflow direction with an increase in amplitude by approximately 200 %.

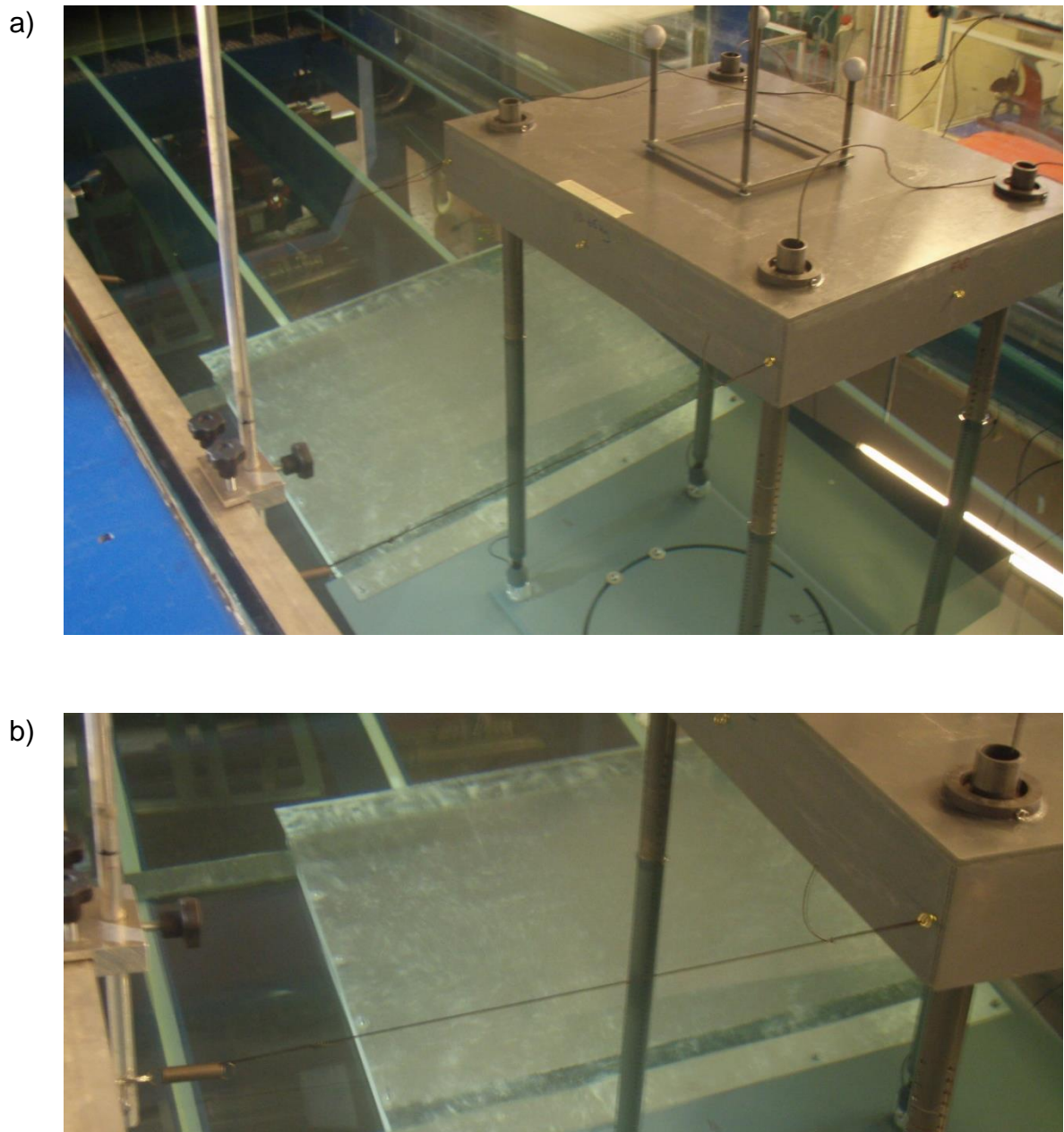


Figure 6-89: a) Transversely constrained model configuration, b) Forward starboard transverse guy line

Figure 6-91 displays the inline average steady and oscillatory base shear response of the free and constrained models with the reduced velocity. The force coefficient  $\left(C_{FX} = F_X / \left[4 \times \frac{1}{2} \rho D h U^2\right]\right)$  represented in the  $y$  axis is analogous to the average drag coefficient of the legs. It can be observed that for the free model, both the mean and

oscillatory inline forces are significantly higher due to the force amplification with the crossflow response. The crossflow motion responses ( $y_0/D$ ) of both the models are also displayed with reference to the secondary axis. It can be inferred that the increase in the oscillatory inline force is partially due to the increase in oscillatory drag caused by the enhanced synchronisation of the vortices along the legs during crossflow lock-in and partially due to the inertial acceleration of the elevated mass with the coupled inline vibrations.

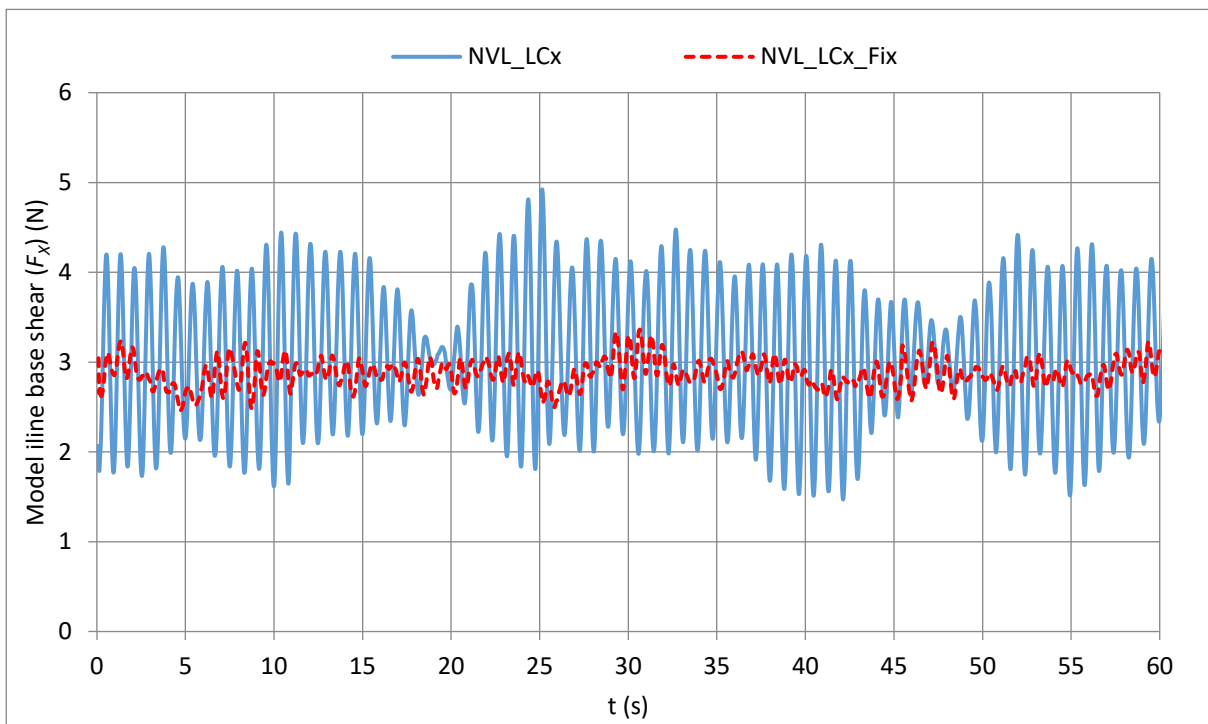


Figure 6-90: Inline base shear force time series in steady current for NVL around a reduced velocity of 5, for the free and constrained models

Figure 6-92 shows the variation of the steady inline force coefficient ( $\bar{C}_{FX}$ ) with the crossflow amplitude ratio. It can be seen that the values lie on a linear expression, almost similar to the equation proposed for mean drag amplification (Blevins, 2001) based on experiments with circular cylinders, demonstrated in Figure 1-8. It can be inferred that the amplification of the mean inline force is due to the mean drag amplification on the vibrating legs, caused due to the increase in the effective projected area to the flow.

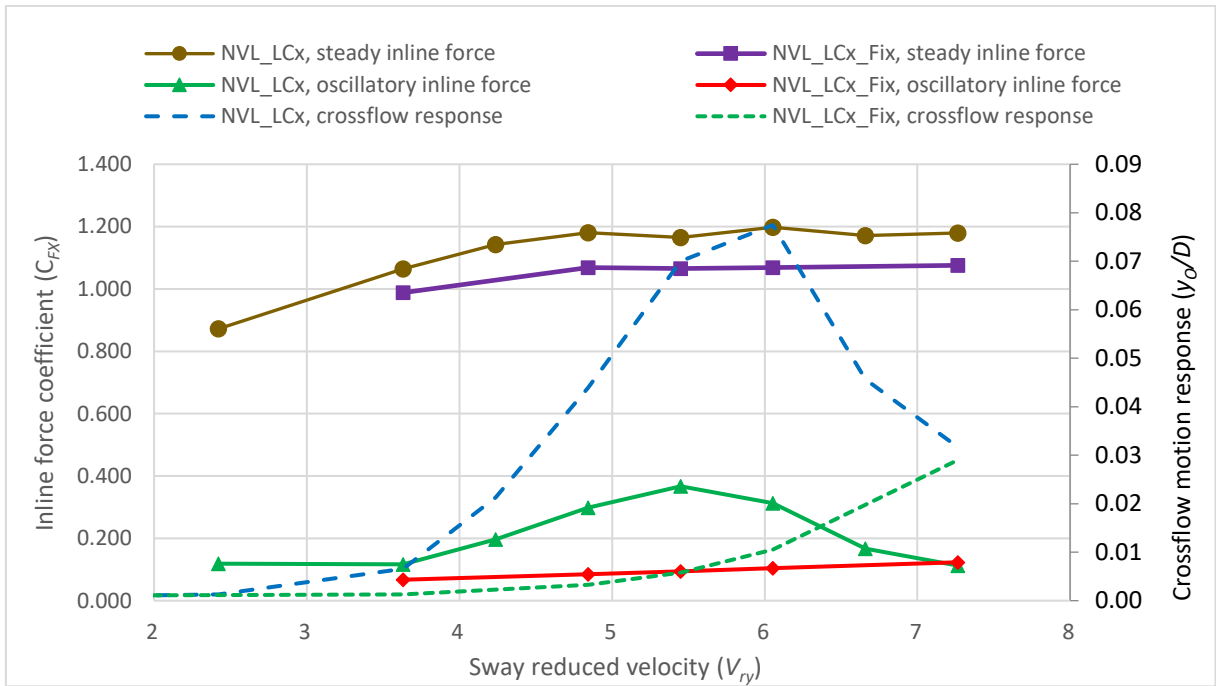


Figure 6-91: Inline force response versus reduced velocity

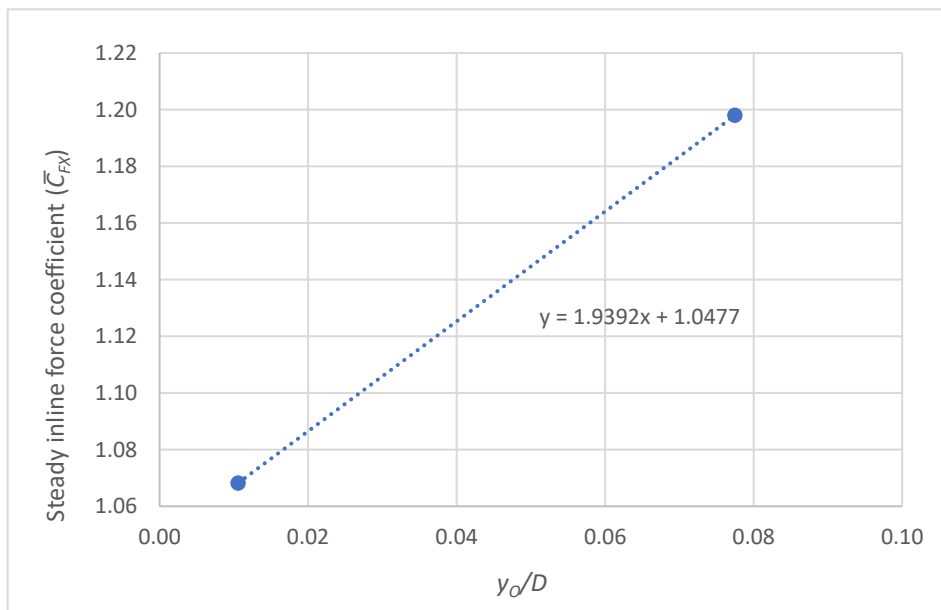


Figure 6-92: Mean drag amplification with crossflow response

### 6.11.2 Crossflow Force

The crossflow force tests were carried out by using a free model. The tests were carried out for the three loading conditions of the jack-up shown in Table 6-15. Figure 6-93 illustrates the time series of the total leg crossflow base shear ( $F_y$ ) during crossflow lock-in condition in the steady current. It can be seen that the crossflow base shear

force assumes very high values during crossflow lock-in vibrations. This can be partially attributed to the lift amplification due to enhanced vortex synchronisation along and about the legs, and partially due to the inertial acceleration of the elevated mass with the crossflow lock-in vibrations.

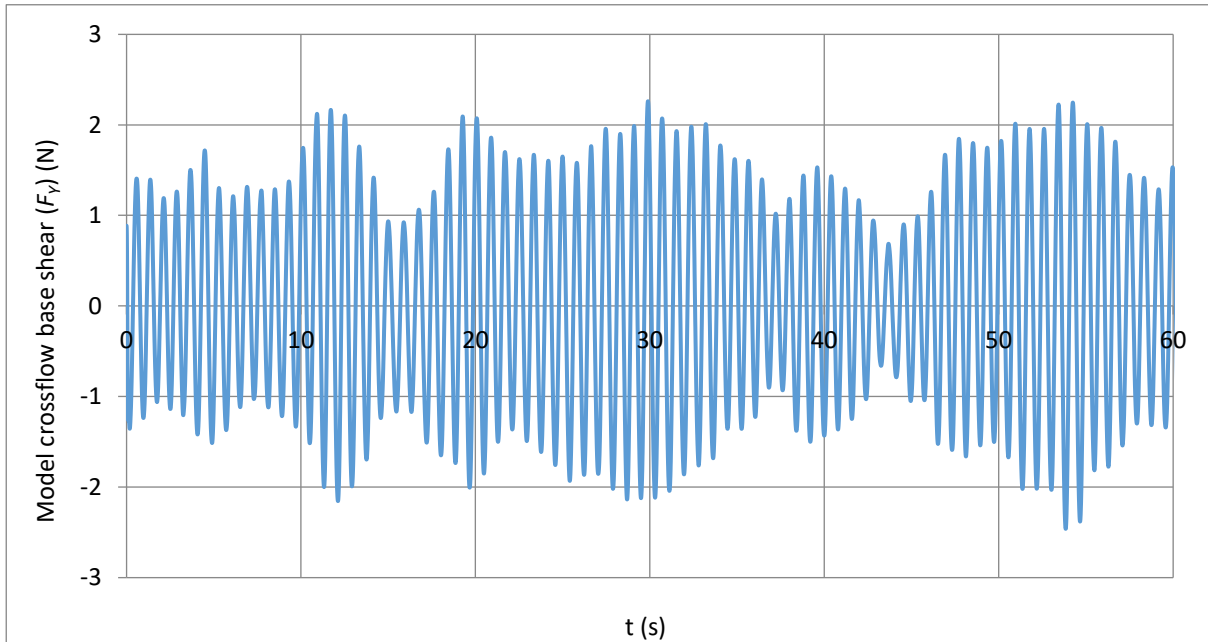


Figure 6-93: Crossflow base shear force time series in steady current for the test case, NVL at a reduced velocity approximately 5

The rms amplitude of the oscillatory crossflow force coefficient ( $C_{FY} = F_Y / [4 \times \frac{1}{2} \rho D h U^2]$ ), which is analogous to the lift coefficient is illustrated in Figure 6-94, for all three mentioned load cases. The force coefficient presented is the average of the force response of the four legs. The rms crossflow motion response is also displayed in the same figure. It can be observed that the crossflow force response increases with the response ratio, indicating lift amplification and dynamic inertial loading. It can be observed that the mean force response assumes very low value during yaw lock-in, as evident from the load case, NVL\_LCy for reduced velocity greater than 8. This can be attributed to the cancellation of the crossflow forces of the upstream and downstream legs, which are out of phase to each other causing yaw excitation. The synchronised out of phase vortex shedding from the upstream and downstream legs during yaw VIV is evident from the results of the numerical simulations, presented in Section 7.8.8.

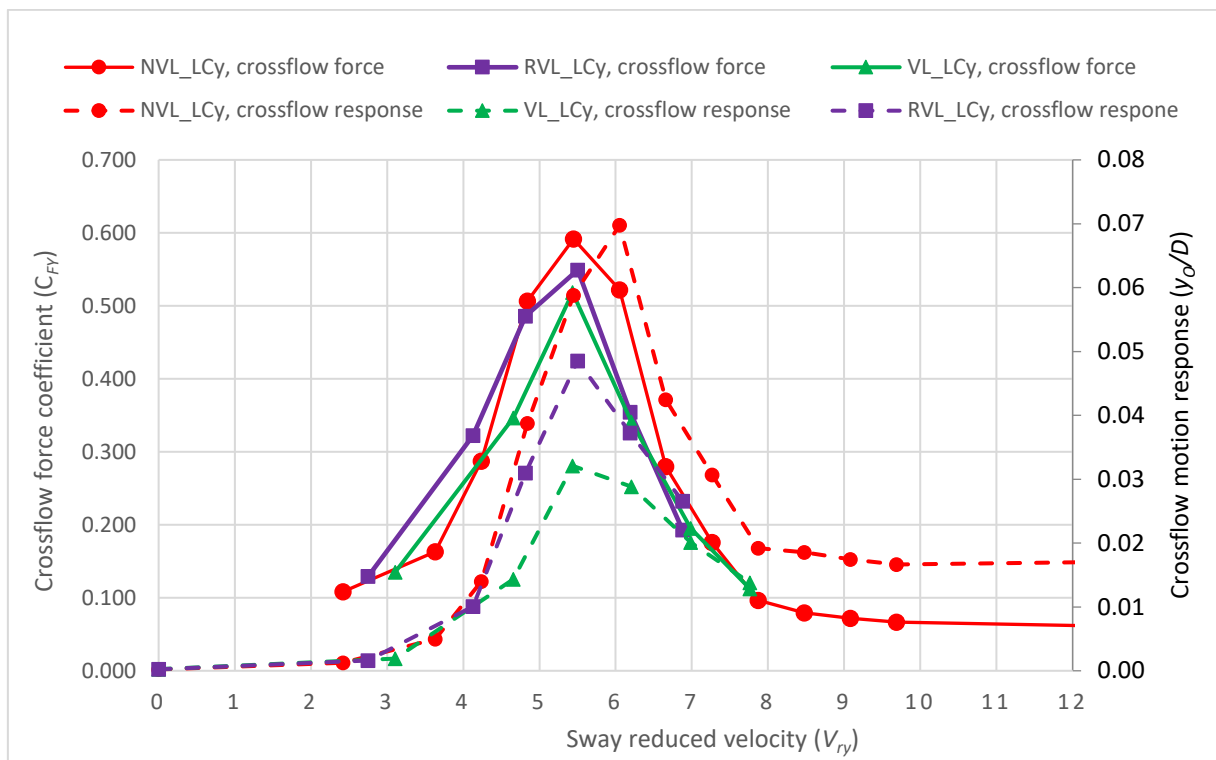


Figure 6-94: Crossflow average oscillatory force response of the legs versus reduced velocity

Figure 6-95 demonstrates the variation of the individual leg oscillatory crossflow force coefficient ( $C_{FYL}$ ) with the reduced velocity for the lightest load case, NVL\_LCy. The crossflow and yaw amplitude ratios are also illustrated in the figure for consideration. It can be observed that during crossflow lock-in, the maximum leg individual crossflow force coefficient approaches 0.80, much higher than the average value. An average force coefficient lower than the mathematical average of individual leg values indicates that a part of the individual leg crossflow forces, out of phase with each other is utilised towards yaw excitation, as evident from the coupled yaw vibrations observed during crossflow lock-in (see Sections 6.6.2 and 6.6.3). Further, the mean crossflow force is much lower than the individual values in the yaw lock-in regime. This can also be interpreted as yaw moment amplification during yaw lock-in, wherein the mean crossflow force of the model reduces considerably due to the enhanced synchronisation of the lift forces of the upstream (forward) and downstream (aft) legs which are at opposite phases, as demonstrated in Section 7.8.8.

The crossflow force coefficient, when plotted against the respective response amplitude ratio yields the curve illustrated in Figure 6-96. It can be observed that the force amplification is nearly linear with respect to the amplitude response due to the

combined effect of lift amplification and inertial amplification. It is a clear demonstration that aggressive vibrations can considerably increase the leg base shear forces and correspondingly leg bending moments and induced stresses.

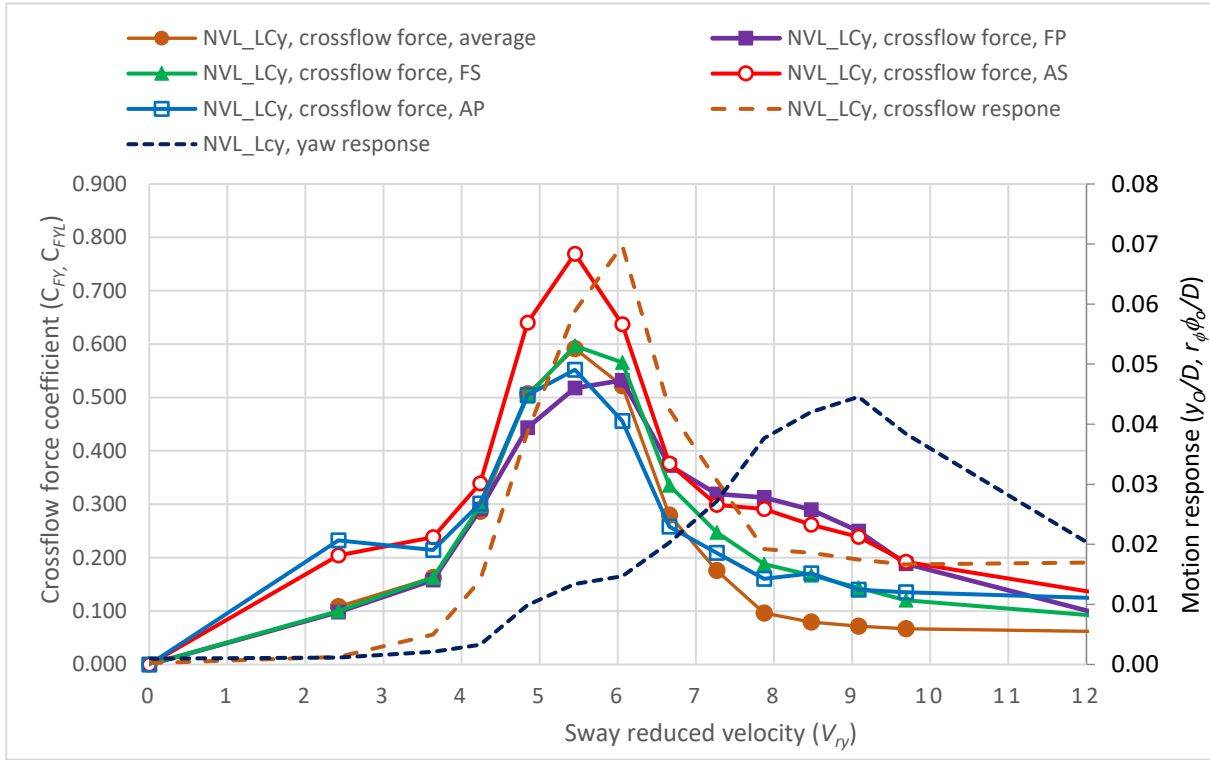


Figure 6-95: Crossflow oscillatory force response of the leg versus reduced velocity

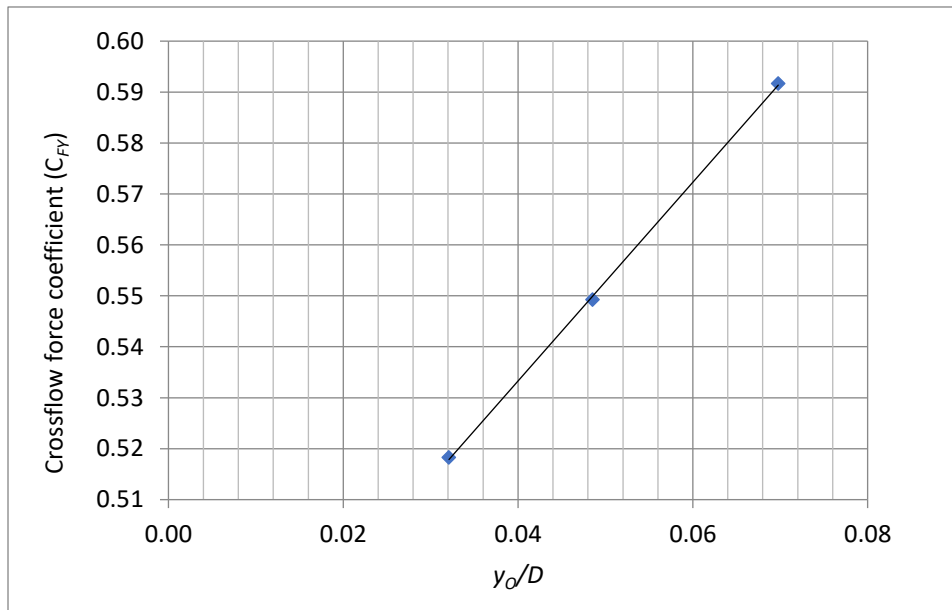


Figure 6-96: Crossflow mean oscillatory force coefficient versus amplitude ratio.

## 6.12 Discussion

The experimental investigation revealed that jack-up experiences significant crossflow and yaw VIV with large lock-in regimes in uniform currents, with maximum amplitude ratios in excess of 0.1D. The lock-in regimes of both the VIV modes were found to extend over the corresponding reduced velocity range, from 3 to 7. In general, the crossflow and yaw responses were found to reduce with increase in effective mass damping and inertia damping parameters respectively. The crossflow and yaw VIV were also observed to couple at higher current speeds, causing very high combined leg amplitude response. The jack-up was found not to experience inline and yaw VIV due to oscillatory drag excitation. However, inline coupled VIV with crossflow lock-in was found to occur during oblique environmental headings in uniform currents. Experiments conducted in the wind did not reveal any of the VIV modes and lock-in vibrations, validating the developed VIV model, criteria and the importance of effective mass and inertial damping parameters in the uniform current.

The crossflow VIV in regular waves is found to be more aggressive than that observed in uniform currents. However, the lock-in regimes are found to be much narrower, and the yaw VIV is found to be less significant in regular waves. The experiments also established the inverse proportionality of the crossflow and yaw amplitude responses with the effective mass damping and inertia damping parameters respectively in regular waves. The lock-in range of the crossflow VIV was found to overlap with the lock-in range of yaw VIV, particularly in light operating conditions, causing very high combined leg amplitude response in both uniform current and regular waves. The yaw VIV was found to occur due to the lift excitation when the lift frequency approaches the yaw natural frequency of the jack-up.

The jack-up is found not to experience any significant VIV in irregular waves, possible due to the irregularities in the lift oscillations. In regular waves with imposed current, the jack-up is found to experience crossflow VIV at resonating waves with low currents in the presence of flow reversal, when the resultant horizontal particle velocity causes an effective reduced velocity around 5. When flow reversal is not present in regular waves with high imposed current, the yaw VIV is found to occur as a function of the current speed.

The leg design LD1H3 with a local heading of 0 is found to reduce the response of both the sway and yaw VIV modes considerably. On the contrary, the leg design LD1H0 is found to increase the VIV response due to the reduction in mass ratio. Free decay tests in uniform current also revealed that the added mass and fluid damping during crossflow and yaw lock-in vibrations are negative. Hence the theoretical assumption of not considering the crossflow component of the fluid damping during crossflow and yaw lock-in vibrations is validated. The force tests revealed considerable drag and lift amplification and additional dynamic loading due to the inertial acceleration of the elevated mass on the legs. Test results demonstrate that jack-up VIV can increase the leg base shear forces and correspondingly leg bending moments and dynamic stresses.

### 6.12.1 *Experimental Challenges*

The primary challenge of the experimental investigation was to obtain the similitude of structural deflections or stiffness while adopting Froude scaling law. This was achieved by selecting the appropriate material for the model and introducing correct flexibility at the leg-hull interface as per Cauchy scaling law. Another major challenge was to ensure that the scale effect on the experimental results due to the difference in model and prototype  $Re$  was minimal. This was ensured by means of the high turbulence intensity generated by the inlet grid along with the free vibrations of the legs, which represented a sufficient approximate to the prototype flow scenario.

Simulation of the pinned boundary conditions at the leg footings of the model by means of ball joints was also equally challenging. The ball joint was found to experience dry friction, which further caused nonlinear stiffness and nonlinear damping. Ensuring absolute linear dynamic behaviour of the model was a great difficulty due to the presence of ball joint friction and leg-hull interface nonlinear stiffness. Testing the jack-up model at various environmental headings was also demanding, and this had to be accomplished by means of a custom designed turntable base. The limitations on the number of available data channels made it hard for the load cells to measure forces along both the horizontal axes simultaneously. Hence, the experiments had to be conducted separately for measuring the inline and crossflow forces by changing the orientations of the load cells.

### 6.12.2 *Experimental Uncertainty*

The random nature of VIV makes the uncertainty analysis very essential in experimental investigations. A brief assessment of the experimental uncertainty was carried out based on IITC guidelines (ITTC, 2011; ITTC, 2014a; ITTC, 2014b; ITTC, 2017a), for the case of VL, 890WD in the uniform current. The crossflow rms amplitude response at the reduced velocity of 5, corresponding to the resonance was selected as the measurand for the uncertainty analysis. The uncertainty due to randomness in a single measurement was minimised by measuring the response time series for around 300 vibration cycles, resulting in a standard uncertainty of one reading as 2.5%. The contributions from the model and instrument calibration were also considered in the uncertainty analysis. The overall or combined experimental uncertainty of the crossflow rms amplitude response was evaluated based on Equation 5-41, using the principle of uncertainty propagation and root-sum-square (RSS) method.

The uncertainty contribution due to the model mass was found to be negligible due to the high resolution (10 g) of the digital scale used. However, the standard uncertainty of leg diameter (0.09%) was found to cause a relative uncertainty of 0.36% in rms amplitude response. The uncertainty in the leg diameter is found to create uncertainty in  $Re$  and consequently in the lift coefficient. The sources of uncertainties due to the instrument calibration were the tank level gauge, thermometer, velocity profilers and Qualisys measuring water depth, water temperature, current velocity and crossflow response respectively. The uncertainty contribution due to Qualisys was found to be negligible due to its high accuracy and resolution. The standard uncertainties of the water depth (0.37%), current velocity (0.88%) and temperature (0.70%) were primarily due to the low resolutions of the level gauge (0.01 m), and manufacturer specified bias limits of the velocity profiler (0.5%+1mm/s) and thermometer (0.20°C) respectively.

The standard uncertainties of the water depth and current velocity were found to result in relative uncertainties of 0.64% and 2.58% respectively in rms amplitude response. The high relative uncertainty contribution from the current velocity can be attributed to significant variation of the lift coefficient with  $Re$  in the test flow regime (Norberg, 2003). The standard uncertainty of the temperature was also found to substantially contribute to the relative uncertainty of rms amplitude response by 0.92%, attributable to the high dependency of the viscosity on the temperature which in turn affects  $Re$  and

consequently the lift coefficient. The combined uncertainty for one reading was calculated as 3.76% using RSS method and considering uncertainty propagation.

As six repeat tests were conducted over the course of the experimental investigation, the uncertainty of repeat measurement was also evaluated. The temperature range during the repeat measurements was found to be 14.1°C - 17.5°C with a mean value of 15.85°C. The range of crossflow rms amplitude response was 1.09 mm – 2.32 mm (0.03D to 0.07D) with a mean value of 1.50 mm (0.04D). In the mean of repeat tests, the relative uncertainty contribution from the mean of temperature was found to be 5.03% due to the effect of the kinematic viscosity, and the standard uncertainty of the mean of crossflow rms amplitude response was found to be 12.54%.

It was found that the overall combined uncertainty of the cross flow rms amplitude response repeat mean is 13.78%, and this corresponds to an expanded uncertainty of 27.55% at the confidence level of 95%. It can be inferred from the combined and expanded uncertainties that a larger number of repeat tests should be ideally conducted to reduce the inherent uncertainty due to the randomness of the VIV. It is emphasised that the predicted uncertainties are exclusive of the contributions from extrapolation and full scale predictions. Further, the effect of the tank blockage was also neglected in the uncertainty analysis.

### 6.12.3 *Model Nonlinearities*

The jack-up model was found to exhibit softening nonlinearity and significant hysteresis. The model hysteresis is the source of nonlinear damping, which increases with the vibration amplitudes. The leg-hull interface of the jack-up model is also affected by contact nonlinearity, causing the contact points between the legs and hull O rings to be different during successive vibration half cycles. The contact points are subjected to only compression loading, leading to the compression set built up and Mullin's softening during successive vibrations. Additionally, the ball joint supports were found to have dry friction, which is also a source of nonlinear damping. The prototype material being steel, a nearly linear material, the responses can be higher than the model results.

## Chapter 7. Numerical Investigation

This chapter presents limited numerical investigations carried out on the jack-up VIV. 2D CFD and FSI simulations were carried out in the model scale with rigidly coupled multiple cylinders representing the legs of the jack-up. The numerical simulations were carried out for a range of mass damping parameters, and various modes of the jack-up VIV were investigated. The numerical results were also compared with the results of the experimental investigation. The simulations were carried out by using the software, ANSYS Fluent.

### 7.1 ANSYS Fluent

ANSYS Fluent is a state-of-the-art computer program, used for incompressible and compressible fluid flow simulations. ANSYS Fluent supports unstructured meshes and allows to refine or coarsen the mesh based on the flow solution, called mesh adaptation. The dynamic mesh model in ANSYS Fluent can be used to model flows where the shape of the domain is changing with time due to motion on the domain boundaries. The 6DOF solver in ANSYS Fluent can be used to compute the translational and angular motion of the COG of a rigid body due to the fluid forces and moments acting on it (ANSYS, 2013a; ANSYS, 2013b).

For all flows, ANSYS Fluent solves conservation equations for mass and momentum. Additional transport equations are also solved when the flow is turbulent. ANSYS Fluent employs two numerical methods; pressure-based solver and density-based solver. In both methods, the velocity field is obtained from the momentum equations. In the density-based approach, the continuity equation is used to obtain the density field while the pressure field is determined from the equation of state. On the other hand, in the pressure-based approach, the pressure field is extracted by solving a pressure correction equation which is obtained by manipulating continuity and momentum equations. The software employs a finite volume discretization process (ANSYS, 2013b).

### 7.2 Reynolds Averaged Navier Stokes Equations

In Reynolds averaging, the solution variables in the instantaneous Navier-Stokes equations are decomposed into the time-averaged mean and fluctuating components.

Considering the velocity components ( $u_i$ ):

$$u_i = \bar{u}_i + u'_i \quad \text{Equation 7-1}$$

where  $\bar{u}_i$  and  $u'_i$  represents the mean and fluctuating velocity components respectively.

Substituting the above equation into the instantaneous continuity and momentum equations and dropping the overbar on the mean velocity yields the ensemble-averaged momentum equations or Reynolds Averaged Navier-Stokes (RANS) equations.

For incompressible flow,

$$\frac{\partial (\rho u_i)}{\partial x_i} = 0 \quad \text{Equation 7-2}$$

$$\frac{\partial (\rho u_i)}{\partial t} + \frac{\partial (\rho u_i u_j)}{\partial x_j} = -\frac{\partial p}{\partial x_i} + \frac{\partial}{\partial x_j} \left[ \mu \left( \frac{\partial u_i}{\partial x_j} + \frac{\partial u_j}{\partial x_i} \right) \right] + \frac{\partial (-\overline{\rho u'_i u'_j})}{\partial x_j} \quad \text{Equation 7-3}$$

Equation 7-2 and Equation 7-3 are called the RANS equations for the Newtonian incompressible flow (Anderson, 1995). These equations have similar general form as the instantaneous Navier-Stokes equations, with the solution variables represented as time-averaged) values. The additional terms representing the effects of turbulence ( $-\overline{\rho u'_i u'_j}$ ) is called Reynolds stresses, which is modelled to solve the equations.

### 7.3 SST $k\omega$ Turbulence Model

The turbulence model is based on the transport equations for the turbulence kinetic energy ( $k$ ) and the specific dissipation rate ( $\omega$ ). The specific dissipation rate can be defined as the ratio of the turbulence dissipation rate ( $\varepsilon$ ) to the turbulence kinetic energy. The SST model was developed to effectively blend the robust and accurate formulation of the standard  $k\omega$  model in the near-wall region with the freestream independence of the  $k\varepsilon$  model in the far field. The SST model is found to be an accurate and reliable turbulence model for adverse pressure gradient flows (Menter, 1996).

The transport equations for the SST  $k\omega$  model are (ANSYS, 2013b),

$$\frac{\partial(\rho k)}{\partial t} + \frac{\partial(\rho k u_i)}{\partial x_j} = \frac{\partial}{\partial x_j} \left[ \Gamma_k \left( \frac{\partial k}{\partial x_j} \right) \right] + G_k - Y_k + S_k \quad \text{Equation 7-4}$$

$$\frac{\partial(\rho \omega)}{\partial t} + \frac{\partial(\rho \omega u_i)}{\partial x_j} = \frac{\partial}{\partial x_j} \left[ \Gamma_\omega \left( \frac{\partial \omega}{\partial x_j} \right) \right] + G_\omega - Y_\omega + D_\omega + S_\omega \quad \text{Equation 7-5}$$

where  $G_k$  and  $G_\omega$  represent the production of turbulence kinetic energy and specific dissipation rate respectively.  $\Gamma_k$  and  $\Gamma_\omega$  represent the effective diffusivity of  $k$  and  $\omega$  respectively.  $Y_k$  and  $Y_\omega$  represent the dissipation of  $k$  and  $\omega$  due to the turbulence,  $D_\omega$  represents the cross-diffusion term, and  $S_k$  and  $S_\omega$  are the source terms. These terms are modelled by means of empirical formulations.

#### 7.4 Transition SST Model

It is verified that the SST model if used in combination with a grid resolving the near wall boundary layer, can qualitatively predict the boundary layer transition and the associated drag crisis (Benim *et al.*, 2007). The transition SST model is based on the coupling of the SST  $k\omega$  transport equations with two other transport equations, one for the intermittency and one for the transition onset criteria, momentum-thickness  $Re$  (ANSYS, 2013b). The model is capable of capturing the effect of inlet turbulence, laminar-turbulent transition in the boundary layer and turbulence in the wake. Thus, the transition SST model is used for the numerical simulations for ensuring consistency with the experimental conditions having high inlet turbulence.

##### 7.4.1 Wall Modelling

Near wall modelling approach is preferred over wall functions to fully resolve the boundary layer. Fluent recommends a maximum  $y^+$  of 1, a wall normal expansion ratio of less than 1.1, and about 75–100 mesh nodes in the streamwise direction for Transition SST model. Additional mesh nodes in the streamwise direction are recommended if the separation-induced transition is present. It is found that with an increase in  $y^+$ , the transition onset location moves upstream and too small a  $y^+$  (below 0.001) causes movement of transition location downstream. For unstructured meshes,

it is recommended to generate prism layers near the wall with 15 or more nodes covering the boundary layer.

### 7.4.2 Inlet Turbulence

The turbulence intensity specified at an inlet decays quite rapidly depending on the inlet viscosity ratio; the larger the inlet viscosity ratio, the smaller the turbulent decay rate. Figure 7-1 illustrates the typical decay of the inlet turbulence intensity ( $Tu$ ) with the streamwise distance from the inlet ( $x$ ). Hence, turbulence intensity and turbulence viscosity ratio at the inlet are specified such that the leading edge of the upstream cylinders will experience a turbulence intensity of around 13%, consistent with the experimental results.

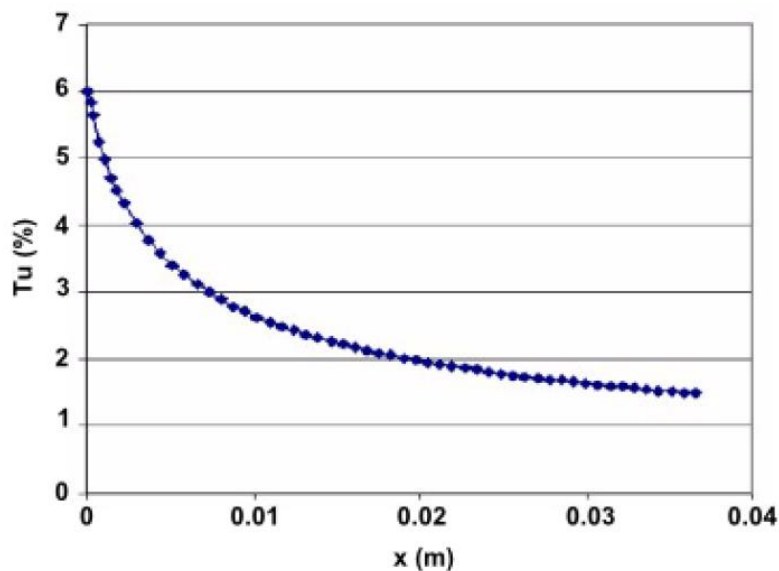


Figure 7-1: Decay of inlet turbulence intensity with the streamwise distance (ANSYS, 2013b)

## 7.5 Pressure Velocity Coupling

The pressure-based solver in Fluent solves the flow problem in either a segregated or coupled manner. The segregated algorithm solves the momentum equation and pressure correction equations separately while the coupled algorithm solves the momentum and pressure-based continuity equations together. ANSYS Fluent provides five pressure-velocity coupling algorithms: SIMPLE, SIMPLEC, PISO, Coupled, and Fractional Step Method (FSM) (ANSYS, 2013b).

The Pressure-Implicit with Splitting of Operators (PISO) pressure-velocity coupling scheme is based on the higher degree of the approximate relation between the corrections for pressure and velocity. A segregated PISO algorithm is selected for the numerical simulation due to its better efficiency on unstructured meshes with some degrees of skewness. Further, though PISO algorithm takes a little more computation time per solver iteration, it decreases the number of iterations required for convergence, especially for transient problems.

## 7.6 Discretisation Scheme and Solver

A second order discretization is used for better accuracy rather than a faster solution. The spatial discretisation scheme employed is summarised in Table 7-1. The Second Order scheme reconstructs the face pressure using a central differencing scheme, which provides improved accuracy.

Temporal discretization involves the integration of every term in the differential equations over a time step. The pressure-based solver in ANSYS Fluent uses an implicit discretization of the transport equation. All convective, diffusive, and source terms are evaluated implicitly by default in Fluent, as fully implicit schemes are unconditionally stable with respect to time step size. A first order implicit scheme is selected for the numerical simulations as dynamic remeshing is not supported by the 2nd order scheme.

Table 7-1: Discretisation scheme for the numerical simulations

Variable	Scheme
Pressure	Second Order
Momentum	Second Order Upwind
Turbulent Kinetic Energy	Second Order Upwind
Specific Dissipation Rate	Second Order Upwind
Intermittency	Second Order Upwind
Momentum Thickness $Re$	Second Order Upwind

The time step is selected at 0.001s, considerably smaller than the characteristic vortex shedding period of 0.34s at the maximum model steady flow velocity of 0.5m/s, to ensure that the vortex shedding phenomenon and the vortex street are captured well in the simulations (Ai *et al.*, 2013). It was further ensured that the streamwise Courant Number ( $CN$ ) is sufficiently low to guarantee numerical stability, where  $CN = \frac{U\Delta t}{\Delta x}$  and

$U$ ,  $\Delta t$  and  $\Delta x$  are the flow velocity, time step and minimum mesh size respectively. A time step convergence study was also carried out along with the mesh independence study, as demonstrated in Section 7.7.4.

## 7.7 Mesh Independence

A mesh sensitivity study has been carried out to ensure that the solution is mesh independent. As the transition model is found to be adversely affected by mesh refinement, Fluent recommended meshing scheme is adopted for the near wall region. The meshing is carried out based on a low  $Re$  approach (Stringer *et al.*, 2014). Mesh convergence study is carried out for the stationary single cylinder case and then similar meshing is adopted for the multi-cylinder simulations. Further, the randomness of the vortex modes about multiple cylinders is expected to make the conventional mesh independence study irrelevant. It is observed that the vortex shedding from four cylinders in an inline square arrangement can be in-phase, anti-phase or with a phase difference, exhibiting intermittency and bistability (Lam *et al.*, 2008).

### 7.7.1 Computational Domain

The fluid domain is idealised as a rectangle, as shown in Figure 7-2. The diameter ( $D$ ) of the cylinder is taken as 33.8 mm consistent with the leg diameters used for the physical experiments. The inlet is defined as a velocity inlet, and the outlet has been specified as a pressure outlet with a gauge pressure equals to 0.00 Pa. The cylinder has been defined as a wall with a no-slip condition. The side boundaries are defined as symmetry.

The prototype  $Re$  corresponding to crossflow and yaw VIV are approximately  $1.1 \times 10^6$  and  $1.5 \times 10^6$  respectively, within the critical regime. Though VIV is found to occur in the critical regime (Ding *et al.*, 2004), prototype scale is not considered for the numerical simulations since realistic modelling of the flow in the critical regime is extremely difficult with RANS turbulence models. Further, the scale effect is insignificant for a vibrating cylinder (DNV GL, 2017b) and hence model scale (subcritical regime) can represent real marine conditions at higher  $Re$ , with substantial freestream turbulence.

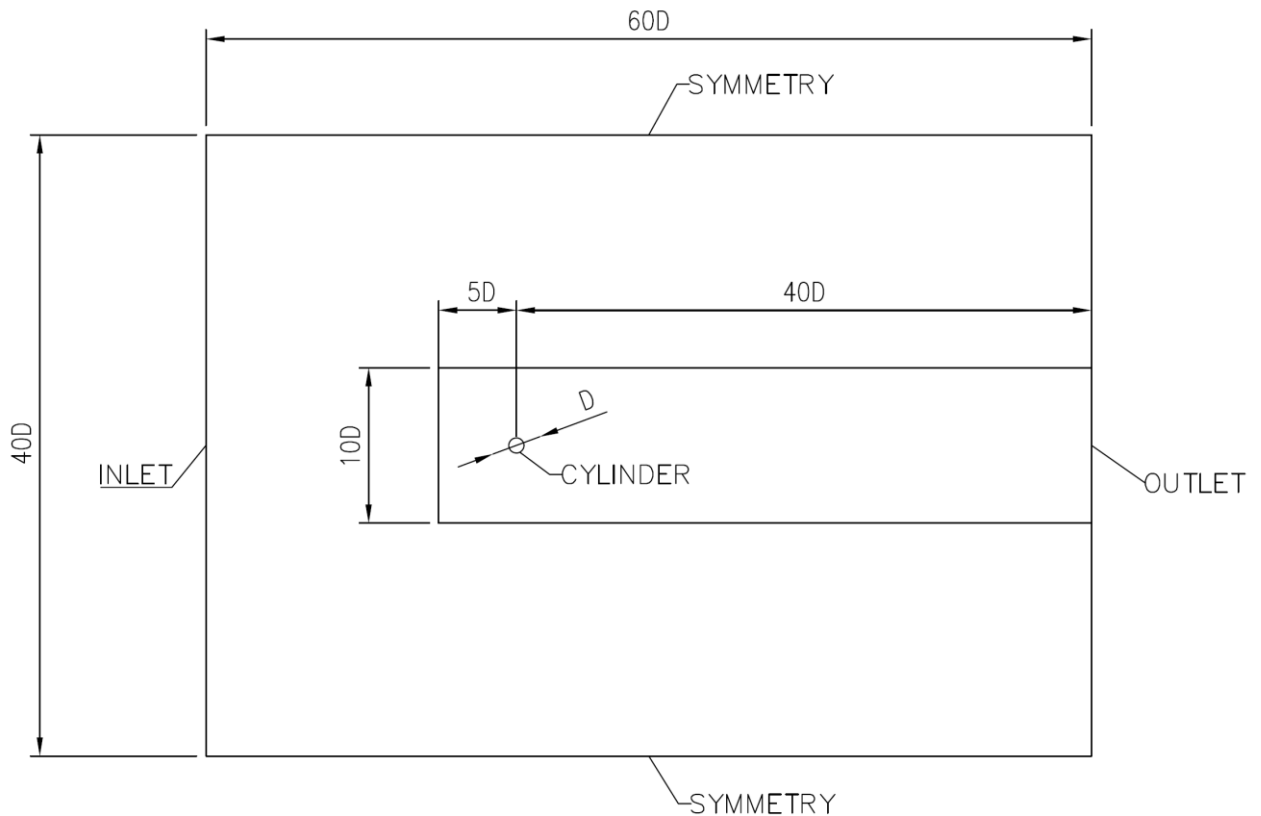


Figure 7-2: Computational Domain for 2D single cylinder

### 7.7.2 Numerical Mesh

Hybrid meshing is adopted for the ease of mesh generation and to optimise the meshing. The outer domain and boundary layer are provided with a structured meshing, and the near cylinder and wake region are provided with unstructured meshing. Quadrilateral cells are used for the structured meshes and triangular cells for the unstructured meshes. 74 quadrilateral layers are provided near the cylinder by means of inflation. A  $y^+$  of around 0.10 is considered along with a wall normal expansion ratio of 1.10. 360 streamwise nodes are provided at every 0.50-degree angular separation along the cylinder. The numerical mesh and the unstructured meshing around the cylinder are illustrated in Figure 7-3 and Figure 7-4 respectively.

The maximum aspect ratio of the boundary layer mesh is also kept at a relatively low value of 51.61. The skewness of the cells is checked, and the average value is 0.03, and the maximum value is found to be 0.91, which is less than the default limiting value of 0.97. The total numbers of cells used for meshing are 79,310, considering the time demand for dynamic mesh refinements.

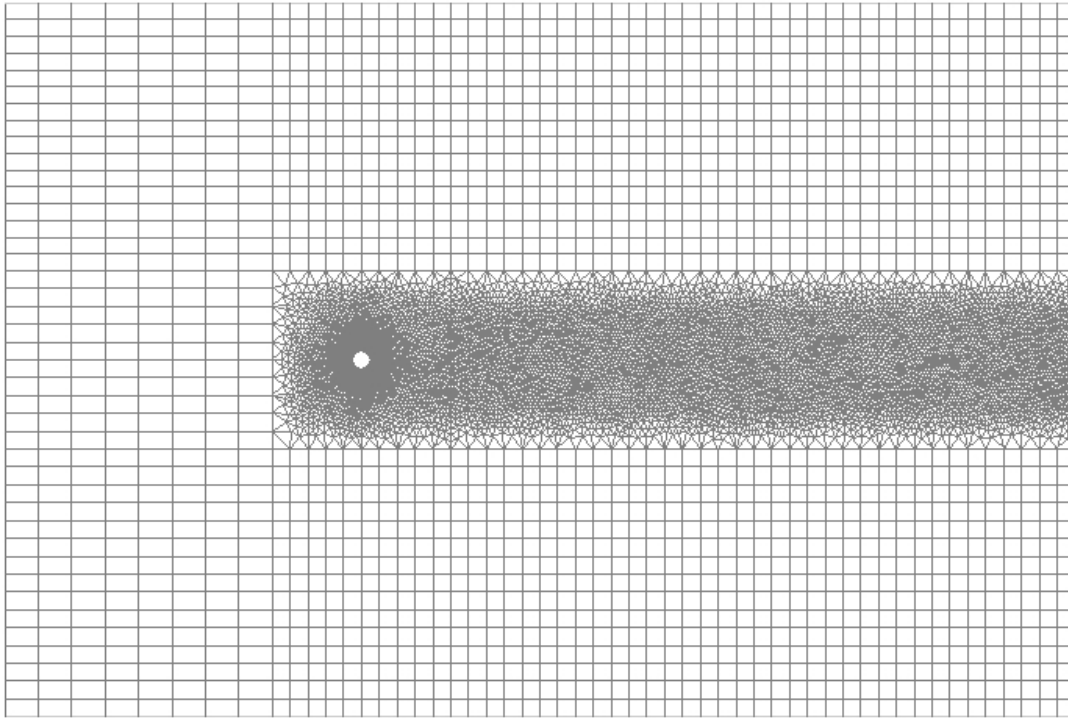


Figure 7-3: Typical numerical mesh for 2D single cylinder

### 7.7.3 Mesh Convergence Study

The mesh convergence study was carried out for the maximum steady flow velocity of the model; 0.5m/s which corresponded to a  $Re$  of  $1.47 \times 10^4$ . The mesh convergence study is carried out in two stages. In stage 1, the effect of domain size and mesh intensity are investigated with negligible inlet turbulence. Inlet turbulence is omitted for this study since it is found that the turbulence intensity declines exponentially with the streamwise distance from the inlet leading to different turbulence intensity in way of the cylinder. The results of the study are presented in Table 7-2, a). It can be seen that the mesh with a near wall thickness of 0.000003 m ( $y^+ = 0.1$ ) and a streamwise node spacing of 0.50 degrees show excellent convergence. Further, it can be inferred that the results are not much affected by the distances of the inlet and the outlet from the cylinder if they are more than 10D and 20D respectively.

Mesh convergence study was conducted for the wake mesh also with around 6% turbulence intensity in way of the cylinder. Table 7-2, b) demonstrates the results achieved for the three different wake meshes. It can be observed that the results are independent of the refinement of the wake mesh. Table 7-2, c) presents the results of the mesh convergence study with around 13% inlet turbulence intensity in way of the

cylinder. Experimental results from Surry (1972) corresponding to a  $Re$  of  $3.38 \times 10^4$  and a turbulence intensity of 14.7% are also demonstrated in the table. It can be observed that the mesh with a near wall thickness of 0.000003 m ( $y^+ = 0.1$ ) and a streamwise node spacing of 1 degree show fair mesh convergence. Nevertheless, a near wall thickness of 0.000003 m and a streamwise node spacing at 0.50 degree angular separation are selected for the numerical simulations to ensure enhanced accuracy and better agreement with the experiment.

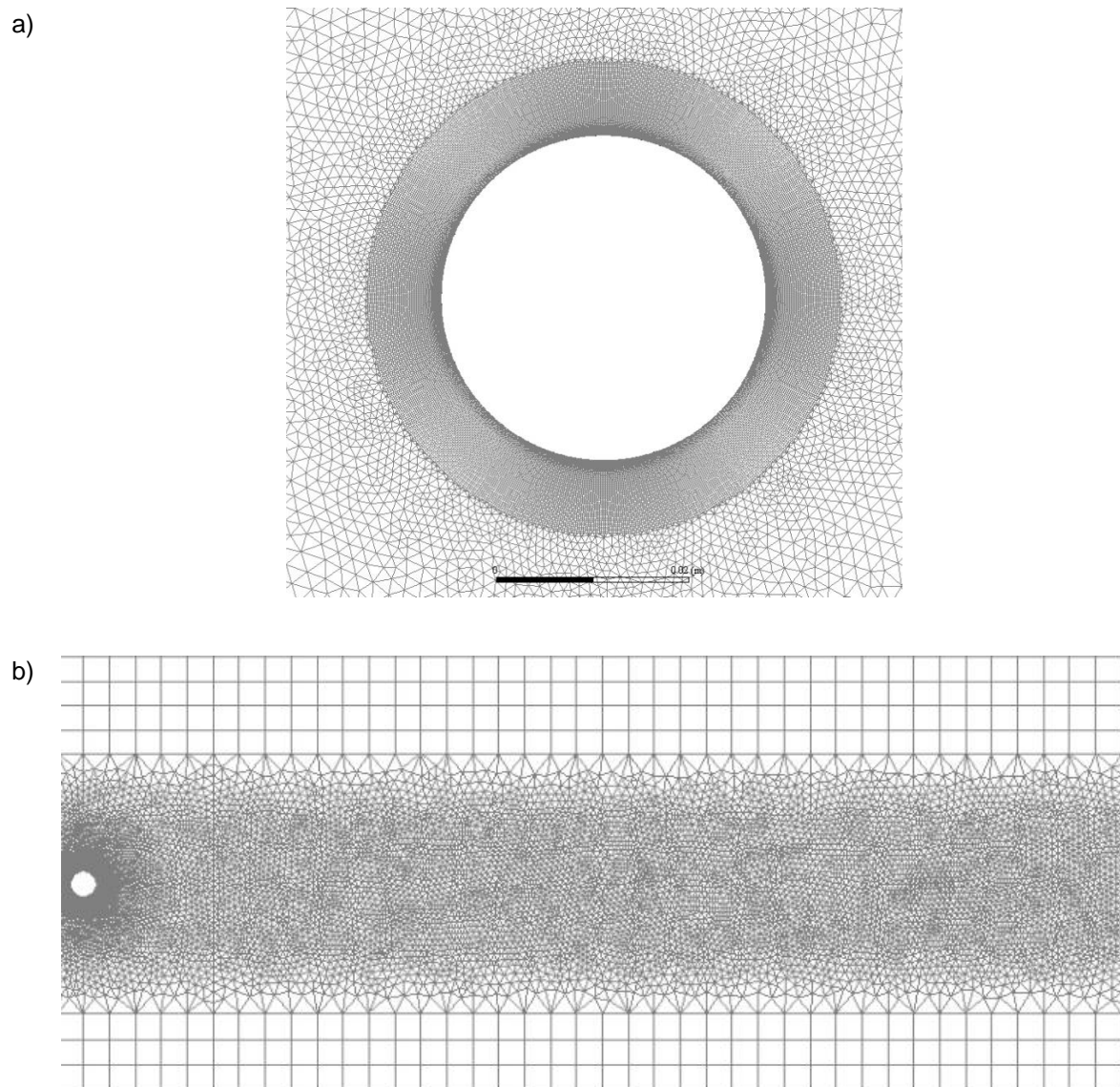


Figure 7-4: Unstructured mesh, a) boundary layer inflation and near cylinder, b) wake

Table 7-2: Summary of mesh convergence study a) without inlet turbulence, b) with 6% turbulence intensity in way of the cylinder, wake refinement, c) with 13% turbulence intensity in way of the cylinder

a)	Mesh	Domain Size (Inlet x Width x Outlet)	No of cells	Near Wall thickness (m)	Streamwise node spacing (degrees)	$C_D$	$St$
	1	20D x 40D x 40D	31649	0.000003	1	1.54	0.226
	2	10D x 30D x 20D	36762	0.000003	1	1.56	0.227
	3	20D x 40D x 40D	70198	0.000003	0.5	1.60	0.219

b)	Mesh	Domain Size (Inlet x Width x Outlet)	No of cells	Near Wall thickness (m)	Streamwise node spacing (degrees)	$C_D$	$St$
	1	20D x 40D x 40D	31649	0.000003	1	1.39	0.229
	2	20D x 40D x 40D	40695	0.000003	1	1.41	0.230
	3	20D x 40D x 40D	61356	0.000003	1	1.40	0.230

c)	Mesh	Domain Size (Inlet x Width x Outlet)	No of cells	Near Wall thickness (m)	Streamwise node spacing (degrees)	$C_D$	$St$
	1	20D x 40D x 40D	31649	0.000003	1	1.00	0.229
	2	20D x 40D x 40D	79310	0.000003	0.5	1.07	0.237
	3	Experiment (Surry, 1972)				1.14	0.200

#### 7.7.4 Time Step Convergence Study

The time step convergence study was carried out with negligible inlet turbulence at the maximum model  $Re$  of  $1.47 \times 10^4$ . The study was carried out with two time steps and two meshes for three  $CN$  cases, as demonstrated in Table 7-3. It can be observed that the selected mesh with a near wall thickness of 0.000003 m ( $y^+ = 0.1$ ) and a streamwise node spacing at 0.50 degree angular separation shows fair convergence at a  $CN$  of 3.39, corresponding to a time step of 0.001s. Consequently, a time step of 0.001s is selected for the numerical simulations.

#### 7.7.5 Numerical uncertainty

Numerical uncertainty was evaluated as per ITTC recommendations (ITTC, 2017b; ITTC, 2017c; ITTC, 2017d). The variable selected for the uncertainty analysis was the drag coefficient, and the verification was based on iterative and grid convergence results. The uncertainty analysis was carried out with 6% turbulence intensity at the

maximum model  $Re$  of  $1.47 \times 10^4$ . The iterative uncertainty was found to be negligible due to the tight convergence criteria adopted for the simulations. As the mesh size and  $CN$  (time step) convergence studies were not based on uniform grid refinement ratios (see Table 7-2, b) and Table 7-3), the drag coefficient values of the coarse grids were corrected using extrapolation. The drag coefficient exhibited oscillatory convergence with both mesh size and  $CN$  refinements, and the uncertainties were found to be 0.75% and 7.08% respectively. The simulation numerical uncertainty considering the contributions from both the parameters was found to be 7.11%. Though the numerical uncertainty can be further reduced by employing finer time steps or  $CNs$ , numerical simulations may become unviable due to the very high computational demands.

Table 7-3: Summary of time step convergence study

Time Step	Streamwise $CN$	Domain Size (Inlet x Width x Outlet)	No of cells	Near Wall thickness (m)	Streamwise node spacing (degrees)	$C_D$	$St$
0.001	1.70	20D x 40D x 40D	31649	0.000003	1	1.54	0.226
0.001	3.39	20D x 40D x 40D	70198	0.000003	0.5	1.60	0.219
0.0001	0.17	20D x 40D x 40D	31649	0.000003	1	1.63	0.234

## 7.8 Steady Flow around Cylindrical Legs of the Jack-up

### 7.8.1 Computational Domain

2D numerical simulations are carried out by using the High Performance Computing (HPC), Topsy at Newcastle University. The fluid domain is idealised as a rectangle. The leg design, LD1H0 with no pin holes is selected for the numerical simulations due to its simplicity. The leg diameter ( $D$ ) is considered as 33.8 mm consistent with the model for the physical experiments. Based on the domain sensitivity study with a single cylinder, the inlet and outlet of the flow domain are provided at a distance of  $20D$  from the upstream and downstream cylinders respectively. The width of the flow domain is kept at 1.80m, same as the width of the WWC tank used for model testing.

The inlet is defined as a velocity inlet. The outlet has been specified as a pressure outlet with a gauge pressure equals 0.00 Pa. The legs are defined as walls with no-slip condition. The side boundaries are defined as symmetry. The computational domain and the boundary conditions are displayed in Figure 7-5.

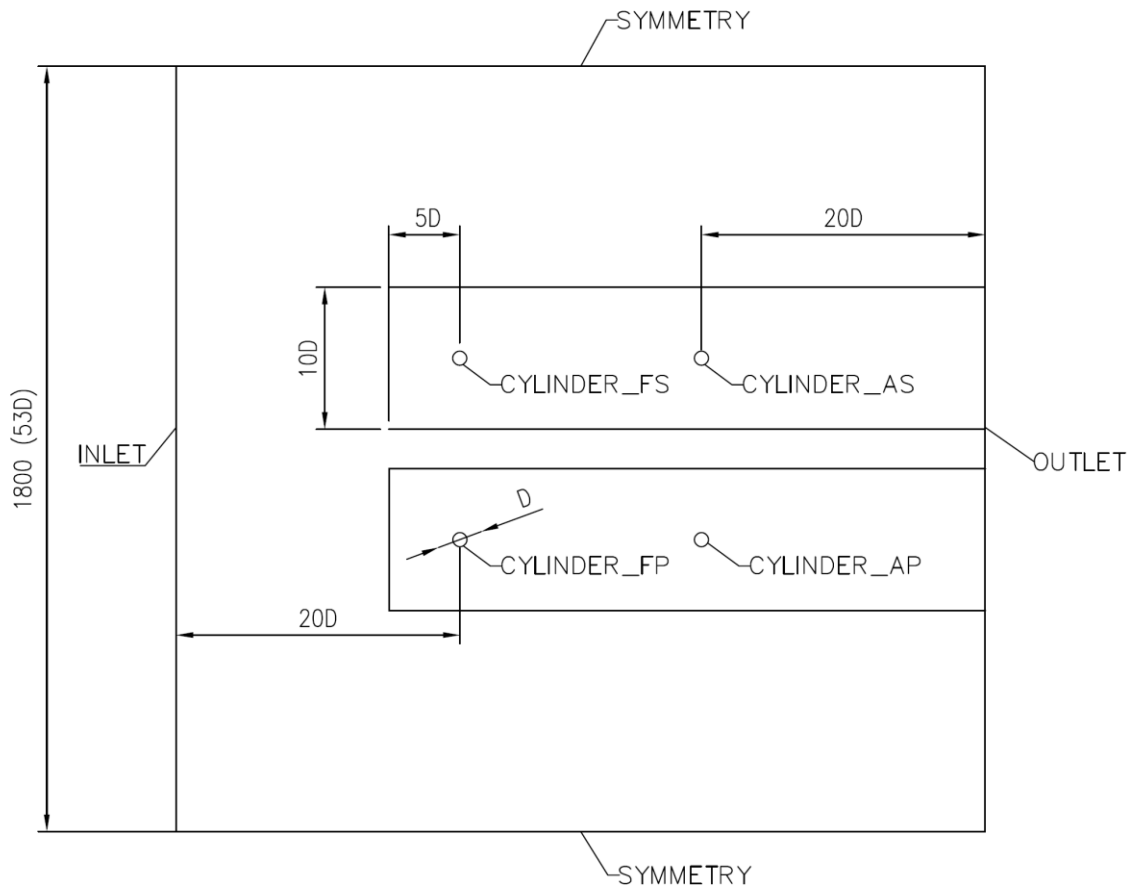


Figure 7-5: Computational Domain for 2D jack-up legs

### 7.8.2 Numerical Mesh

The meshing strategy adopted was same as that for the single cylinder simulations. The outer domain and boundary layer are provided with structured quadrilateral meshing while the near cylinder and wake are provided with unstructured triangular meshing. Consistent to the mesh convergence study carried out with the single cylinder, body fitted 74 quadrilateral layers are provided for the boundary layer by means of the inflation algorithm. A  $y^+$  of around 0.10 is considered for the boundary layer meshing along with a wall normal expansion ratio of 1.10. Correspondingly, the size of the 1st cell adjacent to the legs along the radial direction is retained as 0.000003 m along with the streamwise node spacing at 0.50-degree angular separation. Fine meshing is adopted for the wake of the upstream legs while medium meshing is adopted for the wake of the downstream legs based on the mesh sensitivity study and to optimise the time demands for dynamic mesh refinements. The mesh quality is ensured to be same as that of the single cylinders. The total numbers of cells used for

meshing are 278,576. The numerical mesh and the unstructured meshing around the legs are illustrated in Figure 7-6 and Figure 7-7 respectively.

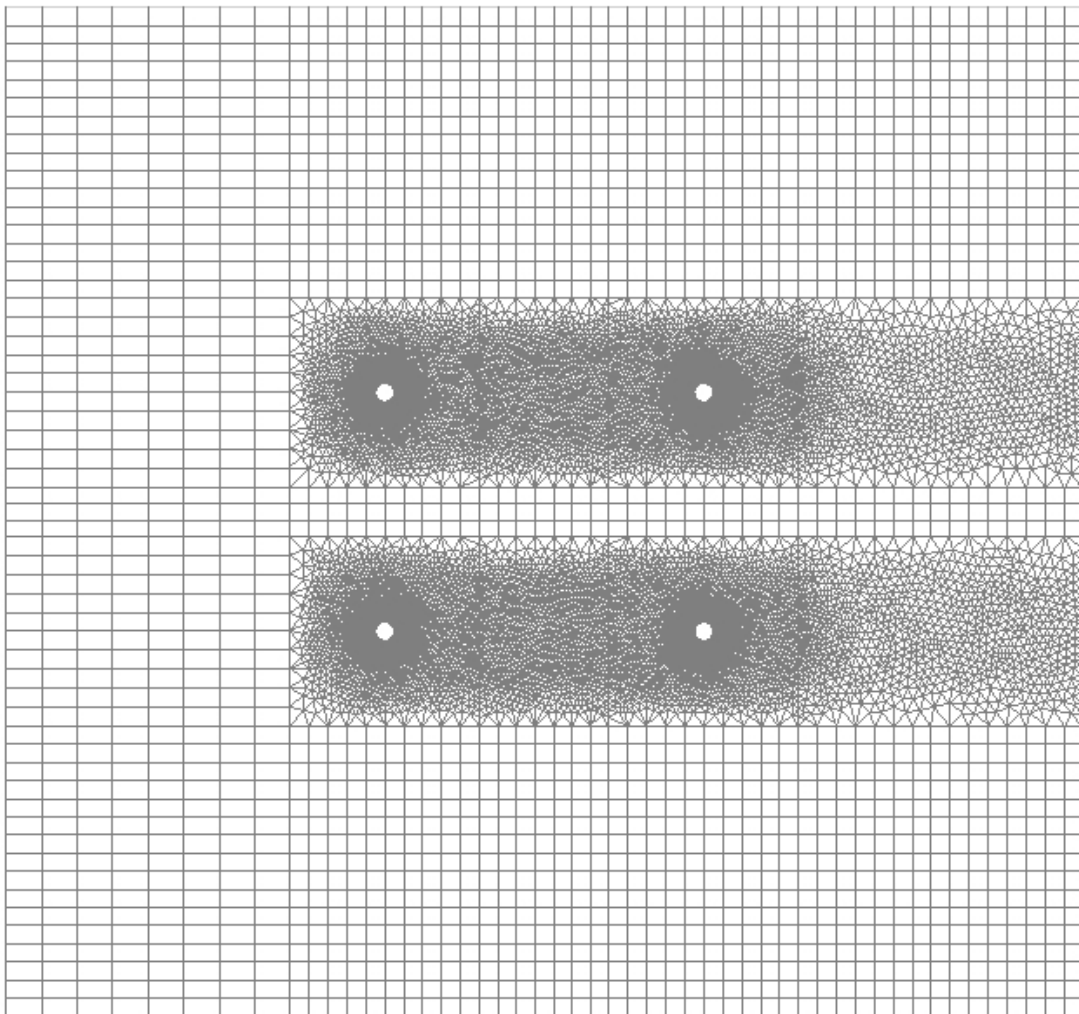
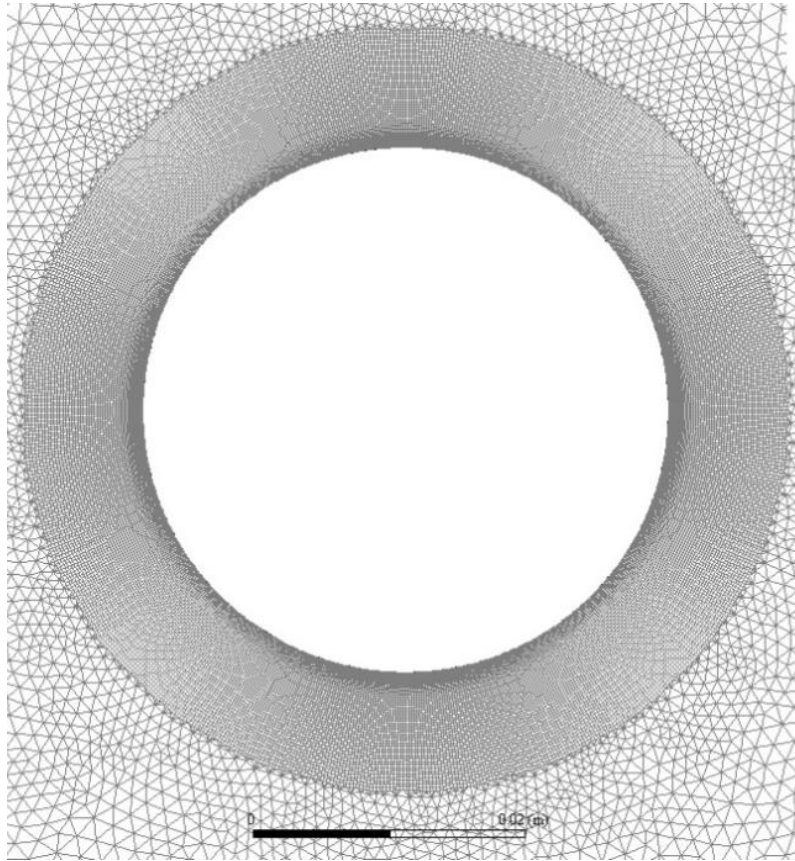


Figure 7-6: Numerical Mesh for the jack-up cylindrical legs

The results of individual legs are compared to that of the single cylinder to ensure mesh independence. The mesh convergence study was carried out for the maximum steady flow velocity of the model; 0.5 m/s which corresponded to a  $Re$  of  $1.47 \times 10^4$ . Table 7-4 demonstrates the results of the mesh convergence study with around 13% inlet turbulence intensity in way of the upstream cylinders (legs). Experimental results for the single cylinder (Surry, 1972) corresponding to a  $Re$  of  $3.38 \times 10^4$  and a turbulence intensity of 14.7% as well as the results of the physical experiment with the jack-up model (see Section 6.11.1) are also demonstrated in the table. It can be observed that the values obtained are in good agreement with the single cylinder results and are fairly concurrent with the experimental values.

a)



b)

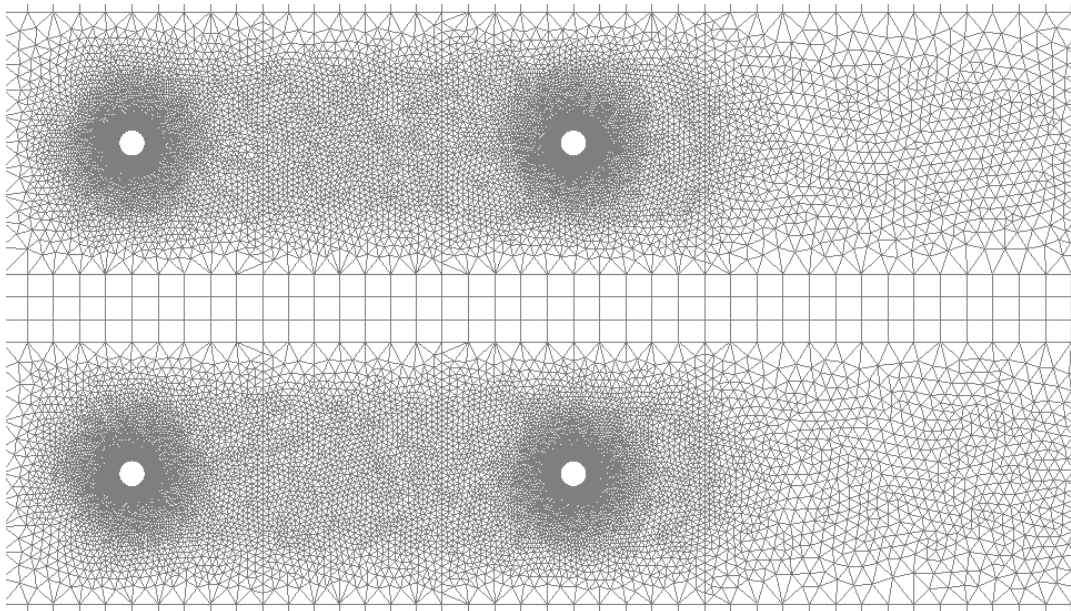


Figure 7-7: Unstructured mesh around jack-up legs, a) boundary layer inflation, b) near cylindrical legs and wake

Table 7-4: Summary of mesh convergence study with 13% turbulence intensity in way of the upstream cylinders

Mesh	Domain Size (Inlet x Width x Outlet)	No of cells	Near Wall thickness (m)	Stream wise node spacing (degrees)	Cylinder	$C_D$	$St$
1	20D x 40D x 40D	31,649	0.000003	1	Single	1.00	0.229
2	20D x 40D x 40D	79,310	0.000003	0.5	Single	1.07	0.237
3	Experiment (Surry, 1972)				Single	1.14	0.200
4	20D x 53D x 20D	278,576	0.000003	0.5	Upstream Starboard	0.98	0.226
					Upstream Port	0.98	0.226
					Downstream Starboard	1.05*	0.226*
					Downstream Port	1.05*	0.226*
5	Jack-up model test (Section 6.11.1)				Upstream Starboard	1.05**	-
					Upstream Port	1.16**	
					Downstream Starboard	0.89**	
					Downstream Port	0.92**	
* corrected for wake speed							
** corrected for leg sway and yaw motions							

### 7.8.3 Dynamic Mesh

The dynamic mesh model in ANSYS Fluent can be used to model flows where the shape of the domain is changing with time due to motion on the domain boundaries. The update of the volume mesh is handled automatically by ANSYS Fluent at each time step based on the new positions of the boundaries. The motion of the boundaries can be described using either boundary profiles, user-defined functions (UDFs), or the six degrees of freedom (6dof) solver.

The four legs are defined as a rigidly coupled single rigid body, 'cylinders' which is the dynamic zone with moving boundaries. The entire fluid domain is defined as the deforming dynamic zone which adjusts its shape to suit the motion of the cylinders. The methods, spring based smoothing and remeshing are selected to handle the dynamic volume mesh updating automatically in Fluent. The remeshing parameters (length scales and skewness) are defined as same as the original mesh. The motion of the cylinders is described by using the 6dof solver in Fluent. Figure 7-8 illustrates

the deformed dynamic mesh around the jack-up legs to suit the leg VIV. It can be observed that the location of the cylinders has moved transversely, and the dynamic mesh is updated to suit the instantaneous shape of the domain.

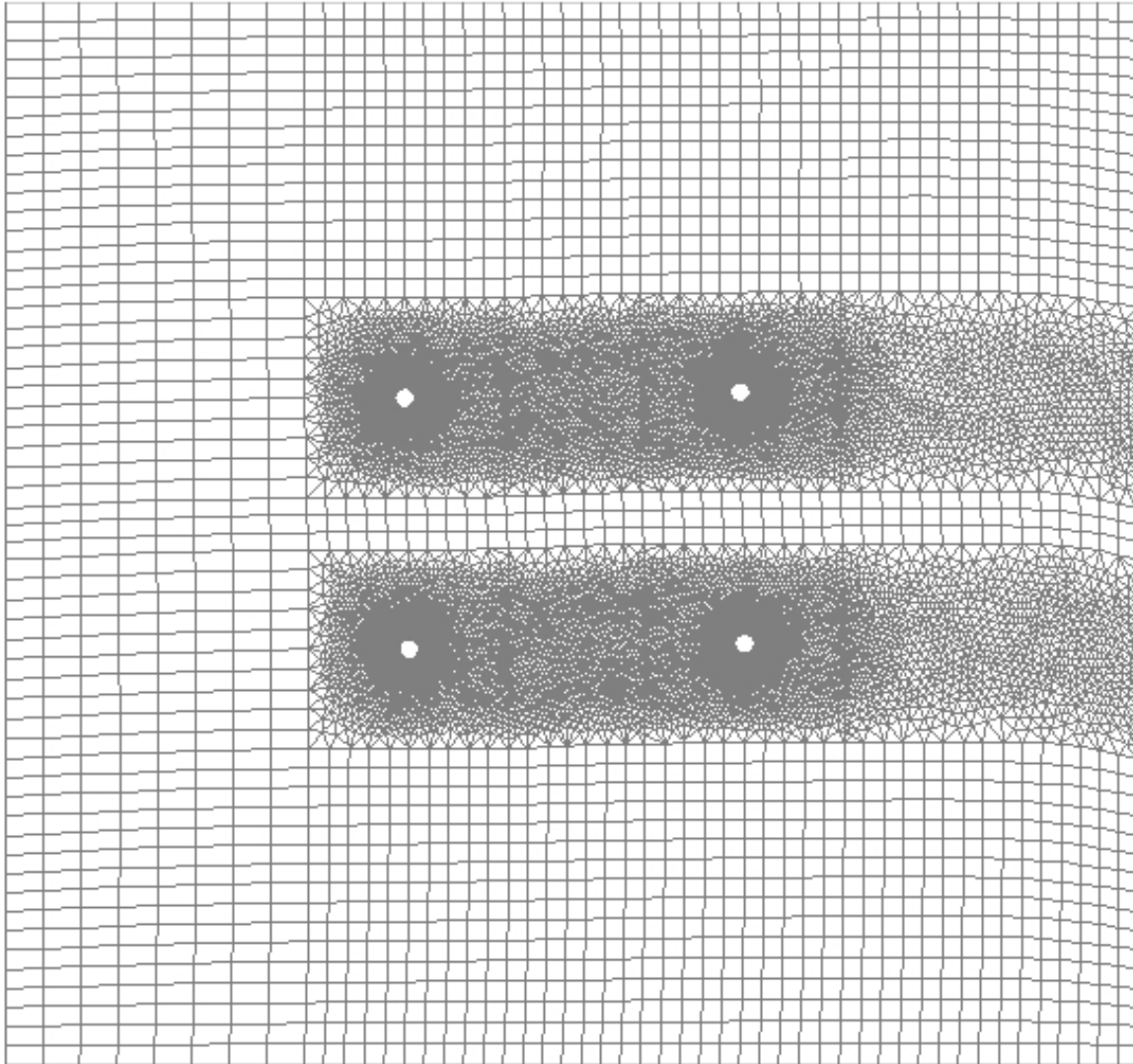


Figure 7-8: Deformed dynamic mesh around the jack-up legs

#### 7.8.4 *Rigid Body (Jack-up) Modelling*

All the four legs are modelled as a rigidly coupled single rigid body in ANSYS Fluent. The mass, stiffness and damping properties of the rigid body, as well as the initial location of its COG, are defined by means of a UDF written in C language. The damping and stiffness forces are computed as defined in the UDF and applied to the rigid body. The 6DOF solver in ANSYS Fluent computes the translational and angular motion of the COG of the rigid body based on the forces and moments acting on it.

The translational and angular accelerations of the COG are computed by solving the equations of translational and angular motions respectively, and the velocities and displacements are derived by numerical integration. The angular and translational velocities are used in the dynamic mesh calculations to update the rigid body position. The properties of the jack-up rigid body considered for the numerical simulation is defined in Table 7-5. The loading condition considered for the numerical simulation is NVL, the operating condition with no variable load (see Table 6-3).

Table 7-5: Properties of the jack-up rigid body

<b>2D Rigid Body Properties: NVL</b>		
$M_e$	28.87	kg
$I_{e\phi}$	2.07	kgm <sup>2</sup>
$K_{ex}$	1974.98	N/m
$K_{ey}$	1872.98	N/m
$K_{e\phi}$	316.72	Nm/radian

### 7.8.5 *Response in Steady flow*

2D numerical simulations were carried out in the steady flow. The global heading was considered as 0 degrees for the simulations. The leg design considered was LD1H0 due to the simplicity of modelling. The loading condition considered was the lightest with no variable load, NVL. The damping ratio of the rigid body is varied to arrive at a range of mass damping parameters ( $m^*\zeta$ ) forming various cases for the simulations. The case with zero mass damping parameter value was also considered to investigate the self-limiting nature of the VIV.

2D CFD and FSI simulations were carried out for the stationary and free jack-up respectively. The response time series were obtained from the simulations and post processed. The inline, crossflow and yaw time series were post processed and the rms amplitudes and vibration frequencies were calculated for various reduced velocities. The details and results of the numerical simulations are summarised in Table 7-6. The results of the physical experiments with the leg design LD1H0, loading condition NVL and global heading 0 are also included in the table under the case, NVL\_LD1H0. As the damping of the jack-up physical model was found to be nonlinear and increasing with the amplitude ratio, the damping ratio presented in the table corresponds to the rms amplitude ratio.

It can be observed in Table 7-6 that the damping ratio of the physical model is unrealistically higher than the typical jack-up damping. Hence, numerical simulations were carried out for a range of realistic damping ratios up to 10% critical damping. The results of the numerical simulations are further validated with the theoretical formulations developed in Chapter 5.

Table 7-6: Jack-up crossflow and yaw responses from the numerical simulations (CFD)

a)

Crossflow / Sway								
Case	$m^*$	MF	$\zeta$	$m^*\zeta$	MF	$V_{ry}$	$y_{O, rms}/D$	$y_{O, max}/D$
NVL_LD1H0_LSND	8.05	1.000	0.000	0.00	5.82	0.63	0.76	
NVL_LD1H0_LSLD2	8.05	1.000	0.020	0.16	6.40	0.54	0.67	
NVL_LD1H0_LSLD4	8.05	1.000	0.040	0.32	5.23	0.44	0.45	
NVL_LD1H0_LSLD10	8.05	1.000	0.100	0.81	5.23	0.14	0.46	
NVL_LD1H0_LSLD	8.05	1.000	0.095	0.77	5.82	0.19	0.23	
NVL_LD1H0	4.46	1.812	0.133	1.07	5.82	0.11	0.18	

b)

Yaw						
Case	$\zeta$	$k_\phi$ (m)	$m^*\zeta$ MF $k_\phi^2$ (m <sup>2</sup> )	$V_{r\phi}$	$R_{\phi\phi O, rms}/D$	$R_{\phi\phi O, max}/D$
NVL_LD1H0_LSND	0.000	0.268	0.0000	6.04	0.85	0.90
NVL_LD1H0_LSLD2	0.020	0.268	0.0115	6.04	0.67	0.72
NVL_LD1H0_LSLD4	0.040	0.268	0.0231	6.04	0.52	0.60
NVL_LD1H0_LSLD10	0.100	0.268	0.0577	4.53	0.08	0.11
NVL_LD1H0	0.109	0.269	0.0637	5.66	0.06	0.13

#### 7.8.5.1 Inline/Surge Response

The inline rms amplitude response of the numerical jack-up model normalised with the leg diameter and plotted against the corresponding reduced velocity is displayed in Figure 7-9, for all the simulation cases. The results of the physical experiments for the case, NVL\_LD1H0 is also included in the figure. It can be seen that the jack-up experiences considerable inline VIV with amplitudes up to 0.08D for low mass damping parameters (damping < 4%). It can also be observed that the inline amplitude ratios exhibit the first peak at reduced velocities between 5 to 8 and continue to increase at higher reduced velocities, possibly due to the galloping response observed at high currents. The increase in response amplitude ratio with the reduction in mass damping parameter verified the mathematical model qualitatively.

The inline frequency responses of the jack-up for various simulation cases were calculated from the time series, normalised with the respective natural frequencies and

plotted against the corresponding reduced velocities in Figure 7-10. It can be observed that the inline frequency response of the model reveals a lock-in range with a frequency ratio of around 1, corresponding to the aggressive inline vibrations. It can be inferred that this corresponds to oscillatory drag at the lift frequencies, revealing coupled inline vibrations with the crossflow lock-in. The coupling is strong and continuous for the cases with the low mass-damping parameter, while weak and intermittent for the other cases.

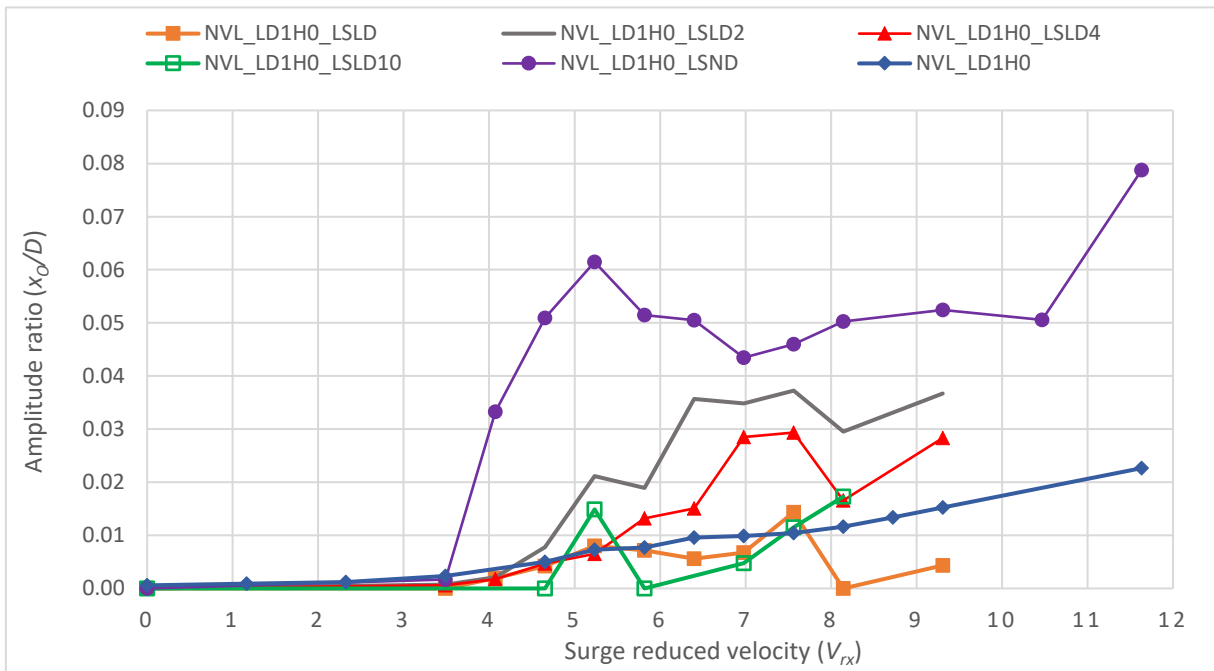


Figure 7-9: Inline amplitude response of the jack-up in steady flow, with corresponding reduced velocity ( $U/f_{Nx}D$ )

#### 7.8.5.2 Crossflow/Sway Response

Based on the crossflow VIV criteria developed in Section 5.3.2, the jack-up was expected to undergo significant crossflow VIV for all the simulation cases. Further, crossflow VIV was expected to be very aggressive for the cases with negligible and low values of mass damping parameters. Figure 7-11 shows the variation of the normalised crossflow rms amplitude responses, plotted with respect to the corresponding reduced velocities. It is demonstrated that the jack-up is highly vulnerable to aggressive crossflow VIV with large lock-in regimes and rms amplitudes even above  $0.50D$  for low damping ratios. As evident in Figure 7-11, the crossflow lock-in regime was found to extend between the reduced velocity values from 3 to 8. It is

found that the response amplitude increases considerably and the lock-in range increases nominally with the decrease in mass damping parameter. The case with the lowest mass damping parameter exhibits the largest crossflow response amplitude and lock-in regime.

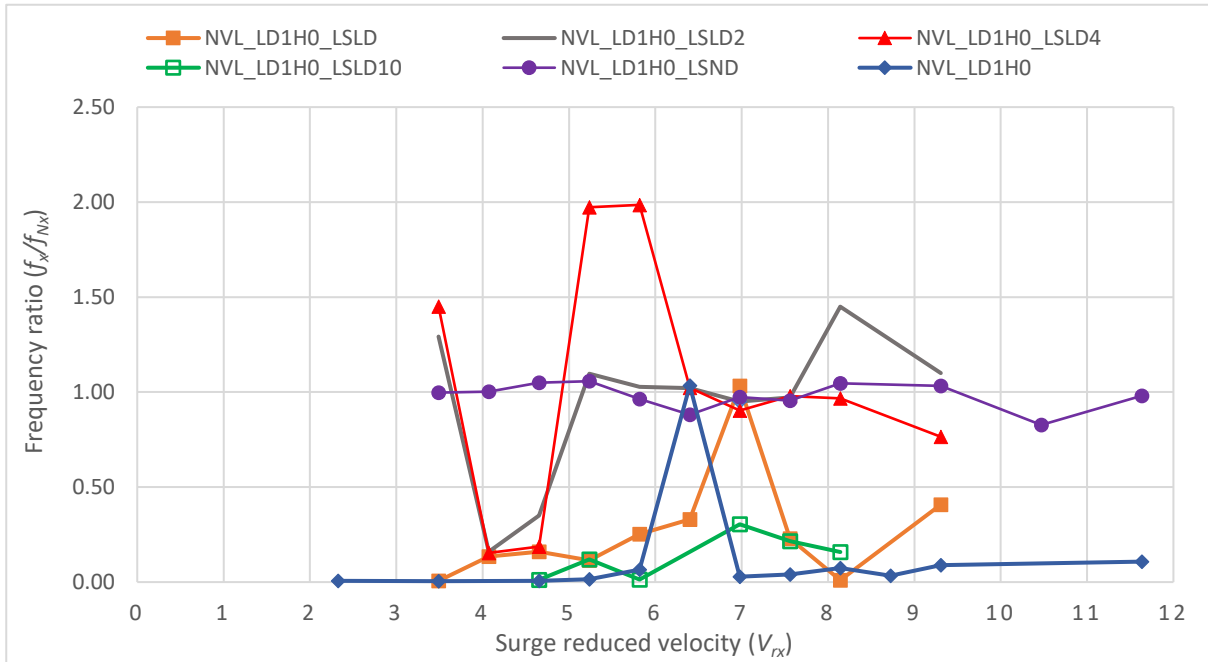


Figure 7-10: Inline frequency response of the jack-up in steady flow

Further, the case with zero mass damping parameter, NVL\_LD1H0\_LSND revealed that the crossflow jack-up VIV is self-limiting; the corresponding rms and maximum amplitude responses are found to be  $0.63D$  and  $0.76D$  respectively. This verifies that the self-limiting nature of VIV observed for single cylinders (Khalak and Williamson, 1997b) is applicable to jack-ups also, and can be attributed to the change in the vortex mode about the legs at higher amplitudes reducing the lift excitation (Sarpkaya, 1995); vortex mode changes from 2S (2 single vortices shed per vibration cycle) to 2P (2 vortex pairs shed per vibration cycle) (Carberry *et al.*, 2004). It can be observed that the peak observed in the crossflow response curve is consistently around a reduced velocity of 5, which correspond to lift excitation. This validated the mathematical model, crossflow VIV criteria and the significance of the mass ratios in containing the VIV of the jack-ups.

Figure 7-12 illustrates the crossflow frequency responses of the jack-up for the simulation cases, plotted against the respective reduced velocity. It can be observed

that the crossflow frequency response of the model reveals two separated lock-in regimes for highly damped cases, a lower regime with a frequency ratio of around unity and an upper regime with a frequency ratio of above 1.40. On comparing with Figure 7-11, it can be understood that the lower regime corresponds to the crossflow lock-in responses in the sway mode. Further investigation revealed that the upper regime corresponded to lock-in responses in the yaw or torsional mode as explained later in Section 7.8.5.4. It can be inferred that the crossflow vibrations in the upper regime are coupled vibrations with the yaw lock-in frequencies. The upper regime is found to be absent for the lightly damped cases.

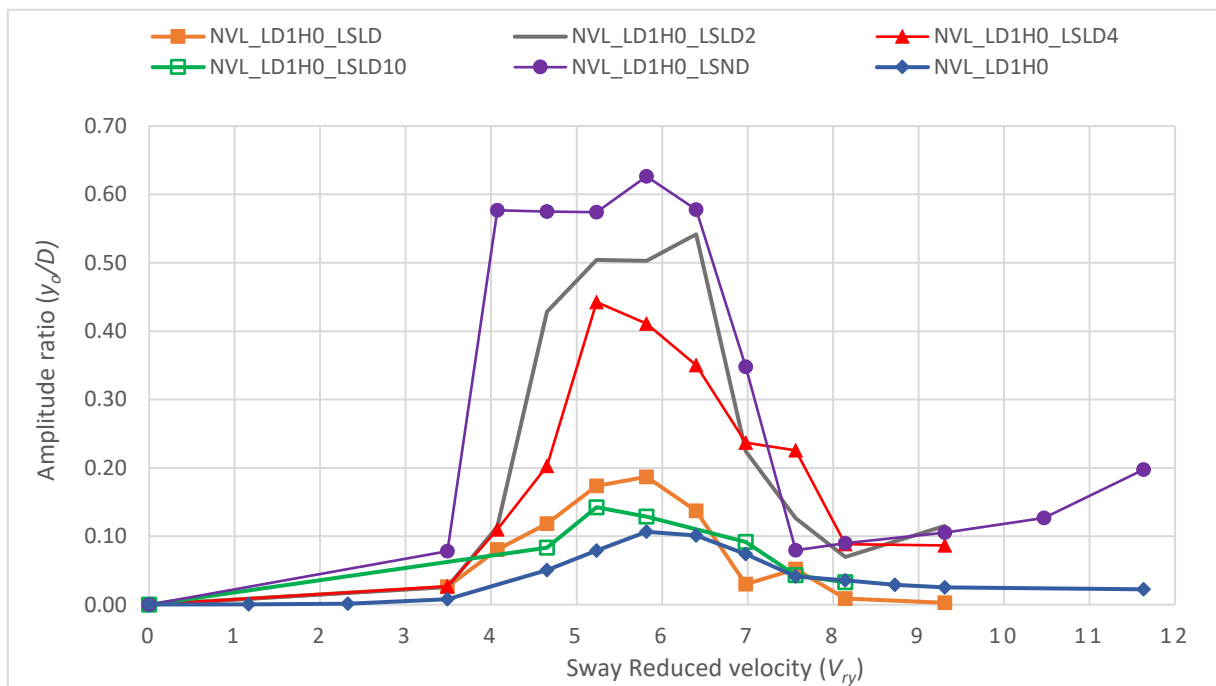


Figure 7-11: Crossflow amplitude response of the jack-up in steady flow, with corresponding reduced velocity ( $U/f_{Ny}D$ )

### 7.8.5.3 Effect of Mass Damping Parameter

It is observed that the increase in mass damping parameter reduced the crossflow amplitude response. The normalised crossflow rms response amplitude ratios fitted reasonably well in a straight line when plotted against the mass damping parameter multiplied with the mode factor, as illustrated in Figure 7-13. This reemphasised the significance of the effective mass damping parameter in controlling the crossflow VIV response. The model test case, NVL\_LD1H0 also fitted well into the trend, when the corrected damping ratio is considered. Hence, the product of mass damping parameter

with the mode factor, also called modified or effective mass damping parameter, can be considered as the universal parameter governing crossflow VIV. This validated the theoretical investigation demonstrated in Sections 5.2.2 and 5.3.2.

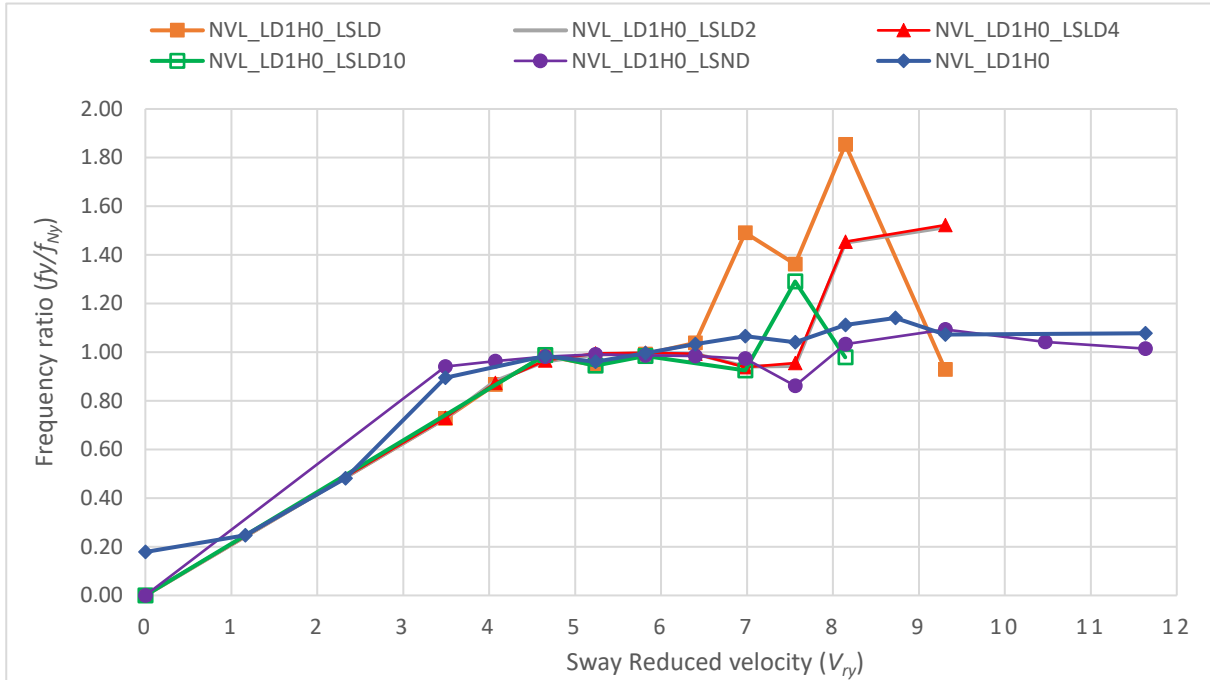


Figure 7-12: Crossflow frequency response of the jack-up in steady flow

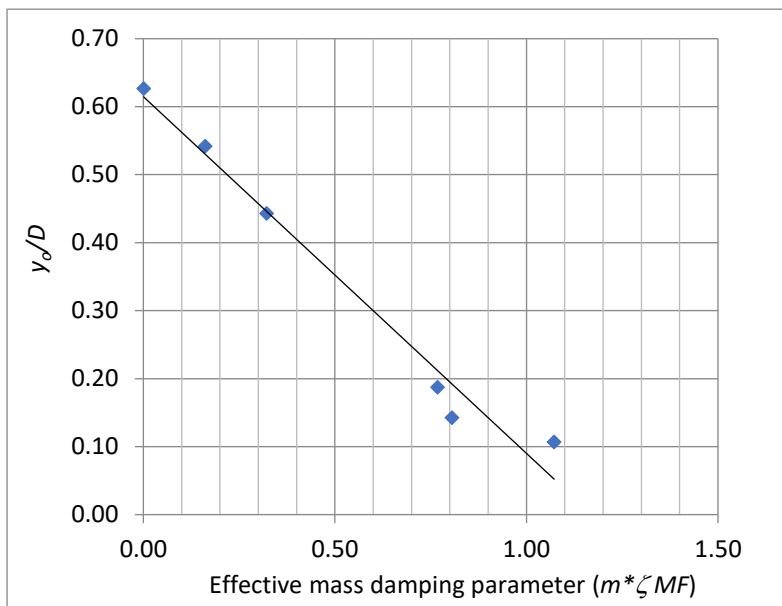


Figure 7-13: Crossflow amplitude response with effective mass damping parameter

## 7.8.5.4 Yaw Response

The jack-up was expected to experience significant yaw VIV also as per the criteria developed in Section 5.3.4. Numerical simulations revealed that the jack-up experiences significant torsional or yaw VIV response at higher steady flow speeds. The normalised yaw rms amplitude response as a function of yaw reduced velocity is plotted in Figure 7-14. It can be observed that the peak yaw response occurs around a yaw reduced velocity of around 5 - 6, confirming that the yaw VIV is due to crossflow lift excitation. The rms response amplitudes are found to be above 0.50D for the cases with low damping. The lock-in regime is found to extend between the yaw reduced velocities of 3 to 8. Further, the case with zero inertia damping parameter revealed that yaw VIV of the jack-up is also self-limiting in nature similar to that observed for single cylinders (Khalak and Williamson, 1997b). It can be inferred from Figure 7-14 that the rms self-limiting amplitudes are in the order of 0.80D.

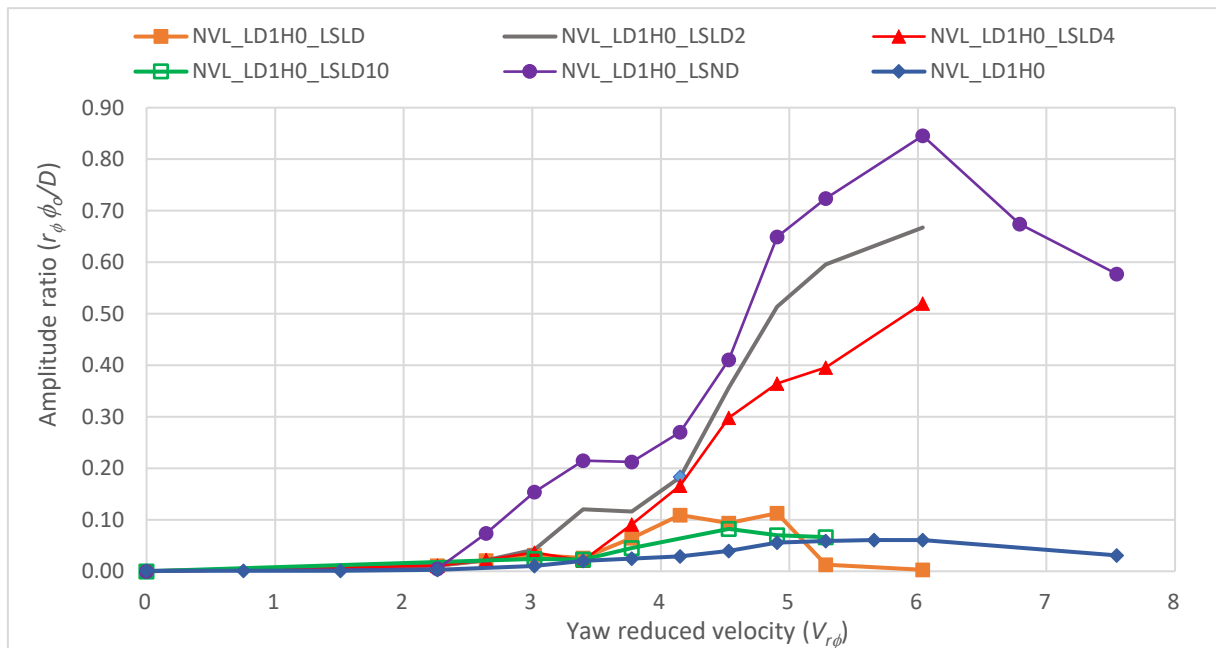


Figure 7-14: Yaw amplitude response of the jack-up in steady flow, with corresponding reduced velocity ( $U/f_{N\phi}D$ )

The yaw frequency responses of the jack-up normalised with the corresponding natural frequencies and plotted against the yaw reduced velocities are displayed in Figure 7-15. Similar to crossflow frequency response, the yaw frequency response of the model also revealed two separated lock-in regimes, a weak lower regime with a frequency ratio around 0.60 and an upper regime with a frequency ratio of around 1.

In comparison with Figure 7-11 and Figure 7-14, it can be understood that the lower regime corresponds to the coupled yaw vibrations due to crossflow lock-in and the upper regime represents lock-in responses in the model's yaw mode. Further, it is evident that the lower coupling regime weakens with the reduction in damping ratio and is almost absent with zero damping.

#### 7.8.5.5 Effect of Inertia Damping Parameter

It is observed that the increase in inertia damping parameter reduced the yaw amplitude response and the lock-in ranges. The response amplitude ratio fitted reasonably well in a straight line when plotted against an inertia damping parameter, as illustrated in Figure 7-16. The model test case, NVL\_LD1H0 also fitted well into the trend, with the corrected damping ratio. Hence, inertia damping parameter, the product of the mass damping parameter, mode factor and the square of yaw radius of gyration and can be considered as the universal parameter determining the yaw VIV response of jack-ups. This validates the theoretical investigation presented in Sections 5.2.4 and 5.3.4.

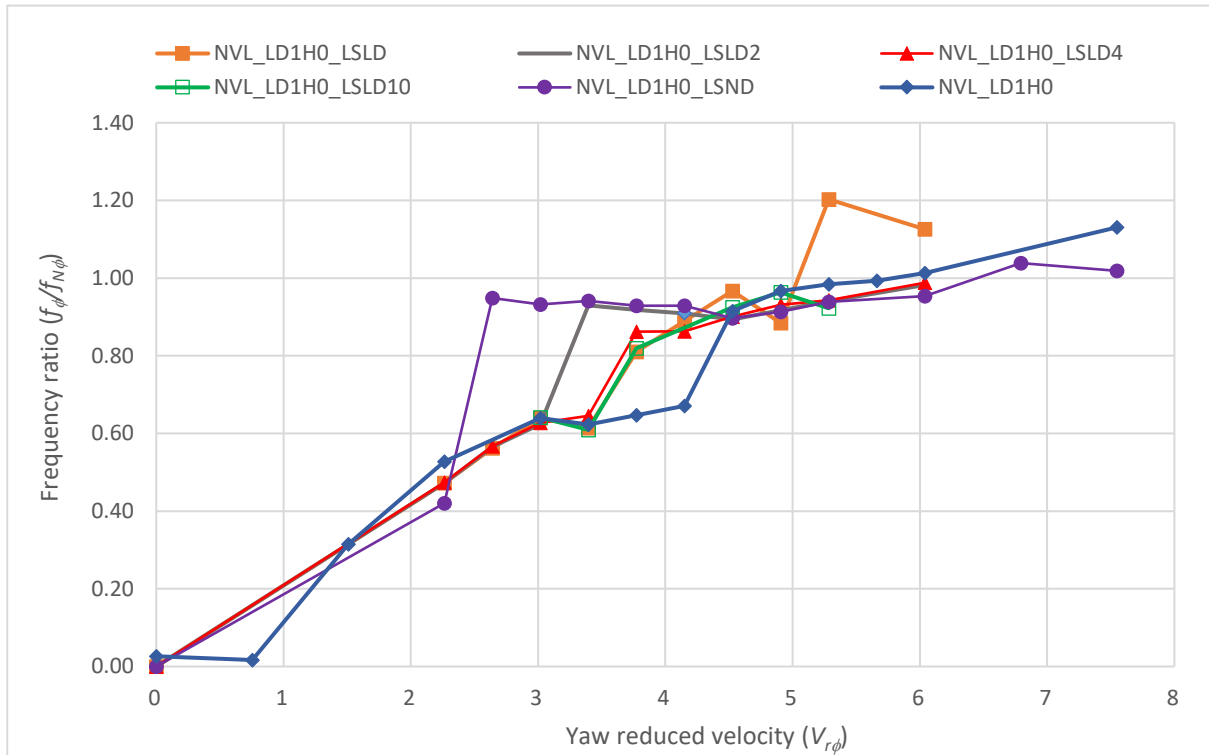


Figure 7-15: Yaw frequency response of the jack-up in steady flow

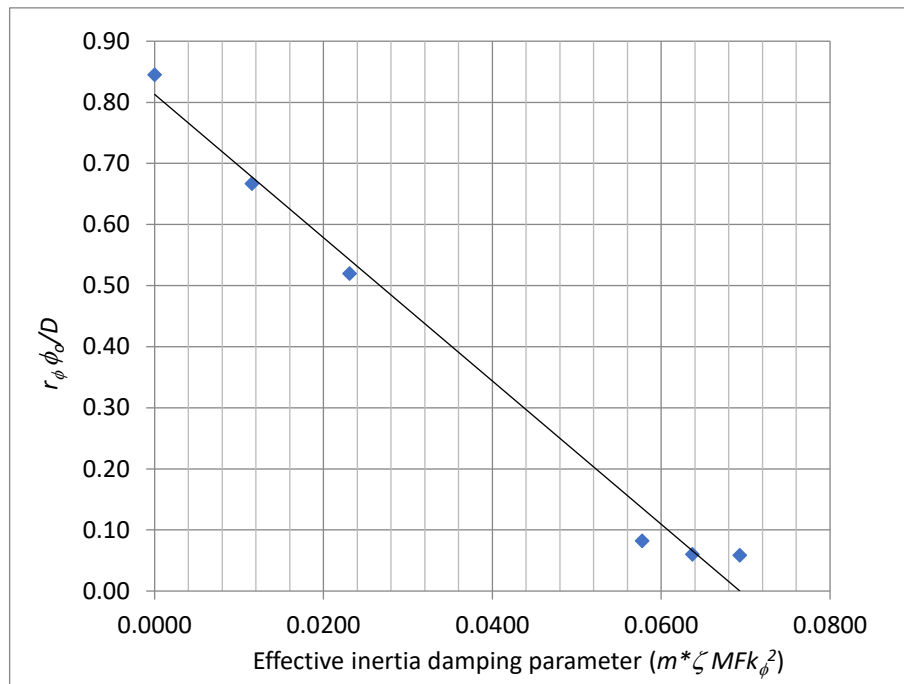


Figure 7-16: Yaw amplitude response with effective inertia damping parameter

#### 7.8.5.6 Mean Response

The mean or steady inline responses of the simulation cases were also ascertained as a function of the flow speed, and the normalised results are plotted in Figure 7-17. It can be observed that the mean inline response roughly follows a quadratic variation (also see Section 6.6.5) with the flow speeds and hence is a good representation of the mean drag force acting on the model. It can be observed that the case with the lowest mass damping parameter exhibits the highest mean inline response. It is clearly evident that the jack-up VIV amplified the mean drag on the jack-up and consequently the mean inline responses throughout the flow speeds. The mean crossflow and yaw responses were found to be insignificant as expected for all the cases.

#### 7.8.5.7 Combined Response

It can be observed that the yaw response range overlaps with the crossflow response range particularly for the low mass damping parameters, causing very large combined lock-in range. The combined crossflow amplitude response of the leg derived from the corresponding crossflow and yaw responses is plotted against the steady flow speeds in Figure 7-18. The combined vibrations achieved higher response amplitudes than the individual values, particularly for low mass damping parameters. Further the combined lock-in range was extending over almost throughout the flow speed range (0.10 m/s to

0.40 m/s) making the jack-up practically redundant, except at low flow speeds. The combined crossflow response of the self-limiting vibrations is found to be around 0.80D.

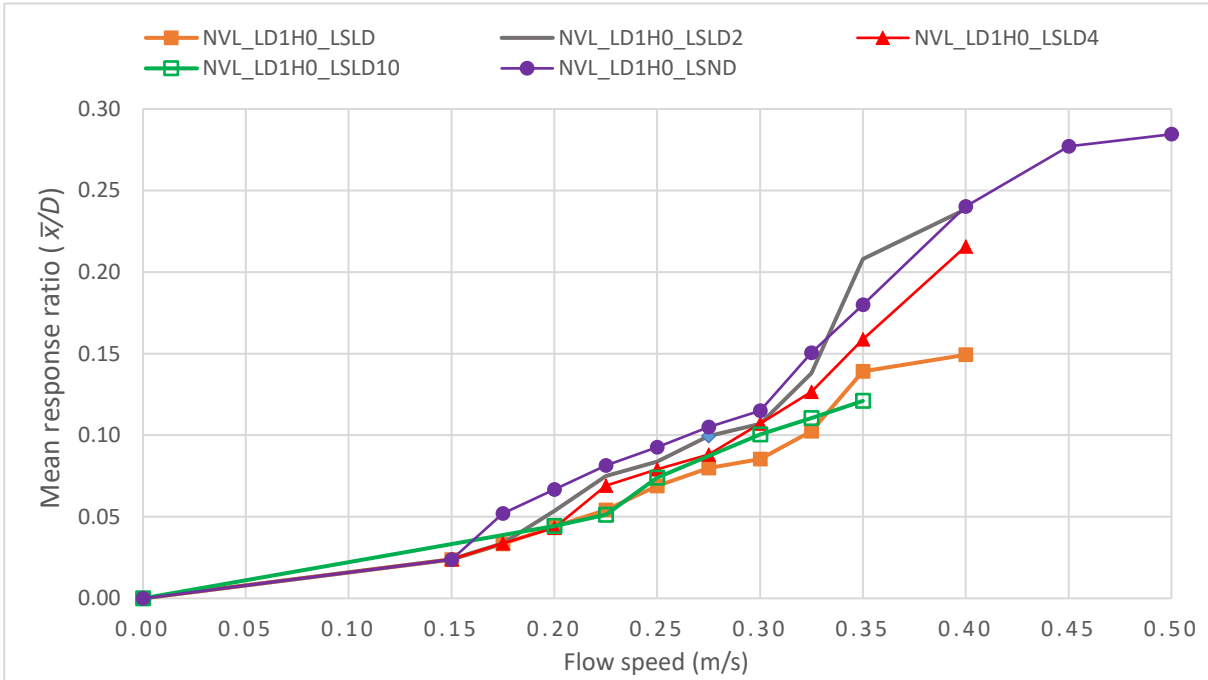


Figure 7-17: Mean inline response of the jack-up versus steady flow speed

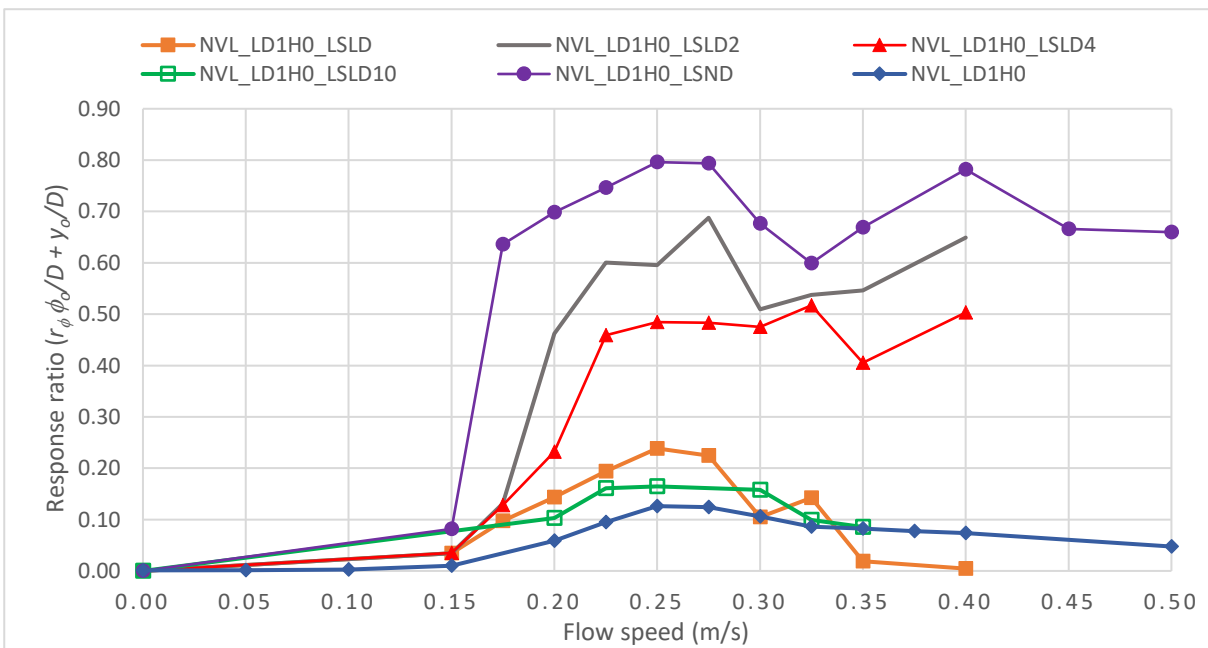


Figure 7-18: Combined crossflow response of the leg in steady flow

### 7.8.6 Forces in Steady Flow

The drag and lift time series of the legs were also obtained from the numerical simulations and post processed to obtain the respective rms amplitudes and mean values. The results are summarised in Table 7-7. The sway and yaw reduced velocities ( $V_{ry}$  and  $V_{r\phi}$  respectively) during the respective lock-in, and the corresponding average inline mean drag ( $C_D$ ), inline oscillatory drag ( $C_{Do}$ ) and lift ( $C_L$ ) coefficients of the jack-up legs are presented in the table. The results of the CFD simulations for stationary jack-up case (LD1H0\_MC) and stationary single cylinder case (LD1H0\_SC) are also shown.

Table 7-7: Jack-up average leg forces from numerical simulations, a) crossflow VIV, b) yaw VIV

a) Force Summary: Sway				
Case	$V_{ry}$	$C_D$	$C_{Do}$	$C_L$
NVL_LD1H0_LSND	5.82	1.46	0.43	0.61
NVL_LD1H0_LSLD2	6.40	1.30	0.31	0.53
NVL_LD1H0_LSLD4	5.23	1.35	0.33	0.74
NVL_LD1H0_LSLD10	5.23	1.05	0.18	0.62
NVL_LD1H0_LSLD	5.82	1.09	0.16	0.63
LD1H0_MC (Fixed)	5.23	0.92	0.03	0.33
LD1H0_SC (Fixed)	5.23	0.99	0.03	0.70
b) Force Summary: Yaw				
Case	$V_{r\phi}$	$C_D$	$C_{Do}$	$C_L$
NVL_LD1H0_LSND	Vrq	1.48	0.51	0.40
NVL_LD1H0_LSLD2	6.04	1.47	0.54	0.59
NVL_LD1H0_LSLD4	6.04	1.33	0.38	0.50
NVL_LD1H0_LSLD10	6.04	1.07	0.15	0.49
NVL_LD1H0_LSLD	4.53	0.96	0.14	0.39
LD1H0_MC (Fixed)	6.04	0.94	0.03	0.45
LD1H0_SC (Fixed)	6.04	1.11	0.08	1.12

#### 7.8.6.1 Lift Force

The rms amplitude of the oscillatory lift coefficient for all the simulation cases is illustrated in Figure 7-19, a) and b) against the crossflow and yaw reduced velocity respectively. The lift coefficient demonstrated is the average value of the four legs. By comparing Figure 7-19 a) with Figure 7-11, it can be inferred that the lift coefficient increases with the crossflow response, indicating lift amplification. It can be observed that the lift coefficient exhibits a single peak response corresponding to crossflow lock-

in. Further, the low value of the average lift coefficient of the stationary jack-up, even less than the single stationary cylinder indicates weak vortex synchronisation among the legs in the absence of crossflow VIV.

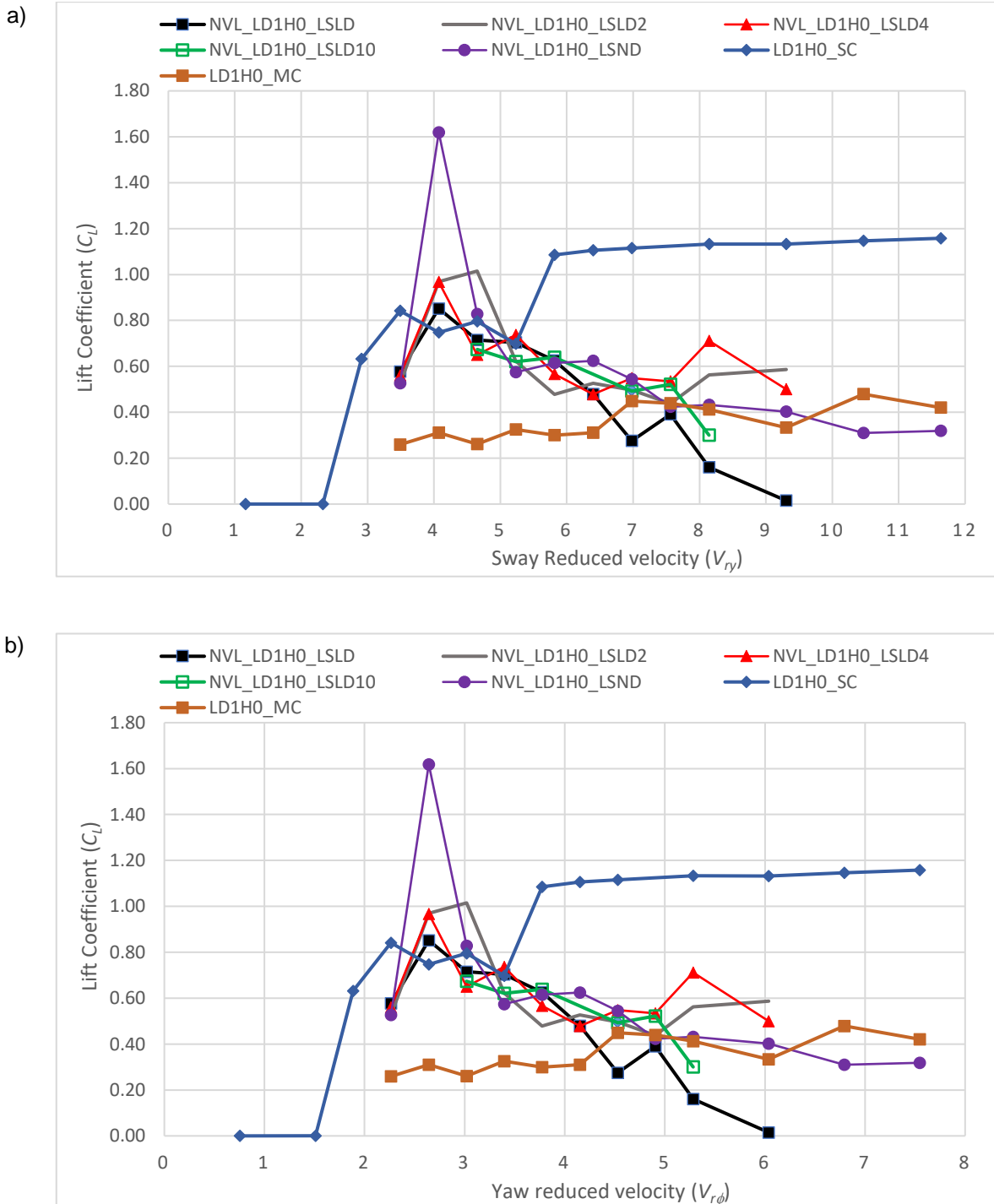


Figure 7-19: Average lift coefficient of the leg in steady flow, a) versus crossflow reduced velocity, b) versus yaw reduced velocity

By comparing Figure 7-19 b) with Figure 7-14, it can be inferred that the mean lift coefficient appeared to be very low value during yaw lock-in, nearly same or even lesser than the stationary jack-up. This can be attributed to the cancellation of the increased out of phase components of the lift forces of the upstream and downstream legs during yaw lock-in, due to enhanced vortex synchronisation about the legs causing yaw moment amplification. Hence, it can be concluded that the lift amplification at the individual leg level will not be reflected in the average lift coefficient of the jack-up leg during yaw lock-in.

Figure 7-20 illustrates the fundamental lift frequency ( $f_L$ ) responses of the jack-up for the simulation cases, normalised with the respective crossflow natural frequencies and plotted against the crossflow reduced velocity. It can be observed that the lift frequency response reveals two separated lock-in regimes; a lower regime with a frequency ratio of around unity and an upper regime with a frequency ratio of above 1.40. In comparison with Figure 7-11 and Figure 7-14, it can be inferred that the lower and upper regimes correspond to the crossflow and yaw lock-in responses respectively. This further demonstrates that both the crossflow and yaw VIVs are causing enhanced vortex synchronisation among the jack-up legs.

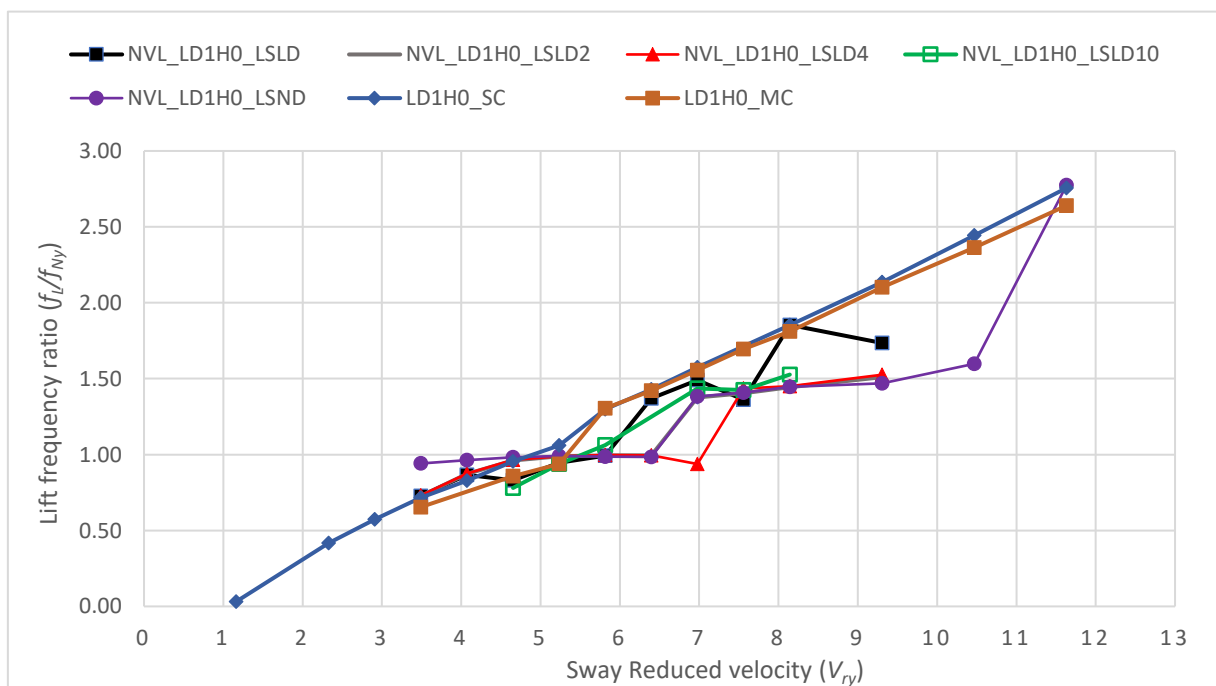


Figure 7-20: Lift frequency in steady flow for the jack-up legs

## 7.8.6.2 Drag Force

Figure 7-21 displays the average rms amplitude of the oscillatory drag coefficient of the jack-up leg for all the simulation cases, plotted against the crossflow reduced velocity. It can be observed that for the oscillatory drag coefficient is significantly higher for the cases with a low mass damping parameter. Further, the oscillatory drag coefficient exhibits a twin peak response, particularly at low mass damping parameter corresponding to the crossflow and yaw lock-in response. This behaviour reveals that the oscillatory drag coefficient is amplified due to both crossflow and yaw VIV, and it can be attributed to the enhanced vortex synchronisation among the legs during lock-in vibrations in these modes.

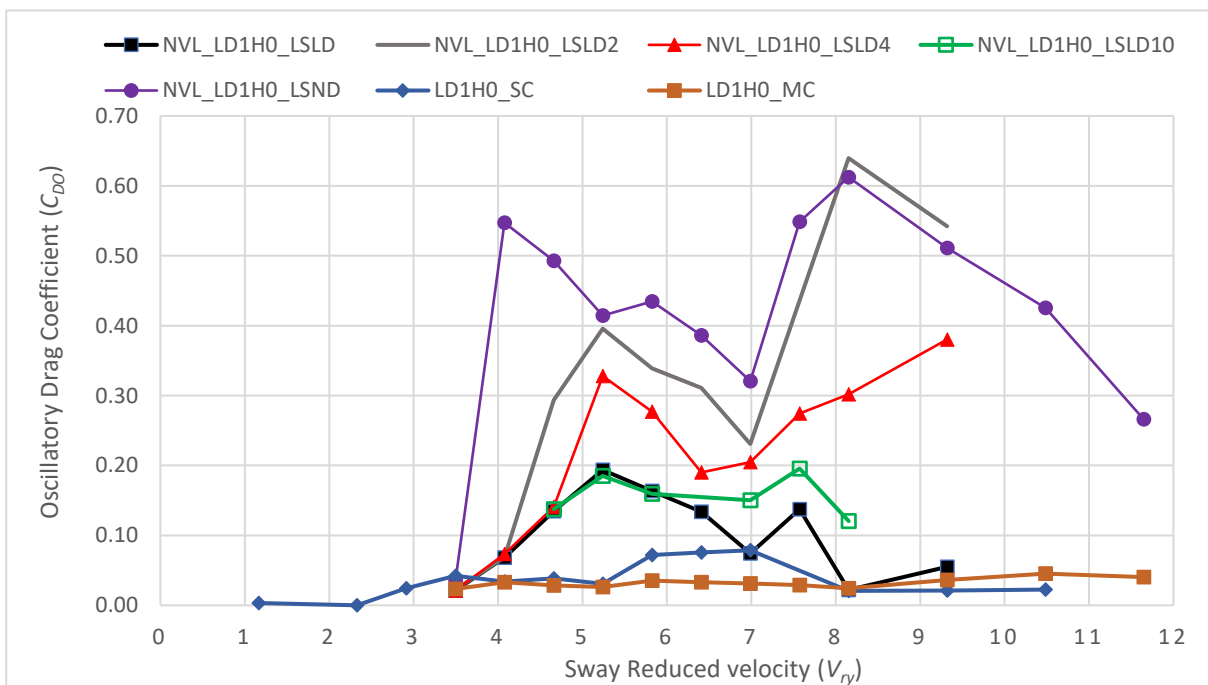


Figure 7-21: Average oscillatory drag coefficient of the leg in steady flow

The fundamental oscillatory drag frequency ( $f_{D0}$ ) of the jack-up for various simulation cases were calculated from the time series, normalised with the respective crossflow natural frequencies and plotted against the corresponding reduced velocities in Figure 7-22. It can be observed that the drag frequency response reveals two separated lock-in regimes; a lower regime with a frequency ratio of around 2 and an upper regime with a frequency ratio of around 3. Considering that the drag force oscillates at twice the lift frequency, it can be inferred that the lower and upper regimes correspond to the crossflow and yaw lock-in regimes respectively. However, for the cases with large

values of mass damping parameters, the oscillatory drag exhibits a low frequency behaviour.

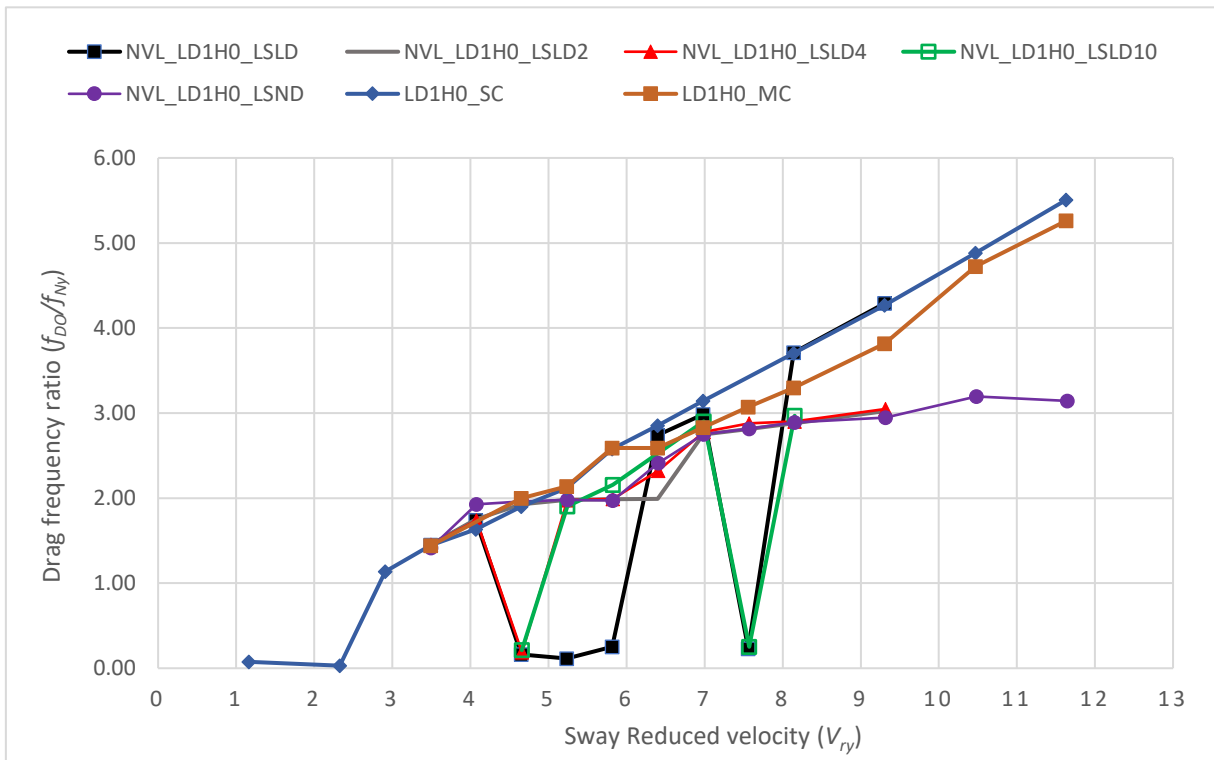


Figure 7-22: Oscillatory drag frequency in steady flow for the jack-up legs

Figure 7-23 presents the average mean drag coefficient of the jack-up legs for various simulation cases, plotted against the steady flow speed from operational consideration. It can be observed that the mean drag coefficient also exhibits a twin peak curve similar to the oscillatory drag coefficient. The corresponding reduced velocity ranges reveal that the peaks correspond to the crossflow and yaw lock-in vibrations. The peaks reveal significant amplification of the mean drag due to both crossflow and yaw VIV, causing increased synchronisation about the legs.

#### 7.8.6.3 Force Amplification

Table 7-8 a) and b) presents the crossflow and yaw VIV response amplitudes and the corresponding leg forces respectively for a given reduced velocity. The forces corresponding to the stationary jack-up leg (LD1H0\_MC) are also demonstrated in the table.

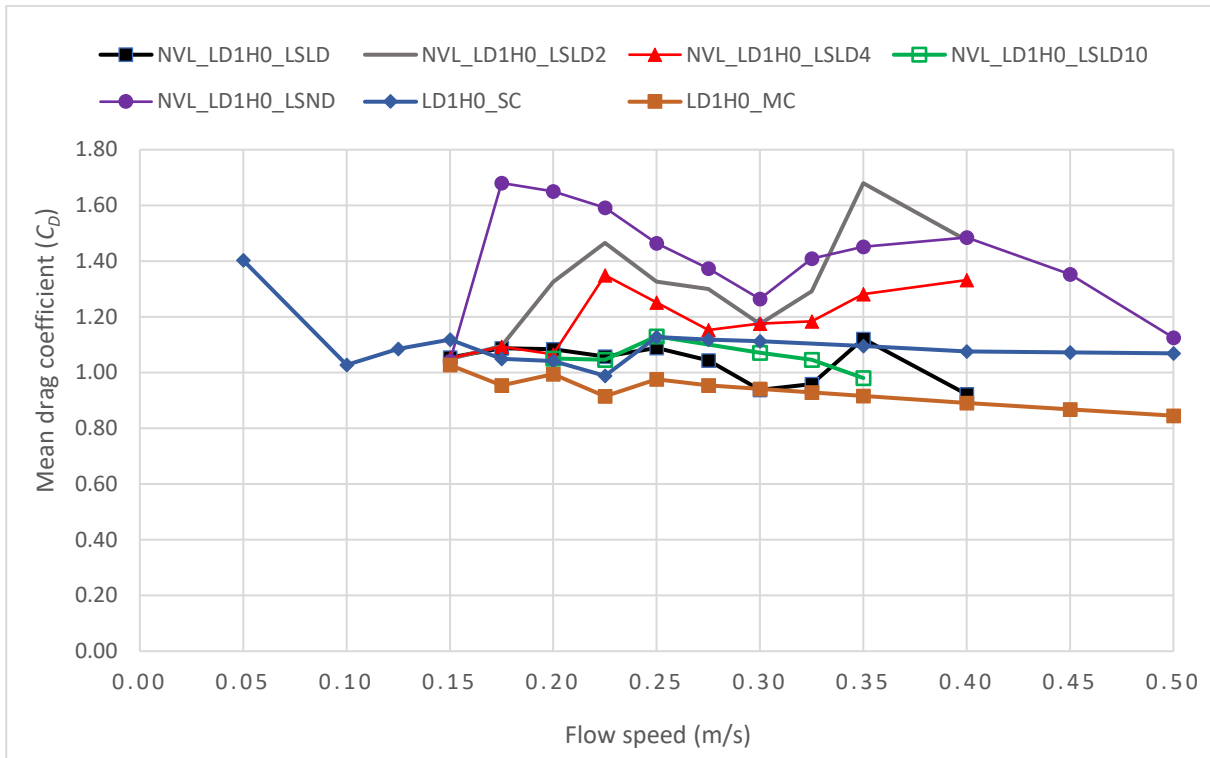


Figure 7-23: Average mean drag coefficient of the leg in steady flow

Table 7-8: Jack-up leg force amplification from numerical simulations, a) crossflow VIV, b) yaw VIV

a) Crossflow /Sway VIV						
Case	$V_{ry}$	$y_{0,rms}/D$	$C_D$	$C_{D0}$	$C_L$	
NVL_LD1H0_LSND	5.23	0.57	1.59	0.41	0.57	
NVL_LD1H0_LSLSL2	5.23	0.50	1.47	0.40	0.62	
NVL_LD1H0_LSLSL4	5.23	0.44	1.35	0.33	0.74	
NVL_LD1H0_LSLSL10	5.23	0.14	1.05	0.18	0.62	
NVL_LD1H0_LSLSL	5.23	0.17	1.06	0.19	0.70	
LD1H0_MC (Fixed)	5.23	0.00	0.92	0.03	0.33	

b) Yaw VIV						
Case	$V_{r\phi}$	$R_{\phi\phi 0,rms}/D$	$R_{\phi\phi 0,rms}/D$	$C_D$	$C_{D0}$	$C_L$
NVL_LD1H0_LSND	4.91	0.65	0.52	1.41	0.55	0.42
NVL_LD1H0_LSLSL2	4.91	0.51	0.41	1.29	0.44	0.44
NVL_LD1H0_LSLSL4	4.91	0.36	0.29	1.18	0.27	0.53
NVL_LD1H0_LSLSL10	4.91	0.07	0.06	1.05	0.20	0.52
NVL_LD1H0_LSLSL	4.91	0.11	0.09	0.96	0.14	0.39
LD1H0_MC (Fixed)	4.91	0.00	0.00	0.93	0.03	0.44

Figure 7-24 illustrates the average force coefficients of the legs plotted against the respective crossflow response amplitude ratios. It can be observed that significant

oscillatory drag and mean drag amplifications occur approximately linearly with the crossflow amplitude ratios, revealing increasing vortex synchronisation along and across the legs with the response amplitude. However, the mean drag amplification is found to be less than that predicted by Blevins (2001), presented in Section 5.4. The lift force exhibited a parabolic curve with a nearly linear increase at small amplitude ratios, saturation at a maximum value around an amplitude ratio of 0.40 and a decrease with the further increase of amplitude ratio, revealing the self-limiting nature of crossflow VIV. This validates the dependence of the lift force on the response amplitude, considered in Section 0. Hence, it can be evidently concluded that aggressive crossflow vibrations can considerably increase the drag and lift forces on the jack-up legs and consequently, the induced stresses.

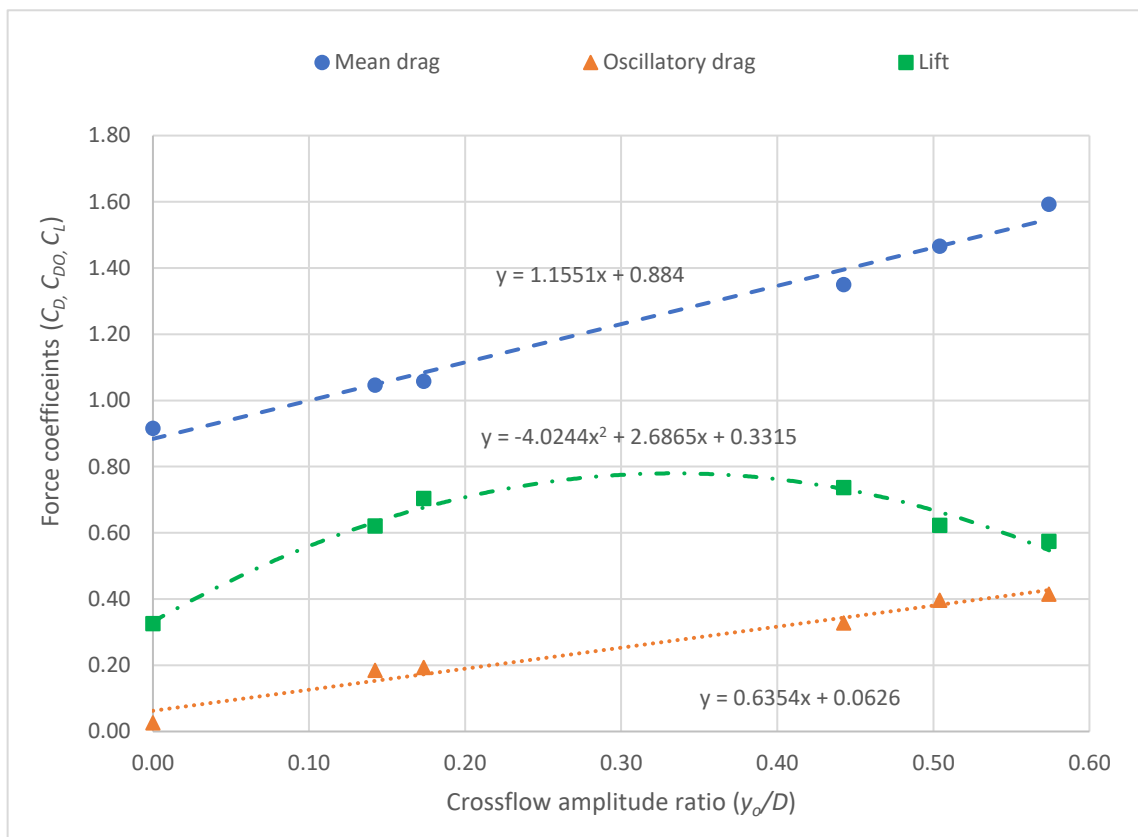


Figure 7-24: Force amplification on the jack-up during crossflow VIV in steady flow

Figure 7-25 shows the variation of the average force coefficients of the legs with the yaw amplitude ratios. Similar to crossflow VIV, near linear increase of mean and oscillatory drag coefficients with the amplitude ratios can be observed for yaw VIV also. This can be attributed to the enhanced vortex synchronisation along and among the legs of the jack-up undergoing yaw VIV, discussed in Sections 7.8.7 and 7.8.8.2.

However, lift coefficient even though exhibits a parabolic behaviour, its dependence on the yaw amplitude ratios is insignificant. This can be attributed to the cancellation of the out of phase lift forces of the upstream and downstream legs during yaw lock-in, leaving a net nearly constant value. Hence, it can be concluded that the lift amplification experienced by the individual leg is not fully captured in the average value displayed and the average yaw moment coefficient would have been a better measure to quantify this effect.

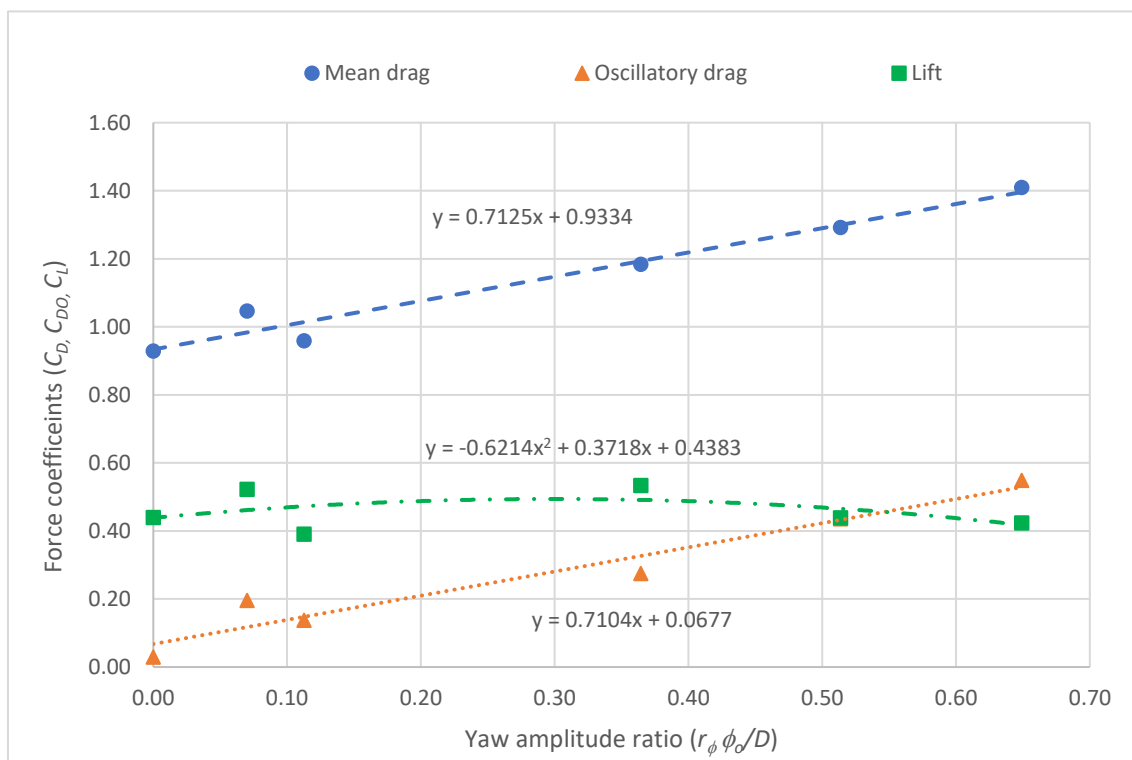


Figure 7-25: Force amplification on the jack-up under yaw VIV in steady flow

### 7.8.7 Vortex Synchronisation about the Legs

The vortex synchronisation about the legs for various VIV modes is investigated by analysing the frequency components of the total lift force coefficient of the jack-up, which has contributions from both the upstream and downstream legs. The self-limiting simulation case, NVL\_LD1H0\_LSND is considered for the investigation owing to significant VIV amplitude response. Figure 7-26 and Figure 7-27 illustrate the results of the FFT of the total lift coefficient of the nonvibrating or stationary jack-up, corresponding to crossflow and yaw lock-in steady flow speeds respectively of NVL\_LD1H0\_LSND.

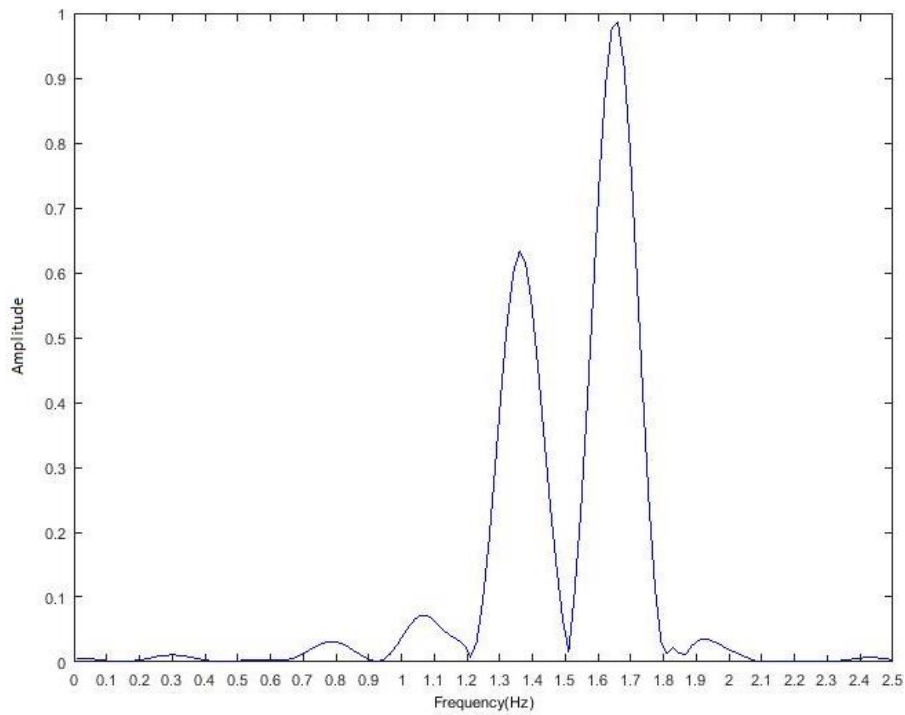


Figure 7-26: FFT of the total lift coefficient of the stationary jack-up corresponding to crossflow VIV, steady flow speed 0.25 m/s, reduced velocity of 5.82

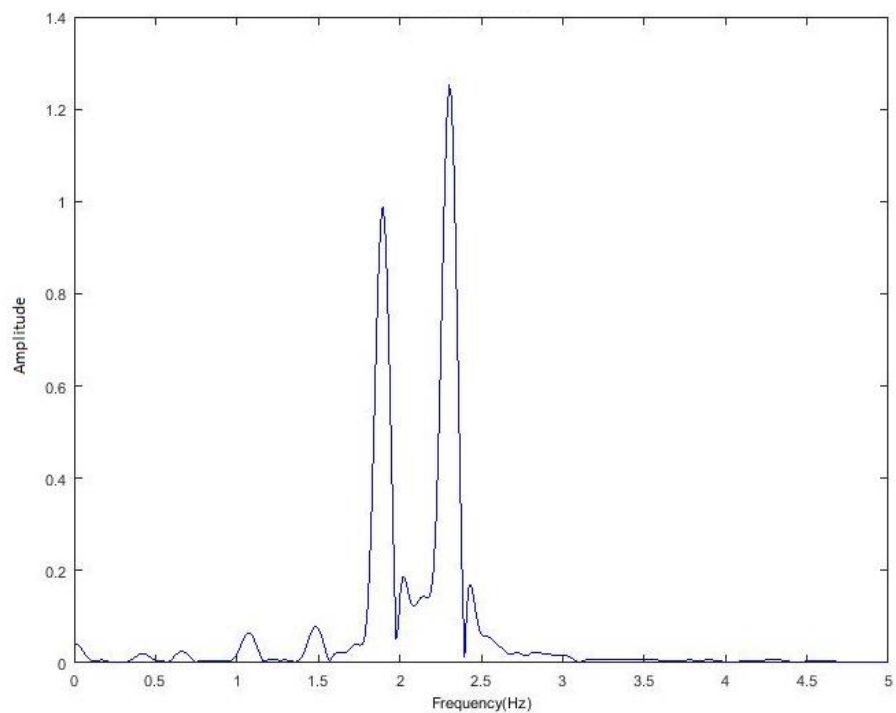


Figure 7-27: FFT of the total lift coefficient of the stationary jack-up corresponding to yaw VIV, steady flow speed 0.35 m/s, yaw reduced velocity of 5.28

It is evident in Figure 7-26 and Figure 7-27 that the total lift force of the nonvibrating jack-up is characterised by a twin peak curve, revealing that the frequency components are predominantly present at two near but separated frequencies. Analysis of the phenomenon further revealed that the two frequency peaks corresponded to the vortex shedding frequencies from the upstream and downstream cylinders. The relatively higher frequency peak corresponds to the upstream cylinder shedding frequency while the other corresponds to that of the downstream cylinder. The lower frequency shedding of the downstream cylinder can be attributed to a lower incoming flow speed due to the wake of the upstream cylinder than the free stream velocity.

The FFT of the total lift coefficient of the jack-up experiencing crossflow and yaw lock-in vibrations is illustrated in Figure 7-28 and Figure 7-29 respectively. It can be observed in Figure 7-28 that the lift force has become slightly broad banded with frequency components at almost all the frequencies. However, the twin peak behaviour has given way to a single fundamental frequency peak, which is same as the crossflow lock-in frequency. Similarly, Figure 7-29 also reveals that the lift force has become relatively broad banded during yaw VIV with a single fundamental frequency peak at the yaw lock-in frequency.

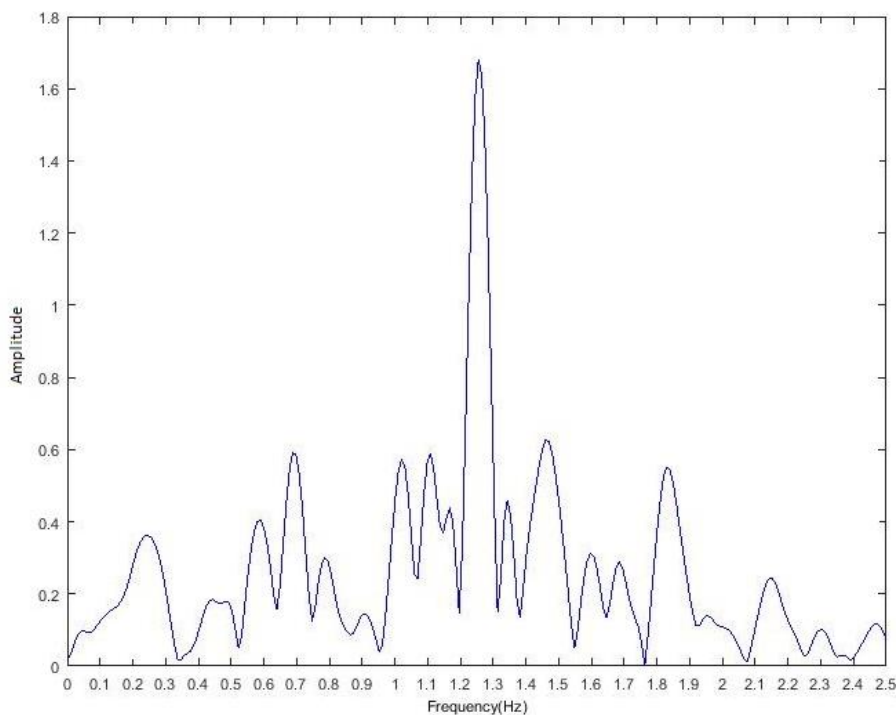


Figure 7-28: FFT of the total lift coefficient of the freely vibrating jack-up during crossflow VIV, steady flow speed 0.25 m/s, reduced velocity of 5.82

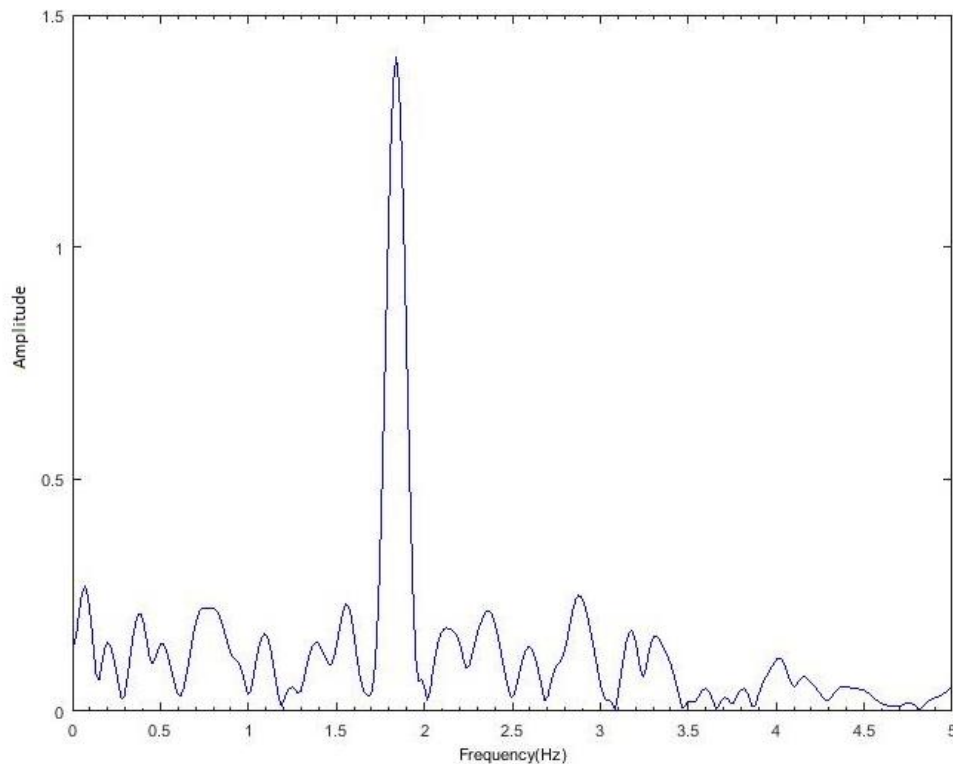


Figure 7-29: FFT of the total lift coefficient of the freely vibrating jack-up during yaw VIV, steady flow speed 0.35 m/s, yaw reduced velocity of 5.28

The observed single frequency peak behaviour of the total lift force indicates that the lock-in vibrations about both the crossflow and yaw VIV modes tend to synchronise the lift or shedding frequencies of the upstream and downstream legs. Further, the lock-in vibrations of the jack-up take control of the shedding frequencies and the vortex shedding from all the legs occurring at the vibration frequency. The slightly broad banded nature of the lift force suggests that the lock-in vibrations disrupt the regular vortex shedding from the upstream and downstream cylinders.

#### 7.8.8 *Vortex Pattern about the Legs*

The vortex patterns about the legs during the VIV modes are investigated by analysing the vortex swirling strength contours about the vibrating legs. The vortex contours at various time shots within a vortex shedding period are analysed to classify the vortex patterns. The self-limiting simulation case, NVL\_LD1H0\_LSND is considered for the investigation owing to its significant VIV response. Figure 7-30 defines the vortex contour colour coding scheme adopted for the investigation.

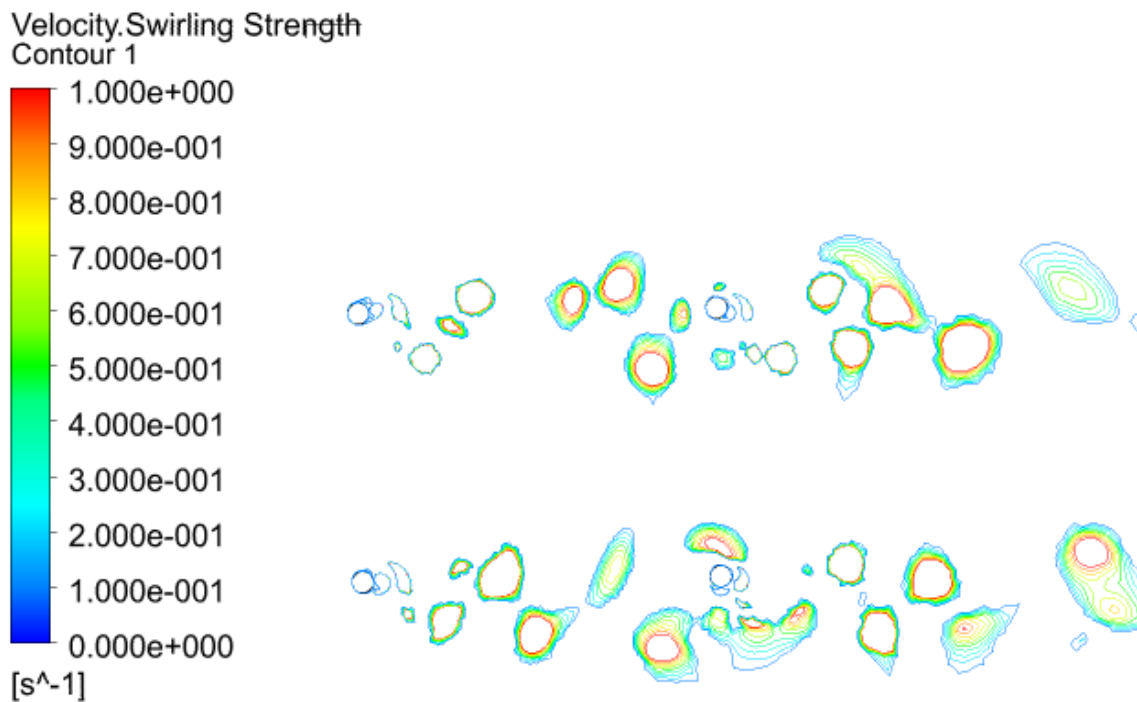
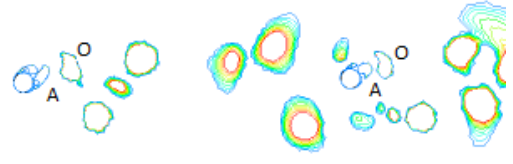
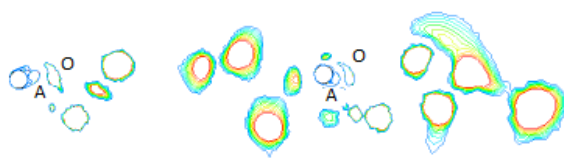


Figure 7-30: Vortex swirling strength contours colour coding scheme

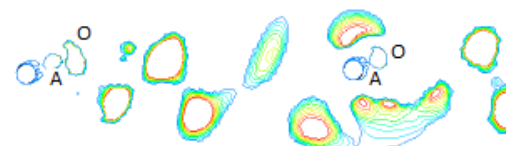
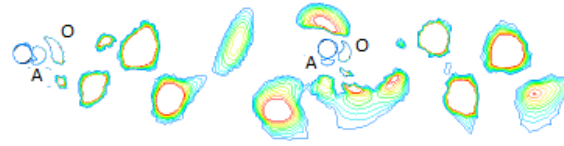
#### 7.8.8.1 Crossflow VIV

Figure 7-31, a) to j) illustrates the vortex patterns around the legs during crossflow VIV at a reduced velocity of 5.82, at time shots equally spaced at 0.10s comprehensively covering one typical vortex shedding period. Figure 7-31 a) demonstrates that the legs are just shedding the vortex A near the downward side of the cylindrical legs. The previously shed vortex O from the upward side is also visible in the figure. It can be seen in Figure 7-31 b) and c) that the vortex A joins the vortex O to form a vortex pair at the upward side. It can be observed in Figure 7-31 d) that all but upstream top leg, are also shedding a secondary vortex A' from the same downward side. The development of vortex B about the upward sides of the legs is also visible in the figure. Figure 7-31 f) shows the synchronised shedding of the vortex B from the upward side of all the legs, demonstrating that the crossflow VIV is synchronising the vortex shedding about the legs. The downstream legs are also found to shed the secondary vortex B' from the upward side, as illustrated in Figure 7-31 i). All the four legs are also found to shed the vortex C almost synchronously from the downward side in Figure 7-31 j).



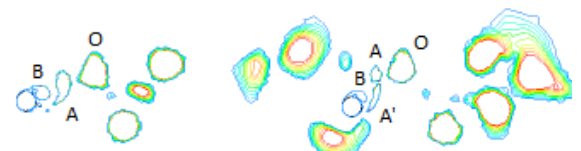
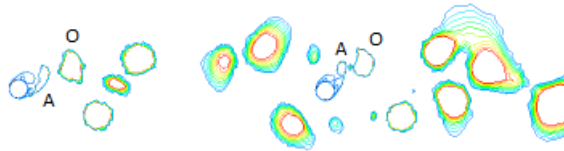
a)

b)



c)

d)



e)

f)

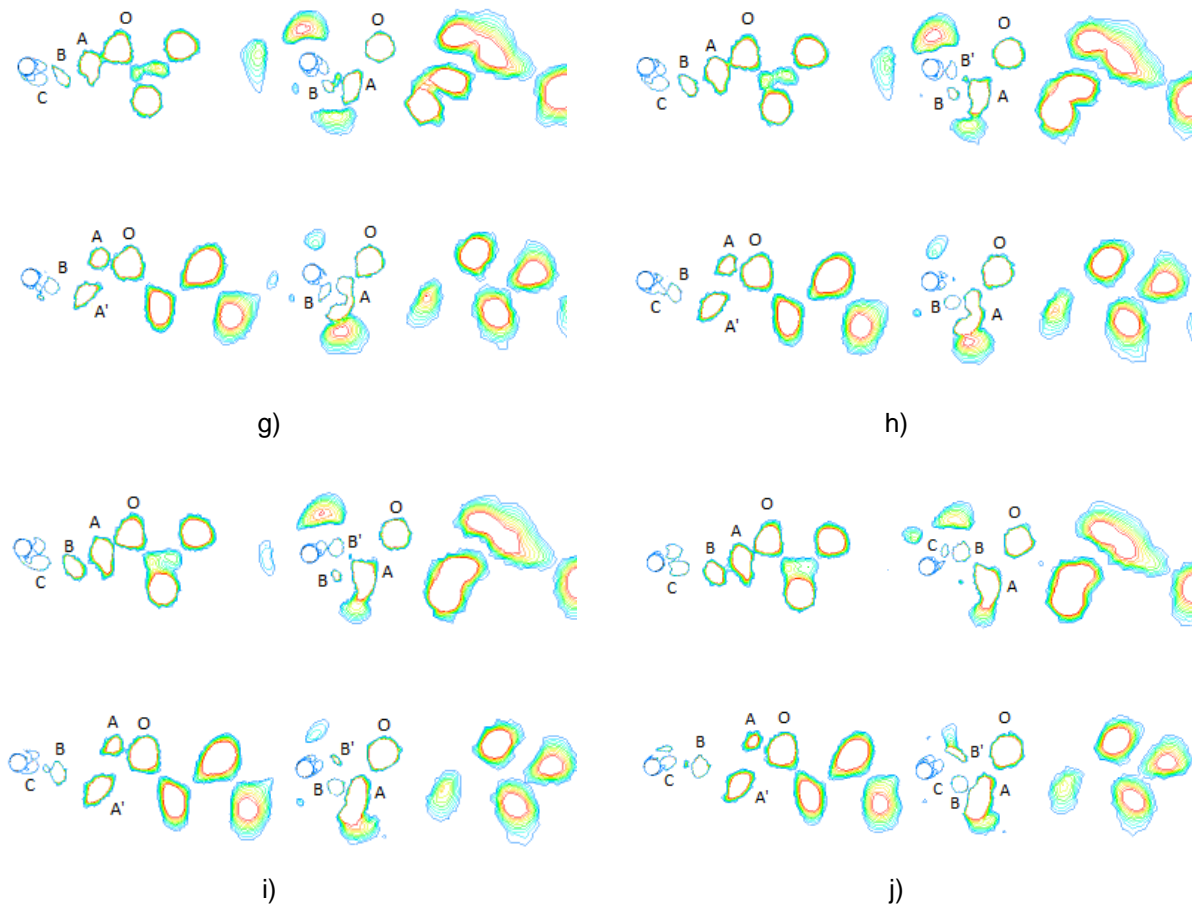


Figure 7-31: Vortex pattern about the jack-up legs during crossflow VIV, steady flow speed 0.25 m/s, reduced velocity of 5.82, a)  $t = 53.5$  s, b)  $t = 53.6$  s, c)  $t = 53.7$  s, d)  $t = 53.8$  s, e)  $t = 53.9$  s, f)  $t = 54$  s, g)  $t = 54.1$  s, h)  $t = 54.2$  s, i)  $t = 54.3$  s, j)  $t = 54.4$  s

It can be concluded that the crossflow VIV of the jack-up synchronises the vortex shedding and vortex phases across the legs. The vortex modes are found to be either 2S or P+S (a vortex pair shed from one side and a single vortex from the other side per vibration cycle) for the upstream legs and 2P for the downstream legs.

#### 7.8.8.2 Yaw VIV

Figure 7-32, a) to f) demonstrate the vortex pattern about the leg during yaw VIV at a yaw reduced velocity of 5.28, at time shots equally spaced at 0.10s covering one typical vortex shedding period. Figure 7-32, a) shows that the cylindrical legs are just shedding the vortex A, upstream legs about the downward side and downstream cylinders about the upward side. The previously shed vortex O, from the upward and downward sides of the upstream and downstream legs respectively is also visible in the figure. It can

be observed from Figure 7-32, c) that the subsequent shedding of the vortex B is from the upward sides of the upstream cylinders and downward sides of the downstream cylinders.

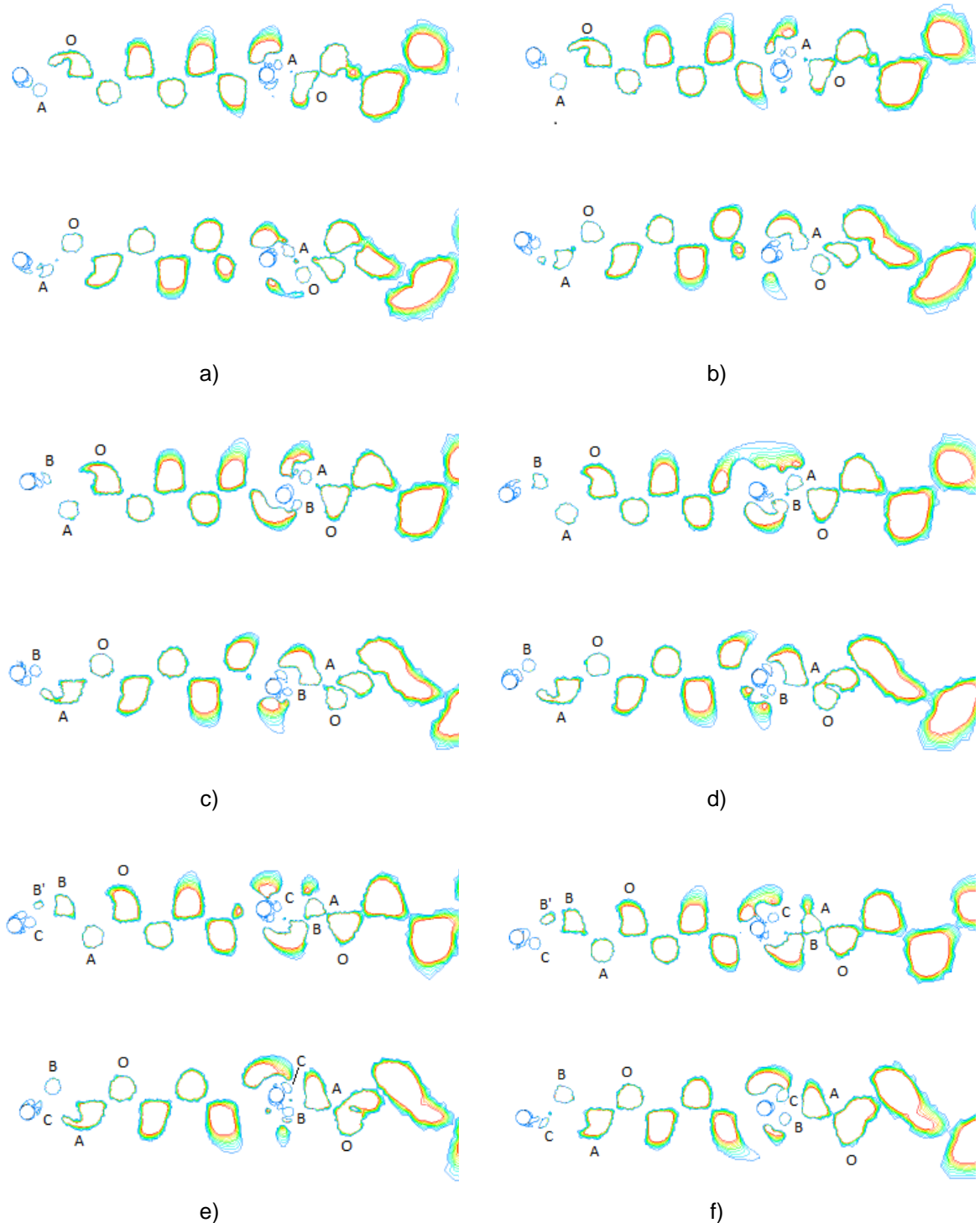


Figure 7-32: Vortex pattern about the jack-up legs during yaw VIV, steady flow speed 0.35 m/s, yaw reduced velocity of 5.28, a)  $t = 48.6\text{s}$ , b)  $t = 48.7\text{s}$ , c)  $t = 48.8\text{s}$ , d)  $t = 48.9\text{s}$ , e)  $t = 49\text{s}$ , f)  $t = 49.1\text{s}$ , g)  $t = 49.2\text{s}$ , h)  $t = 49.3\text{s}$

It is evident that the vortex shedding is more or less synchronised across the legs, though the vortex phase difference is approximately 180 degrees between the upstream and downstream legs. The upstream top leg is also found to shed the secondary vortex B' from the upward side, as illustrated in Figure 7-32, e). The development of the new vortex C at the downward and upward sides of the upstream and downstream legs respectively is also demonstrated in the figure. All the four legs are found to shed the vortex C almost synchronously in Figure 7-32, f), with a 180 degree phase difference between the upstream and downstream legs. It can be concluded that the yaw VIV of the jack-up synchronises the vortex shedding across the legs with a phase difference of 180 degrees between the upstream and downstream cylinders. The vortex modes are found to be either 2S or P+S for the upstream legs and 2S for the downstream legs.

## 7.9 Discussion

The limited 2D numerical investigation carried out for a global heading on 0 degrees validated that the jack-up experiences significant crossflow and yaw VIV with large lock-in regimes in uniform steady currents. The inline lock-in VIV was found not to occur for the cases investigated, though inline coupled VIV was found to occur with the crossflow and yaw modes for low values of mass damping parameters. The crossflow and yaw VIV amplitude responses are found to have an inverse proportionality with the mass damping parameter and inertia damping parameter respectively, as revealed in the theoretical investigation. The lock-in regime of the crossflow VIV is found to be more or less unaffected by the reduction in mass damping parameter while that of yaw VIV is found to increase considerably with the reduction in inertia damping parameter. However, both the crossflow and yaw VIV are found to be self-limiting at amplitude ratios of around 0.60D and 0.85D respectively.

The analysis of leg forces revealed considerable drag and lift amplification due to the crossflow VIV and drag amplification due to the yaw VIV. Oscillatory drag shows a considerable increase in the order of around 10 times during the lock-in vibrations. This can be attributed to the enhanced vortex synchronisation along the legs as well as the consequent increase in the vortex strength (Sumer and Fredsøe, 2006). The mean drag also shows considerable amplification, possibly due to the increase in the effective projected area (Blevins, 2001). However, the lift force displays significant

amplification only in crossflow lock-in regime, whereas in the yaw lock-in regime, the average lift coefficient exhibits much smaller value than the single cylinder.

The investigation of the total lift forces of the stationary jack-up revealed two closely separated frequency components, corresponding to the vortex shedding frequencies of the upstream and downstream legs. The lower frequency component can also be inferred as the effect of the wake of the upstream legs on the vortex shedding about the downstream legs. However, for the jack-up experiencing VIV, the analysis revealed that both the frequency components merged to a single fundamental lift frequency equal to the vibrating frequency. This phenomenon was observed for both the crossflow and yaw modes, revealing lock-in vibrations and consequent vortex synchronisation among the legs.

The investigation of the vortex pattern about the legs during crossflow and yaw lock-in vibrations also revealed enhanced vortex synchronisation about the legs. It is found that during crossflow lock-in, the vortex phase and shedding are both synchronised across all the four legs causing considerable lift amplification. In the case of yaw lock-in, the vortex shedding is found to be synchronised across the four legs but with a vortex phase difference 180 degrees between the upstream and downstream cylinders, causing low total lift force but possibly significant yaw moment amplification. It can be inferred that though the individual legs experience lift amplification during yaw lock-in, the whole jack-up experiences lift reduction due to the out of phase nature of the upstream and downstream lift forces.

Figure 7-33, a) and b) illustrate the simplified vortex patterns about the jack-up legs for the crossflow and yaw VIV modes respectively. However, it is highlighted that the observations correspond to  $0^\circ$  global heading of the jack-ups under uniform flow. As the response behaviour and the vortex patterns can be different for oblique headings and nonuniform or oscillatory flows, further investigation is warranted.

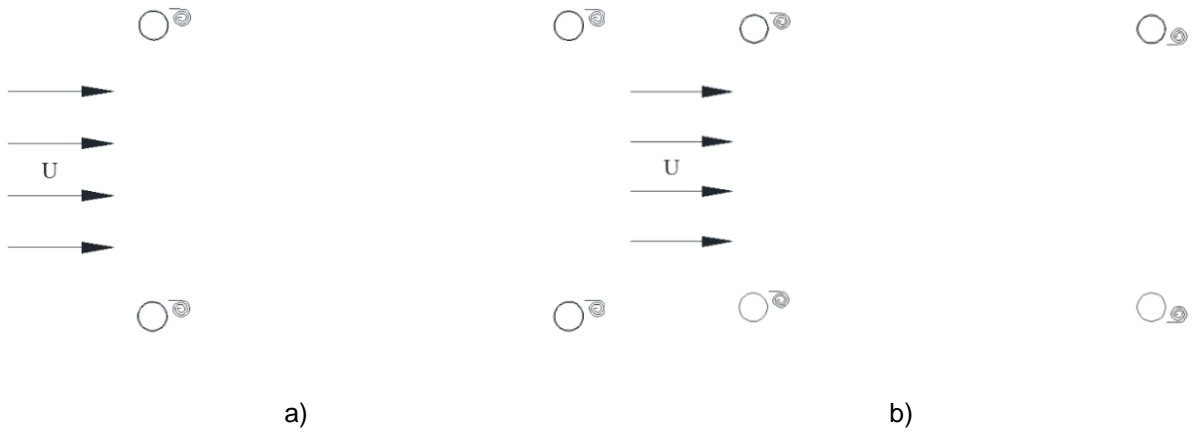


Figure 7-33: Vortex pattern for the VIV modes, a) crossflow, b) yaw

## Chapter 8. Suppression of Jack-up VIV

This chapter demonstrates that streamlined leg fairing can be used as an excellent VIV suppression device for the jack-ups. A simplified mathematical model is developed based on the principle of conservation of energy, which could be used to decide the optimum location and geometry of the fairings for the cylinders undergoing VIV in a uniform flow. The model can be used to optimise the location and thickness (depth) of the fairings fitted on the jack-up legs. Two optimum fairing profiles are developed and successfully tested on the cylindrical legs of the scaled Jack-up model. The two fairing section offsets presented may be readily used by the industry for practical applications.

### 8.1 Fairing Theory

Streamlined fairings work on the principle of delayed boundary layer separation. The streamline nature reduces the rear adverse pressure gradient, eliminates or delays the flow separation and considerably reduces the pressure fluctuations around the body. Consequently, significant reduction of the mean drag, lift and oscillating drag is achieved and so the structural response and the VIV.

#### 8.1.1 Sway Mode of the Jack-up in Uniform Current

##### 8.1.1.1 Excitation

Considering that the portion of the leg covered by the fairings will not contribute to the excitation because of vortex suppression, the effective crossflow excitation per leg ( $F_{eLy}$ ) can be expressed similar to Equation 5-33 as,

$$F_{eLy} = \int_0^h f_{Oy}(z) \frac{A \sin(\kappa_L z + B) + E}{A \sin(\kappa_L L + B) + E} dz - \sum_1^{n_f} F_{fyi} \frac{y_{fi}}{y_L} \quad \text{Equation 8-1}$$

where  $f_{Oy}$ ,  $n_f$ ,  $F_{fyi}$  and  $y_{fi}$  represent the distribution of the oscillatory crossflow excitation force along the leg, the number of leg fairings per leg, the excitation force on the leg at the fairing location if the fairing is not fitted and leg deflection at the fairing location respectively.

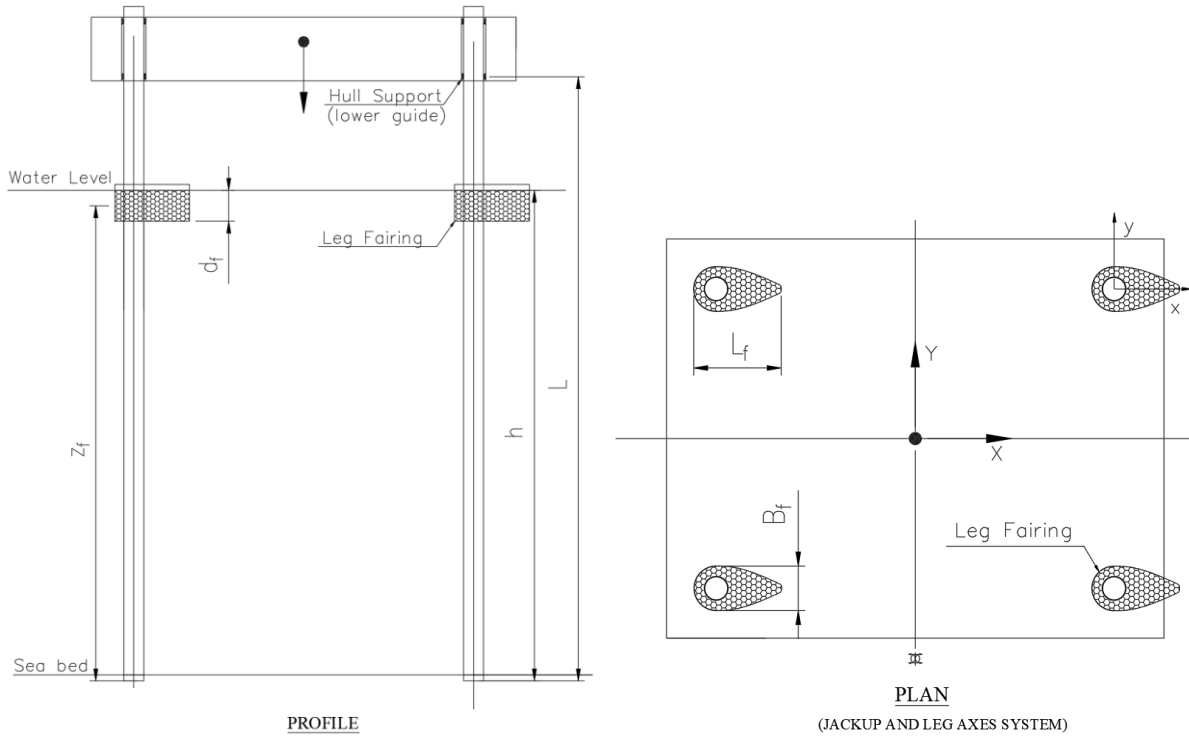


Figure 8-1: Jack-up with leg fairings

Approximating fairing as a two dimensional (2D) body with depth considerably lesser than the leg length and water depth,

$$F_{eLy} = \int_0^h f_{Oy}(z) \frac{A \sin(\kappa_L z + B) + E}{A \sin(\kappa_L L + B) + E} dz - \sum_{i=1}^{n_f} f_{Oy}(z_{fi}) d_f \frac{A \sin(\kappa_L z_{fi} + B) + E}{A \sin(\kappa_L L + B) + E}$$

Equation 8-2

where  $z_{fi}$  and  $d_f$  represent the vertical location of the fairing from the seabed and the depth (thickness) of the fairing along the leg respectively.

It can be observed from Equation 8-2 that for minimal excitation, the magnitude of the second term on the right hand side (RHS) should be as high as possible, which is possible by placing the fairings near the antinodes, where modal displacement is maximum.

For a jack-up, this is at the water level and considering a single fairing per leg as illustrated in Figure 8-1, the expression shall be simplified as,

$$F_{eLy} = \int_0^h f_{Oy}(z) \frac{A \sin(\kappa_L z + B) + E}{A \sin(\kappa_L L + B) + E} dz - f_{Oy}(h) d_f \frac{A \sin(\kappa_L h + B) + E}{A \sin(\kappa_L L + B) + E} \quad \text{Equation 8-3}$$

In the uniform current, neglecting the effect of lift amplification for simplicity and by defining,

$$f_{Oy} = \frac{1}{2} \rho C_L D U^2 \quad \text{Equation 8-4}$$

Defining the lift force as  $F_L = f_{Oy} h$ , Equation 8-3 becomes,

$$F_{eLy} = \frac{F_L}{h [A \sin(\kappa_L L + B) + E]} \left\{ \int_0^h [A \sin(\kappa_L z + B) + E] dz - d_f [A \sin(\kappa_L h + B) + E] \right\}$$

$$\text{Equation 8-5}$$

#### 8.1.1.2 Fluid damping

Consequently, based on Equation 5-156 the linear crossflow fluid damping coefficient per leg ( $C_{eLfy}$ ) can be expressed as,

$$C_{eLfy} = \frac{4}{3\pi [A \sin(\kappa_L L + B) + E]^3} \rho C_{DW} D \omega y_L \int_0^h [A \sin(\kappa_L z + B) + E]^3 dz + \sum_{i=1}^{n_f} \frac{4}{3\pi} \rho (C_{DWyf} L_f - C_{DW} D) d_f \omega y_L \left[ \frac{A \sin(\kappa_L z_{fi} + B) + E}{A \sin(\kappa_L L + B) + E} \right]^3 \quad \text{Equation 8-6}$$

where  $C_{DWyf}$  and  $L_f$  represent the crossflow drag coefficient of the fairing in oscillatory flow and the length of the fairing respectively.

In the uniform current, the whole length of the leg will experience lock-in and the fluid damping on the leg should be due to the fluid drag experienced by the fairings only; the crossflow fluid damping of circular cylinders is found to be negative during lock-in vibrations (Sarpkaya, 1995) and is revealed as lift amplification.

Approximating fairing as a 2D body, the crossflow fluid damping shall be expressed as,

$$C_{eLfy} = \sum_{i=1}^{n_f} \frac{4}{3\pi} \rho C_{DWyf} L_f d_f \omega y_L \left[ \frac{A \sin(\kappa_L z_{fi} + B) + E}{A \sin(\kappa_L L + B) + E} \right]^3 \quad \text{Equation 8-7}$$

It can be observed from Equation 8-7 also that for maximum fluid damping, the magnitude of the RHS term should be as high as possible, which is again possible by placing the fairings at the water level, near the antinodes.

Considering a single fairing per leg at the water level as illustrated in Figure 8-1,

$$C_{eLfy} = \frac{4}{3\pi} \rho C_{DWyf} L_f d_f \omega y_L \left[ \frac{A \sin(\kappa_L h + B) + E}{A \sin(\kappa_L L + B) + E} \right]^3 \quad \text{Equation 8-8}$$

### 8.1.1.3 Response

Similar to Equation 5-34, the crossflow resonant response of the SDOF can be derived as,

$$y_L = \frac{F_L}{C_{eLy} \omega_{Ny}} \left( \frac{1}{h [A \sin(\kappa_L L + B) + E]} \right) \left\{ \int_0^h [A \sin(\kappa_L z + B) + E] dz - d_f [A \sin(\kappa_L h + B) + E] \right\}$$

$$\text{Equation 8-9}$$

Considering Equation 8-4, Equation 8-8 and Equation 5-158 in Equation 8-9, Strouhal relationship and crossflow resonance/lock-in condition,

$$\frac{y_L}{D} = \frac{\rho C_L D^2 \omega_{Ny}}{8\pi^3 St^2 [A \sin(\kappa_L L + B) + E]} \frac{\left\{ \int_0^h [A \sin(\kappa_L z + B) + E] dz - d_f [A \sin(\kappa_L h + B) + E] \right\}}{\left[ C_{eLsy} + \frac{4}{3\pi} \rho C_{DWyf} L_f d_f \omega y_L \left[ \frac{A \sin(\kappa_L h + B) + E}{A \sin(\kappa_L L + B) + E} \right]^3 \right]}$$

$$\text{Equation 8-10}$$

Equation 8-10 shows clearly how the fairings are reducing the crossflow VIV. The reduction in excitation and increase in fluid damping are well captured in the above equation. Similar expressions can also be developed for other rigid vertical cylinders used in marine operations including rigid riser, TLP tether, monopile.

The relative response ratio (response normalised with respect to the response without fairing) in a uniform flow of a fully immersed rigid vertical cylinder with a pinned support at the bottom end, undergoing crossflow VIV with a mode shape of quarter sinusoid, having negligible structural damping and fitted with an antinode fairing is illustrated in Figure 8-2 as a function of fairing depth ratio (fairing depth normalised with respect to the cylinder length). A fairing depth ratio of 0.02 was considered to approximate the response without fairings since Equation 8-10 is found to be asymptotic for a fairing depth ratio of 0, in the absence of any structural damping.

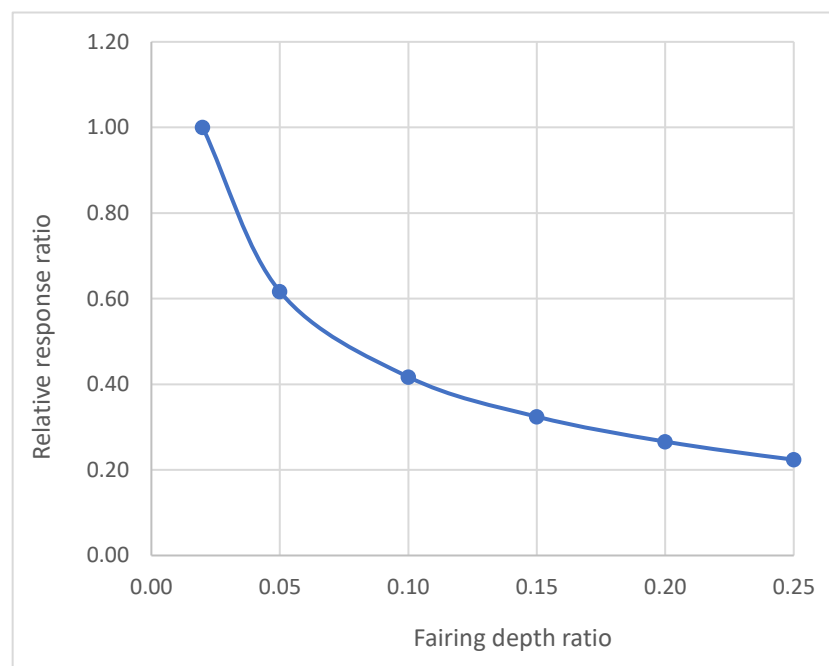


Figure 8-2: Relative response ratio versus fairing depth ratio of a fully immersed vertical cylinder with negligible structural damping

It can be observed from Figure 8-2 that considerable reduction, even up to 80% of the VIV response is possible by means of streamlined fairings. It can also be observed that the response reduction tends to saturate beyond a depth ratio of around 20% the cylinder length for the mentioned mode shape.

## 8.1.2 Yaw Mode of the Jack-up with four cylindrical legs in Uniform Current

### 8.1.2.1 Excitation

The total yaw moment due to crossflow excitation ( $M_{oe\phi}$ ) considering fairings on all four legs as illustrated in Figure 8-1, shall be expressed as,

$$M_{oe\phi} = \int_0^h 4 m_{o\phi}(z) \frac{A \sin(\kappa_L z + B) + E}{A \sin(\kappa_L L + B) + E} dz - 4 \sum_{i=1}^{n_f} M_{f\phi i} \frac{\phi_{fi}}{\phi_L} \quad \text{Equation 8-11}$$

where  $m_{o\phi}$ ,  $M_{f\phi i}$  and  $\phi_{fi}$  represent the distribution of the oscillatory yaw excitation moment along the leg, the yaw excitation moment on the leg at the fairing location if the fairing is not fitted and leg yaw deflection at the fairing location respectively.

Approximating fairing as a 2D body,

$$M_{oe\phi} = \int_0^h 4 m_{o\phi}(z) \frac{A \sin(\kappa_L z + B) + E}{A \sin(\kappa_L L + B) + E} dz - 4 \sum_{i=1}^{n_f} m_{o\phi}(z_{fi}) d_f \frac{A \sin(\kappa_L z_{fi} + B) + E}{A \sin(\kappa_L L + B) + E}$$

Equation 8-12

For minimal yaw excitation, the magnitude of the second term on the RHS should be as high as possible, which is possible by placing the fairings near the antinodes.

Considering a single fairing per leg at the water level, the yaw moment due to crossflow excitation becomes,

$$M_{oe\phi} = \int_0^h 2 f_{oy}(z) a \frac{A \sin(\kappa_L z + B) + E}{A \sin(\kappa_L L + B) + E} dz - 2 f_{oy}(h) d_f a \frac{A \sin(\kappa_L h + B) + E}{A \sin(\kappa_L L + B) + E}$$

Equation 8-13

In the uniform current, neglecting lift amplification, the yaw excitation can be simplified as,

$$M_{oe\phi} = \frac{2 F_L a}{h [A \sin(\kappa_L L + B) + E]} \left\{ \int_0^h [A \sin(\kappa_L z + B) + E] dz - d_f [A \sin(\kappa_L h + B) + E] \right\}$$

Equation 8-14

### 8.1.2.2 Fluid damping

Based on Equation 5-162, the yaw damping coefficient of the jack-up due to inline fluid drag ( $C_{ef\phi x}$ ) becomes,

$$C_{ef\phi x} = 4 \left\{ \frac{4}{3\pi [A \sin(\kappa_L L + B) + E]^3} \rho C_D D \omega \phi_L \left(\frac{b}{2}\right)^3 \int_0^h [A \sin(\kappa_L z + B) + E]^3 dz \right. \\ \left. + \sum_{i=1}^{n_f} \frac{4}{3\pi} \rho (C_{Dxf} B_f - C_D D) d_f \omega \phi_L \left(\frac{b}{2}\right)^3 \left[ \frac{A \sin(\kappa_L z_{fi} + B) + E}{A \sin(\kappa_L L + B) + E} \right]^3 \right\}$$

Equation 8-15

where  $C_{Dxf}$  and  $B_f$  represent the inline drag coefficient and breadth of the fairing respectively. As the inline drag coefficient of the fairing can be quite low due to its streamline nature, fluid damping contribution from the fairings due to inline fluid drag may be neglected. Further, the fluid damping due to inline drag on the legs may also be negligible in comparison with the crossflow drag on the fairings as the length of the fairing is considerably higher than the leg diameter.

Similarly, based on Equation 5-163, the yaw damping coefficient of the jack-up due to crossflow fluid drag ( $C_{eLf\phi y}$ ) becomes,

$$C_{eLf\phi y} = 4 \left\{ \frac{4}{3\pi [A \sin(\kappa_L L + B) + E]^3} \rho C_{DW} D \omega \phi_L \left(\frac{a}{2}\right)^3 \int_0^h [A \sin(\kappa_L z + B) + E]^3 dz \right. \\ \left. + \sum_{i=1}^{n_f} \frac{4}{3\pi} \rho (C_{DWyf} L_f - C_{DW} D) d_f \omega \phi_L \left(\frac{a}{2}\right)^3 \left[ \frac{A \sin(\kappa_L z_{fi} + B) + E}{A \sin(\kappa_L L + B) + E} \right]^3 \right\}$$

Equation 8-16

As the whole length of the leg will experience crossflow lock-in excitation in uniform current, the crossflow fluid damping on the leg should be due to the fairings only; the crossflow fluid damping of circular cylinders is found to be negative during lock-in vibrations (Sarpkaya, 1995).

$$C_{ef\phi y} = 4 \sum_{i=1}^{n_f} \frac{4}{3\pi} \rho C_{DWy_f} L_f d_f \omega \phi_L \left(\frac{a}{2}\right)^3 \left[ \frac{A \sin(\kappa_L z_{fi} + B) + E}{A \sin(\kappa_L L + B) + E} \right]^3 \quad \text{Equation 8-17}$$

It can be observed from Equation 8-17 that for maximum fluid damping, the fairings should be placed near the antinodes, which corresponds to the water level.

Considering single fairing per leg at the water level,

$$C_{ef\phi x} = \frac{2}{3\pi [A \sin(\kappa_L L + B) + E]^3} \rho C_D D \omega \phi_L b^3 \int_0^h [A \sin(\kappa_L z + B) + E]^3 dz + \frac{2}{3\pi} \rho (C_{Dxf} B_f - C_D D) d_f \omega \phi_L b^3 \left[ \frac{A \sin(\kappa_L z_{fi} + B) + E}{A \sin(\kappa_L L + B) + E} \right]^3 \quad \text{Equation 8-18}$$

$$C_{ef\phi y} = \frac{2}{3\pi} \rho C_{DWy_f} L_f d_f \omega \phi_L a^3 \left[ \frac{A \sin(\kappa_L h + B) + E}{A \sin(\kappa_L L + B) + E} \right]^3 \quad \text{Equation 8-19}$$

$$C_{ef\phi} = C_{ef\phi x} + C_{ef\phi y} \quad \text{Equation 8-20}$$

### 8.1.2.3 Response

The yaw resonant response can be found based on Equation 5-46 as,

$$\phi_L = \frac{2 F_L a}{C_{e\phi} \omega_{N\phi}} \left( \frac{1}{h [A \sin(\kappa_L L + B) + E]} \right) \left\{ \int_0^h [A \sin(\kappa_L z + B) + E] dz - d_f [A \sin(\kappa_L h + B) + E] \right\}$$

$$\text{Equation 8-21}$$

Considering Equation 8-4, Equation 8-20 and Equation 5-165 in Equation 8-21, Strouhal relationship and yaw lock-in due to crossflow excitation,

$$\frac{\phi_L}{D} = \frac{\rho C_L D^2 \omega_{N\phi} a}{4 \pi^3 St^2 [A \sin(\kappa_L L + B) + E]} \frac{\left\{ \int_0^h [A \sin(\kappa_L z + B) + E] dz - d_f [A \sin(\kappa_L h + B) + E] \right\}}{[C_{es\phi} + C_{ef\phi}]}$$

Equation 8-22

Neglecting the yaw damping due to inline fluid drag,

$$\frac{\phi_L}{D} = \frac{\rho C_L D^2 \omega_{N\phi} a}{4 \pi^3 St^2 [A \sin(\kappa_L L + B) + E]} \frac{\left\{ \int_0^h [A \sin(\kappa_L z + B) + E] dz - d_f [A \sin(\kappa_L h + B) + E] \right\}}{\left[ C_{eLs\phi} + \frac{2}{3\pi} \rho C_{DWyf} L_f d_f \omega \phi_L a^3 \left[ \frac{A \sin(\kappa_L h + B) + E}{A \sin(\kappa_L L + B) + E} \right]^3 \right]}$$

Equation 8-23

Similar to sway VIV, Equation 8-23 demonstrates clearly how the fairings reduce the yaw VIV. The reduction in excitation and increase in fluid damping are well captured in the above equation.

## 8.2 Fairing Profiles

The mathematical investigation in the previous section revealed that the optimum location for the installation of the fairings is the vicinity of the antinodes of the concerned mode, which corresponds to the water level for the jack-up leg. Two compact leg fairing designs are developed for practical applications, based on the standard NACA0018 profile with  $L_f/B_f$  ratios equalling 3.00 and 2.40.  $L_f/B_f$  ratios of the fairing designs are considered as low as practically possible considering installation and manufacturing, ensuring minimum bearing on the aerofoil performance. The location of the pivot point with respect to the centre of pressure of the profile was decided considering the weathervaning stability.

The two fairing designs are illustrated in the model scale in Figure 8-3 and Figure 8-4 respectively. The fairing designs were subsequently tested experimentally on the scaled Jack-up model in uniform flow.

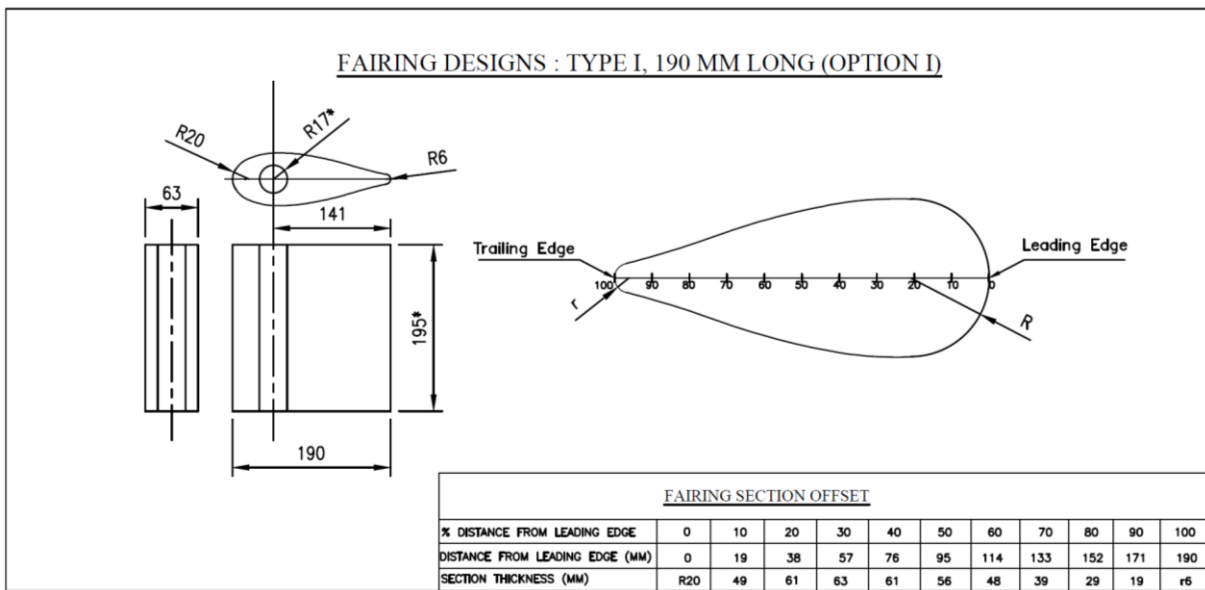


Figure 8-3: Fairing Profile/Design 1 in the model scale

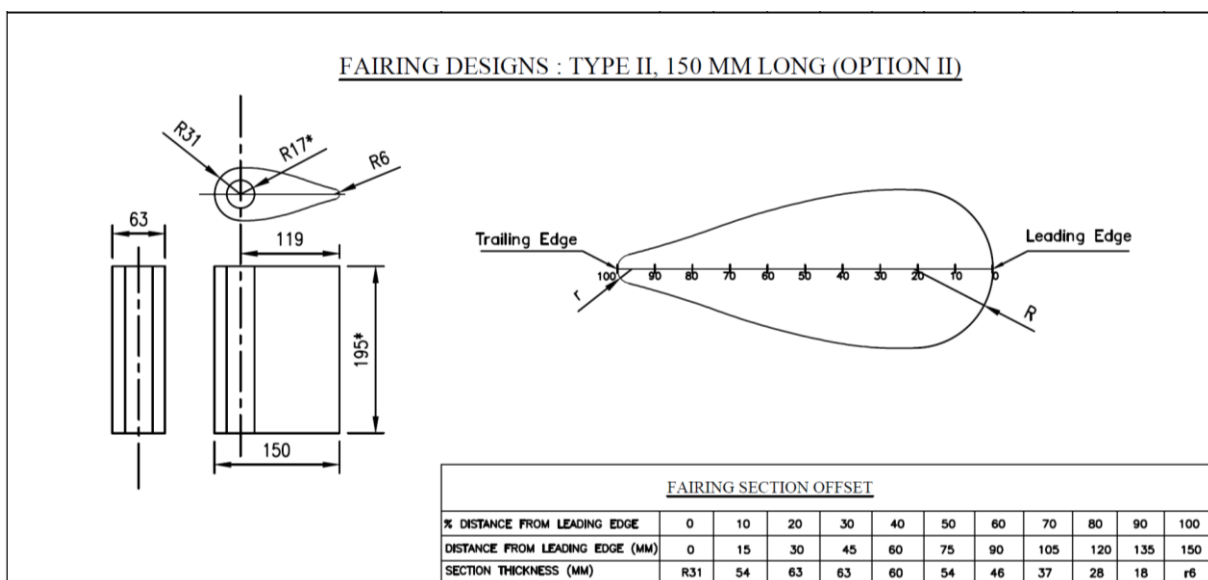


Figure 8-4: Fairing Profile/Design 2 in the model scale

### 8.3 Fairing Models

The leg fairing models were made of foam and installed as neutrally buoyant, even keel, upright and free floating on all the four legs of the jack-up model. Neutral buoyancy and free floatation are provided to ensure that the fairings are self-supporting and thereby to prevent unwarranted frictional forces and moments between the legs and the fairings. Further, there is no effect of the net weight or buoyancy of the fairings on the static mass ratio and the stiffness of the model. Figure 8-5, a) illustrates the

fairing models; the larger and the smaller ones correspond to fairing design 1 and fairing design 2 respectively.

The fairing breadth ( $1.86D$ ) and congruently the length ( $5.62D / 4.44D$ ) were selected considering the diameter of the leg ( $D$ ) and the strength of the fairing. The required immersion or draft of the fairings was achieved by means of solid ballast in the form of streamlined lead plates. The fairings achieved a maximum draft of 180 mm, which corresponded to an effective water depth ratio of 0.23. Four draft marks at forward-starboard, forward-port, aft-starboard and aft-port were provided on the fairings to monitor the draft, trim and heel. Figure 8-5, b) displays the fairing design 2 fitted with draft marks and lead ballast.

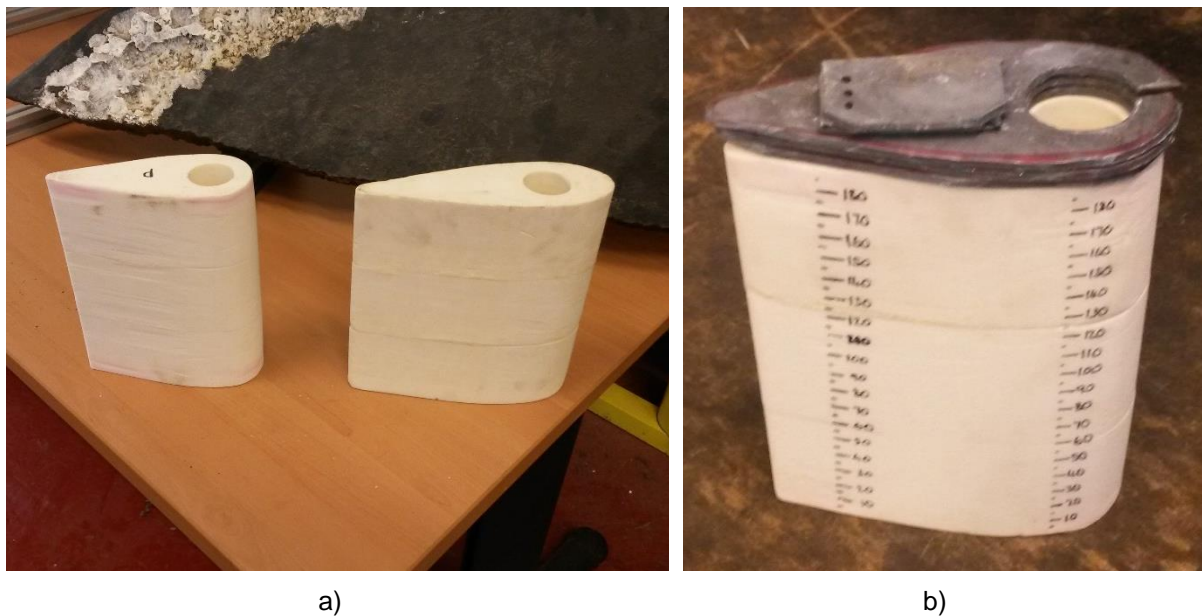


Figure 8-5: a) Fairing models, b) Fairing design 2 with draft marks and lead ballast

The SDOF formulations in Section 8.1 (Equation 8-2, Equation 8-7, Equation 8-12 and Equation 8-17) were used to decide on the optimum location and effective depth of leg fairings for VIV suppression. Accordingly, the water level was decided as the optimum location for the fairings. A maximum effective fairing depth of around 23% of the water depth was selected as a conciliation between size and efficacy, based on the response behaviour illustrated in Figure 8-2. Table 8-1 presents the main properties of the fairing model.

Table 8-1: Fairing properties

<b>Properties</b>	<b>Design 1</b>	<b>Design 2</b>
Length (mm)	190	150
Breadth (mm)	63	63
Depth (mm)	195	195
Profile	Modified NACA0018	Modified NACA0018
L/B Ratio	3.02	2.38
Dry Weight (g)	120	90
Material	Foam	Foam
LCG from Trailing Edge (mm)	96	75
Pivot from Trailing Edge (mm)	141	119

## 8.4 Physical Experiments

### 8.4.1 *Experimental Setup*

The same jack-up model used for the VIV experiments described in Chapter 6 was fitted with the fairings, positioned at the measuring section of the WWC tank and exposed to currents with various speeds. The lightest operating condition of the jack-up model (NVL) was considered for the tests to keep the mass ratio and consequently the mass damping parameter at minimum. The effective water depth of 0.78m was maintained for the tests, corresponding to the maximum operating water depth of the jack-up model. The experimental setup is kept similar to that of the VIV experiments, as illustrated in Figure 8-6.

### 8.4.2 *Test Procedures*

The tests include mass tests, stiffness tests, free decay tests, weathervaning stability tests and response tests. The ability of the fairings to weathervane and align along the flow in a stable configuration with the leading edge facing the flow was ascertained through weathervaning tests. The effect of the fairing depth ratio on the VIV suppression was also investigated by varying the fairing drafts.

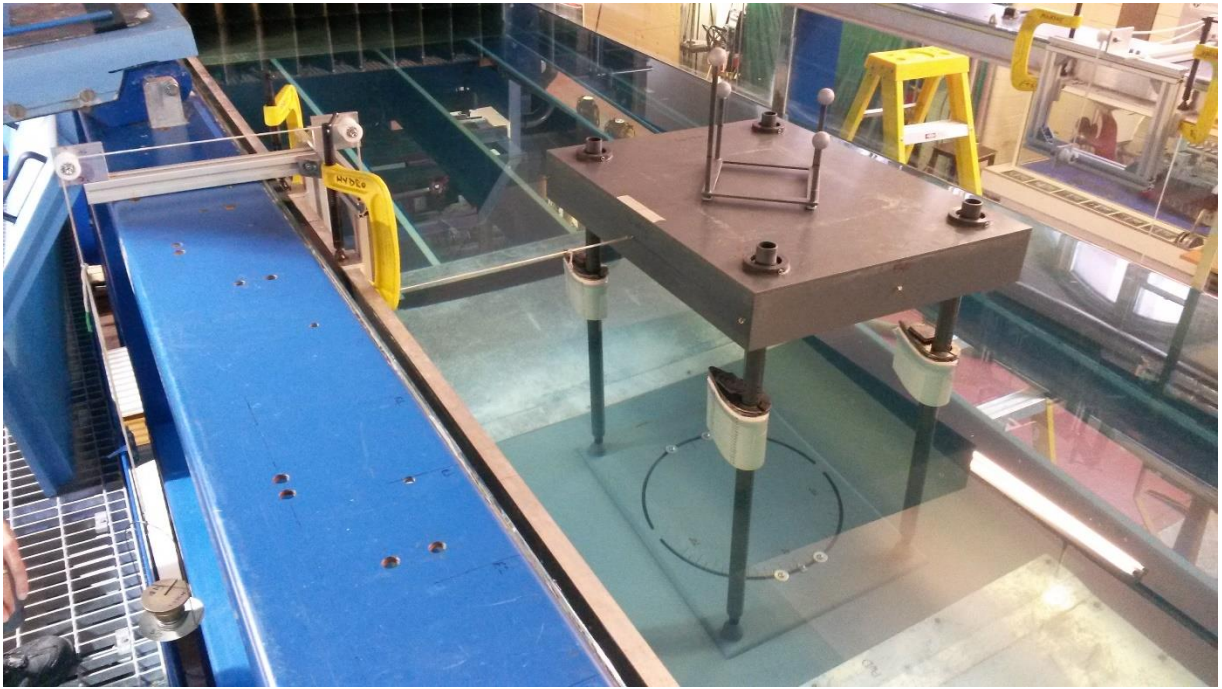


Figure 8-6: Experimental setup for VIV test of the jack-up model fitted with fairings

#### 8.4.3 *Mass and Stiffness Tests*

The mass and COG of the fairings were found by means of weighing test and edge test respectively. Table 8-1 demonstrates the mass and COG details of the fairing designs obtained from the tests. The locations of the COG for both fairing designs are found to be reasonably aft of the pivot point, indicating a reasonable weathervaning stability. As the model stiffness is expected to be unaffected by the free-floating fairings, the stiffness test was carried out only with fairing design 2, selected arbitrarily. Figure 8-7, a) and b) demonstrates the sway and yaw stiffness tests of the model respectively.

The stiffnesses of the model were found to be unaffected by the leg fairings as expected, as later are designed as free floating, even keel and upright. Figure 8-8 illustrates the comparison of the sway deflections of the bare jack-up model with the model fitted with fairings. It can be seen that at small deflections both the curves are almost coinciding revealing no effect of the fairings on the stiffness. The small differences between the stiffnesses at larger deflections are due to the uncertainties and nonlinearities associated with the ball joint friction and leg-hull interface stiffness respectively.



Figure 8-7: Stiffness tests a) sway, b) yaw

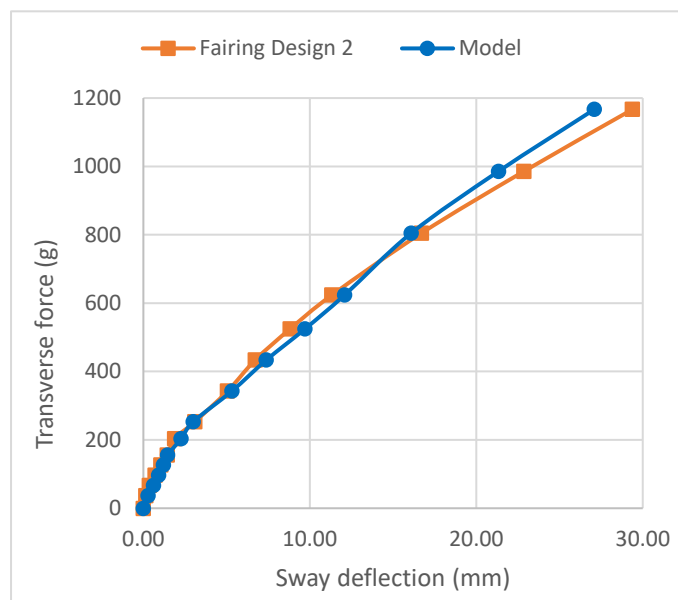
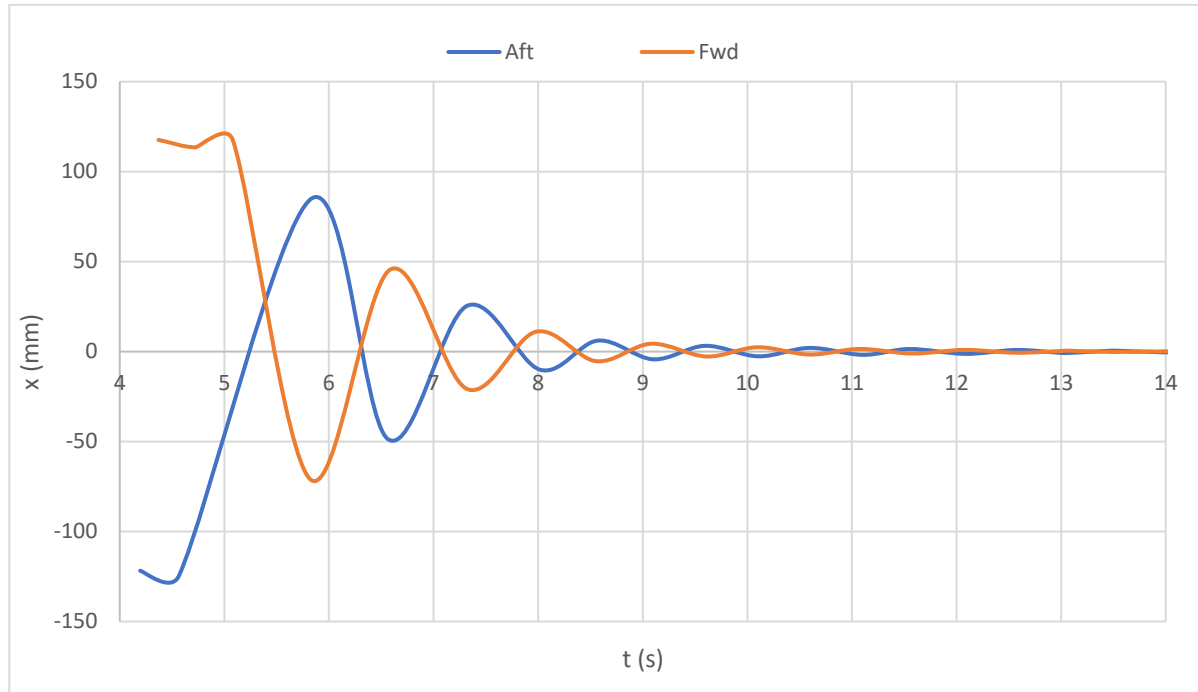


Figure 8-8: Sway deflections of the jack-up model with and without fairings

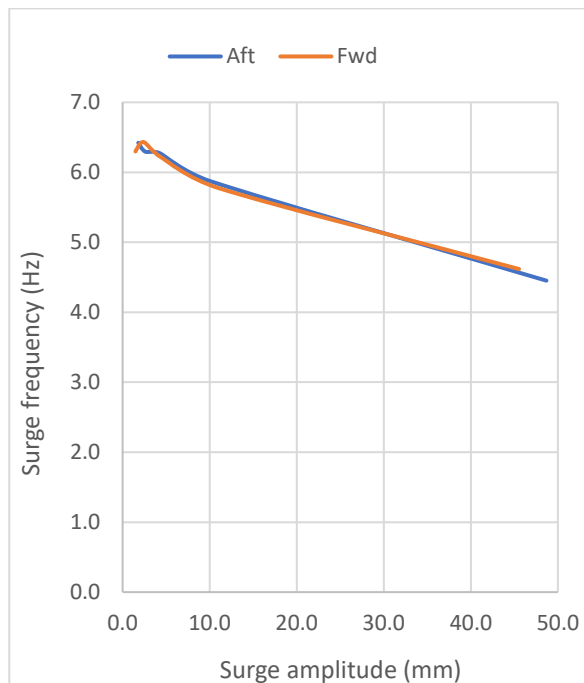
#### 8.4.4 Free Decay Tests with Fairings

Free decay tests were carried out for the jack-up model installed with the fairings for various VIV modes. The added mass of the fairings was calculated from the differences in the natural frequencies of the model with and without fairings. The damping properties of fairings were calculated from the differences in the damping coefficients of the jack-up model with and without fairings. Figure 8-9 illustrates the results of the surge free decay test of the model fitted with fairings of design 1. The free decay time series, softening nonlinearity and nonlinear damping are presented in Figure 8-9, a),

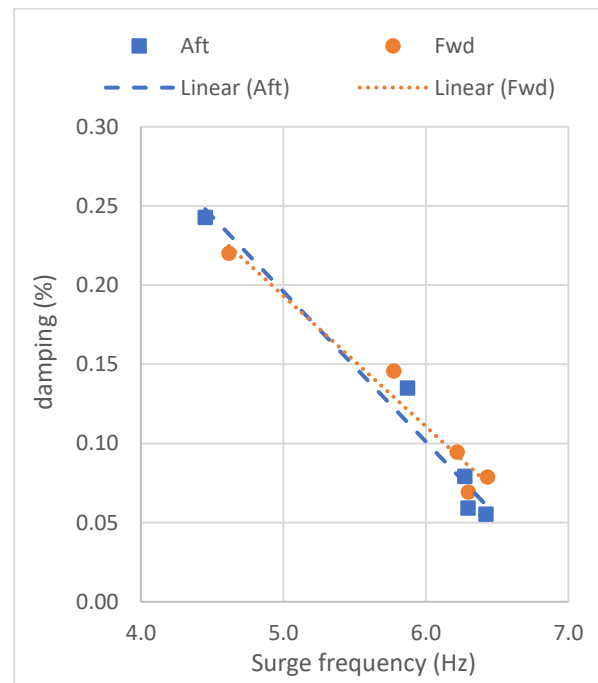
b) and c) respectively. It can be observed in Figure 8-9 b) that the surge frequency decreases with the increase in vibration amplitude. The reduction of damping with the increase in surge frequency is evident in Figure 8-9 c), which indicates that the damping increases with the vibration amplitude.



a)



b)



c)

Figure 8-9: Surge free decay test in still water with fairing design 1, a) free decay time series, b) natural frequency versus amplitude, c) damping ratio versus frequency

Table 8-2, Table 8-3 and Table 8-4 display the summary of the surge, sway and yaw free decay test results respectively. The added mass and damping contributions of the leg fairings calculated from the test results are also provided in the tables.

Table 8-2: Fairing added mass and damping from surge free decay tests

Test Condition	System Properties			Fairing Properties			
	Damping Ratio	Natural Frequency (Hz)	Natural Period (s)	Added Mass (kg)	Added Mass Coefficient	Damping Coefficient (Ns/m)	Damping Ratio
Model in air	0.036	1.37	0.73	0	0	0	0
Model in water	0.040	1.22	0.82	0	0	0	0
Model with Fairing Design 1	0.063	1.03	0.97	14.16	2.68	7.27	0.03
Model with Fairing Design 2	0.096	1.08	0.93	9.58	2.30	14.49	0.06

Table 8-3: Fairing added mass and damping from sway free decay tests

Test Condition	System Properties			Fairing Properties			
	Damping ratio	Natural Frequency (Hz)	Natural Period (s)	Added Mass (kg)	Added Mass Coefficient	Damping Coefficient (Ns/m)	Damping ratio
Model in air	0.036	1.37	0.73	0	0	0	0
Model in water	0.040	1.22	0.82	0	0	0	0
Model with Fairing Design 1	0.166	0.94	1.06	25.90	4.90	36.80	0.14
Model with Fairing Design 2	0.104	1.13	0.88	4.75	1.14	15.18	0.07

Table 8-4: Fairing added mass and damping from yaw free decay tests

Test Condition	System Properties			Fairing Properties			
	Damping ratio	Natural Frequency (Hz)	Natural Period (s)	Added Inertia (kgm <sup>2</sup> )	Added Mass Coefficient (kg)	Damping Coefficient (Nms/rad)	Damping ratio
Model in air	0.037	2.05	0.49	0	0	0	0
Model in water	0.038	1.81	0.55	0	0	0	0
Model with Fairing Design 1	0.149	1.23	0.81	3.02	4.46	3.92	0.12
Model with Fairing Design 2	0.105	1.52	0.66	0.95	1.78	1.90	0.07

#### 8.4.4.1 *Fairing Damping*

Free decay tests revealed that the damping of the system increased as anticipated with the presence of the fairings, due to an increase in the fluid damping. By comparing the surge and sway test results, it can be observed that the fairings have a larger damping ratio along the crossflow direction than the inline direction. The difference is found to be significant for fairing design 1 possibly due to a superior streamlined geometry, while for fairing design 2 the difference is nominal. The yaw damping of the fairings is found to be comparable to the sway damping in still water.

#### 8.4.4.2 *Fairing Added Mass and Natural Frequency*

The surge, sway and yaw natural frequencies of the model fitted with the fairings are demonstrated in Table 8-2, Table 8-3 and Table 8-4 respectively. It can be observed that the natural frequencies of the model reduced with the installation of the leg fairings. This can be attributed to the increase in mass and added mass of the model due to the presence of the fairings.

The corresponding added mass properties of the fairings calculated for various VIV modes are also included in Table 8-2, Table 8-3 and Table 8-4. The sway added mass coefficient is found to be high for fairing design 1 while for fairing design 2, it is found to be less than the respective surge value. The surge added mass coefficients of both the fairing designs are found to be comparable while the yaw added mass coefficients unveiled intermediate values between surge and sway.

Figure 8-10, a) to f) illustrates the results of the FFT of the free decay signals of the model fitted with the fairings. It can be observed from the amplitude peaks that the fairings reduce the natural frequency of the model. The model with the leg fairing design 1 is found to experience a bimodal response with approximately the same amplitude in the crossflow direction; one near to the expected natural frequency and the other at a much lower frequency. Though not clearly understood, the reason for the low frequency mode is suspected to be the pivoting motion of the fairings about the legs during free sway vibrations.

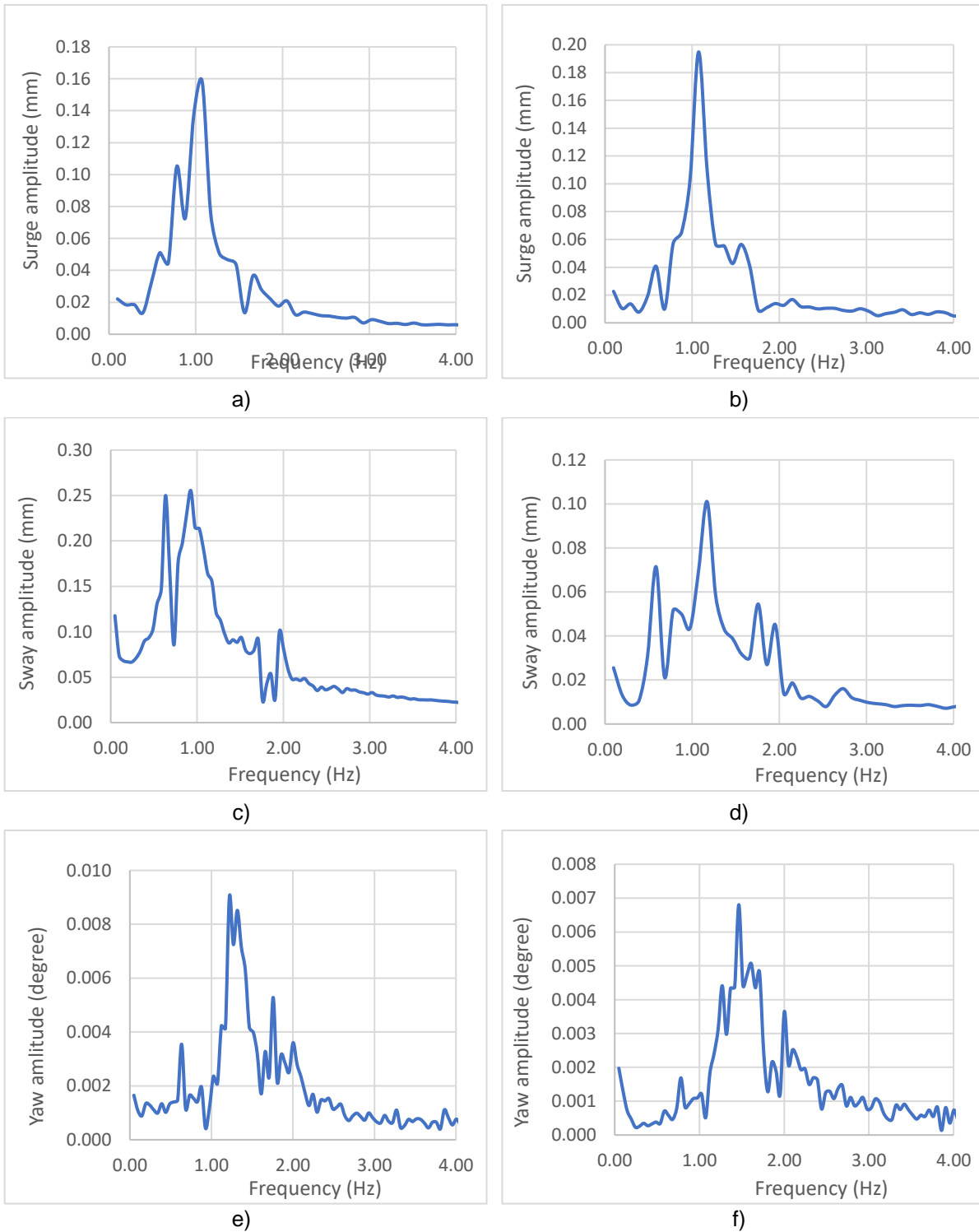


Figure 8-10: FFT of the free decay tests with fairings, a) surge, fairing design1, b) surge, fairing design 2, c) sway, fairing design1, d) sway, fairing design 2, e) yaw, fairing design1, f) yaw, fairing design 2

#### 8.4.5 *Weathervaning Stability Tests*

The response test was preceded by the weathervaning stability test of the fairings. The ability of the fairing to weathervane and align along the direction of the flow, with the leading edge facing the flow was established in the uniform current. Weathervaning stability of the fairings was determined by exposing the jack-up model with fairings to incremental current about the trailing edge (180 degrees angle of attack) and observing the angular response characteristics. Figure 8-11 illustrates the weathervaning test setup, and it can be observed that the local heading of the fairings is 180 degrees; trailing edges are fronting the flow.

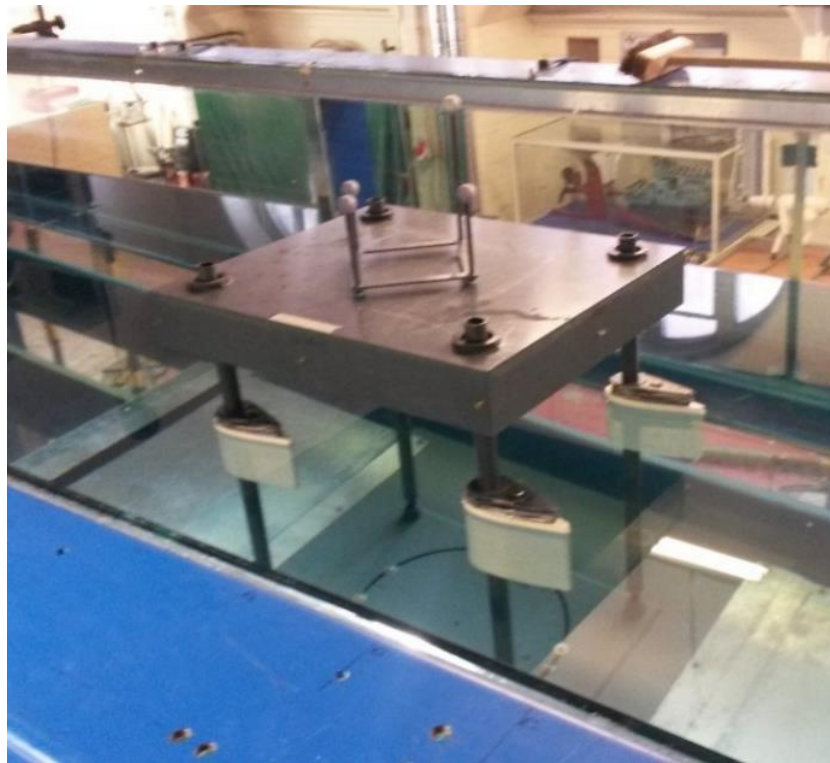


Figure 8-11: Weathervaning test

Both the fairing designs were found to exhibit satisfactory weathervaning stability at all flow speeds except for very low speeds. However, fairing design 2 was found to be sluggish at all the flow speeds and both the designs were found to develop severe galloping at stronger currents. The weathervaning stability was verified for 180 mm, 115 mm and 50 mm drafts and the performance was found to be similar. The results of the weathervaning stability test are presented in Table 8-5.

Table 8-5: Weathervaning performance of fairings

Performance	Design 1	Design 2
Still	up to 0.05 m/s	up to 0.10 m/s
Slow	0.05 - 0.15 m/s	above 0.10 m/s
Quick	above 0.15 m/s	-
Galloping	above 0.30 m/s	above 0.30 m/s

#### 8.4.6 Response Test with Fairings in Steady Current

Response tests were carried out by exposing the jack-up model with fairings to incremental current from the head direction (0 degree angle of attack). The resulting crossflow (sway) and yaw responses are illustrated as time series in Figure 8-12 and Figure 8-13 respectively. The responses of the bare model (model) are also demonstrated in the figure. It can be observed from both figures that the responses are reduced considerably.

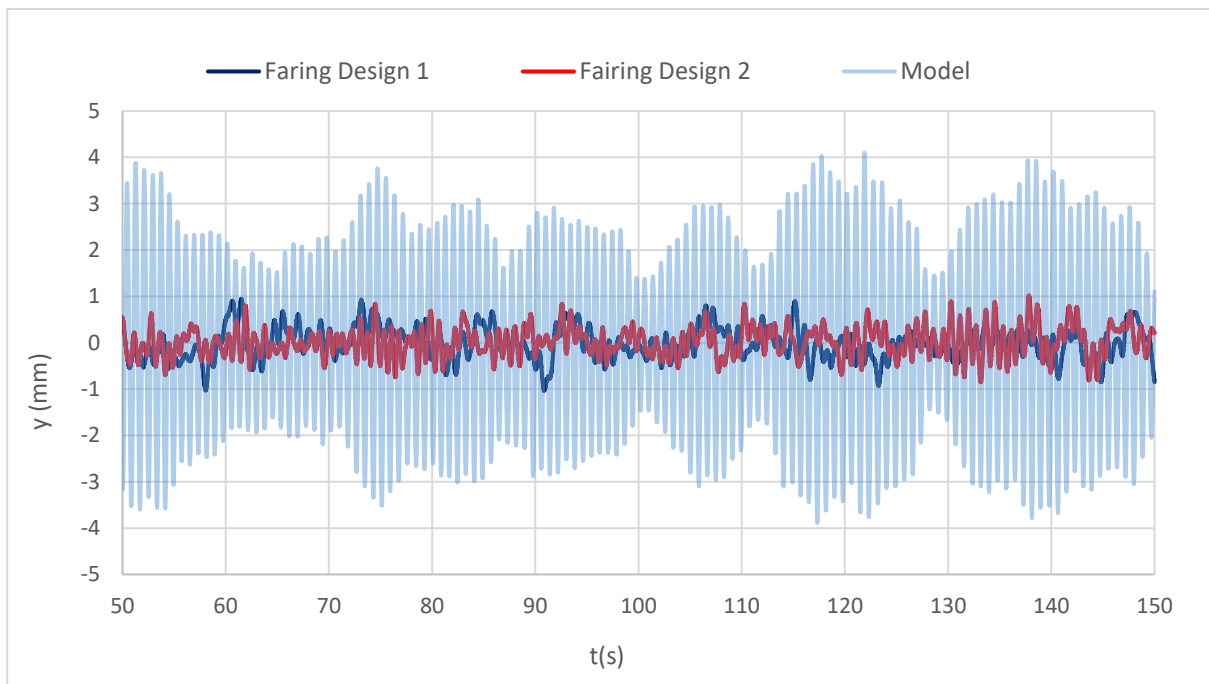


Figure 8-12: Model sway response at a reduced velocity of around 5 (0.225 m/s current)

##### 8.4.6.1 Amplitude Response

Figure 8-14 shows the variation of the inline and crossflow rms amplitude responses, normalised with the model leg diameter and plotted with respect to the corresponding

reduced velocities. It is observed that the crossflow response reduced considerably in the entire lock-in regime with the installation of either of the leg fairings. The crossflow rms response amplitude is found to reduce by around 80% as revealed in Figure 8-14. Further, the fairings are observed to be effective throughout the lock-in regime. This result validated the mathematical model, the significance of the antinode location, and the efficacy of the tested fairing profiles. Though the fairings are found to suppress VIV throughout the lock-in regime, the same are found to increase the response significantly at reduced velocities above 8. The near linear increase of the crossflow response amplitude with the reduced velocity, as illustrated in Figure 8-14 verifies that the phenomenon is galloping.

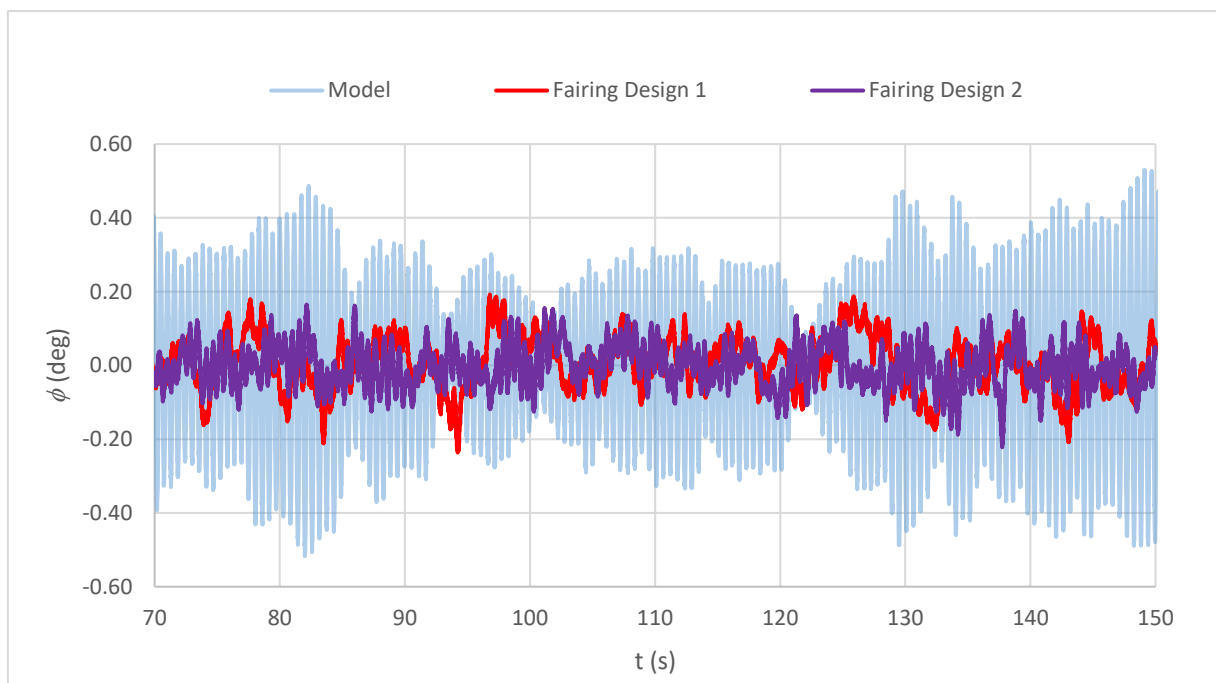


Figure 8-13: Model yaw response at a yaw reduced velocity of around 5 (0.325 m/s current)

Figure 8-15 illustrates the variation of the normalised yaw rms amplitude response (amplitude response multiplied with the radius of motion and normalised with the model leg diameter) plotted with respect to the respective yaw reduced velocity. It can be observed that the yaw responses are also reduced considerably in the entire lock-in regime with the installation of either of the leg fairings. The rms yaw response amplitude is found to reduce by around 70% as revealed in the figure. The fairings are again found to be effective throughout the lock-in regime.

The mathematical model was further validated along with the effectiveness of the tested fairing profiles in the suppression of yaw VIV. Like crossflow VIV, the fairings are found to increase the yaw response at reduced velocities above 8. It can be inferred from the near linear increase of the response, exemplified in Figure 8-15 that the phenomenon is yaw galloping.

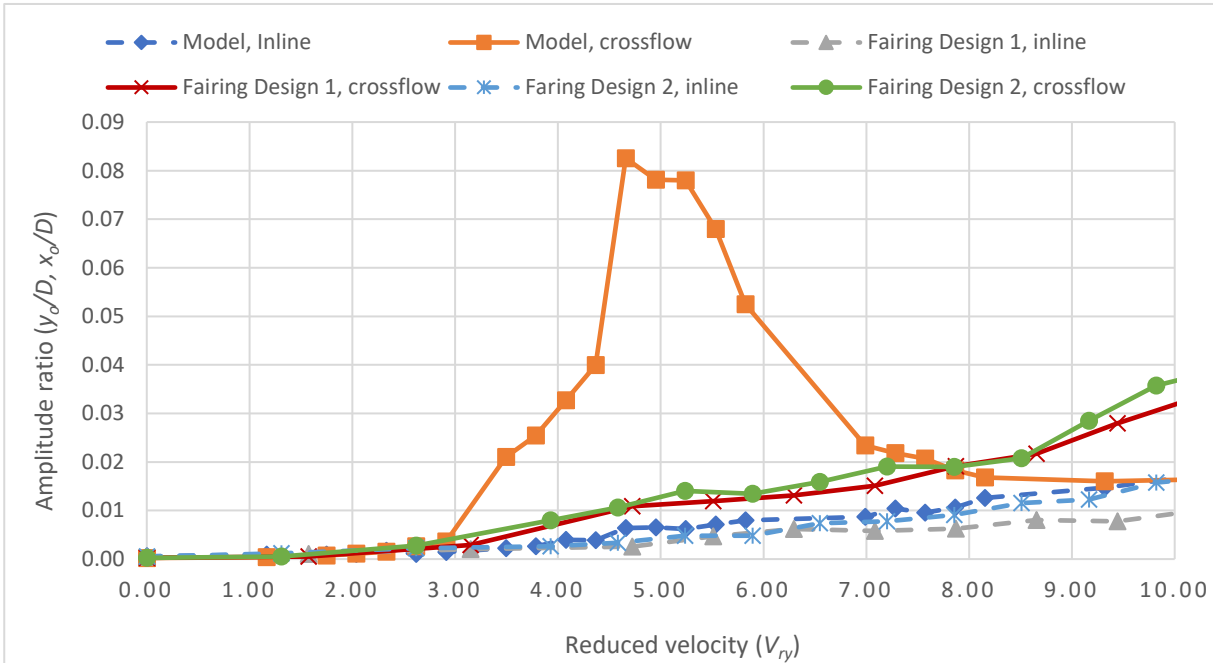


Figure 8-14: In-line and crossflow amplitude responses for the fairing profiles

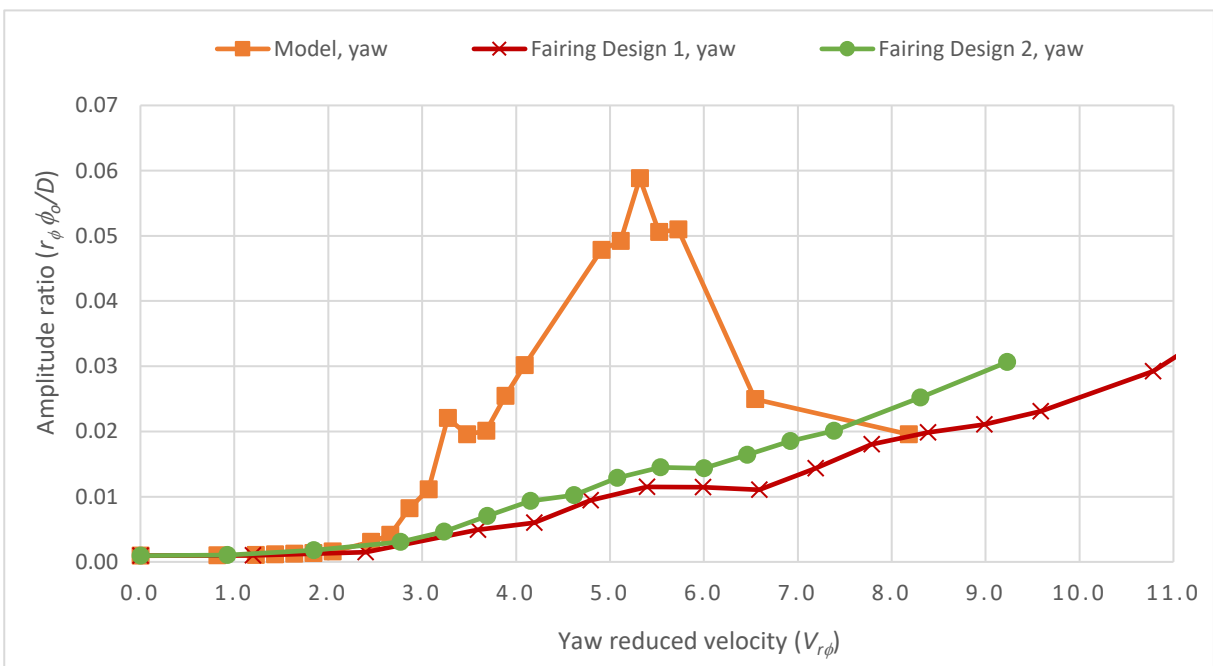


Figure 8-15: Yaw amplitude response versus yaw reduced velocity

## 8.4.6.2 Frequency Response

Figure 8-16 illustrates the crossflow frequency responses of the models with and without fairings, plotted against the corresponding reduced velocity. For the model with the fairings, the lower lock-in regime of crossflow VIV was found to be present for both fairing designs while the upper coupling regime was observed to be totally disrupted. Further, the crossflow responses at higher speeds are found to be of low frequency nature, particularly for design 1, as evident in Figure 8-16. The observed low frequency crossflow responses at higher speeds correspond well to the galloping observed during the experiments.

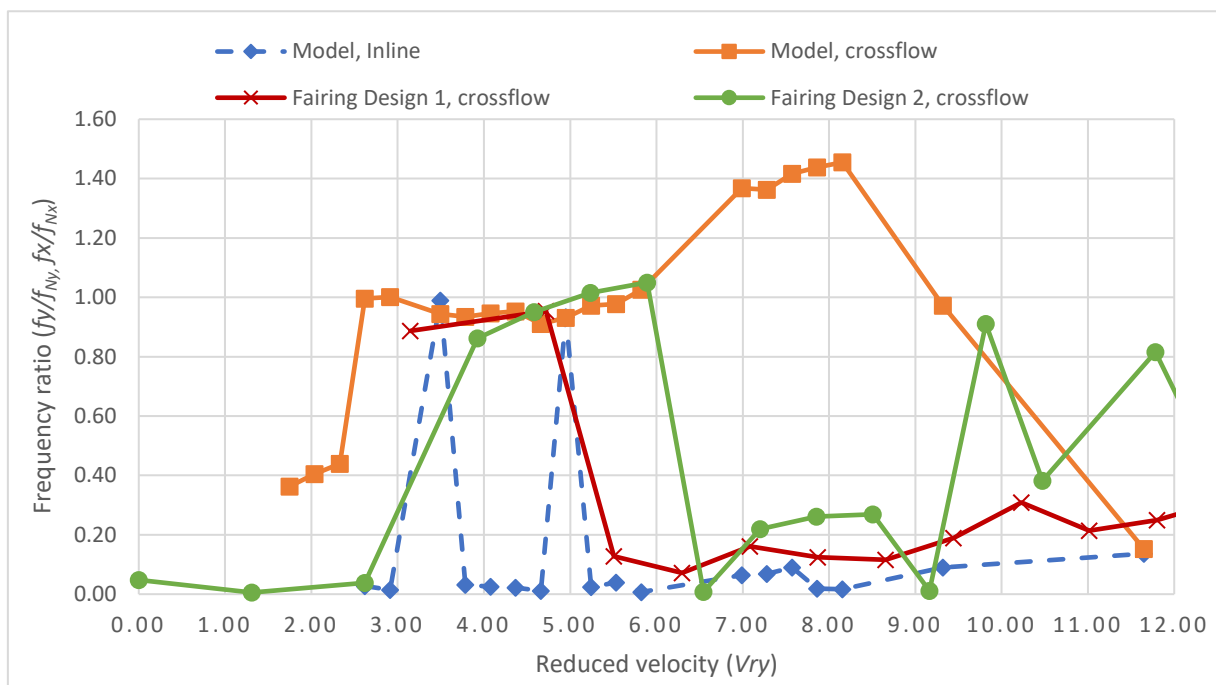


Figure 8-16: Inline and crossflow frequency responses for the fairing profiles

Figure 8-17 illustrates the frequency responses of the models with and without fairings undergoing yaw VIV. For the model with the fairings, upper lock-in regime is observed to be present only for the fairing design 2, while the lower coupling regime is totally disrupted for both the fairing designs. Further, the yaw responses at higher speeds are also found to be of low frequency nature for both fairing designs. The low frequency yaw responses at higher current speeds correspond well to the yaw galloping observed during the experiments.

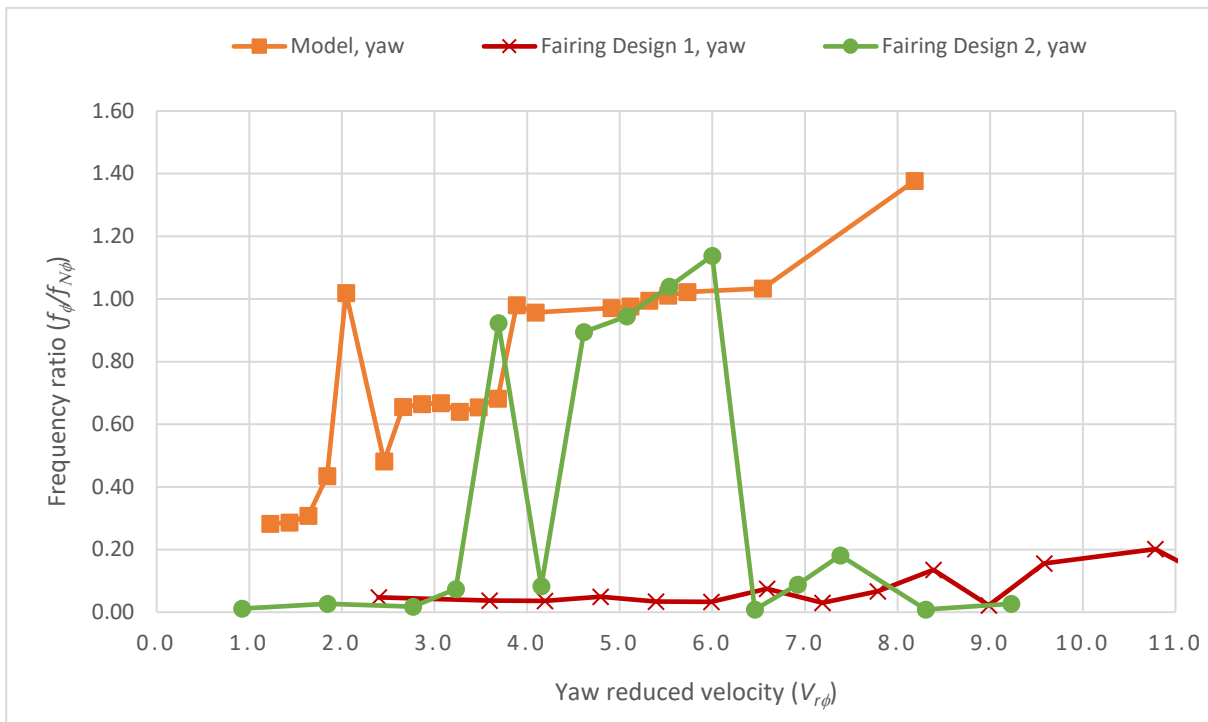


Figure 8-17: Yaw frequency response versus yaw reduced velocity

#### 8.4.6.3 Mean Response

The mean or steady inline and crossflow responses were also measured, and the normalised results are plotted as a function of current speed in Figure 8-18. It is evident that the presence of fairings reduced the mean inline responses and correspondingly mean drag at the practical speed ranges. Fairing design 1 is found to have better drag reduction characteristics when compared to fairing design 2. However, both fairings seem to increase the mean drag at high current speeds, possibly due to the drag amplification caused by the increasing crossflow and yaw response due to galloping. It is also observed that the model fitted with fairing design 1 is experiencing mean crossflow response and consequently mean lift forces throughout the current speeds.

The mean or steady yaw responses were also measured, and the normalised results are plotted as a function of current speed in Figure 8-19. It can be observed that all models experience mean yaw response at high current speed while fairing design 1 experiences mean yaw even at lower current speed, similar to crossflow mean response.

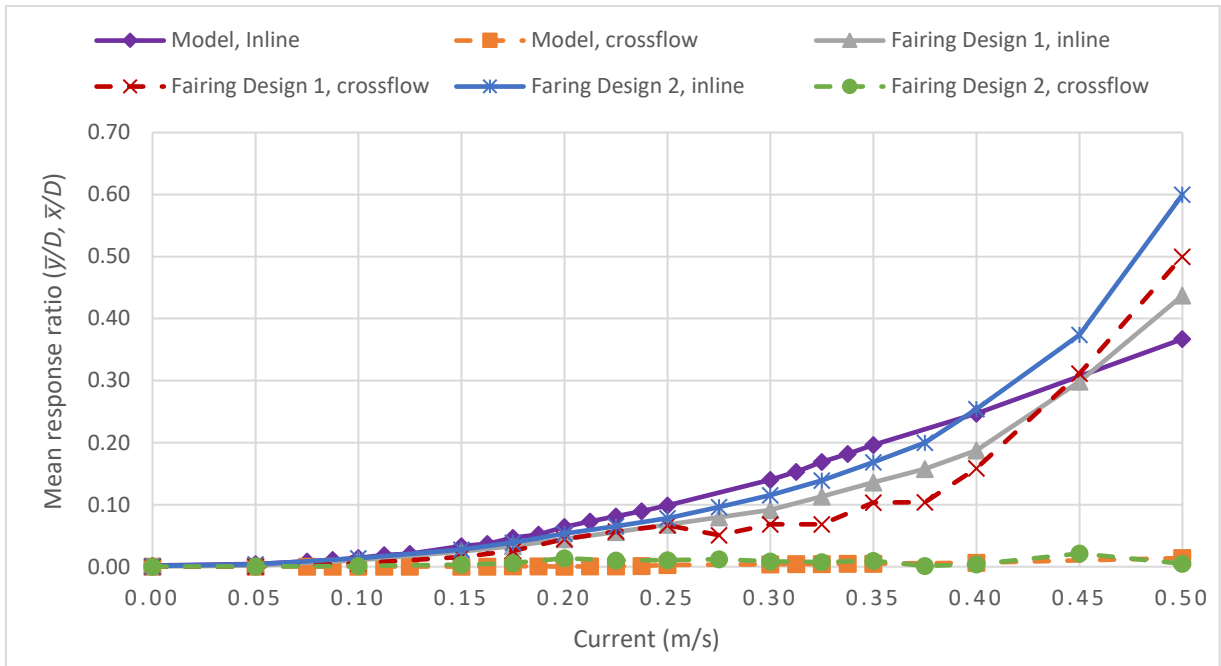


Figure 8-18: Mean inline and crossflow responses versus current

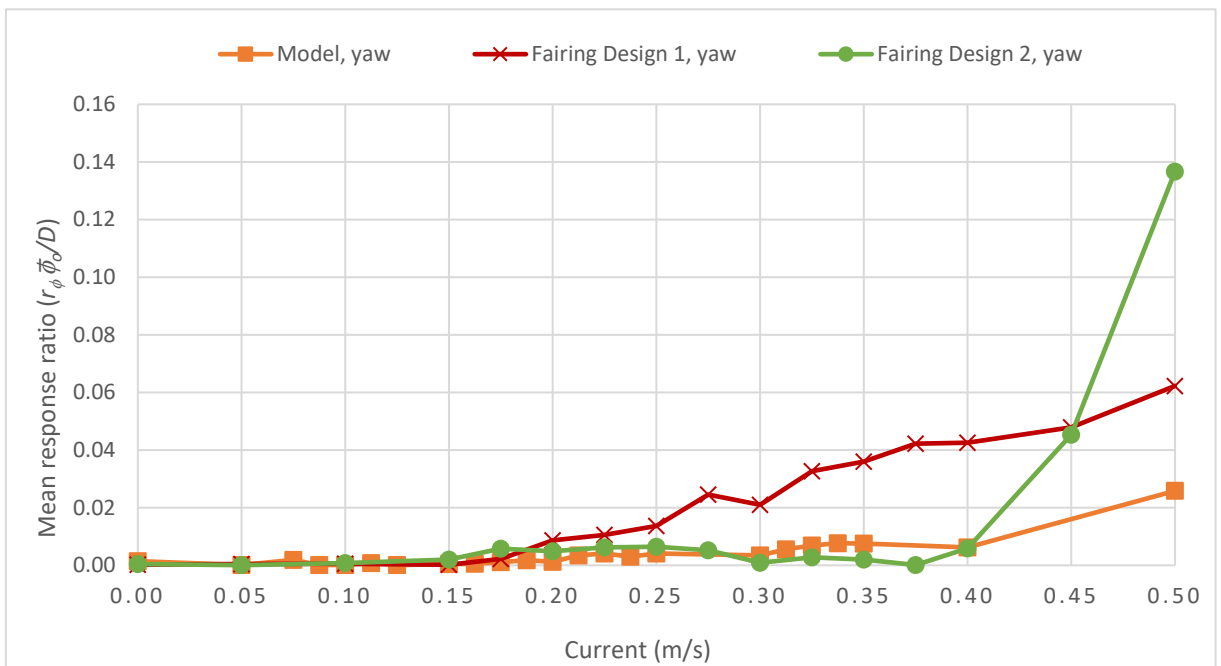


Figure 8-19: Mean yaw response versus current

### 8.5 Effect of Fairing Depth Ratio

The effect of fairing depth ratio (fairing depth over water depth) was investigated by means of model testing at various fairing drafts. The draft variation of the fairings was achieved by varying the lead ballast. Fairing Design 1 is selected for the investigation due to its better response reduction characteristics. The natural frequencies of the

model corresponding to intermediate fairing depth ratios of the fairings were calculated based on the added mass characteristics derived during free decay tests. The test cases and corresponding natural frequencies are presented in Table 8-6.

Table 8-6: Details of fairing depth test

Test Case	Fairing Properties			Sway		Yaw	
	$d_F$	$d_F/L$	$d_F/h$	Natural Frequency (Hz)	$(y_o/D)_{VIV}$ (RMS)	Natural Frequency (Hz)	$(r_{\phi\phi_o}/D)_{VIV}$ (RMS)
Model	0.00	0.00	0.00	1.22	0.08	1.81	0.069
Fairing Design 1_50df	50.00	0.05	0.06	1.09	0.05	1.51	0.027
Fairing Design 1_115df	115.00	0.12	0.15	0.99	0.02	1.32	0.014
Fairing Design 1_180df	180.00	0.19	0.23	0.94	0.02	1.23	0.011

Response tests were also carried out for the intermediate fairing drafts and the amplitude, frequency and mean responses are compared with the results of the bare model and the fairing at the maximum draft.

### 8.5.1 Amplitude Response

Figure 8-20 illustrates the crossflow amplitude responses of the fairing for various depth ratios, plotted with respect to the corresponding reduced velocities. It can be observed that the crossflow VIV response reduces with the increasing fairing depth ratio while the galloping response at higher current speed increases with the same.

The yaw amplitude responses of the fairing for various depth ratios, plotted with respect to the corresponding reduced velocities are presented in Figure 8-21. Like crossflow response, yaw response is also found to reduce with the increasing fairing depth ratio while the yaw galloping at high current speed increases. The peak yaw response occurring at a high reduced velocity of around 6.5 for the fairing depth ratio of 0.06 indicates either a drop in fairing added mass from the still water values or occurrence of significant excitation still at the natural frequency of the bare model. A decrease in the added mass of the fairings due to the vibrations can increase the natural frequency of the model and consequently shift the resonant response peak to a higher reduced velocity. Alternatively, the occurrence of significant excitation and subsequent yaw response at the natural frequency of the bare model can also shift the resonant response peak to a higher reduced velocity, as evident from Table 8-6.

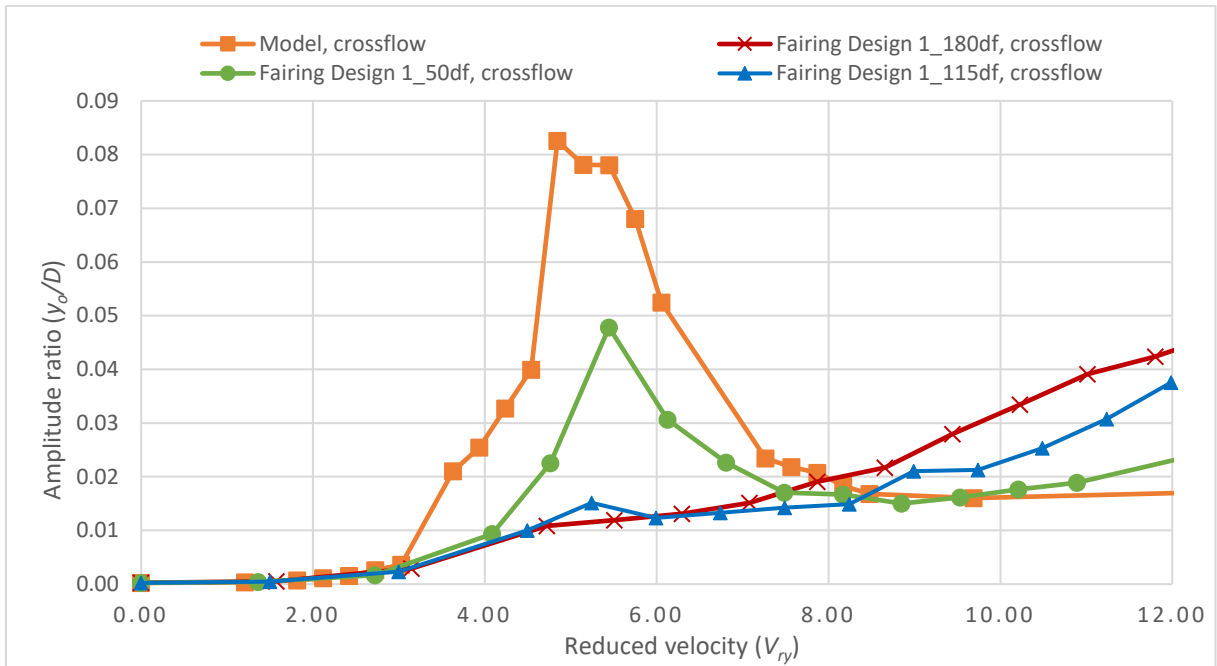


Figure 8-20: Crossflow amplitude response for various fairing depth ratios

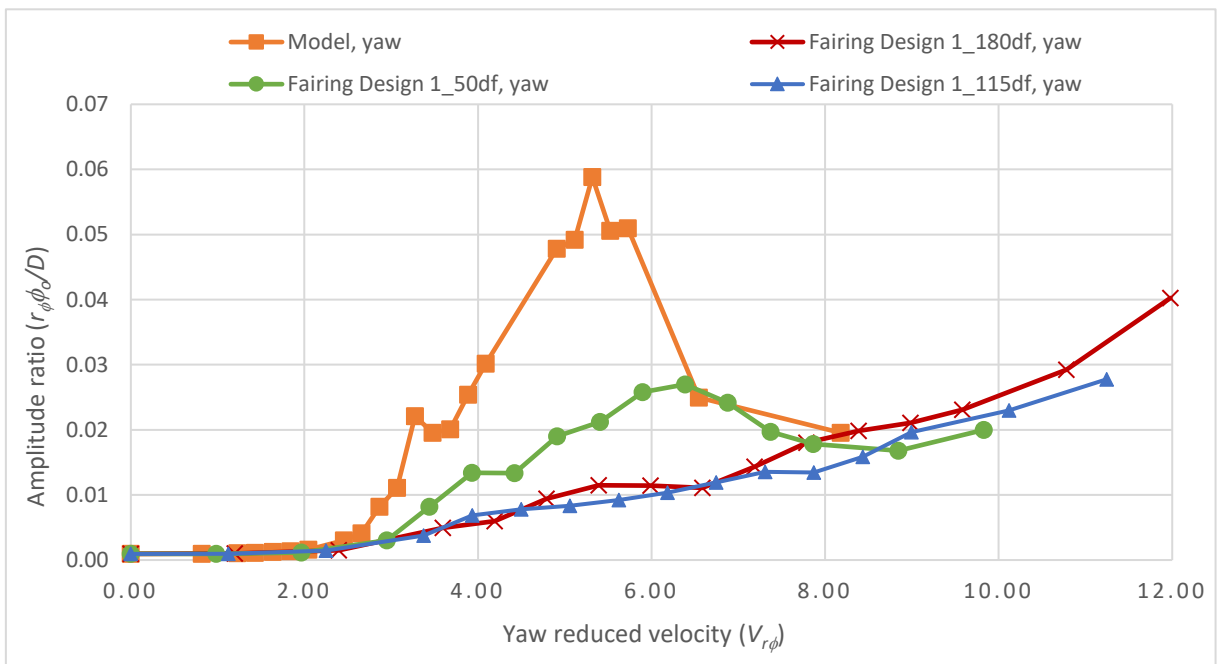


Figure 8-21: Yaw amplitude response for various fairing depth ratios

### 8.5.2 Frequency Response

The frequency responses of the crossflow VIV for various fairing depth ratios are illustrated in Figure 8-22, with respect to the corresponding reduced velocities. It can be observed that both the lower sway lock-in and the upper yaw coupling VIV regimes are increasingly disrupted with the increasing fairing depth ratios. For the fairing depth

ratios of 0.15 and 0.23, the lock-in regime is significantly, and the coupling regime is totally disrupted. However, for the low fairing depth ratio of 0.06, significant disruptions of the lock-in and coupling regimes are not observed indicating unignorable excitation on the cylindrical legs. The frequency response is not presented for the case, 180\_df at very low reduced velocities since the corresponding current speeds are too small with nil response.

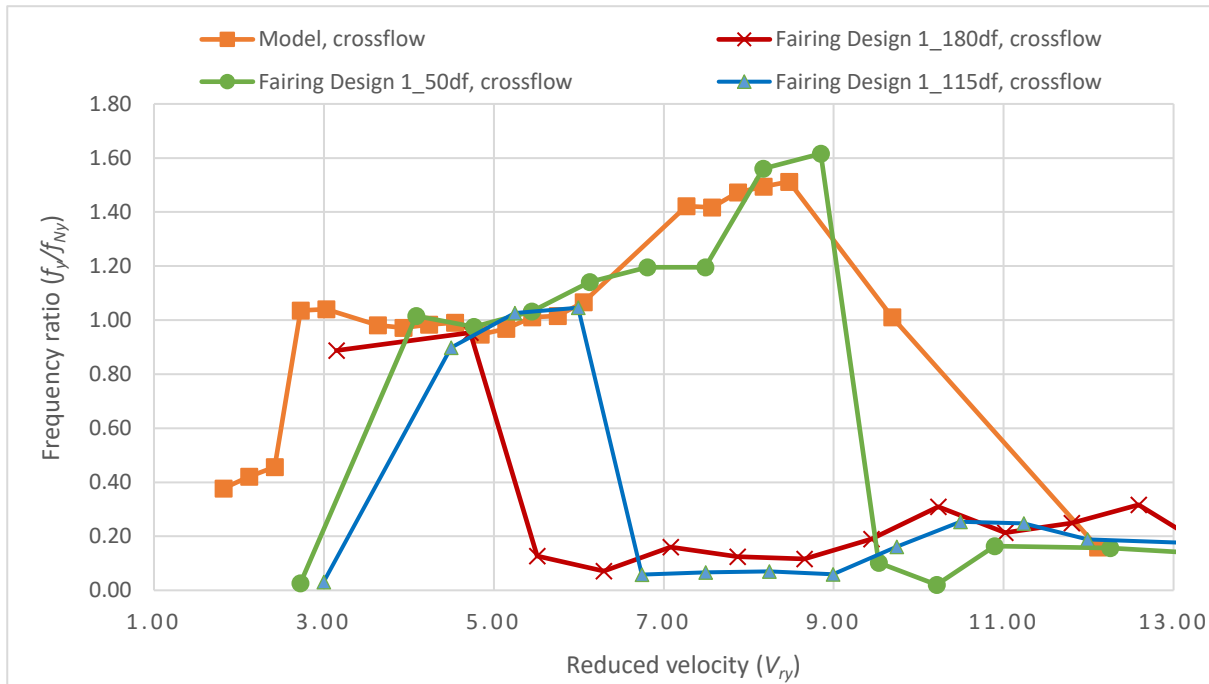


Figure 8-22: Crossflow frequency response for various fairing depth ratios

Figure 8-23 displays the yaw frequency responses of the model for various fairing depth ratios, plotted against the respective yaw reduced velocities. The increasing disruption of the lower sway coupling and upper yaw lock-in regimes with the increasing fairing depths is evident in the figure. It can be observed that both the regimes are totally disrupted for the fairing depth ratio of 0.23. The increase of the frequency responses above 1 in the upper yaw lock-in regime for both the intermediate fairing depth ratios indicates that either added mass of the fairings are dropping from the still water values or considerable yaw excitation is still happening at the natural frequency of the bare model.

Figure 8-24 illustrates the yaw frequency response normalised with the bare model natural frequency and plotted against the bare model reduced velocity for various fairing depth ratios. It can be observed that the frequency response is totally disrupted

for the high depth ratio case, 1\_180df. However, the upper lock-in regimes are found to partially collapse well around a value of 1 for the lower fairing depth ratios, indicating that the yaw lock-in excitation is still dominating at the bare model natural frequency.

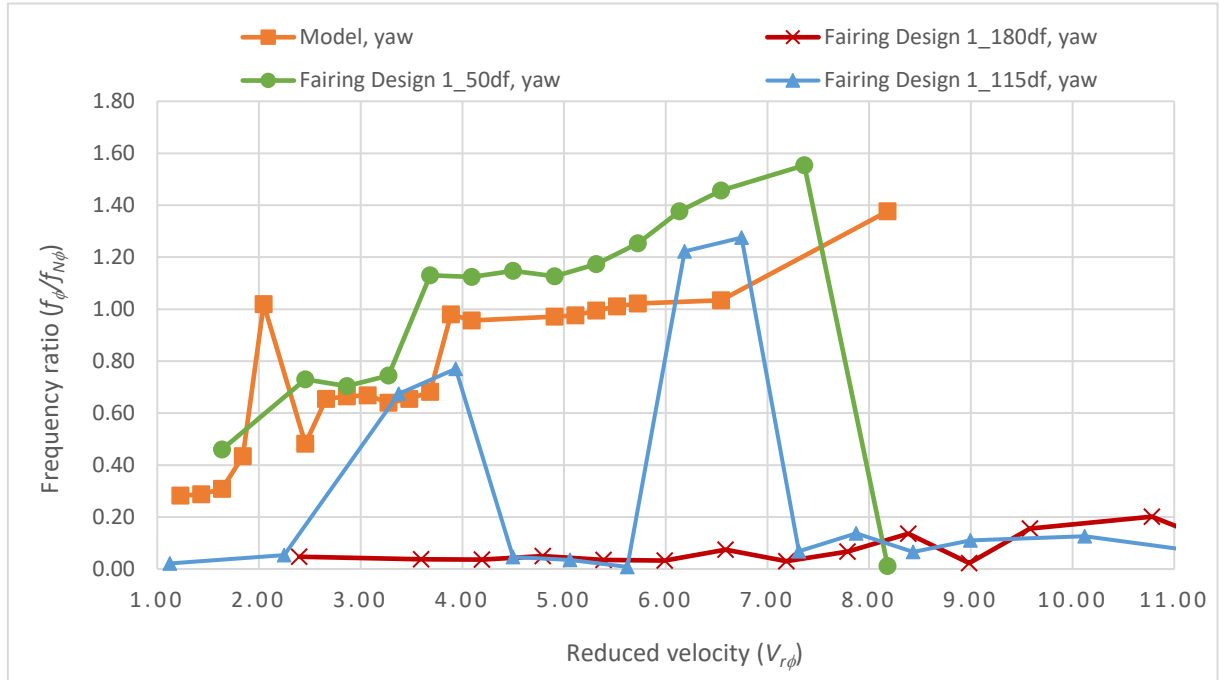


Figure 8-23: Yaw frequency response for various fairing depth ratios

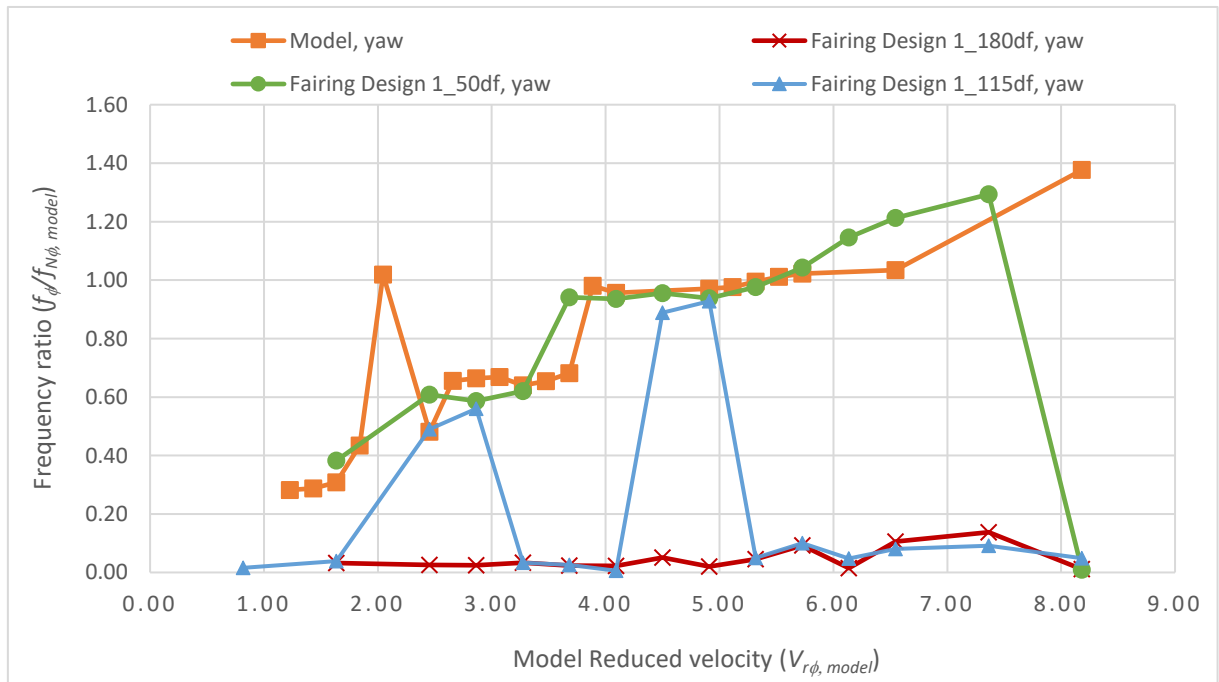


Figure 8-24: Yaw frequency response normalised with bare model parameters for various fairing depth ratios

### 8.5.3 Mean Response

The mean inline and crossflow responses of the model for various fairing depth ratios are plotted against the current speed in Figure 8-25. It can be seen that the mean inline response reduces consistently with increasing fairing depth ratios at the practical speed range though the response is increasing at very high current speeds. This indicates that even fairings with small depth ratios are able to reduce the mean drag acting on the jack-up by means of VIV attenuation. Figure 8-25 demonstrates that mean crossflow response is generally insignificant for the jack-up model without fairings. However, the introduction of fairings is found to cause a mean crossflow response of the model at and above medium current speeds, which increases with increasing fairing depth ratio. It can be evidently observed from the figure that the fairings with the largest depth ratio of 0.23 induce uncharacteristically high mean crossflow response throughout the current speeds.

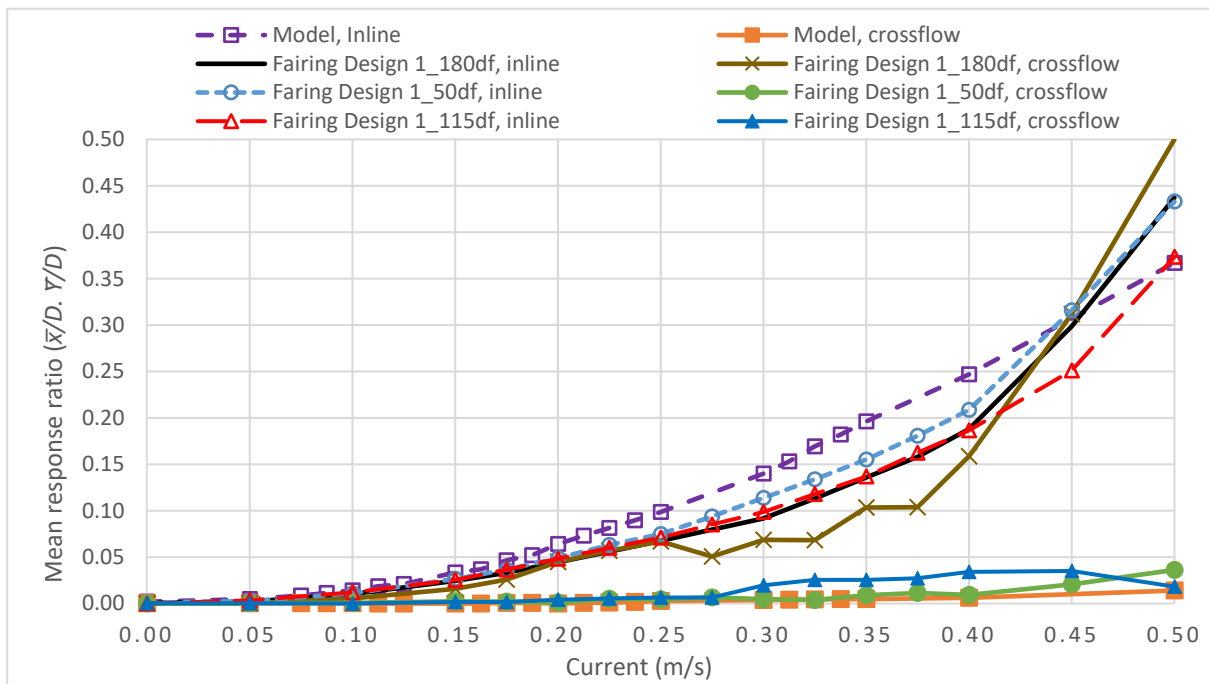


Figure 8-25: Mean inline and crossflow response for various fairing depth ratios

The mean yaw response of the model for various fairing depth ratios is plotted in Figure 8-26 against the current speed. It can be observed that the mean yaw is generally insignificant for the bare jack-up model and for the lowest fairing depth ratio of 0.06, except at very high speed. However, significant mean yaw responses are observed at and above medium current speed for the highest two fairing depth ratios of 0.15 and

0.23. Similar to crossflow response, the fairings with the largest depth ratio of 0.23 is found to cause uncharacteristically high mean yaw response throughout the current speed. This unusually high mean crossflow and yaw response can be attributed to the possibility of reattachment of the separated shear layers from the leading edge of the fairings owing to its high length, causing an off-centre line deflected stable position inducing a steady lift force and yaw moment (Assi *et al.*, 2011; Assi *et al.*, 2014). It can also be inferred from the unceasing trend of the respective curves in Figure 8-25 and Figure 8-26 that the mean forces are further amplified due to galloping.

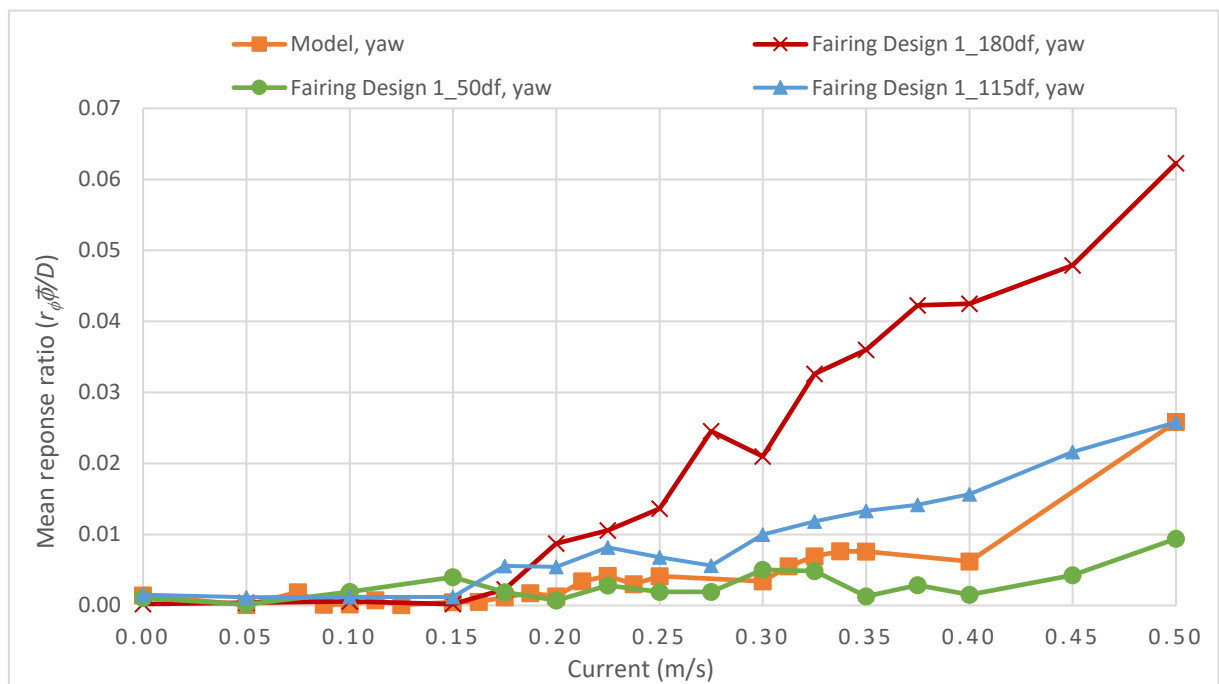


Figure 8-26: Mean yaw response for various fairing depths

#### 8.5.4 Optimum Fairing Depth

Figure 8-27 a) and b) presents the VIV and galloping responses of the model at various fairing depth ratios for sway and yaw modes respectively. The VIV response corresponds to the peak response around the reduced velocity of 5, while the galloping response is measured at the maximum current speed of 0.5m/s. It can be observed in the figure that the crossflow and yaw VIV responses reduce significantly with the increasing fairing depth ratio. However, the response reduction is found to saturate at a fairing depth of approximately 15% of the water depth. Further, the trend of the VIV response for both sway and yaw modes are in line with the trend obtained in Figure 8-2, thereby validating the mathematical solutions.

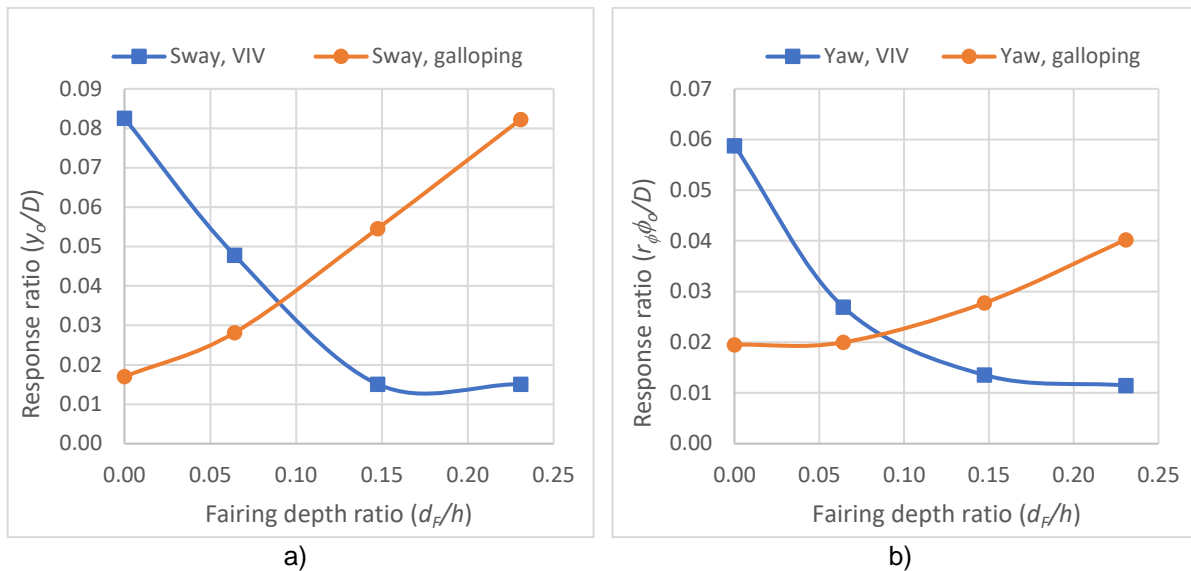


Figure 8-27: VIV and galloping responses versus fairing depth ratios; a) crossflow b) yaw

It can be seen in Figure 8-27 that the increase in fairing depth ratio increases the galloping response of the jack-up in both sway and yaw VIV modes. Hence, the optimum fairing depth ratio should be selected as a compromise between VIV suppression and galloping initiation. It is evident in Figure 8-27 that further response reduction achievable is nominal above a fairing depth ratio of 0.15 and hence it can be concluded that 0.15 is the optimum fairing depth ratio for the application on jack-up legs. Apart from the galloping response, the unwarranted mean crossflow and yaw responses are also found to be tolerable with values of  $0.04D$  and  $0.025D$  respectively for a depth ratio of 0.15.

## 8.6 Fairing Offsets

The nondimensional offsets of the fairing design 1 and 2 are presented in Table 8-7 and Table 8-8 respectively. The offsets can be readily used for practical applications.

## 8.7 Detachable Fairing Concept

As the fairings are found to have adverse effects like severe crossflow galloping, yaw galloping, mean crossflow response, mean yaw responses and drag amplifications at high operating current, it is recommended that the same should be detachable type.

Table 8-7: Nondimensionalised offset table of fairing design 1

Distance from Leading Edge Section thickness	1.00	0.90	0.80	0.70	0.60	0.50	0.40	0.30	0.20	0.10	0.00
Camber	0.00	0.10	0.15	0.21	0.25	0.29	0.32	0.33	0.32	0.26	0.00
Leading Edge Radius	0.11										
Trailing Edge Radius	0.03										
Pivot from Trailing Edge	0.74										
Pivot Radius	0.09										

Table 8-8: Nondimensionalised offset table of fairing design 2

Distance from Leading Edge Section thickness	1.00	0.90	0.80	0.70	0.60	0.50	0.40	0.30	0.20	0.10	0.00
Camber	0.00	0.12	0.19	0.25	0.31	0.36	0.40	0.42	0.42	0.36	0.00
Leading Edge Radius	0.21										
Trailing Edge Radius	0.04										
Pivot from Trailing Edge	0.94										
Pivot Radius	0.11										

## 8.8 VIV Suppression by means of Leg Diameter Selection

### 8.8.1 Steady Current

The Jack-up VIV in steady current can be suppressed by ensuring that the reduced velocity is sufficiently low corresponding to the maximum operating current.

Defining a criterion based on the model response curves as,

$$V_r \leq 3 \quad \text{Equation 8-24}$$

Considering the Strouhal relationship and the lowest natural frequency of the sway mode, the minimum diameter of the leg can be expressed as,

$$D \geq \frac{U_{max}}{3 f_{Ny}} \quad \text{Equation 8-25}$$

where  $U_{max}$  and  $f_{Ny}$  represent the maximum current and the sway natural frequency respectively. Equation 8-25 can be used effectively to decide the leg diameter of the jack-ups, primarily operating in low operating currents. However, the equation may yield very large leg diameters for high currents and low sway frequencies.

### 8.8.2 Regular Waves

Asymmetric vortex shedding and thereby oscillatory lift excitation can be suppressed in regular waves by choosing the diameter of the leg such that that  $KC$  number at the water level is less than 7 (Sumer and Fredsøe, 2006).

$$KC(h) \leq 7 \quad \text{Equation 8-26}$$

Considering the  $KC$  relationship in Equation 8-26, the minimum leg diameter shall be,

$$D \geq \left(\frac{\pi}{7}\right) \frac{H_W}{\tanh(\kappa_W h)} \quad \text{Equation 8-27}$$

As per linear wave theory (Journée and Massie, 2001),

$$\tanh(\kappa_W h) = \frac{\omega_W^2}{g \kappa_W} \quad \text{Equation 8-28}$$

where  $g, h, \kappa_W$  and  $\omega_W$  represent the acceleration due to gravity, water depth, wave number and wave circular frequency respectively.

Equation 8-28 in Equation 8-27 and further simplification,

$$D \geq \frac{H_W g T_W^2}{14 L_W} \quad \text{Equation 8-29}$$

where  $D, H_W, L_W$  and  $T_W$  represent the leg diameter, wave height, wavelength and wave period respectively.

8.8.2.1 Deep water ( $\kappa_W h \rightarrow \infty$ )

$$KC(h) = \frac{\pi H_W}{D} \quad \text{Equation 8-30}$$

Hence,

$$D \geq \left(\frac{\pi}{7}\right) H_W \quad \text{Equation 8-31}$$

Table 8-9 shows the minimum diameter of the circular leg as a function of wave height required in deep water to suppress asymmetric vortex shedding and hence VIV.

Table 8-9: Minimum leg diameter in deep water for vortex suppression in regular waves.

$H_W$ (m)	1	2	3	4	5	6	7	8	9	10
$D$ (m)	0.45	0.9	1.35	1.8	2.25	2.7	3.15	3.6	4.05	4.5

8.8.2.2 Shallow water ( $\kappa_W h \rightarrow 0$ )

With some simplification,

$$KC(h) = KC = \frac{H_W L_W}{2hD} = \frac{H_W T_W}{2D} \sqrt{\frac{g}{h}} \quad \text{Equation 8-32}$$

Hence,

$$D \geq \frac{H_W}{14} \sqrt{\frac{g}{h}} T_W \quad \text{Equation 8-33}$$

## 8.8.2.3 Fatigue Strength and Minimum Leg Diameter

Fatigue strength of an offshore structure is dominated by a large number of small stress ranges experienced over its lifetime (Bartrop and Adams, 1991) rather than the extreme stress ranges with low probabilities of occurrence. A typical sea can have its energy concentrated at around 10 seconds (Sumer and Fredsøe, 2006). A location with 10 m wave height at a return period of 100 years will correspond to a wave height

of around 5 m for a daily return period if a two-parameter Weibull distribution is considered for the long-term statistics (ABS, 2018c). Therefore, the fatigue life of the legs can be enhanced considerably if the leg diameter is chosen corresponding to a wave height of 5m, based on Equation 8-29,

$$D \geq 2.25 \text{ m}, \text{ if deep water}$$

$$\geq 2.89 \text{ m}, \text{ at 20m water depth}$$

It can be inferred from Table 8-9 that by selecting a leg diameter of 2.00 m, VIV can be totally suppressed in deep water waves up to 4 m height, which usually covers the design envelope of the jack-ups with independent cylindrical legs. However, in shallow water, the required leg diameter for VIV suppression can be very high due to the inverse proportionality with the square root of the water depth, as evident in Equation 8-33. Similarly, the fatigue concerns can also be totally eliminated in deep and intermediate water waves by selecting a leg diameter around 2.50 m as demonstrated above.

### 8.9 Jack-up with Fixed Footing

Legs with fixed footing also can be used as an efficient way of reducing VIV. It can be seen that the mode factor, defined in Section 5.3 is around 35% greater for a fixed footing in uniform current than that of a pinned footing, at a practical water depth ratio (water depth over leg length) of 0.80. This indicates that around 35% reduction of VIV amplitudes is possible at these water depths by the provision of fixed footings. However, the materialisation of the footing fixity by means of leg mats can make the jack-up designs cumbersome.

### 8.10 Discussion

Based on the mathematical investigation, modal antinodes are found to be the optimum locations for the installation of the streamlined fairings for VIV suppression. Congruently, the water level is found to be the optimum location for the installation of streamlines fairings on the jack-up legs. Two optimum fairing profiles are developed along with the offsets, based on NACA0018 profiles but with reduced L/B ratios of around 2.40 and 3.00, for practical applications. The tests with scaled down jack-up models with cylindrical legs demonstrated that both the fairing designs could reduce

VIV amplitudes significantly, by around 80%. The fairing designs are found to be effective in reducing both the crossflow and yaw VIV of the jack-up. A fairing depth of around 15% of the water depth is found to be optimum for the jack-up legs.

Free decay tests revealed considerable crossflow and yaw damping, above 7% for both the fairing designs. The weathervaning stability of the fairing designs was also found to be satisfactory, though the fairing design 2 with the lower L/B ratio was found to be slightly sluggish. From the mathematical investigation and experimental results, it is inferred that fairings contribute to the reduction of VIV in three ways: reduction of excitation force, disruption of vortex synchronisation and the increase in fluid damping. Fairings are also found not to have a significant bearing on the drag coefficient of the structure. The fairing design with the lesser L/B ratio of 2.40 is found to be an optimal solution for VIV suppression when the structure is not sensitive to drag forces. However, fairings are found to initiate galloping responses at higher flow speed above the lock-in range and hence it is recommended that the same should be of the detachable type for cylinders exposed to large flow speed variations. Further, the fairings should be neutrally buoyant and stable while afloat for ease of handling and optimum weathervaning performance. The mathematical approach presented will enable practising engineers to design and optimise antinode fairings for structures experiencing VIV. The two fairing section offsets presented can be readily used by the industry for practical applications.

## Chapter 9. Conclusions and Recommendations

This research work carried out a detailed investigation of the VIV of jack-ups with cylindrical legs under various flow scenarios. The research consisted of the analysis of design data from the industry, theoretical, experimental and numerical investigations, and investigations on the suppression of jack-up VIV. The investigations revealed that the jack-up was vulnerable to both crossflow and yaw VIV in uniform currents and regular waves. The conclusions of this research and the recommendations for the future are encapsulated in the following sections.

### 9.1 Conclusions

This section presents the conclusions of various investigations carried out during this research, under the respective subheadings. The recommendations for future jack-up designs to mitigate the undesirable effect of VIV are also presented in this section.

#### 9.1.1 *Design Data Analysis*

1. Most of the current designs of jack-ups with cylindrical legs are vulnerable to various VIV modes in current and regular waves within the design envelopes.
2. The potential VIV modes are inline, crossflow and yaw modes.
3. The mass ratios of the jack-ups can be as low as 2, potentially leading to aggressive VIV with large lock-in ranges.
4. The proximity of natural periods of the VIV modes can lead to overlap of lock-in regimes making the jack-up practically redundant throughout the operating currents.
5. The  $Re$  and  $KC$  ranges of the jack-up VIV are found to cover subcritical to transcritical regimes and single vortex pair regime respectively.

#### 9.1.2 *Theoretical Investigation*

1. Effective mass damping parameter (product of mass ratio, damping ratio and mode factor) is found to be the central parameter controlling the inline and crossflow VIV of jack-ups.
2. Effective inertia damping parameter (product of mass ratio, damping ratio, mode factor and the square of yaw radius of gyration) is found to be the important parameter governing the yaw VIV of jack-ups.

3. The criteria developed can be used to evaluate the potential occurrence of the various modes of jack-up VIV in uniform current and regular waves.
4. The SDOF formulations developed can be used for evaluating the response of the jack-ups undergoing various VIV modes.
5. Significant dynamic stresses are found to be induced in the jack-up legs due to VIV.
6. The fatigue strength of the jack-ups is also found to be considerably affected by the VIV.

### 9.1.3 *Experimental Investigation*

1. Jack-up experiences significant crossflow and yaw VIV with large lock-in regimes in uniform current.
2. Jack-up experiences inline coupled VIV with crossflow lock-in vibrations in oblique environmental headings in uniform currents.
3. Jack-up experiences aggressive crossflow VIV and moderate yaw VIV in regular waves with narrow lock-in regimes.
4. The lock-in ranges of the crossflow and yaw VIVs are found to overlap causing very high leg combined amplitude response.
5. The crossflow and yaw amplitude responses are inversely proportional with the effective mass damping and inertia damping parameters respectively.
6. Experiments is wind validated the proposed criteria for VIV occurrence.
7. Jack-up is found not to experience any significant VIV in irregular waves.
8. Jack-up is found to experience crossflow and yaw VIV in waves with imposed current.
9. The leg design LD1H3 and LD1H0 are found to respectively decrease and increase the VIV responses.
10. The added mass and fluid damping of the leg are found to be negative during crossflow and yaw lock-in vibrations
11. The jack-up leg is found to experience significant amplification of mean drag, oscillatory drag and lift forces due to crossflow and yaw VIV.
12. The VIV is also found to cause additional dynamic loading on the leg due to the inertial acceleration of the elevated mass.

#### 9.1.4 ***Numerical Investigation***

1. Jack-up experiences significant crossflow and yaw VIV with large lock-in regimes in longitudinal uniform currents.
2. The crossflow and yaw VIV amplitude responses have inverse proportionality relation with the mass damping and inertia damping parameters respectively.
3. The jack-up VIV is found to be a self-limiting phenomenon.
4. Jack-up experiences considerable drag, lift and yaw moment amplification due to crossflow and yaw VIV.
5. During crossflow VIV, both the vortex phase and shedding are synchronised across the jack-up legs.
6. During yaw VIV, vortex shedding is found to be synchronised across the jack-up legs but out of phase between the upstream and downstream legs.

#### 9.1.5 ***Investigations on Suppression of Jack-up VIV***

1. Water level is found to be the optimum location for the installation of streamlines fairings on the jack-up legs.
2. Two optimum fairing profiles are developed along with the offsets, based on NACA0018 profiles and successfully tested for practical applications.
3. The mentioned fairing designs effectively reduced both the crossflow and yaw VIV amplitudes in uniform current, by around 80% and 70% respectively.
4. A fairing depth of around 15% of the water depth is found to be the optimum for VIV suppression.
5. The fairings are found to initiate crossflow and yaw galloping responses at higher flow speeds above the lock-in range and hence should be detachable type.
6. The fairings should be neutrally buoyant and free floating for ease of handling and optimum weathervaning performance.

#### 9.1.6 ***Cross-Validation of Theoretical, Experimental and Numerical Models***

1. The theoretical predictions of the crossflow and yaw amplitude responses are found to be in good agreement with the results of the experimental model in uniform current at higher water depth.

2. The crossflow and yaw amplitude response predictions of the theoretical model are found to be conservative in comparison with the experimental results at lower water depths, attributable to the effect of the tank bottom on the uniform current profile.
3. The crossflow and yaw responses in the steady flow of the 2D numerical model correlated well with the experimental results in the uniform current, corresponding to the maximum water depth.
4. The predictions of all the three models correlated well with correct consideration of the nonlinear damping.

### 9.1.7 *Design Recommendations for Jack-ups*

The following considerations shall be made during the design process of jack-ups to ensure that the VIV is minimum.

#### 9.1.7.1 *High Mass Ratio*

High mass ratio can be accomplished by the following considerations during design.

- Adequate water ballast tanks should be provided in the jack-up hull to increase the mass ratio as required during the elevated operations. However, the leg design should consider the corresponding increase in the elevated load.
- The leg diameter of the jack-up should be made as low as practically possible by the use of high tensile steels (HTS) or by introducing footing fixity. Though leg mats make the leg footing fully fixed, it can increase the cost and make the design cumbersome. Hence provision of spud cans of appropriate size along with the usage of HTS shall be considered.
- Though non buoyant legs demand enhanced corrosion considerations, the response will be lesser as demonstrated by the experimental investigation.

#### 9.1.7.2 *High Mode Factor*

Another important design consideration is to maximise the mode factor to increase the effective mass ratio or mass damping parameter. This can be accomplished by introducing footing rotational stiffness or fixity on the legs, by the provision of leg mats or spudcans of adequate size, as appropriate.

#### 9.1.7.3 *Increased Damping*

The material damping of the jack-up can be increased by introducing materials with high damping factors in the leg-hull interface. Provision of rubber pads or other polymers in leg-hull interface shall be considered during design. Spudcans also can enhance the soil damping properties of the jack-up.

#### 9.1.7.4 *Increased Yaw Radius of Gyration*

Maximising the yaw radius of gyration will considerably increase the yaw inertia and thereby the inertial damping parameter. The yaw inertia can be increased by providing the ballast and consumable tanks at the farthest distance from the yaw centre. Figure 9-1 shows the recommended tank plan of a jack-up considering enhancement of mass ratio and yaw radius of gyration.

#### 9.1.7.5 *Leg Design and Local Heading*

The leg design with 3 pin holes (LD1H3) at a global and local heading of 0 degrees is found to be very effective in VIV reduction. Hence it is recommended to adopt this leg design as far as practically possible. However, a smaller number of pin holes will increase the rated capacity of the pins and hydraulic cylinders. Provisions shall be incorporated in the designs to change the leg local orientation, as a change of global heading may not always be practical. It is recommended not to use the leg design without pin holes (LD1H0) if there is a potential VIV concern.

#### 9.1.7.6 *Environmental Heading*

Oblique environmental headings reduce the crossflow VIV of the jack-up in regular waves (Section 6.7.6) but in steady current induce inline coupled VIV (Section 6.6.6). Hence it is recommended to adopt longitudinal or transverse environmental headings (0 or 90 degree global headings respectively) during operations in uniform currents and oblique environmental headings in regular waves.

#### 9.1.7.7 *Detachable Fairings*

The jack-up design with cylindrical legs should be supplemented with the design of detachable leg fairings for VIV suppression. The fairing design may be based on the two fairing profiles presented in Chapter 8 or of any other published profiles. The leg

fairing material may be HTS, foam, aluminium, etc based on weight considerations. Ballast chambers should be provided to make the fairings neutrally buoyant and free floating at the intended draft.

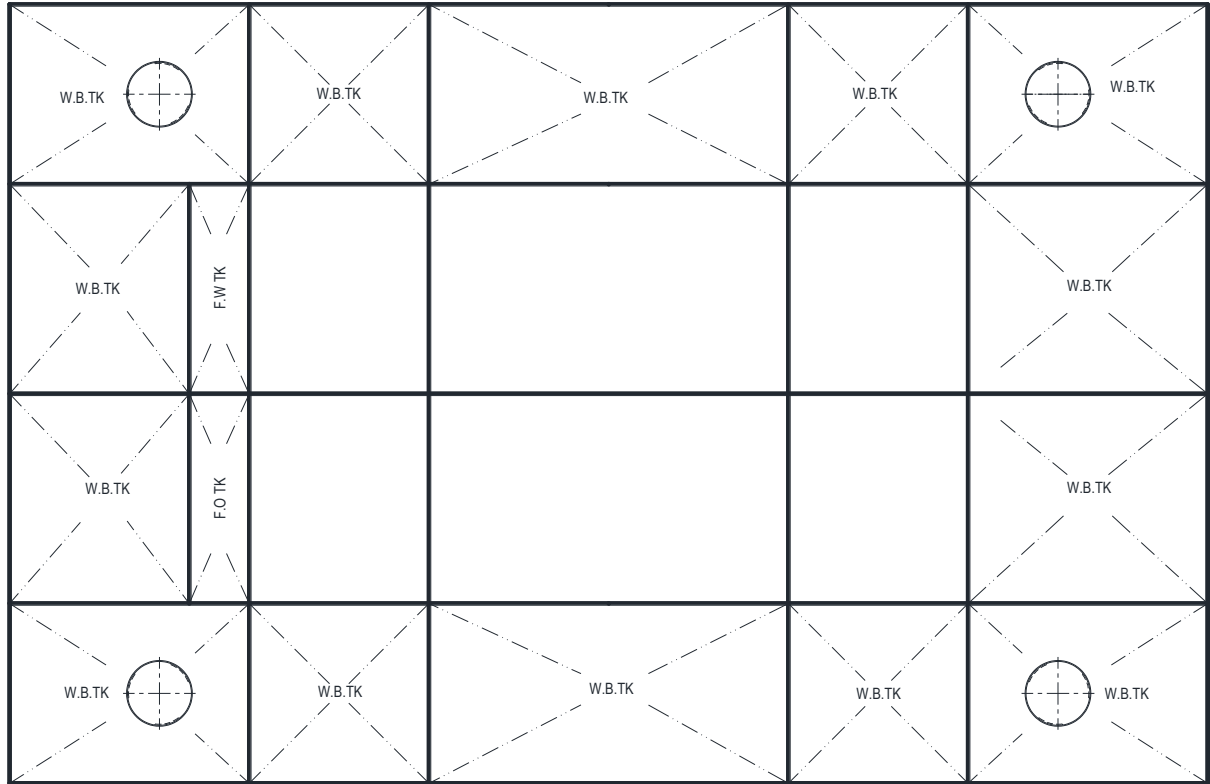


Figure 9-1: Recommended tank plan for a typical jack-up

## 9.2 Recommendations for Future Work

This section presents the recommendations for future research related to the subject. The gaps and shortcomings in the current investigation are analysed to arrive at the below mentioned propositions.

### 9.2.1 *Theoretical Investigation*

The response based models should be extended to evaluate the jack-up VIV in sheared current and irregular waves. Simple formulations should be developed and incorporated in the response based models to account for the variation of the vortex correlation along the legs with the response amplitudes. Mathematical investigation should also be carried out for the leg fairings in regular waves.

## 9.2.2 *Experimental Investigation*

### 9.2.2.1 *Linear Leg-Hull Interface Stiffness*

The leg-hull interface stiffness of the current model is found to exhibit nonlinear stiffness and hysteresis (Section 6.3.2), causing nonlinear structural damping, which increases with the vibration amplitudes. As the responses would have been higher with linear structural damping, as revealed from the numerical simulations, it is recommended that the experiments should be conducted with rigid leg-hull connections with negligible nonlinearities.

### 9.2.2.2 *Footing without Coulomb Damping*

In the present investigation, the ball joints provided in way of legs footing are found to exhibit nominal friction (Section 6.4). As the ball joint friction causes nonlinearity and hysteresis in the model stiffnesses, it is recommended to conduct the experiments with ball joints having negligible friction along with a linear leg-hull interface.

### 9.2.2.3 *Fixed Footing*

Experimental investigations should be carried out with jack-up model having fixed leg footings to evaluate the VIV of the jack-ups with leg bottom mats or large spudcans. Footing fixity will reduce the nonlinearities of the model, increase the effective mass damping parameter (Sections 5.3 and 5.6), and correspondingly reduce the VIV response.

### 9.2.2.4 *Planar Oscillatory flow*

Experimental investigation should be conducted with the jack-up model experiencing planar oscillatory flow conditions as in shallow water the regular waves assume a near planar oscillatory flow behaviour. Further planar oscillatory flow considerably simplifies the oscillatory flow physics by eliminating the orbital particle motion and exponential decay.

### 9.2.2.5 *Inline VIV*

As there are jack-up designs with considerably low mass ratios up to around 2.50 (Table 4-2), experimental investigations should be carried out with the models having

low mass ratios to comprehensively investigate the vulnerability of the jack-ups to inline VIV.

#### *9.2.2.6 Yaw Excitation*

Experimental investigation should be carried out specifically with an aim to examine yaw excitation. During yaw VIV, the total lift force on the jack-up is found to be lesser than the individual legs though yaw excitation can be significantly high. The variation of the individual lift forces on the legs as well as the amplification of the total yaw moment with the response amplitudes should be investigated experimentally.

#### *9.2.2.7 Flow Visualisation*

Flow visualisation should be carried out by means of Particle Image Velocimetry (PIV) to investigate the vortex patterns and synchronisation about the legs during various modes of jack-up VIV. Flow visualisation should also be carried out with various leg designs to evaluate the effect of leg appurtenances including fairings, pin holes, etc on the vortex modes and excitations.

#### *9.2.2.8 Fairings in oscillatory flow*

The leg fairing designs presented (Chapter 8) should be tested in oscillatory flows or regular waves to verify the efficacy in VIV suppression under flow reversal.

### **9.2.3 Numerical Investigation**

#### *9.2.3.1 Enhanced 2D FSI for Steady Flow*

Enhanced 2D FSI simulations should be carried out for the jack-up in steady flow by means of superior turbulence models like Detached Eddy Simulation (DES), LES, etc. The investigation should focus on vortex synchronisation about the legs during various modes of VIV, physics of yaw excitation, the effect of environmental heading, etc., which are relatively unresearched areas, and arrive at a reliable 2D FSI methodology suitable for industrial applications.

#### *9.2.3.2 2D FSI for Planar Oscillatory Flow*

2D FSI simulation of the jack-up in planar oscillatory flow conditions should be carried out to provide a better understanding of the jack-up VIV due to regular waves. The

vortex pattern around the legs and the vortex synchronisation in regular waves can be understood to a reasonable extent from the planar oscillatory flow simulations. Further, the phenomena like added mass, fluid damping, drag amplification, lift amplitude dependence, etc. in oscillatory flows should also be investigated.

#### 9.2.3.3 3D FSI

3D FSI simulations should be carried out for the jack-up in uniform current, sheared current, surface current, regular waves, regular wave with imposed current or any flow conditions to understand all the finer aspects of the jack-up VIV. Though such an investigation can be computationally intensive, it will overcome the limitations of 2D FSI simulations to handle 3D flows like sheared current, regular waves, waves with imposed current, etc.

#### 9.2.3.4 Supercritical Regimes

It is found (Table 4-4 to Table 4-9) that the critical  $Re$  of various modes of many of the jack-up designs are in the supercritical regime. Though scale effect is minimal for a vibrating cylinder (DNV GL, 2017b), it is recommended to carry out numerical simulations in the prototype scale for evaluating the jack-up VIV in supercritical and transcritical regimes of practical significance. Since numerical investigation in prototype scale can be computationally expensive, appropriate URANS turbulence models may be used.

### 9.2.4 **Investigations on Jack-up Design**

#### 9.2.4.1 Square Tubular Legs

Tubular legs with square cross section are also occasionally used for jack-ups due to the ease of fabrication. Square legs offer a much simpler flow scenario as the separation points and consequently, the  $St$  of the square legs are nearly constant. Investigations should be carried out for jack-ups with square legs to evaluate the vulnerability to various modes of VIV. However, square legs may be counterproductive unless considerable reduction in VIV is possible since square sections are vulnerable to galloping response and fatigue cracks.

#### 9.2.4.2 Leg Splitter Plates

Investigations should be carried to establish the efficacy of detachable splitter plates as vortex suppression devices for the jack-up legs. Splitter plate though easy to fabricate, being non-buoyant and non-free-floating, may be challenging to handle and install if not compact. Figure 9-2 illustrates a schematic comparison between the splitter plate and the fairing.



Figure 9-2: Splitter plate fairing comparison, a) splitter plate, b) fairing (Blevins, 2001)

#### 9.2.4.3 Vibration Isolation

Though, an unexpected outcome of the present investigation, a nonlinear jack-up stiffness might be used favourably to reduce VIV responses. Hence, it is highly recommended to conduct investigations towards favourably utilising the following nonlinearities for vibration reduction.

##### 9.2.4.3.1 Nonlinear Leg-Hull Interface Stiffness

Pads of rubber or other suitable polymeric materials provided in way of the leg-hull interface can introduce softening nonlinearity due to nonlinear stiffness, compression sets and Mullin's effect (Diani *et al.*, 2009), which can isolate the jack-up from large amplitude vibrations, by tuning the system away from the excitation frequency with the increasing vibration amplitudes.

##### 9.2.4.3.2 Nonlinear Soil Rotational Stiffness

Soil rotational stiffness exhibits a softening nonlinearity with the vibration amplitudes, as illustrated in Figure 9-3. It can be seen that the spudcan behaves as fully fixed,

pinned and partially fixed footings at small, large and intermediate deflections respectively. The corresponding changes in leg mode shape are also visible in the figure. Efficient spudcan designs should be developed to favourably induce a nonlinearity which tunes away the jack-up from the excitation frequency.

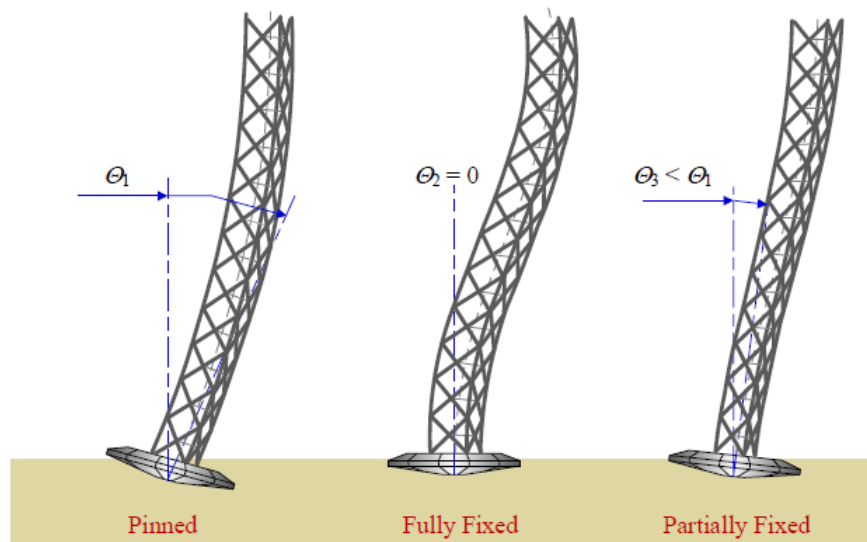


Figure 9-3: Spudcan soil rotational stiffness (ABS, 2018b)

### 9.3 Concluding Note

This investigation demonstrated that the jack-up experienced both crossflow and yaw VIV in uniform currents and regular waves. As evident from the research, the combined lock-in range of both the crossflow and yaw modes can extend over the entire operating flow regimes of a jack-up, making it practically redundant. Hence, necessary modifications to the present classification rules or guidelines are warranted to adequately account the effect of VIV in the design of jack-ups. The mathematical approach developed as a part of this research will enable practising engineers to evaluate the jack-up and design suitable antinode fairings for VIV suppression. The design recommendations presented can be effectively used by the industry to develop VIV resistant jack-up designs. The research also emphasised the significance of yaw or torsional VIV in the case of jack-ups or rigidly coupled multi-cylinder structures in general, and the need to subject the same to exhaustive research.

## References

- ABS (2016) *Guidance Notes on Structural Analysis of Self-Elevating Units*. Houston: American Bureau of Shipping.
- ABS (2017) *Guidance Notes on Dynamic Analysis Procedure for Self-Elevating Units*. Houston: American Bureau of Shipping.
- ABS (2018a) 'Fatigue Assessment of Offshore Structures'.
- ABS (2018b) *Guidance Notes on Geotechnical Performance of Spudcan Foundations*. Houston: American Bureau of Shipping.
- ABS (2018c) *Guide for Fatigue Assessment of Offshore Structures*. Houston: American Bureau of Shipping.
- ABS (2018d) *Rules for Building and Classing Mobile Offshore Drilling Units*. Houston: American Bureau of Shipping.
- Ai, Y., Feng, D., Ye, H. and Li, L. (2013) 'Unsteady numerical simulation of flow around 2-D circular cylinder for high Reynolds numbers', *Journal of Marine Science and Application*, 12(2), pp. 180-184.
- Allen, D.W. and Henning, D.L. (2001) 'Surface Roughness Effects on Vortex-Induced Vibration of Cylindrical Structures at Critical and Supercritical Reynolds Numbers', *Offshore Technology Conference*. Houston, Texas, 2001/1/1/. OTC: Offshore Technology Conference.
- American Petroleum Institute (2000) *API RP 2A-WSD, Recommended Practice for Planning, Designing and Constructing Fixed Offshore Platforms: Working Stress Design*. American Petroleum Institute.
- Anderson, J.D. (1995) *Computational fluid dynamics : the basics with applications*. New York: McGraw-Hill.
- Angrilli, F. and Cossalter, V. (1982) 'Transverse Oscillations of a Vertical Pile in Waves', *Journal of Fluids Engineering*, 104(1), pp. 46-52.
- ANSYS (2013a) *ANSYS Fluent Getting Started Guide*. Canonsburg: ANSYS, Inc.
- ANSYS (2013b) *ANSYS Fluent Theory Guide*. Canonsburg: ANSYS, Inc.
- Assi, G.R.S., Bearman, P.W. and Meneghini, J.R. (2010) 'On the wake-induced vibration of tandem circular cylinders: the vortex interaction excitation mechanism', *Journal of Fluid Mechanics*, 661, pp. 365-401.
- Assi, G.R.S., Bearman, P.W. and Tognarelli, M.A. (2014) 'On the stability of a free-to-rotate short-tail fairing and a splitter plate as suppressors of vortex-induced vibration', *Ocean Engineering*, 92(Supplement C), pp. 234-244.
- Assi, G.R.S., Bearman, P.W., Tognarelli, M.A. and Rodrigues, J.R.H. (2011) 'The Effect of Rotational Friction on the Stability of Short-Tailed Fairings Suppressing Vortex-Induced Vibrations', (44397), pp. 389-394.

- Bartrop, N.D.P. and Adams, A.J. (1991) *Dynamics of Fixed Marine Structures (Third Edition)*. Butterworth-Heinemann.
- Bearman, P.W. (1988) 'Wave loading experiments on circular cylinders at large scale', *Proceedings of the BOSS Conference*. Trondheim. pp. 471-487.
- Bearman, P.W. (2009) 'Understanding and predicting vortex-induced vibrations', *Journal of Fluid Mechanics*, 634, pp. 1-4.
- Bearman, P.W. (2011) 'Circular cylinder wakes and vortex-induced vibrations', *Journal of Fluids and Structures*, 27(5–6), pp. 648-658.
- Bearman, P.W. and Currie, I.G. (1979) 'Pressure-fluctuation measurements on an oscillating circular cylinder', *Journal of Fluid Mechanics*, 91(04), pp. 661-677.
- Bearman, P.W., Graham, J.M.R. and Obasaju, E.D. (1984) 'A model equation for the transverse forces on cylinders in oscillatory flows', *Applied Ocean Research*, 6(3), pp. 166-172.
- Benim, A.C., Cagan, M., Nahavandi, A. and Pasqualotto, E. (2007) *International Conference on Fluid Mechanics and Aerodynamics*. Athens, Greece. IASME/WSEAS.
- Bennett Jr, W.T. and Patel, R.K. (1989) 'Jack-up behavior in elevated condition: model test and computer simulation'. NJ: SNAME.
- Bishop, R.E.D. and Hassan, A.Y. (1964) 'The Lift and Drag Forces on a Circular Cylinder in a Flowing Fluid', *Proceedings of the Royal Society of London A: Mathematical, Physical and Engineering Sciences*, 277(1368), pp. 32-50.
- Blackburn, H.M. and Melbourne, W.H. (1997) 'SECTIONAL LIFT FORCES FOR AN OSCILLATING CIRCULAR CYLINDER IN SMOOTH AND TURBULENT FLOWS', *Journal of Fluids and Structures*, 11(4), pp. 413-431.
- Blevins, R.D. (2001) *Flow-Induced Vibration*. Reprint edn. Florida: Krieger Publishing Company.
- Blevins, R.D. and Burton, T.E. (1976) 'Fluid Forces Induced by Vortex Shedding', *Journal of Fluids Engineering*, 98(1), pp. 19-24.
- Blevins, R.D. and Coughran, C.S. (2009) 'Experimental investigation of vortex-induced vibration in one and two dimensions with variable mass, damping, and reynolds number', *Journal of Fluids Engineering, Transactions of the ASME*, 131(10), pp. 1012021-1012027.
- Botterill, N., Morvan, H.P. and Owen, J.S. (2013) 'Numerically Modelling the Effect of the Drag Crisis on Vortex Induced Vibration of a Circular Cylinder', (55416), p. V007T08A014.
- Branković, M. and Bearman, P.W. (2006) 'Measurements of transverse forces on circular cylinders undergoing vortex-induced vibration', *Journal of Fluids and Structures*, 22(6–7), pp. 829-836.

- Brouwers, J.J.H. and Meijssen, T.E.M. (1985) 'Viscous damping forces on oscillating cylinders', *Applied Ocean Research*, 7(3), pp. 118-123.
- Cammaert, A.B., Hoving, J.S. and Vermeulen, R. (2014) 'Experimental program for ice loads on an arctic jack-up structure', *HYDRALAB IV User Meeting*. Lisbon, Portugal.
- Carberry, J., Govardhan, R., Sheridan, J., Rockwell, D. and Williamson, C.H.K. (2004) 'Wake states and response branches of forced and freely oscillating cylinders', *European Journal of Mechanics - B/Fluids*, 23(1), pp. 89-97.
- Carberry, J., Sheridan, J. and Rockwell, D. (2001) 'FORCES AND WAKE MODES OF AN OSCILLATING CYLINDER', *Journal of Fluids and Structures*, 15(3-4), pp. 523-532.
- Catalano, P., Wang, M., Iaccarino, G. and Moin, P. (2003) 'Numerical simulation of the flow around a circular cylinder at high Reynolds numbers', *International Journal of Heat and Fluid Flow*, 24(4), pp. 463-469.
- Chakrabarti, S. (2005) 'Physical Modelling of Offshore Structures', in *Handbook of Offshore Engineering, Volumes 1-2*. Elsevier.
- Chaplin, J.R. (1988) 'Loading on a cylinder in uniform oscillatory flow: Part I— Planar oscillatory flow', *Applied Ocean Research*, 10(3), pp. 120-128.
- Chaplin, J.R. and Subbiah, K. (1998) 'Hydrodynamic damping of a cylinder in still water and in a transverse current', *Applied Ocean Research*, 20(4), pp. 251-259.
- Chen, H.-I., Dai, S.-s., Li, J. and Yao, X.-I. (2009) 'Three-dimensional numerical simulation of the flow past a circular cylinder based on LES method', *Journal of Marine Science and Application*, 8(2), pp. 110-116.
- Diana, G. and Falco, M. (1971) 'On the forces transmitted to a vibrating cylinder by a blowing fluid', *Meccanica*, 6(1), pp. 9-22.
- Diani, J., Fayolle, B. and Gilormini, P. (2009) 'A review on the Mullins effect', *European Polymer Journal*, 45(3), pp. 601-612.
- Ding, Z.J., Balasubramanian, S., Lokken, R.T. and Yung, T.W. (2004) 'Lift and Damping Characteristics of Bare and Straked Cylinders at Riser Scale Reynolds Numbers', 2004/1/1/. OTC: Offshore Technology Conference.
- Directorate-General for Research (2005) *SEAFLOW Pilot project for the exploitation of marine currents*. EUROPEAN COMMISSION Communities, E.
- DNV GL (2015) *DNVGL-RP-C104, Recommended Practice, Self-Elevating Units*. Oslo: DNV GL AS.
- DNV GL (2017a) *DNVGL-OS-C104, Offshore Standard, Structural Design of Self-Elevating Units - LRFD Method*. Oslo: DNV GL AS.
- DNV GL (2017b) *DNVGL-RP-C205, Recommended Practice, Environmental Conditions and Environmental Loads*. Oslo: DNV GL AS.

- DNV GL (2018) *DNVGL-RU-OU-O104, Rules for Classification, Self-Elevating Units, including Wind Turbine Installation Units and Liftboats*. Oslo: DNV GL AS.
- European Commission (2005) *SEAFLOW Pilot project for the exploitation of marine currents*. Brussels: Directorate-General for Research Communities, E.
- Feng, C.C. (1968) *The measurement of vortex induced effects in flow past stationary and oscillating circular and D-section cylinders*. Text thesis [Online]. Available at: <https://open.library.ubc.ca/collections/831/items/1.0104049>.
- Ferguson, N. and Parkinson, G.V. (1967) 'Surface and Wake Flow Phenomena of the Vortex-Excited Oscillation of a Circular Cylinder', *Journal of Manufacturing Science and Engineering*, 89(4), pp. 831-838.
- Fu, S., Wang, J., Baarholm, R., Wu, J. and Larsen, C.M. (2013) 'Features of Vortex-Induced Vibration in Oscillatory Flow', *Journal of Offshore Mechanics and Arctic Engineering*, 136(1), pp. 011801-011801.
- Fujarra, A.L.C., Rosetti, G.F., de Wilde, J. and Gonçalves, R.T. (2012) 'State-of-Art on Vortex-Induced Motion: A Comprehensive Survey After More Than One Decade of Experimental Investigation', (44915), pp. 561-582.
- Gonçalves, R.T., Freire, C.s.M., Rosetti, G.F., Franzini, G.R., Fujarra, A.L.C. and Meneghini, J.R. (2011a) 'Experimental Comparisons to Assure the Similarity Between VIM (Vortex-Induced Motion) and VIV (Vortex-Induced Vibration) Phenomena', (44397), pp. 11-22.
- Gonçalves, R.T., Rosetti, G.F., Fujarra, A.L.C., Nishimoto, K. and Oliveira, A.C. (2011b) 'Experimental Study on Vortex-Induced Motions (VIM) of a Large-Volume Semi-Submersible Platform', (44397), pp. 1-9.
- Gonçalves, R.T., Fujarra, A.L.C., Rosetti, G.F., Kogishi, A.M. and Koop, A. (2018a) 'Experimental study of the column shape and the roughness effects on the vortex-induced motions of deep-draft semi-submersible platforms', *Ocean Engineering*, 149, pp. 127-141.
- Gonçalves, R.T., Pinto, L.A. and Fujarra, A.L.C. (2018b) 'Concomitant Wave and Current Effects on Vortex-Induced Motion (VIM) of a Large-Volume Semisubmersible Platform', *The 28th International Ocean and Polar Engineering Conference*. Sapporo, Japan, 2018/7/30/. ISOPE: International Society of Offshore and Polar Engineers, p. 7. Available at: <https://doi.org/>.
- Gonçalves, R.T., Rosetti, G.F., Fujarra, A.L.C., Nishimoto, K. and Oliveira, A.C. (2012) 'Wave Effects on Vortex-Induced Motion (VIM) of a Large-Volume Semi-Submersible Platform', (44922), pp. 471-482.
- Govardhan, R. and Williamson, C.H.K. (2004) 'Critical mass in vortex-induced vibration of a cylinder', *European Journal of Mechanics - B/Fluids*, 23(1), pp. 17-27.
- Grant, R. and Patterson, D. (1977) 'Riser Fairing For Reduced Drag And Vortex Supression', *Offshore Technology Conference*. Houston, Texas, 1977/1/1/. OTC: Offshore Technology Conference, p. 10. Available at: <https://doi.org/10.4043/2921-MS>.

- Griffin, O.M. (1980) 'Vortex-Excited Cross-Flow Vibrations of a Single Cylindrical Tube', *Journal of Pressure Vessel Technology*, 102(2), pp. 158-166.
- Griffin, O.M. and Koopmann, G.H. (1977) 'The vortex-excited lift and reaction forces on resonantly vibrating cylinders', *Journal of Sound and Vibration*, 54(3), pp. 435-448.
- Grundlehner, G.J. (1997) 'Systematic model tests on a harsh environment jack-up in elevated condition', *Marine Structures*, 10(2–4), pp. 159-180.
- Halse, K. (1997) *On vortex shedding and prediction of vortex-induced vibrations of circular cylinders*. GEN thesis. Norwegian University of Science and Technology.
- Han, X., Lin, W., Tang, Y., Zhao, C. and Sammut, K. (2015a) 'Effects of natural frequency ratio on vortex-induced vibration of a cylindrical structure', *Computers & Fluids*, 110, pp. 62-76.
- Han, Z., Zhou, D., He, T., Tu, J., Li, C., Kwok, K.C.S. and Fang, C. (2015b) 'Flow-induced vibrations of four circular cylinders with square arrangement at low Reynolds numbers', *Ocean Engineering*, 96, pp. 21-33.
- Harding, S.F. (2013) *Unsteady velocities of energetic tidal currents: An investigation into dynamic flow effects on lifting surfaces at field and experimental scale*. The University of Edinburgh.
- Hayashi, K., Higaki, F., Shigemura, T. and Chaplin, Jr. (2003) 'Vortex-excited vibration of a circular cylinder in planar oscillating flow', *International Journal Of Offshore And Polar Engineering*, 13(4), pp. 266-273.
- Hirst, T.J., Steele, J.E., Remy, N.D. and Scales, R.E. (1976) 'Performance of Mat Supported Jack-Up Drilling Rigs', *Offshore Technology Conference*. Houston, Texas, 1976/1/1/. OTC: Offshore Technology Conference, p. 10. Available at: <https://doi.org/10.4043/2503-MS>.
- Humphries, J.A. and Walker, D.H. (1988) 'Vortex-Excited Response of Large-Scale Cylinders in Sheared Flow', *Journal of Offshore Mechanics and Arctic Engineering*, 110(3), pp. 272-277.
- ISO (2016) *ISO 19905-1, Petroleum and natural gas industries — Site-specific assessment of mobile offshore units, Part 1: Jack-ups*. Geneva, Switzerland: International Organization for Standardization.
- ITTC (2011) *Seakeeping Experiments*. ITTC.
- ITTC (2014a) *Example for Uncertainty Analysis of Resistance Tests in Towing Tanks*. ITTC.
- ITTC (2014b) *Guide to the Expression of Uncertainty in Experimental Hydrodynamics*. ITTC.
- ITTC (2017a) *General Guideline for Uncertainty Analysis in Resistance Tests*. ITTC.
- ITTC (2017b) *Uncertainty Analysis in CFD Verification and Validation, Methodology and Procedures*. ITTC.

- ITTC (2017c) *Uncertainty Analysis in CFD, Examples for Resistance and Flow*. ITTC.
- ITTC (2017d) *Uncertainty Analysis in CFD, Guidelines for RANS Codes*. ITTC.
- Iwan, W.D. and Blevins, R.D. (1974) 'A Model for Vortex Induced Oscillation of Structures', *Journal of Applied Mechanics*, 41(3), pp. 581-586.
- Jauvtis, N. and Williamson, C.H.K. (2003) 'Vortex-induced vibration of a cylinder with two degrees of freedom', *Journal of Fluids and Structures*, 17(7), pp. 1035-1042.
- Jiang, R. (2012) 'FLOW-INDUCED VIBRATIONS OF TWO TANDEM CYLINDERS IN A CHANNEL', *Thermal Science*, 16(5), pp. 1377-1381.
- Johnson, T.L. and Patel, R.K. (1992) 'The use of small scale physical models and numerical models for jack-up design', in *Recent Developments in Jack Up Platforms*. Oxford: Blackwell Scientific Publications.
- Journee, J., Massie, W., Boon, B. and Onnink, R. (1988) *Model experiments on jack-up platform hydrodynamics* (uuid:a4923d28-f07c-48af-b0bd-5412fb6dce51). TU Delft Delft, T.
- Journée, J.M.J. and Massie, W.W. (2001) *Offshore Hydromechanics*. The Netherlands: Delft University of Technology.
- Khalak, A. and Williamson, C.H.K. (1997a) 'FLUID FORCES AND DYNAMICS OF A HYDROELASTIC STRUCTURE WITH VERY LOW MASS AND DAMPING', *Journal of Fluids and Structures*, 11(8), pp. 973-982.
- Khalak, A. and Williamson, C.H.K. (1997b) 'Investigation of relative effects of mass and damping in vortex-induced vibration of a circular cylinder', *Journal of Wind Engineering and Industrial Aerodynamics*, 69–71(0), pp. 341-350.
- Khalak, A. and Williamson, C.H.K. (1999) 'MOTIONS, FORCES AND MODE TRANSITIONS IN VORTEX-INDUCED VIBRATIONS AT LOW MASS-DAMPING', *Journal of Fluids and Structures*, 13(7–8), pp. 813-851.
- Khorasanchi, M. and Huang, S. (2014) 'Instability analysis of deepwater riser with fairings', *Ocean Engineering*, 79(Supplement C), pp. 26-34.
- King, R. (1977) 'A review of vortex shedding research and its application', *Ocean Engineering*, 4(3), pp. 141-171.
- King, R., Prosser, M.J. and Johns, D.J. (1973) 'On vortex excitation of model piles in water', *Journal of Sound and Vibration*, 29(2), pp. 169-188.
- Klamo, J.T., Leonard, A. and Roshko, A. (2005) 'On the maximum amplitude for a freely vibrating cylinder in cross-flow', *Journal of Fluids and Structures*, 21(4), pp. 429-434.
- Kozakiewicz, A., Sumer, B.M. and Fredsøe, J. (1992) 'Spanwise correlation on a vibrating cylinder near a wall in oscillatory flows', *Journal of Fluids and Structures*, 6(3), pp. 371-392.

- Lam, K., Gong, W.Q. and So, R.M.C. (2008) 'Numerical simulation of cross-flow around four cylinders in an in-line square configuration', *Journal of Fluids and Structures*, 24(1), pp. 34-57.
- Longoria, R.G., Beaman, J.J. and Miksad, R.W. (1991) 'An Experimental Investigation of Forces Induced on Cylinders by Random Oscillatory Flow', *Journal of Offshore Mechanics and Arctic Engineering*, 113(4), pp. 275-285.
- Lou, M., Wu, W.-g. and Chen, P. (2017) 'Experimental study on vortex induced vibration of risers with fairing considering wake interference', *International Journal of Naval Architecture and Ocean Engineering*, 9(2), pp. 127-134.
- Mauil, D.J. and Milliner, M.G. (1978) 'Sinusoidal flow past a circular cylinder', *Coastal Engineering*, 2, pp. 149-168.
- McConnell, K.G. and Park, Y.S. (1982) 'The frequency components of fluid-lift forces acting on a cylinder oscillating in still water', *Experimental Mechanics*, 22(6), pp. 216-222.
- Menter, F.R. (1996) 'A Comparison of Some Recent Eddy-Viscosity Turbulence Models', *Journal of Fluids Engineering*, 118(3), pp. 514-519.
- Ming, X., Bifeng, S., Dong, L. and Rui, Y.E. (2010) 'Comparison of Predictive Capabilities of DES and RANS Simulations of the Separated Flow Around a Circular Cylinder', in *48th AIAA Aerospace Sciences Meeting Including the New Horizons Forum and Aerospace Exposition*. American Institute of Aeronautics and Astronautics.
- Moe, G. and Wu, Z.J. (1990) 'The Lift Force on a Cylinder Vibrating in a Current', *Journal of Offshore Mechanics and Arctic Engineering*, 112(4), pp. 297-303.
- Morandi, A.C., Frieze, P.A., Birkinshaw, M., Smith, D. and Dixon, A. (1999) 'Jack-up and jacket platforms: a comparison of system strength and reliability', *Marine Structures*, 12(4-5), pp. 311-325.
- Moreau, F.o. and Huang, S. (2010) 'Model Testing on Cross-Flow Vortex-Induced Vibration in Combined In-Line Current and Oscillatory Flows', (49149), pp. 869-874.
- Morse, A.T. (2011) *The transfer of Oil and Gas Technology and Skills to the conceptual design and development of a novel low cost modular Tidal Energy Conversion deployment system*. The Robert Gordon University.
- Morse, T.L. and Williamson, C.H.K. (2009) 'The effect of Reynolds number on the critical mass phenomenon in vortex-induced vibration', *Physics of Fluids (1994-present)*, 21(4), pp. -.
- Nicholls-Lee, R., Hindley, S. and Parkinson, R. (2013a) 'Development of an Economic and Efficient Installation Vessel for Tidal Stream Energy Converter Arrays', *Ocean Renewable Energy*, Volume 8(55423), p. V008T09A037.
- Nicholls-Lee, R., Hindley, S. and Parkinson, R. (2013b) *International Conference on Offshore Mechanics and Arctic Engineering - OMAE*. Nantes, France, June 9-14, 2013. ASME.

- Norberg, C. (2001) 'FLOW AROUND A CIRCULAR CYLINDER: ASPECTS OF FLUCTUATING LIFT', *Journal of Fluids and Structures*, 15(3–4), pp. 459-469.
- Norberg, C. (2003) 'Fluctuating lift on a circular cylinder: review and new measurements', *Journal of Fluids and Structures*, 17(1), pp. 57-96.
- Novak, M. and Tanaka, H. (1977) *4th International Conference on Wind Effects on Buildings and Structures*. Heathrow, U.K. Cambridge University Press.
- Obasaju, E.D., Bearman, P.W. and Graham, J.M.R. (1988) 'A study of forces, circulation and vortex patterns around a circular cylinder in oscillating flow', *Journal of Fluid Mechanics*, 196, pp. 467-494.
- Ong, M.C., Utnes, T., Holmedal, L.E., Myrhaug, D. and Pettersen, B. (2009) 'Numerical simulation of flow around a smooth circular cylinder at very high Reynolds numbers', *Marine Structures*, 22(2), pp. 142-153.
- Otter, A. (1990) 'Damping forces on a cylinder oscillating in a viscous fluid', *Applied Ocean Research*, 12(3), pp. 153-155.
- PANEL OC-7, S.A.O.J.-U.R. (2008) *Guidelines for Site Specific Assessment of Mobile Jack-Up Units*. Houston: SNAME.
- Pantazopoulos, M.S. (1994) 'Vortex-induced vibration parameters: Critical review', *Offshore Mechanics and Arctic Engineering Conference*. ASME, pp. 199-255.
- Pastò, S. (2008) 'Vortex-induced vibrations of a circular cylinder in laminar and turbulent flows', *Journal of Fluids and Structures*, 24(7), pp. 977-993.
- Pilkey, W.D. (2008) *Peterson's stress concentration factors*. 3rd ed.. edn. Hoboken, N.J.: Hoboken, N.J. : John Wiley.
- Qiu, W., Lee, D.-Y., Lie, H., Rousset, J.-M., Mikami, T., Sphaier, S., Tao, L., Wang, X. and Magarovskii, V. (2017) 'Numerical benchmark studies on drag and lift coefficients of a marine riser at high Reynolds numbers', *Applied Ocean Research*, 69, pp. 245-251.
- Ramadasan, S., Tao, L. and Dev, A. (2018) 'Antinode Fairings: An Optimum Solution for Reduction of Vortex Induced Vibration', *Offshore Technology Conference Asia*. Kuala Lumpur, Malaysia, 2018/3/20/. OTC: Offshore Technology Conference.
- Ramadasan, S., Tao, L. and Dev, A.K. (2019) *ASME 2019 38th International Conference on Ocean, Offshore and Arctic Engineering*. V001T01A016. Available at: <https://doi.org/10.1115/OMAE2019-95764> (Accessed: 11/24/2019).
- Ramberg, S.E. and Griffin, O.M. (1976) 'Velocity Correlation and Vortex Spacing in the Wake of a Vibrating Cable', *Journal of Fluids Engineering*, 98(1), pp. 10-18.
- Rashidi, S., Hayatdavoodi, M. and Esfahani, J.A. (2016) 'Vortex shedding suppression and wake control: A review', *Ocean Engineering*, 126(Supplement C), pp. 57-80.

- Revell, A., Craft, T. and Laurence, D. (2008) 'Turbulence Modelling of Strongly Detached Unsteady Flows: The Circular Cylinder', in Peng, S.-H. and Haase, W. (eds.) *Advances in Hybrid RANS-LES Modelling*. Springer Berlin Heidelberg, pp. 279-288.
- Rodríguez, I., Lehmkuhl, O., Borrell, R., Paniagua, L. and Pérez-Segarra, C.D. (2013) 'High Performance Computing of the Flow Past a Circular Cylinder at Critical and Supercritical Reynolds Numbers', *Procedia Engineering*, 61(0), pp. 166-172.
- Roshko, A. (1961) 'Experiments on the flow past a circular cylinder at very high Reynolds number', *Journal of Fluid Mechanics*, 10(03), pp. 345-356.
- Ryan, K., Thompson, M.C. and Hourigan, K. (2005) 'Variation in the critical mass ratio of a freely oscillating cylinder as a function of Reynolds number', *Physics of Fluids (1994-present)*, 17(3), p. 038106.
- Sadeh, W.Z. and Saharon, D.B. (1982) 'Turbulence effect on crossflow around a circular cylinder at subcritical Reynolds numbers - NASA-CR-3622' [Contractor Report]. NASA.
- Sainsbury, R.N. and King, D. (1971) 'THE FLOW INDUCED OSCILLATION OF MARINE STRUCTURES', *Proceedings of the Institution of Civil Engineers*, 49(3), pp. 269-302.
- Sakai, T., Morishita, M., Iwata, K. and Kitamura, S. (2002) 'Experimental Study on the Avoidance and Suppression Criteria for the Vortex-Induced Vibration of a Cantilever Cylinder', *Journal of Pressure Vessel Technology*, 124(2), pp. 187-195.
- Sarpkaya, T. (1975) 'Forces on Cylinders and Spheres in a Sinusoidally Oscillating Fluid', *Journal of Applied Mechanics*, 42(1), pp. 32-37.
- Sarpkaya, T. (1986) 'Force on a circular cylinder in viscous oscillatory flow at low Keulegan—Carpenter numbers', *Journal of Fluid Mechanics*, 165, pp. 61-71.
- Sarpkaya, T. (1987) 'Oscillating Flow About Smooth and Rough Cylinders', *Journal of Offshore Mechanics and Arctic Engineering*, 109(4), pp. 307-313.
- Sarpkaya, T. (1995) 'Hydrodynamic Damping, Flow-Induced Oscillations, and Biharmonic Response', *Journal of Offshore Mechanics and Arctic Engineering*, 117(4), pp. 232-238.
- Sarpkaya, T. (2004) 'A critical review of the intrinsic nature of vortex-induced vibrations', *Journal of Fluids and Structures*, 19(4), pp. 389-447.
- Sarpkaya, T. and Isaacson, M. (1981) *Mechanics of wave forces on offshore structures*. Van Nostrand Reinhold Co.
- Skop, R.A. and Griffin, O.M. (1973) 'A model for the vortex-excited resonant response of bluff cylinders', *Journal of Sound and Vibration*, 27(2), pp. 225-233.
- Slocum, S.T., Ding, Z.J., Frank, W.R. and Cox, M.R. (2004) 'Flutter Instability in Riser Fairings', *Offshore Technology Conference*. Houston, Texas, 2004/1/1/. OTC: Offshore Technology Conference.

- So, R.M.C. and Savkar, S.D. (1981) 'Buffeting forces on rigid circular cylinders in cross flows', *Journal of Fluid Mechanics*, 105, pp. 397-425.
- Stringer, R.M., Zang, J. and Hillis, A.J. (2014) 'Unsteady RANS computations of flow around a circular cylinder for a wide range of Reynolds numbers', *Ocean Engineering*, 87(0), pp. 1-9.
- Sumer, B.M. and Fredsøe, J. (1988) 'Transverse Vibrations of an Elastically Mounted Cylinder Exposed to an Oscillating Flow', *Journal of Offshore Mechanics and Arctic Engineering*, 110(4), pp. 387-394.
- Sumer, B.M. and Fredsøe, J. (1989) 'Effect of Reynolds Number on Vibrations of Cylinders', *Journal of Offshore Mechanics and Arctic Engineering*, 111(2), pp. 131-137.
- Sumer, B.M. and Fredsøe, J. (2006) *Hydrodynamics around Cylindrical Structures (Revised Edition)*. World Scientific.
- Sumer, B.M., Fredøe, J. and Jensen, K. (1994) 'A Note on Spanwise Correlation on a Freely Vibrating Cylinder in Oscillatory Flow', *Journal of Fluids and Structures*, 8(3), pp. 231-238.
- Sumer, B.M. and Kozakiewicz, A. (1995) 'Visualization Of Flow Around Cylinder In Irregular Waves', *International Journal of Offshore and Polar Engineering*, 5(04), p. 3.
- Sumner, D. (2010) 'Two circular cylinders in cross-flow: A review', *Journal of Fluids and Structures*, 26(6), pp. 849-899.
- Surry, D. (1972) 'Some effects of intense turbulence on the aerodynamics of a circular cylinder at subcritical Reynolds number', *Journal of Fluid Mechanics*, 52(03), pp. 543-563.
- Thake, J. (2005) *Development, Installation and Testing of a Large-Scale Tidal Current Turbine* Department of Trade and Industry, UK Department of Trade and Industry, U.
- Timoshenko, S. (1937) *Vibration problems in engineering*. 2nd ed edn. New York: New York, Van Nostrand.
- Toebe, G.H. (1969) 'The Unsteady Flow and Wake Near an Oscillating Cylinder', *Journal of Fluids Engineering*, 91(3), pp. 493-502.
- Travin, A., Shur, M., Strelets, M. and Spalart, P. (2000) 'Detached-Eddy Simulations Past a Circular Cylinder', *Flow, Turbulence and Combustion*, 63(1-4), pp. 293-313.
- Tsahalis, D.T. (1987) 'Vortex-Induced Vibrations due to Steady and Wave-Induced Currents of a Flexible Cylinder Near a Plane Boundary', *Journal of Offshore Mechanics and Arctic Engineering*, 109(2), pp. 112-118.
- Tutar, M. and Holdø, A.E. (2001) 'Computational modelling of flow around a circular cylinder in sub-critical flow regime with various turbulence models', *International Journal for Numerical Methods in Fluids*, 35(7), pp. 763-784.
- Van Den Abeele, F. and Vande Voorde, J. (2011a) *OMAE 2011*. Rotterdam, The Netherlands, June 19-24. ASME.

- Van Den Abeele, F. and Vande Voorde, J. (2011b) 'Stability of offshore structures in shallow water depth', *Sustainable Construction & Design*, 2(2), pp. 320-333.
- Vandiver, J.K. (2012) 'Damping Parameters for flow-induced vibration', *Journal of Fluids and Structures*, 35, pp. 105-119.
- Vandiver, J.K., Allen, D. and Li, L. (1996) 'THE OCCURRENCE OF LOCK-IN UNDER HIGHLY SHEARED CONDITIONS', *Journal of Fluids and Structures*, 10(5), pp. 555-561.
- Verley, R.L.P. (1982) 'A simple model of vortex-induced forces in waves and oscillating currents', *Applied Ocean Research*, 4(2), pp. 117-120.
- Vickery, B.J. and Watkins, R.D. (1964) 'FLOW-INDUCED VIBRATIONS OF CYLINDRICAL STRUCTURES A2 - SILVESTER, RICHARD', in *Hydraulics and Fluid Mechanics*. Pergamon, pp. 213-241.
- Vikestad, K., Larsen, C.M. and Vandiver, J.K. (1997) 'EXPERIMENTAL STUDY OF EXCITED CIRCULAR CYLINDER IN CURRENT', *OMAE*. Yokohama, Japan, April 13-17. ASME.
- Vikestad, K., Larsen, C.M. and Vandiver, J.K. (2000a) 'Norwegian Deepwater Program: Damping of Vortex-Induced Vibrations', *Offshore Technology Conference*. Houston, Texas.
- Vikestad, K., Vandiver, J.K. and Larsen, C.M. (2000b) 'ADDED MASS AND OSCILLATION FREQUENCY FOR A CIRCULAR CYLINDER SUBJECTED TO VORTEX-INDUCED VIBRATIONS AND EXTERNAL DISTURBANCE', *Journal of Fluids and Structures*, 14(7), pp. 1071-1088.
- Walker, S. and Brazier, S. (1980) 'Vortex-shedding forces and the fatigue analysis of offshore structures', *European Petroleum Conference*. pp. 423-429.
- Wang, X.K., Gong, K., Liu, H., Zhang, J.X. and Tan, S.K. (2013) 'Flow around four cylinders arranged in a square configuration', *Journal of Fluids and Structures*, 43(0), pp. 179-199.
- Williamson, C. and Roshko, A. (1988) 'Vortex formation in the wake of an oscillating cylinder', *Journal of Fluids and Structures*.
- Williamson, C.H.K. (1985) 'Sinusoidal flow relative to circular cylinders', *Journal of Fluid Mechanics*, 155, pp. 141-174.
- Williamson, C.H.K. (1996) 'Vortex Dynamics in the Cylinder Wake', *Annual Review of Fluid Mechanics*, 28(1), pp. 477-539.
- Williamson, C.H.K. and Govardhan, R. (2004) 'VORTEX-INDUCED VIBRATIONS', *Annual Review of Fluid Mechanics*, 36(1), pp. 413-455.
- Wissink, J.G. and Rodi, W. (2008) 'Numerical study of the near wake of a circular cylinder', *International Journal of Heat and Fluid Flow*, 29(4), pp. 1060-1070.

- Wolfram, J. (1991) 'The effect of marine growth on vortex shedding and the fatigue life of tubular members: Results from a case study', *International Offshore and Polar Engineering Conference*. pp. 362-369.
- Wootton, L.R. (1969) 'The oscillations of large circular stacks in wind', *ICE Proceedings*. pp. 573-598.
- [www.all-energy.co.uk](http://www.all-energy.co.uk) (2012) 'Subsea drilling in aggressive tidal locations', *ALL\_ENERGY 2013*, September 2012, p. 24.
- Xu, W.-H., Gao, X.-F. and Du, J. (2012) 'The prediction on in-line vortex-induced vibration of slender marine structures', *Acta Mechanica Sinica*, 28(5), pp. 1303-1308.
- Zdravkovich, M.M. (1981) 'Review and classification of various aerodynamic and hydrodynamic means for suppressing vortex shedding', *Journal of Wind Engineering and Industrial Aerodynamics*, 7(2), pp. 145-189.
- Zdravkovich, M.M. (1982) 'Modification of Vortex Shedding in the Synchronization Range', *Journal of Fluids Engineering*, 104(4), pp. 513-517.
- Zdravkovich, M.M. (1985) 'Flow induced oscillations of two interfering circular cylinders', *Journal of Sound and Vibration*, 101(4), pp. 511-521.
- Zedan, M.F., Yeung, J.Y., Salane, H.J. and Fischer, F.J. (1981) 'Dynamic Response of a Cantilever Pile to Vortex Shedding in Regular Waves', *Journal of Energy Resources Technology*, 103(1), pp. 32-40.
- Zhao, M. and Cheng, L. (2012) 'Numerical simulation of vortex-induced vibration of four circular cylinders in a square configuration', *Journal of Fluids and Structures*, 31(0), pp. 125-140.
- Zhu, Z. and Chen, Z. (2013) '3D LES Prediction of Unsteady Pressure on a Circular Cylinder at  $Re=4.1 \times 10^4$ ', *Procedia Engineering*, 61(0), pp. 2-8.

## Appendix A. Generic Literature Review on VIV

### A.1 Vortex Shedding around Bluff Bodies

When fluid flows around a bluff body like a circular cylinder, the flow will separate from the surface of the cylinder except at very low velocities and form vortices that are convected downstream. In the viscous flow around a bluff body, the kinetic energy of the fluid particles in the boundary layer reduces substantially due to the friction and results in a boundary layer separation. This gives rise to a vortex at the separation point that will grow and get separated from the cylinder. The vortices shed alternately from either side of the body are convected downstream, forming the Von Karman vortex street (Halse, 1997), shown in Figure A-1.

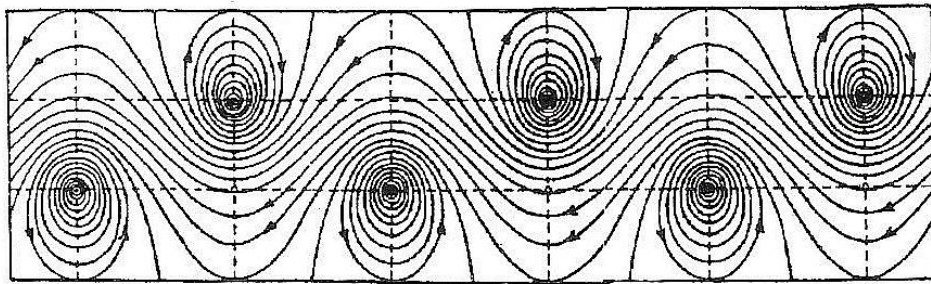


Figure A-1: Von Karman vortex street (Blevins, 2001)

#### A.1.1 *Steady Flow around a Circular Cylinder*

In a steady flow, the phenomenon of alternate vortex shedding is observed around circular cylinders for all the  $Re$  above 40 (Sumer and Fredsøe, 2006). The flow regimes around the circular cylinder are shown in Figure A-2. It can be seen in the figure that for  $Re$  above 40 alternate shedding of vortices takes place. The laminar vortex shedding forms the Karman's vortex street until a  $Re$  of 150. Between  $Re = 150$  and 300, the wake becomes turbulent although boundary layer on the cylinder remains laminar. The  $Re$  range  $300 < Re < 3 \times 10^6$  is called subcritical, where the wake is turbulent while the boundary layer is laminar and separates at  $80^\circ$ .

In the transitional or critical range,  $Re$  between  $3 \times 10^5$  to  $3.5 \times 10^6$ , the laminar boundary layer undergoes turbulent transition causing disappearance of the regular vortex street, decrease of wake width and a low drag coefficient of 0.3. In this range

the flow undergoes at first a laminar separation at  $100^\circ$  and reattaches to the cylinder wall, forming an attached separation bubble, before separating downstream at  $140^\circ$ . In the supercritical regime, for  $Re > 3.5 \times 10^6$ , the separation bubble gradually disappears, fully turbulent separation occurs at  $110^\circ$ , the wake width increases, drag coefficient reaches a stable value of 0.54, and a turbulent vortex street is established (Blevins, 2001).

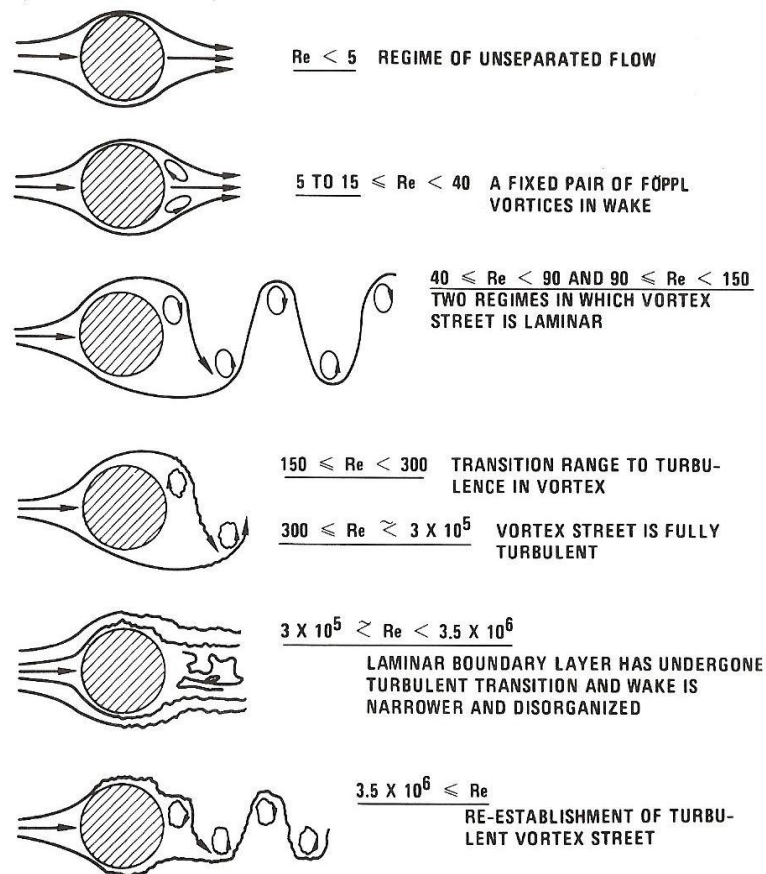


Figure A-2: Flow regimes around a cylinder in steady flow (Blevins, 2001)

### A.1.2 Oscillatory Flow around a Circular Cylinder

In the case of a circular cylinder in an oscillatory flow, the vortex shedding and lift frequencies are found to be the functions of  $KC$  number. The flow regimes in an oscillatory flow are represented Figure A-3. It can be seen in Figure A-3 that the asymmetric vortex shedding phenomenon starts at  $KC$  numbers above 7.

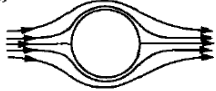
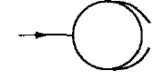
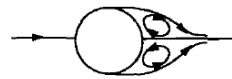
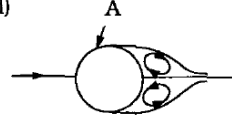
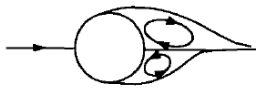
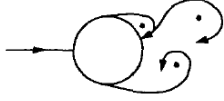
a)		No separation. Creeping (laminar) flow.	$KC < 1.1$
b)		Separation with Kármán vortices. See Figs. 3.3 and 3.4	$1.1 < KC < 1.6$
c)		A pair of symmetric vortices	$1.6 < KC < 2.1$
d)		A pair of symmetric vortices. Turbulence over the cylinder surface (A).	$2.1 < KC < 4$
e)		A pair of asymmetric vortices	$4 < KC < 7$
f)		Vortex shedding	$7 < KC$ Shedding regimes

Figure A-3: Flow regimes around a smooth circular cylinder in an oscillatory flow (Sumer and Fredsøe, 2006)

At  $KC$  higher than 7, there are distinct vortex shedding regimes with respective flow patterns for different  $KC$  ranges, like  $7 < KC < 15$ ,  $15 < KC < 24$ , etc. (Sumer and Fredsøe, 2006). For a particular  $KC$  regime, the number of vortex pairs shed within a flow cycle increases by one from that of the preceding lower regime starting with a single vortex pair for  $7 < KC < 15$ . The vortex shedding regimes in an oscillatory flow are presented in Table A-1 along with the respective  $Re$ . The shedding frequency and the lift frequency are found to be functions of both  $KC$  and  $Re$ .

## A.2 VIV in Steady Flow

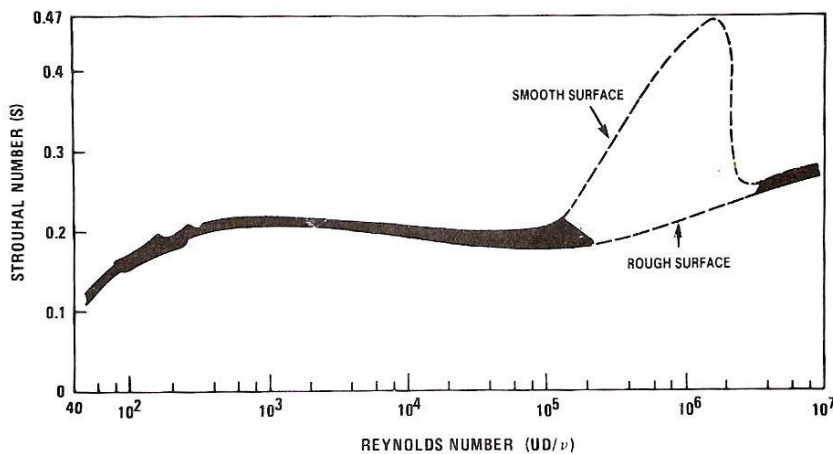
VIV in steady flow is relatively a well understood phenomenon. Comprehensive reviews on VIV are presented by Sarpkaya and Isaacson (1981), Blevins (2001), Sarpkaya (2004), Williamson and Govardhan (2004) and Sumer and Fredsøe (2006).

Table A-1: Vortex shedding regimes versus  $KC$  number in an oscillatory flow (Sumer and Fredsøe, 2006)

$KC$ regime	$KC$ range	Reynolds number $Re$	Normalised fundamental lift frequency (= the number of oscillations in the lift per flow cycle) $N_L = \frac{f_v}{f_w}$
Single pair	$7 < KC < 15$	$1.8 - 3.8 \times 10^3$	2
Double pair	$15 < KC < 24$	$3.8 - 6.1 \times 10^3$	3
Three pairs	$24 < KC < 32$	$6.1 - 8.2 \times 10^3$	4
Four pairs	$32 < KC < 40$	$8.2 - 10 \times 10^3$	5

### A.2.1 Strouhal Relation

On a fixed cylinder, a linear relation is found between the vortex shedding frequency and the flow velocity (Halse, 1997). The vortex shedding frequency ( $f_v$ ) when normalised with the flow velocity ( $U$ ) and the cylinder diameter ( $D$ ) is called the Strouhal Number ( $St = \frac{f_v D}{U}$ ), which is a function of  $Re$  and to a lesser extent surface roughness and free stream turbulence (Blevins, 2001). Figure A-4 shows the variation of  $St$  with  $Re$ . It can be observed that for low  $Re$ ,  $St$  increases with  $Re$  and exhibits a constant value of 0.20 in the subcritical regime. In the critical regime, a broad banded spectrum is found for a smooth cylinder, and in supercritical regime, a constant value of around 0.30 is again re-established.

Figure A-4:  $St$  versus  $Re$  (Blevins, 2001)

Roshko (1961) observed no vortex shedding in the critical regime with a certain peak frequency up to a  $Re$  of  $3.5 \times 10^6$ . An onset of definite shedding was again observed at  $Re = 3.5 \times 10^6$  with a  $St$  of 0.27. The following classification of flow was proposed; in the subcritical regime the separation is laminar, in the supercritical regime there is a laminar separation bubble followed by turbulent separation, and in the transcritical regime the separation is purely turbulent.

### A.2.2 *Excitation / Vortex Induced Forces*

As a consequence of the alternate vortex shedding phenomenon, the cylinder will experience oscillatory drag and lift forces due to the periodic change in the pressure distribution around the cylinder. The lift force oscillates at the vortex shedding frequency with a zero mean, while the drag force oscillates at twice the vortex shedding frequency with a nonzero mean (Sumer and Fredsøe, 2006). The periodic pressure field around a cylinder is illustrated in Figure A-5.

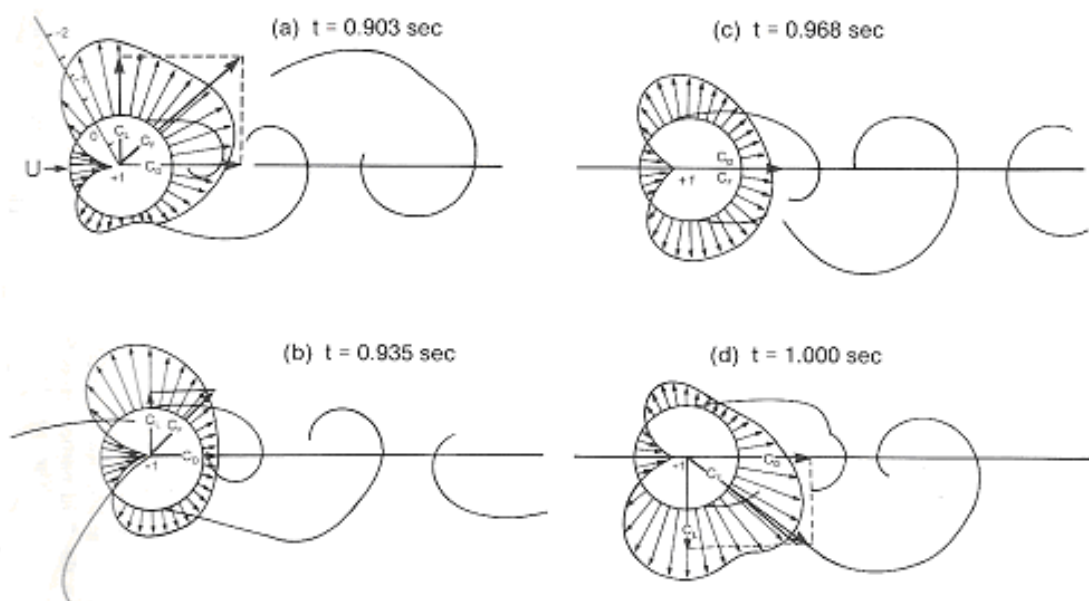


Figure A-5: Pressure distribution in a vortex (Blevins, 2001)

At the critical steady flow velocities, the oscillatory force frequency coincides with the natural frequency of the cylinder and results in resonant inline or lateral vibrations, called as VIV. The phenomenon called lock-in happens when the vortex shedding frequency locks on to the structural natural frequency and the cylinder experiences lateral vibrations at or near the natural frequency (DNV GL, 2017b). In the range of

lock-in vibration, the product of the  $St$  and the reduced Velocity ( $V_r$ ) will be near to unity, where  $V_r = \frac{U}{Df_N}$  and  $f_N$  is the natural frequency of the cylinder (Sumer and Fredsøe, 2006).

#### A.2.2.1 Drag Force

For a smooth cylinder, the (mean) drag coefficient ( $\bar{C}_D$  or  $C_D$ ) is a function of  $Re$ , as shown in Figure A-6. It can be observed that  $C_D$  is practically constant at 1.2 throughout the subcritical regime ( $Re$  300 to  $3 \times 10^5$ ), followed by dropping to a value of 0.30 due to drag crisis in the critical regime and attains a constant value of approximately 0.50 in the transcritical regime.

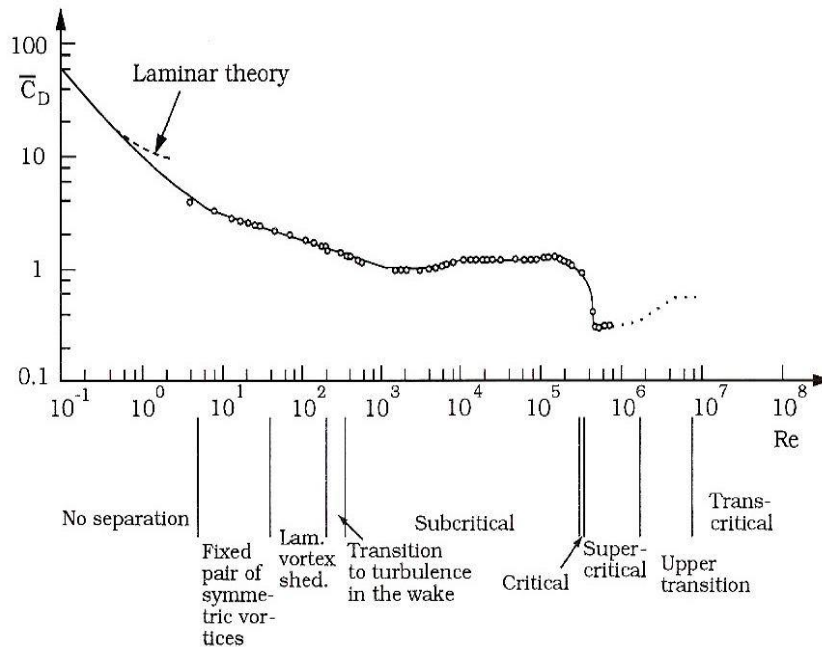


Figure A-6: Mean drag coefficient of a smooth cylinder as a function of  $Re$  (Sumer and Fredsøe, 2006)

Roshko (1961) carried out wind tunnel measurements on a large circular cylinder at  $Re$   $10^6$  to  $10^7$  and found a high  $Re$  transition at  $Re > 3.5 \times 10^6$ , where the drag coefficient achieved a constant value of around 0.7 and definite vortex shedding reappeared with a  $St$  of 0.27. Ding *et al.* (2004) conducted experiments in the  $Re$  range from  $10^4$  to  $10^6$  and found that the drag crisis is insignificant for the cylinders with large roughness and absent for the straked cylinders.

The variation of the root-mean-square (rms) value of the oscillatory drag ( $C'_D$  or  $C_{DO}$ ) with the  $Re$  is presented in Figure A-7. It can be seen that the magnitude of the oscillatory drag is considerably less than the mean drag though both follow a similar trend.

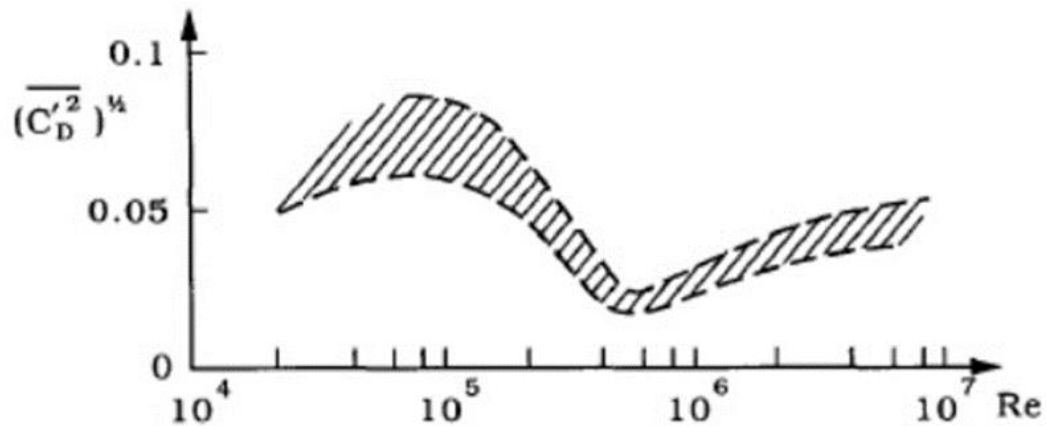


Figure A-7: Oscillatory drag coefficient of a smooth cylinder as a function of  $Re$  (Sumer and Fredsøe, 2006)

#### A.2.2.2 Lift Force

Blevins (2001) compiled the published results from various authors and demonstrated that the measurements of the lift coefficient show a considerable scatter, as shown in Figure A-8. Barltrop and Adams (1991) proposed a design curve for lift coefficient ( $C_L$  or  $C'_L$ ) based on Blevin's compilation to conservatively estimate the lift forces on a stationary circular cylinder in a steady flow, as illustrated in Figure A-9 a). Sumer and Fredsøe (2006) also compiled rms values of the oscillating lift data from various authors and presented the curve in Figure A-9 b). It can be seen that the *r.m.s.*-value of  $C_L$  experiences a sudden drop in the critical flow regime and attains an extremely low value in the supercritical flow regime, analogous to the drag crisis.

Norberg (2001; 2003) presented the experimental data on rms values of the sectional lift coefficients of a smooth stationary cylinder in Figure A-10. It was proposed to name the sudden drop in lift coefficient at  $Re\ 1.6 \times 10^3$  as lift crisis. Flow visualisations revealed that the lift crisis is due to initiation of a low-quality shedding at  $Re$  around  $10^3$ , with a transitional change in the three dimensionalities of the wake. A rapid fall in  $C_L$  was again observed at  $Re$  of  $2 \times 10^5$  when entering the critical regime.

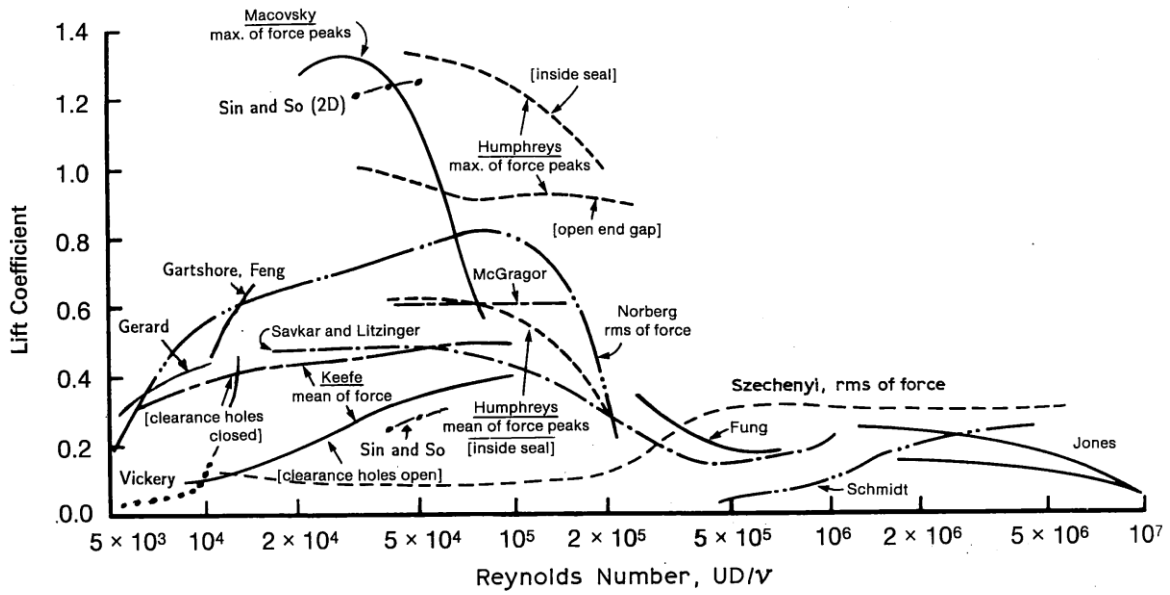


Figure A-8: Lift coefficient versus  $Re$  from various sources (Blevins, 2001)

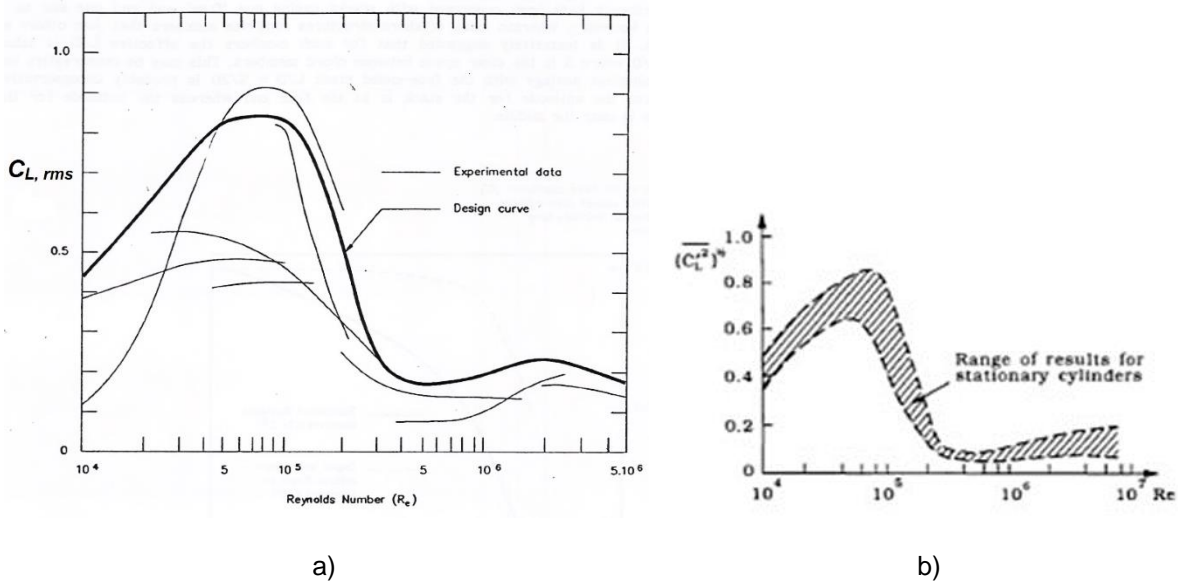


Figure A-9: Lift coefficient versus  $Re$ , a) (Bartrop and Adams, 1991), b) (Sumer and Fredsøe, 2006)

Sumer and Fredsøe (2006) presented the variation of the spanwise correlation length with the  $Re$  for a smooth cylinder based on the data compiled by King (1977). Norberg (2001; 2003) conducted experiments and compiled the normalised spanwise correlation length ( $\lambda/D$ ) of the lift force of a smooth cylinder, as illustrated in Figure A-11. It can be observed that the correlation length generally decreases with increasing  $Re$ , and the decrease is drastic for the turbulent shedding conditions.

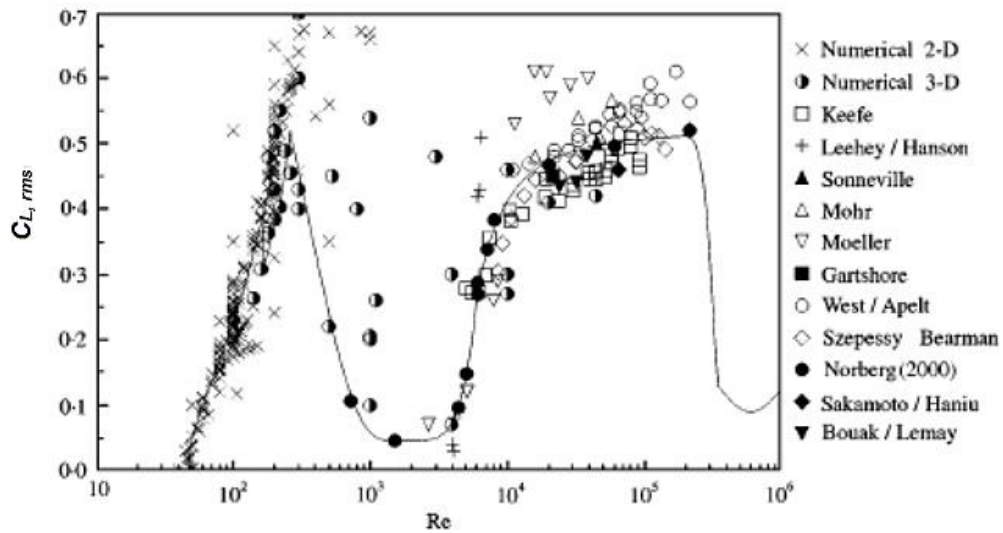


Figure A-10: Sectional lift coefficient versus  $Re$  (Norberg, 2001)

Bartrop and Adams (1991) present the effect of finite cylinder aspect ratio on the normalised lift coefficient (ratio of lift coefficient of a finite length cylinder to that of an infinitely long cylinder) with the aspect ratio ( $L/D$ ) in Figure A-12. It was noted that the loading could be considerably reduced due to 3D effects if the aspect ratio is less than about 30 in subcritical and 10 in the super and post critical flow regimes.

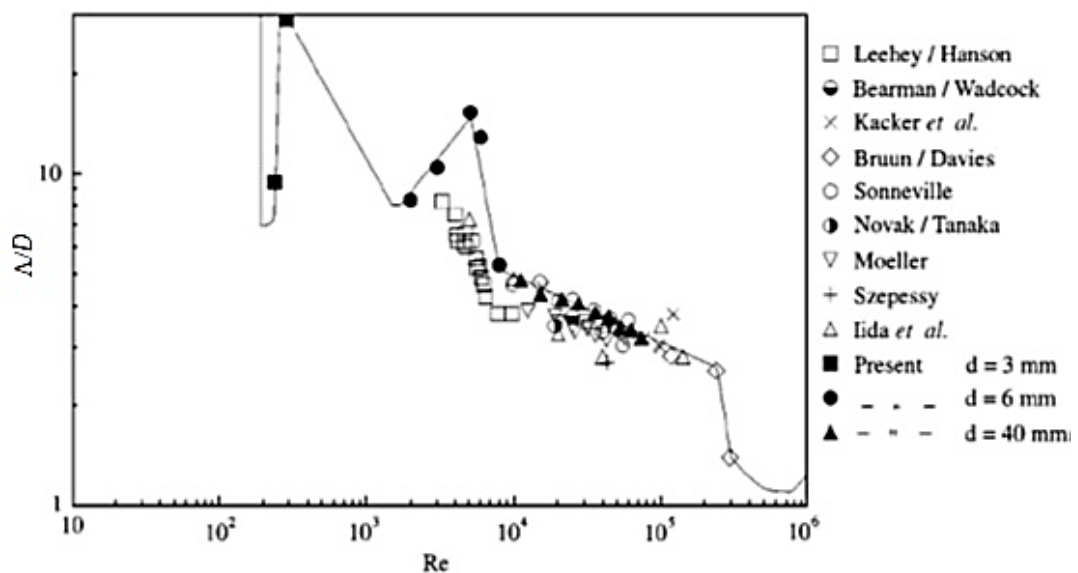


Figure A-11: Spanwise correlation length versus  $Re$  (Norberg, 2001)

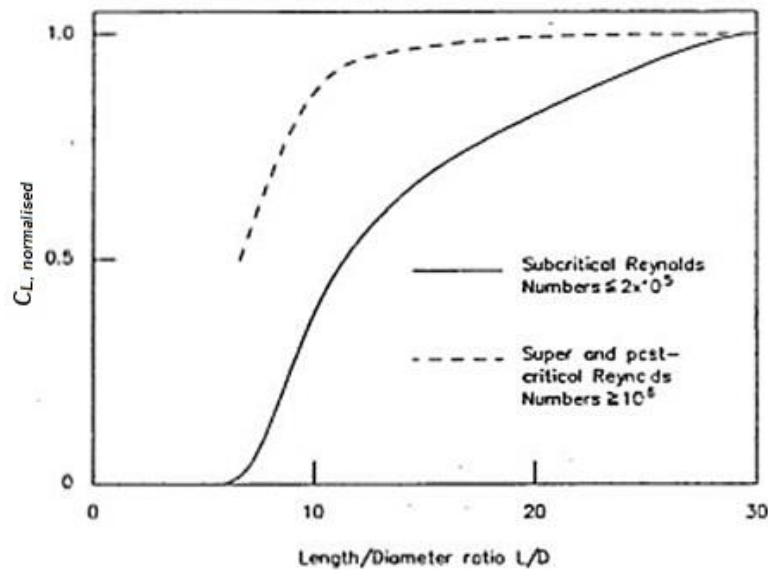


Figure A-12: Reduction in lift force due to finite aspect ratios (Barltrop and Adams, 1991)

#### A.2.2.3 Effect of Free Stream Turbulence

Surry (1972) investigated the effect of free stream turbulence on the flow around a circular cylinder at subcritical  $Re$  experimentally. It was observed that large scale turbulence is qualitatively equivalent to an increase in effective  $Re$ . Vortex shedding is found not disrupted even by severe turbulence, but the forces are affected by low frequencies. The unsteady lift and drag were found to be predominantly due to vortex shedding and turbulence respectively. So and Savkar (1981) observed that the effect of the free stream turbulence is to shift the transitional region to a lower  $Re$ . However, at pre transitional  $Re$ , the free stream turbulence is found not to have any bearing on the steady and unsteady forces. It was observed that the unsteady drag and lift forces exhibited variation similar to that of mean drag with  $Re$ .

Blackburn and Melbourne (1997) measured the sectional lift forces on a circular cylinder undergoing forced crossflow oscillation with an amplitude of  $0.03 D$  in smooth and turbulent flows, at a  $Re$   $1.6 \times 10^5$ . It was observed that in a smooth flow, motion correlated lift was found to be well correlated in the spanwise direction, and the uncorrelated lift was found to be similar to those of a fixed cylinder. In turbulent flows (up to 18% intensity) motion correlated lift was found to be much smaller than in smooth flow. It was further found that high free stream turbulence induced the critical transition at a lower  $Re$  than the smooth flow. At very high turbulence intensity (18%), the

correlation length of lift increased nominally, and broadband vortex shedding re-established at a  $St$  of 0.23.

### A.2.3 *Inline VIV*

VIV in water is characterised by low mass ratio, high added mass and significant fluid damping. King et al. (1973) investigated the nature of VIV in water using model piles and observed VIV along both inline and crossflow directions. Two inline vibration modes were identified, one associated with symmetric vortex shedding and the other with alternate vortex shedding, with response peaks at reduced velocities 2.2 and 3.2 respectively. It was observed that the inline vibrations occur at twice the vortex shedding frequency. Figure A-13 illustrates the inline base bending moment response of a model pile due to inline VIV, for various values of the stability parameter ( $k_s = \pi^2 m^* \zeta_s$ ), plotted against the reduced velocity ( $V_r$ );  $m^*$  and  $\zeta_s$  represent the mass ratio and structural damping ratio respectively.

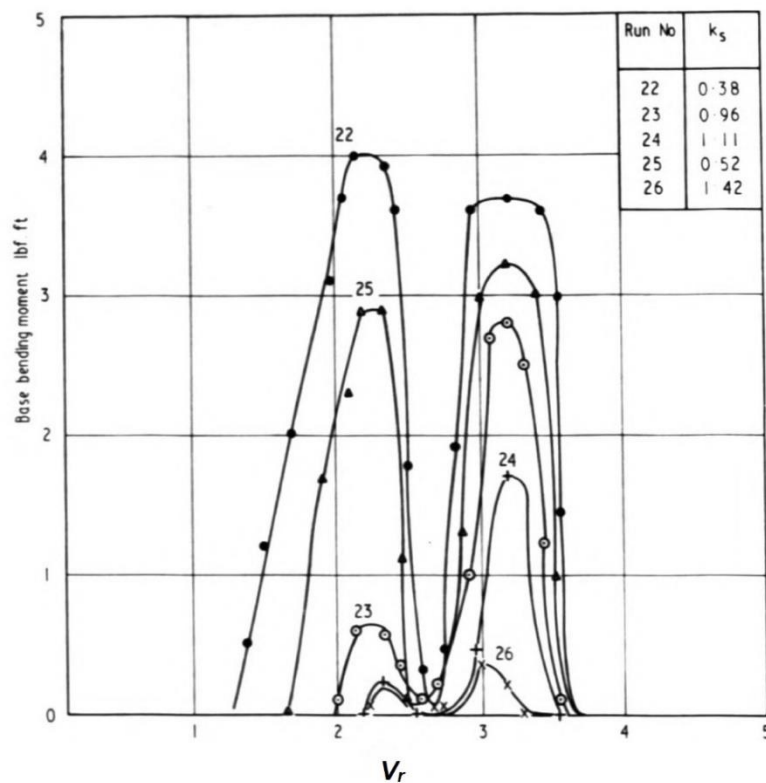


Figure A-13: Base bending moment response of a model pile due to inline VIV (King *et al.*, 1973)

The findings of King et al. (1973) were further verified by Humphries and Walker (1988) and Jauvtis and Williamson (2003). Vandiver (2012) also notes that the inline cylinder vibrations are at twice the shedding frequency.

#### A.2.4 **Crossflow VIV**

Khalak and Williamson (1997a; 1997b) conducted experiments with elastically mounted rigid cylinders constrained to oscillate transversely only with very low damping, and with a low mass ratio of around 1% of that of Feng (1968). The mass damping parameter ( $m^*\zeta_s$ ) was 4% of the Feng's experimental value, and it was observed that the cylinder excitation regime extended over a larger range of reduced velocity, around four times that of Feng. Further, the amplitude response ( $A_{max} = \frac{y_o}{D}$ ) was also found to be twice that of Feng, as illustrated in Figure A-14 (see Figure 1-4 also). Four distinct regions of crossflow response were identified, the initial excitation region, the upper branch with very high amplitude response, the lower branch with moderate amplitude response, and the desynchronization region. The vibration frequency is found to increase above the natural frequency through the excitation regime and the upper branch, as evident from the frequency ratio ( $f^* = \frac{f}{f_n}$ );  $f$  represents the vibration frequency. Further, the phase difference between the lift force and the displacement is found to be 0 and 180 degrees in the upper and lower branches respectively, similar to a resonance phase jump of a low damped linear system.

Khalak and Williamson (1999) conclude that there exist two distinct transverse responses for an elastically mounted cylinder depending on the mass damping parameter ( $m^*\zeta$ ). For low  $m^*\zeta$ , three modes namely initial, upper and lower branches and for high  $m^*\zeta$ , initial and lower branches are found. It was further demonstrated that the amplitude response plots collapsed well when plotted against the true reduced velocity based on the vibration frequency. Jauvtis and Williamson (2003) investigated the response of an elastically mounted cylinder, which is free to move in 2 DOF in a fluid flow, having low mass and damping and observed the initial, upper and lower response branches. It was found that the freedom to move in two directions has minimal effect on the transverse response, the modes of vibration, or the vortex wake dynamics. Carberry *et al.* (2004) also observed that for cases with relatively high mass damping parameter, only the initial and lower branches exist and for small values of

mass damping parameter, the upper branch response also exists with amplitude ratios typically greater than 0.7, between the initial and lower branches.

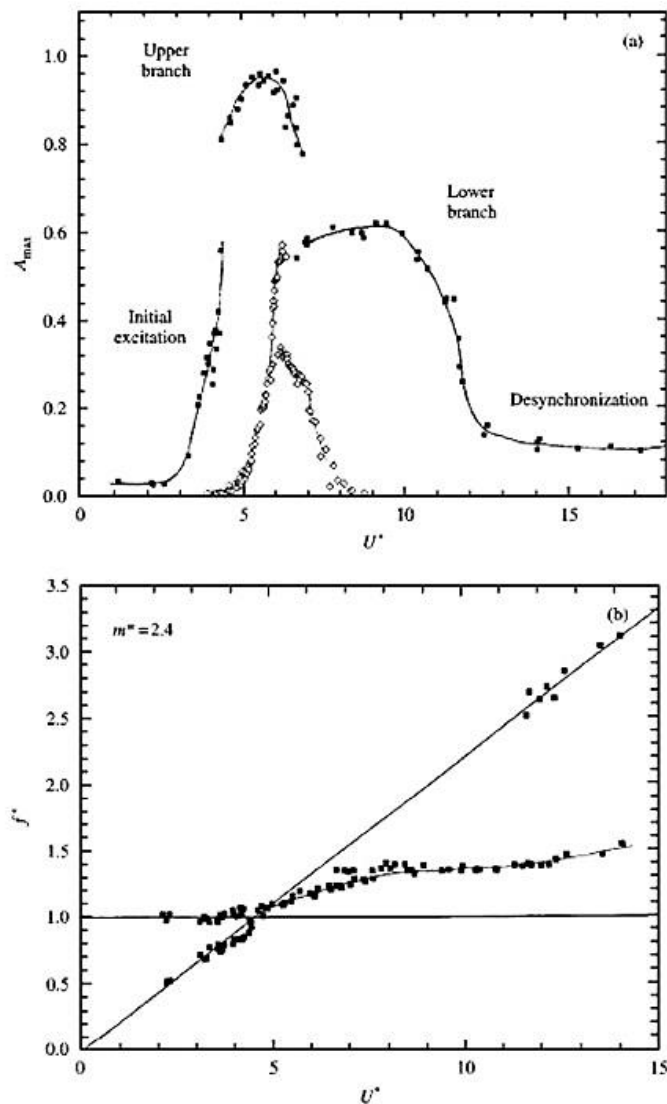


Figure A-14: Crossflow amplitude and frequency response for low mass and damping (Khalak and Williamson, 1997a)

Moe and Wu (1990) observed large self-excited crossflow motions for a wider range of true reduced velocity (based on the actual vibration frequency) if the cylinder is free to execute figure eight motions than restrained in the in-line direction. It was observed that relatively large random effects like amplitude modulations and additional frequency components exist in the lift force of the cylinder undergoing VIV, though the displacement time series was found to be harmonic. The randomness was found to be stronger for the in-line fixed cases than for the in-line spring-supported ones. Pastò

(2008) also observed that the frequency and amplitude of oscillations are modulated during self-excited vibrations.

Ding *et al.* (2004) investigated the crossflow VIV of smooth and rough cylinders with various spring stiffnesses. It was observed that aggressive VIV occurred even in the critical regime for the smooth, small roughness and medium roughness cylinders. Further, VIV amplitude in the order of  $2D$  was observed for the smooth cylinders in  $Re$  from 70,000 to 250,000. The crossflow response ( $\frac{A}{D} = \frac{y_o}{D}$ ) of the small roughness cylinders in critical regime is illustrated in Figure A-15;  $R_n$  in the figure represents  $Re$ .

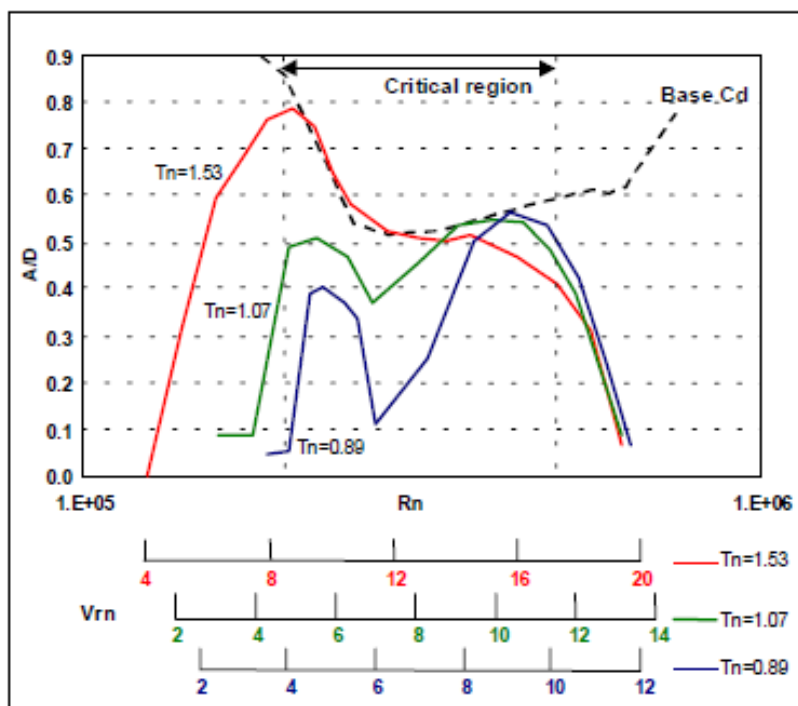


Figure A-15: Crossflow VIV of small roughness cylinder in critical regime (Ding *et al.*, 2004)

Humphries and Walker (1988) noted that during crossflow lock-in an inline motion at twice the natural frequency occurs for a free cylinder and orbital trace of the displacement describes a figure-eight motion. Sarpkaya (1995) observed that if the structure's natural frequency in the in-line direction is twice that of the transverse direction, the excitations lock-on to the respective natural frequencies and the body traces an 8-shaped path. It was further observed that the cylinder traces a crescent shape or circular arc for identical natural frequencies in the inline and crossflow directions.

### A.2.5 Spanwise Correlation

Ferguson and Parkinson (1967) conducted measurements of the fluctuating pressures on the surface and in the wake of stationary and vortex excited circular cylinders at subcritical  $Re$ . It was observed that throughout the synchronisation range, displacement and pressure amplitudes exhibited insignificant modulations indicating highly organised wake and vortices due to the cylinder oscillations. Diana and Falco (1971) carried out wind tunnel experiments with a circular cylinder and observed that the randomness reduced and the wake became bidimensional with increasing vibration amplitudes.

The correlation length along the cylinder and the vortex strength are found to increase with vibrations, leading to larger exciting forces and response amplitudes. Figure A-16 presented by Sumer and Fredsøe (2006) shows the variation of the correlation length ( $L_c$ ) normalised with the diameter as a function of the amplitude-to-diameter ratio ( $\frac{A}{D} = \frac{y_0}{D}$ ), based on the results of Novak and Tanaka (1977). It can be seen that the correlation length increases considerably for a smooth cylinder at vibration amplitudes above 0.1D.

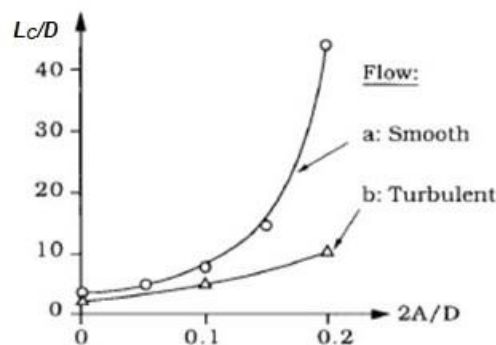


Figure A-16: Correlation length versus amplitude ratio (Sumer and Fredsøe, 2006)

Toebes (1969) carried out correlation measurements in the turbulent wake of a vibrating circular cylinder for  $Re$  up to  $1.2 \times 10^5$  and found that cylinder vibrations lead to increased axial correlation. Ramberg and Griffin (1976) conducted experiments with vibrating cables at various  $Re$  and found that the degree and extent of correlated shedding within the synchronised region, above a lower threshold amplitude of 0.1D are independent of the amplitude, frequency and  $Re$ . The measured correlation coefficient was found to approach unity and limited only by the turbulence level.

Pastò (2008) demonstrated that the relationship between the amplitude of oscillation and the wake correlation length was more evident in laminar and low turbulence flows; the correlation length was found to be higher for higher response amplitudes. However, it is found that in the high turbulence, for both smooth and rough cylinders, the correlation length decreases considerably, attributable to the three-dimensional wake. It is further observed that the wake correlation length decreases as the  $Re$  enters critical regime.

### A.2.6 Surface Roughness

Ding *et al.* (2004) investigated the effect of surface roughness on crossflow VIV and the resulted amplitude ratio  $\left(\frac{A}{D} = \frac{y_o}{D}\right)$ , for different cylinder roughness are plotted against the reduced velocity in Figure A-17. It can be seen that the small and medium roughness cylinders show the two peak phenomena demonstrating the  $Re$  dependence of VIV. It can be observed that in the critical regime, the bare cylinder VIV amplitude is sensitive to both  $Re$  and surface roughness. Further, smooth cylinders were found to experience large VIV amplitudes even in the critical regime.  $V_m$  in the figure represents reduced velocity ( $V_r$ )

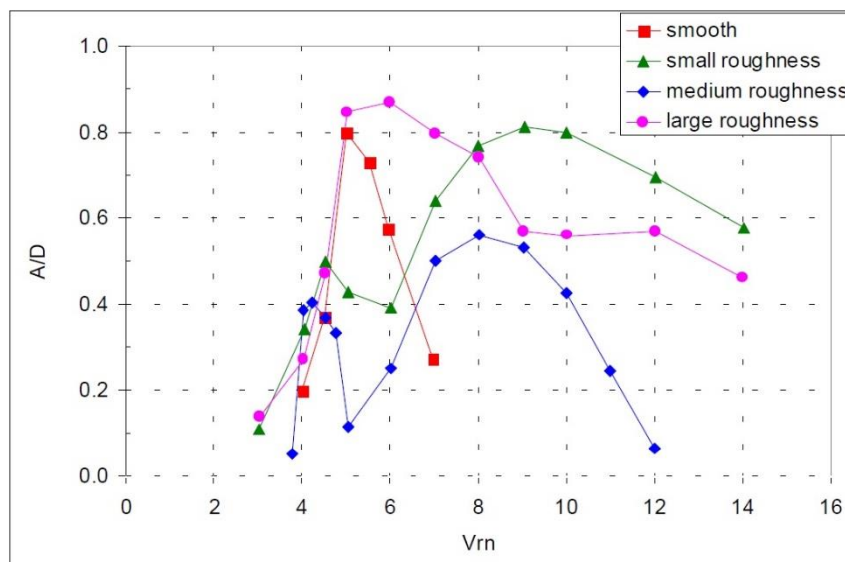


Figure A-17: Crossflow VIV of smooth and rough cylinders (Ding *et al.*, 2004)

On the contrary, Allen and Henning (2001) observed that the smooth cylinder experienced low drag and virtually no VIV in the critical  $Re$  range. Further, it was noticed that as the surface roughness increased, the VIV amplitude also increased to

a saturation point. The authors argued that the VIV of a circular cylinder could be virtually eliminated if the surface is made sufficiently smooth.

### A.2.7 *Response Branches and Vortex Modes*

Zdravkovich (1982) carried out flow visualisation within the synchronisation range and found that the oscillating cylinder controlled both the frequency as well as the timing of the vortex shedding in the wake. It was observed that in the lower reduced velocity region of the synchronization range, the vortex shedding was out of phase with the cylinder motion and in the upper synchronization range, the vortex shedding was in phase with the cylinder motion. The two modes were found to be separated by the critical reduced velocity, with the maximum amplitude and a discontinuous change in phase angle between the cylinder displacement and the fluctuating pressure. Khalak and Williamson (1997a; 1999) observed that if the phase of the upper branch is near  $0^\circ$ , the lower branch phase is near  $180^\circ$ , similar to a low damped linear system going through resonance. Further, flow visualisation studies (Khalak and Williamson, 1999) revealed that the initial and lower branches are associated with 2S and 2P modes respectively.

Carberry *et al.* (2001) investigated the wake states of a cylinder subjected to forced oscillations at frequencies close to vortex shedding frequency. It was observed that as the oscillation frequency increases, there is simultaneously a jump in the lift force and change in the vortex mode. The jump in lift force consists of an abrupt increase in the lift coefficient and a phase shift by  $180^\circ$  from out of phase to in phase. Further, the vortex shedding mode changed from 2P to 2S. In the 2P mode, a vortex pair is shed alternately from either side of the cylinder in a vibration cycle whereas, in the 2S mode, a single vortex is shed alternately from either side. Jauvtis and Williamson (2003) investigated the wake modes of the response branches of a freely vibrating cylinder having low mass and damping and found 2S for initial and 2P for upper and lower branches. Govardhan and Williamson (2004) verified the wake modes of the branches by superimposing the responses on the classical wake mode map from Williamson and Roshko (1988), as illustrated in Figure A-18.  $A^*$ ,  $f_v$ ,  $f$  represents amplitude ratio  $\left(\frac{y_0}{D}\right)$ , vortex shedding frequency of the stationary cylinder and the vibration frequency respectively.

Carberry *et al.* (2004) observed that for free oscillations, the jump in lift occurs at the transition between the lower and upper branches, whereas the jump in vortex strength occurs at the transition between the upper and initial branches. The shedding modes for the lower and upper branches were found to be 2P, while the vortex mode in the initial branch wake was 2S. However, in the upper branch, the second vortex in each pairing is found to be significantly weaker than the first. Carberry *et al.* (2004) further observed that although the forced sinusoidal oscillations replicate many features of the VIV, they result in negative energy transfer where free oscillations are known to occur.

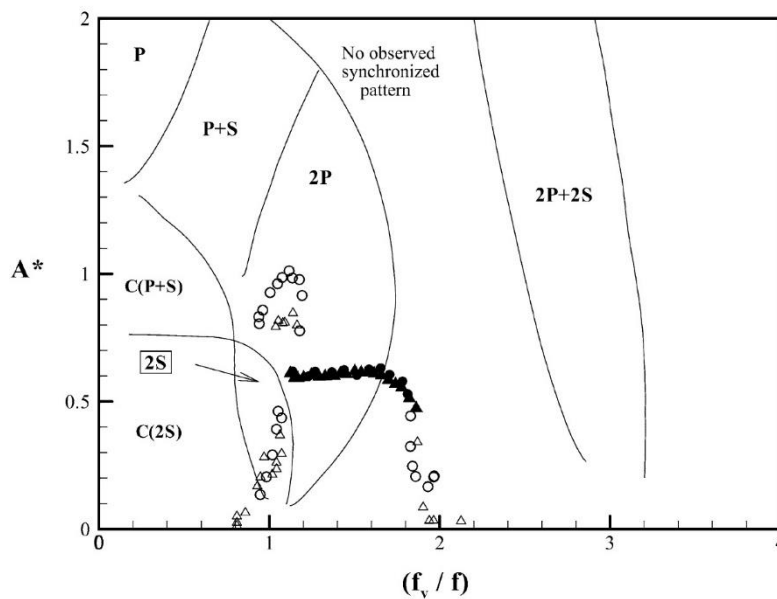


Figure A-18: Response branches and vortex modes from the wake mode map (Govardhan and Williamson, 2004)

Bearman (2009) elaborates the various modes of vortex shedding for large amplitude vibrations, greater than one diameter. Figure A-19, extracted from his work, shows various modes of vortex shedding as captured from forced oscillation tests. The 2P mode consists of an arrangement of roughly equal strength vortex pairs whereas the P+S mode has a single vortex shed from one side and a pair shed from the other, which is not expected to be found in the wake of a freely vibrating cylinder as verified by energy measurements. The 2Po mode is similar to the 2P mode except that the paired vortices are of considerably different strengths. It was named the 2P overlap mode (2Po) since it can occur in regions where other modes are possible. 2S is the normal Von Karman vortex mode. Bearman (2009) also

mentions about the initial, upper and lower response branches and the respective 2S, 2Po and 2P vortex modes.

Pastò (2008) also observed a phase jump, passing through the resonance in laminar and low turbulence flows around a circular cylinder. It was observed that just before this phase shift, the responses approach their maximum value. However, in high turbulence flow, such a clear phase shift was not observable as the phase was constant at  $90^\circ$  during the synchronization range.

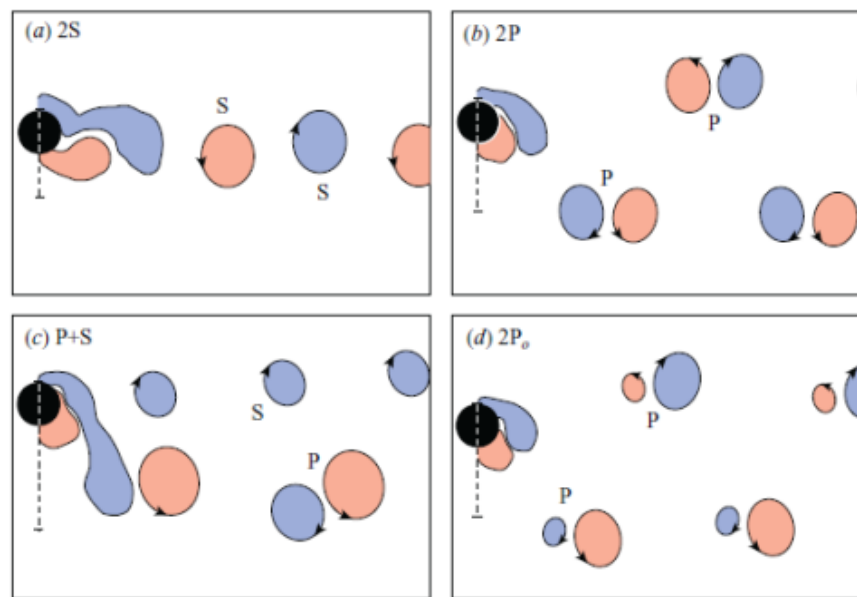


Figure A-19: Vortex modes of a vibrating cylinder (Bearman, 2009)

### A.2.8 Fluid Damping

Brouwers and Meijssen (1985) explain that for cylindrical bodies undergoing transverse vibrations with small amplitudes compared with their diameter, damping is due to the viscous forces in the thin boundary layer attached to the body and can be calculated using Stokes' equation. For vibrations with amplitudes of the same order of the diameter or larger, the boundary layer undergoes separation, and the damping force is the quadratic fluid drag. Further, It was found that fluid damping changes rather abruptly from viscous shear to quadratic drag around amplitude ratio in the order of 1.

Otter (1990) conducted experiments on the vibrating cylinders in still water and observed that the fluid damping is not only dependent on the amplitude ratio  $\left(\frac{x_o}{D}\right)$  but also on the ratio of the cylinder diameter to the thickness of the unsteady boundary

layer. It was noted that above an amplitude ratio of 0.30, the fluid damping deviates from Stoke's solution. Vikestad *et al.* (1997) define the transverse drag coefficient in terms of energy dissipation from the cylinder into the fluid. It was found that the drag coefficient has a minimum value of approximately 0.5 at an amplitude ratio of 0.3, and for low amplitudes,  $C_D$  follows Stokes law.

Vikestad *et al.* (2000a) define VIV as an energy balance problem where excitation forces add an equal amount of energy to the system that is dissipated by the damping forces. It was explained that the fluid damping is dependent on the amplitude and that the dynamic equilibrium should be found by iteration. Based on experimental results in still water, the authors recommended that the damping force must be expressed as a function of the amplitude ratio and reduced velocity. Sarpkaya (1995) compiled the fluid force measurements on the oscillating cylinders in current from various studies and observed that drag coefficient or the normalised out-of-phase component of the total instantaneous transverse force ( $C_{dy}$ ) becomes negative primarily in the neighbourhood of resonance ( $f/f_N = 1$ ). This region was called the negative damping region where the transverse drag force helps to magnify the oscillations (lift amplification). Figure A-20, extracted from the author's work illustrates the variation of drag as a function of  $Vr.St$ , for a relative amplitude ( $\frac{A_y}{D} = \frac{y_o}{D}$ ) of 0.50.

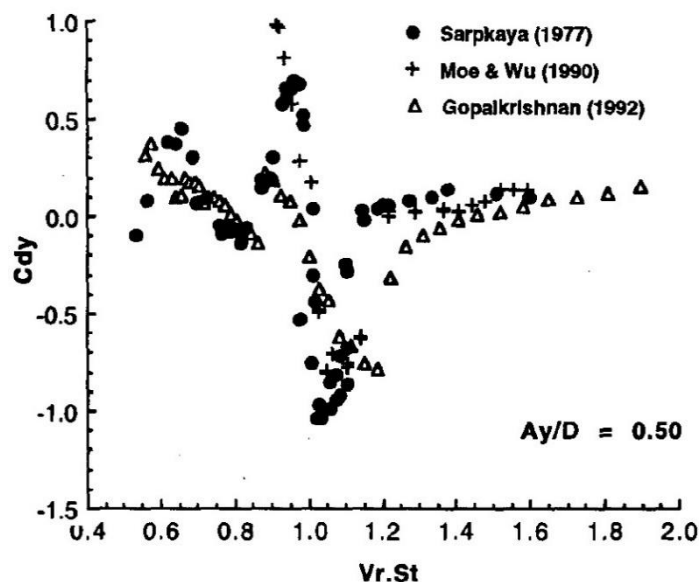


Figure A-20: Fluid damping of a vibrating cylinder at an amplitude ratio of 0.50 (Sarpkaya, 1995)

Chaplin and Subbiah (1998) presented laboratory measurements of the hydrodynamic damping of smooth and roughened circular cylinders in still water and transverse current. It was concluded that for low  $KC$  numbers, Morison's equation leads to severe overestimation of the damping. Further, below a certain velocity, a transverse current is found to have a negligible effect on the damping, but over stronger currents the damping almost doubled from the still water value. It was also found that surface roughness generated an increase in damping of about 35% in still water, but only 5% in a current. Sarpkaya (1986) presented the inline force coefficients for circular cylinders in planar oscillatory flows of small amplitude. Four broad regimes were identified as far as damping is concerned; Stokes-Wang regime where the laminar flow is attached and stable, transition regime where the laminar flow becomes unstable to axially periodic vortices, single vortex pair regime ( $8 < KC < 13$ ) where  $C_D$  increases and the effects of vortex shedding become increasingly important, and Von Karman regime ( $KC > 13$ ) where  $C_D$  decreases as the number of shed vortices increase.

Vandiver (2012) proposed an alternative damping parameter ( $C^*$ ) to overcome the limitation of mass damping parameter. It was argued that the alternative parameter could be used to characterise VIV at all reduced velocities in the lock-in or synchronisation range and multiplied with the amplitude ratio to calculate the lift coefficient. Pastò (2008) found that in laminar and low turbulence flows the synchronisation range narrows when damping is increased. The range of synchronisation was found to be larger for the smooth cylinder than the rough cylinders immersed in the flow with high turbulence.

### A.2.9 *Mass Ratio*

Jauvtis and Williamson (2003) mention that the typical mass ratios in the air are in the order of 100 while in the water it can be in order 1 or 10. Sumer and Fredsøe (2006) explain the effect of the mass ratio ( $M = m^*$ ) in the amplitude response  $\left(\frac{A}{D} = \frac{y_0}{D}\right)$  with the help of Figure A-21. It can be seen that the cylinder with the larger mass ratio responds over a much narrower range, in spite of having a lower damping ( $\zeta_s$ ) and stability parameter ( $K_s$ ).

Khalak and Williamson (1997b; 1999) demonstrated that for low mass ratios, the frequency of oscillation deviates and becomes higher than the natural frequency at higher reduced velocities. It can be observed with respect to Figure A-22 that at a mass

ratio ( $m^*$ ) of 2.4, throughout the upper branch the nondimensional frequency ( $f^* = \frac{f}{f_n}$ ) deviates from 1 and reaches a final value near 1.5 in the lower branch. The overall range of excitation as well as the shape of the response curve was found to be determined by the mass ratio while the amplitude response was controlled by the mass damping parameter.

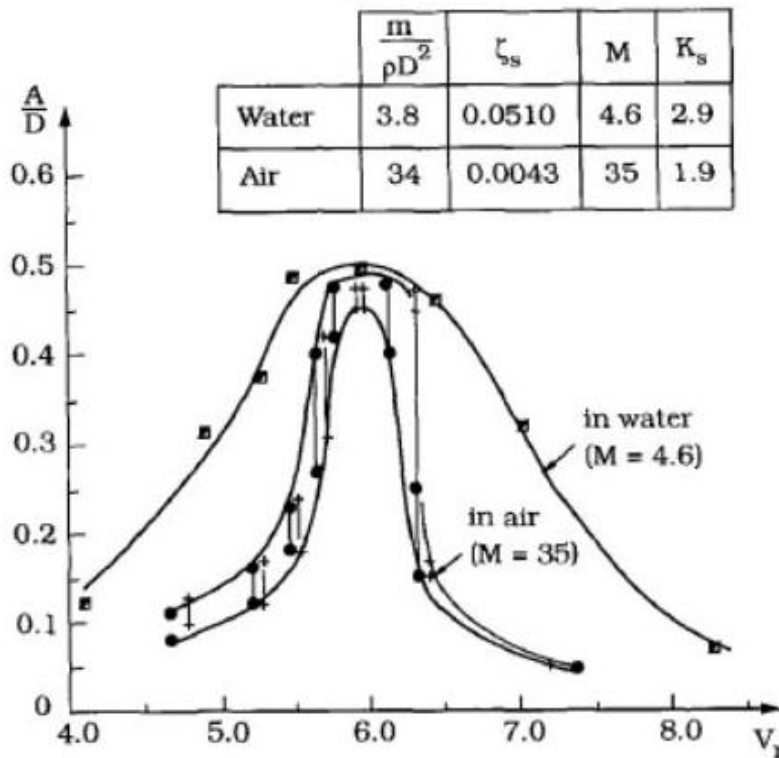


Figure A-21: Effect of mass ratio ( $m^*$ ) on crossflow amplitude response (Sumer and Fredsøe, 2006)

Govardhan and Williamson (2004) confirmed that the vibration frequency during lock-in is primarily dependent on mass ratio and can reach remarkably large values when the mass ratio is in the order of unity. The authors discovered a critical mass ratio below which the structure will vibrate until infinite flow speed in the upper branch. Blevins and Coughran (2009) conducted tests on VIV of an elastically supported cylinder in water and observed that the lock-in range increased with decrease in mass ratio and the vibration frequency increased even up to 50% above cylinder's natural frequency. Bearman (2009) regards in addition to damping, mass ratio also as an important parameter for structures in water as it is two to three orders of magnitude smaller than that typically found in the air.

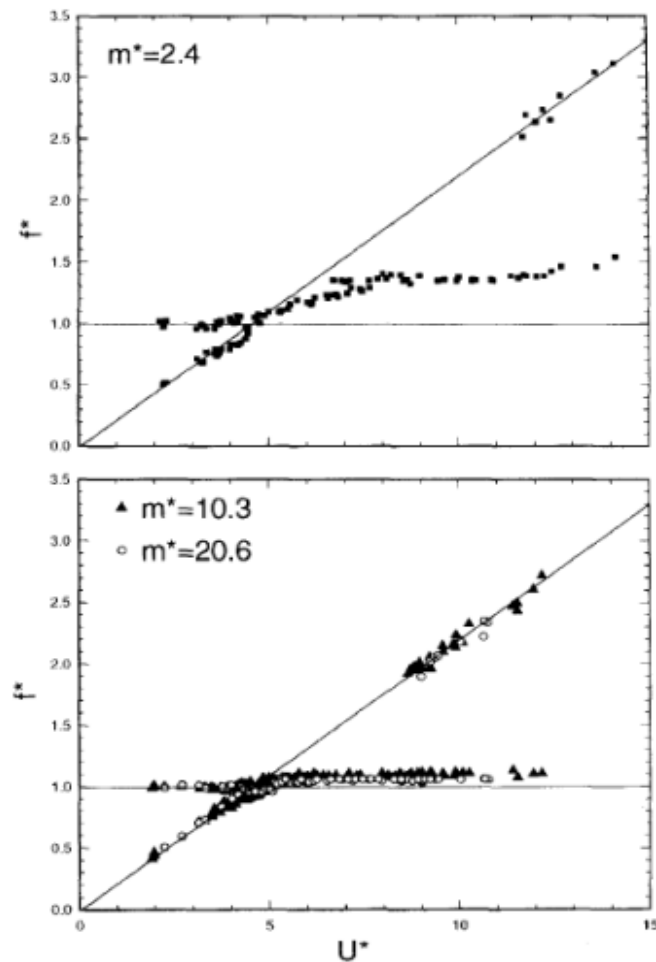


Figure A-22: Effect of mass ratio ( $m^*$ ) on crossflow frequency response (Khalak and Williamson, 1997b)

#### A.2.10 *Added Mass*

Moe and Wu (1990) argued that the added mass of the water varies strongly within the lock-in range, and therefore the actual natural frequency of a spring supported cylinder may increase from the beginning to the end of the lock-in range. Sarpkaya (1995) observed that the natural frequency of the structure does not remain constant over the excitation range because of the change of added mass with the amplitude ratio. Vikestad *et al.* (2000b) conducted experiments with lightly damped elastically mounted rigid cylinder under steady flow conditions in subcritical  $Re$ . It was found that the natural frequency predicted based on the measured added mass was same as the vibration frequency. It was concluded that the response frequency variation in the lock-in range is an added mass dependent variation in the natural frequency of the cylinder.

## A.2.10.1 Negative added mass

Sarpkaya (1995) demonstrates in Figure A-23, added mass coefficient ( $C_{my} = C_A$ ) as a function of  $Vr.St$ , and for an amplitude ratio ( $\frac{A_y}{D} = \frac{y_0}{D}$ ) of 0.50, from 3 investigations. It can be observed that the added mass is negative for the  $Vr.St$  values around and above 1, corresponding to the lock-in range. It can be inferred from the negative values of added mass that the potential flow around a vibrating cylinder is significantly affected by the synchronised vortex shedding process.

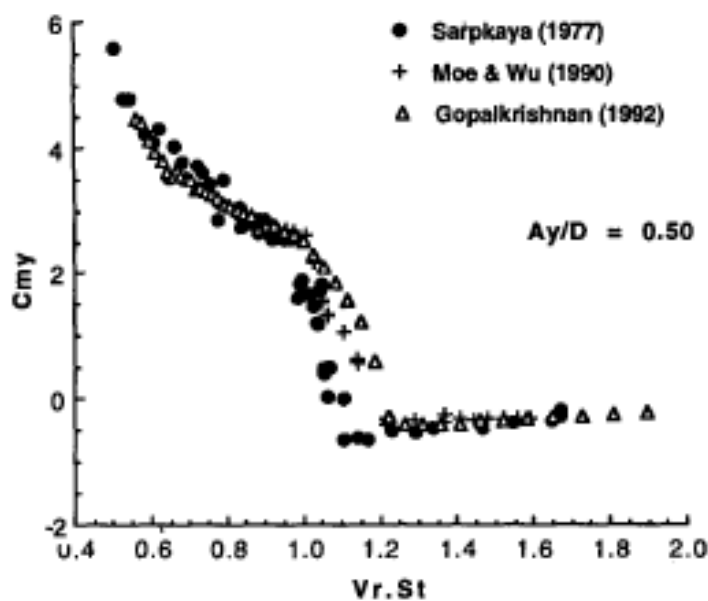


Figure A-23: Added mass of a vibrating cylinder at an amplitude ratio of 0.50 (Sarpkaya, 1995)

Vikestad *et al.* (1997) conducted experiments with riser models and found that the added mass coefficient is approximately 1.0 for vibrations with small amplitudes in still water. However, it was found that the added mass varied considerably and became negative for high reduced velocities and the ratio between the oscillation frequency and the true natural frequency (considering the added mass variation) was approximately unity. It was revealed that the added mass adapts to a value giving oscillations at the resonant frequency. Govardhan and Williamson (2004) also discovered that the added mass of cylinders during large amplitude crossflow vibration is negative.

## A.2.10.2 Critical mass ratio

Govardhan and Williamson (2004) found that when the mass ratio is less than a critical mass ratio, lower branch ceases to exist and the upper branch will continue indefinitely until infinite flow speeds with vigorous oscillations. It was observed that large-amplitude oscillations suddenly appeared for a wide range of flow speeds when the mass ratio is less than a critical mass ratio of 0.542 at a  $Re$  of 22000. Morse and Williamson (2009) found that the critical mass ratio gradually increases with  $Re$  from a value of 0.36 to 0.54 over the  $Re$  range of 4000 to 30000 respectively. In addition to the jump in response amplitude, a sudden change in the oscillation frequency was also observed when the mass ratio is decreased below the critical value. It was demonstrated that for a system of low mass damping, the end of synchronisation ( $V_{r,end}$ ) can be expressed as in Equation A-1. The synchronisation regime is illustrated in Figure A-24 as a function of mass ratio ( $m^*$ ) and reduced velocity ( $U^* = V_r$ ).

$$V_{r,end} = 9.5 \sqrt{\frac{m^* + C_A}{m^* - m^*_{crit}}} \quad \text{Equation A-1}$$

where  $m^*$ ,  $m^*_{crit}$  and  $C_A$  represent the mass ratio, critical mass ratio and potential added mass coefficient respectively.

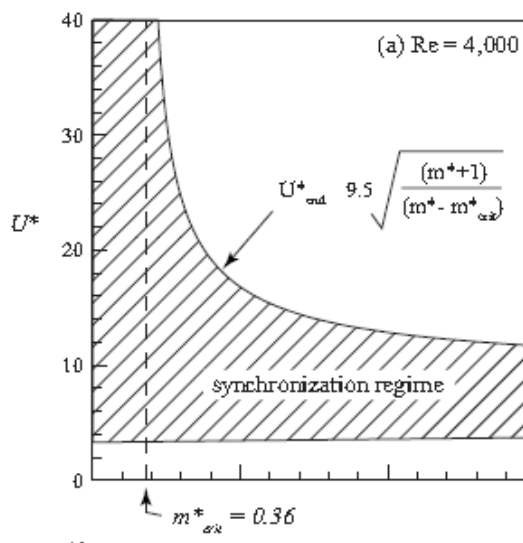


Figure A-24: Effect of mass ratio ( $m^*$ ) on synchronisation regime (Morse and Williamson, 2009)

Ryan *et al.* (2005) investigated the critical mass ratio of a circular cylinder by means of numerical simulations and found that there are for two regions of critical mass ratio, a low viscous region ( $Re < 100$ ) and a higher region ( $Re > 180$ ) with no critical mass ratio between these two regions.

### A.2.11 *Mass Damping Parameter*

Sarpkaya (1995) highlighted the inadvisability of combining mass and damping into one parameter and argued that the dynamic response is governed by mass ratio and damping independently. Khalak and Williamson (1997b) concluded that the overall range of excitation, as well as shape of response are defined by the mass ratio ( $m^*$ ) while the response in the upper branch is decided by the combined mass-damping parameter ( $m^*\zeta$ ). The upper and lower branch maxima ( $A = \frac{y_0}{D}$ ) were plotted as a function of  $m^*\zeta$ , as in Figure A-25 and it was demonstrated that the upper branch maximum has a continuous dependence upon  $m^*\zeta$ . Jauvtis and Williamson (2003) also compared the Griffin Plots (vibration amplitude v/s mass damping parameter) obtained for both the upper and lower response branches with that of Khalak and Williamson (1997b) and found good agreement.

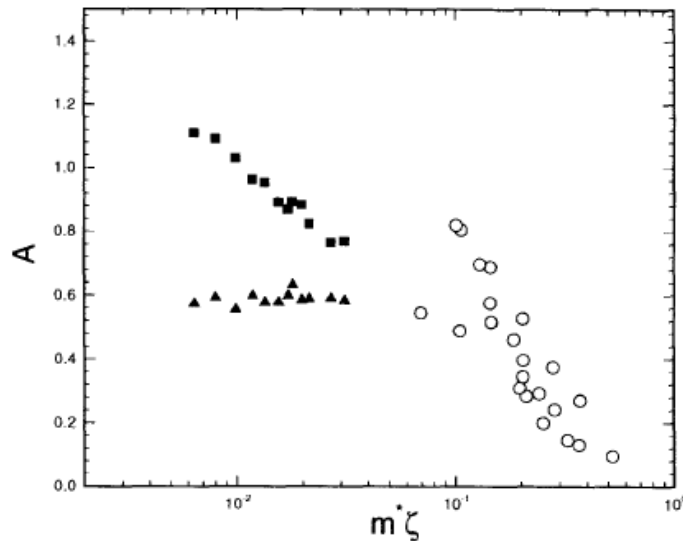


Figure A-25: Effect of mass damping parameter ( $m^*\zeta$ ) on crossflow amplitude ratio (Morse and Williamson, 2009)

Khalak and Williamson (1999) proposed a combined mass damping parameter ( $m^*+C_A$ ) $\zeta$ , considering the effect of added mass and demonstrated that the peak

amplitude data collapsed well in the Griffin plot if the combined parameter is used. Amplitude ratio in the order of 1.2D was observed without saturation indicating a higher self-limiting amplitude.

Blevins and Coughran (2009) evaluated the VIV of an elastically supported circular cylinder in water for a wide range of reduced velocity, damping and mass ratios at  $Re$  up to 150,000. It was revealed that high amplitudes are self-limiting while a linear forced vibration model is appropriate at low amplitudes. Further, the maximum amplitudes were found to be nearly identical and at the same reduced velocity for a particular mass damping parameter. Sumer and Fredsøe (2006) concluded based on published experimental data that the cylinder remains virtually stationary along the crossflow direction for stability parameter ( $K_s = \pi^2 m^* \zeta$ ) larger than around 18, demonstrated in Figure A-26.

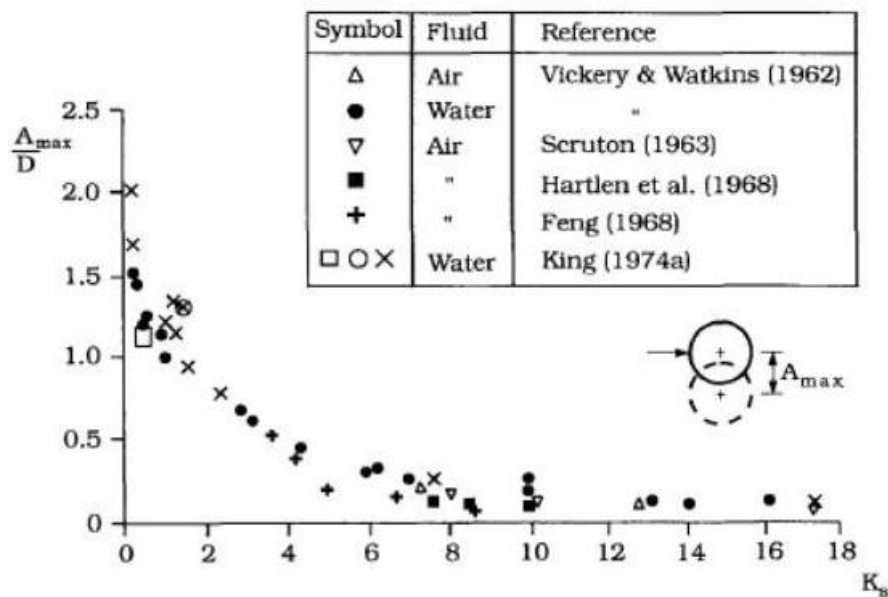


Figure A-26: Crossflow amplitude ratio as a function of stability parameter (Sumer and Fredsøe, 2006)

Xu *et al.* (2012) presented inline amplitude ratios as a function of mass damping parameter based on experimental results in Figure A-27. It was demonstrated that the inline VIV ( $x_{max}$ ) response is equally dependent on the stability parameter ( $C_n = \frac{1}{2} \pi^2 m^* \zeta$ )

### A.2.12 VIV frequency

Moe and Wu (1990) found large variations in the frequency response in the “lock-in” range during free vibration tests. It was found that the self-excited frequency of a spring-supported cylinder varies significantly, especially when the cylinder is free to execute figure-eight motions, and the factor deciding the frequency response is the mass ratio. Khalak and Williamson (1997b) investigated the frequency response for various mass ratios and found that for low mass ratios, the nondimensional frequency deviated slowly from 1 throughout the upper branch and reached its final value in the lower branch. Further, the lower branch frequency did not correspond to either the natural frequency or the Strouhal frequency, as demonstrated in Figure A-14.

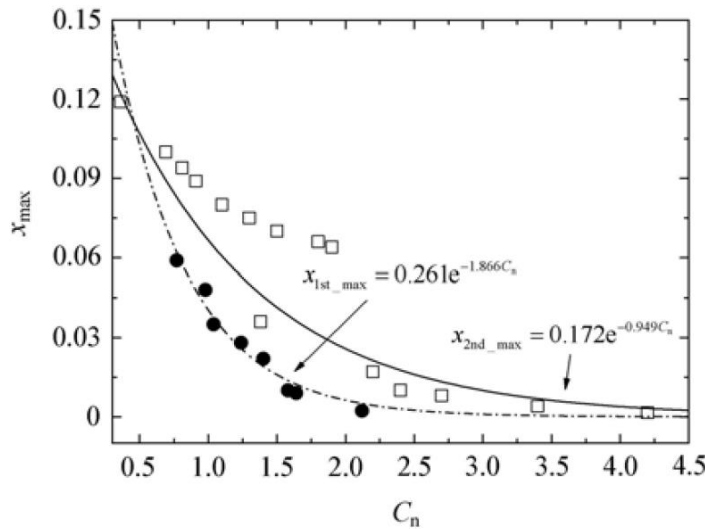


Figure A-27: Inline amplitude response versus mass-damping parameter (Xu *et al.*, 2012)

Govardhan and Williamson (2004) studied the transverse VIV of an elastically-mounted cylinder at low mass-damping values and found that the oscillation frequency is primarily dependent on the mass ratio ( $m^*$ ). The authors expressed the cylinders frequency response ( $f^*$ ) as,

$$f^* = \frac{f}{f_N} = \sqrt{\frac{m^* + C_A}{m^* + C_{EA}}}$$

Equation A-2

where  $f$  and  $f_N$  are the vibration frequency and the natural frequency in still water respectively,  $C_{EA}$  is the effective added mass coefficient due to wake vortex dynamics, and  $C_A$  is the potential added mass coefficient. It was observed that the frequency response is sinusoidal, periodic and constant in the lower branch and hence concluded that the effective added mass is constant throughout the lower branch. It was found that  $C_{EA} = -0.54$  for the  $Re$  tested and hence the lower-branch frequency response ( $f_{lower}^*$ ) becomes,

$$f_{lower}^* = \frac{f_{lower}}{f_N} = \sqrt{\frac{m^* + 1}{m^* - 0.54}} \quad \text{Equation A-3}$$

where  $f_{lower}$  is the vibration frequency in the lower branch.

The denominator of Equation A-3 demonstrates that the critical mass ratio is 0.54 for the  $Re$  tested by Govardhan and Williamson (2004). Sumer and Fredsøe (2006) observe that the natural frequency of a cylinder is not maintained at the still water value in the lock-in range, but undergoes a linear increase with increasing  $V_r$ . It can be seen from Figure A-28 that the normalised natural frequency ( $f^* = \frac{f}{f_n}$ ) remains almost same for the very high mass ratio of 200 (in air) but increases almost linearly with reduced velocity ( $V_r$ ) for small mass ratios, 2.5 and 5 (in water);  $A/D$  in the figure represents amplitude ratio.

### A.2.13 **Force amplification**

Bishop and Hassan (1964) measured the fluctuating drag and lift, and the steady drag on a transversely oscillating cylinder in a steady flow. It was found that the forces were magnified with the increase in the amplitude ratio, with the fluctuating drag and lift exhibiting around a fivefold increase at an amplitude ratio of 0.75. It was concluded that the phenomenon could be represented by the existence of a nonlinear self-excited wake oscillator. Toebe (1969) measured the base pressure near to the aft stagnation point of a vibrating cylinder and demonstrated a 20 percent decrease for a response amplitude of 0.1D, revealing drag amplification.

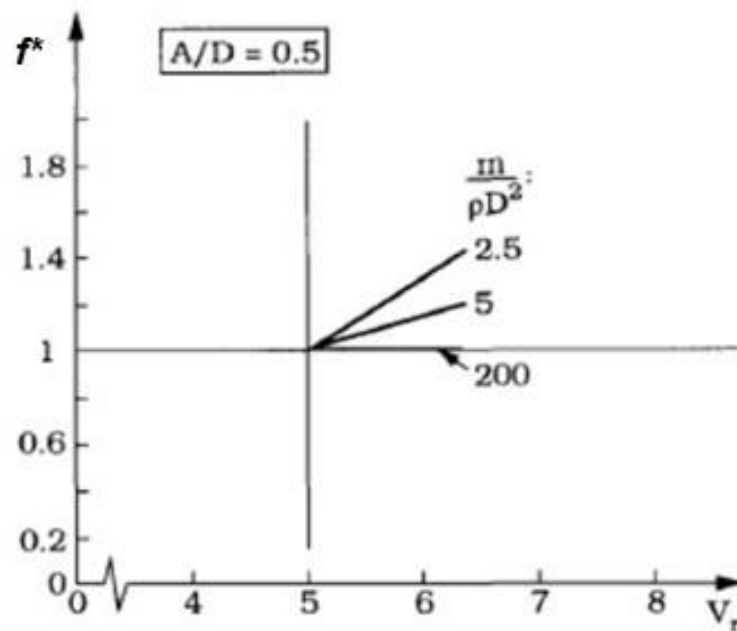


Figure A-28: Natural frequency ratio versus reduced velocity for various mass ratios (Sumer and Fredsøe, 2006)

Zdravkovich (1982) identifies the main feature of synchronised vortex shedding as the magnification of the fluctuating forces on the oscillating cylinder. The magnification is attributed to three causes, the shortening of the length of the vortex formation region, the increase in vortex correlation and the increased period of vortex shedding. Khalak and Williamson (1997a) observed a very sharp peak in the lift coefficient, at the transition between the initial excitation region and the upper branch. It was concluded based on test results that the induced forces increase with the increase in response. It was observed that the lift and total drag increased more than five-fold and oscillatory drag up to 100 times for a vibration amplitude of around  $1D$ . It was found that both the drag and lift increase rapidly through the initial excitation regime, peak at the beginning of the upper-branch region, decrease rapidly throughout the upper branch, and then gradually diminish to values even smaller than the corresponding stationary case in the lower-branch region. Sumer and Fredsøe (2006) explain that both the drag and the lift increase considerably in the synchronisation range due to the increase in the spanwise correlation and vortex synchronisation.

#### A.2.13.1 Lift Amplitude Interaction

Diana and Falco (1971) found that the lift force initially increases with increasing vibration amplitudes, then decreases with the vibration amplitudes for amplitude ratios

above 0.4 – 0.5 and disappears around an amplitude ratio of 1. It was proposed that the decline and eventual disappearance of the lift above an amplitude ratio of 0.5 can be attributed to the increase in fluid damping with amplitude ratios. Griffin and Koopmann (1977) measured the fluid damping and the lift force out of phase and in phase respectively with the velocity of the cylinders undergoing VIV for a  $Re$  range from 300 to 1000. It was observed that the lift is dependent on the vibration amplitudes, increasing till an amplitude ratio of around  $0.3D$ , reducing with further increase and vanishing at a self-limiting amplitude ratio of  $0.75D$ . The authors confirmed the nonlinear wake-oscillator effects proposed by early investigators.

Griffin (1980) summarises based on measurements and other published results on elastically mounted rigid cylinders that the lift force peaks at amplitudes between  $0.3D$  –  $0.5D$  and then decreases to zero at amplitudes between  $1D$  –  $1.5D$ , resulting in a limiting amplitude for VIV. Moe and Wu (1990) conducted forced vibration tests and showed that the transverse force in the lock-in range would add energy to the cylinder at moderate motion amplitudes and subtract energy at large amplitudes, revealing lift variation with the amplitude. The authors observed that vibrations are unstable at small amplitudes, stable at moderate amplitudes, and nonexistent at very large amplitudes.

Sarpkaya (1995) noted that for amplitude ratios ( $\frac{y_o}{D}$ ) larger than about 0.5, the forcing decreases due to changes in vortex shedding, the amplitude reaches a self-limiting value and the phase, sequence, and pattern of vortices in the wake are altered. Blevins and Coughran (2009) measured the amplitude response at various damping values and found that the high amplitudes are self-limiting while suggesting a linear forced vibration model for low amplitudes. Barltrop and Adams (1991) describe that owing to the interaction between the motion of the structure and the mechanism of vortex shedding, the coefficient of fluctuating lift,  $C_L$  increases with amplitude first and then falls again as shown in Figure A-29.

Bearman and Currie (1979) performed pressure fluctuation measurements on an oscillating circular cylinder in a steady flow. The pressure was recorded at a point  $90^\circ$  from the forward stagnation point, and the amplitudes were up to  $1.33D$ . It was found that the maximum lift occurs within the lock-in regime at an amplitude of about  $0.5D$  and the self-limiting oscillation amplitude was predicted to be around  $2D$ .

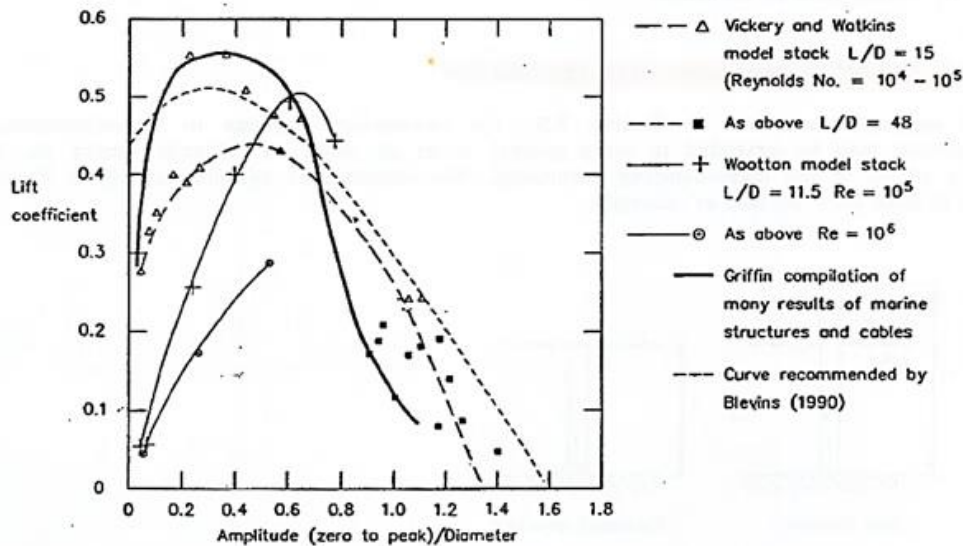


Figure A-29: Variation of lift coefficient with crossflow amplitude ratio (Bartrop and Adams, 1991)

#### A.2.13.2 Drag Amplification

Diana and Falco (1971) observed that the mean drag increased monotonically with the vibration amplitudes. Sarpkaya (1995) presented the mean inline drag coefficient of the oscillating cylinder ( $C_d$ ), normalised with the mean drag coefficient of the non-oscillating cylinder ( $C_{d0}$ ) at the same  $Re$ , in Figure A-30. It can be observed that the drag coefficient of a vibrating cylinder increases around three folds of the fixed cylinder.

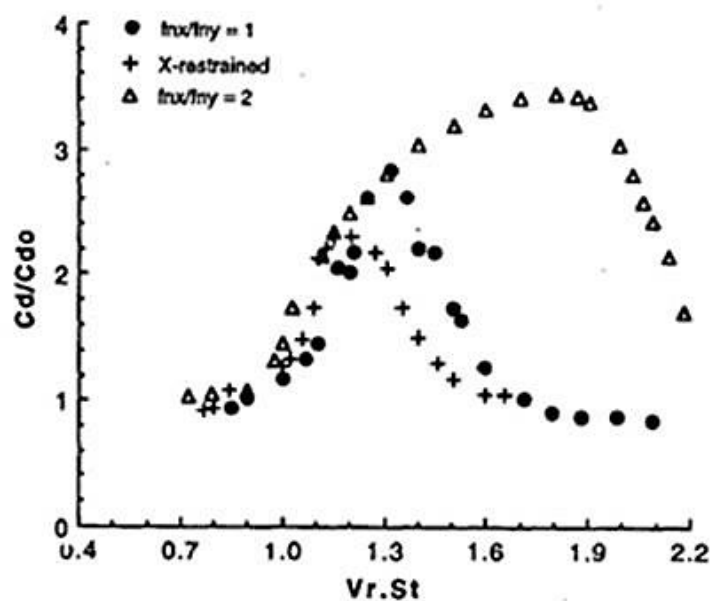


Figure A-30: Drag amplification due to VIV in steady flow (Sarpkaya, 1995)

Sumer and Fredsøe (2006) presented Equation A-4 originally proposed by Sarpkaya for the drag coefficient of a vibrating cylinder ( $C_{DA}$ ) based on the assumption that the transversely vibrating cylinder presented a larger projected area to the mean flow as,

$$C_{DA} = C_D \left( 1 + \frac{2 y_o}{D} \right) \quad \text{Equation A-4}$$

where  $C_D$  is the drag coefficient of a stationary cylinder and  $\frac{y_o}{D}$  represents the crossflow amplitude ratio.

Allen and Henning (2001) observed that the drag coefficient of the vibrating cylinders is strongly coupled to the vibration amplitudes. Blevins and Coughran (2009) showed that the drag on an excited cylinder with 1D amplitude is three times that of the stationary cylinder, in agreement with Sarpkaya's findings. Blevins (2001) also presented a linear model for the increase of mean drag with transverse vibration amplitude during crossflow lock-in, as illustrated in Figure 1-8.

#### A.2.14 Reynolds Number Dependence

Wootton (1969) investigated the effect of  $Re$  on the crossflow vibrations and Figure A-31 based on his work illustrates the crossflow amplitude ratio as a function of  $Re$  (Sumer and Fredsøe, 2006). It is found that the amplitude follows the trend of the lift force variation with  $Re$  and experiences a crisis in the critical and supercritical regimes.

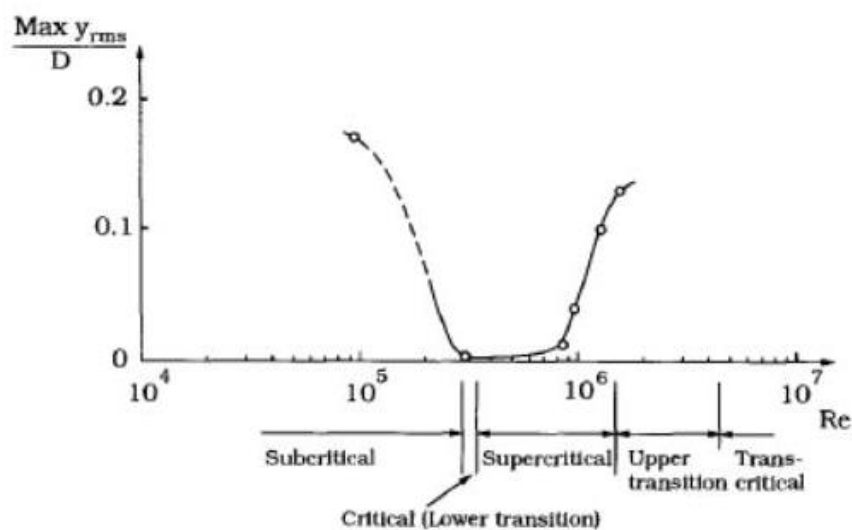


Figure A-31: Crossflow amplitude response versus  $Re$  (Sumer and Fredsøe, 2006)

Sarpkaya (1995) questioned the assumption that the lock-in region is not  $Re$  dependent, and argued that the response would exhibit significantly different behaviour in the critical regime due to the dramatic changes in vortex shedding and the resulting forces. Klamo *et al.* (2005) conducted experiments and demonstrated that the maximum amplitude depends not only on the damping but also on the  $Re$ . It was also concluded that there is no dependence of the vibration amplitude only on the mass-ratio ( $m^*$ ).

Pastò (2008) found that along with the mass-damping parameter ( $m^*\zeta$ ),  $Re$  also influences the response amplitudes. It was observed that even in the critical regime, synchronization occurs as the cylinder oscillations take control of the vortex shedding. Further, in the critical  $Re$  regime in high turbulence flow, the vortex shedding is found to disappear outside the lock-in regime. Pastò (2008) observed a reduction in  $C_L$  of a vibrating cylinder in the critical regime and concluded that the response amplitude depends on both  $m^*\zeta$  and  $Re$ . Bearman (2011) plotted the maximum amplitude against  $Re$ , based on published data and demonstrated that the amplitude is a function of  $Re$ . Further, the author anticipated an amplitude crisis as the critical regime is entered.

### A.3 VIV in Oscillatory Flow

#### A.3.1 Lift force

Sumer and Fredsøe (2006) present Figure A-32 based on Justesen's work, illustrating the evolution of the lift force ( $F_y$ ) with the  $KC$  number. It can be seen that the lift force is initiated when  $KC$  becomes 4 due to the asymmetry of the wake vortices and the lift due to vortex shedding start after  $KC$  is 8.

Figure A-33 from Williamson (1985), reproduced by Sumer and Fredsøe (2006) demonstrates that the lift coefficient attains maximum values at  $KC = 11, 18$  and  $26$ , the centres of the respective vortex pair regimes where the correlation is measured to be the highest, and the minimum values at the boundaries between the  $KC$  regimes. Barltrop and Adams (1991) also confirm that the strength of the lift force is strongest in the middle of the  $KC$  ranges than the boundaries, where a definite integer number of vortices are shed per half-wave cycle.

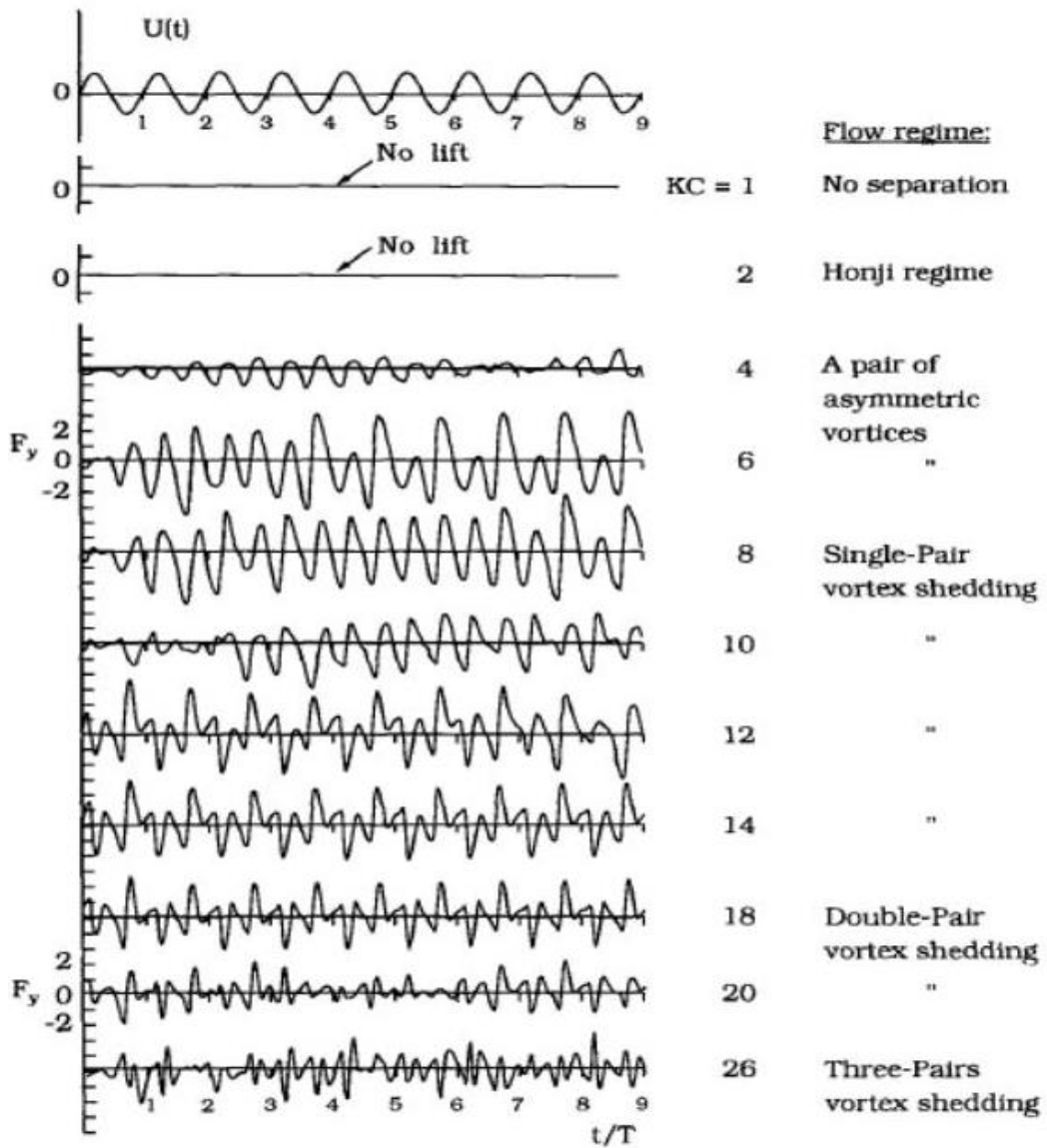


Figure A-32: Lift forces in oscillatory flow with  $KC$  (Sumer and Fredsøe, 2006)

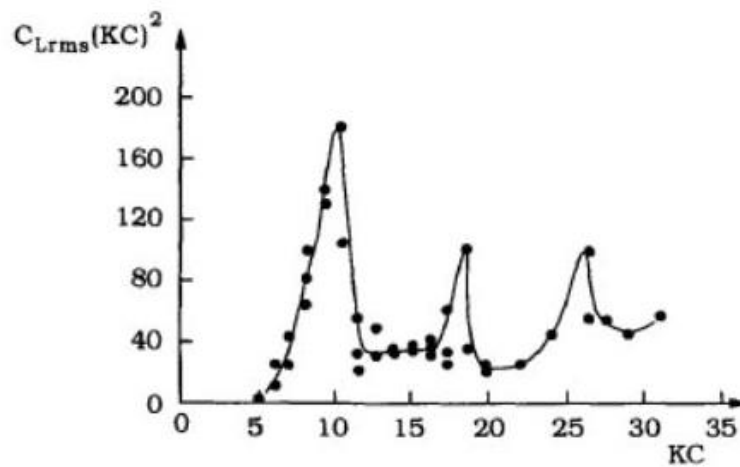


Figure A-33: Lift coefficient versus  $KC$  number (Sumer and Fredsøe, 2006)

The time history of the oscillating lift force ( $F_L$ ) in an oscillatory flow corresponding to a  $KC$  of 16 is illustrated in Figure A-34. It can be inferred that the lift force frequency is not identical to the vortex shedding frequency and is dependent on both vortex shedding and flow reversal. For every  $KC$  regime, the lift frequency is found to be a multiple of flow frequency and the multiplier increases by one from that of the preceding lower regime starting with 2 for  $7 < KC < 15$  (Sumer and Fredsøe, 2006).

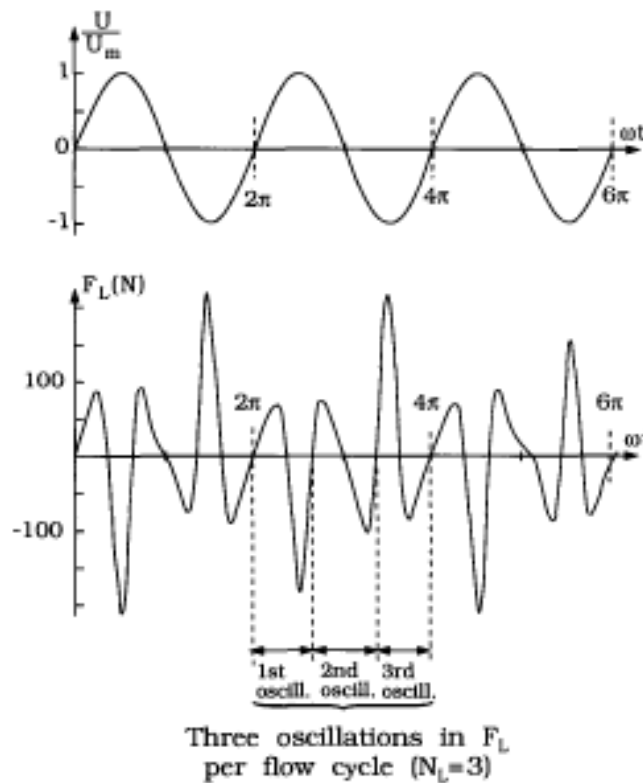


Figure A-34: Oscillatory lift histogram in oscillatory flow (Sumer and Fredsøe, 2006)

It can be inferred from Figure A-34 that the peak in the lift force immediately after the flow reversal is related to the return of the most recently shed vortex to the cylinder, while the rest of the peaks are associated with the vortex shedding. It can be noticed that the multiplier is greater than the number of vortices shed in a flow half cycle by integer 1. Figure A-35 represents the variation of the maximum lift coefficient for a smooth cylinder in an oscillatory flow along with the corresponding values in a steady flow. It can be observed that the lift force in an oscillatory flow is a function of both  $Re$  and  $KC$  and the lift coefficient at low  $Re$  can be considerably higher than in steady flow.

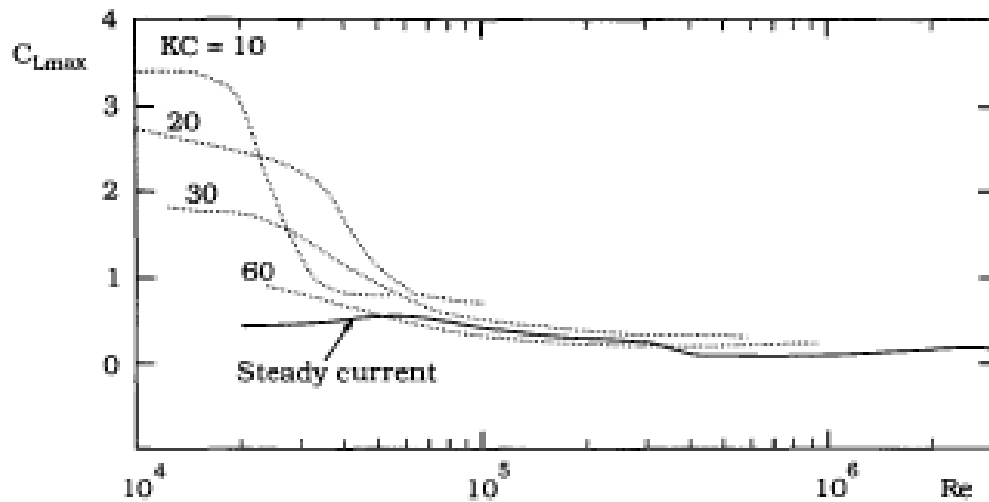


Figure A-35: Lift force coefficient of a smooth cylinder in oscillatory flow (Sumer and Fredsøe, 2006)

Sumer and Fredsøe (2006) noticed a substantial increase in the lift force of a vibrating cylinder in an oscillatory flow based on the numerical simulation carried out by Kozakiewicz and attributed the behaviour to the increase in the strength of the vortices due to better correlation and synchronisation. McConnell and Park (1982) studied the frequency components of lift forces in an oscillatory flow by oscillating a cylinder sinusoidally in still water. Velocity ratio (the product of amplitude ratio ( $A/D$ ) and the natural frequency-wave frequency ratio ( $f_n/f_w$ )) was proposed as the significant non-dimensional parameter defining the cylinder VIV, and it was demonstrated that the excitation, natural frequency and the added mass were dependent on the velocity ratio.

Sarpkaya (1975) evaluated the inline and transverse forces acting on a circular cylinder in a harmonically oscillating fluid in a U shaped vertical tunnel and found that transverse forces can be as large as the inline forces. It was observed that the lift coefficient reaches a value as high as 3 at  $KC$  less than 10, the transverse forces alternate at frequencies that are one to four times the flow frequency and several frequencies are present in a lift cycle. Sarpkaya (1987) conducted experiments with smooth and sand roughened cylinders in oscillatory flow for a range of  $KC$  numbers and Reynolds numbers ( $Re$ ) and investigated the first ten harmonics of the lift force acting on the cylinder. It was found that all the ten harmonics are present in the lift force, and second and fourth harmonics are predominant in the drag-inertia dominated regimes.

Mauil and Milliner (1978) studied the unidirectional sinusoidal flow past a circular cylinder in a U tube for  $KC$  numbers up to 30 and observed lift coefficients of considerable magnitudes between  $KC$  numbers of 10 and 15 due to stable lift generation with minimal intermittency. It was found that the lift force components at double, triple and quadruple of the flow frequency are maximum at  $KC$  numbers of 13, 18 and 25 respectively. Strong lift frequency components at four and five times the flow frequency were also observed at  $KC$  13 and 25 respectively.

### A.3.2 Crossflow VIV

Sumer and Fredsoë (1988) carried out experimental studies with an elastically mounted circular cylinder exposed to oscillatory flows and concluded that the number of vortices shed per flow cycle for a vibrating cylinder is dependent not only on  $KC$  number but also on reduced velocity. It was noted that lock-in occurred more than once, leading to the typical multi-peak amplitude response. The frequency and amplitude response of the cylinder at a  $KC$  of 20 is illustrated in Figure A-36. It can be inferred from the figure that at a given  $KC$ , the vibration frequency to wave frequency ratio ( $f/f_w$ ) drops to the lower integer value at the lock-in points, for any further increase in  $V_r$  since  $f_w$  increases to maintain the  $KC$ . Once the value  $f/f_w = 2$  is reached, this value is maintained for further increase in  $V_r$ , as this is the absolute minimum number of vibrations in one cycle of the flow oscillation. It was observed that the cylinder vibration frequency follows the stationary cylinder vortex shedding frequency from  $V_r = 0$  to the first lock-in point. In the figure,  $\frac{A}{D}$ ,  $f$ ,  $f_w$ ,  $f_n$  and  $V_r$  represent amplitude ratio ( $\frac{y_0}{D}$ ), vibration frequency, wave frequency, natural frequency and reduced velocity respectively.

The effects of mass ratio and mass damping (stability) parameter are found to be similar to the case of steady flow (Sumer and Fredsoë, 1988). It was observed that higher the mass ratio, the narrower the response range and smaller the mass damping parameter, larger the response amplitude. Sumer and Fredsoë (1988) further demonstrated that cylinder vibrations with amplitudes as large as  $0.7D$  are possible at  $KC$  less than 8, attributable to the lift force due to the asymmetry in the strength of the two attached vortices, formed behind the cylinder for every half cycle of the flow. This asymmetry occurs once the  $KC$  number exceeds 4, giving rise to a lift force at the frequency of the flow (Williamson, 1985).

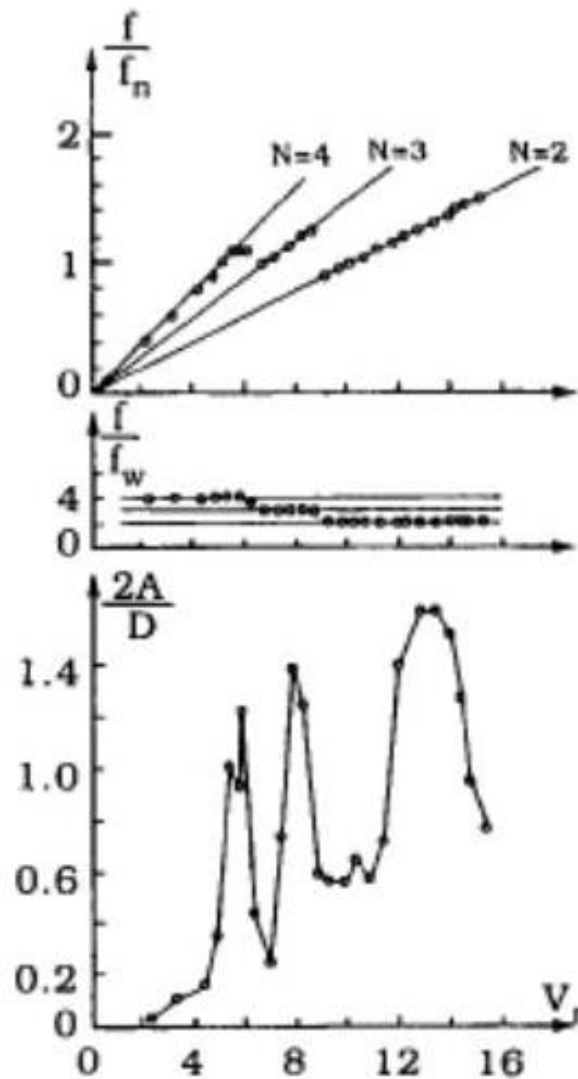


Figure A-36: Crossflow amplitude and frequency response with reduced velocity in planar oscillatory flow (Sumer and Fredsøe, 1988)

Fu *et al.*, (2013) studied the response of steel catenary risers under vessel oscillatory motions using model tests and confirmed the occurrence of intermittent VIV in high  $KC$  flows. The authors separated the half oscillatory period into three parts in terms of the VIV developing process; building-up, lock-in, and dying out regions. Higher harmonics, approximately three times of the maximum shedding frequency, was observed in the VIV. Hayashi *et al.* (2003) conducted laboratory investigation to study the dynamic transverse response of a cylinder in planar oscillatory flow and observed twin peaks in the transverse VIV amplitude response similar to that observed for a vertical circular cylinder in waves.

Sumer and Fredsøe (1989) investigated the effect of  $Re$  on the VIV in oscillatory flow and found that the lock-in points are reached earlier in terms of  $Vr$  when the  $Re$  number is larger than approximately  $2 \times 10^5$ , the critical transition point. It is inferred that as the lift force decreases considerably, the hydroelastic excitation takes over rapidly and the lock-in point is reached earlier. It was observed that the number of vibrations per flow cycle ( $N$ ) jumps from 4 and 10 direct to 2 for  $KC = 40$  and 100 respectively at the critical  $Re$ .

Sumer and Fredsøe (1989) further observe that the frequency response of the rough cylinder is same as the frequency response of the smooth cylinder in subcritical flow regime and the phenomenon where the number of vibrations per flow cycle abruptly drops to 2 disappears in the case of the rough cylinder. It was concluded that the  $Re$  effect on the vibration of cylinders disappears for roughness greater than  $0.003D$ , which the marine growth on flexible offshore structures normally satisfies.

### A.3.3 **Spanwise Correlation.**

Sumer *et al.* (1994) did spanwise correlation measurement for an elastically mounted cylinder exposed to oscillatory flow undergoing crossflow VIV at a  $KC$  of 10. It was observed that during the lock-in, the correlation continuously increased until the maximum amplitude ratio ( $\frac{A}{D} = \frac{y_0}{D}$ ) of 0.60, as illustrated in Figure A-37. Sumer and Fredsøe (2006) show that the correlation coefficient takes very large values when  $KC$  is small, and it takes the lowest value when  $KC$  is at about 22. It is argued that the correlation is high at  $KC = 10$  because it lies in the centre of the  $KC$  regime,  $7 < KC < 15$ . The variation of the correlation coefficient with  $KC$  numbers is illustrated in Figure A-38, based on the work of Obasaju *et al.* (1988).

Sumer and Fredsøe (2006) further presented the correlation coefficient ( $R$ ) as functions of the double amplitude ratio for various  $KC$  numbers, based on the forced oscillation experiment results from Kozakiewicz *et al.* (1992). It was observed that the correlation coefficient increased with the double amplitude ratio up to about 0.2 - 0.3 and reduced with further increase in amplitudes attributable to the change in the flow regime.

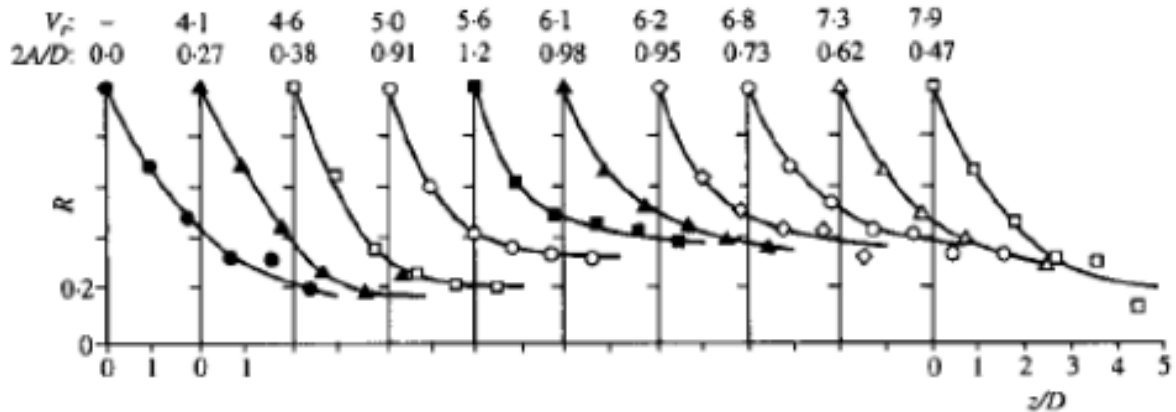


Figure A-37: Correlation coefficient for a cylinder undergoing self-induced vibrations in oscillatory flow (Sumer *et al.*, 1994)

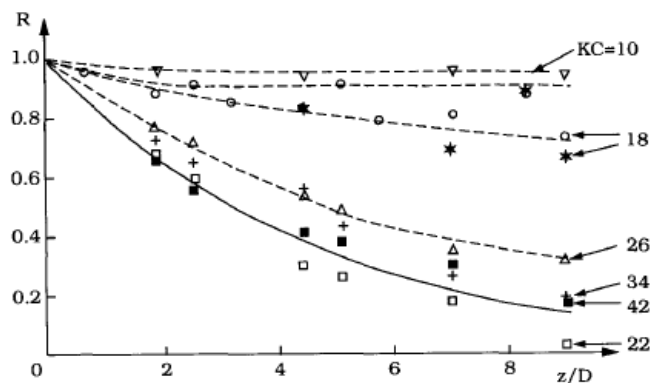


Figure A-38: Correlation coefficient of the lift forces on a cylinder in oscillatory flow (Sumer and Fredsøe, 2006)

#### A.4 VIV in Regular Waves

Chaplin (1988) conducted experimental studies on smooth and rough cylinders at high  $Re$  in planar oscillatory flow. The  $Re$  were in the range of 20000 to 280,000, the  $KC$  from 6 to 20 and it was observed that the lift coefficients are in close agreement with that of vertical cylinders in waves. Wolfram (1991) demonstrated using experiments in shallow waters that the wave closely approximates the planar oscillatory flow and lift forces has a high degree of spanwise coherence. Barltrop and Adams (1991) proposed the curve illustrated in Figure A-39 for the lift coefficient of a vertical cylinder in waves at post-critical  $Re$ , as a function of  $KC$  number based on the results of large scale tests in a wave flume and planar oscillatory flow experiments.

It can be seen in the figure that the transverse force on a rigid cylinder is strongest when the  $KC$  number is around 10.

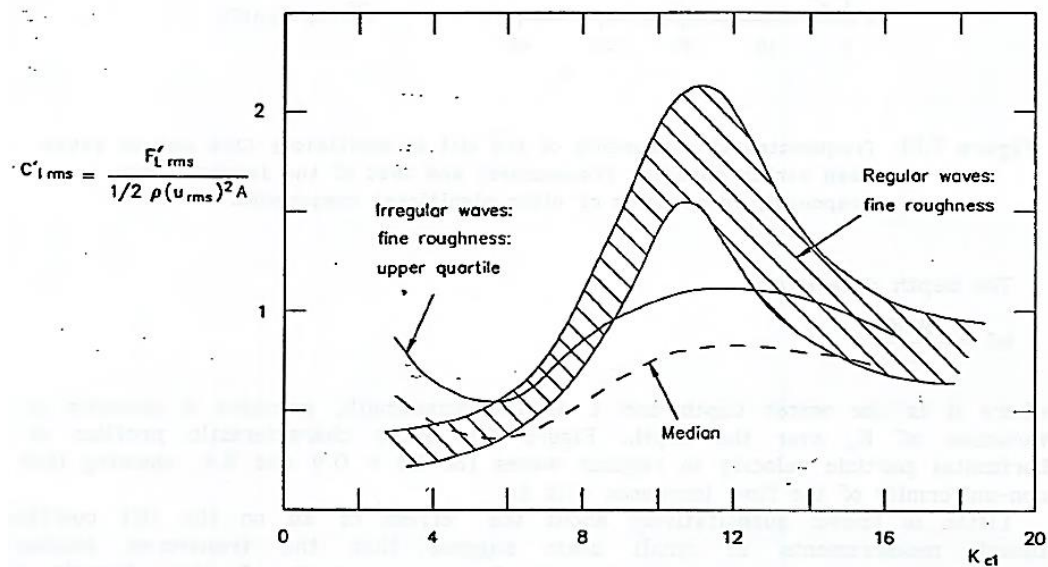


Figure A-39: Lift coefficient of a vertical cylinder in waves (Barltrop and Adams, 1991)

Figure A-40 presents the variation of the normalised horizontal particle velocity ( $U_w$ ) in waves with the elevation, represented by a depth parameter defined as  $kd = \frac{2\pi d}{L_w}$ , where  $d$  is the water depth and  $L_w$  is the wavelength. At values of  $kd$  less than 2 in waves, the vortex shedding is better correlated over the water depth, and the magnitude of transverse forces can be expected to follow that of a planar oscillatory flow (Barltrop and Adams, 1991).  $H$  and  $T$  in the figure represent wave height and wave period respectively.

Zedan *et al.* (1981) carried out an experimental investigation with a cantilever pile in regular waves under vortex-shedding lock-in conditions. It was observed that neither pile oscillations nor structural flexibility affected the shedding frequency and the fixed cylinder results shall be used to predict vortex-shedding in waves. The response energy was found to be concentrated in two frequency bands, twice the wave frequency and the pile natural frequency. An SDOF analysis of the response was carried out, and the variation with the reduced velocity ( $V_r$ ) and the frequency ratio ( $f^*$ ) were presented as in Figure A-41 and Figure A-42 respectively. The sharp peak at a frequency ratio of 0.99 in Figure A-42 indicates lock-in conditions. It was observed that for intermediate water depth ( $K_d = 1.63$ ) very fine tuning between pile natural frequency

and shedding frequency was required to achieve lock-in, while deeper water ( $K_d = 2.6$ ) required less tuning.

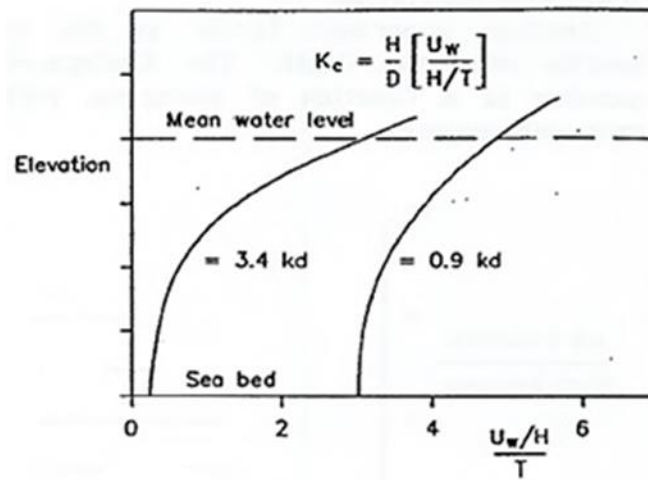


Figure A-40: Distribution of  $KC$  with depth in regular waves (Bartrop and Adams, 1991)

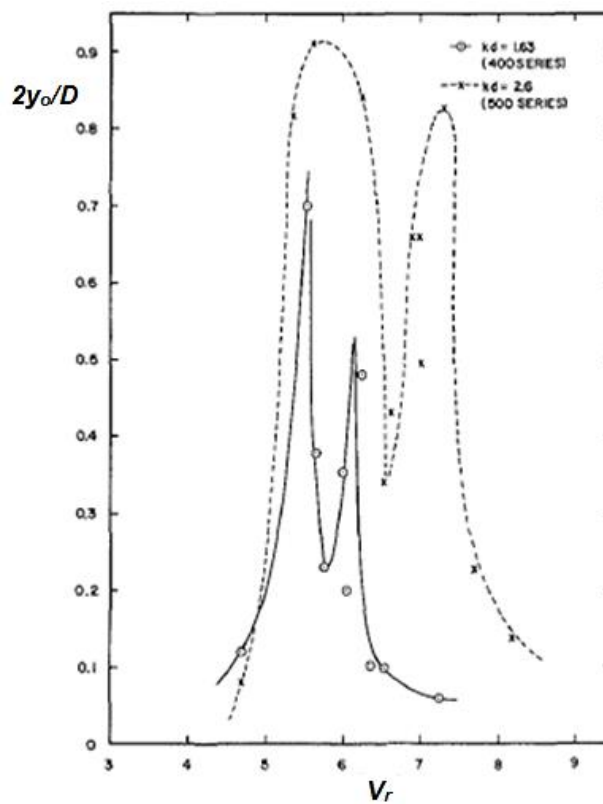


Figure A-41: Crossflow amplitude response a vertical pile in regular waves versus reduced velocity (Zedan *et al.*, 1981)

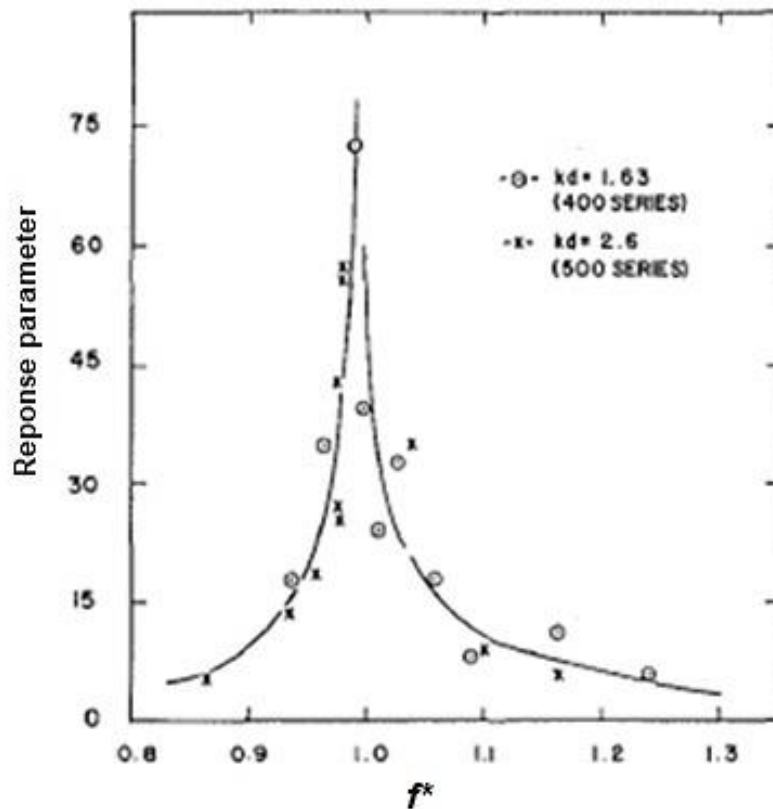


Figure A-42: Crossflow response parameter of a vertical pile in regular waves versus frequency ratio (Zedan *et al.*, 1981)

Zedan *et al.* (1981) found that the inline response energy was concentrated in two bands, around the wave frequency ( $f_w$ ) and the shedding frequency ( $2f_w$ ). It was further observed that at perfect lock-in, the inline response occurs at a frequency equal to the shedding frequency, and the inline response was found to be amplified substantially due to the transverse and inline oscillations. The authors also discussed the inadequacy of the Morison equation to represent the in-line force under vortex-shedding lock-in.

Angrilli and Cossalter (1982) conducted experiments with a vertical pile in regular waves and found that transverse resonant vibrations at natural frequency are induced by lift forces due to vortex shedding. The lock-in behaviour observed for a narrow wave frequency range of  $0.9 - 1.1 f_N$ , where  $f_N$  is the natural frequency. Barltrop and Adams (1991) present the increase in the drag coefficient ( $C_d$ ) with the amplitude of crossflow oscillation in regular waves, as illustrated in Figure A-43 based on the large scale experimental results from Bearman (1988).

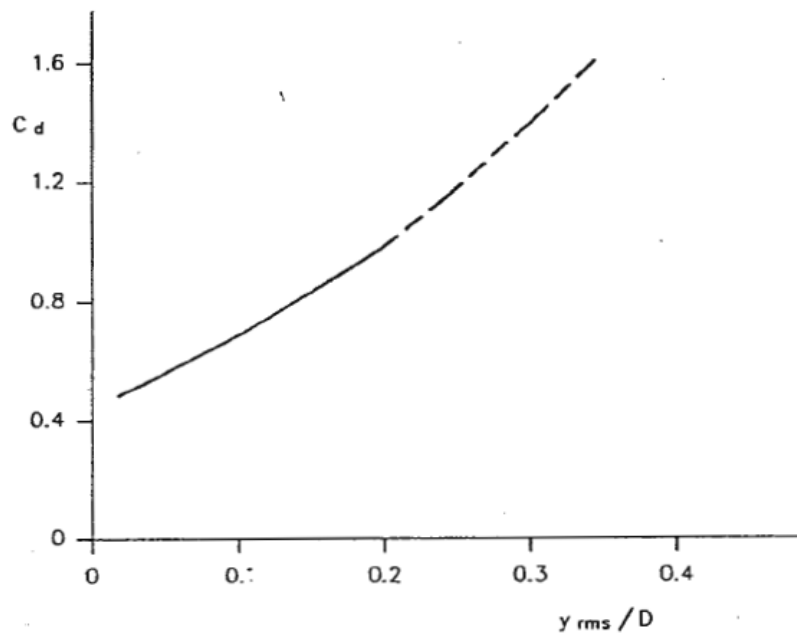


Figure A-43: Drag coefficient versus crossflow amplitude ratio in regular waves (Barltrop and Adams, 1991)

### A.5 VIV in sheared current

Vandiver *et al.* (1996) investigated VIV of a cable in a sheared current and have conceptually illustrated the phenomenon in Figure A-44. It is found that in the case of uniform flow, a single mode extracts power from the long length of the cable and a spectrum with a single peak results, as shown in (a). In the case of mild shear, several modes have significant available input power, but not a single mode is sufficiently strong to prevent the other modal responses, leading to a multi-peak response spectrum with low amplitudes, as shown in (b). In the strongly sheared flow, one of the modes (k) as depicted in (c), has much greater input power preventing the responses of the lesser excited modes and resulting in a single peak response.

Humphries and Walker (1988) found that for higher shear, the excitation frequency exists over a larger flow velocity range causing an extended vibration range but the excitation along the cylinder would be less leading to reduced peak values. Figure A-45 illustrates the effect of the linear shear profiles on the observed crossflow response. It was also observed that the VIV of the cylinder caused amplification of the mean hydrodynamic drag forces acting on the cylinder. Further, it was found that VIV occurs within the critical  $Re$  transition, and the sheared velocity profiles reduce the critical  $Re$  and drag amplification.

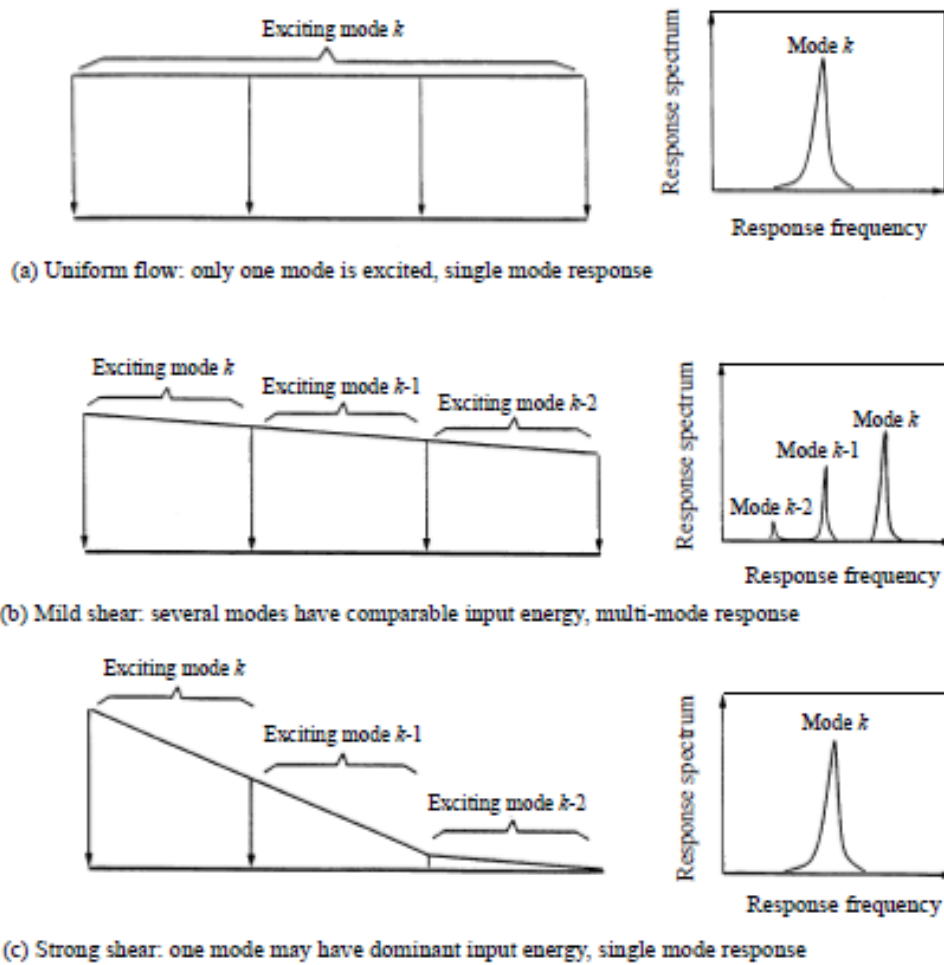


Figure A-44: Effect of shear on the crossflow response of a flexible cylinder (Vandiver *et al.*, 1996)

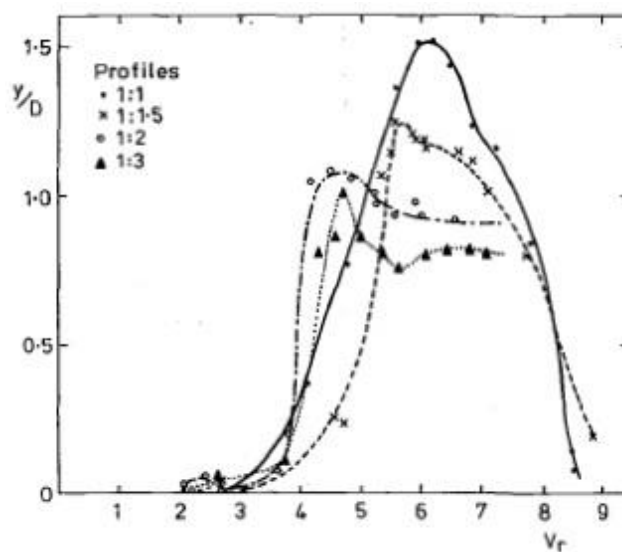


Figure A-45: Crossflow VIV in sheared current, amplitude ratio versus reduced velocity (Humphries and Walker, 1988)

## A.6 VIV Suppression

Zdravkovich (1981) presents an exhaustive review of various suppression devices, classifying them as surface protrusions, shrouds and near wake stabilisers. A recent in-depth review by Rashidi *et al.* (2016) on vortex suppression and wake control broadly classifies them as active and passive means with nine sub-classifications. Of all the passive devices, helical strakes are the most widely used vortex suppression device, but the mean drag is increased considerably. However, the omnidirectionality, effectivity under periodic flows, ease of pre-installation and minimum maintenance still make it the preferred solution in most cases. Even though streamlined fairings are found to suppress VIV and reduce the mean drag considerably, unidirectionality, discreteness, difficulty in installation and maintenance, ineffectiveness during flow reversal and cumbersome nature act as a deterrent for extensive applications. Concepts like splitter plates, axial slats, etc have also been successfully deployed.

Figure A-46 illustrates the effect of various passive vortex suppression devices on the mean drag of a smooth cylinder. It can be observed that the helical strakes cause the largest increase of the mean drag while guiding vanes or fairings enable the largest drag reduction. Streamlined fairings work on the principle of delayed boundary layer separation, preventing shear layer interaction and considerably reducing the pressure fluctuations around the body. Grant and Patterson (1977) presented the design of a weathervaning fairing for a drilling riser with an aspect ratio of around 2.1. The wind tunnel model test results and field measurements demonstrated that the fairing reduced fluid drag and eliminated VIV in currents upto 6 knots.

Assi *et al.* (2011; 2014) carried out physical experiments on stability of a short tail fairing fitted on a rigid cylinder and found that the rotation friction between the two should be above a lower threshold for efficient vortex suppression and should not be above an upper threshold to avoid severe galloping. It was observed that the fairings found a stable off flow position and developed a steady lift force towards the deflected side. Khorasanchi and Huang (2014) developed an analytical model to predict the instability onset of a fairing fitted on a rigid riser. The authors highlighted the significance of hydrodynamic damping in providing stability and distinguished fishtailing from instability. Lou *et al.* (2017) conducted experiments with stationary fairings and found that the caudal horn angle shall be less than  $60^\circ$  for efficient VIV

reduction. It was found that though the fairing provided significant drag reduction, it increased the drag force on the downstream cylinder.

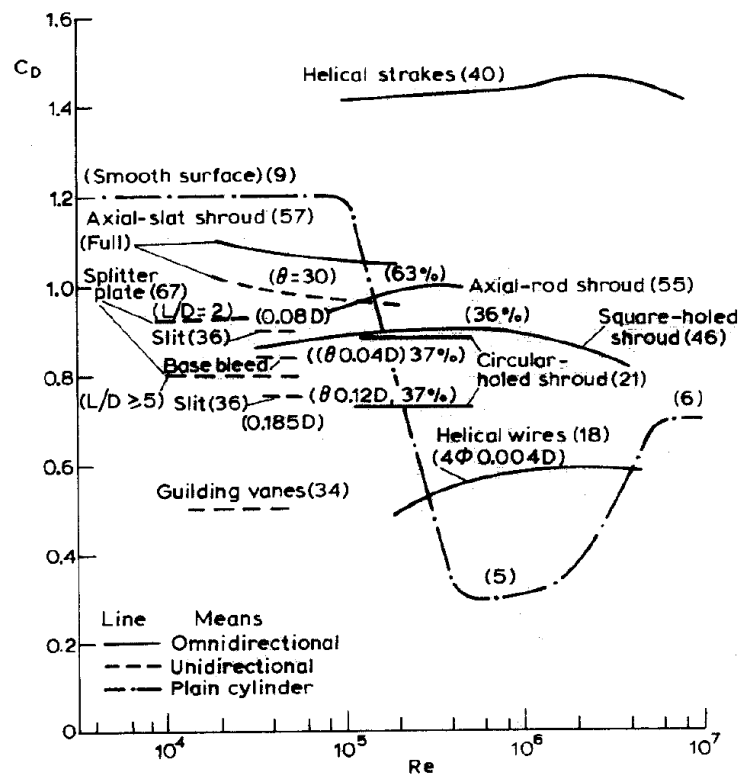


Figure A-46: Drag coefficient of vortex suppression devices (Zdravkovich, 1981)

Branković and Bearman (2006) carried out experiments on a circular cylinder, with and without helical strakes in subcritical flow regime with very low mass ratio and damping and observed that the amplitude of the straked cylinder response reduced by 60% and the response range became narrower. Further, the straked cylinder had a phase close to zero over the entire reduced velocity range. Slocum *et al.* (2004) conducted experiments with fairings, which were neutrally buoyant with a mass ratio of approximately 1. Over the lock-in range the fairings were found to be highly effective in eliminating VIV and reducing drag compared to the bare pipe. However, It was observed that at higher reduced velocities above 8, significant transverse oscillations developed with an accompanying angular oscillation of the fairing, similar to galloping showing an increasing trend with increasing speed. It was also established mathematically that the unstable motion occurs once the flow speed exceeds a critical flutter speed. Roshko (1961) conducted experiments on cylinder fitted with splitter plates and observed the main effects as the suppression of the shedding and an

insignificant decrease in mean drag. It was found that the splitter plate at transcritical  $Re$  was vulnerable to fluttering.

## **A.7 Structural Dynamics**

### **A.7.1 Conservation of Energy**

The effective mass, stiffness and consequently, the natural frequency of an SDOF or a mode in a multi-degree-of-freedom (MDOF) system can be found by using conservation of energy (Barltrop and Adams, 1991). The effective excitation, mass and stiffnesses of a particular mode can be found from work done, kinetic energy and potential energy respectively. The modal response under VIV can subsequently be evaluated using an appropriate harmonic model.

### **A.7.2 SDOF Approximation**

The forced vibration of an MDOF system is represented by a set of coupled differential equations. However, these equations uncouple in a principal axis system and can be solved independently. The transformation to the principal axes is equivalent to describing the deflection of a structure as the summation of individual modal deflections. Each modal deflection is solved as an independent SDOF system, and the MDOF response is found by superposition; the results are then transformed back to the Cartesian coordinates. This is a standard method adopted for both frequency domain and time domain analyses and is also applicable to a lightly damped system with negligible coupling effects. The method is outlined schematically in Figure A-47 (Barltrop and Adams, 1991).

The method is applicable for both discrete and continuous MDOF systems. For continuous or distributed system, the mode shapes and natural frequencies can be calculated analytically, and the transformation of the equations to the principal coordinates can be performed by integration. The method is described for the discrete and continuous systems and compared in Figure A-48 (Barltrop and Adams, 1991). It can be observed that the equations for the distributed system's modal mass and stiffness are derived by using the conservation of energy.

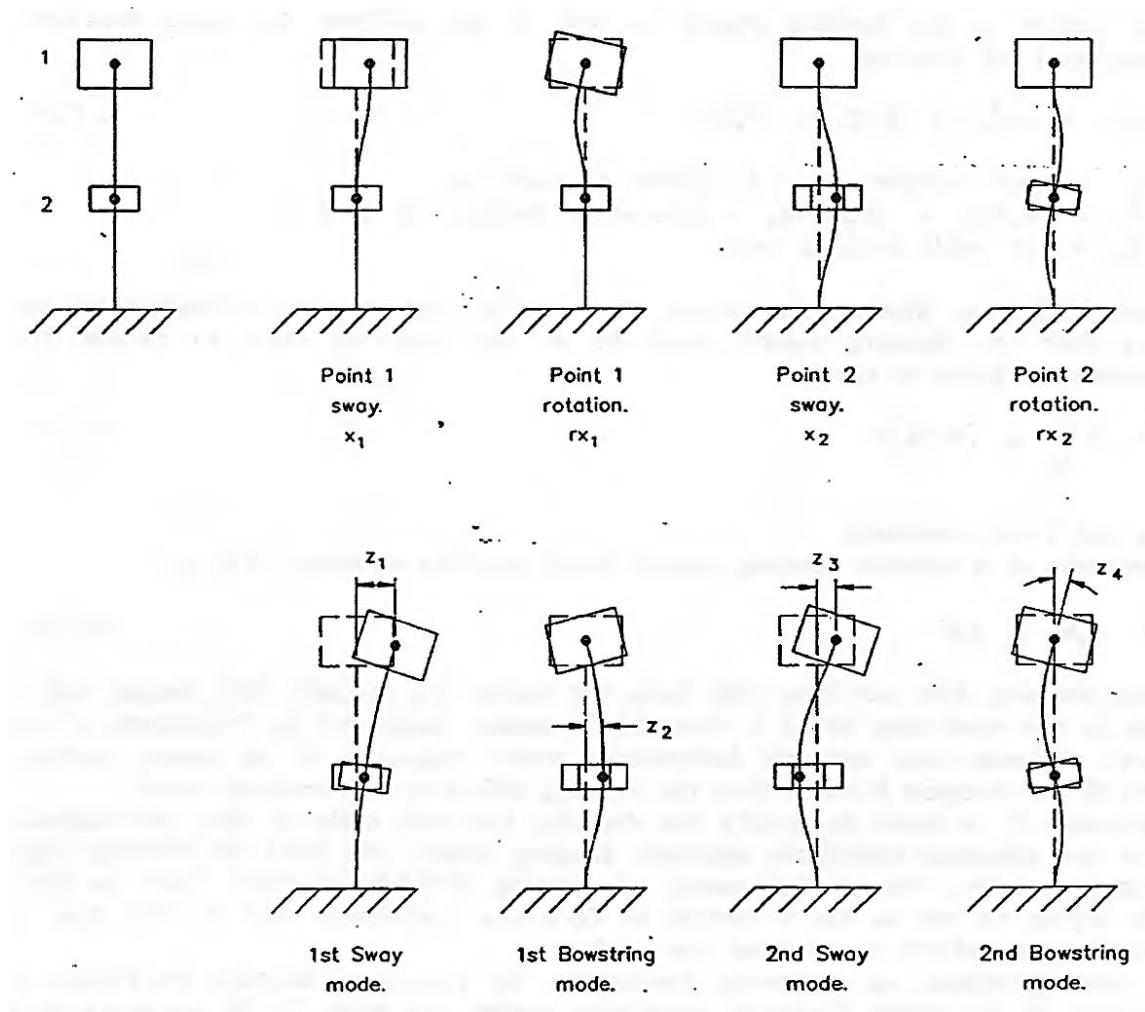


Figure A-47: SDOF approximation of an MDOF system (Barltrop and Adams, 1991)

## A.8 CFD Investigations on Flow around Circular Cylinders

Menter (1996) compared various eddy viscosity turbulence models and observed that though the SST model and the standard  $k-\varepsilon$  model yield identical results for free shear layers, the  $k-\varepsilon$  model under predicts the spreading rate of the far wake. Figure A-49 extracted from his work compares the turbulent shear stresses profiles of various turbulence models. It was found that Renormalisation-group (RNG)  $k-\varepsilon$  model did not significantly improve the predictions for the adverse pressure gradient flows, compared to the standard  $k-\varepsilon$  model. Spalart–Allmaras (SA) model gave significantly better results than  $k-\varepsilon$  model but somewhat underpredicted separation. It was concluded that the SST model gave the best results for the adverse pressure gradient cases, due to its calibration for these flows.

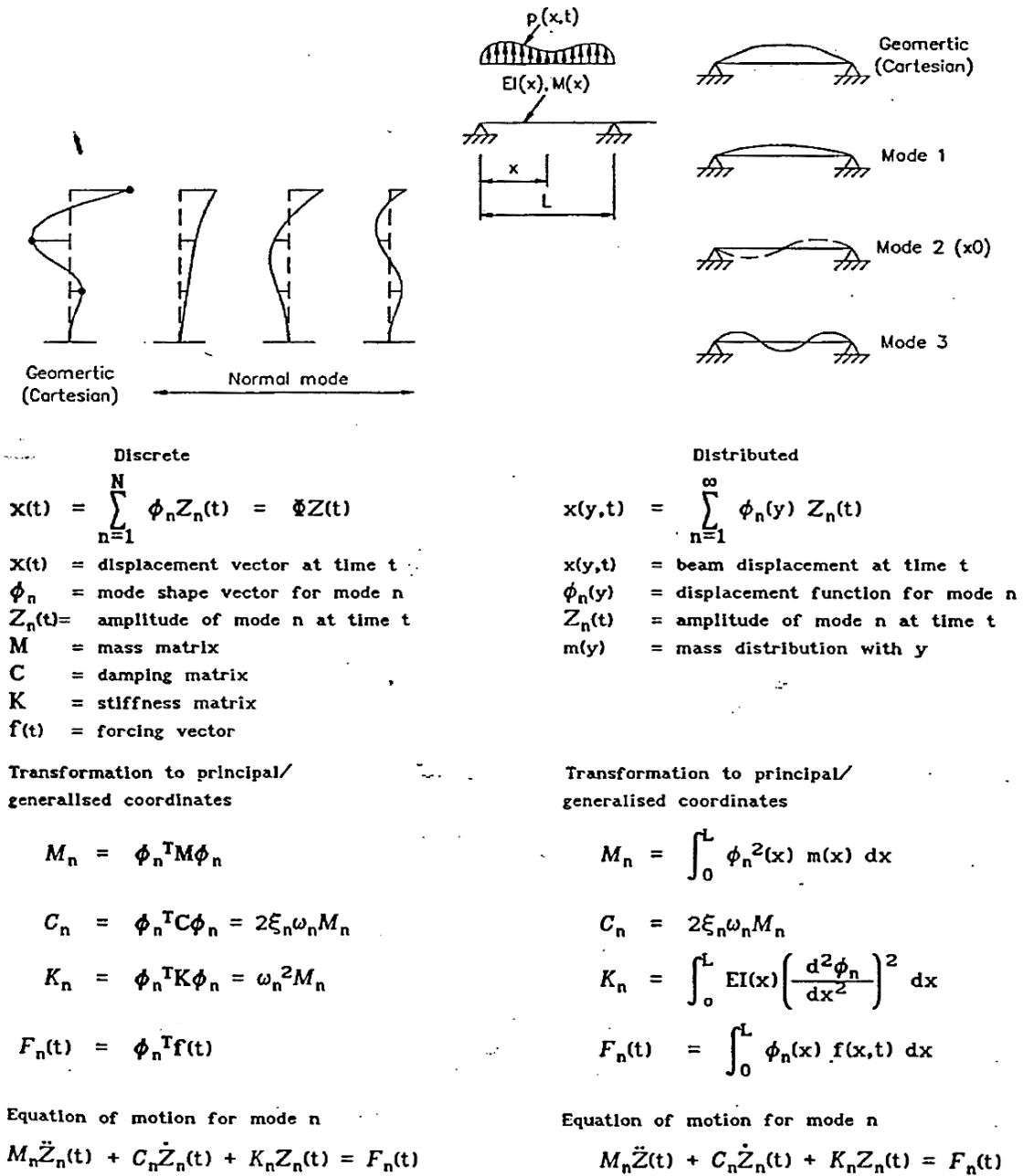


Figure A-48: Displacement of discrete and distributed MDOF systems and effective mass, damping, stiffness and excitation of an SDOF (Bartrop and Adams, 1991)

Travin *et al.* (2000) performed DES for the flow past the circular cylinder with laminar separation at  $Re$  of  $5 \times 10^4$  and  $1.4 \times 10^5$ , and with turbulent separation at  $Re$  of  $1.4 \times 10^5$  and  $3 \times 10^6$ . The results were also compared with the experimental and RANS results, and it was observed that URANS is less accurate than DES for laminar separation, but the results are very near for the turbulent separation. Tutar and Holdø (2001) performed numerical simulations for flow around circular cylinders in transitional regime by using URANS and LES. The RANS models employed were standard, RNG

and anisotropic  $k - \epsilon$  models and LES was based on standard sub-grid scale (SGS) model with near wall approach. The inlet, side wall and outlet were at  $7D$ ,  $7D$  and  $15D$  respectively from the cylinder. It was found that the enhanced  $k - \epsilon$  models have better capability than the standard model to predict vortex shedding, though they still have limitation in predicting time dependent phenomena. LES was found to exhibit better results in the transitional flow regimes.

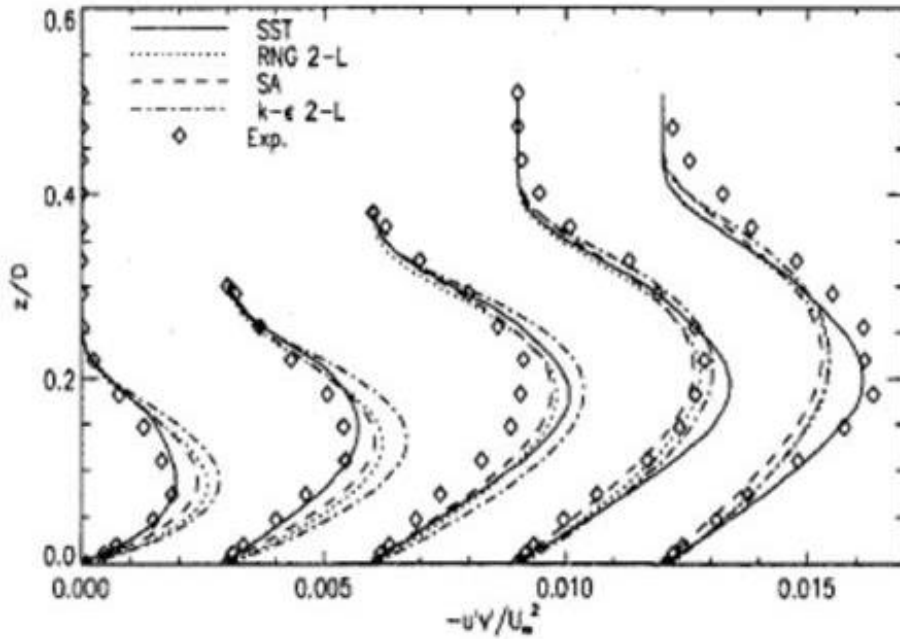


Figure A-49: Turbulent shear stress profiles of various turbulence models (Menter, 1996)

Catalano *et al.* (2003) used a flow domain with C-mesh around the circular cylinder for LES and RANS simulations. The computational domain extended  $22D$ ,  $17D$  and  $24D$  upstream, downstream and far field respectively from the cylinder and the spanwise domain size was  $2D$ , over which the flow was assumed periodic. In the streamwise direction, 144 grid points were provided on the cylinder surface. LES was carried out for the critical and supercritical regime with a simple wall stress model providing the approximate wall boundary conditions. LES was performed at  $Re\ 5 \times 10^5$  and  $2 \times 10^6$  and the mean drag coefficients showed remarkable agreement with the drag curve of Achenbach. However, it was found that LES could not capture the  $Re$  dependence at increased  $Re$ . The results of the LES simulations were compared with that of URANS solutions carried out using the standard  $k - \epsilon$  model with wall functions and published

experimental data. The contours of the vorticity magnitude, as computed by LES and URANS for a  $Re$  of  $10^6$  are illustrated in Figure A-50.

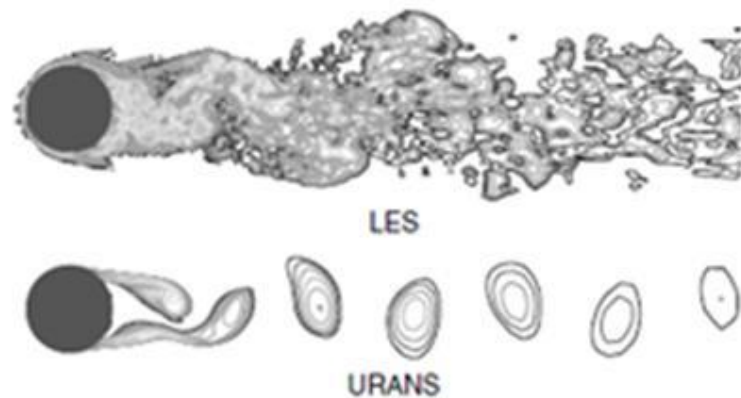


Figure A-50: Comparison of the vortex contours of LES and RANS at  $Re$   $1 \times 10^6$  (Catalano *et al.*, 2003)

It can be observed in Figure A-50 that the LES can capture much more coherent structures in the wake. It was observed that LES predicts the delayed boundary layer separation and a narrower wake, resulting in a smaller drag coefficient and a higher  $St$  where RANS shows a thicker wake, resulting in a higher drag coefficient and a lower  $St$ . It was found that LES lift and drag time histories are able to capture the randomness in the flow. It was concluded that LES is considerably more accurate than the RANS since it captures the delayed boundary layer separation and drag crisis.

Benim *et al.* (2007) numerically investigated the flow past a circular cylinder in critical regime by using RANS turbulence models in Fluent. SST and  $k - \epsilon$  turbulence models were used along with the resolution of the wall boundary layer. A  $y^+ < 1$ , 400 half-cylinder streamwise divisions, aspect ratio of 5 and expansion ratio of 1.02 - 1.05 were maintained for the near wall mesh.  $y^+$  is the nondimensional distance to the wall, where  $y^+ = \frac{u_\tau y}{\nu}$ ,  $u_\tau$  is the friction velocity,  $y$  is the distance to the wall and  $\nu$  is the kinematic viscosity of the fluid. Computations were also performed by using the wall function approach. It was found that the  $k - \epsilon$  model performs poorly in the laminar and transition regimes while SST model performs well at low  $Re$  and predicts sharp transition to turbulence. Further, it was observed that wall functions failed to achieve mesh independence, exhibiting continuous variation with the  $y^+$ . The domain size study revealed that the optimum inlet, side wall and outlet location from the cylinder is  $6D$ ,

6D and 12D respectively. The drag coefficient was compared with the experimental results, and it was found that wall functions ignored the transition completely while SST model could qualitatively predict drag crisis, though the values were underestimated. Figure A-51 illustrates the drag crisis captured by the SST turbulence model.

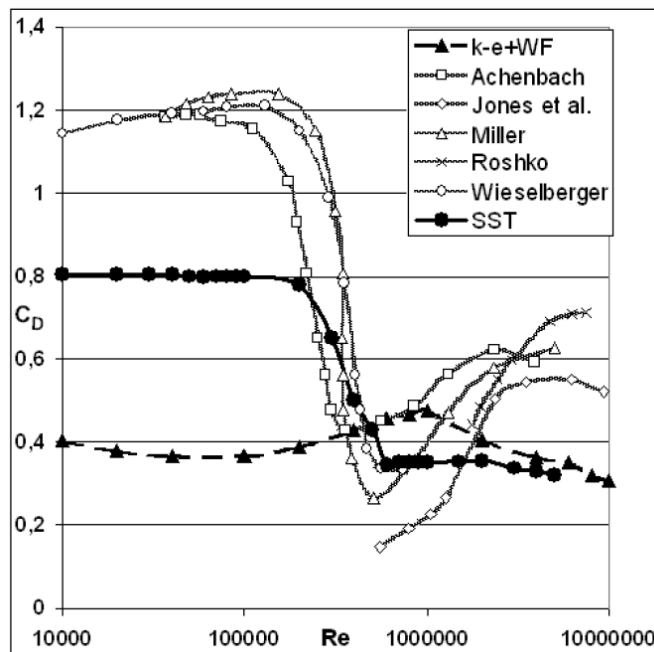


Figure A-51:  $C_D$  versus  $Re$ , RANS predictions and measurements

Revell *et al.* (2008) investigated the flow around a circular cylinder by using 2D and 3D URANS and DES, coupled with standard SST model. The results were also compared with that of the newly developed SST-Cas model, sensitive to the lag between turbulent stress and mean strain rate. It was found that the RANS simulations could not capture the coherent structures in the wake except very close to the cylinder while DES SST and SST-Cas could. It was concluded that SST-Cas improved the predictions compared to the standard SST model though the results are far from DES SST. Ong *et al.* (2009) numerically investigated high  $Re$  flows covering the supercritical to upper transition regimes around a smooth circular cylinder using 2D URANS equations with a standard  $k - \epsilon$  turbulence model. The inlet, outlet and side walls were at 7D, 20D and 7D respectively from the cylinder. It was found that the inlet and outlet distances are sufficient to eliminate the far field effects on the flow. The drag lift and  $St$  obtained were compared with published data, and it was concluded that URANS with the standard high  $Re$   $k - \epsilon$  model gives satisfactory results in the supercritical and the upper transition flow regimes.

Chen *et al.* (2009) used unstructured meshes to simulate the 3D flow around a cylinder by means of LES at a  $Re$  of 14000. The inlet, outlet and side walls were at  $4D$ ,  $20D$  and  $4D$  respectively from the cylinder and the depth of the domain considered was  $10D$ . It was observed that the vortex showed twisted phenomena, suggesting 3D nature of that the flow. The computational mesh used is illustrated in Figure A-52. On comparison with the published results of numerical simulations and experiments, it was concluded that LES results are of very high accuracy.

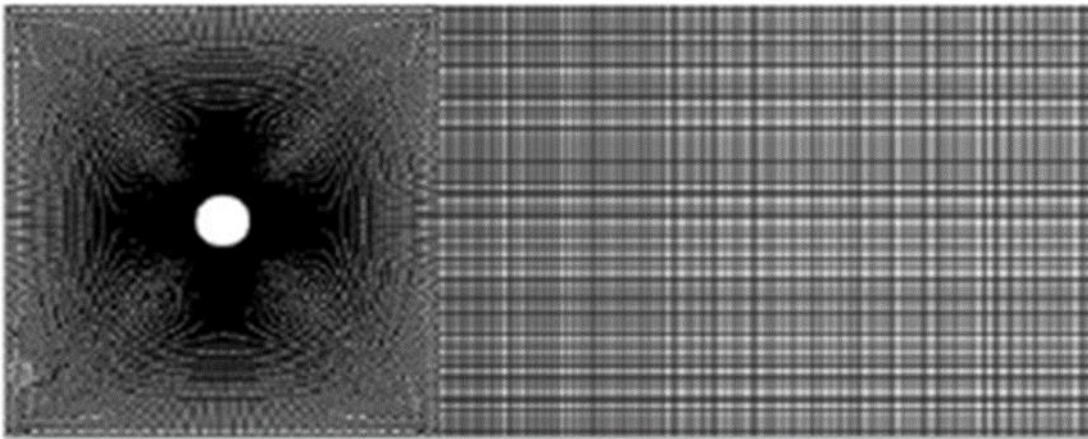


Figure A-52: Computational mesh for LES (Chen *et al.*, 2009)

Ming *et al.* (2010) investigated 3D separated turbulent flow around a circular cylinder by using DES and URANS, coupled with SA turbulence model. It was found that the hybrid DES is very suitable for the separated flows, with RANS turbulence model near the wall and LES in the separated flow. It was found that the secondary vortices are captured by DES compared to RANS and hence is a more suitable model for complex separated turbulent flows. Ai *et al.* (2013) investigated the flow around a circular cylinder by using the 2D URANS equations with a  $k-\epsilon$  turbulence model in the supercritical and upper transition flow regimes. The inlet, outlet and side walls were at  $15D$ ,  $30D$  and  $15D$  respectively from the cylinder. Second order discretisation method for convection and second order upwind scheme for the viscous terms were utilised. The commercial software Fluent was used for the simulations and the lift coefficient around obtained was around  $0.40 - 0.50$ . Though the authors claimed that the reduction in drag coefficient with  $Re$  was due to drag crisis, certain inconsistencies are observed in their results.

Wissink and Rodi (2008) performed 3D DNS of flow past a circular cylinder at a  $Re$  of 3900 and compared the results with that of published experiments. The results were found to be in good agreement with the experimental results. Further, DNS produced excellent contours of vortex street, capturing almost all the coherent structures in the wake. Rodríguez *et al.* (2013) performed LES on a supercomputer for the critical  $Re$  regime of a circular cylinder. Unstructured grid with up to 70 million control volumes was employed for the simulations. Not only the variation of the drag coefficient exhibited fair agreement with the published experimental data but also the simulations predicted mean lift at a  $Re$  of  $2.5 \times 10^5$ , consistent with the experimental observation. Zhu and Chen (2013) performed 3D LES for the flow around a circular cylinder at a  $Re$  of  $4.1 \times 10^4$  and found that the mean drag coefficient, lift coefficient and the  $St$  are in good agreement with the published results. It was demonstrated that the wake flow behind the cylinder is fully 3D.

Stringer *et al.* (2014) compared the performance of OpenFOAM and ANSYS CFX for a range of  $Re$  covering laminar to supercritical regimes. The inlet, outlet and side walls were at 20D, 40D and 20D respectively from the cylinder. Figure A-53 shows the near wall meshing adopted for the simulations; a  $y^+$  of the order 1 is maintained with a minimum of 5 cells in the boundary layer. The meshing scheme consisted of a body fitted hexahedral region with an expansion ratio of 1.1 with a total of 30 layers surrounding the cylinder with the unstructured wedges filling the remaining far field domain. The aspect ratio of the wall layer is kept below 20:1 for most cases. The softwares employ finite volume method to solve the Navier–Stokes equations.

The methodology incorporated the SST turbulence model, a fully resolved boundary layer, dense conformal grid, cell aspect ratio control and adaptive time stepping. It was found that the lack of symmetry of the unstructured grids aids the development of vortex shedding. It was concluded that OpenFOAM displays high correlation with experimental data at low to sub-critical values, whereas ANSYS CFX is more effective in high sub-critical and critical regions. At  $Re 10^5$ , OpenFOAM is seen to generate zero lift and at  $Re 10^6$  recovers to closely match Norberg's result. In the subcritical region, CFX highly overpredicts the lift at  $Re 10^3 - 10^4$  while showing recovery at high  $Re$ .

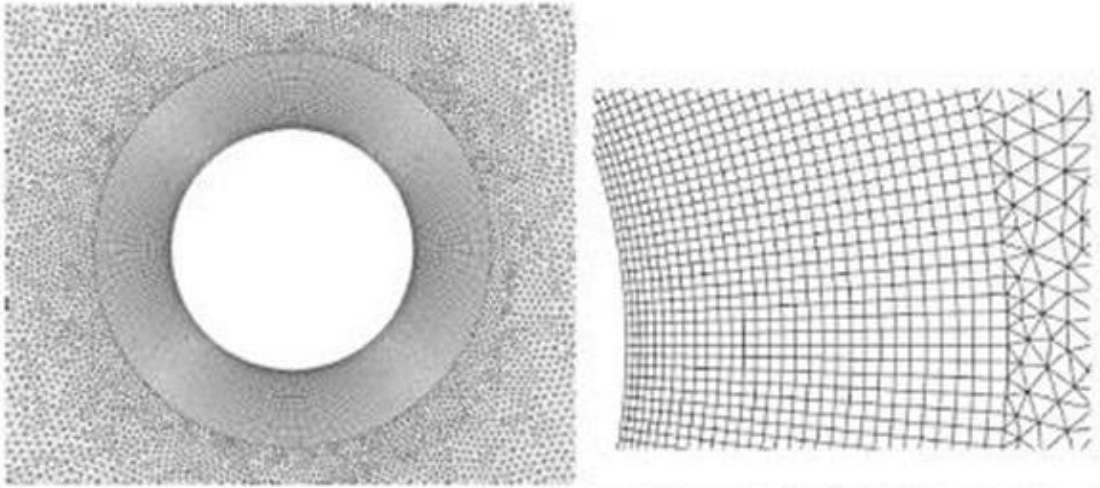


Figure A-53: Near wall and boundary layer meshing (Stringer *et al.*, 2014)

## A.9 Physical Experiments with Scaled Models

### A.9.1 *Laws of Similitude*

Chakrabarti (2005) presents the scaling laws for the FSI problems in Table A-2. As the simultaneous satisfaction of  $Fr$  and  $Re$  is extremely difficult, Froude law is the accepted method of model scaling in hydrodynamics (Chakrabarti, 2005).

Table A-2: Scaling laws in offshore engineering (Chakrabarti, 2005)

Symbol	Dimensionless number	Force ratio	Definition
$Fr$	Froude Number	Inertia/Gravity	$u^2/gD$
$Re$	Reynolds Number	Inertia/Viscous	$uD/\nu$
$Eu$	Euler Number	Inertia/Pressure	$p/\rho u^2$
$Ch$	Cauchy Number	Inertia/Elastic	$\rho u^2/E$
$KC$	Keulegan–Carpenter Number	Drag/Inertia	$uT/D$
$St$	Strouhal Number	Eddy/Inertia	$f_e D/u$

Table A-3 shows the scale factor of the common variables that the Froude model satisfies. The elasticity of the structural members should be scaled with a suitable material like plasticised PVC, based on Cauchy similarity along with the Froude similarity (Chakrabarti, 2005). Scaling parameters for the important structural variables

are presented in Table A-4 as the ratio of full scale to model values in terms of the scale factor.

Table A-3: Froude scaling of model parameters (Chakrabarti, 2005)

Variable	Symbol	Scale factor
All linear dimensions	$D$	$\lambda$
Fluid or structure velocity	$u$	$\lambda^{1/2}$
Fluid or structure acceleration	$\dot{u}$	1
Time or period	$t$	$\lambda^{1/2}$
Structure mass	$m$	$\lambda^3$
Structure moment of inertia	$I$	$\lambda^5$
Section moment of inertia	$I$	$\lambda^4$
Structure displacement volume	$V$	$\lambda^3$
Structure restoring moment	$C$	$\lambda^4$
Force	$F$	$\lambda^3$
Moment	$M$	$\lambda^4$
Stress	$\sigma$	$\lambda$
Spring constant	$K$	$\lambda^2$
Wave period	$T$	$\lambda^{1/2}$
Wave length	$L$	$\lambda$
Pressure	$p$	$\lambda$
Gravity	$g$	1
Fluid density	$\rho$	1
Fluid kinematic viscosity	$\nu$	1
Reynolds number	$Re$	$\lambda^{3/2}$
Keulegan–Carpenter number	$KC$	1

Table A-4: Scaling of stiffness parameters for combined Froude-Cauchy similarity (Chakrabarti, 2005)

Item	Formula	Prototype/Model
Bending moment	$M_{yp} = \lambda^5 M_{ym}$	$\lambda^5$
Bending stiffness	$(EI)_p = \lambda^5 (EI)_m$	$\lambda^5$
Axial stiffness	$(EA)_p = \lambda^3 (EA)_m$	$\lambda^3$
Section modulus	$I_p = \lambda^4 I_m$	$\lambda^4$
Young's modulus	$E_p = \lambda E_m$	$\lambda$
Stress	$\sigma_p = \lambda \sigma_m$	$\lambda$
Torsional rigidity	$(GI)_p = \lambda^5 (GI)_m$	$\lambda^5$
Torsional modulus	$G_p = \lambda G_m$	$\lambda$

### A.9.2 **Model Scale Selection**

Chakrabarti (2005) explains that the choice of model scale is often limited by the experimental facilities. A very small scale can result in scale effects, while a very large model can be cumbersome and expensive. It is advised to adopt a large scale when viscous effects are important to minimise the scale effects. Further, for circular cylindrical structures, the overall transverse dimension shall not exceed  $1/5^{\text{th}}$  the width of the tank.

### A.9.3 **Model Scale Effect**

Chakrabarti (2005) describes the methods to account for the scale effects for a Froude model; maximise scale of the model to simulate the prototype effect closer, correct Reynolds effect when scaling up of data to full scale, trip the incoming flow by roughing the model surface in the forward area or induce turbulence by external means placed upstream of the model, like a mesh barrier. Further, measured forces should be corrected if fresh water is used to represent the seawater and mass similitude may be achieved by impregnation of powdered lead.

### A.9.4 **Data Acquisition and Instrumentation**

The standard instruments that are required during a typical fixed or floating structure test and their applications are listed in Table A-5. Each instrument should be checked for waterproofing and calibration before setting up the test in the tank. Regular checks of the instrumentation should be performed during testing to ensure reliability. Instruments should be electrically connected to an automatic data acquisition system (DAS), using an A/D (analogue to digital converter) system to convert the analogue signal from the instruments to digital form. All data are to be collected in the time domain using a suitable high pass filter that removes the high-frequency electrical noise inherently present in the system (Chakrabarti, 2005).

Table A-5: Typical instrumentation for offshore model testing (Chakrabarti, 2005)

Instrument	Application	Accuracy	Comments
Wave probes	Measures incident and phase waves	1/16 in.	Mounted from the air above the water surface
Air gap probes	Measures air gap between the free surface and the deck of the model	1/16 in.	Splashing of water introduces inaccuracy in measurement
Non-contact optical tracking system	Six degrees of freedom (DOF) motion of floating structures	1/8 in. and 1/2 deg. after application of software	Cameras are mounted on the side wall or the carriage
Motion sensing transducer (MST)	Light specially built mechanical system having linear and angular potentiometers to measure six DOF	1/8 in. linear and 1/2 deg. angular	Inertia and damping effect of the mechanical system on the structure should be known
Load cells	Measures loads between the model parts where attached, e.g. towing loads, and wave loads on member	0.1 lb or less depending on load range; 5% cross talk	Attaches between model and fixtures or two members of a model
Ring gauges	Measures line tensions of the mooring lines at the fairlead	0.1 lb	Mounts on model at the mooring line fairlead
Strain gauges	Measures the stresses on the mounting point on the model	0.01 $\mu$	May be mounted directly on elastic members
Accelerometers	Measures (XYZ) accelerations at the point of attachment, e.g. CG of the model	0.01g	Mounted on the model where acceleration/displacement is desired
Towing speed indicator	Records towing speed of the towing carriage	0.1 ft/s	Part of the towing carriage
Towing dynamometer	Two component (XY) load cell capable of measuring the towing load on the structure	0.1 lb	A hinge provided between the staff and dynamometer to allow freedom in pitch